UNIVERSIDAD DE EXTREMADURA

TESIS DOCTORAL

APLICACIONES DE LA TELEDETECCIÓN EN LA MODELIZACIÓN HIDROLÓGICA

Laura Fragoso Campón

Programa de Doctorado en Desarrollo Territorial Sostenible

La conformidad de los Directores de la tesis consta en el original en papel de esta Tesis Doctoral

2021

JUNTA DE EXTREMADURA
Consejería de Economía, Ciencia y Agenda Digital

Unión Europea

La presente investigación se ha realizado gracias a la financiación de la **Consejería de Economía, Ciencia y Agenda Digital de la Junta de Extremadura**, antigua Consejería de Economía e Infraestructuras, que ha financiado el contrato predoctoral PD16018, mediante **Fondo Social Europeo: Una manera de hacer Europa**, a través de la **Ayuda para la Financiación de Contratos Predoctorales para la Formación de Doctores en los Centros Públicos de I+D pertenecientes al Sistema Extremeño de Ciencia, Tecnología e Innovación (Expediente PD16018).**

Fondo Social Europeo *Una manera de hacer Europa*.

JUNTA DE EXTREMADURA
Consejería de Economía, Ciencia y Agenda Digital

Unión Europea

La edición de las publicaciones científicas en inglés, la difusión de los trabajos en congresos científicos nacionales e internacionales, así como la edición e impresión de la Tesis, han sido posible gracias a la financiación concedida por el **Fondo Europeo de Desarrollo Regional (FEDER)** y la **Consejería de Economía, Ciencia y Agenda Digital de la Junta de Extremadura** a través de la ayuda con referencia GR18052.

Fondo Europeo de Desarrollo Regional *Una manera de hacer Europa*.

A Jimena y a Ramón

Y, a todos los que me han acompañado en este viaje

JUNTA DE EXTREMADURA

Consejería de Economía, Ciencia y Agenda Digital

Unión Europea

UNIVERSIDAD DE EXTREMADURA

TESIS DOCTORAL

APLICACIONES DE LA TELEDETECCIÓN EN LA MODELIZACIÓN HIDROLÓGICA

Laura Fragoso Campón

Programa de Doctorado en Desarrollo Territorial Sostenible

2021

Fondo Social Europeo

Una manera de hacer Europa

La Tesis Doctoral se presenta como compendio de publicaciones siguiendo los criterios establecidos en el "Artículo 46. Tesis doctorales presentadas como compendio de publicaciones" de la normativa de doctorado según la RESOLUCIÓN de 18 de febrero de 2014, del Gerente, por la que se ejecuta el acuerdo adoptado por el Consejo de Gobierno por el que se aprueba la modificación de la normativa de los estudios de Doctorado.

Los requisitos exigidos por el Artículo 46 son los siguientes:

1. La Comisión Académica del Programa podrá autorizar el depósito de tesis doctorales como compendio de publicaciones, siempre que se reúnan los siguientes requisitos:

a. Una introducción general, en la que se presenten temáticamente las publicaciones y se justifique la coherencia e importancia unitaria de la Tesis.

b. Un resumen global estructurado de los resultados y de la discusión de los mismos, así como las conclusiones finales.

c. Una copia completa de los trabajos publicados, haciendo constar claramente el nombre y la filiación de todos los coautores de los trabajos y la referencia completa de la revista en que se han publicado o aceptado para su publicación. En este último caso deberá aportar la documentación justificativa de la aceptación, así como la referencia completa de la revista a la que se han enviado el trabajo para su publicación. En caso de que se presente algún trabajo realizado en coautoría, hay que incluir también el informe a que hace referencia el apartado 2 de este artículo

d. En caso de que alguno de los trabajos presentados se haya publicado en una lengua distinta de las especificadas en el Programa de Doctorado, debe adjuntar un resumen del trabajo en cuestión redactado en alguna de las lenguas del Programa.

e. De estas aportaciones al menos dos tendrán que estar publicadas en revistas indexadas en el ISI-JCR o tratarse de alguna contribución relevante en su campo científico según los criterios de la Comisión Nacional Evaluadora de la Actividad Investigadora (CNEAI).

f. Cualquier otro requisito que pueda establecer la Comisión Académica del Programa de Doctorado con el visto bueno de la Comisión de Doctorado.

2. Como procedimiento general, se adjuntará obligatoriamente un informe del director de la tesis doctoral sobre el factor de impacto o la categorización de las publicaciones incluidas en la tesis doctoral y sobre los trabajos realizados en coautoría, especificando exhaustivamente cual ha sido la participación del doctorando en cada artículo y, si procede, la utilización, implícita o explícita, por parte de los coautores de los trabajos presentados para la elaboración de una tesis doctoral."

Por tanto, cumpliendo con los requisitos expuestos anteriormente, el contenido de la Tesis Doctoral se estructura de la siguiente manera:

- CAPÍTULO 1 – Introducción General
- CAPÍTULO 2 – Resumen global estructurado de los resultados, discusión y conclusiones
- CAPÍTULO 3 – Trabajos publicados

Contenido

Resumen

Disponer de una estimación adecuada de los procesos hidrológicos en una cuenca es fundamental ya que, de ellos dependen la correcta gestión de los recursos hídricos. La eficiencia en la modelización hidrológica depende en gran medida de la disponibilidad de datos de entrada al modelo y, de las incertidumbres de los valores de los parámetros que intervienen. Además, la incertidumbre es aún mayor en las cuencas no aforadas, donde la calibración de los parámetros del modelo no es factible, convirtiéndose así en un reto hidrológico. En esta Tesis Doctoral se aplica la teledetección como apoyo en la modelización hidrológica con el propósito de disminuir la incertidumbre asociada a la estimación de parámetros hidrológicos desde dos enfoques: en primer lugar, con miras a la generación de cartografía *ad hoc* para modelización hidrológica y, en segundo lugar, con el objeto de la regionalización de parámetros hidrológicos en cuencas no aforadas.

Muchos de los datos de entrada requeridos en la modelización hidrológica son datos derivados de la teledetección y, de entre los factores que intervienen en la respuesta hidrológica, la caracterización de los tipos del suelo y la tipología de vegetación tienen una gran influencia en el balance hídrico. Por tanto, se plantea en esta tesis generar la cartografía *ad hoc* mediante la clasificación supervisada de la fusión de datos de los satélites Sentinel 1 y Sentinel 2 del Programa Copernicus de la Comisión Europea. En primer lugar se aborda una metodología para definir las áreas de entrenamiento a partir de la clasificación supervisada de imágenes de ultra alta resolución espacial del PNOA y considerando los datos derivados del LiDAR-PNOA como apoyo. De esta forma, se minimiza el trabajo manual asociado a la fotointerpretación y a las campañas de campo. Los mapas obtenidos representan la cobertura del suelo agrupados según su capacidad potencial de escorrentía, en términos del parámetro NRCS-CN, caracterizando la respuesta hidrológica de las cuencas y su variación estacional debido a cambios fenológicos. El resultado es la representación veraz y detallada del territorio específicamente diseñado para abordar simulaciones hidrológicas a escala regional en pequeñas cuencas forestales, disminuyendo la incertidumbre asociada a los usos y características hidrológicas del suelo.

Por otro lado, se estudia la capacidad de la firma espectral de las cuencas para la regionalización de los parámetros hidrológicos mediante un enfoque de aprendizaje automático basado en la regresión. En la propuesta de regionalización se consideran tres modalidades: un novedoso enfoque que utiliza exclusivamente la firma espectral de las cuencas, el método clásico que utiliza las propiedades físicas y un método mixto que utiliza los datos espectrales y físicos. Los datos de la cartografía *ad hoc*, permiten abordar la calibración de los modelos hidrológicos utilizando un

enfoque espacial semi-distribuido, y los resultados obtenidos en la fase de calibración son excelentes. En la fase de regionalización, en términos globales, el escenario espectral alcanza casi la misma eficiencia que el método clásico, y no se observan mejores exactitudes al fusionar la información espectral y la física. Además, se detecta relación entre la eficiencia de los modelos hidrológicos y el entorno climático de las cuencas, siendo la eficiencia de los modelos más elevada en las cuencas más húmedas. Nuestros resultados confirman que la regionalización sigue siendo un reto en las variantes bioclimáticas mediterráneas, donde el nuevo enfoque espectral propuesto en esta Tesis muestra resultados prometedores al obtener los mejores resultados en los entornos más secos. Se plantean futuras líneas de investigación en la regionalización de parámetros a escala europea, especialmente para llenar el vacío de los estudios de regionalización en el entorno Mediterráneo. Además, la cobertura continua de los datos de Sentinel en todo el mundo ofrece nuevas posibilidades en zonas donde no se dispone de información cartográfica. Y, por último, sería también destacable que las series temporales de datos satelitales podrían mejorar los enfoques de regionalización estacional caracterizando la respuesta hidrológica de las cuencas y su variabilidad estacional.

CAPÍTULO 1

Introducción General

La Tesis Doctoral se presenta como compendio de las siguientes publicaciones (ordenadas en orden cronológico de publicación):

- Publicación N.º 1 (**P1**) en revista indexada WOS (JCR) *Forest Systems*, con un índice de impacto en 2017 de 0,96 situada en el Q3 en la categoría *Forestry*:

  FRAGOSO-CAMPÓN, L., QUIRÓS, E. & DURÁN-BARROSO, P. 2017. Resource communication: Variability in estimated runoff in a forested area based on different cartographic data sources. *Forest systems,* 26, 2. DOI: 10.5424/fs/2017262-10921

- Publicación N.º 2 (**P2**) en revista indexada WOS (JCR) Environmental Science and Pollution Researh Journal, con un índice de impacto en 2019 de 3,056 situada en el Q2 de la categoría *Environmental Science:*

  FRAGOSO-CAMPÓN, L., QUIRÓS, E., MORA, J., GUTIÉRREZ GALLEGO, J. A. & DURÁN-BARROSO, P. 2020. Overstory-understory land cover mapping at the watershed scale: accuracy enhancement by multitemporal remote sensing analysis and LiDAR. *Environmental Science and Pollution Research,* 27, 75-88. DOI: 10.1007/s11356-019-04520-8

- Publicación N.º 3 (**P3)** en revista indexada WOS (JCR) *Stochastic Environmental Research and Risk Assessment,* con un índice de impacto en 2019 de 2.351 situada en el Q1 de la categoría *Statistics and Probability* y Q2 de las categorías *Civil Engineering, Water Science and Technology:*

  FRAGOSO-CAMPÓN, L., QUIRÓS, E. & GUTIÉRREZ GALLEGO, J. A. 2020. Dehesa environment mapping with transference of a Random Forest classifier to neighboring ultra-high spatial resolution imagery at class and macro-class land cover levels. *Stochastic Environmental Research and Risk Assessment*, 1-32. DOI: 10.1007/s00477-020-01880-3

- Publicación N.º 4 (**P4**) en revista indexada WOS (JCR) *Stochastic Environmental Research and Risk Assessment,* con un índice de impacto en 2019 de 2.351 situada en el Q1 de la categoría *Statistics and Probability* y Q2 de las categorías *Civil Engineering, Water Science and Technology:*

  FRAGOSO-CAMPÓN, L., QUIRÓS, E. & GUTIÉRREZ GALLEGO, J. A. 2021. Optimization of land cover mapping through improvements in Sentinel-1 and Sentinel-2 image dimensionality and data mining feature selection for hydrological modeling. *Stochastic Environmental Research and Risk Assessment*. DOI: 10.1007/s00477-021-02014-z

- Publicación N.º 5 (**P5**) en revista indexada WOS (JCR) *Journal of Selected Topics in Applied Earth Observations and Remote Sensing* con un índice de impacto en 2019 de 3,827 situada en el Q1 de la categoría Geography, Physical y en el Q2 de la categoría Remote Sensing*:*

  QUIRÓS , E., POLO, M. E. & FRAGOSO-CAMPÓN, L. 2021. GEDI Elevation Accuracy Assessment: A Case Study of Southwest Spain. *IEEE Journal of Selected Topics in Applied Earth Observations and Remote Sensing*. DOI: 10.1109/JSTARS.2021.3080711

- Publicación N.º 6 (**P6**), enviada a revista WOS (JCR), el manuscrito en su formato preprint y el estado de la revisión por pares está disponible para su consulta en Authorea:

  FRAGOSO-CAMPÓN, L., DURÁN-BARROSO, P. & QUIRÓS , E. 2021. Analysing the Capability of the Catchment's Spectral Signature for the Regionalization of Hydrological Parameters. *Preprint posted on Authorea*. DOI: 10.22541/au.162100995.56312514/v1

Otros méritos adicionales relacionados con la investigación desarrollada en esta Tesis Doctoral:

- Publicación nº7 (**P7**): FRAGOSO-CAMPÓN, L., QUIRÓS, E. & GUTIÉRREZ GALLEGO, J. A. 2019. Clasificación supervisada de imágenes PNOA-NIR y fusión con datos LiDAR-PNOA como apoyo en el inventario forestal. Caso de estudio: Dehesas. *Cuadernos de la Sociedad Española de Ciencias Forestales,* 45**,** 77-96. DOI: 10.31167/csecfv0i45.19882

- Comunicación congreso (**C1**): FRAGOSO, L., DURÁN-BARROSO, P., QUIRÓS, E. & GUTIÉRREZ, J. A. 2017. Análisis de la sensibilidad en la generación de escorrentía en zonas forestales ante las variaciones de la fracción de cabida cubierta. Caso de estudio: Valle del Jerte. *In:* FORESTALES, S. E. D. C. (ed.) *7º Congreso Forestal Español.* Plasencia (Cáceres).

- Comunicación congreso (**C2**): FRAGOSO-CAMPÓN, L., GUTIÉRREZ, J. A., MORA, J. & QUIRÓS, E. 2018a. Integración de datos LiDAR e imágenes Sentinel 2A para la evaluación de la densidad de cobertura vegetal en una cuenca hidrológica de carácter forestal. *XVIII Congreso Nacional TIG* Valencia: Universitat de València.

- Comunicación congreso (**C3**): FRAGOSO-CAMPÓN, L., QUIRÓS, E., MORA, J., GUTIÉRREZ, J. A. & DURÁN-BARROSO, P. 2018. Accuracy enhancement for

land cover classification using LiDAR and multitemporal Sentinel 2 images in a forested watershed. *Multidisciplinary Digital Publishing Institute Proceedings,* 2**,** 1280. DOI: 10.3390/proceedings2201280

- Comunicación congreso (**C4**): FRAGOSO-CAMPÓN, L. & QUIRÓS, E. 2019b. Sentinel Toolbox Application (SNAP) aplicado a la clasificación supervisada de imágenes PNOA. *In:* UVA (ed.) *XVIII Congreso de la Asociación Española de Teledetección: Hacia una visión global del cambio climático.* Valladolid (España).

La investigación desarrollada en esta Tesis Doctoral aplica la teledetección como apoyo en la modelización hidrológica y plantea dos objetivos generales:

- Objetivo N.º 1 (O1): Desarrollar una metodología para la generación de cartografía *ad hoc* específica para modelización hidrológica mediante técnicas de teledetección.
- Objetivo N.º 2 (O2): Analizar la capacidad de la respuesta espectral de las cuencas para la regionalización de parámetros hidrológicos.

Méritos relacionados con el O1, sobre la aplicación de la teledetección en la elaboración de cartografía *ad hoc* para modelización hidrológica:

El análisis sobre la problemática existente derivada del uso de cartografía oficial para modelización hidrológica se presentó como comunicación oral en congreso nacional **(C1)** y, en la revista indexada WOS (JCR) *Forest Systems*, con un índice de impacto en 2017 de 0,96 situada en el Q3 en la categoría *Forestry* **(P1)**.

De este modo, se planteó la elaboración de cartografía de la cobertura vegetal mediante teledetección, inicialmente se diseñó mediante la aplicación de técnicas de clasificación supervisadas, sobre imágenes de los satélites de la misión Sentinel del Programa Europeo Copernicus, y su fusión con los datos de la estructura 3D de la vegetación mediante información LIDAR capturada para el Plan Nacional de Ortofotografía Aérea (PNOA).

Este análisis de fusión de datos Sentinel y LiDAR, se refleja en dos contribuciones científicas: una comunicación (en formato póster) en congreso nacional **(C2)** (que obtuvo el Premio a mejor póster en el XVIII Congreso TIG) y en otra presentada como comunicación oral en congreso internacional **(C3)**.

Finalmente, esta fase de trabajo culminó con la publicación de los resultados en la revista indexada en la WOS (JCR) *Environmental Science and Pollution Researh Journal*, con un índice de impacto en 2019 de 3,056 situada en el Q2 de la categoría *Environmental Science* **(P2).**

Seguidamente surgió uno de los principales escollos de la propuesta metodológica inicial: la desactualización de los datos LiDAR respecto de la fecha de captura de las imágenes del satélite. Los datos LiDAR disponibles al inicio de los trabajos de la tesis eran los de la primera cobertura de 2010 y en principio, se preveía su actualización a finales del 2019. La metodología propuesta en la **(P2)**, propone un método para distinguir entre la vegetación de los estratos inferiores y las del dosel arbóreo y solventar este desfase temporal mediante el uso de una métrica booleana. Sin embargo, esta metodología exige una tarea de verificación de las áreas de entrenamiento utilizando una serie temporal de imágenes PNOA que cubra el desfase entre las fechas de adquisición de los datos, que limita la aplicación del método en áreas extensas. Considerando el volumen de datos LiDAR a procesar en toda la extensión de estudio, y los plazos previstos por el proyecto LiDAR-PNOA, se valoró la posibilidad del procesamiento, en todo el ámbito de estudio de la segunda cobertura del vuelo LiDAR, cuyos datos fueron adquiridos durante 2018, y por lo tanto estaban en la misma ventana temporal que las imágenes Sentinel-2, y que, además, cuentan con una densidad de puntos (1-2 puntos/m^2) superior a la de la primera cobertura (0,5 puntos/m^2). No obstante, la segunda cobertura en el ámbito de la provincia de Cáceres (lote EXT N) y suroeste de Castilla La Mancha (lote CLM SW) se fue demorando en el tiempo y, a fecha de redacción del presente documento, siguen sin estar disponible. Por este motivo, surgió la necesidad de buscar alternativas en el análisis de las alturas de vegetación.

En este sentido, aprovechando el lanzamiento de la misión *The Global Ecosystem Dynamics Investigation (GEDI)* en 2018, se investigó la posibilidad de aplicar estos datos para conocer la estructura vertical de la vegetación, en distintos entornos como los pastizales, la dehesa, o bosques. La misión GEDI proporciona datos discretos sobre la altura de vegetación en huellas de 25 m de diámetro sobre la superficie terrestre, que pueden ser extrapolados al resto del territorio mediante distintas técnicas de regresión. Sin embargo, en base a los resultados obtenidos específicamente en la estimación de las alturas de vegetación en el estrato del sotobosque (pastos-matorral) consideramos no adecuada su aplicación en trabajos posteriores relacionados con el objeto específico de la tesis.

La investigación relacionada con esta fase de los trabajos está incluida en la en la revista indexada WOS (JCR) *Journal of Selected Topics in Applied Earth Observations and Remote Sensing* con un índice de impacto en 2019 de 3,827 situada en el Q1 de la categoría Geography, Physical y en el Q2 de la categoría Remote Sensing **(P5).**

Así pues, una vez que se descartó la posibilidad de incluir la estructura de la vegetación en altura como predictor en el análisis de la vegetación, la propuesta metodológica se replanteó para alcanzar el objetivo de nuestro propósito, el de ser

capaz de distinguir las coberturas vegetales según su capacidad de generar escorrentía utilizando datos relativos a imágenes satélites y adquiridas por naves aerotransportadas, con cobertura en nuestra área de estudio, reduciendo el uso de los datos LiDAR sólo como apoyo en la creación de las áreas de entrenamiento.

En este sentido, uno de los elementos claves a la hora de abordar una clasificación supervisada de una imagen, es la calidad y representatividad de las áreas de entrenamiento utilizadas, ya que la exactitud de los mapas finales dependerá de la veracidad de dichas áreas de entrenamiento. Para dar respuesta a esta necesidad, se desarrolló una metodología capaz de obtener de manera precisa la definición automática de estas áreas de entrenamiento utilizando como base las imágenes de alta resolución espacial PNOA, utilizando los datos LiDAR-PNOA como apoyo.

Esta fase de la investigación dio lugar a varias publicaciones presentadas como comunicaciones orales en un congreso nacional **(C4)**, así como, en la Jornada científico-técnica del Grupo de trabajo Ibérico de Inventario y Teledetección Forestal celebrado en el INIA y la posterior publicación en la revista Cuadernos de la Sociedad Española de Ciencias Forestales (artículo con revisión por pares) **(P7)**.

Los resultados de esta etapa se publicaron en la revista indexada WOS (JCR) *Stochastic Environmental Research and Risk Assessment,* con un índice de impacto en 2019 de 2.351 situada en el Q1 de la categoría *Statistics and Probability* y Q2 de las categorías *Civil Engineering, Water Science and Technology* **(P3)**.

A continuación, se aplicó la metodología anterior con el fin de definir las áreas de entrenamiento en todo el ámbito de estudio para la clasificación supervisada de fusión de imágenes radar y ópticas, de Sentinel -1 y Sentinel-2. El resultado final representa la respuesta hidrológica en el ámbito de estudio en términos del número de curva (CN), permitiendo el análisis de la escorrentía potencial y su variación debido a la fenología estacional.

Así pues, esta fase de los trabajos culminó con la publicación en revista indexada WOS (JCR) *Stochastic Environmental Research and Risk Assessment,* con un índice de impacto en 2019 de 2.351 situada en el Q1 de la categoría *Statistics and Probability* y Q2 de las categorías *Civil Engineering, Water Science and Technology* **(P4)**.

Méritos relacionados con el O2, relacionadas con la aplicación de la teledetección en la regionalización de parámetros hidrológicos.

La última etapa de la investigación consistió en la utilización de la cartografía *ad hoc* obtenida para la implementación de los modelos hidrológicos en las cuencas aforadas, que llamaremos cuencas pilotos, utilizando el modelo conceptual HBV. El

conocimiento detallado de las coberturas según su capacidad de generar escorrentía permitió calibrar los modelos semi-distribuidos alcanzando unas excelentes eficiencias en la modelización. Además, la metodología desarrollada en la Tesis propone un novedoso enfoque en la regionalización de parámetros hidrológicos en cuencas no aforadas aplicando técnicas de regresión con aprendizaje automático considerando la firma espectral de las cuencas basada en los datos del Sentinel-1 y Sentinel-2, contrastando los resultados respecto al enfoque tradicional que utiliza datos físicos (tipo de suelo, vegetación, geología, litología, pendientes, etc).

La investigación relacionada con esta fase de los trabajos se ha enviado para su consideración a revista indexada **WOS (JCR),** el manuscrito en su formato preprint y el estado de la revisión por pares está disponible para su consulta en Authorea: **"***Analyzing the Capability of Catchment's Spectral Signature for the Regionalization of Hydrological Parameters*" (Laura Fragoso-Campón, Pablo Durán-Barroso, Elia Quirós)**.**

CAPÍTULO 2

Resumen global estructurado de los resultados, discusión y conclusiones finales

1. Contexto

1.1. Contexto general [1]

Disponer de una estimación adecuada de los procesos hidrológicos en una cuenca hidrográfica es fundamental ya que, de ellos dependen la correcta gestión de los recursos hídricos como el suministro de agua, la evaluación de las inundaciones y las sequías. Históricamente se han desarrollado distintos tipos de modelos hidrológicos, cada uno con diferentes grados de suposición y simplificación para simular los procesos de escorrentía: en cuanto a la conceptualización de los procesos podemos diferenciar entre modelo empírico, modelo conceptual y modelo físico; respecto a la estructura espacial de los procesos hidrológicos dentro de la cuenca, podemos diferenciar entre modelos agregados, semi-distribuidos o distribuidos; y, en cuanto a la temporalidad del análisis, podemos diferenciar entre los basados en eventos de precipitación y los de modelización continua (Brocca et al., 2011).

En este sentido, el uso de los modelos conceptuales está muy extendido ya que presentan una estructura sencilla, y cuentan con un número de parámetros a considerar muy inferior a de los modelos físicos, minimizando la dificultad y la incertidumbre en su estimación. Muchos de los datos de entrada requeridos, independientemente del modelo utilizado (estructura espacial o temporalidad), son datos derivados de la teledetección, tales como modelos digitales de elevaciones (MDE), datos meteorológicos y, mapas de suelo y cobertura del suelo (Athira et al., 2016, Becker et al., 2019, Chen et al., 2019, Martínez-Salvador and Conesa-García, 2020, Parajuli et al., 2018). De entre todos los factores que intervienen en la respuesta hidrológica de una cuenca, la caracterización de los tipos del suelo y, especialmente, la tipología de vegetación tiene una gran influencia en el balance hídrico (Astuti et al., 2019, Sajikumar and Remya, 2015), puesto que la cobertura vegetal está relacionada con aspectos como la evapotranspiración, la escorrentía y la capacidad de infiltración (Becker et al., 2019, Dias et al., 2015, Dionizio and Costa, 2019, Luan et al., 2018, Netzer et al., 2019, Parajuli et al., 2018). La eficiencia en la modelización hidrológica depende en gran medida de la disponibilidad de datos de

[1] Adapted/Translated by permission from Springer Nature:

(a) Springer Nature, Stochastic Environmental Research and Risk Assessment, Optimization of land cover mapping through improvements in Sentinel-1 and Sentinel-2 image dimensionality and data mining feature selection for hydrological modeling, Laura Fragoso-Campón et al, COPYRIGHT 2021, and

(b) Springer Nature Environmental Science and Pollution Research, Overstory-understory land cover mapping at the watershed scale: accuracy enhancement by multitemporal remote sensing analysis and LiDAR, Laura Fragoso-Campón et al, COPYRIGHT 2020.

entrada al modelo y, de las incertidumbres de los valores de los parámetros que intervienen en el modelo, que idealmente, deberían ser calibrados para obtener una buena exactitud en las simulaciones de los caudales (Beck et al., 2020). Sin embargo, la calibración podría conducir a una combinación no única de los mejores parámetros (Bárdossy, 2007). Por lo tanto, la incertidumbre es aún mayor en las cuencas no aforadas, donde la calibración de los parámetros del modelo no es factible, convirtiéndose así en un reto hidrológico.

El modelo del Número de Curva (*Curve Number* – CN) del *Natural Resources Conservation Service* (NRCS) (NRCS, 2009), es un modelo conceptual diseñado para el análisis de eventos de precipitación, que tiene una formulación sencilla y que requiere pocos datos de entrada. Por este motivo, ha sido ampliamente utilizado a nivel mundial desde su aparición. Este método, relaciona el volumen de escorrentía tras un aguacero con tres parámetros hidrológicos: la cobertura del suelo (que a su vez incluye información del uso del suelo y clase de tratamiento), características hidrológicas y del tipo de suelo. Sin embargo, el método no ha estado exento de polémica, ya que una de las mayores debilidades del método se produce precisamente en las zonas forestales (Kim and Lee, 2008, Choi et al., 2016, Tedela et al., 2012, Walega et al., 2020). Además, la formulación del método original ha sido estudiada por muchos autores y replanteada en algún caso para la mejora de la estimación de los caudales (Bartlett et al., 2016). Sea cual fuere, la versión del método utilizada, los parámetros de entrada al modelo no varían, y aun siendo pocos parámetros, no está exento de incertidumbre. Del análisis de la problemática inicial (véase P1) la estimación de los factores que intervienen se realiza de manera tradicional por interpretación del usuario considerando la información procedente de diversas fuentes cartográficas oficiales. Sin embargo, la decisión sobre el uso de del suelo y la definición de las características hidrológicas más apropiadas, son los aspectos más complicados de valorar, ya que, en primer lugar, existen usos del suelo en los que no existen criterios objetivos para determinar las características hidrológicas más adecuadas, y por otro lado, ninguna fuente de datos cartográfica oficial proporciona, en sí misma, todos los datos necesarios para determinar, de manera objetiva, las características hidrológicas. Este aspecto provoca una gran incertidumbre sobre la validez del valor finalmente propuesto. Además, aunque la aplicación en modelos físicos está fuera del alcance de esta tesis, en una reciente revisión realizada por Marin et al. (2020), en la que se analizaron modelizaciones basadas en el modelo físico que utiliza la aplicación *Soil and Water Assessment Tool* (SWAT) en pequeñas cuencas forestales, los autores concluyeron que el valor del parámetro del CN, resultó ser uno de los parámetros más sensibles en los procesos hidrológicos en todos los estudios analizados.

Por este motivo, es necesario conocer distribución espacial, tanto del tipo de suelo como, de los usos del suelo y tipología de la vegetación. Además, dependiendo de la escala del modelo, la resolución espacial de esta información también influye en la eficiencia de la modelización. Según el análisis de Sajikumar and Remya (2015), la resolución de los mapas de coberturas a gran escala puede no ser apropiada cuando se aborda un análisis regional, en el que se requieren mapas con mayor resolución espacial para lograr una simulación hidrológica adecuada. Por lo tanto, en los análisis regionales, en los que se necesita un conocimiento detallado de la cobertura del suelo, se recomienda utilizar mapas *ad hoc* especialmente diseñados para un propósito específico, y las técnicas de teledetección son una opción adecuada para crear estos mapas.

Para abordar una modelización hidrológica continua, existen otros métodos conceptuales, como el método HBV (Bergström, 1995), que modeliza el proceso precipitación-escorrentía de manera global a través de varias rutinas, en las que intervienen un número razonable de parámetros, que están a su vez relacionados con las características físicas de las cuencas: usos del suelo, tipo de suelo, características geológicas y morfológicas. Como se ha mencionado anteriormente, los parámetros en este tipo de modelos deben ser calibrados para caracterizar la respuesta hidrológica de las cuencas de manera precisa, y cuantos más parámetros, mayor la incertidumbre de la modelización. En el caso de las cuencas no aforadas, donde es imposible realizar la calibración de los parámetros, éstos se suelen obtener mediante lo que se denomina regionalización, que consiste en transferir los patrones de respuesta hidrológica de las cuencas aforadas a las no aforadas (Hrachowitz et al., 2013). En este sentido, existen distintos métodos de regionalización como el de proximidad espacial, el basado en la similitud, el basado en la regresión de las características de las cuencas y el basado en las firmas hidrológicas de los caudales (Hrachowitz et al., 2013, Parajka et al., 2013, Guo et al., 2021). Sin embargo, no hay un modelo de regionalización óptimo, y la eficacia de la regionalización dependerá del entorno y de los atributos hidro climáticos particulares de una zona (Parajka et al., 2013). En particular, uno de los grupos de métodos existentes, los métodos basados en la regresión, utilizan las propiedades físicas de las cuencas (usos del suelo, tipo de suelo, características geológicas y propiedades morfológicas). Tradicionalmente, esta información se obtiene de cartografía temática, que como ya se ha mencionado anteriormente, muchas veces se genera a partir de datos de teledetección. Sin embargo, ya que la respuesta hidrológica depende de los atributos físicos y estos últimos están relacionados con la respuesta espectral del territorio, en esta tesis se propone relacionar directamente la respuesta espectral con el comportamiento hidrológico de una cuenca.

Así pues, la investigación desarrollada en esta Tesis Doctoral aplica la teledetección como apoyo en la modelización hidrológica con el propósito de disminuir la incertidumbre asociada a la estimación de parámetros hidrológicos desde dos enfoques: en primer lugar, para la generación de cartografía *ad hoc* a ser utilizada la modelización hidrológica y, en segundo lugar, para la regionalización de parámetros hidrológicos en cuencas no aforadas.

Por tanto, los objetivos generales planteados en esta Tesis son los siguientes:

- Objetivo N.º 1 (O1): Desarrollar una metodología con el fin de generar cartografía *ad hoc* específica para modelización hidrológica mediante técnicas de teledetección.

- Objetivo N.º 2 (O2): Analizar la capacidad de la respuesta espectral de las cuencas para la regionalización de parámetros hidrológicos.

1.2. Contexto específico del O1 sobre la aplicación de la teledetección en la elaboración de cartografía *ad hoc* para modelización hidrológica [1]

En relación con el estudio de las áreas forestales, la capacidad de generación de escorrentía se verá disminuida debido a las intercepciones del dosel arbóreo y de la vegetación del sotobosque (Gökbulak et al., 2016). Esta reducción depende en gran medida, no sólo del volumen de las precipitaciones, también de la densidad de los árboles, el tipo de bosque y su estructura vertical. En entornos Mediterráneos, las áreas forestales se caracterizan por la presencia de formaciones ramificadas: árboles y arbustos que coexisten en un mismo hábitat. Para distinguir entre el dosel arbóreo superior y la vegetación del sotobosque, la inclusión de datos LiDAR y técnicas de aprendizaje automático en los procesos de clasificación han demostrado ser eficientes (Bork and Su, 2007, Erdody and Moskal, 2010, García et al., 2011, Mundt et al., 2006, Mutlu et al., 2008). Esta fusión de datos aprovecha la información proporcionada por los datos LiDAR sobre la estructura vertical de la vegetación, y la capacidad de los datos multiespectrales para captar la distribución horizontal de la vegetación, así como para diferenciar los tipos de vegetación en función de su respuesta espectral (García et al., 2011).

Existen muchos estudios a nivel mundial que han demostrado las grandes capacidades de la aplicación de las técnicas de teledetección para el estudio de la cobertura del suelo desde un punto de vista general (Akike and Samanta, 2016, Bolton et al., 2018), y, en particular, para estudios de la estructura forestal y las especies arbóreas (Fassnacht et al., 2016, Ferreira et al., 2016, Ghosh et al., 2014), estudios realizados exclusivamente en el estrato del sotobosque (Magiera et al., 2016, Stavrakoudis et al., 2014, van Lier et al., 2009), estudios centrados en zonas

agrícolas (Brinkhoff et al., 2020, Verma et al., 2019) y, estudios centrados específicamente en zonas urbanas (Matikainen and Karila, 2011, Tavares et al., 2019). No obstante, si bien es importante disponer de la distribución espacial de la cubierta vegetal para la modelización hidrológica, sólo unos pocos estudios han abordado los mapas regionales de vegetación *ad hoc* mediante técnicas de teledetección específicamente elaborados para sus modelos hidrológicos. Entre ellos, encontramos algunos trabajos basados en imágenes Landsat-8, con una resolución espacial de 30 m (Astuti et al., 2019, Martínez-Salvador and Conesa-García, 2020, Wang et al., 2020), y otro estudio que combinó datos de Landsat-5, Sentinel-1 (S1) y Sentinel 2 (S2), también con una resolución espacial de 30 m, para estudiar la influencia del cambio de la cubierta vegetal en los recursos hídricos y los ecosistemas de Tanzania (Leemhuis et al., 2017). Otros trabajos utilizaron el LISS-IV, con una resolución espacial de 5,8 m, en la India (Karunanidhi et al., 2020, Nageswara Rao, 2020).

En la actualidad, se dispone de una gran cantidad de imágenes de teledetección para su uso en la cartografía de la cubierta terrestre, y estos datos pueden clasificarse, según las características del sensor, como pasivos (multiespectrales o hiperespectrales) o activos de radar de apertura sintética (*Synthetic Aperture Radar* - SAR)), y pueden utilizarse solos, en combinación entre ellos o en combinación con otros datos. Además, es posible añadir la variable temporal; por lo tanto, el análisis de la cubierta terrestre podría abordarse desde varios puntos de vista en función del número de sensores y de la temporalidad de las imágenes analizadas. Varios estudios señalan que la exactitud final es mayor cuanta más información se utiliza (Stromann et al., 2020, Zhao et al., 2016). Algunos estudios han utilizado series multitemporales de sensores ópticos multiespectrales, como las imágenes Landsat (Ahmed et al., 2015, Bolton et al., 2018, Zhao et al., 2016), Sentinel-2 (Hoscilo and Lewandowska, 2019, Immitzer et al., 2019), o una combinación de ambas (Carrasco et al., 2019, Li et al., 2019).

La mayor limitación a hora de usar imágenes de sensores pasivos es que éstos se ven afectados por las condiciones atmosféricas y, por lo tanto, en las regiones lluviosas con alta probabilidad de nubosidad, el uso del SAR es casi la única opción y, en estos casos, se suele abordar el análisis multitemporal (Wei et al., 2019, Yu et al., 2019). Además, en las regiones en las que la climatología permite disponer de datos de ambos sensores, se puede realizar la fusión de las dos fuentes y obtener buenos resultados. En este sentido, desde el lanzamiento de los satélites Sentinel, estas imágenes se han utilizado en muchos estudios, y la fusión de S1 y S2 se ha demostrado ser eficaz para el cartografiado de distintas coberturas de la superficie terrestre.

Hay muchas formas de combinar la información de los datos ópticos y del SAR. Hay algunos estudios en los que los autores combinan únicamente la intensidad de la retrodispersión del S1 en ambas polarizaciones con las bandas ópticas S2 (Feng et al., 2019, Khan et al., 2020, Steinhausen et al., 2018). Otros autores también añadieron información derivada de las bandas del S2, como los índices radiométricos o biofísicos (Brinkhoff et al., 2020, Denize et al., 2019, Heckel et al., 2020, Ienco et al., 2019, Lopes et al., 2020, Mahdianpari et al., 2020, Mercier et al., 2019, Whyte et al., 2018). Además, es posible combinar la información de la intensidad de la retrodispersión del S1 exclusivamente con los índices radiométricos o biofísicos derivados del S2 (Van Tricht et al., 2018). Otros autores también combinan la intensidad de la retrodispersión del S1 con varios sensores ópticos (S2, Landsat, LISS) y los índices radiométricos o biofísicos derivados (Carrasco et al., 2019, Muthukumarasamy et al., 2019, Poortinga et al., 2019). Asimismo, otros trabajos añadieron información textural de la matriz de color de nivel de gris (*Gray level color Matrix* - GLCM) al análisis, utilizando sólo texturas derivadas del S1 (Numbisi et al., 2019, Tavares et al., 2019, Verma et al., 2019), sólo texturas del S2 (Liu et al., 2018), o ambas (Mishra et al., 2019, Stromann et al., 2020). Nos encontramos entonces ante un *big data* en teledetección, al servicio de la ciencia, que nos brinda una oportunidad única en la búsqueda de nuevas metodologías. Sin embargo, el considerable aumento del volumen de datos a procesar hace que la capacidad de almacenamiento necesaria y, el tiempo de cálculo también aumenten considerablemente. Por lo tanto, los problemas no se refieren únicamente a la disponibilidad de datos (series multitemporales de imágenes ópticas sin nubes y SAR), sino también a la capacidad de almacenar, gestionar y disponer de los requisitos computacionales mínimos necesarios.

Por último, uno de los elementos claves a la hora de abordar una clasificación supervisada, sea cual sea el origen de los predictores que intervienen, es la calidad y representatividad de las áreas de entrenamiento utilizadas para entrenar al clasificador ya que, la exactitud de los mapas finales, dependerán de la veracidad de dichas áreas de entrenamiento. La definición de estas áreas de referencia se realiza tradicionalmente a partir del trabajo de campo, que es una tarea que requiere mucho tiempo y es bastante costosa (Ghimire et al., 2012). Dicho trabajo de campo también se complementa con técnicas de fotointerpretación de imágenes a alta resolución, lo que minimiza e incluso en ocasiones, puede llegar a evitar, la dura tarea de las visitas de campo, sobre todo en áreas de difícil acceso. Sin embargo, este procedimiento, igualmente manual, también es laborioso, requiere mucho tiempo y es poco práctico para áreas extensas (Müllerová et al., 2013). Una alternativa al método tradicional fue propuesta por Paris et al. (2017) donde se planteaba la definición de un "pseudo" conjunto de entrenamiento obtenido a partir de un mapa temático analizando las muestras que tuvieran la mayor probabilidad de pertenecer a zonas donde no se

produjeran cambios sobre el terreno. Finalmente, tras una validación, estas pseudo-muestras de entrenamiento podían utilizarse como muestras de entrenamiento para la clasificación supervisada.

Por tanto, dentro del O1 planteado en la Tesis sobre desarrollar una metodología para la generación de cartografía *ad hoc* específica para modelización hidrológica, se plantearon los siguientes objetivos específicos:

- O1.1: Analizar la capacidad de la fusión de datos de imágenes Sentinel-2 y LiDAR-PNOA de baja densidad en el análisis de la cobertura vegetal considerando su estratificación vertical (sotobosque y dosel arbóreo) para generar cartografía de usos de suelo a escala de cuenca hidrográfica. (Este objetivo específico se desarrolla en la P2)

- O1.2: Analizar la capacidad de la misión GEDI para analizar la estructura de la vegetación en los estratos inferiores del sotobosque. (Este objetivo específico se desarrolla en la P5)

- O1.3: Desarrollar una metodología para generar áreas de entrenamiento a partir imágenes de ultra alta resolución espacial.

    - Definir metodología para generar mapas personalizados de alta resolución de la vegetación tanto en el estrato superior como en el inferior, identificando los tipos en función de la capacidad de generación de escorrentía

    - Desarrollar un método para reducir las campañas de campo transfiriendo la información del conjunto de datos de entrenamiento a diferentes imágenes.
    - Evaluar la influencia de la resolución espacial de los mapas de cobertura del suelo en la estimación de la escorrentía potencial.

  (Este objetivo específico se desarrolla en la P3 y P7)

- O1.4: Desarrollar una metodología para la generación de mapas de cobertura de la cubierta terrestre utilizando la fusión de datos SAR y ópticos de imágenes Sentinel:

    - Desarrollar un método para elaborar mapas de alta exactitud mediante la selección de predictores más influyentes y la minimización de los requisitos de capacidad de almacenamiento y el tiempo de cálculo,

- Identificar las categorías de la cubierta terrestre desde el punto de vista hidrológico, en función de la capacidad de generación de escorrentía, y el análisis de la variación estacional de la misma.

(Este objetivo específico se desarrolla en la P4)

1.3. Contexto específico del O2 sobre la aplicación de la teledetección en la regionalización de parámetros hidrológicos

Como se ha adelantado en el contexto general, en cuencas no aforadas, la estimación de los parámetros hidrológicos se suele realizar mediante un proceso denominado regionalización, que consiste en transferir los patrones de la respuesta hidrológica de cuencas aforadas a las no aforadas (Hrachowitz et al., 2013). Existen distintos métodos de regionalización que han demostrado ser eficaces (Hrachowitz et al., 2013, Parajka et al., 2013, Guo et al., 2021) si bien, no hay un modelo de regionalización óptimo, y depende el entorno y de características particulares de cada zona (Parajka et al., 2013).

En relación con la regionalización de parámetros basada en la regresión, los modelos más utilizados son la regresión lineal o múltiple (Merz and Blöschl, 2004, Seibert, 1999) o las funciones de transferencia (Beck et al., 2020, Götzinger and Bárdossy, 2007, Hundecha and Bárdossy, 2004). Este modelo de regionalización basado en regresión transfiere los valores calibrados en las cuencas aforadas a las no aforadas, siembre que ambas presenten similitudes en cuanto a sus propiedades. Estas características suelen ser las propiedades físicas como los datos topográficos, el uso del suelo, propiedades edáficas y geológicas, que tradicionalmente proceden de fuentes cartográficas (Booij, 2005, Hundecha and Bárdossy, 2004, Kult et al., 2014, Merz and Blöschl, 2004, Parajuli et al., 2018). Estudios recientes han incorporado datos de teledetección como predictores, si bien, estos se reducen a varios índices de vegetación (NDVI, NDMI y SAVI) o biofísicos (LAI) derivados de la información espectral del MODIS (Choubin et al., 2019) o Landsat-8 (Bui et al., 2020). Específicamente, estudios relativos a la regionalización basada en regresión, en Beck et al. (2020), utilizaron el índice de vegetación NDVI derivado del programa de vegetación SPOT como predictor en su regionalización de parámetros hidrológicos a nivel mundial.

Sin embargo, a parte de los índices señalados anteriormente, los datos obtenidos por teledetección añaden una valiosa caracterización de las cuencas. En primer lugar, la respuesta espectral del territorio depende de la vegetación, tanto del tipo de especies como de su densidad de cobertura, así como de las características geológicas y litológicas. Además, los tipos de vegetación a su vez también dependen

de la litología del terreno (Costa et al., 2017) y los sensores registran una respuesta espectral distinta en función de la naturaleza del mismo. Por ejemplo, la reflectancia captada por el sensor óptico está relacionada con la mineralogía de la superficie dependiendo de la composición geológica del suelo (Rajendran and Nasir, 2021). Además, la respuesta de la intensidad de la retrodispersión del SAR se ve afectada por la rugosidad de la superficie, el contenido de humedad del suelo (Purinton and Bookhagen, 2020), la constante dieléctrica y la granulometría (Lu et al., 2021). Por tanto, considerando que estas características están directamente implicadas en la respuesta hidrológica del territorio, la respuesta espectral de una cuenca puede relacionarse con su respuesta hidrológica. Si bien, hasta donde sabemos, aún no se ha documentado la capacidad de la firma espectral para estudiar las propiedades de las cuencas y para ser utilizadas como predictores en la regionalización basada en la regresión de los parámetros hidrológicos.

Por tanto, dentro del O2 planteado en la Tesis sobre analizar la capacidad de la respuesta espectral de las cuencas para la regionalización de parámetros hidrológicos, se plantearon los siguientes objetivos específicos:

- O2.1: Obtener la firma espectral de las cuencas basándose en los satélites Sentinel-1 y Sentinel -2.

- O2.2: Caracterizar las propiedades físicas del suelo basándose en la información cartográfica del Centro Europeo de Datos del Suelo (*European Soil Data Centre*).

- O2.3: Evaluar la capacidad del algoritmo de *Random Forest* para realizar la regresión de los parámetros hidrológicos.

- O2.4: Evaluar la eficiencia hidrológica de la regionalización desde dos puntos de vista: las propiedades espectrales y físicas.

(Este objetivo se desarrolla en la P6)

1.4. Contextualización de las misiones Sentinel-1 y Sentinel -2

El Programa Copernicus, se ha convertido en la última década en el Programa de Observación de la Tierra de referencia en Europa, está coordinado por la Comisión Europea y, junto con la colaboración de la Agencia Espacial Europea -European Space Agency (ESA)- ha desarrollado el programa Sentinel. Los datos captados por los sensores de los distintos satélites Sentinel permiten el monitoreo terrestre, el oceánico y atmosférico (ESA, 2019a).

Específicamente para el estudio de la cobertura terrestre, el Programa Copernicus cuenta con tres misiones: Sentinel-1 (S1), Sentinel-2 (S2) y Sentinel-3 (S3). Cada una estas misiones, cuenta con una constelación de dos satélites gemelos (A y B) que orbitan desfasados 180º y están equipados con sensores de distintas tecnologías. Los satélites S1 están equipados con un sensor activo SAR, el satélite S1A fue lanzado el 3 de abril de 2014 y el S1B fue lanzado el 25 de abril de 2016, y trabajando conjuntamente ofrecen un período de revisita de 6 días. Los satélites S2 están equipados con un sensor pasivo multiespectral de la alta resolución espacial. El satélite S2A fue lanzado el 23 de junio de 2015 y el S2B fue lanzado el 7 de marzo de 2017, y trabajando conjuntamente ofrecen un período de revisita de 5 días (ESA, 2019b). Los datos suministrados por los Sentinel son libre distribución a través de la plataforma de descarga Copernicus Open Access Hub (Copernicus Program and ESA, 2014-2021)

El S1 es un SAR que opera en la banda C, cuyas longitudes de onda captan imágenes de la superficie de la Tierra durante el día y la noche, y no se ven restringidos por las condiciones atmosféricas. En las latitudes de la península Ibérica, ofrece datos en modo Interferometría de gran amplitud (*Interferometric Wide Swath Mode - IW*) y doble polarización VV-VH (Transmisión vertical/recepción vertical (VV) - Transmisión vertical/recepción horizontal (VH). Las imágenes captadas en modo IW se procesan para convertirlos en productos de nivel 1: el *Single Look Complex* (SLC) y *Ground Range Detected* (GRD) (ESA, 2019b). En esta Tesis, se han utilizado los productos GRD consistentes en datos proyectados a nivel del suelo usando un modelo de elipsoide terrestre (Figura 1)

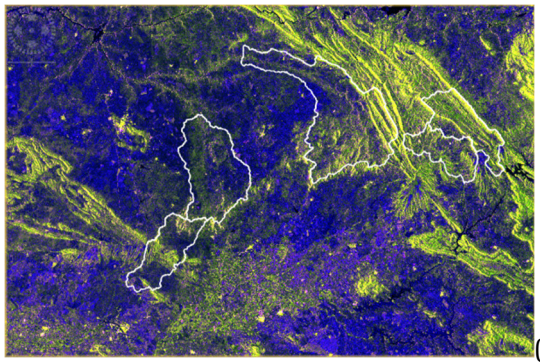
(a)
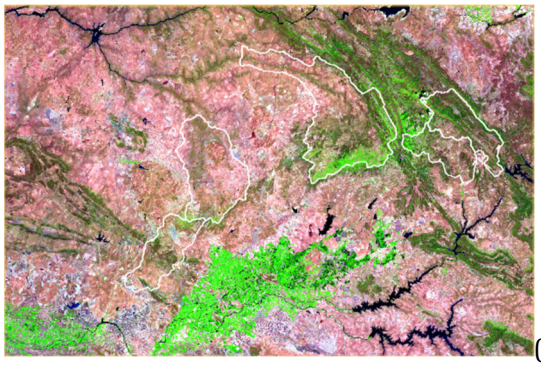
(b)

Figura 1. Ejemplo de la visualización de las imágenes Sentinel en la zona de estudio (a) imagen S1 en composición RGB:VV-VH-VV/VH y (b) imagen S2 en falso color RGB:B11-B8-B4.

El S2 es un sensor óptico multiespectral de la alta resolución espacial con una resolución radiométrica de 13 bandas, que van desde el espectro visible (VIS) del azul al infrarrojo de onda corta (SWIR), incluyendo la región de transición del rojo al infrarrojo cercano (NIR), conocido como *Red Edge* (NIR-RE) (ESA, 2019b). La

resolución espacial, varía entre 10 m, 20 m y 60 m en función de la banda analizada (Tabla 1)

Tabla 1. Resolución radiométrica y espacial de las bandas del satélite Sentinel-2

Espectro electromagnético			Longitud de onda central (nm)	Ancho de banda (nm)	Resolución espacial
Visible (VIS)		B1	443	21	60 m
		B2	490	65	10 m
		B3	560	35	10 m
		B4	665	30	10 m
Infrarrojo cercano (NIR)	*Red Edge* (NIR-RE)	B5	705	15	20 m
		B6	740	15	20 m
		B7	783	20	20 m
		B8	842	115	10 m
		B8A	865	20	20 m
		B9	945	20	60 m
Infrarrojo de onda corta (SWIR)		B10	1375	30	60 m
		B11	1610	90	20 m
		B12	2190	180	20 m

Las imágenes S2 están disponibles en dos niveles de procesamiento: *Level*-1C correspondiente a los valores de las reflectancias en el techo de la atmósfera (*Top of Afmosfere* – TOA) y *Level*-2A correspondientes reflectancias a nivel de terreno (*Bottom of Atmosfere* – BOA), con la corrección atmosférica ya aplicada, que son las que se han utilizado en esta Tesis.

Las bandas del S2 nos aportan información sobre la reflectividad de la superficie del terreno en cada una de las longitudes de onda, y nos permite diferenciar coberturas de diferente naturaleza en función la esta energía reflejada por cada tipo de superficie, esta respuesta también se conoce como firma espectral. La firma espectral de una misma superficie puede variar a lo largo del tiempo, por ejemplo, en la vegetación debido a cambios fenológicos. Además, la información espectral puede complementarse con el uso de índices radiométricos, que se obtienen a partir de las bandas espectrales y facilitan la discriminación entre coberturas al depender de la coloración, el contenido de agua, la acción fotosintética y la vigorosidad de las plantas, así como de las características del suelo. Estos índices se pueden agrupar en distintos grupos como son: los índices de vegetación (*Vegetation Indices* - VI), los índices de suelo (*Soil Indices* - SI) o, los índices agua (*Water Indices* - WI). En el caso específico de la vegetación, además de los VI, existen otros índices más específicos sobre la salud y el crecimiento de la vegetación, los denominados índices biofísicos, que analizan el contenido en agua de las hojas (*Canopy Water Content* - CWC), el

índice de área foliar (*Leaf Area Index* - LAI)o el contenido en clorofila (*Canopy Chlorophyll Content* - CCC). En este Tesis, se han utilizado los índices radiométricos que se describen a continuación, cuya formulación se resume en la Tabla 2, quedando el uso de los índices biofísicos fuera el ámbito de estudio.

- Índice de vegetación de diferencia normalizada verde (*Green Normalized Difference Vegetation Index* – GNDVI): utilizado para medir la vitalidad de la vegetación según la relación de la reflectividad en el espectro del verde (VIS) y el NIR-RE.

- Índice de vegetación de diferencia normalizada (*Normalized Difference Vegetation Index - NDVI*): utilizado para medir la densidad y vitalidad de la vegetación según la relación de la reflectividad en el espectro del rojo (VIS) y el NIR.

- Índice de vegetación de diferencia normalizada (*Normalized Difference Index - NDI*): índice normalizado en relación con la reflectividad en el espectro del rojo (VIS) y el NIR-RE, que basado en la combinación de bandas B5 y B4 (NDI45) está relacionado con el LAI.

- Índice de vegetación Red-edge (*Sentinel-2 Red-Edge Position Index – S2REP*): Estudia el estado de la vegetación en base a la reflectividad en el espectro del rojo (VIS) y el NIR-RE.

- Índice de vegetación ajustado al suelo (*Soil Adjusted Vegetation Index - SAVI*): Similar al NDVI, pero minimizando el efecto del suelo, especialmente útil en superficies parcialmente recubiertas de vegetación.

- Índice de vegetación ajustado al suelo modificado (*Second Modified Soil Adjusted Vegetation Index – MSAVI2)*: Similar al SAVI, pero teniendo en cuenta que diferentes suelos tienen diferente respuesta espectral.

- Índice de luminosidad del suelo (*Brightness Index - BI*): Utilizado para distinguir el suelo y la vegetación de pequeño porte según la relación de la reflectividad en el espectro del verde y el rojo (VIS).

- Índice de color del suelo (*Color Index - CI*): Relacionado con la concentración de carbonatos o sulfatos en el suelo según la relación de la reflectividad en el espectro del verde y el rojo (VIS).

- Índice de agua de diferencia normalizada (*Normalized Difference Water Index* - NDWI): utilizado para discriminar las masas de agua según la relación de la reflectividad en el espectro del rojo (VIS) y el NIR.

Tabla 2. Resumen de los índices radiométricos usados en esta Tesis.

Índice	Ecuación para las bandas S2	Referencia
GNDV	$GNDVI = \frac{B7 - B3}{B7 + B3}$	Gitelson et al. (1996)
NDVI	$NDVI = \frac{B8 - B4}{B8 + B4}$	Rouse Jr et al. (1974)
NDI45	$NDI45 = \frac{B5 - B4}{B5 + B4}$	Delegido et al. (2011)
S2REP	$S2REP = 705 + 35 \cdot \frac{\left(\frac{B4 + B7}{2} - B5\right)}{(B6 - B5)}$	Guyot et al. (1988)
SAVI	$SAVI = (1 + L) \cdot \frac{B8 - B4}{(B8 + B4 + L)}$	Huete (1988)
	con L=0.5	
MSAVI2	$MSAVI2 = \frac{1}{2} \cdot \left[(2 \cdot (B8 + 1) - \sqrt{(2B8 + 1)^2 - 8(B8 - B4)}\right]$	Qi et al. (1994)
BI	$BI = \sqrt{\frac{B4^2 + B3^2}{2}}$	Mathieu et al. (1998)
CI	$CI = \frac{B4 - B3}{B4 + B3}$	Escadafal and Huete (1991)
NDWI	$NDWI = \frac{B3 - B8}{B3 + B8}$	Gao (1996)

1.5. Contextualización del área de estudio[1a]

El área de estudio corresponde a las zonas forestales de la Comunidad Autónoma de Extremadura en España, que se extiende entre las latitudes 37°56'-40°29' N y las longitudes 7°32'-4°39' W (Figura 2).

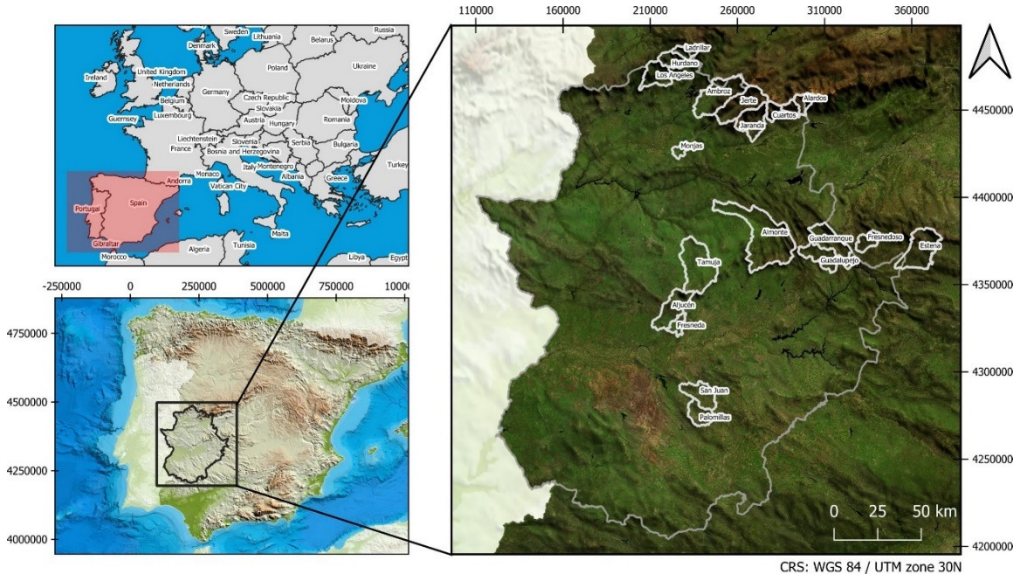

Figura 2. Situación y área de estudio de la Tesis. (Fuente: Figura 1 de la P4)

El análisis se centra en varias cuencas aforadas de toda la región, dentro del ámbito de las Confederaciones Hidrográficas del Guadiana y Tajo, que han sido seleccionadas para la modelización hidrológica del régimen natural del río al disponer serie histórica de datos de aforo y no están afectadas por ninguna regulación de embalses, además todas tienen un tamaño inferior a 1000 km^2 lo que permite despreciar el efecto de propagación del caudal en los cauces (Tabla 3). Las variantes bioclimáticas de las cuencas de la zona de estudio corresponden a la variante pluviseasonal-continental Mediterránea (*Mediterranean pluviseasonal-continental* - Mpc) y, a la variante climática templada oceánica sub Mediterránea (t*emperate oceanic sub-Mediterranean* - Tocsm) (Rivas-Martinez and Rivas-Saenz, 1996-2019).

Tabla 3. Características de las cuencas pilotos estudiadas en la Tesis

Cuenca	Confederación Hidrográfica	Variante Bioclimática*	Tª media (ºC)	Precipitación media (mm)	Área (km^2)	Elevación Media (m)
Alardos	Tajo	Tocsm	10,36	1024,74	87,81	1287,34
Aljucén	Guadiana	Mpc	16,91	551,32	253,57	397,83
Almonte	Tajo	Mpc	15,59	736,99	781,36	639,62
Ambroz	Tajo	Mpc	13,85	1104,15	390,49	760,47
Ángeles	Tajo	Tocsm	13,67	999,29	188,79	788,61
Cuartos	Tajo	Tocsm	10,52	1271,11	68,41	1259,59
Estena	Guadiana	Mpc	15,08	628,31	355,97	788,60
Fresnedoso	Guadiana	Mpc	15,61	579,58	107,07	642,07
Guadalupejo	Guadiana	Mpc	15,76	718,10	199,13	580,41
Guadarranque	Guadiana	Mpc	15,32	698,52	256,56	670,97
Hurdano	Tajo	Tocsm	13,16	974,48	108,58	852,21
Jaranda	Tajo	Tocsm	13,80	1243,26	225,29	815,32
Jerte	Tajo	Tocsm	11,57	1322,85	315,08	1131,62
Ladrillar	Tajo	Tocsm	12,89	980,22	73,11	890,68
Minchones	Tajo	Tocsm	11,10	1112,70	56,41	1305,55
Palomillas	Guadiana	Mpc	16,55	446,02	145,84	494,39
San Juan	Guadiana	Mpc	16,76	453,55	194,05	451,80
Tamuja	Tajo	Mpc	16,52	550,18	458,12	447,49

* Rivas-Martinez and Rivas-Saenz (1996-2019)

Los tipos de cobertura del suelo en Extremadura pueden dividirse en cuatro grupos generales: zonas forestales, zonas agrícolas, masas de agua y superficies impermeables.

En primer lugar, las zonas forestales, que representan el 67% de la región extremeña, pueden subdividirse a su vez en bosques, pastos y dehesas. Las dehesas, son un paisaje típico de Extremadura, definida por Diaz et al. (1997) como *"pastizales poblados por encinas y/o alcornoques, con un sotobosque de pastizales abiertos, cultivos de cereal o matorral mediterráneo".* Las especias arbóreas de las zonas forestales de Extremadura son principalmente: encinas (*Quercus rotundifolia*), alcornoques (*Quercus suber*), robles melojos (*Quercus pyrenaica*), castaño dulce (*Castanea sativa*) y pinos (*Pinus pinaster* y *Pinus pinea*). El estrato arbustivo está compuesto por varias especies de hoja perenne, siendo las principales *Cistus ladanifer, Retama sphaerocarpa, Lavandula stoechas, Thymus mastichina, Genista hirstuta, Phillyrea angustifolia, Erica arborea* y *Erica australis*, con especies de *Cytisus* en las cotas más altas (Devesa Alcaraz, 1995). Los pastos están compuestos por vegetación herbácea y son predominantemente acidófilos con fenología primaveral. En las zonas forestales, también abundan otras coberturas como los afloramientos rocosos y el suelo desnudo, que son en su mayoría, impermeables.

En segundo lugar, las zonas agrícolas de Extremadura, que representan el 32% de la región, pueden dividirse en zonas de secano y de regadío. Los cultivos de secano son principalmente el olivo y el viñedo y los cultivos anuales de invierno como la avena, el trigo y la cebada. Mencionamos también los cerezos típicos del valle del Jerte en el noroeste de la provincia de Cáceres. Los cultivos de regadío incluyen cultivos de verano como el maíz, el tomate, el arroz, el tabaco y los árboles frutales.

Por último, encontramos otras coberturas como las masas de agua, que incluye a los ríos, embalses y pequeñas charcas para el ganado, y otras superficies impermeables como las zonas urbanas y carreteras.

2. Resultados y Discusión

2.1. Resumen de la P1 sobre la variabilidad en la escorrentía estimada en una zona forestal en función de las fuentes de datos cartográficas

Esta publicación se elaboró en la primera fase de la tesis y se basa en parte de los resultados de la investigación desarrollada en el Máster Universitario en Investigación en Ingeniería y Arquitectura. Especialidad Ingeniería Gráfica y Construcción que dio origen a la elaboración de la presente Tesis Doctoral (Fragoso-Campón, 2015).

2.1.1. Resumen

El objetivo de este estudio fue el de analizar las variaciones en los valores del CN en una cuenca forestal, derivados de cuatro fuentes de datos cartográficas oficiales en España, y determinar cuál de ellas estima un volumen de escorrentía mas ajustado a los volúmenes de escorrentía observados. El ámbito del estudio fue una cuenca hidrográfica forestal situada en el oeste de España. Los resultados mostraron que ninguna de las fuentes cartográficas proporcionaba toda la información necesaria para determinar correctamente los valores de CN. La metodología propuesta basada en el factor de cabida cubierta de dosel arbóreo para determinar las características hidrológicas mejoró los resultados obtenidos, y como conclusión, se propuso que la estimación del valor de la CN en las zonas forestales se realice en función del factor de cabida cubierta y que deberían calibrarse a escala local.

2.1.2. Resultados y Discusión

La estimación del valor del CN fue distinta para cada fuente de datos considerada (Sistema de Información sobre Ocupación del Suelo de España -SIOSE, Mapa Forestal de España, Corine Land Cover y el Mapa de Cultivos y Aprovechamientos de España). Los valores del CN más representativos para las zonas forestales oscilaron entre 55 y 65, coincidiendo con los valores obtenidos por Choi et al. (2016) en cuencas forestales experimentales. Desde el punto de la coincidencia en la distribución espacial del CN, se observaron zonas en las que todos los mapas coincidían en el valor del CN propuesto, así como zonas en las que no se observaba ninguna coincidencia (Figura 3a). En término de los valores del CN se observaron diferencias superiores a más de 15 puntos que, en su mayoría, coincidían con las zonas en las que no había acuerdo entre las fuentes de datos (Figura 3b). La mayor

variación de CN se observó en las zonas clasificadas como bosque de matorral y pradera, donde ninguna de las fuentes cartográficas proporcionó los valores del factor de cabida cubierta.

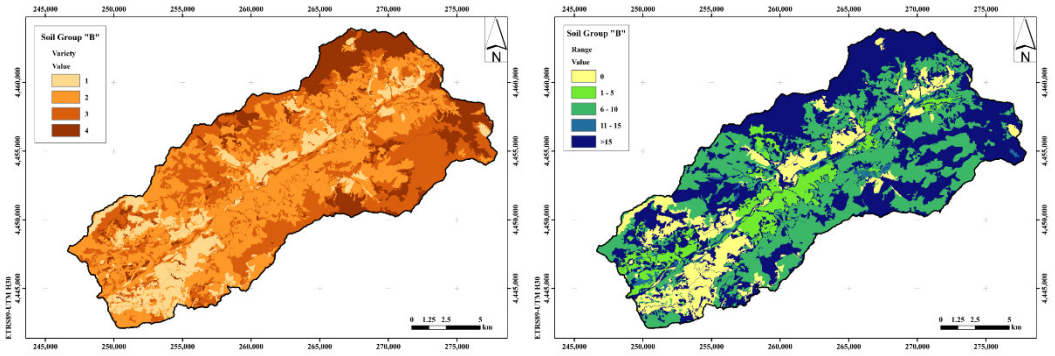

Figura 3. Resultados de la variación del CN para los cuatro mapas generados a partir de cada fuente de datos cartográficos: (a) Mapa de la variedad en los valores de CN obtenidos (b) Mapa del rango de variación en los valores de CN. Fuente: Figura 2 de la P1

De la comparativa de volúmenes de escorrentía estimados y observados, los mejores resultados fueron para el SIOSE y el Mapa Forestal de España. Además, la facilidad para obtener los datos del factor de cabida cubierta de arbolado del Mapa Forestal constituye un claro valor añadido para esta fuente de datos cartográficas. La metodología propuesta para la asignación de las características hidrológicas basada en el factor de cabida cubierta mejoró los resultados obtenidos, siendo necesaria su validación en otras tipologías de cuencas forestales.

2.2. Resumen de la P2 sobre el estudio de la fusión de datos LiDAR y series multitemporales de imágenes Sentinel-2 para la elaboración de cartografía de cobertura vegetal a escala de la cuenca hidrográfica

2.2.1. Resumen

En las cuencas hidrográficas forestales, la densidad, la cubierta vegetal y su estructura vertical son factores cruciales para la gestión de las inundaciones, el manejo de los ecosistemas y el inventario forestal. Hoy en día, la producción de mapas de cobertura del suelo con alta exactitud se ha convertido en una realidad con la aplicación de técnicas de teledetección, pero a veces, no es tan fácil distinguir entre la vegetación del sotobosque y la del arbolado con sólo información espectral. El objetivo principal de este estudio fue analizar la mejora de la exactitud en la cartografía del dosel arbóreo y del sotobosque, a escala de cuenca hidrográfica, mediante la fusión de datos de series temporales estacionales y anuales de imágenes S2 complementadas con LiDAR de baja densidad e índices de suelo y vegetación. El área de estudio estaba compuesta por dos cuencas vecinas en la provincia de Badajoz (España). La exactitud de las clasificaciones de la cobertura del suelo se evaluó de dos maneras: primero, con las series temporales estacionales e índices de suelo-vegetación asociados; y segundo, para la serie temporal anual y los índices de suelo-vegetación asociados. A continuación, se incluyeron ambos análisis los datos LiDAR en base a una métrica booleana relativa a la altura. Los resultados obtenidos mostraron que la exactitud global era mejor con la evaluación anual cuando sólo se utilizaba la información espectral. Además, al incluir los datos LiDAR en la clasificación (fusión de datos), las exactitudes globales mejoraban mucho, especialmente en las estaciones de verano y otoño. Esta mejora puede ser importante en el análisis de la estructura de la vegetación y su distribución espacial, ya que es decisiva para la gestión del ecosistema de la cuenca.

2.2.2. Esquema metodológico

La Figura 4 muestra el esquema metodológico planteado para analizar la mejora de la exactitud en la cartografía en los distintos estratos de vegetación a escala de cuenca hidrográfica mediante la fusión de datos de series temporales estacionales y anuales de imágenes Sentinel-2 complementadas con datos LiDAR de baja densidad.

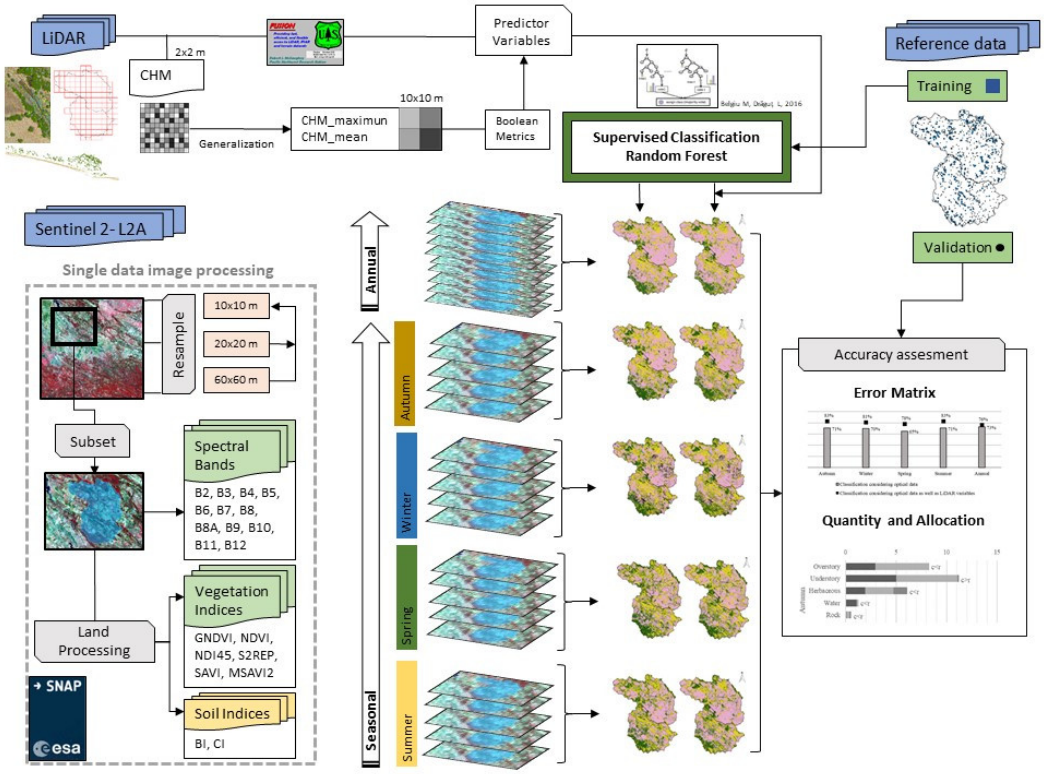

Figura 4. Esquema metodológico de la propuesto en el estudio de la fusión de datos LiDAR y series multitemporales de imágenes satelitales para la elaboración de cartografía de cobertura vegetal a escala de la cuenca hidrográfica. Fuente: Figura 2 de la P2.

2.2.3. Resultados y discusión

La Figura 5 muestra los valores de las exactitudes globales (*Overall Accuracy* - OA) para todos los casos analizados. Se puede observar como, cuando sólo se utilizaba la información espectral, la exactitud global era mejor con la evaluación anual. Sin embargo, si se incluían datos LiDAR en la clasificación (fusión de datos), las precisiones globales mejoraban en todos los casos, especialmente en las estaciones de verano y otoño

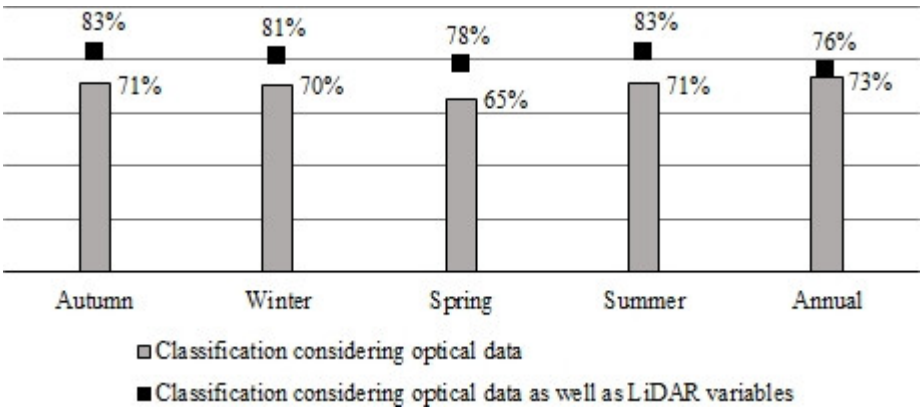

Figura 5. Exactitud global obtenidas en las distintas clasificaciones de la cobertura del suelo (Overall Accuracy - OA). Las columnas representan la OA obtenida para cada clasificación considerando los datos ópticos. Los marcadores negros representan la OA al considerar los datos ópticos así como las variables LiDAR. Fuente: Figura 8 de la P2

Al considerar exclusivamente los datos ópticos, la clasificación anual fue la que obtuvo la mejor exactitud (OA= 73%), estando en consonancia con los resultados obtenidos en Gebhardt et al. (2014), que oscilaban entre el 70% y el 77% en su análisis multitemporal de las imágenes Landsat, y con los obtenidos en Zhao et al. (2016), donde el valor de la OA oscilaba entre el 73% y el 80% con la fusión de los datos multi-estacionales de Landsat.

Por otro lado, cuando se incluyeron los datos LiDAR, la exactitud global mejoró mucho, sobre todo en al análisis estacional, de forma similar a la de otros estudios anteriores (Ahmed et al., 2015, Erdody and Moskal, 2010). Los mejores resultados se obtuvieron para el verano y el otoño (OA= 83%). Este valor resultó ligeramente inferior a los resultados obtenidos en Sánchez Sánchez et al. (2018) donde el OA alcanzó el 88% utilizando imágenes Sentinel-2 y datos LiDAR-PNOA, como en este trabajo. Por otro lado, los resultados fueron inferiores a los de García et al. (2011) del 94%, pero en este caso, el vuelo LiDAR tenía mejor densidad de puntos (1,5-6 puntos/m^2 superior a la disponible y considerada en este trabajo de 0,5 puntos/m^2), además, en su análisis se utilizó con una imagen multiespectral de alta resolución espacial de 2 m, mejor la resolución espacial de Sentinel-2 de 10 m utilizada en este estudio.

La Figura 6 muestra los resultados obtenidos para el análisis anual. En cuanto a la evaluación estacional, los mejores resultados alcanzados en verano-otoño se deben fenología de la vegetación que, en el entorno Mediterráneo, muestra la mejor separabilidad espectral en estas fases fenológicas de menos vigorosidad en las plantas. En este sentido, otros estudios como Godinho et al. (2016a), Godinho et al.

(2017) y Sánchez Sánchez et al. (2018) seleccionaron la fecha de la imagen a utilizar siguiendo bajo este criterio.

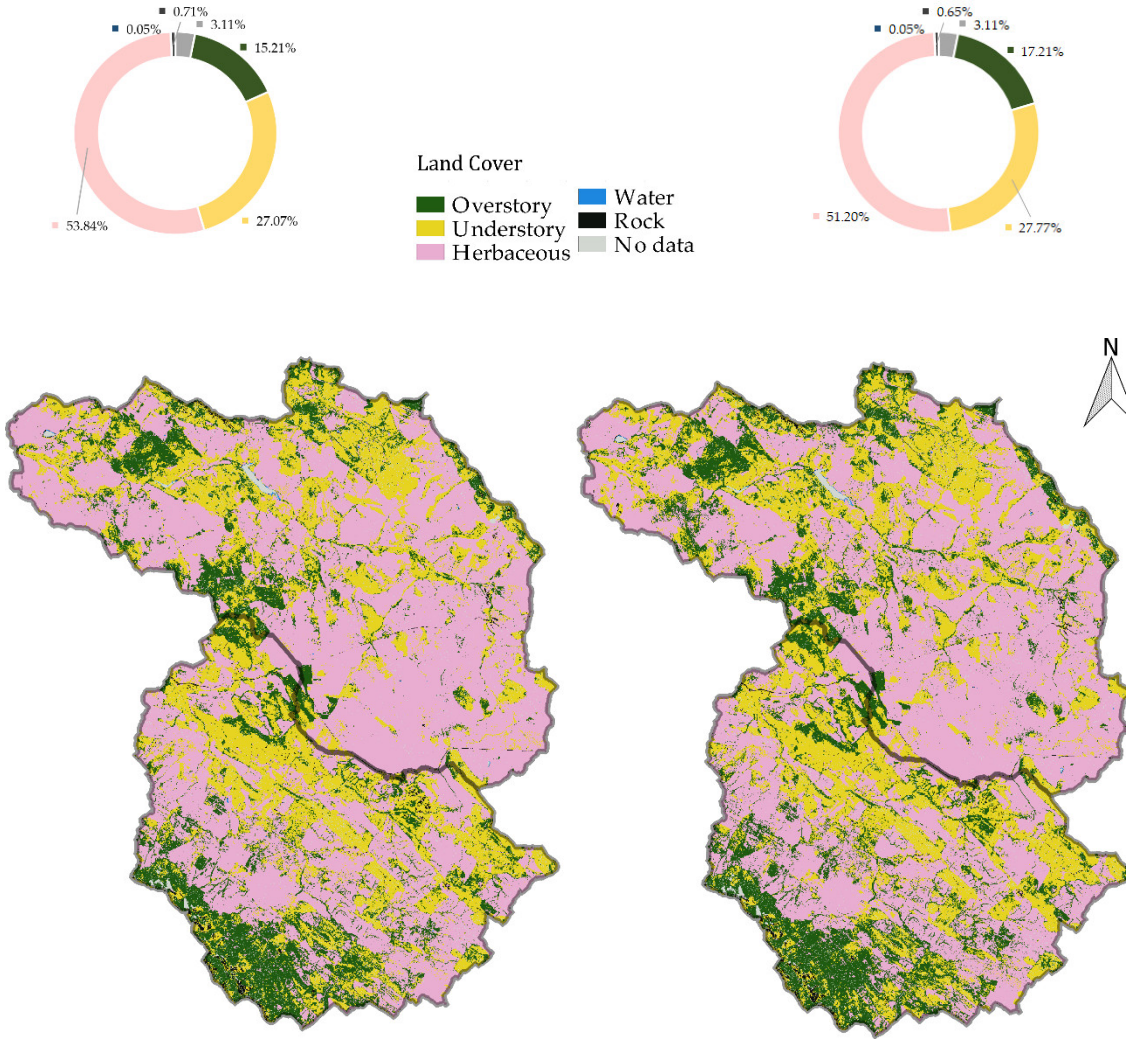

Figura 6. Mapa de coberturas del suelo obtenido a partir del análisis anual considerando (a) datos ópticos y (b) considerando los datos ópticos, así como las variables LiDAR. Fuente: Figura 7 de la P2

En relación con la importancia de los predictores, las bandas del espectro del infrarrojo cercano (NIR) resultaron ser las mas significativas en el escenario de datos ópticos, si bien, en el escenario que consideraron las métricas LiDAR, éstas fueron los predictores más importantes, junto con las NIR y las bandas del infrarrojo de longitud de onda corta (SWIR) B11 y B12 y el índice de color (CI) del suelo.

En cuanto a las exactitudes del usuario (Tabla 4) y productor (Tabla 5), los mejores resultados se obtuvieron al considerar los datos LiDAR. Para los estratos superiores del dosel arbóreo, los mejores valores de usuario oscilaron entre el 72% (primavera) y el 85% (otoño), y en el caso del sotobosque, estos valores oscilaron entre el 64% (invierno y primavera) y el 70-71% (verano-otoño). En el caso de la exactitud del productor las exactitudes obtenidas para el sotobosque del 86 %, resultaron superiores a los valores obtenidos para el dosel arbóreo del 80 %, ambos en el mejor análisis estacional correspondiente al verano.

Tabla 4. Exactitudes del Usuario (Fuente: Tabla2 de la P2)

	Classification considering optical data					Classification considering optical data as well as LiDAR variables				
	Au	Wi	Sp	Su	An	Au	Wi	Sp	Su	An
Overstory	60%	61%	54%	60%	69%	85%	82%	72%	84%	76%
Understory	54%	54%	48%	54%	59%	71%	68%	64%	70%	64%
Herbaceous	96%	97%	96%	96%	95%	96%	95%	96%	96%	96%
Water	67%	100%	100%	100%	100%	69%	100%	100%	100%	100%
Rock	62%	36%	100%	93%	100%	75%	57%	100%	94%	95%

Au: Autumn; Wi: Winter; Sp: Spring; Su: Summer; An: Annual

Tabla 5. Exactitudes del Productor (Fuente: Tabla3 de la P2)

	Classification considering optical data					Classification considering optical data as well as LiDAR variables				
	Au	Wi	Sp	Su	An	Au	Wi	Sp	Su	An
Overstory	51%	46%	58%	61%	49%	73%	68%	75%	80%	63%
Understory	74%	77%	69%	71%	81%	87%	80%	75%	86%	77%
Herbaceous	79%	76%	69%	80%	90%	88%	88%	85%	88%	85%
Water	50%	70%	15%	15%	40%	45%	70%	15%	10%	10%
Rock	90%	80%	75%	70%	89%	90%	85%	80%	80%	90%

Au: Autumn; Wi: Winter; Sp: Spring; Su: Summer; An: Annual

En cuanto a la evaluación los errores de cantidad (*Quantity*), y de asignación (*Allocation*), los resultados obtenidos, al considerar tanto los datos ópticos como las variables LiDAR, fueron mejores que los obtenidos por otros trabajos anteriores (Zhou et al., 2014, Gao et al., 2011) En particular, el sotobosque y herbáceas están ambas por debajo del límite del umbral booleano establecido, por lo que las variables LiDAR, a pesar de haber mejorado mucho la exactitud de la clasificación, no eliminó toda la confusión entre clases.

Por tanto, nuestros resultados apoyan las conclusiones de González-Ferreiro et al. (2012), quienes consideraron los datos LiDAR-PNOA del Instituto Geográfico Nacional de España como una buena fuente de información para la gestión forestal. Además, aunque las actualizaciones de los datos LiDAR-PNOA no son tan frecuentes como se desearía, es posible minimizar los efectos del desfase temporal en las alturas de la vegetación, ya que, aunque la evolución de la vegetación no pueda ser despreciada en el periodo de desfase entre los datos LiDAR y la adquisición de las imágenes del satélite, la falta de información precisa sobre la altura de la vegetación puede ser neutralizada aplicando los valores métricos Booleanos LiDAR como se propone en este trabajo. Sin embargo, la principal limitación de este método es que estos valores sólo podrían aplicarse para separar la vegetación alta de la baja, y probablemente no podría utilizarse para estimar valores precisos de la estructura del bosque o la evaluación de la biomasa.

Reflexión final

Tras finalizar esta fase de los trabajos surgió uno de los principales escollos de la propuesta metodológica inicial: la desactualización de los datos LiDAR respecto de la fecha de captura de las imágenes del satélite. Los datos LiDAR disponibles al inicio de los trabajos de la tesis, los utilizados en esta publicación, corresponden a la primera cobertura de 2010. La metodología propuesta en esta publicación solventa este desfase temporal mediante el uso de una métrica booleana. Esto fue posible ya que el paisaje en la zona estudiada es estable y, para la mayoría de las situaciones, se puede suponer que sólo se han producido cambios fenológicos en el tiempo transcurrido entre el vuelo LiDAR y la fecha de captura de las imágenes Sentinel. Las áreas de entrenamiento se identificaron por fotointerpretación sobre la ortofoto del PNOA, y para garantizar que estas áreas representaran a las mismas coberturas en todas las fechas, se comprobó de manera visual, sobre la serie temporal de imágenes del PNOA, que las áreas de entrenamiento no habían sufrido cambios significativos en el intervalo entre los datos LiDAR y las imágenes Sentinel. Así pues, se verificaron las áreas de entrenamiento sobre imágenes del PNOA de 2009, 2011 y 2016.

Sin embargo, considerando el tiempo y esfuerzo requerido, tanto en la verificación de las áreas de entrenamiento, como del tiempo de procesamiento requerido de los datos LiDAR para toda la extensión de las cuencas en estudio (13 592 hojas LAS en todo él ámbito de estudio de la P4 frente a las 116 usadas en este trabajo), y considerando los plazos previstos por el proyecto LiDAR-PNOA, se consideró que lo ideal hubiese sido haber podido procesar, en todo el ámbito de estudio, la segunda cobertura del vuelo LiDAR. Los datos de la segunda cobertura fueron adquiridos durante 2018, y por lo tanto están en la misma ventana temporal que las imágenes S2, y además, cuentan con una densidad de puntos (1-2 puntos/m^2) superior a la de

la primera cobertura (0,5 puntos/m^2). Sin embargo, la segunda cobertura en el ámbito de la provincia de Cáceres (lote EXT N) y suroeste de Castilla La Mancha (lote CLM SW), cuya actualización estaba prevista a finales del 2019, se fue demorando en el tiempo y, a fecha de redacción del presente documento, sigue sin estar disponible. Por este motivo, se replanteó la propuesta metodológica para buscar alternativas en el estudio de la estructura vertical de vegetación tal y como se expone en la siguiente sección (P5).

2.3. Resumen de la P5 sobre el estudio de la capacidad de datos GEDI para el análisis de altura de vegetación en los estratos inferiores.

Este trabajo surge de la necesidad de buscar una fuente de datos alternativa en el análisis de las alturas de vegetación debido a retrasos en la actualización de la segunda cobertura del vuelo LiDAR-PNOA en la provincia de Cáceres y zona suroeste de Castilla la Mancha. En este sentido, aprovechando el lanzamiento de la misión *The Global Ecosystem Dynamics Investigation* (GEDI) en 2018, investigamos la posibilidad de aplicar estos datos para conocer la estructura vertical de la vegetación, en distintos entornos como los pastizales, la dehesa, o bosques.

Los resultados expuestos en esta sección se recogen en la P5, si bien, ésta contempla unos objetivos más extensos, a continuación, resumimos exclusivamente los aspectos directamente relacionados con el objeto de la Tesis.

2.3.1. Resumen extenso

El sensor LiDAR espacial *Global Ecosystem Dynamics Investigation* (GEDI), lanzado el 5 de diciembre de 2018 por la NASA, es un sistema para medir la superficie terrestre y proporcionar un mapa de biomasa con una resolución espacial de 1 km (Schneider et al., 2020). Se prevé que la misión GEDI, que estará operativa durante al menos dos años, recoja aproximadamente 10.000 millones de observaciones de la superficie terrestre sin nubes. El objetivo de la misión GEDI es proporcionar datos para estudiar las estructuras y la biomasa de los bosques en entornos tropicales y templados de entre 51,6° norte y sur, siguiendo la trayectoria de la estación espacial internacional (Dubayah et al., 2020).

El instrumento GEDI, tal y como se muestra en la Figura 7, se compone de 3 láseres geodésicos, que se interpolan ópticamente para formar 8 pistas de huellas paralelas. Estas pistas paralelas están espaciadas 600 m en la dirección del eje de vuelo, dejando una distancia de 4,2 km entre la primera y la última pista. Cada láser dispara 242 veces por segundo, creando una huella de 25 m de diámetro en la superficie terrestre, y sobre la que se mide la estructura 3D. El borde de cada huella está separado 35 m del siguiente o, lo que es lo mismo, los centros de las huellas están separados 60 m (Dubayah et al., 2020, Duncanson et al., 2020).

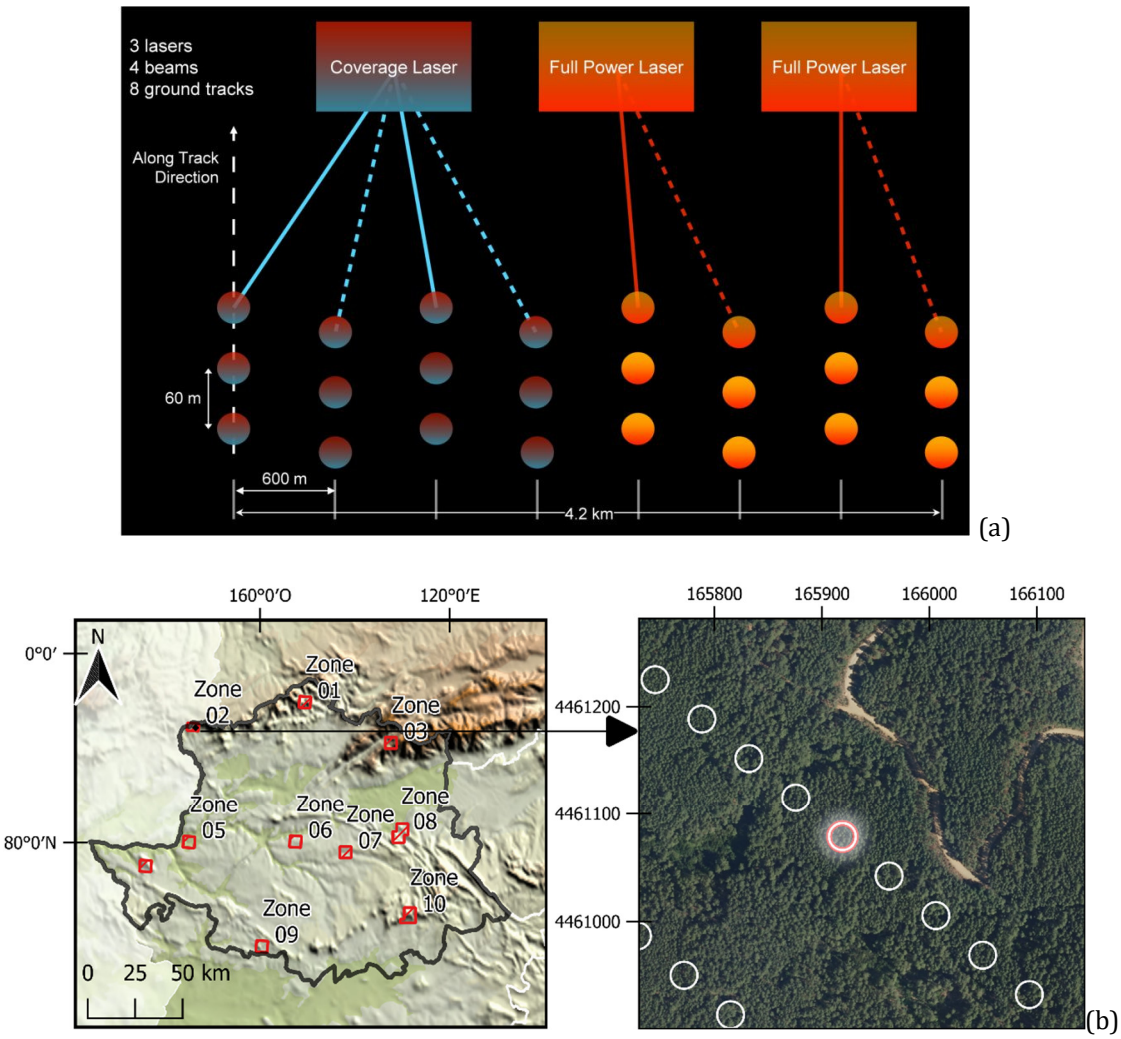

Figura 7. Esquema de la toma de datos del GEDI (a) Disposición del sistema de medida (Fuente: https://gedi.umd.edu/) y (b) ejemplo de las alineaciones en la zona de muestreo de este estudio.

El GEDI proporciona datos en varios niveles para cada huella, que pueden descargarse gratuitamente de la plataforma EarthData de la NASA (Dubayah et al., 2020). Los datos del GEDI se utilizan para múltiples propósitos como, modelar los procesos del ecosistema forestal (Sanchez-Lopez et al., 2020), estimar la biomasa (Duncanson et al., 2020, Qi et al., 2019b) o, estimar la altura del bosque (Qi et al., 2019a).

El mayor inconveniente de los datos del GEDI es su reciente lanzamiento, existiendo áreas todavía sin cobertura, y allá donde existen, son datos discretos, tal y como se ha indicado anteriormente (Figura 7), pero, aun así, es posible salvar estas limitaciones, realizando una extrapolación de la información de alturas de vegetación del GEDI utilizando imágenes multiespectrales (Potapov et al., 2021, Lang et al., 2019).

No obstante, antes de realizar cualquier interpolación de alturas de vegetación, y su posible fusión con las imágenes Sentinel, es necesario evaluar específicamente la exactitud con la que los datos GEDI mide las alturas de vegetación en el ámbito de estudio de la Tesis, cuyas zonas forestales están compuesta mayoritariamente por sistemas agroforestales de dehesas, bosques y vegetación esclerófila.

Para la elaboración de este trabajo se han utilizado los datos GEDI Level 2A en la zona de estudio que han sido procesados con el paquete *rGEDI* de R Software (Silva et al., 2020). En primer lugar, los datos se filtraron, descartando todas las huellas con indicadores de calidad no válidos, y finalmente, la posición espacial de las huellas se exportó a formato *shapefile* para su análisis en el software GIS. Como resultado, se utilizaron en el análisis de alturas un total de 12 031 huellas. Tras dicho procesado se obtiene, para cada huella, datos referentes a métricas de calidad, cota media del suelo y alturas de vegetación relativas (RH) como se muestra en la Figura 8.

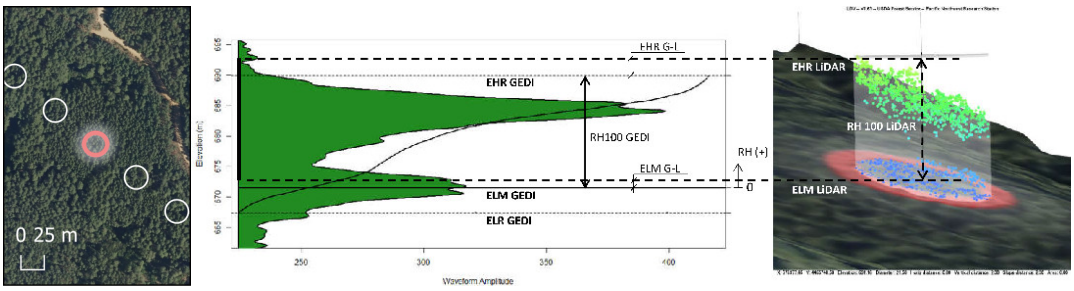

Figura 8. Interpretación de los datos GEDI. Fuente: Figura 2 de la P5

Para poder evaluar la exactitud de los datos capturados por el GEDI, descartamos la primera cobertura del proyecto LiDAR-PNOA por el desase de tiempo entre la adquisición de datos, pero, aunque a fecha de elaboración del estudio, no estaban todavía publicados, se solicitó permiso para poder comparar los datos GEDI con la versión actualizada de la segunda cobertura de los datos LiDAR-PNOA, que fueron finalmente facilitados por la Junta de Extremadura exclusivamente en el ámbito específico de las zonas estudiadas.

2.3.2. Resultados y discusión

Los datos LiDAR se procesaron con el software FUSION (McGaughey, 2009). En primer lugar, con la herramienta *GroundFilter* se filtró la nube de retornos LiDAR para identificar los retornos que se forman la superficie del terreno (McGaugheey, 2020), después, utilizando la herramienta *GridSurfaceCreate*, que calcula las elevaciones de las celdas utilizando la elevación media de todos los puntos dentro de una celda, se generó el modelo digital de elevaciones (*Digital Elevation Model* - DEM). En segundo lugar, se generó el modelo digital de superficie (*Digital Surface Model* - DSM) utilizando la herramienta *CanopyModel*, que crea un modelo de superficie asignando a cada píxel la máxima elevación todos los puntos dentro de la celda. Por último, se calculó el porcentaje de cabida cubierta de la vegetación (*Canopy Cover Model* - CCM), mediante la herramienta *Cover*. estableciendo un valor umbral de altura de 1 m por encima del suelo. Los DEM, DSM y CCM se generaron con una resolución espacial de 2 m.

Finalmente, se obtuvieron las estadísticas zonales de los datos LiDAR (DEM, DSM y CCM) en cada huella GEDI, y se calcularon las siguientes diferencias de alturas:

- ELM G-L: la diferencia en la elevación media del suelo en la huella entre los datos GEDI y LiDAR.

- EHR G-L: la diferencia en el mayor retorno detectado en la huella entre los datos GEDI y LiDAR.

- RH100 G-L: la diferencia de elevación entre el mayor retorno detectado y la elevación media del suelo en la huella entre los datos GEDI y LiDAR.

El análisis estadístico se realizó utilizando el software R (R-Core-Team, 2018) desde el punto de vista global y también por rangos de cobertura. La Figura 9 muestra la correlación entre las elevaciones y las diferencias de altura, observando una alta correlación en las elevaciones ELM y EHR. Sin embargo, desde el punto de vista de los valores de RH100, los resultados son más dispersos. Centrándonos en este último caso, el RMSE global obtenido para RH100 es de 3,56 m pero, si analizamos los resultados considerando los distintos estratos estudiados, vemos que los peores resultados se obtienen para alturas de vegetación inferiores a 1 m (RMSE = 4,41 m), seguidos del tramo con alturas entre 1 y 3 m (RMSE = 3,69m). Los mejores resultados son para el dosel arbóreo, con alturas superiores a 3 m (RMSE =3,53 m).

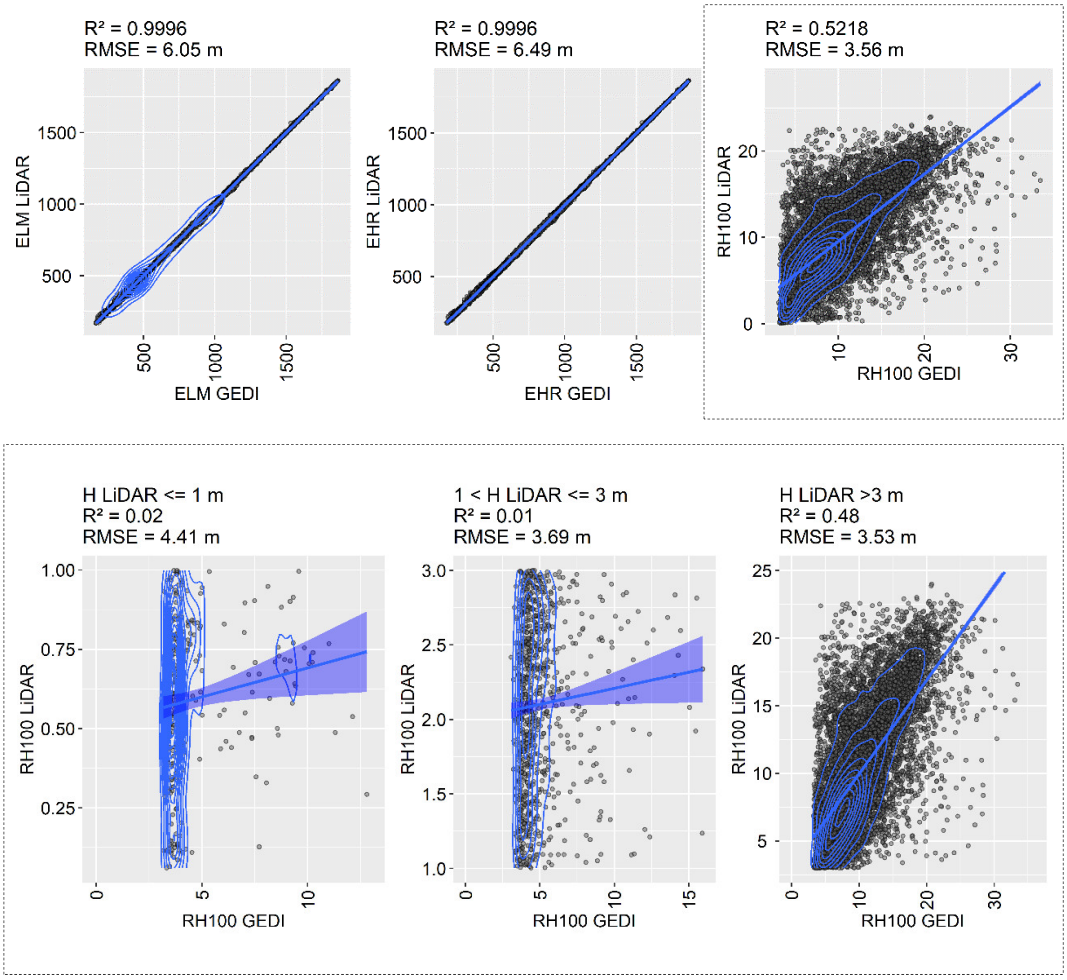

Figura 9. Resultados de la comparación del GEDI y LiDAR. Fuente: adaptación de la Figura 5 de la P5.

La Figura 10 muestra la comparativa de los valores en términos de RH100 G-L en los distintos rangos de cobertura considerados. Para los dos estratos de vegetación inferiores a 3 m, las diferencias entre los datos GEDI y LiDAR son positivas, es decir, que los datos captados por el GEDI son de mayor altura que los medidos por el LiDAR, por el contrario, a partir de una cobertura del 20%, la diferencias entre los datos comienza a ser negativa, es decir, la estimación en altura del GEDI es menor que la registrada por el LiDAR.

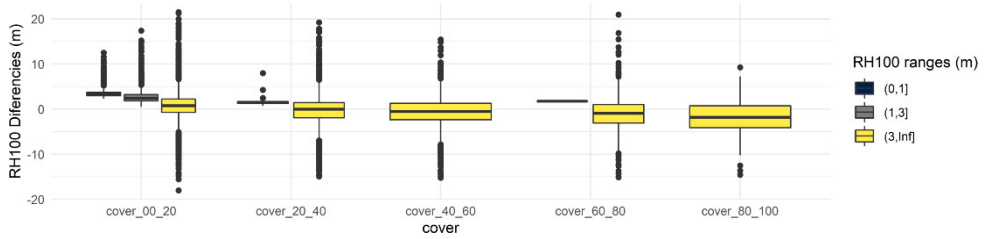

Figura 10. Diferencias en los valores RH100 entre los datos GEDI y LiDAR para cada rango de altura de vegetación y porcentaje de cabida cubierta de la vegetación. Fuente: adaptación de la Figura 11 de la P5.

En los resultados globales de RH100 (RMSE = 3,56 m) son del mismo orden que los obtenidos por Qi and Dubayah (2016).Del mismo modo, Hancock et al. (2019) evaluaron las diferencias en las métricas RH2, RH5, RH25, RH50, RH75 y RH98 del GEDI en comparación con los conjuntos de datos ALS y obtuvieron RMSE de aproximadamente 4,7-5,7 m. Healey et al. (2020) también realizaron predicciones de RH98 obteniendo RMSE que van de 7,08 m a 9,2 m y valores de IQR de 6,89-11,19 m. Nuestros resultados generales muestran un IQR general significativamente mejor de 3,50 m para las diferencias de RH100 y valores que van de 2,15 m a 4,04 m. Considerando tipología de vegetación, el error para vegetación inferior a 1 m (RMSE = 4,41 m) es del mismo orden de magnitud que el obtenido por Healey et al. (2020) quienes lograron un RMSE mínimo de 4,50 m para los pastizales.

Los resultados globales de este trabajo muestran diferencias de elevación de los datos GEDI en relación con otras fuentes de datos (LiDAR), y si bien, los resultados obtenidos concuerdan con otros estudios previos, las diferencias pueden ser o no importantes en función de la escala del trabajo y de la exactitud de la cartografía forestal requerida. En el caso especifico de esta Tesis, los pobres resultados obtenidos en los estratos inferiores, en términos de RMSE, hacen inviable su utilización para la extrapolación de los resultados GEDI, a una cobertura continua de alturas de vegetación.

2.4. Resumen de la P3 sobre el desarrollo de una metodología para generar áreas de entrenamiento utilizando imágenes de ultra alta resolución espacial.

2.4.1. Resumen

En este estudio se propuso una metodología para generar cartografía detallada de los usos del suelo y la vegetación en un entorno de dehesa utilizando imágenes PNOA de ultra alta resolución espacial de 0,25 m con una resolución espectral de cuatro bandas, tres en el espectro visible y una en el infrarrojo cercano (NIR). Las categorías de cobertura del suelo se definieron según la capacidad de generación de escorrentía en dos niveles de desagregación: diferenciando entre especies (nivel de macroclase) y diferenciando clases dentro de una misma especie (nivel de clase). Además, el método se planteó para reducir las campañas de campo y el trabajo manual de fotointerpretación mediante la transferencia de los clasificadores entrenados con un grupo de imágenes (grupo de entrenamiento) a imágenes vecinas (grupo de validación). Los resultados obtenidos en el grupo de entrenamiento fueron notablemente altos, alcanzando una exactitud global del 91,6% a nivel de clase y del 95,8% a nivel de macroclase. Los resultados del grupo de validación, aunque menores, también fueron elevados, con una exactitud global del 78,3% a nivel de clase y del 86,3% a nivel de macroclase. En cuanto a los predictores más importantes, destacamos la banda azul, el índice de color del suelo y las características de textura que tuvieron una gran influencia en la discriminación de especies, especialmente dentro de las especies de arbustos en entornos de dehesa. Finalmente, se evaluó la capacidad potencial de las distintas clases para generar escorrentía comparándose los resultados con los obtenidos a partir de una cartografía global. Los resultados obtenidos destacaron la importancia de disponer de cartografía detallada en estudios regionales ya que el uso de cartografía global llevó a subestimar la escorrentía potencial en la cubierta del suelo más representativa en el entorno de la dehesa.

2.4.2. Esquema metodológico

La Figura 11 muestra esquema metodológico planteado para realizar la clasificación de imágenes de ultra alta resolución espacial y la transferencia de los clasificadores entrenados en un grupo de imágenes (grupo de entrenamiento) a imágenes vecinas (grupo de validación).

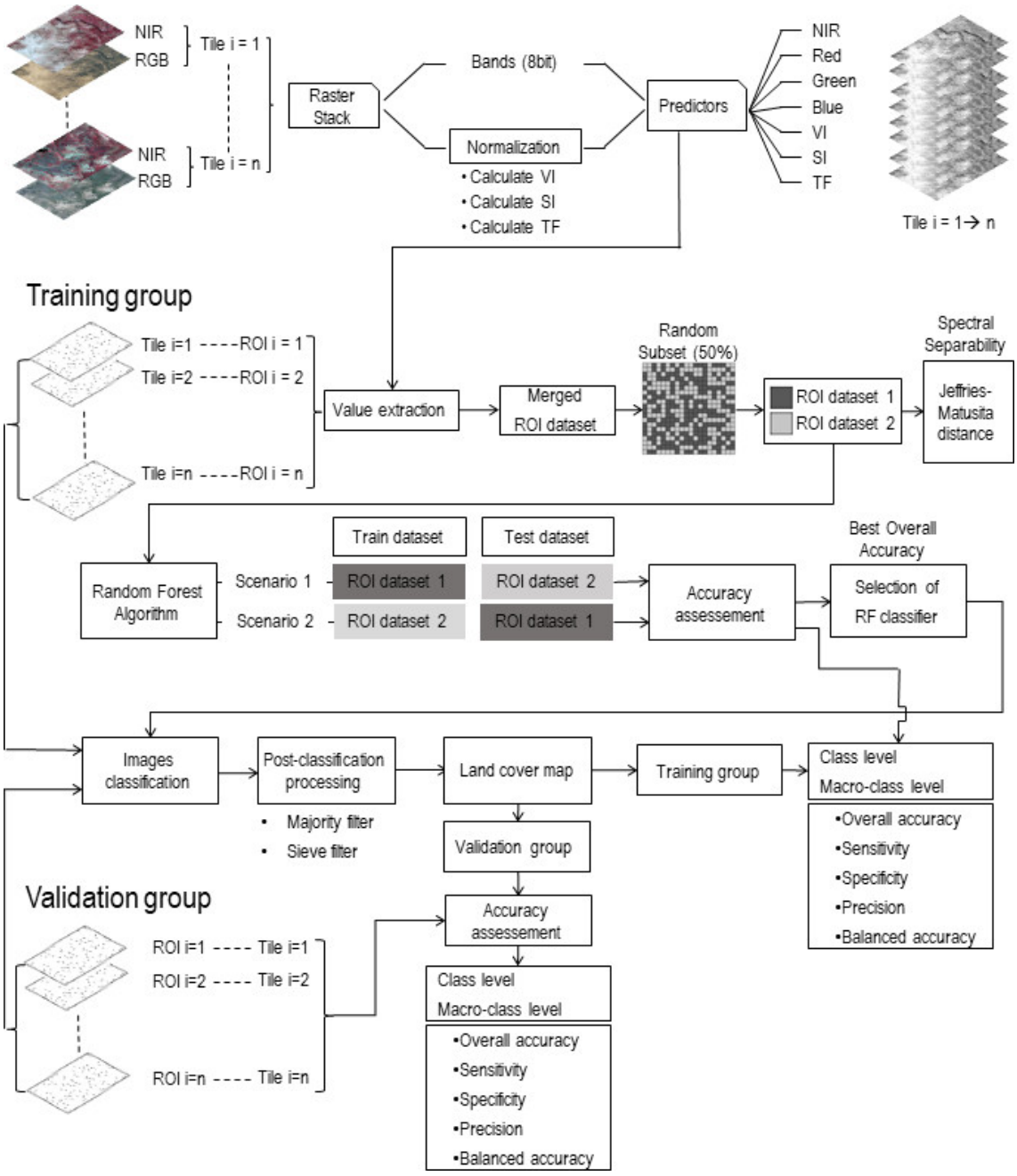

Figura 11. Esquema metodológico propuesto para la clasificación de imágenes de ultra alta resolución espacial. Fuente: Figura 4 de la P3.

La Tabla 6 muestra la nomenclatura de las categorías analizadas en este trabajo agrupadas en los dos niveles de desagregación considerados: clases y macro-clases.

Tabla 6. Nomenclatura de las categorías estudiadas (Fuente: Tabla 3 de la P3)

Stratum	Land cover type	Class-level categories	Runoff generation	Macro-class-level categories
Overstory	Holm Oaks (*Quercus rotundifolia*)	Qc		Quercus (Qc)
	Cork oaks (*Quercus suber*)			
	Pyrenean oaks (*Quercus pyrenaica*)			
Understory	Mixed shrubs (*Lavandula stoechas, Thymus mastichina, Genista hirsute, Phillyrea angustifolia, Erica arborea and Erica australis*)	Smix		Shrub (S)
	Retama sphaerocarpa	Sret		
	Cistus ladanifer	Scis		
	Pasture	P		Herbaceous plants (H)
	Dry agricultural land	L		
Non-vegetation	Bare soil	B		B
	Roads	Rd		Impervious (I)
	Rocky outcrops	Rk		
	Roofs of rural houses	U		
	Shadows	Sh	-	Sh
	Waterbodies	W	-	W
Capacity for run off generation legend:	 very high	 high	 medium	 low

2.4.3. Resultados y discusión

Importancia de los predictores en el algoritmo Random Forest

La Figura 12 representa la importancia de los predictores medidos en términos de la disminución de la exactitud del clasificador, cuando ese predictor se queda fuera de la selección de entrenamiento. Los valores más altos sugieren un papel más importante del predictor en el proceso de clasificación. Los predictores más influyentes fueron el CI, la banda azul, GLCMm y GLCMv, seguidos de la banda verde, BI y la banda NIR. El índice NDVI fue el menos influyente de todos los utilizados (Figura 12a). Además, la importancia de los predictores resultó distinta para de cada categoría (clase o macroclase) (Figura 12b), así se obtuvo que la banda azul tuvo una notable importancia para clasificar las especies de arbustos. El CI y GLCMm lo fueron para clasificar la vegetación herbácea y el CI fue el predictor más valioso en el caso de las superficies impermeables o sin vegetación en consonancia con otros trabajos previos como los de Richardson and Wiegand (1977) y Huete et al. (1984). La importancia de la banda azul y los rasgos de textura (GLCMm y GLCMv) están en concordancia con los resultados de Burnett et al. (2019) y teniendo en cuenta las fechas de adquisición de las imágenes, nuestros resultados también coinciden con los de Fang et al. (2018), que demostraron que las longitudes de onda azules estaban entre las variables más importantes durante la primavera y el verano.

En relación con el NDVI, que resultó ser poco importante, puede explicarse por el patrón fenológico estacional que se observa típicamente durante el inicio del verano en Extremadura (que es la fecha de adquisición de las imágenes), por el que el estrato herbáceo pierde su verdor y los arbustos de hoja perenne se vuelven menos vigorosos, y por tanto el CI y BI pasan a ser más efectivos para la discriminación entre categorías.

Figura 12. Importancia de los predictores en la clasificación mediante Random Forest (a) cómputo global (b) según las distintas categorías analizadas. Fuente: Figuras 9 y 10 de la P3.

Evaluación de la exactitud

Los valores de la exactitud global fueron más altos para análisis en términos de macro-clases (95,8 %) que para el análisis del nivel de clase (91,6 %), y los resultados del grupo de validación fueron inferiores a los del grupo de entrenamiento, los dos niveles de desagregación, macro-clases (86,3 %) y clases (78,3 %). Sin embargo, a pesar de estas diferencias, el rendimiento global del clasificador fue muy bueno en todas las métricas derivadas de las matrices de error (Figura 13a)

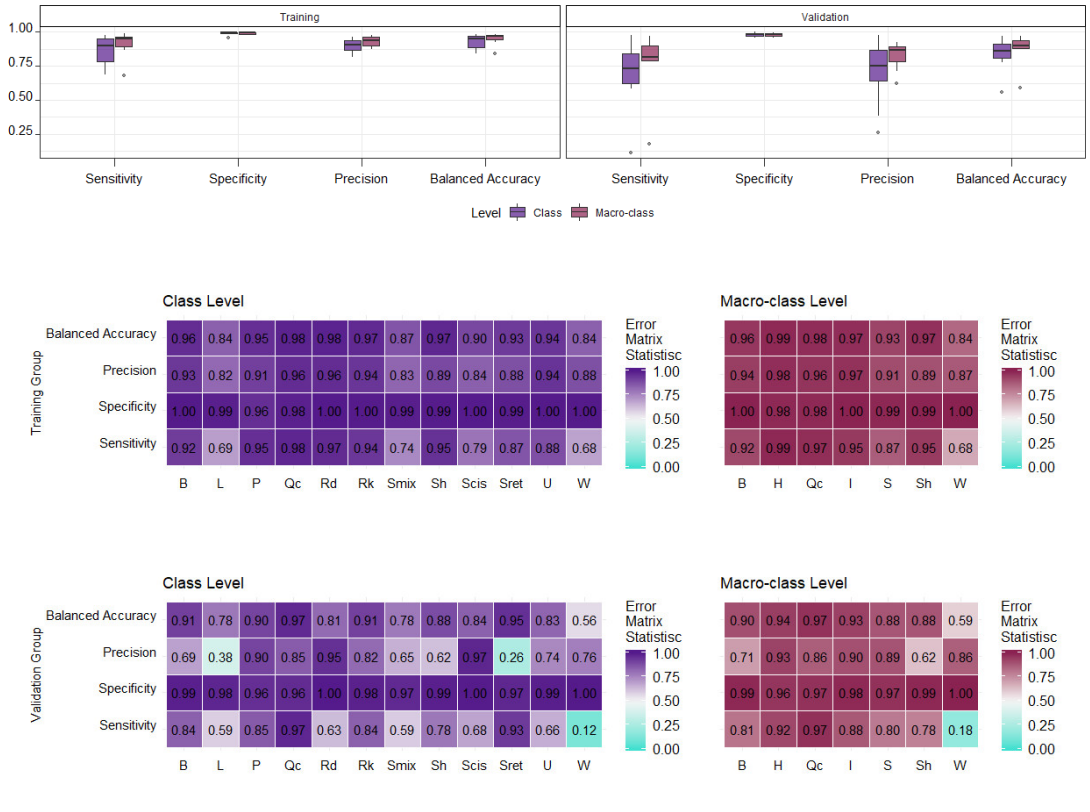

Figura 13. Resumen de los resultados derivados de las matrices de error del clasificador Random Forest (a) cómputo global (b) desagregación de resultados por clases y macro-clases en el grupo de entrenamiento (c) desagregación de resultados por clases y macro-clases en el grupo de validación Fuente: Figuras 11, 12 y 13 de la P3.

En el grupo de entrenamiento las métricas fueron muy altas (Figura 13b), especialmente para el dosel arbóreo Qc que obtuvo excelentes resultados, con una sensibilidad, especificidad y exactitud promediada de 0,98. Además, a nivel de macro-clase, se obtuvieron excelentes resultados para el estrato de arbustos, mostrando una sensibilidad de 0,80, una especificidad de 0,97 y una exactitud promediada de 0,88, mientras que a nivel de clases, los mejores resultados se observaron para Sret, seguido de Scis y Smix. En cuanto al estrato herbáceo, los resultados fueron excelentes a nivel de macroclase. Sin embargo, a nivel de clase, las estadísticas de la clase L fueron más pobres que las de la clase P. En concreto, L presentó unos valores de precisión y sensibilidad equilibrados de 0,84 y 0,69, respectivamente, mientras que P alcanzó un valor de 0,95 para ambos parámetros. Considerando las cubiertas no vegetales, los resultados fueron excelentes para B e I. También se obtuvieron buenos resultados al considerar la desagregación a nivel de clase en Rk, Rd y U. Sin embargo, los valores obtenidos para W fueron menos precisos, con una sensibilidad de 0,68 y una exactitud promediada de 0,84.

En cuanto al grupo de validación (Figura 13c), los valores fueron inferiores a los del grupo de entrenamiento, especialmente a nivel de clase, donde se observaron descensos significativos en la sensibilidad y la precisión. En términos de exactitud promediada, los resultados mostraron valores que van de 0,56 a 0,97 a nivel de clase y de 0,59 a 0,97 a nivel de macro-clase. Las clasificaciones de la vegetación siguieron siendo buenas para Qc, H y S. Por el contrario, para las clases no relacionadas con la vegetación, se observó una importante disminución de la exactitud obteniéndose el peor resultado para las masas de agua.

Los resultados obtenidos en la clasificación del dosel arbóreo son del mismo orden que los trabajos previos que utilizaron imágenes de alta resolución espacial (Boggs, 2010, Dalponte et al., 2014). En la clasificación del sotobosque, particularmente en la discriminación de las especies de arbustos, nuestros resultados fueron ligeramente mejores que los obtenidos en trabajos anteriores, a pesar de que nuestro trabajo utilizó imágenes de muy alta resolución espacial (Eroğlu et al., 2010, Malahlela et al., 2015, van Lier et al., 2009) y mejores que otros específicos del estrato arbustivo (Niphadkar et al., 2017). Respecto a los pobres resultados de las masas de agua, que corresponden a charcas para el ganado, los malos resultados son probablemente debidos a gran variabilidad de la respuesta espectral por la poca profundidad y la existencia de algas y lodos en suspensión que suelen estar presentes durante el periodo de adquisición de imágenes (junio). Además, aunque la exactitud de la clasificación de las masas de agua fue pobre, en nuestro caso concreto de estudio, dichas superficies sólo representaban el 0,5% del área estudiada, por lo que no tienen gran influencia en los resultados finales.

Mapas de usos de suelo

La Figura 14 representa algunos ejemplos de los resultados obtenidos para los tipos de cobertura del suelo más representativos del entorno de la dehesa a escala global de cada imagen PNOA clasificada para el caso del grupo de entrenamiento y la Figura 15 para el caso del grupo de validación. Por último, la Figura 16 muestra algunas áreas con más detalle de visualización.

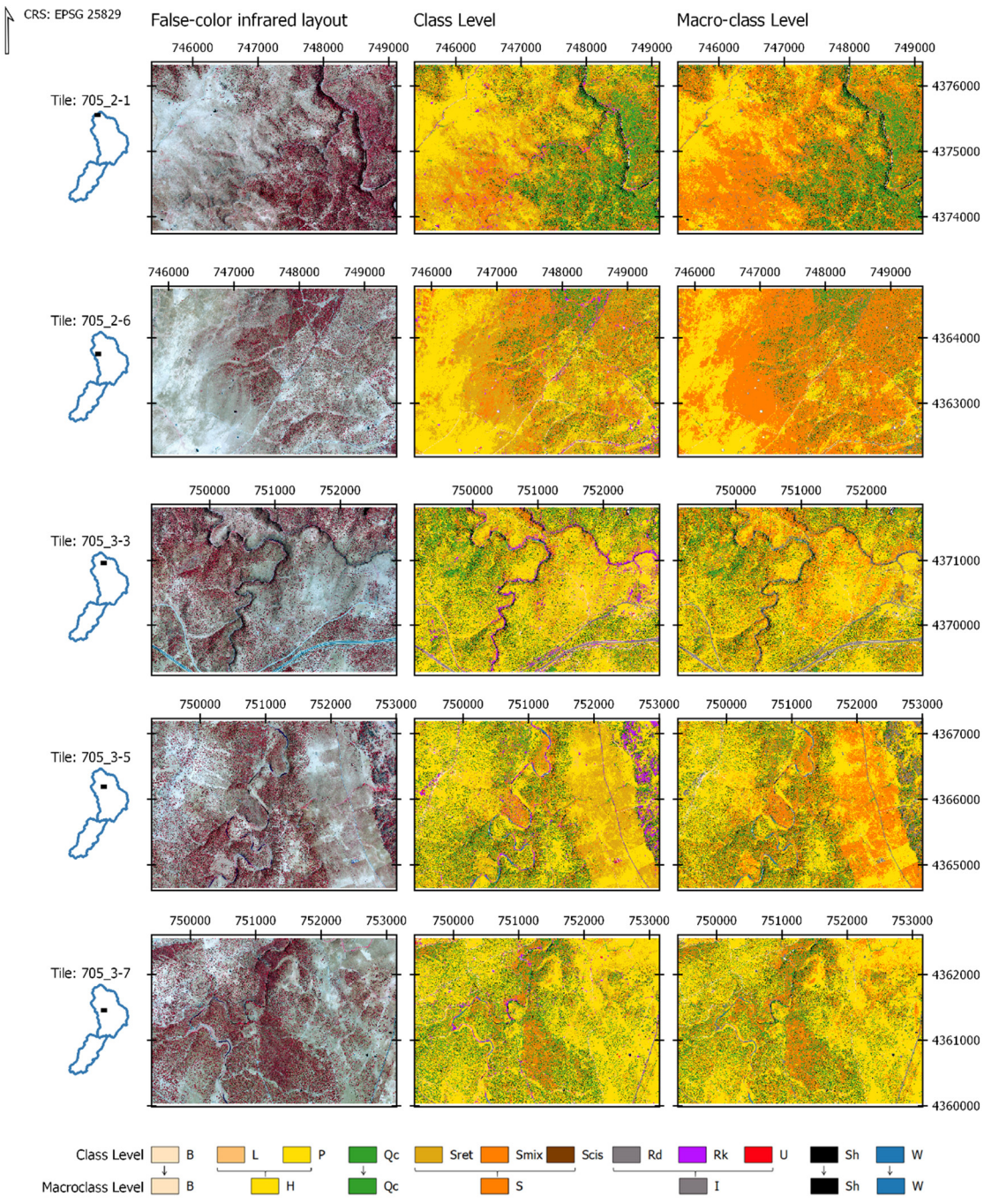

Figura 14. Mapas finales de la cobertura del suelo del entorno de la Dehesa en una selección de imágenes del grupo de entrenamiento. Fuente: Figura S2 de la P3.

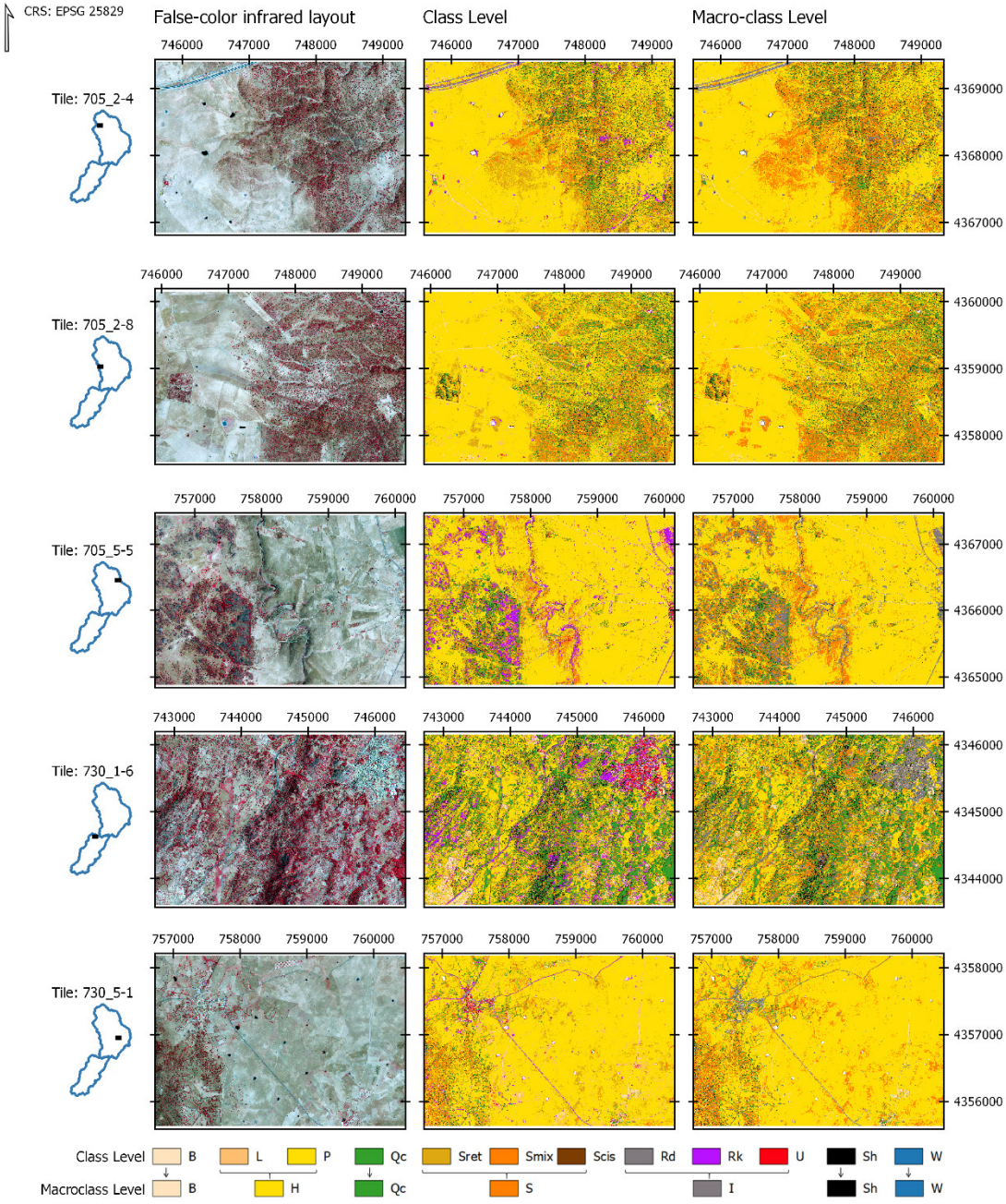

Figura 15. Mapas finales de la cobertura del suelo del entorno de la Dehesa en una selección de imágenes del grupo de validación. Fuente: Figura S6 de la P3.

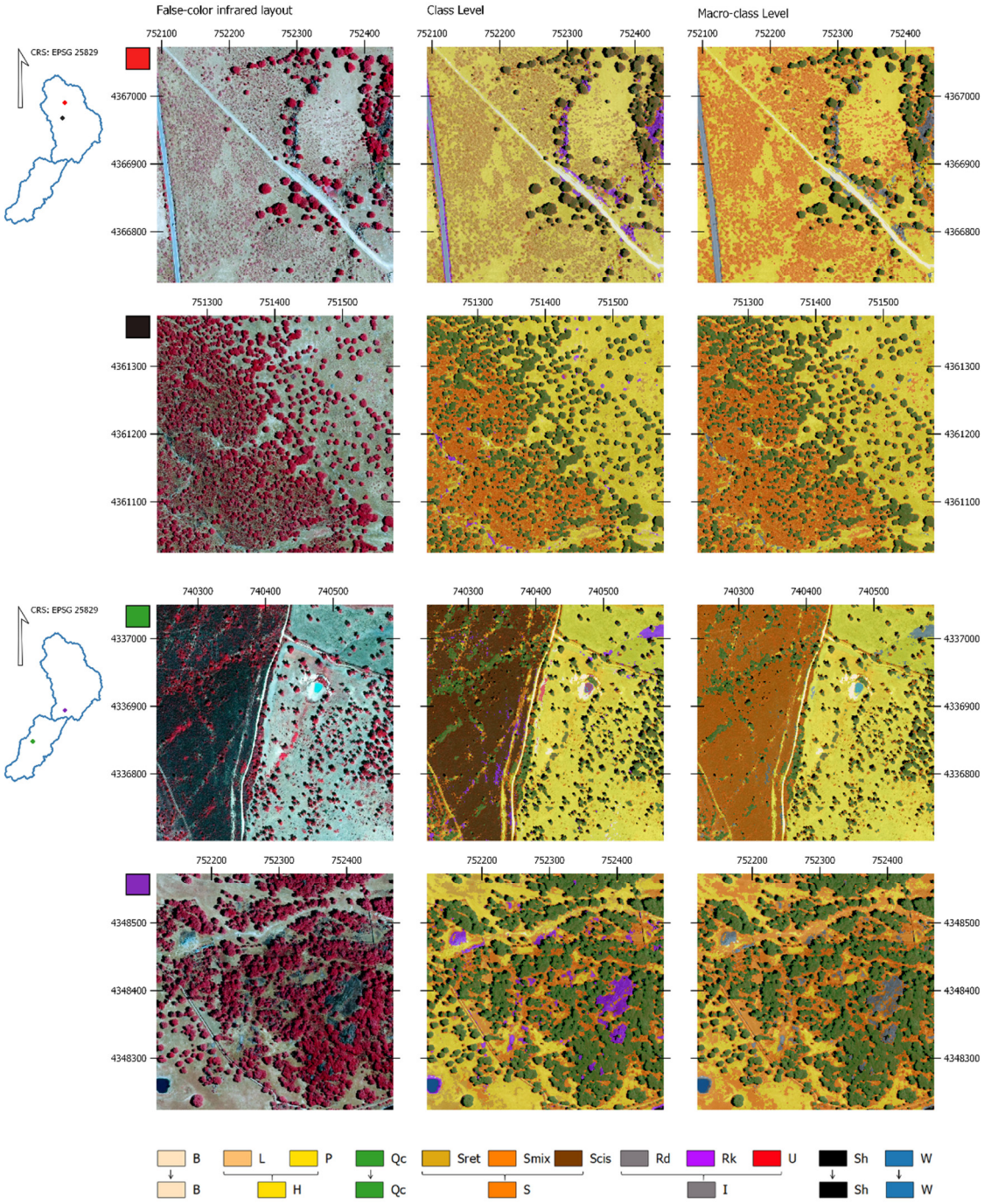

Figura 16. Detalle de los mapas finales de la cobertura del suelo del entorno de la Dehesa Fuente: Figura 15 de la P3.

Los mapas obtenidos y las excelentes exactitudes logradas en los principales tipos de cobertura del suelo representativos del entorno de la dehesa podrían ser muy útiles para calcular los parámetros dendométricos derivados de los árboles individuales, como el área de la copa y el diámetro de la copa, así como otras variables dasométricas relacionadas con el factor de cabida cubierta arbóreo y la densidad del arbolado. Cabe destacar que las especies arbustivas se clasificaron también buena exactitud, lo que permite estudiar la distribución espacial de los

arbustos y sus especies. Este estrato juega un papel crucial en la respuesta hidrológica del terreno, afectando a la productividad de los pastos y al crecimiento de los árboles (Pulido et al., 2010, Rivest et al., 2011), a la aparición de plantas aromáticas y medicinales y a la miel (Canteiro et al., 2011) y finalmente, pero no menos importante, la gestión del ecosistema de la dehesa (Caballero Díaz et al., 2015, Godinho et al., 2016b).

Influencia de la resolución espacial de los mapas de cobertura del suelo en los resultados de la escorrentía

A continuación, se muestran los mapas de la distribución espacial del CN obtenidos a partir de los mapas elaborados en este trabajo, comparándolos con los resultados procesados a partir de la cartografía del proyecto Corine Land Cover (CLC), representados en la misma extensión del territorio que en la sección anterior: en una selección de imágenes del grupo de entrenamiento (Figura 17), en una selección de imágenes del grupo de validación (Figura 18) y detalle de ciertas zonas (Figura 19). Mediante inspección visual ya aprecian diferencias y cómo la distribución espacial de los valores de CN depende de la resolución espacial de la fuente de datos de la cubierta del suelo.

Dado que estas diferencias en el valor del CN tienen un sentido físico, en la Figura 20 se representa si el desacuerdo entre los mapas significa sobreestimación o subestimación del valor del CN. En la Figura 20a, se observa como para valores de CLC-CN por debajo de 66, los valores UHRS-CN equivalentes son menores, lo cual significa una subestimación de la escorrentía del CLC para el frondosas perenne, el bosque mixto, el bosque de transición-arbusto, los pastos, los olivares y los mosaicos de cultivo complejos, correspondiendo éstas a las coberturas más representativas del entorno de la dehesa. Por otro lado, los valores del CLC-CN por encima del valor umbral de 66 son superiores a los valores del UHRS-CN, lo que significa una sobreestimación de la escorrentía para las categorías de vegetación esclerófila, zonas agroforestales, praderas naturales, tierras de cultivo no regadas, tierras ocupadas principalmente por la agricultura, con importantes zonas de vegetación natural, zonas de escasa vegetación, lugares de extracción de minerales y tejido urbano continuo.

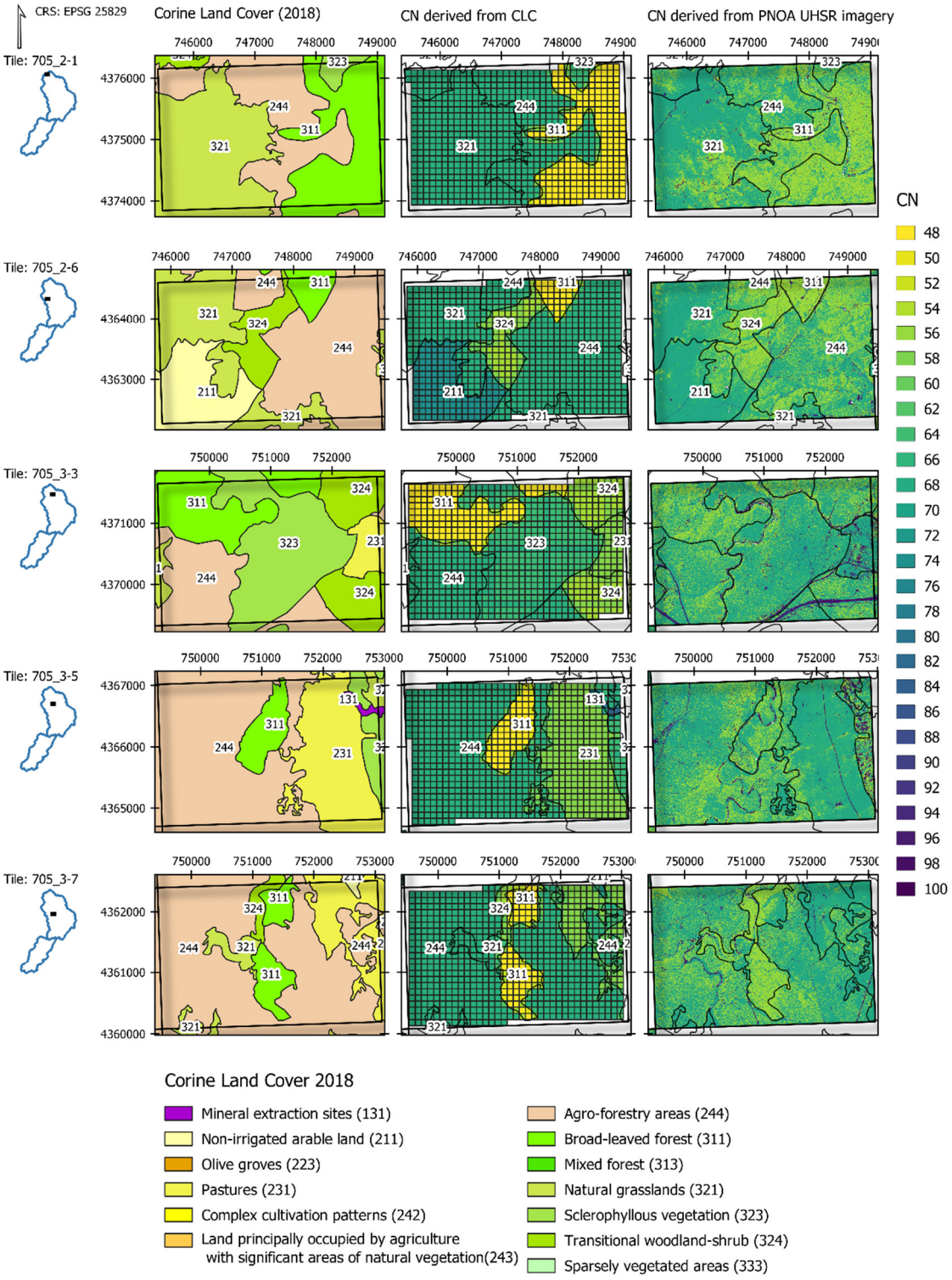

Figura 17. Valores medios ponderados del CN derivados de los mapas de cobertura del suelo obtenidos en este trabajo (UHSR-CN) y los derivados de los mapas del proyecto Corine Land Cover (CLC-CN) en un entorno de dehesa en una selección de imágenes del grupo de entrenamiento. Fuente: Figura S8 de la P3.

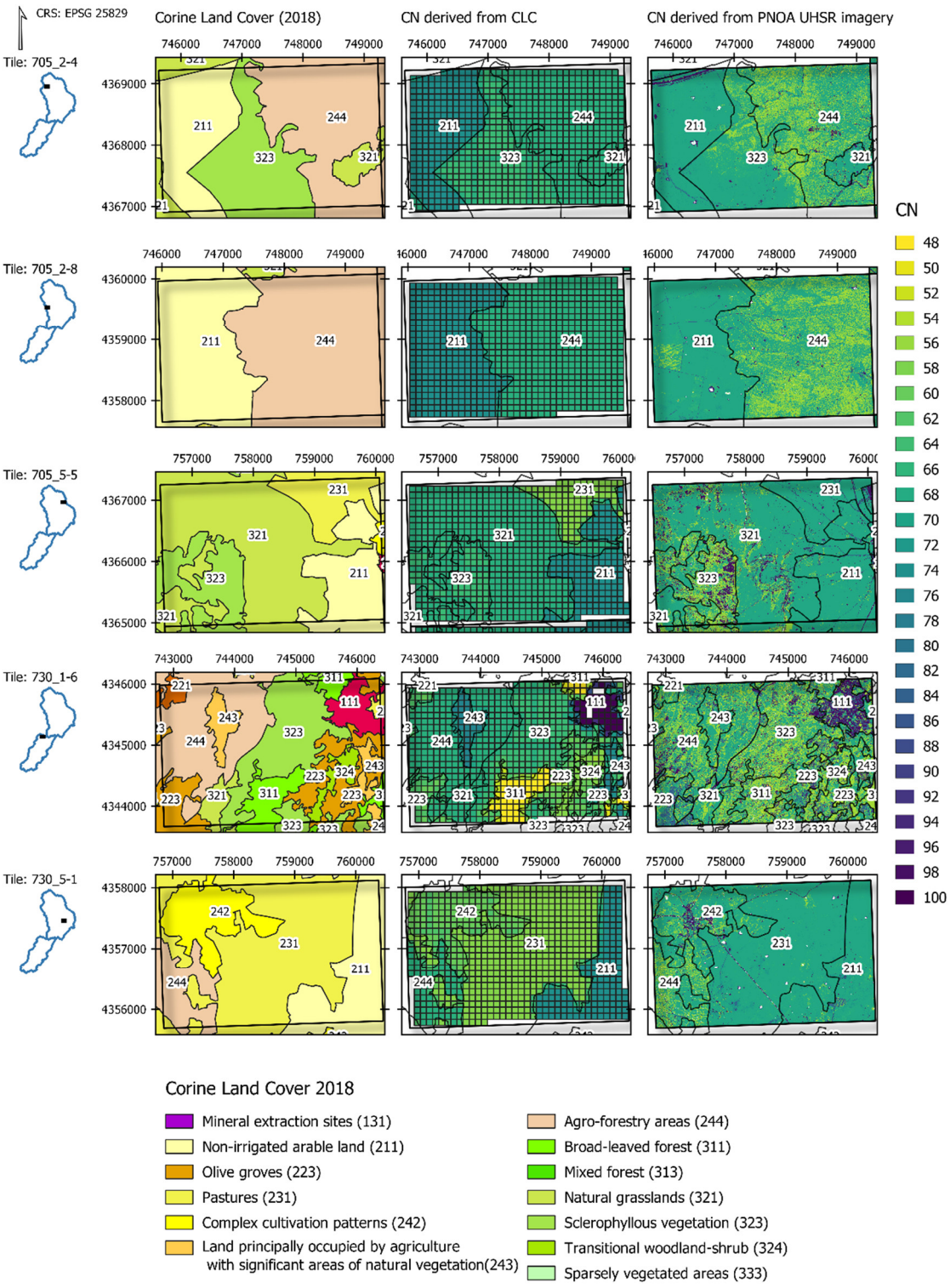

Figura 18. Valores medios ponderados del CN derivados de los mapas de cobertura del suelo obtenidos en este trabajo (UHSR-CN) y los derivados de los mapas del proyecto Corine Land Cover (CLC-CN) en un entorno de dehesa en una selección de imágenes del grupo de validación Fuente: Figura S12 de la P3.

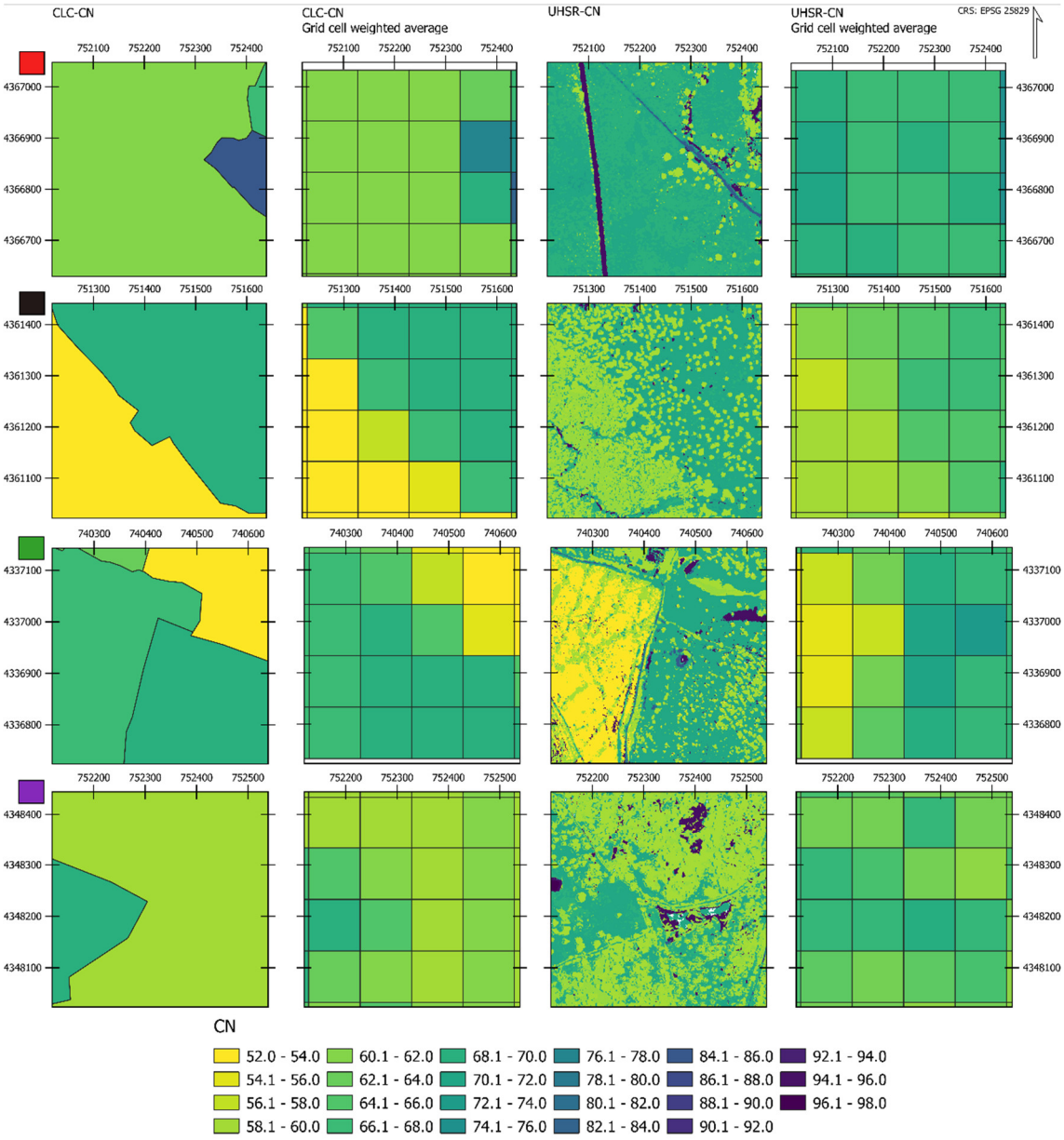

Figura 19. Detalle de los mapas de los valores medios ponderados del CN derivados de los mapas de cobertura del suelo obtenidos en este trabajo (UHSR-CN) y los derivados de los mapas del proyecto Corine Land Cover (CLC-CN) en un entorno de dehesa. Fuente: Figura 16 de la P3.

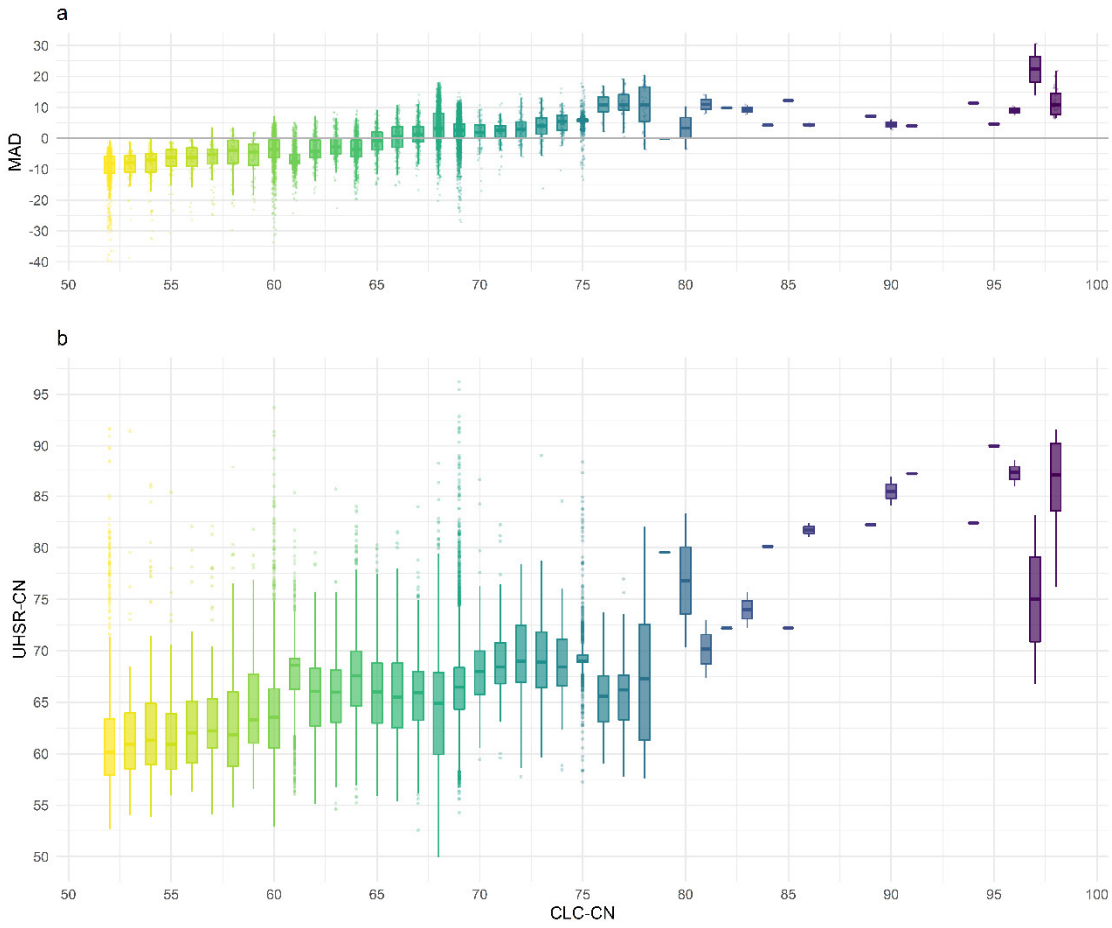

Figura 20. Influencia de la resolución espacial de los mapas de cobertura del suelo la estimación del valor del CN obtenido a partir de la cartografía CLC-CN frente a los valores UHSR-CN (a) diferencia media absoluta (*mean absolute diference* - MAD) (b) box-plot de los valores CLC-CN frente a los valores UHSR-CN. Fuente: Figura 17 de la P3.

La resolución espacial de los mapas *ad hoc* permitieron estimar de forma precisa la distribución espacial de los valores del CN, destacando la influencia de la resolución espacial en la respuesta hidrológica del territorio, ya que la base de datos global del CLC subestima la escorrentía potencial en las coberturas del suelo más representativas en el entorno de la dehesa. Este resultado, está en consonancia con otros estudios como el de Walega and Salata (2019) en el que los autores señalaron que subestimación de la dependía del tamaño de la cuenca debido al riesgo de sobregeneralización de las categorías de cobertura de la tierra del CLC.

Por último, una vez clasificadas las imágenes, tanto para el grupo de entrenamiento como para el de validación, la información sobre la cobertura del suelo puede utilizarse para la definición de nuevos conjuntos de datos de entrenamiento para la clasificación supervisada de imágenes de satélite como, como Sentinel o Landsat. En este trabajo, hemos demostrado la eficacia de aplicar un clasificador a imágenes

vecinas con entornos similares que podrían no participar en la extracción del conjunto de datos de entrenamiento, reduciendo así el trabajo manual de fotointerpretación y visitas de campo lo que resulta especialmente útil en regiones inaccesibles. La principal limitación de nuestro procedimiento propuesto es que las imágenes deben tener las mismas condiciones de vuelo para garantizar la similitud de la información espectral.

Reflexión final

Tras finalizar esta fase de los trabajos, se diseñó el método para la extracción automática de las áreas de entrenamiento de las imágenes de ultra alta resolución espacial extendiendo la aplicación del método descrito en la P3, al ámbito de estudio de la P4, basándonos en parte de la metodología desarrollada en la P7. Como los datos del LiDAR de la segunda cobertura seguían sin estar disponibles para procesarlos en todo el ámbito de estudio de la P4, decidimos utilizar los datos LiDAR de la primera cobertura, exclusivamente como apoyo en la definición de las áreas de entrenamiento de las zonas forestales en la extensión del estudio de la P4. Para ello, planteamos una técnica de fusión entre la clasificación de la imagen del PNOA de ultra alta resolución y las métricas del LiDAR de baja densidad de puntos de la primera cobertura, similar al descrito en la P7 y basado en el límite de altura expuesto en la P2. Asumiendo las siguientes limitaciones:

- Sólo se consideraron polígonos con una superficie superior a 625 m^2 para garantizar el solape con al menos 4 píxeles de la imagen S2 (con una resolución espacial de 10m).

- Sólo los polígonos clasificados como arbolado que presenten una altura media superior al umbral de 2,5 m se considerarán finalmente como árbol.

- Sólo los polígonos clasificados como arbustos, con una altura media inferior al umbral de 2,5 m se considerarán finalmente como arbustos.

- Sólo los polígonos clasificados como pastos, con una altura media inferior al umbral de 0,5 m se considerarán finalmente como pastos.

2.5. Resumen de la P4 sobre la generación de mapas de cobertura terrestre para modelización hidrológica utilizando la fusión de datos SAR y ópticos de imágenes Sentinel

2.5.1. Resumen

La caracterización de la cobertura del suelo en una cuenca tiene una notable influencia en el balance hídrico y, es un factor clave en la evaluación de modelos hidrológicos complejos a escala regional. En este trabajo se propone un método para generar mapas *ad hoc* estacionales de la cobertura del suelo desde el punto de vista hidrológico, basados en la capacidad de generación de escorrentía, utilizando técnicas de teledetección con datos de S1 y S2 y clasificación supervisada con Random Forest. Se propone un estudio minimizando al máximo las imágenes: una sola fecha para los datos de S2 y dos fechas para los datos de S1. A continuación, se mejora la dimensión de los datos de los satélites con métricas de textura e índices espectrales, tras lo cual se lleva a cabo una selección de las características más influyentes para la optimización del algoritmo de clasificación, garantizando la exactitud de los mapas finales. Las exactitudes globales son notablemente altas (93,29%) para el conjunto de entrenamiento y altas (85,24%) para el conjunto de datos de validación. Las métricas de textura son los parámetros de clasificación más importantes y se derivan principalmente de las bandas del VIS (B2 y B3), NIR (B5 y B6) y SWIR (B11). Los resultados mejoraron a otros obtenidos en trabajos anteriores que utilizaban grandes series temporales de imágenes, reduciendo en nuestro trabajo los requisitos de capacidad de almacenamiento y el tiempo de cálculo necesario. En consecuencia, la respuesta hidrológica de las cuencas, en términos de NRCS-CN, se caracteriza de forma veraz, permitiendo el análisis de la escorrentía potencial y su variación debido a la fenología estacional.

2.5.2. Esquema metodológico

La Figura 21 muestra el esquema propuesto para la generación de mapas de cobertura del suelo específicos para modelización hidrológica utilizando la fusión de datos SAR y ópticos de imágenes Sentinel.

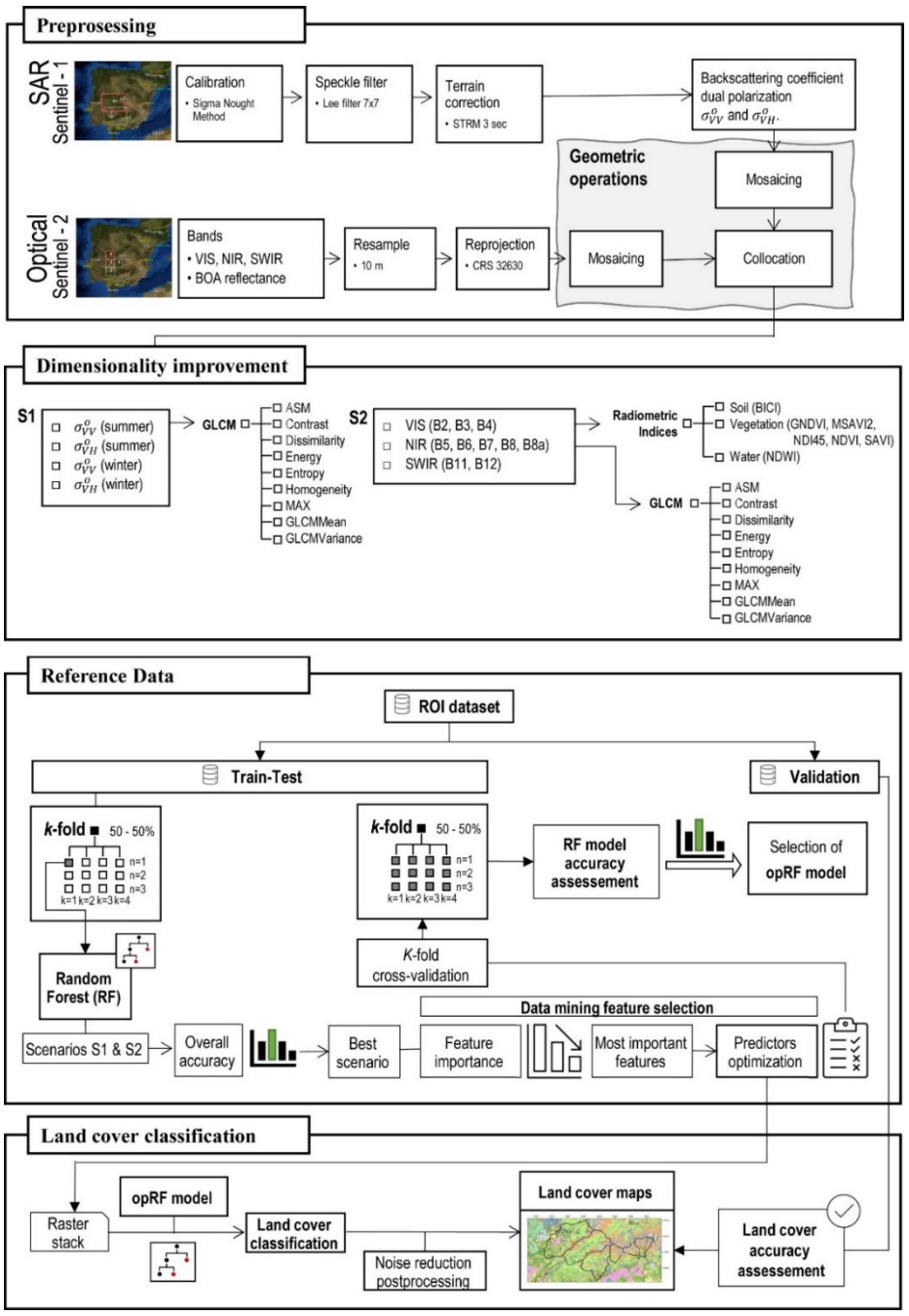

Figura 21. Esquema metodológico propuesto para la generación de mapas de cobertura terrestre para modelización hidrológica utilizando la fusión de datos SAR y ópticos de imágenes Sentinel. Fuente: Figura 2 de la P4.

Las categorías de cobertura del suelo se plantearon considerando la capacidad de generación de escorrentía según la metodología del NRCS-CN (NRCS, 2004), teniendo en cuenta a su vez, la fenología estacional, que afecta principalmente a los árboles de hoja caduca y a los cultivos de temporada, ya que modifica las características hidrológicas de los mismos. El parámetro CN se refiere a la capacidad potencial de escorrentía de una cuenca; un valor de CN más bajo indica una capacidad potencial de escorrentía menor y viceversa. Por lo tanto, para una

determinada categoría de uso suelo, se definen las condiciones hidrológicas en dos períodos: operacional y no operacional. El período operacional se refiere a la fase fenológica que va desde la plantación hasta el laboreo en los cultivos de temporada y a la fase de inicio de la hoja en los árboles de hoja caduca en zonas forestales o en los cultivos de cerezo. Además, para los pastos, también se considera período operacional los meses de primavera, en los que la vegetación experimenta un crecimiento muy vigoroso. Así, el período no operativo se refiere al resto del año, hasta la siguiente fase operativa. La Tabla 7 muestra la nomenclatura de las categorías consideradas y las características hidrológicas asociadas en los períodos operacionales y no operacionales y la Figura 22 muestra las cinco fases fenológicas que se consideran en este trabajo.

Tabla 7. Tipos de coberturas terrestres y la característica hidrológica asociada en los períodos operacionales y no operacionales. Fuente: Tabla 3 de la P4

	Land cover description [1]	Class code	NRCS land cover type		Hydrologic condition	
			Phenological Stage [2]		Phenological Stage [2]	
			Op	Non-op	Op	Non-op
Forested areas	Evergreen needleleaf forest (*Pinus pinaster, Pinus pinea*)	ENF	Woods	Woods	Good	Good
	Evergreen broadleaf forest (*Quercus rotundifolia, Quercus suber*) TCC>60%	EBF	Woods	Woods	Good	Good
	Evergreen broadleaf forest (*Quercus rotundifolia, Quercus suber*) 20<TCC<60%	DHS	Woods	Woods	Fair	Poor
	Deciduous broadleaf forest *(Quercus pyrenaica, Castanea sativa)*	DBF	Woods	Woods	Good	Fair
	Shrub	S	Brush	Brush	Fair	Fair
	Herbaceous vegetation	P	Pasture	Pasture	Fair	Poor
	Rocky outcrops	Rk	Impervious	Impervious	--	--
	Bare soil	B	Road Gravel	Road Gravel	--	--
Agricultural lands	Irrigated warm-season crops	AgIr	Row crops straight row	Fallow	Good	Fallow
	Rainfed cold-season crops	AgRc	Close seeded straight row	Fallow	Good	Fallow

	Crop residue cover	Agf	Fallow	Fallow	Poor	Poor
	Rainfed cherry tree plantations	Agc	Orchard/Tree farm	Orchard/Tree farm	Fair	Poor
	Rainfed olive tree plantations	Ago	Orchard/Tree farm	Orchard/Tree farm	Fair	Fair
	Rainfed vineyard plantations	Agv	Orchard/Tree farm	Orchard/Tree farm	Poor	Poor
Other	Urban and paved roads	Imp	Impervious	Impervious	--	--
	Water bodies	W	Water bodies	Water bodies	--	--

[1] TCC Tree Canopy Cover

[2] Op The operational stage refers to the phenological phase from planting to tillage in seasonal crops and to the leaf-on phase in deciduous trees in forested areas or cherry tree crops.

Non-op The nonoperational period refers to the rest of the period, until the next operational stage

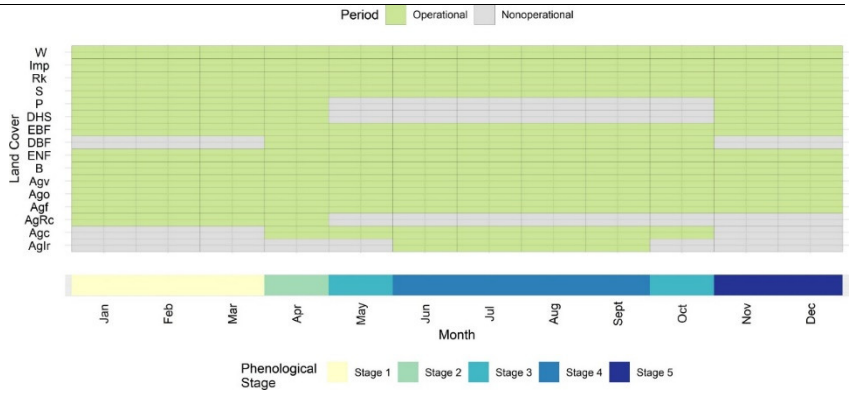

Figura 22. Etapas fenológicas consideradas en función de los períodos operacionales y no operacionales de las categorías de cobertura del suelo en la zona de estudio. Fuente: Figura 3 de la P4.

2.5.3. Resultados y discusión

Selección del escenario de clasificación

Para analizar la influencia de la fusión de datos procedentes de distintos sensores en la exactitud global y el tiempo computacional, estudiamos dieciocho escenarios con diferentes permutaciones de predictores S1 y S2. En la Figura 23 se observa que el tiempo de cálculo aumenta con el número de predictores en todos los escenarios y que la exactitud global depende, no sólo del número de predictores, sino también del sensor utilizado. Los predictores S1 muestran peores resultados, y los escenarios que combinan S1 y S2 alcanzan precisiones superiores al 85%. El escenario con mejor rendimiento es denominado S1tS2it, que es el escenario que comprende los 148 predictores disponibles (bandas, texturas e índices derivados), alcanzando una exactitud global del 92,98% y que fue el escenario escogido para realizar la selección de los predictores.

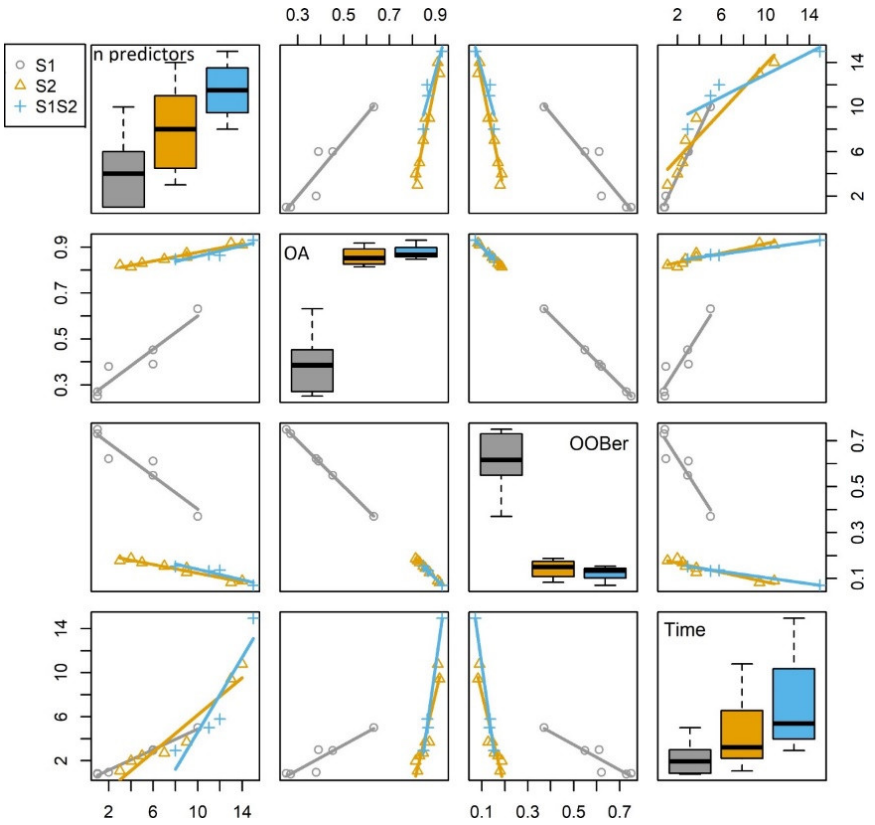

Figura 23. Resultados obtenidos en los distintos escenarios de las permutaciones de los predictores de las imágenes Sentinel-1 y Sentinel-2 considerados en la optimización del algoritmo RF. Fuente: Figura 5 de la P4.

Para realizar la selección de los predictores mas influyentes se utilizaron los valores la disminución de la exactitud del clasificador (MDA) cuando un predictor se queda fuera de la selección de entrenamiento del RF. Se consideraron tres iteraciones en el proceso: la primera iteración (DM1) descartó características con valores de MDA inferiores a 50, la segunda iteración (DM2) descartó características con valores de MDA inferiores a 40 y, finalmente, la tercera iteración (DM3) descartó las características con valores de MDA inferiores a 30. En cada iteración se evaluó de nuevo la exactitud del modelo de RF y el tiempo de cálculo y, finalmente, se compararon con los resultados del escenario de referencia S1tS2it. La Figura 24a representa el origen de las características mas importantes, y resultó que estaban relacionadas casi exclusivamente con las métricas de textura de ambos sensores. En lo que respecta a las bandas, sólo las bandas NIR (B5) y SWIR (B11 y B12) se clasificaron como predictores importantes. Por último, en relación con los índices radiométricos, sólo el CI pareció ser importante. La Figura 24b muestra que las características de textura están relacionadas principalmente con las bandas S2 y con las métricas de textura de S1 en invierno, principalmente la polarización VV, aunque también hay varias características importantes de S1 en verano en la polarización VH. La iteración DM1, que utilizó los 21 predictores más importantes, mostró una disminución del 8,7% en términos de exactitud global, con una optimización del

tiempo de cálculo del 86%. La iteración DM2, que utilizó los 42 predictores más importantes, presentó una disminución del 2,3% en términos de exactitud global, con una reducción del tiempo de cálculo del 74% y la iteración DM3, que utilizó los 75 predictores más importantes, mostró el mismo valor de exactitud global que el escenario original, con una reducción del tiempo de cálculo del 54%. La Figura 24c muestra la disminución de las métricas de exactitud para cada categoría de uso del suelo en las tres iteraciones, y se puede observar cómo la iteración DM3 obtuvo casi el mismo rendimiento para todas las categorías que el escenario original con aproximadamente la mitad de las características. Por lo tanto, las características utilizadas en la iteración DM3 fueron seleccionadas para en entrenamiento del algoritmo RF.

Evaluación de la exactitud del modelo RF

Una vez seleccionados los predictores óptimos se realizó una validación cruzada de los resultados del RF de cuatro grupos con tres repeticiones del algoritmo (*k*-fold *cross-validation* (k=4, n=3)). El valor medio de la exactitud global fue de 93,23% destacando que se logró una estabilidad notable en los resultados tanto de la tasa de error (*ouf of bag* - OOB) como de la exactitud global. De entre todos los clasificadores entrenados se seleccionó el que obtuvo la mayor tasa de acierto de todos, que llamaremos opRF, que alcanzó una exactitud global de 93,29% y con él se realizó la clasificación de la imagen en toda el área de estudio.

Tras el postproceso del resultado (reducción del efecto *salt-and-pepper*), se evaluó la exactitud de los mapas utilizando el conjunto de datos de validación y se obtuvo una exactitud global del 85,24%. Sin embargo, a pesar de ser inferior que la exactitud obtenida para el conjunto de datos de entrenamiento, el rendimiento global del clasificador opRF fue excelente. La Figura 25 representa las métricas de exactitud obtenidas por el opRF para cada categoría de cobertura del suelo en los dos grupos de entrenamiento y validación (Figura 25a). En el conjunto de datos de validación, las clases de cobertura forestal mostraron mejores resultados en que las clases de cobertura agrícola, y la cobertura de suelo desnudo obtuvo los resultados más débiles, si bien tiene poca representatividad dentro del conjunto (Figura 25b). La confusión entre categorías se muestra en el diagrama de la Figura 25c, observándose como el estrato arbustivo (S), que es el que tiene resultados mas bajos dentro de la categoría forestal, se confundió principalmente con DBF (11%), P (7%) y EBP (5%), mientras que la categoría de tierras de barbecho (Agf) que es la que tiene resultados mas bajos dentro de la categoría agrícola, se debió a la confusión principalmente con AgRc (12%), Ago (11%) y S (7%).

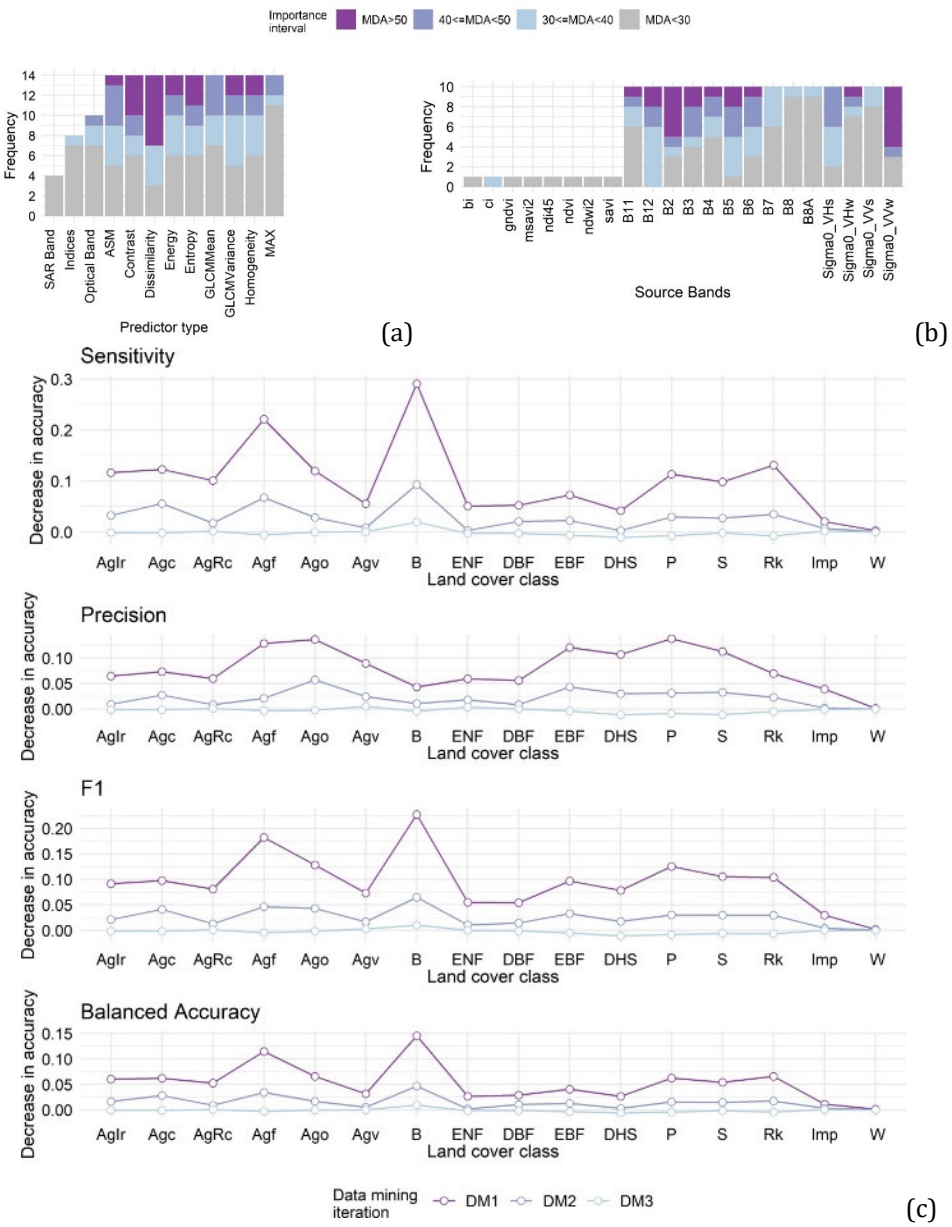

Figura 24. Resultados del proceso de selección de los predictores mas importantes (a) frecuencia de aparición de los tipos de predictores en las características seleccionadas como óptimas. (c) frecuencia de aparición de las métricas derivadas de cada banda en las características seleccionadas como óptimas. (d) disminución de las métricas de exactitud para cada categoría de cobertura del suelo para las tres iteraciones de selección respecto del escenario global con todos los predictores. Fuente: adaptación de la Figura 6 de la P4.

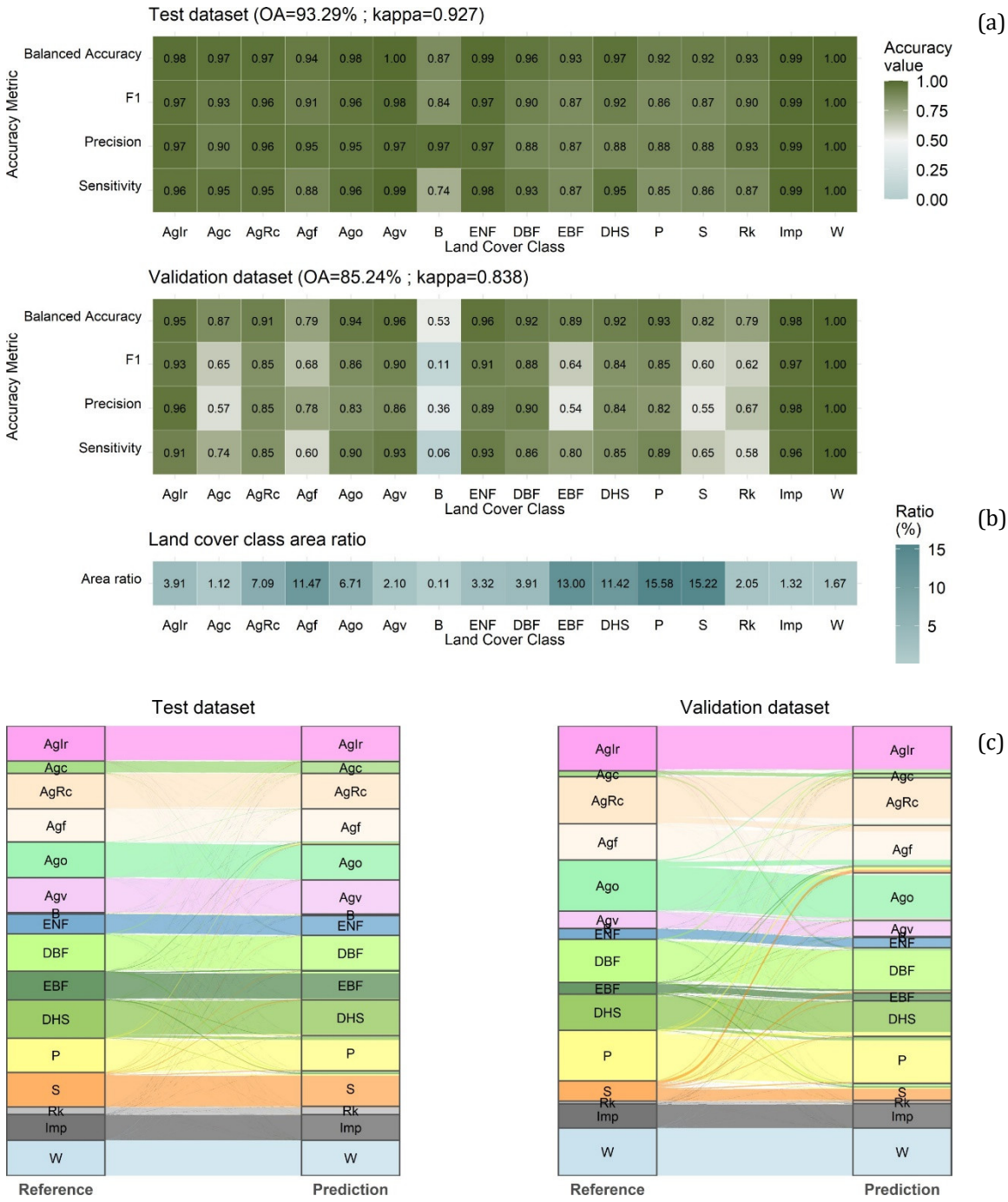

Figura 25. Evaluación de la exactitud (a) Métrica de exactitud obtenida para cada categoría basada en la información de la matriz de error. (b) Proporción de área de cada categoría de cobertura del suelo en el mapa final de cobertura del suelo. (c) Diagrama de errores de clasificación entre categorías. Fuente: Figura 7 de la P4.

Los valores globales de exactitud obtenidos en este trabajo para el grupo de entrenamiento (93,29%) y para el grupo de validación (85,24%) son comparables a los de otros estudios en zonas forestales, como el de Whyte et al. (2018) (83,3%) que utilizó únicamente las bandas de S1 y S2 con índices ópticos para la clasificación

de 15 categorías. Con respecto a otros trabajos anteriores que usaron imágenes de una sola fecha y métricas de textura como predictores, nuestros resultados son mejores que los de Muthukumarasamy et al. (2019) (78,49%) en la fusión de S1 y texturas derivadas de Landsat-8 (se consideraron cinco clases en el análisis). Por último, nuestros resultados fueron ligeramente inferiores a los de Mishra et al. (2019) (87,70%), aunque su análisis fusionó más fuentes de datos, como S1 (polarizaciones VV, VH) y RISAT-1 (polarizaciones HH, HV) y LISS-III, LISS-IV y Landsat-8 para los datos ópticos, y sólo se consideraron siete clases, mientras que nosotros distinguimos entre dieciséis categorías de cobertura del suelo. Además, nuestros resultados son ligeramente mejores que los de otros trabajos anteriores basados en análisis multitemporales y métricas de textura, como el de Verma et al. (2019) (83,97 %), que utilizó métricas de textura derivadas sólo de datos SAR para analizar seis clases, o Liu et al. (2018) (82,78 %) que utilizó métricas de textura derivadas sólo de datos ópticos para clasificar ocho categorías de cobertura del suelo. Además, cabe destacar que nuestros resultados superaron a otros trabajos anteriores basados en análisis multitemporales de S1 y S2 que no incorporaban información de textura, aunque se utilizaran índices radiométricos o biofísicos (Carrasco et al., 2019, Denize et al., 2019, Mahdianpari et al., 2020, Poortinga et al., 2019, Van Tricht et al., 2018).

En cuanto a las diferencias en la exactitud en el conjunto de entrenamiento y de validación, la confusión entre categorías, especialmente entre aquellas con firmas similares, podría deberse a que las áreas de entrenamiento utilizadas no representaran toda la variabilidad espectral dentro de una gran extensión, como la estudiada en este trabajo. Lo cual, confirma el hecho de que la calidad de las áreas de entrenamiento es un factor crucial para obtener resultados de clasificación exactos y fiables (Heckel et al., 2020). No obstante, la exactitud conseguida en el grupo de validación, aún menor que la de entrenamiento fue muy buena, confirmando de este modo la bondad del método propuesto de generación de las áreas de entrenamiento derivadas de la clasificación de las imágenes de ultra alta resolución del PNOA.

Importancia de los predictores en el clasificador RF

Los predictores más influyentes en la clasificación del opRF fueron los relacionados con las métricas de textura de ambos sensores, y la disimilitud, la media GLCM, la varianza GLCM y el contraste. En cuanto a las bandas de origen de las métricas de textura, las más importantes eran principalmente de B2, B3, B5 y B6. Además, la banda SWIR (B11) también tuvo una gran influencia en la clasificación. Además, también tuvieron gran importancia en la clasificación varias métricas de textura derivadas de las bandas del SAR, no en vano; la métrica VH-GLCMMean en invierno

ocupa el primer lugar del ranking general, con gran influencia en la discriminación de los cultivos estacionales de regadío (AgI), las plantaciones de cerezos (Agc), las frondosas de hoja perenne (EBF), las frondosas de hoja caducas (DBF) y las superficies impermeables (Imp). La importante influencia de las métricas de texturas obtenida en este estudio está de acuerdo con los resultados de Mishra et al. (2019), quiénes señalaron que las métricas de textura óptimas dependían del sensor y de las características del área, y en su estudio, encontraron que las más importantes eran la media, la disimilitud y la entropía para los datos ópticos y la media, la varianza, el contraste y la disimilitud para los datos SAR.

Mapas de usos de suelo y características hidrológicas

La Figura 26 representa el mapa final de las coberturas del suelo propuesto en esta tesis. A partir de ellos, se generan los mapas de cobertura y características hidrológicas siguiendo la nomenclatura del NRCS (NRCS, 2004) en cada etapa: etapa fenológica 1 (Figura 27), etapa fenológica 2 (Figura 28), etapa fenológica 3 (Figura 29), etapa fenológica 4 (Figura 30) y para la etapa fenológica 5 (Figura 31).

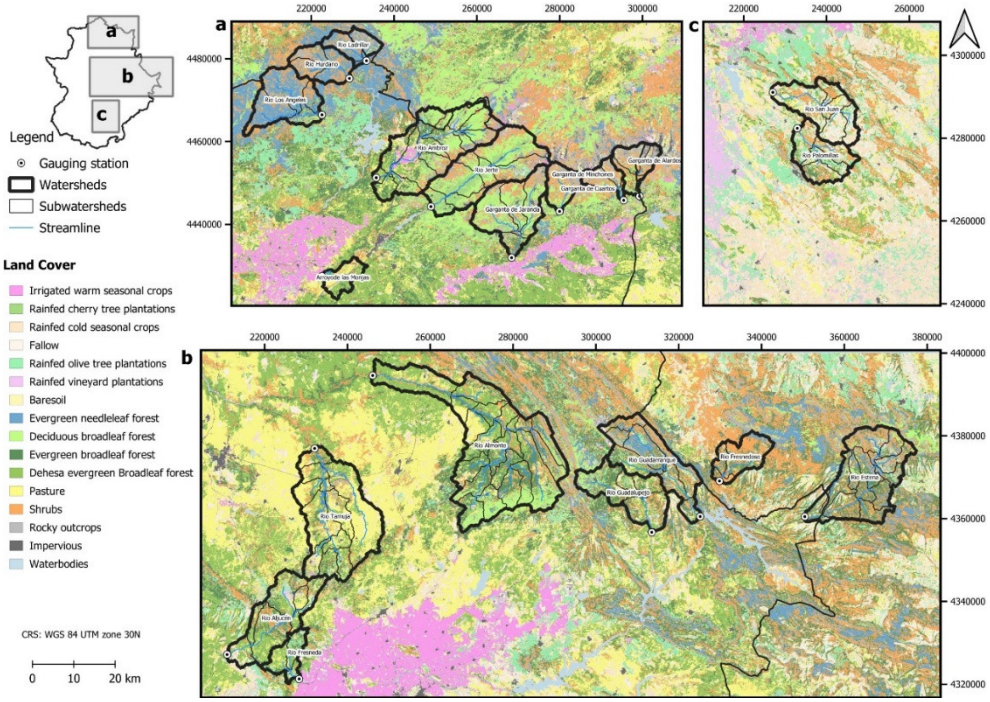

Figura 26. Mapas de cobertura de suelo en el área de estudio. Fuente: Figura 9 de la P4.

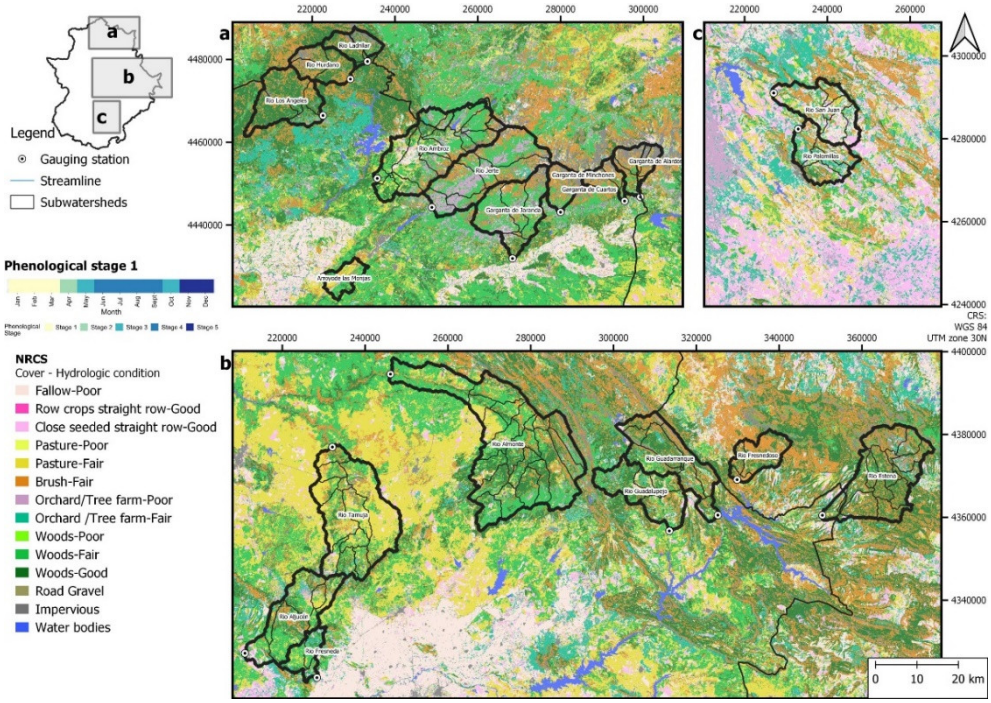

Figura 27. Mapas de cobertura y características hidrológicas según la nomenclatura del NRCS para la etapa fenológica 1 correspondiente a los meses desde enero hasta marzo. Fuente: *Online Resource2* de la P4.

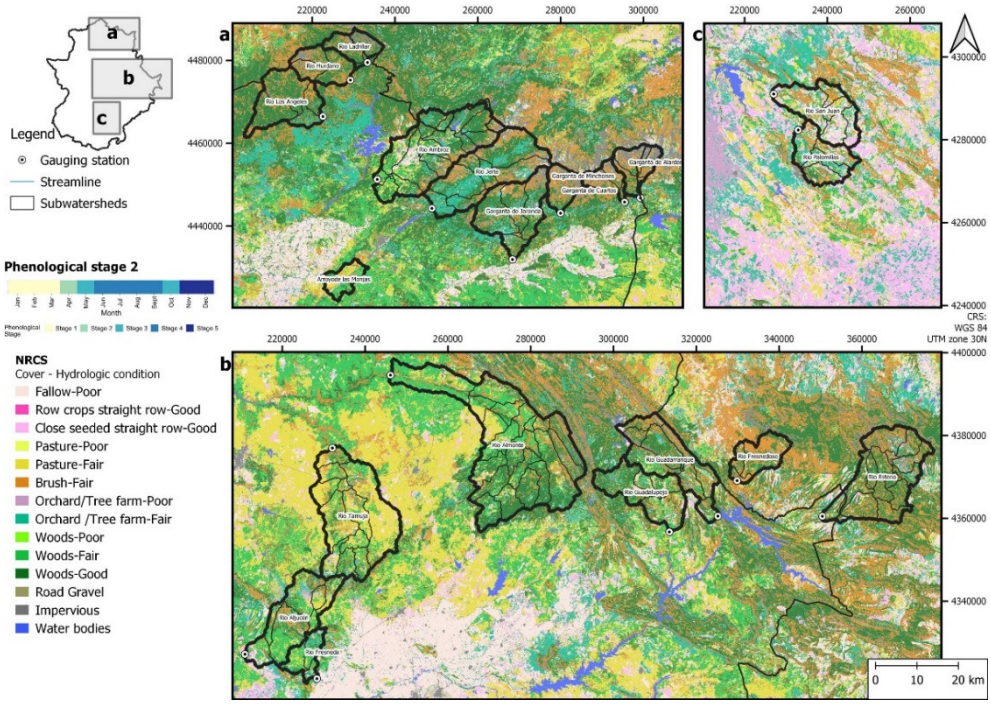

Figura 28. Mapas de cobertura y características hidrológicas según la nomenclatura del NRCS para la etapa fenológica 2 correspondiente al mes de abril. Fuente: *Online Resource2* de la P4.

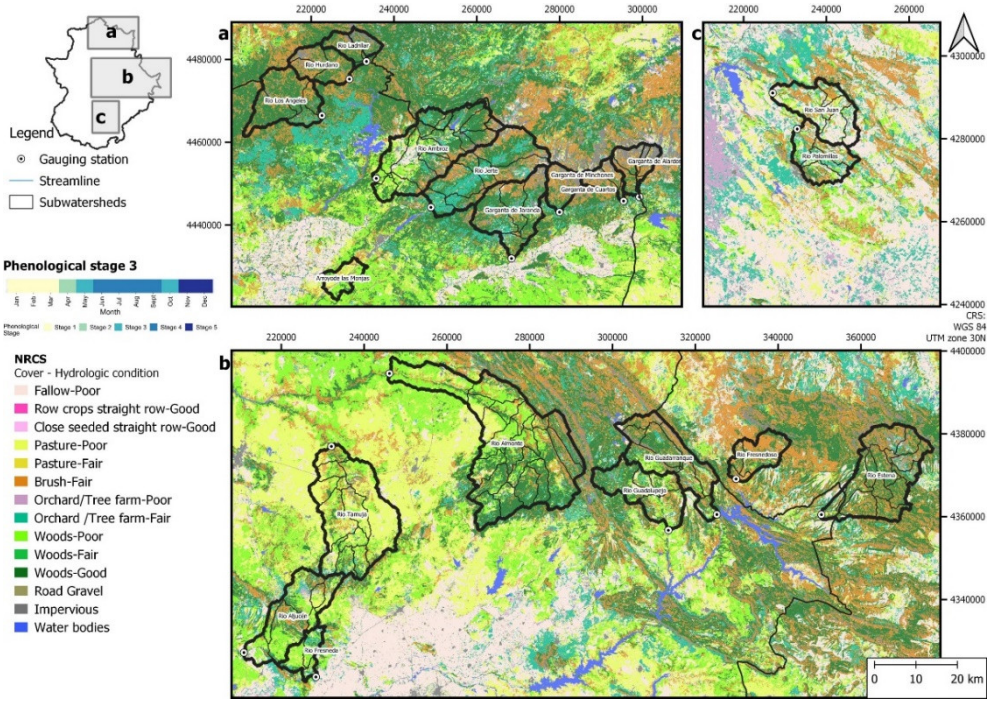

Figura 29. Mapas de cobertura y características hidrológicas según la nomenclatura del NRCS para la etapa fenológica 3 correspondiente a los meses desde mayo y octubre. Fuente: *Online Resource2* de la P4.

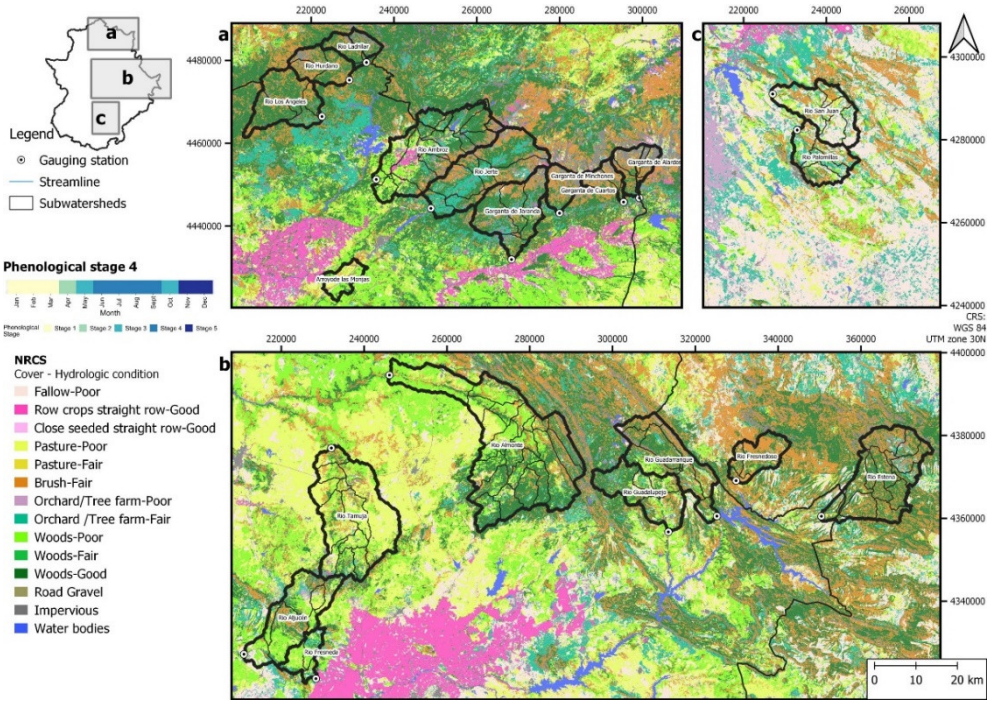

Figura 30. Mapas de cobertura y características hidrológicas según la nomenclatura del NRCS para la etapa fenológica 4 correspondiente a los meses desde junio hasta septiembre. Fuente: *Online Resource2* de la P4.

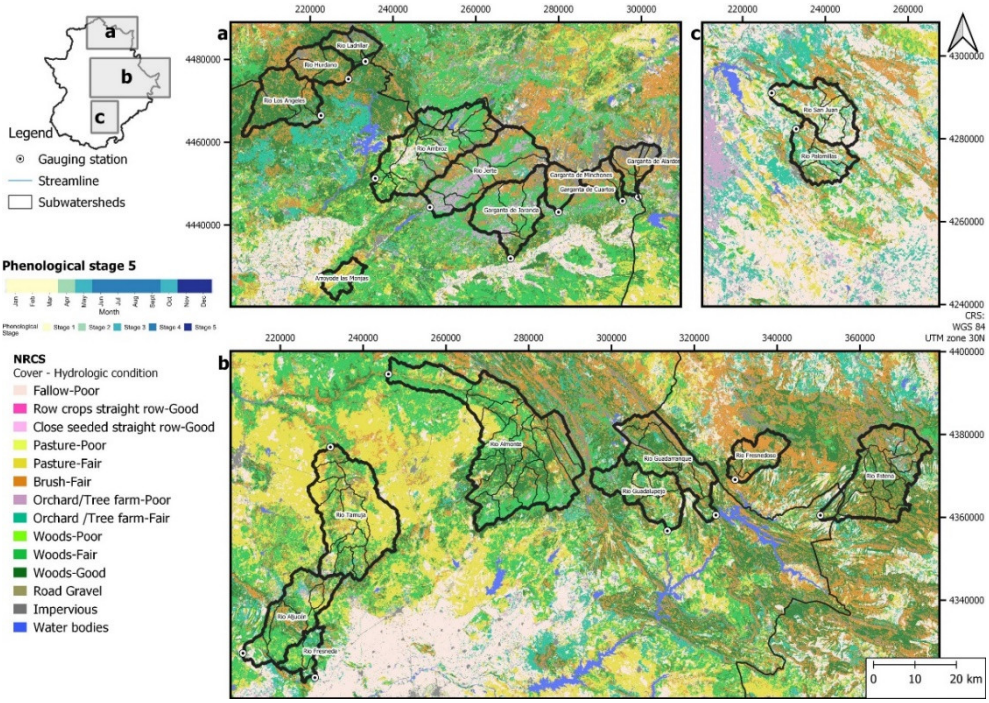

Figura 31. Mapas de cobertura y características hidrológicas según la nomenclatura del NRCS para la etapa fenológica 5 correspondiente a los meses desde noviembre y diciembre. Fuente: *Online Resource2* de la P4.

Mapa del grupo de suelo

El grupo de suelo se analizó considerando los datos de texturas facilitados por el Centro Europeo de Datos de Suelos (*European Soil Data Centre* - ESDAC) (Joint Research Centre, 2020), concretamente se utilizaron los resultados de Ballabio et al. (2016) que estudiaron las clases texturales en Europa según la clasificación del USDA (*United States Department of Agriculture*) basada en la combinación de tres mapas texturales (arcilla, limo y arena) y que se representan en la Figura 32. Las clases texturales del suelo se transformaron en el grupo hidrológico del suelo utilizando los criterios de Hong and Adler (2008).

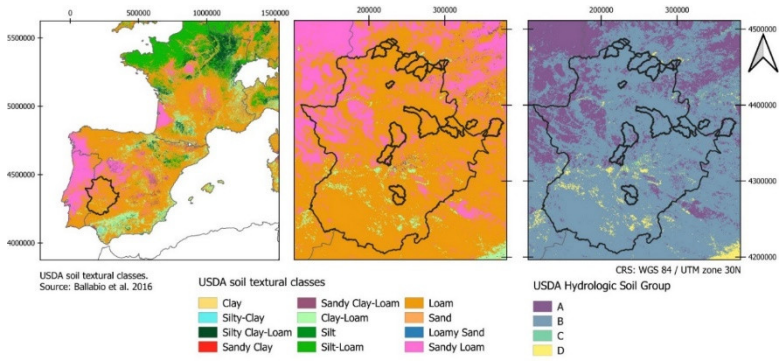

Figura 32. Grupo de suelo hidrológico según la nomenclatura del USDA (*United States Department of Agriculture*) en la zona de estudio. Fuente: Figura 4 de la P4.

Mapas de distribución espacial del número de curva (CN)

Como resultado final, considerando la información de los usos de suelo y características hidrológicas junto con el mapa de grupo de suelo se generaron los mapas equivalentes en términos de valores de CN en cada etapa: etapa fenológica 1 (Figura 33), etapa fenológica 2 (Figura 34), etapa fenológica 3 (Figura 35), etapa fenológica 4 (Figura 36) y para la etapa fenológica 5 (Figura 37).

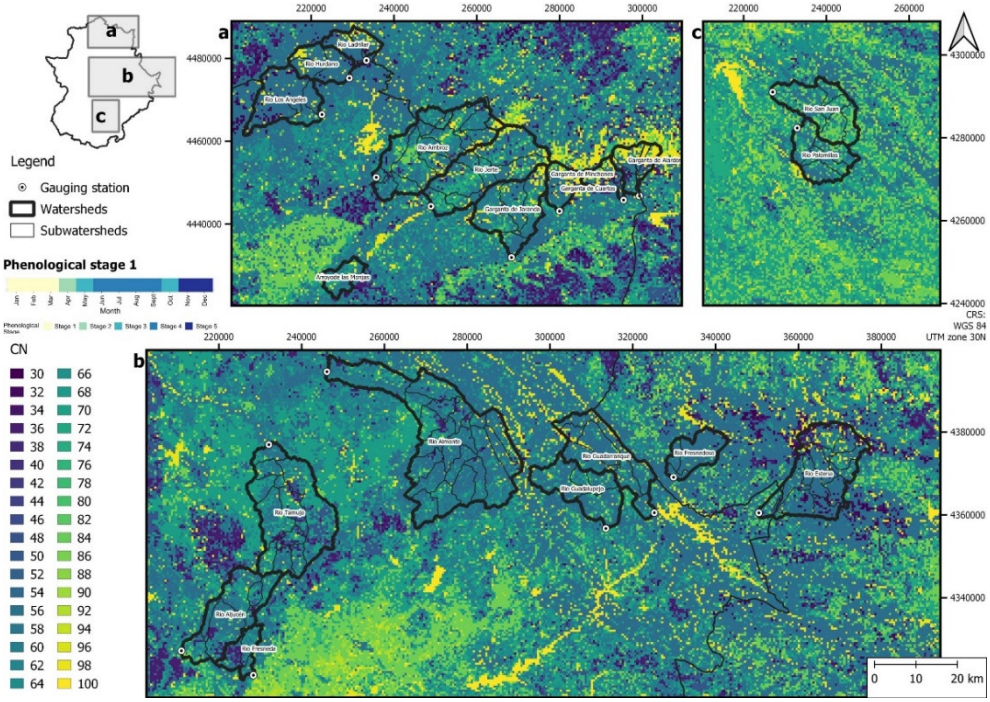

Figura 33. Mapas de la distribución espacial del NRCS-CN en la zona de estudio para la etapa fenológica 1 correspondiente a los meses desde enero hasta marzo. Fuente: *Online Resource 3* de la P4.

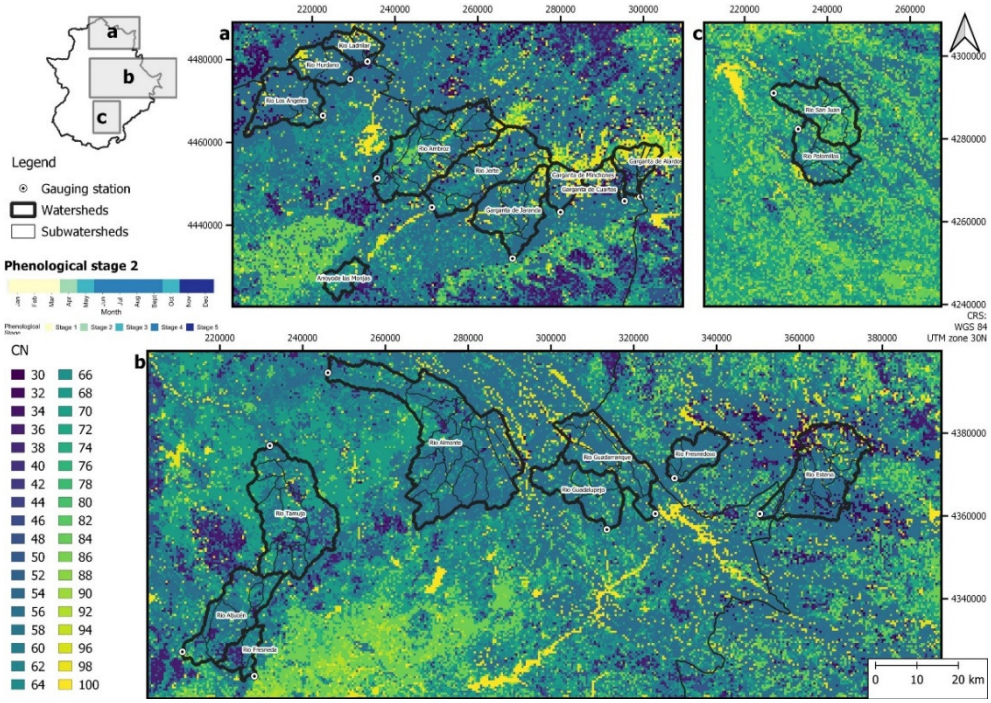

Figura 34. Mapas de la distribución espacial del NRCS-CN en la zona de estudio para la etapa fenológica 2 correspondiente a los meses desde enero hasta marzo Fuente: *Online Resource 3* de la P4.

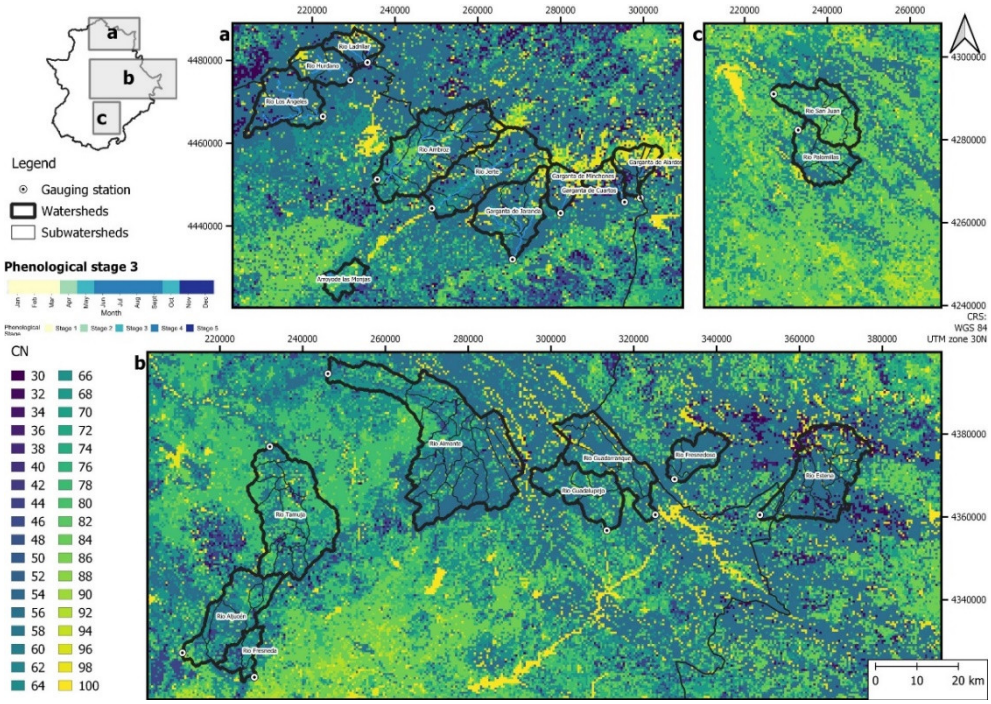

Figura 35. Mapas de la distribución espacial del NRCS-CN en la zona de estudio para la etapa fenológica 3 correspondiente a los meses desde enero hasta marzo Fuente: Figura 10 y *Online Resource 3* de la P4.

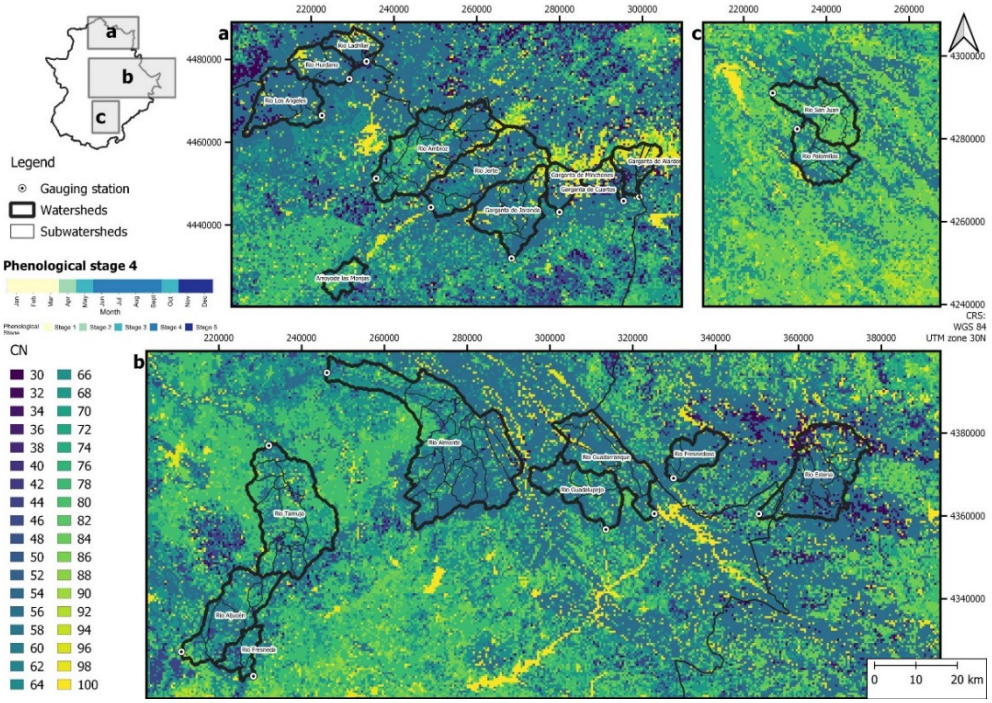

Figura 36. Mapas de la distribución espacial del NRCS-CN en la zona de estudio para la etapa fenológica 4 correspondiente a los meses desde enero hasta marzo. Fuente: *Online Resource 3* de la P4.

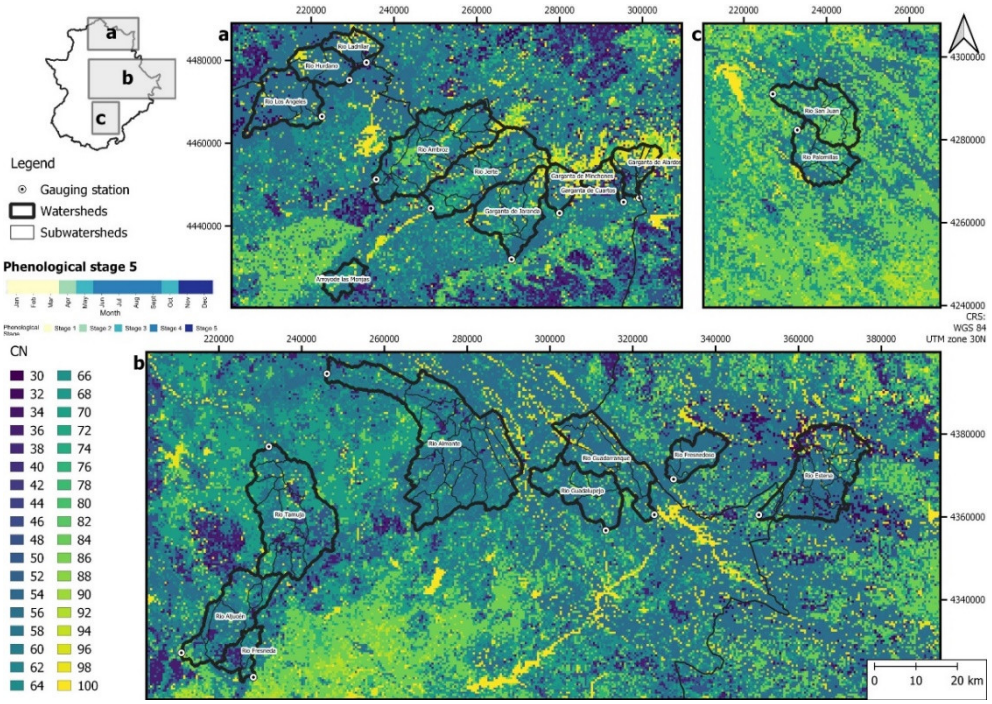

Figura 37. Mapas de la distribución espacial del NRCS-CN en la zona de estudio para la etapa fenológica 5 correspondiente a los meses desde enero hasta marzo. Fuente: *Online Resource 3* de la P4.

Finalmente, se analizaron los valores medios ponderados del CN en cada etapa fenológica a nivel de cuenca y subcuenca, resultando dos comportamientos diferentes en función de las variaciones de los valores del CN a lo largo del año (Figura 38). Un primer grupo, que incluye las cuencas en las que las características hidrológicas de las coberturas permanecen invariables en ambos períodos (operacional y no operacional) y, por tanto, el valor del CN no varía a lo largo de las distintas etapas fenológicas (por ejemplo, Alardos, Minchones, Estena, Hurdano y Ladrillar). Por otro lado, está el grupo de cuencas en las que las características hidrológicas sí varían a lo largo del año y los valores del CN obtenido fue distinto en cada etapa: algunas cuencas tuvieron valores de CN más altos de mayo a octubre (etapas 3 y 4) (por ejemplo, Aljucén, Almonte, Fresneda y Tamuja) y otras tuvieron valores de CN más altos de noviembre a marzo (etapas 1 y 5) (por ejemplo, Jaranda, Ambroz y Jerte).

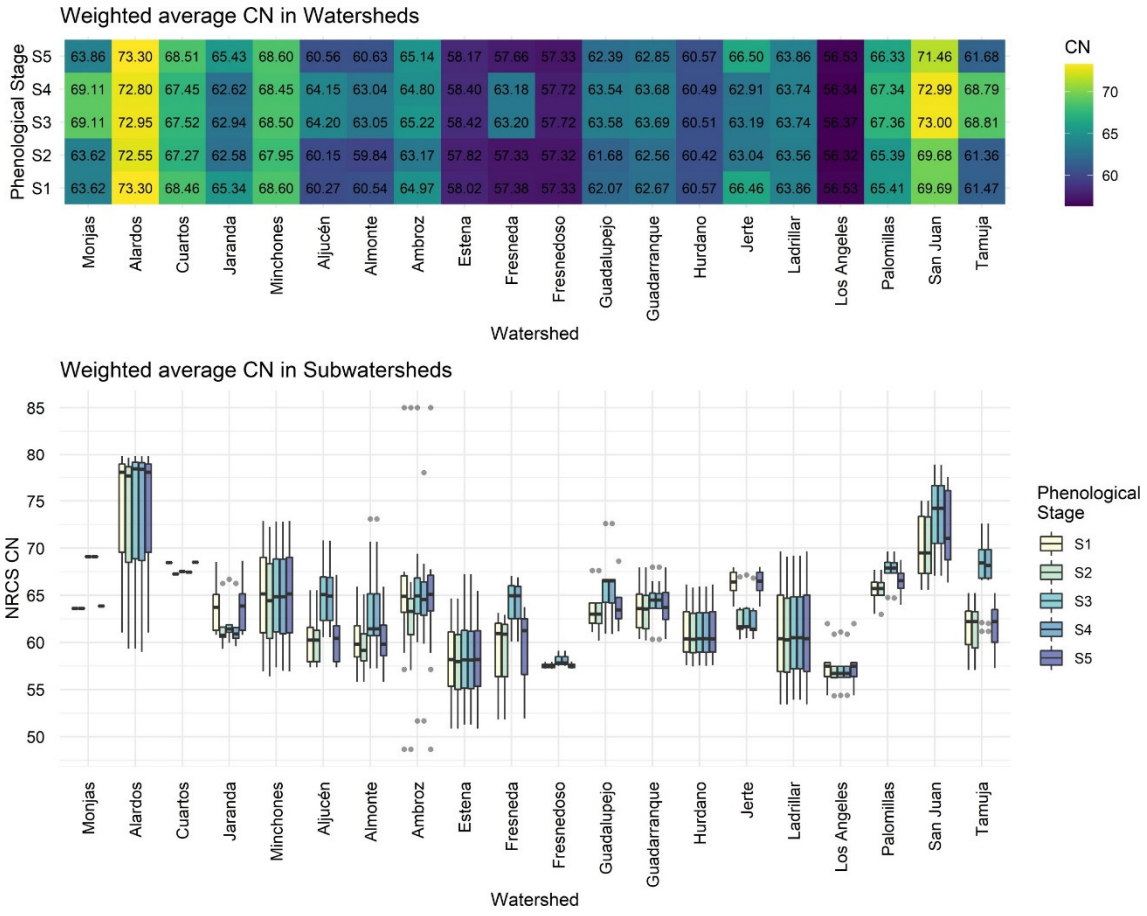

Figura 38. Resultados de los valores de CN obtenidos a nivel de cuenca y subcuenca en las distintas etapas fenológicas. Fuente: Figura 11 de la P4.

Estos resultados, los podemos comparar con los propuestos por Zeng et al. (2017), en su versión actualizada del trabajo original de Hong and Adler (2008), quienes elaboraron un mapa global de CN a partir de imágenes MODIS a una resolución espacial de 1 km. Interpretando los resultados de su publicación (*Fig. 2a: Global map*

of curve number (CN) en *Zeng et al. (2017).*), y teniendo en cuenta la incertidumbre que implica la regionalización de un estudio a escala global, en la región de Extremadura, los valores de CN oscilan entre 60 y 80, mientras que en nuestro estudio los valores del CN oscilan entre 30 y 100 con unos valores medios en las cuencas resultaron entre 56 y 74.

Por tanto, nuestros resultados representan el territorio de forma veraz a una alta resolución espacial adecuados para abordar simulaciones hidrológicas estacionales a escala regional y reduciendo el riesgo de sobre generalización de las categorías de cobertura del suelo en cuencas pequeñas (Sajikumar and Remya, 2015, Walega and Salata, 2019). Este aspecto es especialmente importante en zonas forestales en las que el método NRCS-CN es más débil (Tedela et al., 2012, Walega et al., 2020). Además, otros autores han demostrado que considerar la variabilidad estacional del CN es eficiente en simulaciones continuas de la escorrentía (Gundalia and Dholakia, 2014, Paik et al., 2005).

2.6. Resumen de la P6 sobre la aplicación de la teledetección en la regionalización de parámetros hidrológicos.

La investigación en su formato preprint y el estado de la revisión por pares está disponible para su consulta en Authorea:

Preprint: "Analyzing the Capability of Catchment's Spectral Signature for the Regionalization of Hydrological Parameters" (Laura Fragoso-Campón, Pablo Durán-Barroso, Elia Quirós). https://doi.org/10.22541/au.162100995.56312514/v1.

2.6.1. Resumen

La gestión de los recursos hídricos es compleja debido a las incertidumbres en torno a los parámetros hidrológicos que controlan el comportamiento de la escorrentía, y esta incertidumbre, es aún mayor en cuencas no aforadas. En estos casos se recurre a la regionalización de parámetros, que es un método que consiste en transferir los patrones de respuesta hidrológica conocidos en cuencas aforadas a las no aforadas. De entre los métodos existentes, lo basados en la regresión, relacionan los valores más adecuados de los parámetros con las propiedades físicas de las cuencas, y tradicionalmente, estas propiedades provienen de fuentes de datos cartográficos. Las técnicas actuales de teledetección nos ofrecen nuevos puntos de vista en el procesamiento de la regionalización ya que la respuesta hidrológica depende de los atributos físicos y estos últimos están relacionados con la respuesta espectral del territorio. En este trabajo se estudia la capacidad de la respuesta espectral de la cuenca obtenida de los satélites S1 y S2 para abordar una regionalización basada en la regresión de los parámetros hidrológicos utilizando un enfoque de aprendizaje automático con Random Forest. La modelización hidrológica se realizó mediante el modelo conceptual HBV. Y se planteó la regionalización en dos escenarios: el nuevo enfoque que utiliza la firma espectral de las cuencas, el método tradicional que utiliza las propiedades físicas y una fusión de ellos. Los resultados de la calibración fueron excelentes, con valores de eficiencia KGE entre 0,50 y 0,92 y, los parámetros regionalizados con el algoritmo de Random Forest también obtuvieron buenas eficiencias, similares en los tres escenarios estudiados que alcanzaron un KGE entre 0,45 y 0,50 (mediana). La eficacia de los modelos en las cuencas más húmedas fue superior al de las cuencas más secas. En este último entorno la regionalización basada en datos espectrales obtuvo mejores eficiencias el método físico, que alcanzaron unos valores de KGE de 0,33 y 0,25 (mediana) respectivamente. Los resultados obtenidos en este trabajo confirman que la regionalización en zonas con clima Mediterráneo, sigue siendo un reto, y donde el nuevo enfoque espectral mostró resultados prometedores.

2.6.2. Propuesta metodológica

Modelo hidrológico

La modelización hidrológica se planteó mediante un modelo conceptual-continuo a escala de cuenca utilizando la versión HBV-light (Seibert and Vis, 2012) del modelo HBV (Bergström, 1995). Este modelo conceptual comprende diferentes rutinas. La rutina de precipitación-nieve, que estudia el ciclo lluvia-nieve-escorrentía, la rutina que modeliza los procesos que afectan al cambio de humedad del suelo, la rutina que modeliza el flujo subterráneo y, por último, la rutina que estudia la propagación del hidrograma de escorrentía resultante. Este modelo, simula la escorrentía total que se genera en una cuenca tomando como datos de entrada las series temporales de datos de precipitación, temperatura y evaporación potencial. Se utilizó una estructura de modelo de tres cajas de agua subterránea (GW): el almacenamiento en la zona superficial del suelo (STZ), el almacenamiento en la zona superior del suelo (SUZ) y el almacenamiento en la zona inferior del suelo (SLZ) (Figura 39). La definición de los parámetros que intervienen en el modelo en cada rutina se muestra en la Tabla 8.

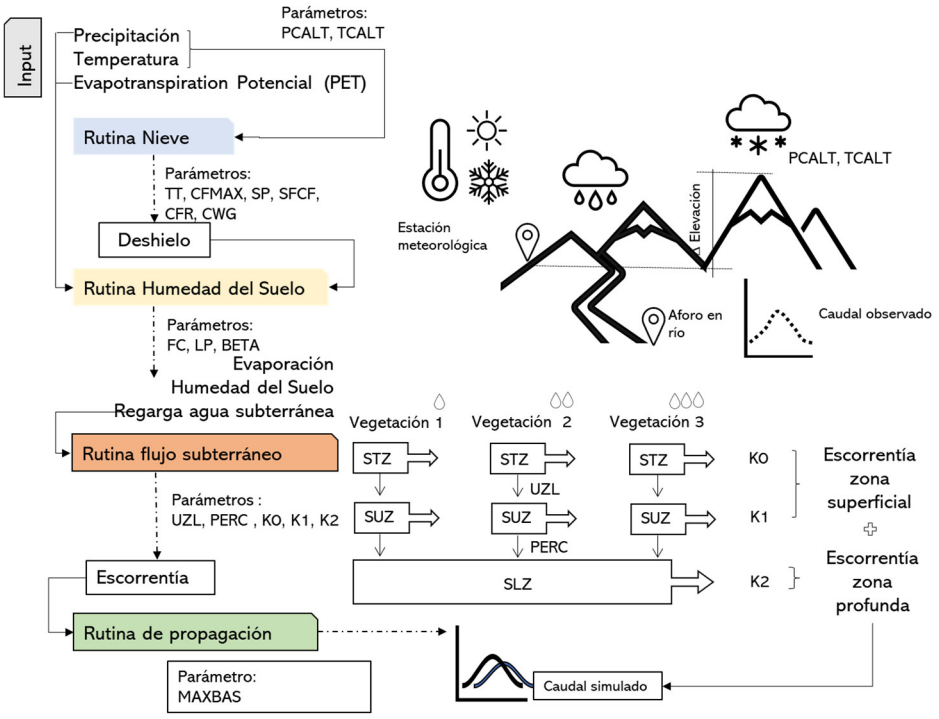

Figura 39. Esquema del modelo hidrológico HBV-light

Tabla 8. Relación de parámetros que intervienen en el modelo HBV-light

Rutina	Datos de entrada	Parámetro	Definición	Unidades	Rango	Dato de salida
-	Precipitación (P_i)	PCALT	Aumento de la precipitación con el incremento de la altura	%/100m	10 – 30	P
-	Temperatura (T_i)	TCALT	Descenso de la temperatura con el incremento de altura	ºC/100m	0,6 – 1	T
-	Evapotranspiración potencial (PET)	-	-	mm/Δt	-	PET
Precipitación - Nieve	P y T	TT	Umbral de temperatura por debajo del cual, la precipitación se acumula en forma de nieve	ºC	-2 – 0,5	Deshielo
		CFMAX	Factor que contrala el deshielo, y la nieve empieza a fundir si la temperatura es superior al umbral TT	mm $ºC^{-1}$ Δt^{-1}	0,5 – 4	
		SP	Variación estacional del factor que controla el deshielo	-	0	
		SFCF	Factor de corrección de nieve	-	0,5 – 0,9	
		CFR	Coeficiente de recongelación	-	0,05	
		CWH	Capacidad de retención del agua que vuelve a congelarse cuando la temperatura desciende por debajo de TT	-	0,01	
Humedad del suelo	P, deshielo y PET	FC	Almacenamiento máximo de la humedad del suelo	mm	50 – 550	AET, humedad del suelo y recarga de aguas subterráneas
		LP	valor de humedad del suelo por encima del cual la evapotranspiración real (AET) alcanza la potencial (PET)	mm	0,3 – 1	

Rutina	Datos de entrada	Parámetro	Definición	Unidades	Rango	Dato de salida
		BETA	parámetro que determina la contribución relativa a la escorrentía de la lluvia o del deshielo	-	1 – 5	
Flujo Subterráneo	Recarga de aguas subterráneas y PET	UZL	Máxima percolación desde STZ hacia SUZ	mm	0 – 70	Escorren-tía
		K_0	Coeficiente de recesión de STZ	Δt^{-1}	0,1 – 0,5	
		K_1	Coeficiente de recesión de SUZ	Δt^{-1}	0,01 – 0,2	
		K_2	Coeficiente de recesión de SLZ	Δt^{-1}	0,00005–0,1	
		PERC	Máxima percolación desde SUZ hacia SLZ	mm Δt^{-1}	0 – 4	
Propagación	Escorrentía	MAXBAX	Coeficiente de respuesta de la cuenca	Δt	1 – 2,5	Hidrogra-ma simulado

STZ: almacenamiento en la zona superficial del suelo
SUZ: almacenamiento en la zona superior del suelo
SLZ: almacenamiento en la zona inferior del suelo

Datos de entrada al modelo

Los datos de los aforos en ríos usados son los registrados por el Sistema Automático de Información Hidrológica (SAIH) de las Confederaciones Hidrográficas del Tajo y del Guadiana. Los SAIH entonces suministran información continua de los puntos de aforos existentes desde 2008. En este trabajo, se ha analizado el flujo diario durante 11 años, desde enero de 2008 hasta diciembre de 2019, dividiendo las series temporales en dos períodos: calibración (enero de 2008 a septiembre de 2014) y validación (octubre de 2014 a diciembre de 2019). Dado que el régimen natural de los ríos estudiados es intermitente, los hidrogramas se analizaron visualmente para garantizar la ausencia de lagunas y valores atípicos, evitando así confundir picos de avenidas con valores numéricos atípicos. (Crochemore et al., 2020).

Los datos de precipitación y temperatura usados en este trabajo fueron los de la base de datos diarios en rejilla de la Agencia Estatal de Meteorología (AEMET) (AEMET, 2019). Los datos de precipitación corresponden a la acumulada en 24 horas, y los datos de temperatura, corresponden a los registros diarios de valores máximos y mínimos. Como se detalla en AEMET (2017), las rejillas de datos se obtuvieron mediante un análisis de interpolación estadística a partir de los datos de las

estaciones de observación, con una resolución espacial de 0,05° en una malla rotada (conforme a CORDEX) basada del modelo de predicción numérica HIRLAM operativo en AEMET.

Para obtener las series diarias en cada cuenca, primero se reproyectaron las cuencas a la malla rotada y luego se obtuvieron las estadísticas zonales de los valores medios diarios en cada cuenca. Además, teniendo en cuenta que la interpolación de estos datos está referida a la ubicación de las estaciones de observación terrestre, para analizar las variaciones de temperatura y precipitación con la altura (PCALT y TCALT), se analizaron las diferencias de cota entre las cuencas y las de las estaciones de referencia. Para ello, se generaron dos ráster auxiliares: uno representando el DEM de las estaciones de observación (gosDEM), obtenido por interpolación IDW de las elevaciones a las que se encuentran las estaciones de observación meteorológicas, y otro, representando en cada celda la distancia euclídea a la estación de observación más cercana (DE).

Por último, la evapotranspiración potencial diaria (*Potential Evapotranspiration* - PET), que, considerando los datos climáticos disponibles, se calculó utilizando la ecuación ETo de Hargreaves de 1985 (véase la ecuación 8 en Hargreaves et al. (2003)). También fue necesario calcular los valores de radiación extraterrestre (Ra) para las diferentes latitudes de las cuencas, y se estimaron siguiendo las ecuaciones de Allen et al. (1998). Finalmente, calcularon los valores medios mensuales de la serie temporal desde enero de 2008 hasta diciembre de 2019.

Características físicas de las cuencas

La regionalización de los parámetros hidrogógicos desde el punto de vista tradicional se ha realizado en base a la topografía y morfología de las cuencas, la cobertura del terreno y características del suelo.

Los datos topográficos y morfológicos se obtuvieron a partir de los DEM a una resolución espacial de 25 m elaborados por el Instituto Geográfico Nacional de España (IGN, 2021). A partir de los DEM se delinearon las cuencas, se obtuvieron las pendientes del terreno y se calcularon: el factor de forma de Horton (Rf), el índice de compacidad de Gravellius (Rc) y el ratio de elongación (Re).

El modelo HBV-light permite analizar las cuencas desde un punto de vista semi-distribuido, considerando distintos rangos de alturas y hasta tres tipos distintos de vegetación. Se plantearon cuatro rangos de altura (considerando en cada cuenca cuatro zonas de elevaciones según cuantiles del DEM en cada una de ellas) y tres clases de vegetación en cada uno de los rangos de altura.

Para la cobertura del terreno se utilizó el mapa elaborado en la Tesis (Figura 26), agrupando las categorías en función de su CN, para lo que se tomó la referencia los valores obtenidos para las estaciones fenológicas 1 (Figura 33) y 5 (Figura 37) ya que son los períodos más lluviosos. Como ya se ha mencionado, las coberturas del terreno estaban limitadas y se agruparon en tres categorías según su capacidad de escorrentía. Así pues, se consideró como tipo 1 la vegetación con baja capacidad que incluye el bosque perenne, el bosque caducifolio, las dehesas y los arbustos; el tipo 2 la vegetación con capacidad media, que incluye la vegetación herbácea y la cubierta de tierras agrícolas; y, por último, el tipo 3, las coberturas con alta capacidad de general escorrentía, que comprende las superficies más impermeables.

Los datos de las propiedades del suelo fueron facilitados, específicamente para la elaboración de esta Tesis Doctoral, por el ESDAC (Joint Research Centre, 2020). Se utilizaron dos bases de datos distintas: para caracterizar la capa más superficial del terreno se utilizaron los datos de Ballabio et al. (2016) en base a la base de datos LUCAS *(Land Use and Cover Area frame Statistical survey)* (ver Figura 32) y para caracterizar las capas más profundas del terreno, se utilizaron los datos de la Base de Datos Europea de Suelos v2.0 (Panagos, 2006).

Para la capa más superficial, se utilizaron los siguientes datos: contenidos de arcilla, limo, arena, densidad aparente del terreno, porcentaje de fragmentos gruesos en la tierra vegetal y la capacidad de agua disponible para la fracción fina del terreno (Ballabio et al., 2016). De todas las características mencionadas se obtuvieron en cada cuenca las estadísticas zonales (valor medio y desviación estándar).

Para el subsuelo, se utilizaron las siguientes propiedades : la clasificación del según la base Referencial Mundial (WRB) de la FAO, la clasificación hidrogeológica, la distancia a la capa impermeable y la capacidad de agua disponible en el subsuelo (Panagos, 2006). De todas las propiedades mencionadas se obtuvieron para cada cuenca los porcentajes de ocupación de cada tipo.

Características espectrales de las cuencas

La respuesta espectral de las cuencas se estudió utilizando las imágenes S1 y S2 procesadas para la P4. Para este caso, se utilizaron tanto las bandas, como los índices radiométricos de suelo, vegetación y agua, así como las métricas de texturas de todas las bandas, tanto de las ópticas como de las del radar, ya que, como se demostró en la P4, resultaron muy útiles para analizar las coberturas del suelo, pero también han sido utilizadas con éxito en otros trabajos previos de análisis litológico (Lu et al., 2021, Radford et al., 2018).

De todas las métricas espectrales, que se muestran en la Figura 40, se obtuvieron las estadísticas zonales para cada cuenca (valor medio, desviación estándar, cuantil 25%, cuantil 50%, cuantil 75%).

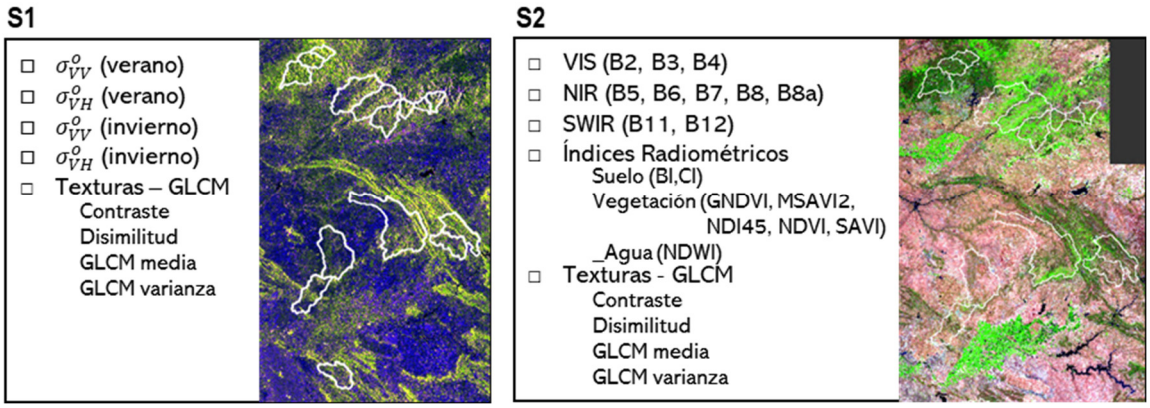

Figura 40. Datos espectrales considerados para la caracterización de la cuencas (visualización de la imagen S1, en composición RGB:VV-VH-VV/VH; visualización S2 en falso color RGB:B11-B8-B3).

Calibración del modelo

La calibración del modelo consistió en obtener para cada cuenca los valores óptimos de los parámetros expuestos en la Tabla 8, y este proceso se abordó en dos etapas: primero cada cuenca individualmente y después se analizaron agrupadas en clústeres de similares características.

La primera etapa, para cada cuenca, comenzó con una simulación de Montecarlo de 50 000 repeticiones, y en cada repetición, los valores de los parámetros se crean aleatoriamente dentro del rango permitido (Tabla 8) garantizando la ausencia de sesgo en el procedimiento de calibración (Seibert, 1999). Tras la primera simulación, se analizaron los resultados obtenidos y se estableció el rango óptimo de los parámetros PCALT y TCALT, que minimizaban el error de volumen del balance hídrico. A continuación, una vez acotados los rangos de PCALT y TCALT, se realizó una segunda simulación de Monte Carlo de 50 000 repeticiones. Los resultados se analizaron para cada parámetro en las distintas funciones de bondad de ajuste (GoF) (Tabla 9) definiendo el rango óptimo para maximizar la exactitud del modelo. El último paso consistió en la aplicación del algoritmo GAP dentro de los límites óptimos de los parámetros obtenidos en los pasos anteriores, y como resultado, se calculó la mejor combinación de valores de los parámetros para una función objetivo utilizando los valores ponderados de Reff, KGE y Reff Peak.

Tabla 9. Funciones de bondad del ajuste (GoF) del modelo hidrológico

Función	Descripción	Ecuación	Valor de ajuste perfecto
Reff	Eficiencia del modelo o Nash-Sutcliffe Efficiency (NSE)	$1 - \frac{\sum(Q_{osb} - Q_{sim})^2}{\sum(Q_{osb} - \overline{Q_{obs}})^2}$	1
KGE	Eficiencia Kling-Gupta	$1 - \sqrt{((r-1)^2 + (\alpha-1)^2 + (\beta-1)^2)}$ r: Pearson correlation coefficient between Q_{sim} and Q_{osb} α: ratio between standard deviation of Q_{sim} and Q_{osb} β: ratio between $\overline{Q_{sim}}$ and $\overline{Q_{osb}}$	1
R^2	Coeficiente de determinación	$\frac{(\sum(Q_{osb} - \overline{Q_{obs}}) \cdot (Q_{sim} - \overline{Q_{sim}}))^2}{\sum(Q_{osb} - \overline{Q_{obs}})^2 \cdot \sum(Q_{sim} - \overline{Q_{sim}})^2}$	1
LogReff	Eficiencia del modelo para log (Q)	$1 - \frac{\sum(\ln Q_{osb} - \ln Q_{sim})^2}{\sum(\ln Q_{osb} - \overline{\ln Q_{obs}})^2}$	1
MeanDiff	Diferencia media de volumen	$\frac{\sum(Q_{osb} - Q_{sim})}{n} \cdot 365$ n : number of times steps	0
VolumeError	Error en volúmen	$1 - \frac{\lvert\sum(Q_{osb} - Q_{sim})\rvert}{\sum(Q_{osb})}$	1
ReffPeak	Eficiencia de los picos del hidrograma	$1 - \frac{\sum(peakQ_{osb} - peakQ_{sim})^2}{\sum(peakQ_{osb} - \overline{peakQ_{obs}})^2}$	1
Objetivo	Función objetivo	0,2·Reff+0,6·KGE +0,2·ReffPeak	1

Para todas las fuciones Gof (excepto MeanDiff):
El valor 1 indica ajuste perfecto entre el caudal observado y el caudal simulado
El valor 0 indica que la simulación es tan buena (o mala) como la predicción del valor medio.
Valores inferiores a 0 indican ajuste insatisfactorio
Para Mean Diff:
El valor 0 indica el ajuste perfecto entre el volumen total observado y el simulado

Durante el proceso de calibración, puede ocurrir que una combinación no única de parámetros obtenga la máxima eficiencia del modelo (Bárdossy, 2007, Hundecha and Bárdossy, 2004). Por tanto, para comprobar la tendencia de los parámetros calibrados en la primera fase en cada cuenca individual, en la segunda etapa, se analizaron los valores en el conjunto del clúster, asumiendo que cuencas con características similares presentarán valores de parámetros similares dentro del mismo clúster. El análisis de clústeres se realizó mediante el método de agrupación jerárquica de Ward (Ward Jr, 1963) con distancias euclídeas utilizando el paquete *Stats Package* de R Software (R-Core-Team, 2018). Este análisis agrupó las cuencas que eran similares, considerando la información, tanto la física y como la espectral, propuesta en este trabajo, y que previamente fueron normalizadas (restando la media y dividiendo por la desviación estándar). De esta manera, los parámetros

fuera de la tendencia de clúster fueron recalculados de nuevo usando el algoritmo GAP. Finalmente, se definió para cada cuenca, la mejor combinación de los parámetros hidrológicos (Best-Par).

Análisis de sensibilidad

Se evaluó la sensibilidad de la modelización a los valores de los parámetros en cada cuenca ejecutando varias simulaciones de Monte Carlo de 10 000 repeticiones, una simulación por cada parámetro, utilizando la combinación Best-Par y variando cada vez, sólo un parámetro dentro del rango original (Tabla 8) y midiendo la disminución de la eficiencia del modelo en todas las GoF respecto al mejor valor de la calibración. Para todas las ejecuciones, se calculó el valor mínimo, medio, mediano y máximo en cada simulación para cada parámetro.

Regionalización de los parámetros

El proceso de regionalización se basa en la hipótesis de que la respuesta hidrológica en cuencas con características similares debe ser también similar. La regionalización se abordó considerando modelos independientes:

- Regionalización climatológica (CR): que comprende el estudio de los parámetros relacionadas con la precipitación, la temperatura y la rutina de la nieve-precipitación, en función de la situación topográfica y la climatología.

- Regionalización del terreno (GR): que comprende el estudio de los parámetros implicados en las rutinas de humedad del suelo, flujo subterráneo y la propagación, en función de las propiedades de la cuenca en términos del perfil espectral, morfología, cobertura del suelo y características del suelo. Además, en este caso, consideramos tres escenarios diferentes para caracterizar las propiedades de la cuenca:

    - Escenario Espectral (SGR): que caracteriza las cuencas considerando exclusivamente la información espectral.
    - Escenario Físico (PGR): que caracteriza las cuencas del modo tradicional en base a sus propiedades físicas: morfología, cobertura del suelo y características del suelo.
    - Escenario Global (GGR): que utiliza la fusión de todas las características, tanto físicas como espectrales.

El análisis de regresión entre los parámetros y las características de las cuencas en cada escenario se realizó con el algoritmo Random Forest (RF) (Breiman, 2001), eficaz trabajando con predictores de origen mixto como los utilizados en este

trabajo. Se utilizó el paquete *RandomForest* de R Software (Liaw and Wiener, 2002) definiendo un número de árboles (Ntree) de 5 000, mientras que el número de variables a seleccionar (Mtry) fue entrenado automáticamente por el algoritmo para cada escenario en función del número de predictores en cada caso.

Para realizar la validación cruzada de las regresiones, se realizó un análisis regresión iterativo, que consistió en dejar fuera del algoritmo las características de una de las cuencas y ejecutar el algoritmo de RF para calcular los parámetros regionalizados (Reg-Par) considerando los datos de las otras. Tras la ejecución de todas las regresiones, los Reg-Par se compararon con los Best-Par, obteniéndose el RMSE de cada parámetro en cada escenario. Por último, la evaluación de efectividad hidrológica de la regionalización en los distintos escenarios se abordó ejecutando el modelo HBV con los Reg-Par obtenidos para cada cuenca y analizando las variaciones en las funciones GoF al compararlas con los resultados del Best-Par.

2.6.3. Resultados y discusión

La agrupación de cuencas en clústeres utilizando agrupación jerárquica de Ward según su similaridad espectral y física se representa en la Tabla 10.

Tabla 10. Dendograma de la agrupación jerárquica de Ward y características bioclimáticas

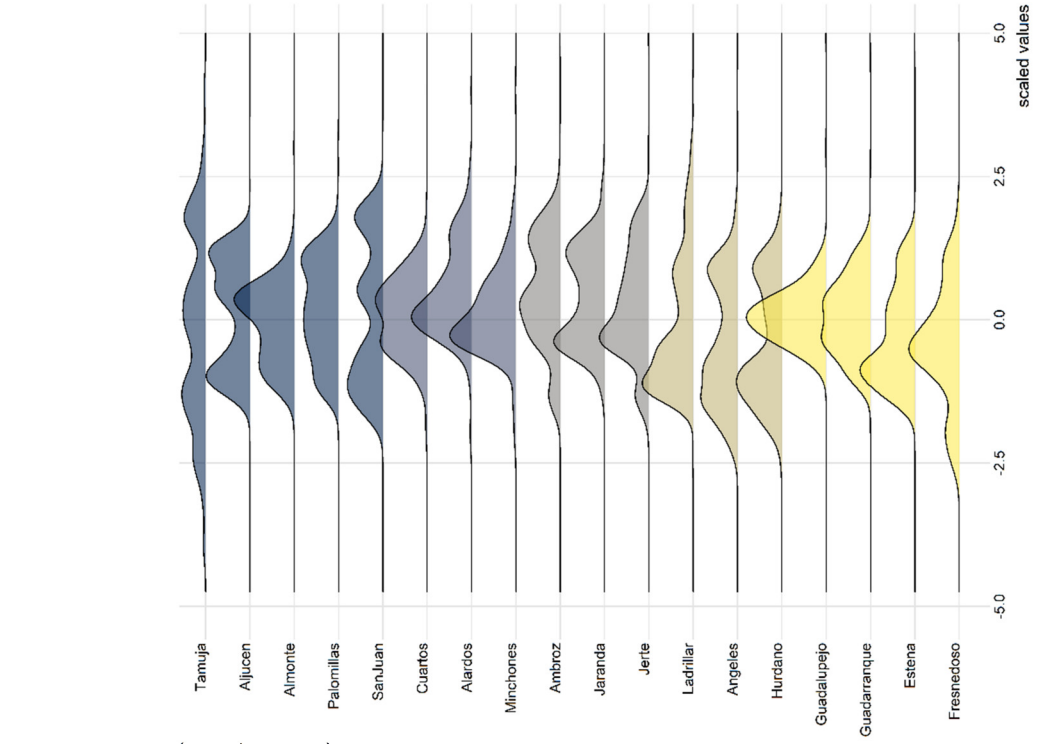

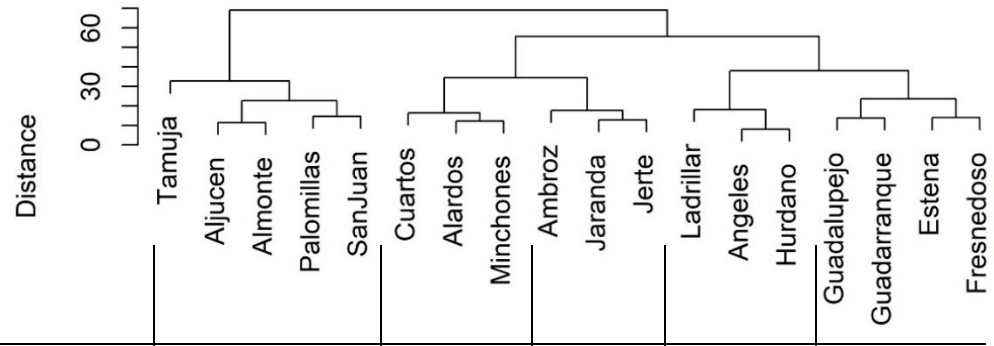

Clúster	1	2	3	4	5
Variante Bioclimática	Mpc	Tocsm	Tocsm	Tocsm	Mpc

Worldwide Bioclimatic Classification System (Rivas-Martinez and Rivas-Saenz, 1996-2019): Mediterranean pluviseasonal-continental (Mpc) and temperate oceanic sub-Mediterranean (Tocsm)

La eficiencia de los obtentidos tras la fase de calibración se resumen en la Tabla 11. Los mejores resutaldos se observaron para los clústeres 2, 3 y 4 (entorno de variante bioclimática Tocsm), mientras en que los clusters 1 y 5 (entorno de variante bioclimática Mpc) son ligeramente inferiores pero igualmente satisfactorios.

Tabla 11. Mediana de los valores de la bondad del ajuste obtenidos en términos globales, por clústeres y por agrupación de clústeres según variedad bioclimática

GoF	Global	Clústeres-Mpc			Clústeres-Tocsm			
		Mpc	Clúster 1	Clúster 5	Tocsm	Clúster 2	Clúster 3	Clúster 4
R2	0,71	0,66	0,63	0,69	0,75	0,73	0,83	0,69
Reff	0,68	0,64	0,63	0,67	0,73	0,72	0,79	0,68
KGE	0,83	0,78	0,78	0,81	0,84	0,84	0,86	0,81
LogReff	-0,36	-0,51	-0,51	-0,97	0,30	-0,29	0,65	0,30
Flow_weighted	0,83	0,81	0,72	0,84	0,86	0,86	0,90	0,71
Reff_peak	0,52	0,42	0,49	0,32	0,73	0,73	0,81	0,61
Volume	0,98	0,98	0,98	0,98	0,98	0,99	0,98	0,97
Objective	0,73	0,69	0,69	0,68	0,79	0,79	0,83	0,74

La Figura 41 muestra los resultados derivados del análisis de sensibilidad. En el computo global (Figura 41a), resultó que las eficiencias de los modelos hidrológicos eran sensibles a las variaciones de los parámetros FC, UZL y K0, asimismo, se detectaron algunas diferencias entre los clústeres (Figura 41b). Los clústeres Mpc (1 y 5), que mostraron sensibilidad a BETA, FC y UZL, mientras que el cluster 3 mostró una alta sensibilidad a FC y PCALT. Por el contrario, la menor sensibilidad apareció para el cluster 2, sensible a K0, PCALT y TCALT y el cluster 4, que resultó sensible a FC, UZL y K0.

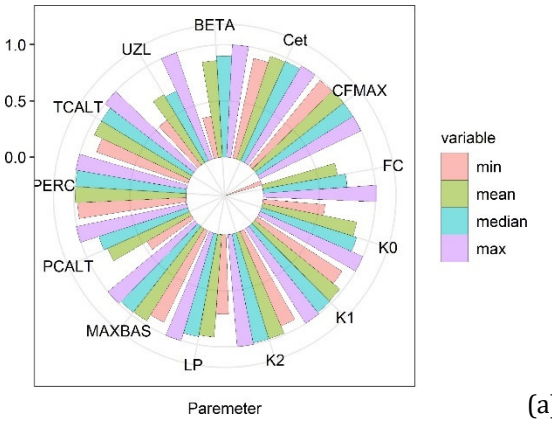

(a)

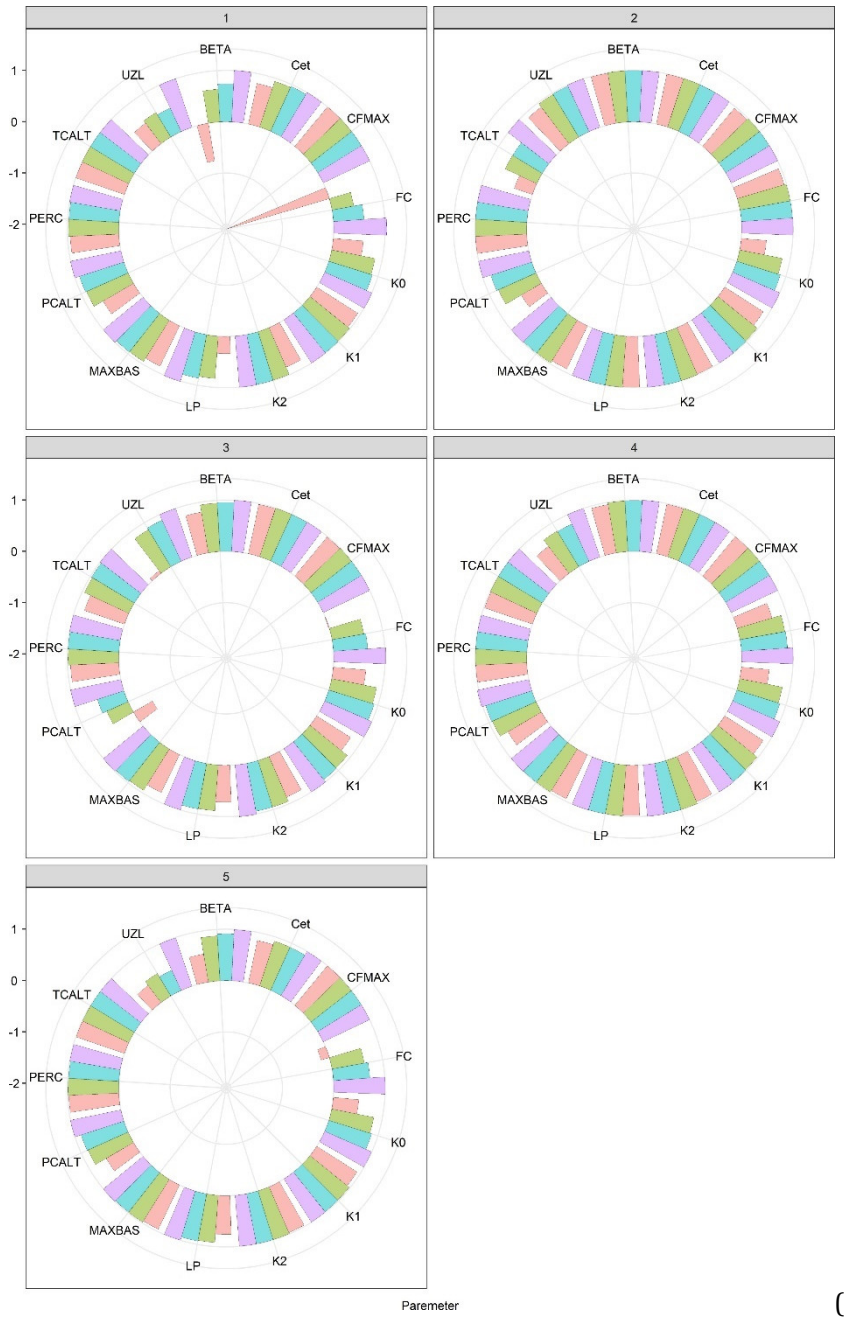

(b)

Figura 41. Sensibilidad del modelo a variaciones de los valores de los parámetros calibrados (a) análisis globlal (b) análisis en clústeres. Los valores de ajuste en torno a 1 implican que el modelo no es sensible a ese parámetro ya que el GoF es tan bueno como los resultados obtenidos por la calibración con la mejor combinación de parámetros.

Los valores de los parámetros tras la calibración y la regionalización de la rutina de precipitación-nieve, rutina de humedad del suelo, rutina de flujo subterráneo y la rutina de propagación, se representan en la Figura 42, Figura 43, Figura 44 y Figura 45 respectivamente. La Tabla 12 muestra los errores en términos del RMSE para cada caso.

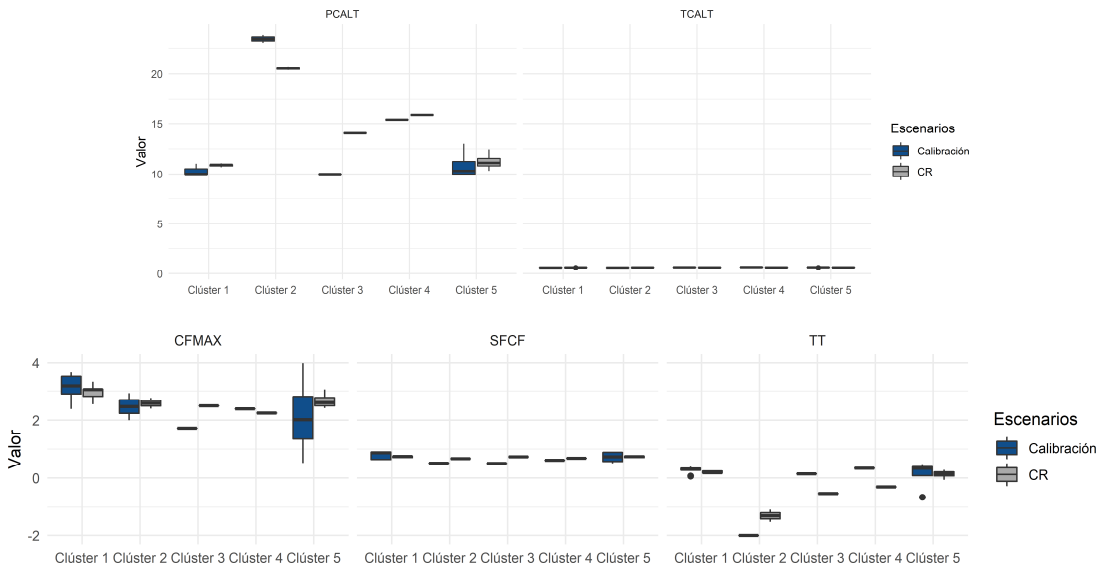

Figura 42. Resultados de la calibración y regionalización de los parámetros hidrológicos relacionados con rutina precipitación-nieve agrupados en clústeres.

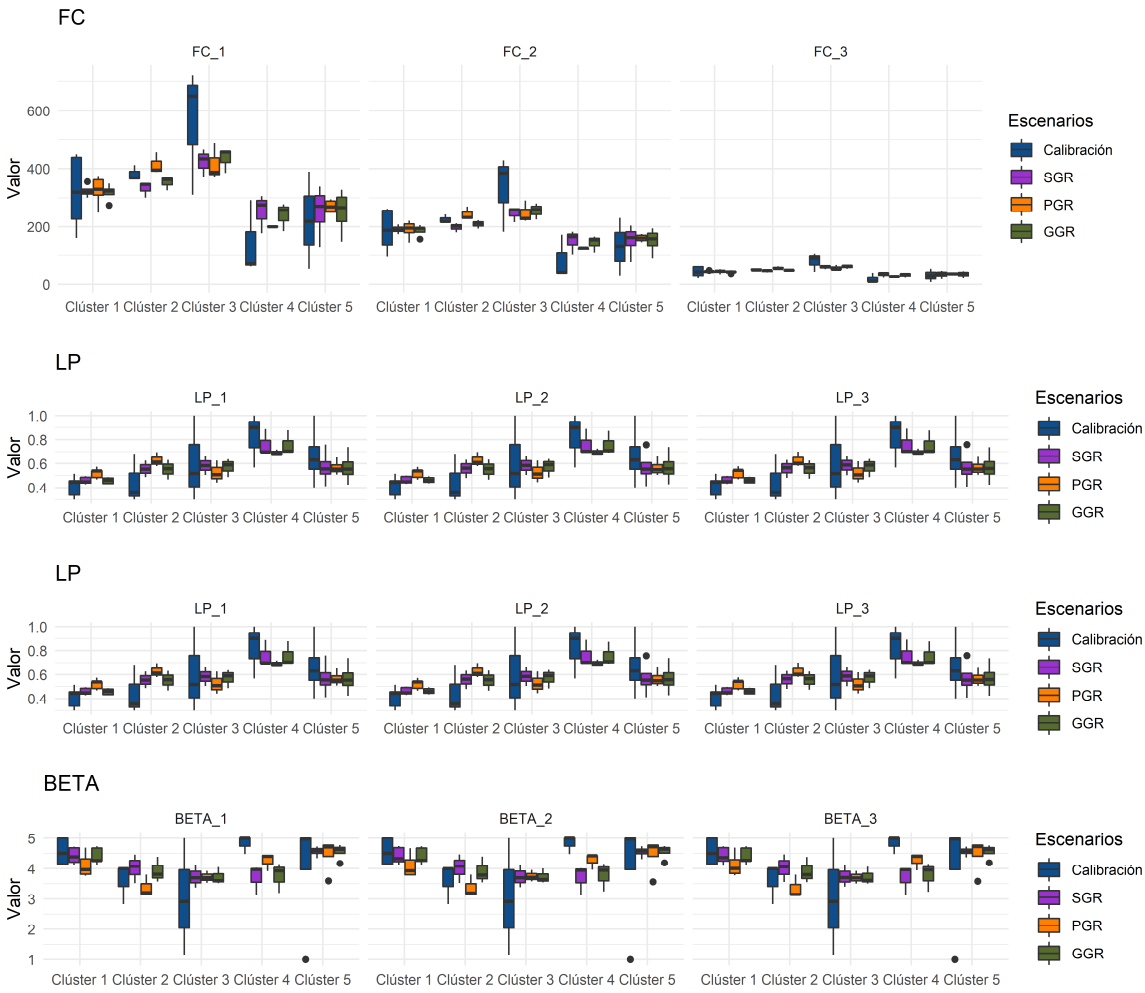

Figura 43. Resultados de la calibración y regionalización de los parámetros hidrológicos relacionados con la rutina de humedad del suelo en los distintos clústeres de cuencas.

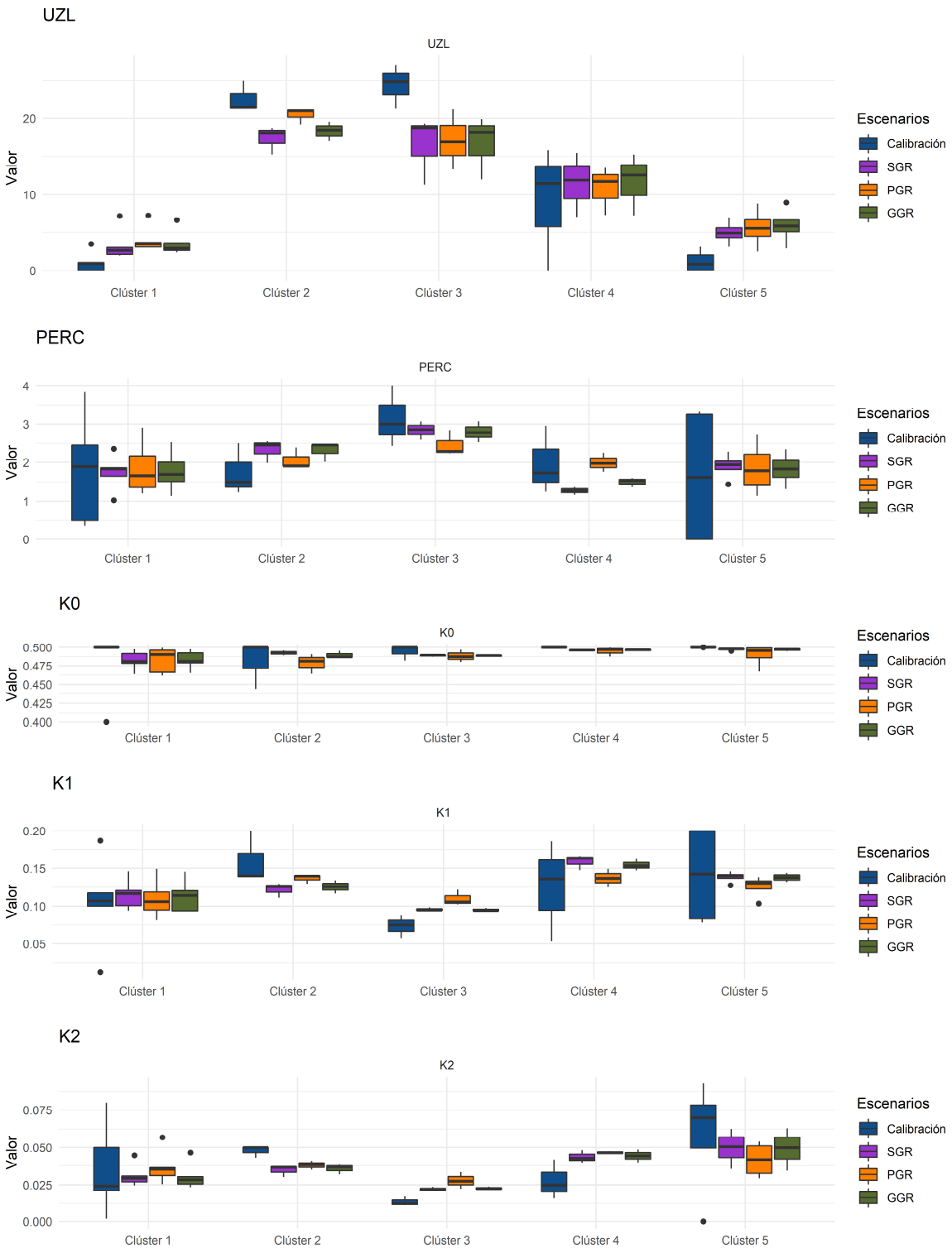

Figura 44. Resultados de la calibración y regionalización de los parámetros hidrológicos relacionados con la rutina de flujo subterráneo en los distintos clústeres de cuencas.

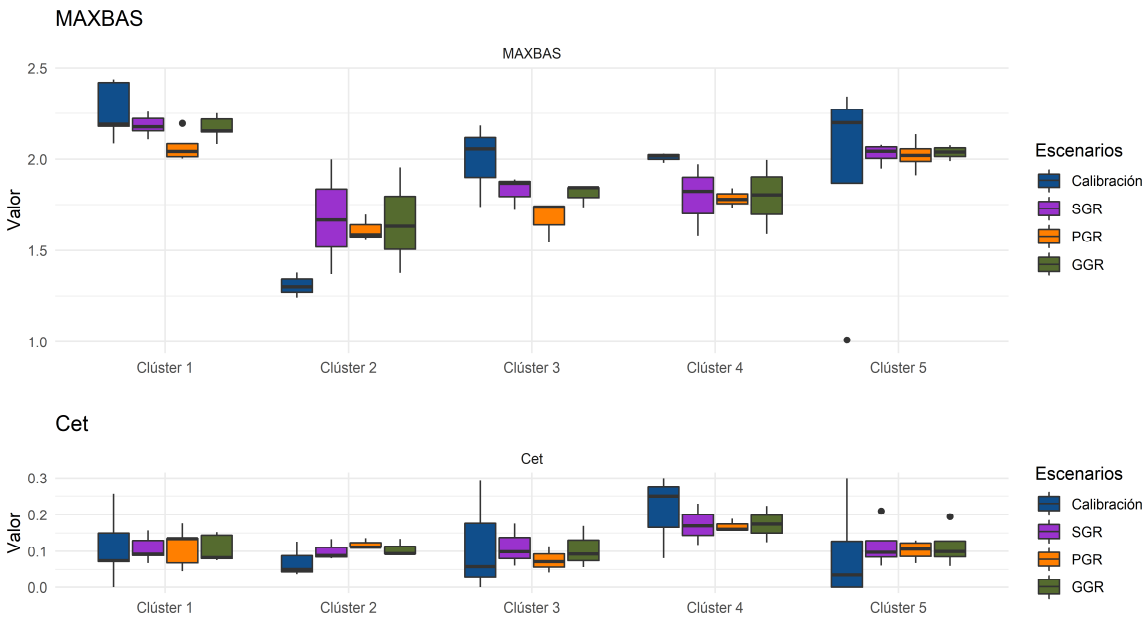

Figura 45. Resultados de la calibración y regionalización de los parámetros hidrológicos relacionados con la rutina de propagación en los distintos clústeres de cuencas.

Tabla 12. RMSE en la regionalización de los parámetros hidrológicos en cada escenario considerado.

Escenario	Parámetros	CR	SGR	PGR	GGR
CR	PCALT	3,59	-	-	-
	TCALT	0,02	-	-	-
	TT	0,56	-	-	-
	CFMAX	0,94	-	-	-
	SFCF	0,18	-	-	-
GR	FC_1	-	168,02	157,84	162,63
	FC_2		101,43	94,59	97,88
	FC_3		24,02	22,44	23,06
	LP	-	0,26	0,26	0,26
	BETA	-	1,39	1,34	1,36
	PERC	-	1,24	1,17	1,18
	UZL	--	6,66	6,16	6,62
	K0	-	0,03	0,03	0,03
	K1	-	0,06	0,06	0,06
	K2	-	0,03	0,03	0,03
	MAXBAS	-	0,36	0,39	0,36
	Cet	-	0,13	0,10	0,12

La Figura 46 representa la importancia de los predictores en la regresión mediante RF, que se evaluó midiendo el aumento del error cuadrático medio cuando un predictor se permuta al azar (%IncMSE) y, por tanto, valores más altos sugieren un papel más importante del predictor en la regresión. En la CR los más influyentes resultaron ser la desviación estándar de las diferencias entre la cota de la cuenca y la cota de referencia de las estaciones de observación de precipitación y temperatura, así como, las variables climáticas medias.

En el caso de la regionalización de los parámetros del terreno, para el escenario SGR, los predictores más influyentes estaban relacionados principalmente con las métricas de texturas, tanto para el SAR como para las bandas ópticas del S2, y también los VI de MSAVI2 y SAVI. En el caso del escenario de PGR, las propiedades de la capa superior del suelo son los predictores más valiosos junto con la cobertura vegetal. Por último, en el escenario GGR, los atributos de la capa superior del suelo siguen siendo predictores influyentes, junto con la cobertura vegetal, las métricas derivadas de la textura de las bandas SAR y NIR y los VI (MSAVI2 y SAVI)

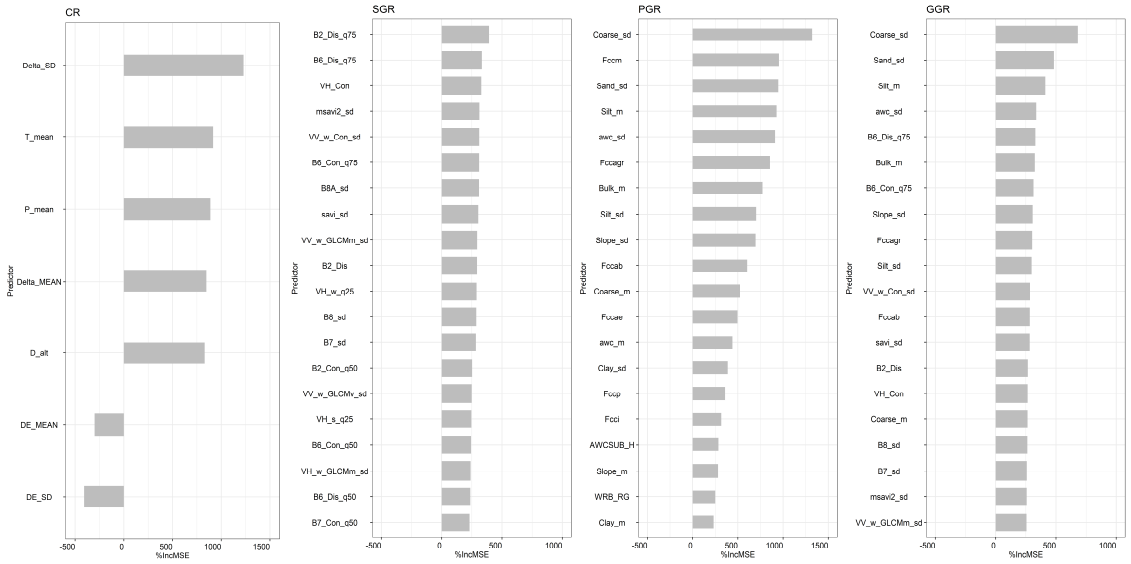

Figura 46. Importancia global de los predictores del algoritmo Random Forest en la estimación de los parámetros hidrológicos. %IncMSE representa el aumento del error cuadrático medio cuando un predictor se permuta al azar.

Por otro lado, analizando los predictores más influyentes específicamente para la regresión de parámetro considerado, en el análisis espectral, SGR, para estimar el valor del parámetro UZL, los valores más influyentes fueron los de las bandas del S2, B2 y B3 y sus texturas (contraste y disimilitud), las bandas del rango NIR-RE y NIR como la B7, B8 y B8A (desviación estándar), los VI (GNDVI, MSAVI2, NDVI y SAVI) y SI (CI), así como y las texturas del SAR en polarización VV. Para estimar el valor del parámetro FC, los predictores más importantes fueron los valores S2 del NIR-RE y

NIR, B6, B7, B8A y B8, y sus texturas derivadas, también los VI (NDVI, SAVI y MSAVI2) y las texturas del SAR en polarización VH (contraste y disimilitud). Por último, para estimar el valor del parámetro K0, las bandas más influyentes fueron las del S2 del espectro SWIR, B11, B12 y sus texturas derivadas (contraste y disimilitud). En el análisis físico, PGR, para estimar el valor del parámetro UZL, los valores más influyentes fueron la pendiente del terreno (desviación estándar), atributos de la capa superficial: el contenido de arena (desviación estándar), limo (media), la densidad aparente (media), y la capacidad de agua disponible (media y desviación estándar). Los predictores mas influyentes para estimar el valor del parámetro FC, fueron, atributos de la capa superficial: contenido de arena (desviación estándar), limo (media y desviación estándar), capacidad de agua disponible (desviación estándar), porcentaje de fragmentos gruesos en la tierra vegetal (desviación estándar), y el porcentaje de cobertura del estrato arbóreo.

La Figura 47 muestra algunos ejemplos de los hidrogramas observados y modelizados, dos en variante bioclimática más seca, Mpc (Tamuja y Almonte) y la Figura 48 dos ejemplos en la variante bioclimática más húmeda, Tocsm (Ángeles y Minchones).

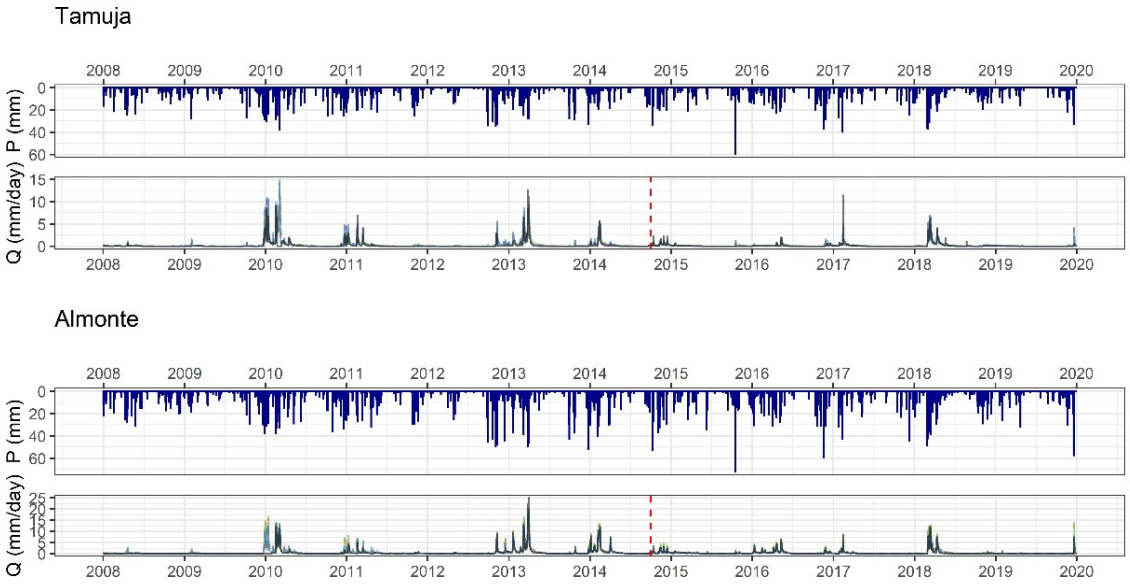

Figura 47. Ejemplos de los hidrogramas observados y simulados en los tres escenarios de regionalización del terreno en cuencas situadas en entorno de variante bioclimática Mpc.. La línea roja vertical representa el fin del período de calibración e inicio del período de validación.

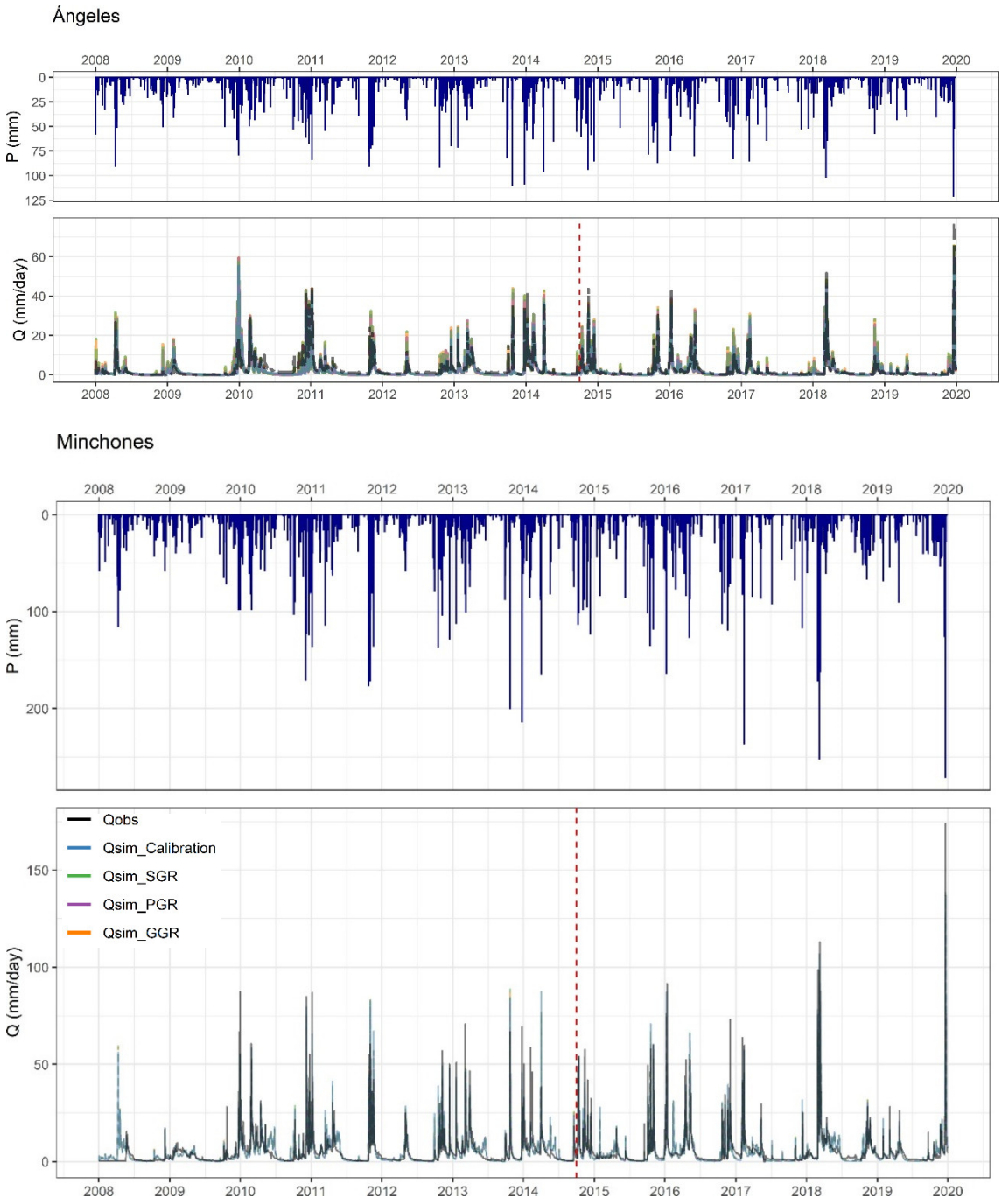

Figura 48. Ejemplos de los hidrogramas observados y simulados en los tres escenarios de regionalización del terreno en cuencas situadas en entorno de variante bioclimática Tocsm. La línea roja vertical representa el fin del período de calibración e inicio del período de validación.

Los resultados detallados en cada cuenca se en muestran en la Tabla 13 para todos los escenarios de regionalización, donde el valor para un ajuste perfecto es 1 y los valores inferiores a 0 indican un ajuste deficiente.

Tabla 13. Tabla resumen de la bondad del ajuste de las simulaciones hidrológicas en las cuencas piloto para todos los escenarios considerados.

Cuenca	R^2	Reff	KGE	LogReff	Flow weighted	Reff peak	Volume	Objetivo	Escenario
Alardos	0,73	0,72	0,84	0,21	0,86	0,44	0,99	0,74	Calibración
	0,56	0,55	0,59	0,26	0,60	0,15	0,91	0,49	CR
	0,71	0,69	0,84	0,29	0,88	0,33	0,98	0,71	SGR
	0,72	0,70	0,84	0,15	0,85	0,39	0,98	0,72	PGR
	0,71	0,69	0,84	0,26	0,88	0,34	0,98	0,71	GGR
	0,55	0,55	0,61	0,29	0,63	0,23	0,89	0,52	CR&GGR
Aljucén	0,63	0,63	0,61	-4,75	0,70	0,31	0,76	0,55	Calibración
	0,63	0,63	0,60	-4,74	0,70	0,30	0,76	0,55	CR
	0,50	0,29	0,16	0,26	0,25	-0,54	0,77	0,05	SGR
	0,52	0,35	0,25	0,15	0,32	-0,43	0,91	0,13	PGR
	0,51	0,29	0,16	0,26	0,26	-0,53	0,77	0,05	GGR
	0,51	0,29	0,17	0,26	0,26	-0,52	0,78	0,05	CR&GGR
Almonte	0,83	0,81	0,91	0,51	0,91	0,70	0,99	0,85	Calibración
	0,83	0,81	0,90	0,50	0,91	0,72	0,98	0,85	CR
	0,78	0,42	0,39	0,50	0,70	0,79	0,64	0,48	SGR
	0,74	0,72	0,77	0,51	0,88	0,57	0,81	0,72	PGR
	0,79	0,56	0,49	0,47	0,78	0,88	0,64	0,58	GGR
	0,79	0,54	0,47	0,47	0,77	0,88	0,62	0,56	CR&GGR
Ambroz	0,83	0,79	0,71	0,65	0,92	0,55	0,72	0,69	Calibración
	0,83	0,60	0,40	0,58	0,86	0,39	0,49	0,43	CR
	0,76	-0,57	-0,23	0,45	0,23	-1,54	0,21	-0,56	SGR
	0,74	-1,07	-0,45	0,39	-0,07	-2,39	0,08	-0,96	PGR
	0,76	-0,54	-0,22	0,45	0,24	-1,48	0,22	-0,54	GGR
	0,73	-1,28	-0,54	0,35	-0,08	-2,55	0,00	-1,09	CR&GGR
Ángeles	0,84	0,83	0,92	0,30	0,88	0,79	0,99	0,87	Calibración
	0,82	0,81	0,90	0,29	0,88	0,76	0,97	0,86	CR
	0,75	0,59	0,64	-2,45	0,87	0,59	0,79	0,62	SGR
	0,77	0,66	0,72	-3,27	0,89	0,68	0,86	0,70	PGR
	0,76	0,61	0,66	-2,48	0,87	0,61	0,80	0,64	GGR
	0,74	0,57	0,63	-2,47	0,87	0,52	0,77	0,59	CR&GGR
Cuartos	0,71	0,69	0,84	-0,68	0,80	0,74	0,99	0,79	Calibración
	0,64	0,64	0,74	-0,41	0,71	0,49	0,94	0,67	CR
	0,72	0,71	0,84	0,27	0,80	0,60	0,96	0,77	SGR
	0,74	0,73	0,83	0,23	0,81	0,56	0,97	0,76	PGR
	0,73	0,72	0,84	0,26	0,80	0,58	0,97	0,76	GGR
	0,66	0,66	0,72	0,29	0,70	0,31	0,98	0,63	CR&GGR
Estena	0,72	0,68	0,84	-0,49	0,87	0,42	0,99	0,73	Calibración
	0,72	0,64	0,79	-0,41	0,87	0,48	0,91	0,70	CR
	0,55	-1,86	-1,06	0,19	0,17	0,00	-0,64	-1,01	SGR
	0,62	0,13	-0,01	0,28	0,77	0,52	0,11	0,12	PGR
	0,57	-1,36	-0,85	0,22	0,31	0,27	-0,48	-0,73	GGR
	0,57	-1,69	-1,03	0,18	0,21	0,14	-0,63	-0,93	CR&GGR

Cuenca	R^2	Reff	KGE	LogReff	Flow weighted	Reff peak	Volume	Objetivo	Escenario
Fresnedoso	0,67	0,66	0,77	-1,45	0,81	0,21	0,88	0,64	Calibración
	0,67	0,66	0,77	-1,46	0,80	0,20	0,87	0,63	CR
	0,65	0,30	-0,06	-2,77	0,37	-1,29	0,21	-0,23	SGR
	0,65	0,30	-0,05	-2,79	0,38	-1,26	0,21	-0,22	PGR
	0,66	0,31	-0,05	-2,79	0,39	-1,25	0,21	-0,22	GGR
	0,64	0,29	-0,06	-3,00	0,37	-1,29	0,20	-0,24	CR&GGR
Guadalupejo	0,84	0,84	0,88	-0,43	0,89	0,53	0,97	0,80	Calibración
	0,84	0,84	0,88	-0,42	0,89	0,53	0,97	0,80	CR
	0,80	0,72	0,57	0,71	0,73	-0,26	0,85	0,43	SGR
	0,80	0,73	0,61	0,65	0,75	-0,14	0,94	0,49	PGR
	0,79	0,71	0,58	0,70	0,73	-0,27	0,87	0,44	GGR
	0,79	0,71	0,58	0,70	0,73	-0,27	0,87	0,43	CR&GGR
Guadarranque	0,62	0,62	0,65	-10,05	0,60	0,11	0,98	0,53	Calibración
	0,62	0,62	0,65	-10,00	0,60	0,11	0,99	0,53	CR
	0,62	0,49	0,33	0,62	0,40	-0,28	0,73	0,24	SGR
	0,60	0,47	0,32	0,64	0,39	-0,29	0,74	0,23	PGR
	0,60	0,47	0,32	0,62	0,39	-0,31	0,74	0,23	GGR
	0,60	0,47	0,33	0,63	0,39	-0,30	0,74	0,23	CR&GGR
Hurdano	0,69	0,68	0,81	0,38	0,71	0,61	0,97	0,74	Calibración
	0,69	0,69	0,74	0,34	0,68	0,55	0,88	0,69	CR
	0,76	0,73	0,63	0,29	0,72	0,45	0,76	0,62	SGR
	0,75	0,74	0,71	0,22	0,73	0,53	0,83	0,68	PGR
	0,76	0,74	0,65	0,32	0,73	0,47	0,78	0,63	GGR
	0,77	0,71	0,54	0,21	0,68	0,34	0,69	0,53	CR&GGR
Jaranda	0,75	0,73	0,86	0,37	0,87	0,81	0,99	0,83	Calibración
	0,75	0,74	0,86	0,38	0,87	0,79	0,98	0,82	CR
	0,76	0,73	0,72	0,36	0,86	0,71	0,75	0,72	SGR
	0,77	0,72	0,68	0,28	0,85	0,69	0,71	0,69	PGR
	0,77	0,73	0,70	0,36	0,85	0,68	0,73	0,70	GGR
	0,77	0,73	0,68	0,36	0,85	0,64	0,72	0,68	CR&GGR
Jerte	0,86	0,85	0,92	0,68	0,90	0,83	0,98	0,89	Calibración
	0,85	0,28	0,21	0,60	0,65	-0,25	0,50	0,13	CR
	0,85	0,56	0,50	0,84	0,79	0,44	0,78	0,50	SGR
	0,81	0,41	0,44	0,84	0,74	0,21	0,81	0,38	PGR
	0,85	0,56	0,51	0,86	0,79	0,45	0,79	0,51	GGR
	0,80	-0,63	-0,22	0,75	0,21	-1,61	0,33	-0,58	CR&GGR
Ladrillar	0,59	0,57	0,54	-6,01	0,51	-0,04	0,88	0,43	Calibración
	0,59	0,54	0,45	-6,38	0,46	-0,17	0,77	0,35	CR
	0,68	0,53	0,34	-0,19	0,43	-0,44	0,69	0,23	SGR
	0,68	0,55	0,38	-0,08	0,46	-0,39	0,73	0,26	PGR
	0,68	0,53	0,35	-0,16	0,44	-0,43	0,70	0,23	GGR
	0,68	0,48	0,25	-0,23	0,38	-0,62	0,59	0,12	CR&GGR
Minchones	0,76	0,74	0,87	-0,29	0,86	0,73	0,98	0,81	Calibración
	0,74	0,72	0,67	-0,52	0,79	0,38	0,76	0,62	CR

Cuenca	R^2	Reff	KGE	LogReff	Flow weighted	Reff peak	Volume	Objetivo	Escenario
	0,76	0,74	0,87	0,28	0,84	0,67	1,00	0,80	SGR
	0,76	0,75	0,87	0,27	0,84	0,62	1,00	0,79	PGR
	0,76	0,74	0,87	0,27	0,84	0,66	1,00	0,80	GGR
	0,74	0,72	0,67	0,14	0,75	0,27	0,78	0,60	CR&GGR
Palomillas	0,43	0,43	0,50	-1,42	0,47	0,13	0,96	0,41	Calibración
	0,43	0,43	0,50	-1,43	0,47	0,13	0,97	0,41	CR
	0,52	0,36	0,18	0,33	0,32	-0,24	0,63	0,13	SGR
	0,49	0,32	0,15	0,32	0,29	-0,32	0,66	0,09	PGR
	0,52	0,35	0,17	0,34	0,32	-0,25	0,63	0,12	GGR
	0,52	0,35	0,17	0,34	0,32	-0,25	0,63	0,12	CR&GGR
San Juan	0,62	0,59	0,78	0,11	0,81	0,49	1,00	0,69	Calibración
	0,67	0,62	0,74	0,10	0,85	0,71	0,82	0,71	CR
	0,66	0,42	0,39	-1,72	0,89	0,87	0,49	0,49	SGR
	0,63	0,09	0,00	-1,71	0,84	0,83	0,14	0,18	PGR
	0,66	0,30	0,25	-1,68	0,87	0,86	0,38	0,38	GGR
	0,66	0,28	0,22	-1,65	0,86	0,86	0,36	0,36	CR&GGR
Tamuja	0,66	0,64	0,81	-0,51	0,72	0,50	0,98	0,71	Calibración
	0,66	0,63	0,81	-0,49	0,72	0,51	0,96	0,71	CR
	0,66	0,66	0,69	0,53	0,59	0,18	0,84	0,58	SGR
	0,65	0,59	0,57	0,37	0,69	0,47	0,62	0,55	PGR
	0,66	0,66	0,69	0,54	0,60	0,20	0,85	0,59	GGR
	0,66	0,66	0,69	0,53	0,60	0,21	0,83	0,59	CR&GGR

Así mismo, la Figura 49 muestra gráficamente resultados en el conjunto global y agrupados según el entorno bioclimático. La tendencia general fue que la disminución exactitud fue menor para la CR que para la GR, donde los tres escenarios en lograron casi la misma eficiencia, y el escenario que combina la regionalización climática y del terreno CR&GGR logró exactitudes ligeramente inferiores. Por el contrario, la eficacia en términos del logaritmo del caudal mejoró mucho en todos los escenarios de GR. En cuanto a las diferencias entre los clústeres, los clústeres 2 y 4 mostraron el mejor rendimiento en la evaluación de la regionalización, mientras que el grupo 5 obtuvo las eficiencias más bajas. Los resultados de SGR fueron mejores que los de PGR las cuencas más secas (Mpc), mientras que en las más húmedas (Tocsm) fue al contrario. La función que evalúa la bondad del ajuste de los caudales punta del hidrograma fue la que obtuvo los peores resultados.

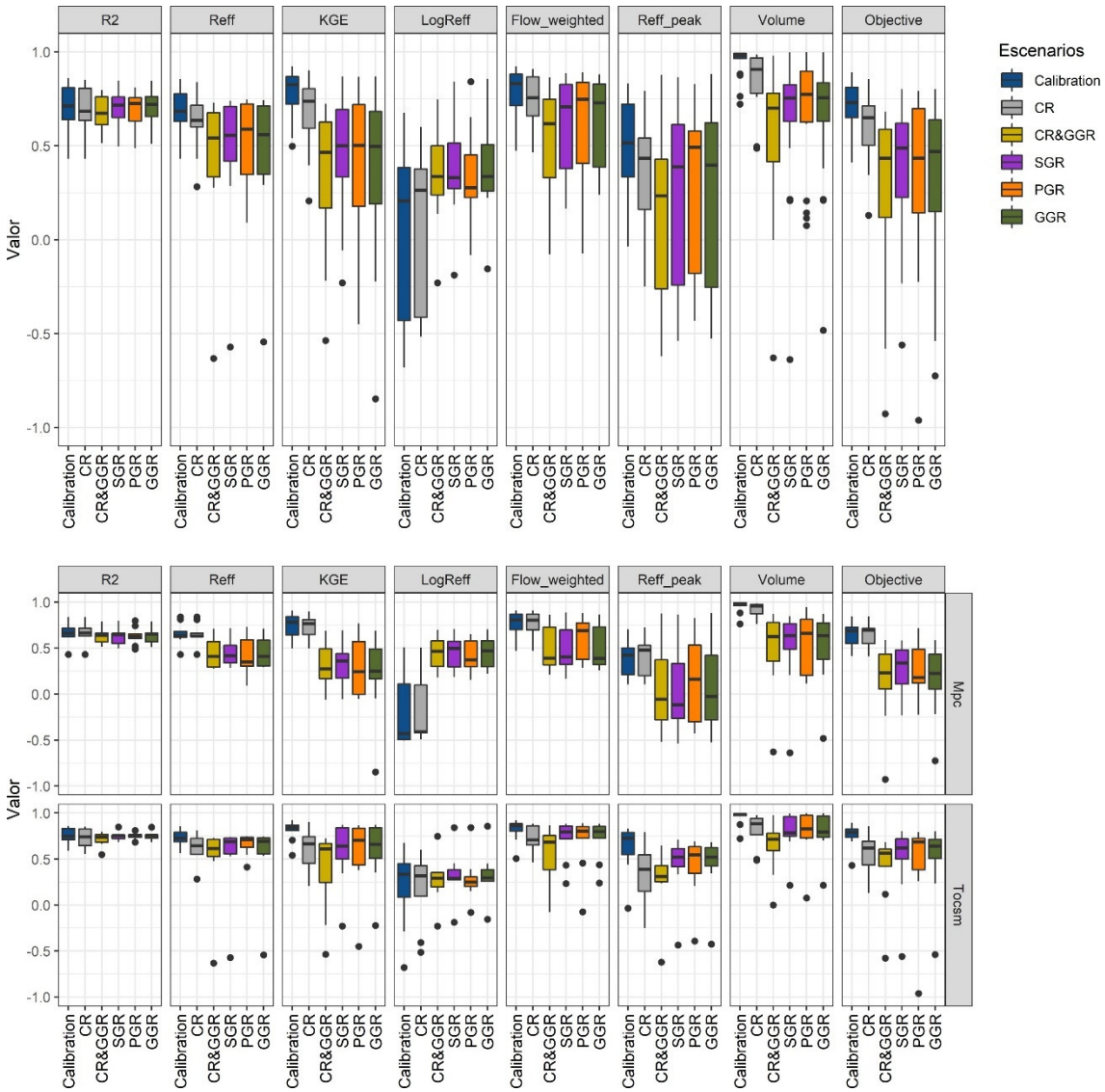

Figura 49. Gráfico Boxplot de los valores de las funciones de bondad del ajuste de los modelos en los diferentes escenarios considerados para la regionalización de los parámetros (Nótese que en esta gráfica no se representan lo valores por debajo de -1 de la Tabla 13).

Antes de comparar los resultados de esta Tesis con estudios anteriores, cabe señalar que existen pocos trabajos en latitudes y variantes climáticas mediterráneas, que sean similares al entorno estudiado en esta Tesis, lo cual dificulta la comparación de la eficacia obtenida. La Tabla 14 resume los resultados obtenidos en esta Tesis en la fase de calibración frente a otros estudios anteriores, sea cual fuere el ámbito de estudio y para cualquier enfoque de regionalización.

Tabla 14. Comparación de los resultados obtenidos en la fase de calibración con otros estudios previos.

Fase de Calibración	KGE (mediana)	NSE (mediana)	Ámbito de estudio
Tesis	0,83	0,68	Mediterraneo
Beck et al. (2020)	0,46	-	Global
	0,30*	-	Clima árido
Alfieri et al. (2020)	0,61	0,35	Global
	0,82 **	-	Europa
Merz and Blöschl (2004)	-	0,63	Austria
Jin et al. (2009)	-	0,78	China
Götzinger and Bárdossy (2007)	-	0,53	Alemania
Parajka et al. (2007)	-	0,66-0,69	Austria

* interpretación visual de la Figura 5 de Beck et al. (2020) para clima árido donde se situaría España según su trabajo

**interpretación visual de la Figura 6 de Alfieri et al. (2020)

En términos de KGE, los resultados de la Tesis superaron a trabajos anteriores, como los obtenidos por Beck et al. (2020) y similares a los obtenidos por Alfieri et al. (2020) para el ámbito europeo. Desde el punto de vista del Reff, también conocido como Eficiencia de Nash-Sutcliffe (NSE), nuestros resultados fueron similares a los de Merz and Blöschl (2004) y Parajka et al. (2007), mejores que los obtenidos por Götzinger and Bárdossy (2007) e inferiores a los obtenidos por Jin et al. (2009). Cabe destacar que nuestra calibración se realizó optimizando una función objetivo en la que Reff y KGE se ponderaron con 0,20 y 0,60.

En cuanto a nuestros resultados regionalizados, el escenario GGR, que combina todos los atributos espectrales y físicos, no obtuvo mejores resultados que los SGR y PGR en ningún caso. Esto quizás es debido a que la respuesta espectral del terreno está condicionada por las características físicas del territorio y la suma de los predictores no aporta información nueva al clasificador sino redundante. Comparando específicamente las eficiencias de SGR frente a PGR, en el cómputo global el SGR fue ligeramente inferior a los resultados en el PGR (Tabla 15).

Tabla 15. Comparación de los resultados obtenidos en la fase de regionalización con otros estudios previos.

	KGE (mediana)			Reff - NSE (mediana)			Ámbito de estudio
	Mpc & Tocsm	Mpc	Tocsm	Mpc & Tocsm	Mpc	Tocsm	
Tesis en escenario SGR	0,45	0,33	0,64	0,54	0,42	0,69	España
Tesis en escenario PGR	0,50	0,25	0,71	0,57	0,35	0,70	España
Merz and Blöschl (2004)		-			0,56		Austria
Götzinger and Bárdossy (2007)		-			0,50		Alemania
Masih et al. (2010)		-			0,47*		Iran (semi-arid)
Jin et al. (2009)		-			0,72		China (subtropical)

*estimado a partir de la Tabla 7 en Masih et al. (2010) usando los siete mejores valores

Los valores de esta Tesis, desde el punto de vista global, son del orden de los obtenidos por Merz and Blöschl (2004) y Götzinger and Bárdossy (2007) y mejores que los logrados por Masih et al. (2010). Sin embargo, si diferenciamos por variedades climáticas, los resultados, tanto para SGR y PGR, en Tocsm, son mejores que los obtenidos por Merz and Blöschl (2004) y Götzinger and Bárdossy (2007) en Austria y Alemania que se encuentran en una variante Toc (*temperate oceanic*) (Rivas-Martinez and Rivas-Saenz, 1996-2019). Del mismo modo, los resultados para SGR en Mpc resultaron ligeramente inferiores a los obtenidos por Masih et al. (2010) en Irán, y los resultados de PGR en Tocsm, resultaron ligeramente inferiores que los obtenidos por Jin et al. (2009) en china (clima subtropical).

Los resultados también se compararon con el obtenido por el conjunto de datos *global high-resolution regionalized parameters* (GloH20) (Beck et al., 2020). Para ello, tras descargar la información disponible, procesamos para cada cuenca, el valor medio de los parámetros disponibles del modelo (BETA, FC, K0, K1, K2, LP, PERC, UZL, TT, CFMAX, CFR y CWH) del conjunto de datos GloH20. Para los parámetros no mencionados anteriormente (PCALT, TCALT, SFCF, MAXBAS y Cet) se asumió el Best-Par obtenido en nuestra calibración y, después, se ejecutaron de nuevo los modelos HBV para cada cuenca y se obtuvieron las eficiencias en cada caso.

La Figura 50 muestra que el enfoque regional propuesto en esta Tesis (SGR, PGR y GGR) superaron en eficiencia a los obtenidos a partir de los globales de GloH20 en todas las funciones de bondad de ajuste consideradas. Específicamente para el caso de KGE, nuestros resultados (mediana) SGR (0,45), PGR y GGR (ambos 0,50) fueron superiores a los obtenidos por GloH20 (0,20).

El área de estudio de esta Tesis, en España, según la Figura 5 de Beck et al. (2020) se clasificaría dentro de la categoría de clima árido y, para esta categoría, los resultados mostraron un KGE aproximadamente de -0,05 (de -0,20 en el percentil 25 a 0,15 en el percentil 75 según la interpretación de la Figura 2 en Beck et al. (2020)). Por lo tanto, teniendo en cuenta que en su trabajo no se observan estudios en la península Ibérica, los resultados obtenidos al aplicar los parámetros regionalizados de GloH20 en las cuencas de esta Tesis, obtuvieron una eficiencia aproximadamente del mismo orden de magnitud que los informados en el estudio original para la clase de clima árido. Además, los parámetros regionalizados de GloH20 lograron bueno resultados en las cuencas más húmedas (Tocsm) en las que alcanzaron un KGE de alrededor de 0,28 (mediana). Por el contrario, los resultados en los entornos más secos (Mpc) fueron peores, con un KGE alrededor de -0,14. La razón principal, se debe a las diferencias en la estimación de los parámetros más sensibles en las cuencas estudiadas, observándose que GloH20 sobreestima los valores de FC y UZL y subestima los valores de K0 en comparación con los Best-Par y Reg-Par obtenidos en nuestro trabajo.

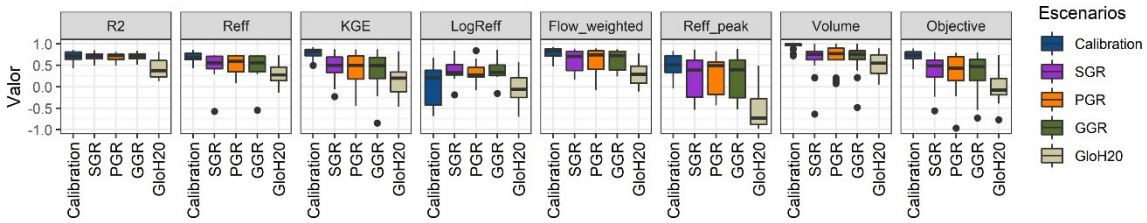

Figura 50. Comparación de las eficiencias de las modelizaciones hidrológicas en los escenarios de regionalización del terreno propuestos en la Tesis, frente a los resultados obtenidos al aplicar los parámetros hidrológicos regionalizados de la base de datos *Global high-resolution regionalized parameters* (GloH20) propuestos en Beck et al. (2020).

Los resultados obtenidos mostraron una eficiencia de los modelos relacionada con el punto de vista climático ya que, las cuencas clasificadas como variante bioclimática Tocsm en general obtuvieron eficiencias superiores a las clasificadas como Mpc (Figura 49). Este aspecto concuerda con los hallazgos de la revisión de Parajka et al. (2013), quienes indicaron que la exactitud de las simulaciones de la escorrentía tiende a ser menor en las regiones áridas que en las frías y húmedas, y también con el hallazgo de Goswami et al. (2007), donde los peores resultados se obtuvieron en la cuenca más seca de su estudio.

En relación con la regionalización de las variables climáticas, encontramos una mayor disminución de la eficiencia de la modelización en las cuencas húmedas que en las más secas, de acuerdo con el análisis de Pianosi and Wagener (2016), quien

indicó que la incertidumbre en la precipitación tiene más influencia en las cuencas húmedas que en las secas.

Los resultados mostraron que la información del suelo suministrada por el ESDAC, tuvo una fuerte influencia en la regresión de los parámetros, ya que las propiedades de la capa superior del suelo resultaron ser los predictores más valiosos en el escenario PGR y también en el GGR, junto con las métricas derivadas de la textura de las bandas SAR, NIR e IV. La regresión en el escenario SGR obtuvo mejores resultados que el PGR en las cuencas de la variante bioclimática Mpc, que son las más secas y se caracterizan por una cobertura vegetal de media a baja. Los predictores más influyentes en el SGR están relacionados principalmente con las métricas de las texturas tanto para el SAR (en ambas polarizaciones) como para las bandas del S2 y algunos VI. Las métricas de texturas del SAR están influenciadas por el tamaño de grano de la superficie (Lu et al., 2021), y la capacidad del radar para estudiar la litología del terreno es mejor en las zonas con cobertura de vegetación escasa que en las de vegetación densa (Radford et al., 2018). Además, la información óptica de las bandas azul y NIR resultaron ser también valiosos predictores en la regresión, y estas bandas, ya habían resultado eficaces en estudios de la geología de regiones áridas (Rajendran and Nasir, 2021). Los dos VI más influyentes, son los que tienen en cuenta el ruido de la reflectancia del suelo sobre la vegetación en áreas con vegetación dispersa (MSAVI2, SAVI), resultando especialmente el influyente el MSAVI2, que considera además que diferentes suelos tienen diferente respuesta espectral (Qi et al., 1994). Además, resultó que varios de lo índices utilizados VI (GNDVI, MSAVI2, NDVI y SAVI) y SI (CI) tuvieron gran influencia en la estimación del parámetro UZL, que fue de los parámetros más sensibles de los modelos hidrológicos y que interviene en la percolación desde zona más exterior del terreno hacia el interior.

De los resultados obtenidos, cabe señalar que la eficacia en los modelos hidrológicos depende en gran medida del entorno climático, y al comparar los resultados con otros estudios, parece muy recomendable analizar los hallazgos desde el punto de vista climático más que desde el metodológico. Una de las cuestiones clave en la regionalización de los parámetros hidrológicos es la disponibilidad de cartografía para extraer los atributos de las cuencas (Merz and Blöschl, 2004)y también, la variabilidad en la nomenclatura de la cartografía temática, si proviene de distintos orígenes (regiones o países). En este sentido, disponer de los datos del suelo en toda Europa, como los suministrados por el ESDAC, junto con la información de los satélites Sentinel suministrados por el Programa Copernicus de la Unión Europea, nos ofrece nuevas oportunidades en la regionalización de los parámetros a escala europea. Los resultados presentados en esta Tesis son los primeros en cuanto a la regionalización de parámetros en entorno climático del Mediterráneo, ya que casi

todos los estudios previos de ámbito regional de latitudes similares se localizan en áreas del norte de Europa o Irán. Nuestros resultados confirman que la regionalización en entornos Mediterráneos sigue siendo un reto, donde el nuevo enfoque espectral SGR mostró resultados prometedores. Además, dado que los eventos de precipitación de las cuencas mediterráneas tienen un marcado carácter estacional, las series temporales de los datos Sentinel podrían mejorar los enfoques de regionalización considerando parámetros hidrológicos con variación estacional, en vez de considerar valores medios anuales como los analizados en este trabajo.

Por último, los resultados obtenidos en la regionalización utilizando exclusivamente datos espectrales, ofrece nuevas posibilidades en territorios donde no se disponga de información cartográfica sobre los usos y tipos de suelo ya que los datos Sentinel ofrecen una cobertura continua en casi todo el mundo.

3. Conclusiones Finales

En la investigación desarrollada en esta Tesis Doctoral se ha aplicado la teledetección como apoyo en la modelización hidrológica con el propósito de disminuir la incertidumbre asociada a la estimación de parámetros hidrológicos desde dos enfoques: en primer lugar, con miras a la generación de cartografía ad hoc para modelización hidrológica y, en segundo lugar, con el objeto de la regionalización de parámetros hidrológicos en cuencas no aforadas.

La cartografía *ad hoc* para modelización hidrológica se elaboró mediante la clasificación supervisada de la fusión de datos S1 y S2 aplicando el algoritmo Random Forest. La información espectral facilitada por los satélites se amplió con métricas de textura e índices radiométricos derivados. El método propuesto, se basó en la selección de los predictores más influyentes para reducir los problemas computacionales y garantizando a su vez, la exactitud de los mapas finales, que representaron los principales tipos de cobertura del suelo a una alta resolución espacial. Los tipos de cobertura del suelo se clasificaron según su capacidad potencial de escorrentía en términos del parámetro NRCS-CN. De este modo, se caracterizó la respuesta hidrológica de las cuencas mediante el análisis de la escorrentía potencial, así como su variación estacional debida a cambios fenológicos. El resultado fue la representación veraz y detallada del territorio específicamente diseñado para abordar simulaciones hidrológicas a escala regional en pequeñas cuencas forestales.

La investigación propone una metodología para definir las áreas de entrenamiento a partir de la clasificación supervisada de imágenes de ultra alta resolución espacial del PNOA y considerando los datos derivados del LiDAR-PNOA como apoyo. La definición adecuada de las áreas de entrenamiento fue un elemento clave en el desarrollo metodológico ya que, la exactitud de los mapas obtenidos por clasificación supervisada depende de la veracidad de dichas áreas de entrenamiento. Así pues, se desarrolló un método para reducir las campañas de campo evaluando la posibilidad de transferir los datos del algoritmo de clasificación a imágenes vecinas que no se utilizaron inicialmente para entrenar el modelo, logrando buenos resultados. De esta forma, se minimizó el trabajo manual asociado a la fotointerpretación y a las campañas de campo, en la amplia extensión del estudio.

En la fase inicial de los trabajos de la Tesis, se estudió la mejora de la exactitud en la clasificación de la cobertura del territorio utilizando fusión de datos LiDAR-PNOA con S2 proponiendo el uso de una serie multitemporal de las imágenes. En esta época eran pocos los trabajos que habían utilizado las imágenes Sentinel debido a

su entonces reciente lanzamiento. Por tanto, el estudio sobre la fusión de datos S2 y el LiDAR-PNOA se planteó en un contexto novedoso. Además, se abordó el estudio temporal a escala anual y estacional. Los resultados obtenidos mostraron que los datos LiDAR-PNOA del Instituto Geográfico Nacional de España eran adecuados para fusionarlos con los datos Sentinel, mejorando notablemente las exactitudes en la clasificación de coberturas. Como existía un desfase importante entre las fechas de adquisición de datos del LiDAR-PNOA y las imágenes S2, se desarrolló un método basado en el uso de métricas booleanas LiDAR para ayudar al clasificador en la separación del sotobosque y dosel arbóreo.

Sin embargo, la principal limitación de esta metodología radica en la difícil tarea de verificación de las áreas de entrenamiento utilizando una serie temporal de imágenes PNOA que cubra el desfase entre las fechas de adquisición de los datos, lo cual, limita la aplicación del método en áreas extensas. Por lo tanto, para aplicar la fusión de datos LiDAR-PNOA e imágenes Sentinel de una forma efectiva en grandes extensiones, se debía realizar utilizando directamente las alturas normalizadas de la vegetación en la clasificación, y para ello, el desfase temporal debía ser mínimo. Sin embargo, varios lotes en el área de estudio de la Tesis sufrieron un retraso en las actualizaciones de la segunda cobertura, que estaba prevista en el segundo semestre del 2019, y no se llegaron a publicar durante el período de elaboración de esta Tesis. Este fue el motivo por el cual, se limitó el uso de los datos LiDAR-PNOA de la primera cobertura de 2010, exclusivamente como apoyo en la definición de las áreas de entrenamiento, y no como predictor en la extensión global del estudio.

Por otro lado, aprovechando el lanzamiento de la misión *The Global Ecosystem Dynamics Investigation* (GEDI) en 2018, se investigó la posibilidad de aplicarlos para conocer la estructura vertical de la vegetación, como fuente de datos alternativa a los datos LiDAR-PNOA. No obstante, debido entonces reciente lanzamiento, antes de poder abordar su posible fusión con las imágenes Sentinel, fue necesario evaluar específicamente la exactitud con la que los datos GEDI medía las alturas de vegetación en el ámbito de estudio de la Tesis. Los resultados globales mostraron diferencias de elevación de los datos GEDI en relación con otras fuentes de datos más exactas y, si bien los errores obtenidos concordaban con otros estudios previos, se obtuvieron resultados pobres en los estratos inferiores. Por este motivo, la utilización de los datos GEDI para la extrapolación a una cobertura continua de alturas de vegetación, resultó inviable para el objetivo de esta Tesis.

En relación con la de generación de la cartografía *ad hoc* para modelización hidrológica, la principal aportación de investigación desarrollada en esta Tesis es la propuesta de una metodología de generación de mapas específicamente diseñados para la elaboración de cálculos hidrológicos, a una resolución espacial detallada, que

disminuye la incertidumbre asociada a los usos y características hidrológicas del suelo, permitiendo abordar modelos a escala regional. Los datos utilizados en su elaboración provienen de fuente de datos abiertas, como el Programa Copernicus, Instituto Geográfico Nacional de España y del Centro Europeo de Datos de Suelos (ESDAC) y, por tanto, la metodología propuesta puede replicarse en cualquier ámbito nacional o europeo (siempre que cuente con los datos equivalentes a los del proyecto PNOA en España).

Tras la fase de generación de la cartografía *ad hoc*, se estudió la capacidad de la firma espectral de las cuencas para la regionalización de los parámetros hidrológicos mediante un enfoque de aprendizaje automático basado en la regresión. Para ello, se analizó la firma espectral de las cuencas basada en los datos S1 y S2, así como la caracterización física de la cobertura del suelo, tomando como referencia la cartografía *ad hoc*, las propiedades morfológicas y datos físicos del suelo. Se aplicó el algoritmo de RF para abordar la regresión de los parámetros hidrológicos que intervienen en la generación de escorrentía desde diferentes puntos de vista: considerando un novedoso enfoque que utiliza exclusivamente la firma espectral de las cuencas, el método clásico que utiliza las propiedades físicas y un método mixto que utiliza los datos espectrales y físicos.

Los datos de la cartografía *ad hoc*, permitieron abordar la calibración de los modelos hidrológicos utilizando un enfoque espacial semi-distribuido, y los resultados obtenidos en la fase de calibración fueron excelentes. En la fase de regionalización, los tres escenarios considerados lograron prácticamente la misma eficiencia en las modelizaciones y se detectó que la eficacia en los modelos hidrológicos dependía del entorno climático. La tendencia fue que la predicción en las cuencas más húmedas obtuvo mejores resultados en las más secas. En los entornos más húmedos, la regionalización en el escenario físico alcanzó mejores eficiencias que el escenario espectral. Sin embargo, en los entornos más secos, la regionalización del escenario espectral mostró los mejores resultados. Nuestros resultados confirmaron que la regionalización sigue siendo un reto en las variantes bioclimáticas mediterráneas, donde el nuevo enfoque espectral mostró resultados prometedores.

La principal aportación de la Tesis en este ámbito es la de la aplicación de la firma espectral de las cuencas en el ámbito de la regionalización de parámetros hidrológicos. Además, se plantean futuras líneas de investigación ya que disponer de datos continuos del suelo en toda Europa, junto con la información de Sentinel, nos ofrece nuevas oportunidades en la regionalización de parámetros a escala europea, especialmente para llenar el vacío de los estudios de regionalización en el entorno mediterráneo. Además, la cobertura continua de los datos de Sentinel en todo el mundo ofrece nuevas posibilidades en zonas donde no se dispone de

información cartográfica. Y, por último, sería también destacable que las series temporales de datos satelitales podrían mejorar los enfoques de regionalización estacional caracterizando la respuesta hidrológica de las cuencas y su variabilidad estacional.

Referencias

AEMET. 2017. *Serie de precipitación diaria en rejilla con fines climáticos. Nota técnica 24 de AEMET.* [Online]. Available: https://www.aemet.es/es/conocermas/recursos_en_linea/publicaciones_y_estudios/publicaciones/detalles/NT_24_AEMET [Accessed June 2019].

AEMET. 2019. *Datos observacionales Precipitación y Temperatura* [Online]. Available: http://www.aemet.es/es/serviciosclimaticos/cambio_climat/datos_diarios?w=2 [Accessed December 2020].

AHMED, O. S., FRANKLIN, S. E., WULDER, M. A. & WHITE, J. C. 2015. Characterizing stand-level forest canopy cover and height using Landsat time series, samples of airborne LiDAR, and the random forest algorithm. *ISPRS Journal of Photogrammetry and Remote Sensing,* 101**,** 89-101. DOI: 10.1016/j.isprsjprs.2014.11.007

AKIKE, S. & SAMANTA, S. 2016. Land Use/Land Cover and Forest Canopy Density Monitoring of Wafi-Golpu Project Area, Papua New Guinea. *Journal of Geoscience and Environment Protection,* 4**,** 1. DOI: 10.4236/gep.2016.48001

ALFIERI, L., LORINI, V., HIRPA, F. A., HARRIGAN, S., ZSOTER, E., PRUDHOMME, C. & SALAMON, P. 2020. A global streamflow reanalysis for 1980–2018. *Journal of Hydrology X,* 6**,** 100049

ALLEN, R. G., PEREIRA, L. S., RAES, D. & SMITH, M. 1998. Chapter 3 - Meteorological data. *In:* NATIONS, F.-F. A. A. O. O. T. U. (ed.) *Crop evapotranspiration - Guidelines for computing crop water requirements - FAO Irrigation and drainage paper 56.* Rome: FAO - Food and Agriculture Organization of the United Nations.

ASTUTI, I. S., SAHOO, K., MILEWSKI, A. & MISHRA, D. R. 2019. Impact of land use land cover (LULC) change on surface runoff in an increasingly urbanized tropical watershed. *Water Resources Management,* 33**,** 4087-4103. DOI: 10.1007/s11269-019-02320-w

ATHIRA, P., SUDHEER, K. P., CIBIN, R. & CHAUBEY, I. 2016. Predictions in ungauged basins: an approach for regionalization of hydrological models considering the probability distribution of model parameters. *Stochastic environmental research and risk assessment,* 30**,** 1131-1149. DOI: 10.1007/s00477-015-1190-6

BALLABIO, C., PANAGOS, P. & MONATANARELLA, L. 2016. Mapping topsoil physical properties at European scale using the LUCAS database. *Geoderma,* 261**,** 110-123. DOI: 10.1016/j.geoderma.2015.07.006

BÁRDOSSY, A. 2007. Calibration of hydrological model parameters for ungauged catchments. *Hydrology and Earth System Sciences,* 11**,** 703-710. DOI: 10.5194/hess-11-703-2007

BARTLETT, M., PAROLARI, A. J., MCDONNELL, J. & PORPORATO, A. 2016. Beyond the SCS-CN method: A theoretical framework for spatially lumped rainfall-runoff response. *Water Resources Research,* 52**,** 4608-4627. DOI: 10.1002/2015WR018439

BECK, H. E., PAN, M., LIN, P., SEIBERT, J., VAN DIJK, A. I. & WOOD, E. F. 2020. Global fully distributed parameter regionalization based on observed streamflow from 4,229 headwater catchments. *Journal of Geophysical Research: Atmospheres,* 125**,** e2019JD031485. DOI: 10.1029/2019JD031485

BECKER, R., KOPPA, A., SCHULZ, S., USMAN, M., BEEK, T. A. D. & SCHÜTH, C. 2019. Spatially distributed model calibration of a highly managed hydrological system using remote sensing-derived ET data. *Journal of Hydrology,* 577**,** 123944. DOI: 10.1016/j.jhydrol.2019.123944

BERGSTRÖM, S. 1995. The HBV model. *Computer models of watershed hydrology.***,** 443-476

BOGGS, G. S. 2010. Assessment of SPOT 5 and QuickBird remotely sensed imagery for mapping tree cover in savannas. *International journal of applied earth observation and geoinformation,* 12**,** 217-224. DOI: 10.1016/j.jag.2009.11.001

BOLTON, D. K., WHITE, J. C., WULDER, M. A., COOPS, N. C., HERMOSILLA, T. & YUAN, X. 2018. Updating stand-level forest inventories using airborne laser scanning and Landsat time series data. *International Journal of Applied Earth Observation and Geoinformation,* 66**,** 174-183. DOI: 10.1016/j.jag.2017.11.016

BOOIJ, M. J. 2005. Impact of climate change on river flooding assessed with different spatial model resolutions. *Journal of hydrology,* 303**,** 176-198. DOI: 10.1016/j.jhydrol.2004.07.013

BORK, E. W. & SU, J. G. 2007. Integrating LIDAR data and multispectral imagery for enhanced classification of rangeland vegetation: A meta analysis. *Remote Sensing of Environment,* 111**,** 11-24

BREIMAN, L. 2001. Random forests. *Machine learning,* 45**,** 5-32. DOI: 10.1023/A:1010933404324

BRINKHOFF, J., VARDANEGA, J. & ROBSON, A. J. 2020. Land Cover Classification of Nine Perennial Crops Using Sentinel-1 and-2 Data. *Remote Sensing,* 12. DOI: 10.3390/rs12010096

BROCCA, L., MELONE, F. & MORAMARCO, T. 2011. Distributed rainfall-runoff modelling for flood frequency estimation and flood forecasting. *Hydrological processes,* 25**,** 2801-2813. DOI: 10.1002/hyp.8042

BUI, Q.-T., NGUYEN, Q.-H., NGUYEN, X. L., PHAM, V. D., NGUYEN, H. D. & PHAM, V.-M. 2020. Verification of novel integrations of swarm intelligence algorithms into deep learning neural network for flood susceptibility mapping. *Journal of Hydrology,* 581**,** 124379. DOI: 10.1016/j.jhydrol.2019.124379

BURNETT, M. W., WHITE, T. D., MCCAULEY, D. J., DE LEO, G. A. & MICHELI, F. 2019. Quantifying coconut palm extent on Pacific islands using spectral and textural analysis of very high resolution imagery. *International Journal of Remote Sensing,* 40**,** 7329-7355. DOI: 10.1080/01431161.2019.1594440

CABALLERO DÍAZ, J., PÉREZ, F., MANUEL, A. & QUIRÓS ROSADO, E. 2015. A state-and-transition model of Iberian dehesas based on spatial patterns. *Forest Systems,* 24. DOI: 10.5424/fs/2015242-06408

CANTEIRO, C., PINTO-CRUZ, C., SIMÕES, M. P. & GAZARINI, L. 2011. Conservation of Mediterranean oak woodlands: understorey dynamics under different shrub management. *Agroforestry Systems,* 82**,** 161-171. DOI: 10.1007/s10457-011-9375-6

CARRASCO, L., O'NEIL, A. W., MORTON, R. D. & ROWLAND, C. S. 2019. Evaluating Combinations of Temporally Aggregated Sentinel-1, Sentinel-2 and Landsat 8 for Land Cover Mapping with Google Earth Engine. *Remote Sensing,* 11. DOI: 10.3390/rs11030288

CHEN, T., REN, L., YUAN, F., TANG, T., YANG, X., JIANG, S., LIU, Y., ZHAO, C. & ZHANG, L. 2019. Merging ground and satellite-based precipitation data sets for improved hydrological simulations in the Xijiang River basin of China. *Stochastic Environmental Research and Risk Assessment,* 33**,** 1893-1905. DOI: 10.1007/s00477-019-01731-w

CHOI, H. T., KIM, J. & LIM, H.-G. Estimating the SCS runoff curve number in forest catchments of Korea. EGU General Assembly Conference Abstracts, 2016. 7210.

CHOUBIN, B., SOLAIMANI, K., REZANEZHAD, F., ROSHAN, M. H., MALEKIAN, A. & SHAMSHIRBAND, S. 2019. Streamflow regionalization using a similarity approach in ungauged basins: Application of the geo-environmental signatures in the Karkheh River Basin, Iran. *Catena,* 182**,** 104128. DOI: j.catena.2019.104128

COPERNICUS PROGRAM & ESA. 2014-2021. *Copernicus Open Access Hub* [Online]. Available: https://scihub.copernicus.eu [Accessed 01 2018].

COSTA, S., SANTOS, V., MELO, D. & SANTOS, P. Evaluation of Landsat 8 and Sentinel-2A data on the correlation between geological mapping and NDVI. 2017 First IEEE International Symposium of Geoscience and Remote Sensing (GRSS-CHILE), 2017. IEEE, 1-4.

CROCHEMORE, L., ISBERG, K., PIMENTEL, R., PINEDA, L., HASAN, A. & ARHEIMER, B. 2020. Lessons learnt from checking the quality of openly accessible river flow data worldwide. *Hydrological Sciences Journal,* 65**,** 699-711. DOI: 10.1080/02626667.2019.1659509

DALPONTE, M., ØRKA, H. O., ENE, L. T., GOBAKKEN, T. & NÆSSET, E. 2014. Tree crown delineation and tree species classification in boreal forests using

hyperspectral and ALS data. *Remote sensing of environment,* 140**,** 306-317. DOI: 10.1016/j.rse.2013.09.006

DELEGIDO, J., VERRELST, J., ALONSO, L. & MORENO, J. 2011. Evaluation of sentinel-2 red-edge bands for empirical estimation of green LAI and chlorophyll content. *Sensors,* 11**,** 7063-7081

DENIZE, J., HUBERT-MOY, L., BETBEDER, J., CORGNE, S., BAUDRY, J. & POTTIER, E. 2019. Evaluation of Using Sentinel-1 and-2 Time-Series to Identify Winter Land Use in Agricultural Landscapes. *Remote Sensing,* 11. DOI: 10.3390/rs11010037

DEVESA ALCARAZ, J. A. 1995. *Vegetación y flora de Extremadura,* Badajoz, Universitas Editorial.

DIAS, L. C. P., MACEDO, M. N., COSTA, M. H., COE, M. T. & NEILL, C. 2015. Effects of land cover change on evapotranspiration and streamflow of small catchments in the Upper Xingu River Basin, Central Brazil. *Journal of Hydrology: Regional Studies,* 4**,** 108-122. DOI: 10.1016/j.ejrh.2015.05.010

DIAZ, M., CAMPOS, P. & PULIDO, F. J. 1997. The Spanish dehesas: a diversity in land-use and wildlife. *In:* PAIN, D. & PIENKOWSKI, M. (eds.) *Farming and birds in Europe.* London: Academic Press.

DIONIZIO, E. A. & COSTA, M. H. 2019. Influence of land use and land cover on hydraulic and physical soil properties at the cerrado agricultural frontier. *Agriculture,* 9**,** 24. DOI: 10.3390/agriculture9010024

DUBAYAH, R., BLAIR, J. B., GOETZ, S., FATOYINBO, L., HANSEN, M., HEALEY, S., HOFTON, M., HURTT, G., KELLNER, J., LUTHCKE, S., ARMSTON, J., TANG, H., DUNCANSON, L., HANCOCK, S., JANTZ, P., MARSELIS, S., PATTERSON, P. L., QI, W. & SILVA, C. 2020. The Global Ecosystem Dynamics Investigation: High-resolution laser ranging of the Earth's forests and topography. *Science of Remote Sensing,* 1**,** 100002. DOI: 10.1016/j.srs.2020.100002

DUNCANSON, L., NEUENSCHWANDER, A., HANCOCK, S., THOMAS, N., FATOYINBO, T., SIMARD, M., SILVA, C. A., ARMSTON, J., LUTHCKE, S. B., HOFTON, M., KELLNER, J. R. & DUBAYAH, R. 2020. Biomass estimation from simulated GEDI, ICESat-2 and NISAR across environmental gradients in Sonoma County, California. *Remote Sensing of Environment,* 242**,** 111779. DOI: 10.1016/j.rse.2020.111779

ERDODY, T. L. & MOSKAL, L. M. 2010. Fusion of LiDAR and imagery for estimating forest canopy fuels. *Remote Sensing of Environment,* 114**,** 725-737

EROĞLU, H., ÇAKıR, G., SIVRIKAYA, F. & AKAY, A. E. 2010. Using high resolution images and elevation data in classifying erosion risks of bare soil areas in the Hatila Valley Natural Protected Area, Turkey. *Stochastic environmental research and risk assessment,* 24**,** 699-704. DOI: 10.1007/s00477-009-0356-5

ESA. 2019a. Available: https://www.esa.int/Our_Activities/Observing_the_Earth [Accessed 03 2019].

ESA. 2019b. *Sentinel Technical Guides* [Online]. Available: https://sentinels.copernicus.eu/web/sentinel/home [Accessed 01 2019].

ESCADAFAL, R. & HUETE, A. 1991. Etude des propriétés spectrales des sols arides appliquée à l'amélioration des indices de végétation obtenus par télédétection. *Comptes rendus de l'Académie des sciences. Série 2, Mécanique, Physique, Chimie, Sciences de l'univers, Sciences de la Terre,* 312**,** 1385-1391

FANG, F., MCNEIL, B. E., WARNER, T. A. & MAXWELL, A. E. 2018. Combining high spatial resolution multi-temporal satellite data with leaf-on LiDAR to enhance tree species discrimination at the crown level. *International journal of remote sensing,* 39**,** 9054-9072. DOI: 10.1080/01431161.2018.1504343

FASSNACHT, F. E., LATIFI, H., STEREŃCZAK, K., MODZELEWSKA, A., LEFSKY, M., WASER, L. T., STRAUB, C. & GHOSH, A. 2016. Review of studies on tree species classification from remotely sensed data. *Remote Sensing of Environment,* 186**,** 64-87. DOI: 10.1016/j.rse.2016.08.013

FENG, Q., YANG, J., ZHU, D., LIU, J., GUO, H., BAYARTUNGALAG, B. & LI, B. 2019. Integrating Multitemporal Sentinel-1/2 Data for Coastal Land Cover Classification Using a Multibranch Convolutional Neural Network: A Case of the Yellow River Delta. *Remote Sensing,* 11. DOI: 10.3390/rs11091006

FERREIRA, M. P., ZORTEA, M., ZANOTTA, D. C., SHIMABUKURO, Y. E. & FILHO, C. R. D. S. 2016. Mapping tree species in tropical seasonal semi-deciduous forests with hyperspectral and multispectral data. *Remote Sensing of Environment,* 179**,** 66-78. DOI: 10.1016/j.rse.2016.03.021

FRAGOSO-CAMPÓN, L. 2015. *Estimación de parámetros hidrológicos mediante el uso de Sistemas de Información Geográfica para el análisis de la escorrentía superficial generada en una cuenca.* Trabajo Fin de Máster - Máster Universitario en Investigación en Ingeniería y Arquitectura, Universidad de Extremadura.

GAO, B.-C. 1996. NDWI—A normalized difference water index for remote sensing of vegetation liquid water from space. *Remote sensing of environment,* 58**,** 257-266

GAO, Y., MARPU, P., NIEMEYER, I., RUNFOLA, D. M., GINER, N. M., HAMILL, T. & PONTIUS, R. G. 2011. Object-based classification with features extracted by a semi-automatic feature extraction algorithm–SEaTH. *Geocarto International,* 26**,** 211-226

GARCÍA, M., RIAÑO, D., CHUVIECO, E., SALAS, J. & DANSON, F. M. 2011. Multispectral and LiDAR data fusion for fuel type mapping using Support Vector Machine and decision rules. *Remote Sensing of Environment,* 115**,** 1369-1379. DOI: 10.1016/j.rse.2011.01.017

GEBHARDT, S., WEHRMANN, T., RUIZ, M. A. M., MAEDA, P., BISHOP, J., SCHRAMM, M., KOPEINIG, R., CARTUS, O., KELLNDORFER, J. & RESSL, R. 2014. MAD-MEX: automatic wall-to-wall land cover monitoring for the Mexican REDD-MRV program using all Landsat data. *Remote Sensing,* 6**,** 3923-3943

GHIMIRE, B., ROGAN, J., GALIANO, V. R., PANDAY, P. & NEETI, N. 2012. An evaluation of bagging, boosting, and random forests for land-cover classification in Cape Cod, Massachusetts, USA. *GIScience & Remote Sensing,* 49**,** 623-643. DOI: 10.2747/1548-1603.49.5.623

GHOSH, A., FASSNACHT, F. E., JOSHI, P. K. & KOCH, B. 2014. A framework for mapping tree species combining hyperspectral and LiDAR data: Role of selected classifiers and sensor across three spatial scales. *International Journal of Applied Earth Observation and Geoinformation,* 26**,** 49-63. DOI: 10.1016/j.jag.2013.05.017

GITELSON, A. A., KAUFMAN, Y. J. & MERZLYAK, M. N. 1996. Use of a green channel in remote sensing of global vegetation from EOS-MODIS. *Remote sensing of Environment,* 58**,** 289-298

GODINHO, S., GIL, A., GUIOMAR, N., COSTA, M. J. & NEVES, N. 2016a. Assessing the role of Mediterranean evergreen oaks canopy cover in land surface albedo and temperature using a remote sensing-based approach. *Applied Geography,* 74**,** 84-94. DOI: 10.1016/j.apgeog.2016.07.004

GODINHO, S., GUIOMAR, N. & GIL, A. 2017. Estimating tree canopy cover percentage in a mediterranean silvopastoral systems using Sentinel-2A imagery and the stochastic gradient boosting algorithm. *International Journal of Remote Sensing***,** 1-23. DOI: 10.1080/01431161.2017.1399480

GODINHO, S., GUIOMAR, N., MACHADO, R., SANTOS, P., SÁ-SOUSA, P., FERNANDES, J. P., NEVES, N. & PINTO-CORREIA, T. 2016b. Assessment of environment, land management, and spatial variables on recent changes in montado land cover in southern Portugal. *Agroforestry Systems,* 90**,** 177-192. DOI: 10.1007/s10457-014-9757-7

GÖKBULAK, F., ŞENGÖNÜL, K., SERENGIL, Y., ÖZHAN, S., YURTSEVEN, İ., UYGUR, B. & ÖZÇELIK, M. S. 2016. Effect of forest thinning on water yield in a sub-humid Mediterranean oak-beech mixed forested watershed. *Water resources management,* 30**,** 5039-5049

GONZÁLEZ-FERREIRO, E., DIÉGUEZ-ARANDA, U. & MIRANDA, D. 2012. Estimation of stand variables in Pinus radiata D. Don plantations using different LiDAR pulse densities. *Forestry,* 85**,** 281-292. DOI: 10.1093/forestry/cps002

GOSWAMI, M., O'CONNOR, K. & BHATTARAI, K. 2007. Development of regionalisation procedures using a multi-model approach for flow simulation in an ungauged catchment. *Journal of Hydrology,* 333**,** 517-531

GÖTZINGER, J. & BÁRDOSSY, A. 2007. Comparison of four regionalisation methods for a distributed hydrological model. *Journal of Hydrology,* 333**,** 374-384. DOI: 10.1016/j.jhydrol.2006.09.008

GUNDALIA, M. & DHOLAKIA, M. 2014. Impact of monthly curve number on daily runoff estimation for Ozat catchment in India. *Open Journal of Modern Hydrology,* 4**,** 144. DOI: 10.4236/ojmh.2014.44014

GUO, Y., ZHANG, Y., ZHANG, L. & WANG, Z. 2021. Regionalization of hydrological modeling for predicting streamflow in ungauged catchments: A comprehensive review. *Wiley Interdisciplinary Reviews: Water***,** e1487. DOI: 10.1002/wat2.1487

GUYOT, G., BARET, F. & MAJOR, D. 1988. High spectral resolution: Determination of spectral shifts between the red and the near infrared. *International Archives of Photogrammetry and Remote Sensing,* 11

HANCOCK, S., ARMSTON, J., HOFTON, M., SUN, X., TANG, H., DUNCANSON, L. I., KELLNER, J. R. & DUBAYAH, R. 2019. The GEDI simulator: A large-footprint waveform lidar simulator for calibration and validation of spaceborne missions. *Earth and Space Science,* 6**,** 294-310. DOI: 10.1029/2018EA000506

HARGREAVES, G. H., ASCE, F. & ALLEN, R. G. 2003. History and Evaluation of Hargreaves Evapotranspiration equation. *Journal of Irrigation and Drainage Engineering,* 129**,** 53-63. DOI: 10.1061/(ASCE)0733-9437(2003)129:1(53)

HEALEY, S. P., YANG, Z., GORELICK, N. & ILYUSHCHENKO, S. 2020. Highly Local Model Calibration with a New GEDI LiDAR Asset on Google Earth Engine Reduces Landsat Forest Height Signal Saturation. *Remote Sensing,* 12**,** 2840. DOI: 10.3390/rs12172840

HECKEL, K., URBAN, M., SCHRATZ, P., MAHECHA, M. D. & SCHMULLIUS, C. 2020. Predicting Forest Cover in Distinct Ecosystems: The Potential of Multi-Source Sentinel-1 and-2 Data Fusion. *Remote Sensing,* 12. DOI: 10.3390/rs12020302

HONG, Y. & ADLER, R. 2008. Estimation of global SCS curve numbers using satellite remote sensing and geospatial data. *International Journal of Remote Sensing,* 29**,** 471-477. DOI: 10.1080/01431160701264292

HOSCILO, A. & LEWANDOWSKA, A. 2019. Mapping Forest Type and Tree Species on a Regional Scale Using Multi-Temporal Sentinel-2 Data. *Remote Sensing,* 11. DOI: 10.3390/rs11080929

HRACHOWITZ, M., SAVENIJE, H., BLÖSCHL, G., MCDONNELL, J., SIVAPALAN, M., POMEROY, J., ARHEIMER, B., BLUME, T., CLARK, M., EHRET, U., FENICIA, F., FREER, J. E., GELFAN, A., GUPTA, H., HUGHES, D., HUT, R., MONTANARI, A., PANDE, S., TETZLAFF, D., TROCH, P., UHLENBROOK, S., WAGENER, T., WINSEMIUS, H., WOODS, R., ZEHE, E. & CUDENNEC, C. 2013. A decade of Predictions in Ungauged Basins (PUB)—a review. *Hydrological sciences journal,* 58**,** 1198-1255. DOI: 10.1080/02626667.2013.803183

HUETE, A. 1988. A soil-adjusted vegetation index (SAVI). *Remote Sensing of Environment,* 25**,** 259-309. DOI: 10.1016/0034-4257(88)90106-X

HUETE, A. R., POST, D. F. & JACKSON, R. D. 1984. Soil spectral effects on 4-space vegetation discrimination. *Remote sensing of environment,* 1984 v.15 no.2**,** pp. 155-165. DOI: 10.1016/0034-4257(84)90043-9

HUNDECHA, Y. & BÁRDOSSY, A. 2004. Modeling of the effect of land use changes on the runoff generation of a river basin through parameter regionalization of a watershed model. *Journal of hydrology,* 292**,** 281-295. DOI: j.jhydrol.2004.01.002

IENCO, D., INTERDONATO, R., GAETANO, R. & DINH HO TONG, M. 2019. Combining Sentinel-1 and Sentinel-2 Satellite Image Time Series for land cover mapping via a multi-source deep learning architecture. *Isprs Journal of Photogrammetry and Remote Sensing,* 158**,** 11-22. DOI: 10.1016/j.isprsjprs.2019.09.016

IGN. 2021. *Centro de Descargas.*

Centro Nacional de Información Geográfica [Online]. Available: http://centrodedescargas.cnig.es/CentroDescargas/index.jsp [Accessed April 2017].

IMMITZER, M., NEUWIRTH, M., BÖCK, S., BRENNER, H., VUOLO, F. & ATZBERGER, C. 2019. Optimal Input Features for Tree Species Classification in Central Europe Based on Multi-Temporal Sentinel-2 Data. *Remote Sensing,* 11**,** 2599. DOI: 10.3390/rs11222599

JIN, X., XU, C.-Y., ZHANG, Q. & CHEN, Y. D. 2009. Regionalization study of a conceptual hydrological model in Dongjiang basin, south China. *Quaternary International,* 208**,** 129-137. DOI: 10.1016/j.quaint.2008.08.006

JOINT RESEARCH CENTRE. 2020. *European Soil Data Centre (ESDAC)* [Online]. European Commission. Available: https://esdac.jrc.ec.europa.eu/ [Accessed 20/07/2020.

KARUNANIDHI, D., ANAND, B., SUBRAMANI, T. & SRINIVASAMOORTHY, K. 2020. Rainfall-surface runoff estimation for the Lower Bhavani basin in south India using SCS-CN model and geospatial techniques. *Environmental Earth Sciences,* 79**,** 1-19. DOI: 10.1007/s12665-020-09079-z

KHAN, A., GOVIL, H., KUMAR, G. & DAVE, R. 2020. Synergistic use of Sentinel-1 and Sentinel-2 for improved LULC mapping with special reference to bad land class: a case study for Yamuna River floodplain, India. *Spatial Information Research*. DOI: 10.1007/s41324-020-00325-x

KIM, N. W. & LEE, J. 2008. Temporally weighted average curve number method for daily runoff simulation. *Hydrological Processes,* 22**,** 4936-4948

KULT, J. M., FRY, L. M., GRONEWOLD, A. D. & CHOI, W. 2014. Regionalization of hydrologic response in the Great Lakes basin: Considerations of temporal scales of analysis. *Journal of Hydrology,* 519**,** 2224-2237. DOI: 10.1016/j.jhydrol.2014.09.083

LANG, N., SCHINDLER, K. & WEGNER, J. D. 2019. Country-wide high-resolution vegetation height mapping with Sentinel-2. *Remote Sensing of Environment,* 233**,** 111347. DOI: 10.1016/j.rse.2019.111347

LEEMHUIS, C., THONFELD, F., NÄSCHEN, K., STEINBACH, S., MURO, J., STRAUCH, A., LÓPEZ, A., DACONTO, G., GAMES, I. & DIEKKRÜGER, B. 2017. Sustainability in the food-water-ecosystem nexus: The role of land use and land cover change for water resources and ecosystems in the Kilombero Wetland, Tanzania. *Sustainability,* 9**,** 1513. DOI: 10.3390/su9091513

LI, L., LI, N., LU, D. & CHEN, Y. 2019. Mapping Moso bamboo forest and its on-year and off-year distribution in a subtropical region using time-series Sentinel-2 and Landsat 8 data. *Remote Sensing of Environment,* 231**,** 111265. DOI: 10.1016/j.rse.2019.111265

LIAW, A. & WIENER, M. 2002. Classification and regression by randomForest. *R News,* 2/3

LIU, R., REN, H., LIU, S., LIU, Q., YAN, B. & GAN, F. 2018. Generalized FPAR estimation methods from various satellite sensors and validation. *Agricultural and Forest Meteorology,* 260**,** 55-72. DOI: 10.1016/j.agrformet.2018.05.024

LOPES, M., FRISON, P.-L., DURANT, S. M., TO BUHNE, H. S., IPAVEC, A., LAPEYRE, V. & PETTORELLI, N. 2020. Combining optical and radar satellite image time series to map natural vegetation: savannas as an example. *Remote Sensing in Ecology and Conservation*. DOI: 10.1002/rse2.139

LU, Y., YANG, C. & MENG, Z. 2021. Lithology Discrimination Using Sentinel-1 Dual-Pol Data and SRTM Data. *Remote Sensing,* 13**,** 1280. DOI: 10.3390/rs13071280

LUAN, X.-B., WU, P.-T., SUN, S.-K., LI, X.-L., WANG, Y.-B. & GAO, X.-R. 2018. Impact of land use change on hydrologic processes in a large plain irrigation district. *Water Resources Management,* 32**,** 3203-3217. DOI: 10.1007/s11269-018-1986-5

MAGIERA, A., FEILHAUER, H., TEPHNADZE, N., WALDHARDT, R. & OTTE, A. 2016. Separating reflectance signatures of shrub species - a case study in the Central Greater Caucasus. *Applied Vegetation Science,* 19**,** 304-315. DOI: 10.1111/avsc.12205

MAHDIANPARI, M., SALEHI, B., MOHAMMADIMANESH, F., BRISCO, B., HOMAYOUNI, S., GILL, E., DELANCEY, E. R. & BOURGEAU-CHAVEZ, L. 2020. Big Data for a Big Country: The First Generation of Canadian Wetland Inventory Map at a Spatial Resolution of 10-m Using Sentinel-1 and Sentinel-2 Data on the Google Earth Engine Cloud Computing Platform. *Canadian Journal of Remote Sensing*. DOI: 10.1080/07038992.2019.1711366

MALAHLELA, O. E., CHO, M. A. & MUTANGA, O. 2015. Mapping the occurrence of Chromolaena odorata (L.) in subtropical forest gaps using environmental and

remote sensing data. *Biological Invasions,* 17**,** 2027-2042. DOI: 10.1007/s10530-015-0858-7

MARIN, M., CLINCIU, I., TUDOSE, N. C., UNGUREAN, C., ADORJANI, A., MIHALACHE, A. L., DAVIDESCU, A. A., DAVIDESCU, Ş. O., DINCA, L. & CACOVEAN, H. 2020. Assessing the vulnerability of water resources in the context of climate changes in a small forested watershed using SWAT: A review. *Environmental Research***,** 109330. DOI: doi.org/10.1016/j.envres.2020.109330

MARTÍNEZ-SALVADOR, A. & CONESA-GARCÍA, C. 2020. Suitability of the SWAT Model for Simulating Water Discharge and Sediment Load in a Karst Watershed of the Semiarid Mediterranean Basin. *Water Resources Management***,** 1-18. DOI: 10.1007/s11269-019-02477-4

MASIH, I., UHLENBROOK, S., MASKEY, S. & AHMAD, M. 2010. Regionalization of a conceptual rainfall–runoff model based on similarity of the flow duration curve: A case study from the semi-arid Karkheh basin, Iran. *Journal of hydrology,* 391**,** 188-201. DOI: 10.1016/j.jhydrol.2010.07.018

MATHIEU, R., POUGET, M., CERVELLE, B. & ESCADAFAL, R. 1998. Relationships between satellite-based radiometric indices simulated using laboratory reflectance data and typic soil color of an arid environment. *Remote sensing of environment,* 66**,** 17-28. DOI: 10.1016/S0034-4257(98)00030-3

MATIKAINEN, L. & KARILA, K. 2011. Segment-based land cover mapping of a suburban area—Comparison of high-resolution remotely sensed datasets using classification trees and test field points. *Remote Sensing,* 3**,** 1777-1804

MCGAUGHEEY, R. J. 2020. Manual FUSION/LDV Software for LiDAR Data Analysis and Visualization. *US Department of Agriculture, Forest Service.* 4.00 ed.

MCGAUGHEY, R. J. 2009. FUSION/LDV: Software for LIDAR data analysis and visualization. *US Department of Agriculture, Forest Service, Pacific Northwest Research Station: Seattle, WA, USA.*

MERCIER, A., BETBEDER, J., RUMIANO, F., BAUDRY, J., GOND, V., BLANC, L., BOURGOIN, C., CORNU, G., CIUDAD, C., MARCHAMALO, M., POCCARD-CHAPUIS, R. & HUBERT-MOY, L. 2019. Evaluation of Sentinel-1 and 2 Time Series for Land Cover Classification of Forest-Agriculture Mosaics in Temperate and Tropical Landscapes. *Remote Sensing,* 11. DOI: 10.3390/rs11080979

MERZ, R. & BLÖSCHL, G. 2004. Regionalisation of catchment model parameters. *Journal of hydrology,* 287**,** 95-123. DOI: 10.1016/j.jhydrol.2003.09.028

MISHRA, V. N., PRASAD, R., RAI, P. K., VISHWAKARMA, A. K. & ARORA, A. 2019. Performance evaluation of textural features in improving land use/land cover classification accuracy of heterogeneous landscape using multi-sensor remote sensing data. *Earth Science Informatics,* 12**,** 71-86. DOI: 10.1007/s12145-018-0369-z

MÜLLEROVÁ, J., PERGL, J. & PYŠEK, P. 2013. Remote sensing as a tool for monitoring plant invasions: Testing the effects of data resolution and image classification approach on the detection of a model plant species Heracleum mantegazzianum (giant hogweed). *International Journal of Applied Earth Observation and Geoinformation,* 25**,** 55-65. DOI: 10.1016/j.jag.2013.03.004

MUNDT, J. T., STREUTKER, D. R. & GLENN, N. F. 2006. Mapping sagebrush distribution using fusion of hyperspectral and lidar classifications. *Photogrammetric Engineering & Remote Sensing,* 72**,** 47-54

MUTHUKUMARASAMY, I., SHANMUGAM, R. S. & USHA, T. 2019. Incorporation of textural information with SAR and optical imagery for improved land cover mapping. *Environmental Earth Sciences,* 78. DOI: 10.1007/s12665-019-8654-9

MUTLU, M., POPESCU, S. C., STRIPLING, C. & SPENCER, T. 2008. Mapping surface fuel models using lidar and multispectral data fusion for fire behavior. *Remote Sensing of Environment,* 112**,** 274-285

NAGESWARA RAO, K. 2020. Analysis of surface runoff potential in ungauged basin using basin parameters and SCS-CN method. *Applied Water Science,* 10**,** 1-16. DOI: 10.1007/s13201-019-1129-z

NETZER, M. S., SIDMAN, G., PEARSON, T. R., WALKER, S. M. & SRINIVASAN, R. 2019. Combining global remote sensing products with hydrological modeling to measure the impact of tropical forest loss on water-based ecosystem services. *Forests,* 10**,** 413. DOI: 10.3390/f10050413

NIPHADKAR, M., NAGENDRA, H., TARANTINO, C., ADAMO, M. & BLONDA, P. 2017. Comparing pixel and object-based approaches to map an understorey invasive shrub in tropical mixed forests. *Frontiers in plant science,* 8**,** 892. DOI: 10.3389/fpls.2017.00892

NRCS 2004. Chapter 9: Hydrologic Soil-Cover Complexes. *NRCS National Engineering Handbook, Part 630: Hydrology.* Washington, DC: Engineering Division, US. Department of Agriculture.

NRCS 2009. *National Engineering Handbook, section 4, Hydrology, version (1956, 1964, 1971, 1985, 1993, 2004, 2009),* Washington, DC, Engineering Division, US. Department of Agriculture.

NUMBISI, F. N., VAN COILLIE, F. M. B. & DE WULF, R. 2019. Delineation of Cocoa Agroforests Using Multiseason Sentinel-1 SAR Images: A Low Grey Level Range Reduces Uncertainties in GLCM Texture-Based Mapping. *Isprs International Journal of Geo-Information,* 8. DOI: 10.3390/ijgi8040179

PAIK, K., KIM, J. H., KIM, H. S. & LEE, D. R. 2005. A conceptual rainfall-runoff model considering seasonal variation. *Hydrological Processes: An International Journal,* 19**,** 3837-3850. DOI: 10.1002/hyp.5984

PANAGOS, P. 2006. The European soil database. *GEO: connexion,* 5**,** 32-33

PARAJKA, J., BLÖSCHL, G. & MERZ, R. 2007. Regional calibration of catchment models: Potential for ungauged catchments. *Water Resources Research,* 43. DOI: 10.1029/2006WR005271

PARAJKA, J., VIGLIONE, A., ROGGER, M., SALINAS, J., SIVAPALAN, M. & BLÖSCHL, G. 2013. Comparative assessment of predictions in ungauged basins–Part 1: Runoff-hydrograph studies. *Hydrology and Earth System Sciences,* 17**,** 1783-1795. DOI: 10.5194/hess-17-1783-2013

PARAJULI, P. B., JAYAKODY, P. & OUYANG, Y. 2018. Evaluation of using remote sensing evapotranspiration data in SWAT. *Water resources management,* 32**,** 985-996. DOI: 10.1007/s11269-017-1850-z

PARIS, C., BRUZZONE, L. & FERNÁNDEZ-PRIETO, D. A novel automatic approach to the update of land-cover maps by unsupervised classification of remote sensing images. Geoscience and Remote Sensing Symposium (IGARSS), 2017 IEEE International, 2017. IEEE, 2207-2210.

PIANOSI, F. & WAGENER, T. 2016. Understanding the time-varying importance of different uncertainty sources in hydrological modelling using global sensitivity analysis. *Hydrological Processes,* 30**,** 3991-4003. DOI: 10.1002/hyp.10968

POORTINGA, A., TENNESON, K., SHAPIRO, A., QUYEN, N., SAN AUNG, K., CHISHTIE, F. & SAAH, D. 2019. Mapping Plantations in Myanmar by Fusing Landsat-8, Sentinel-2 and Sentinel-1 Data along with Systematic Error Quantification. *Remote Sensing,* 11. DOI: 10.3390/rs11070831

POTAPOV, P., LI, X., HERNANDEZ-SERNA, A., TYUKAVINA, A., HANSEN, M. C., KOMMAREDDY, A., PICKENS, A., TURUBANOVA, S., TANG, H., SILVA, C. E., ARMSTON, J., DUBAYAH, R., BLAIR, J. B. & HOFTON, M. 2021. Mapping global forest canopy height through integration of GEDI and Landsat data. *Remote Sensing of Environment,* 253**,** 112165. DOI: 10.1016/j.rse.2020.112165

PULIDO, F., GARCÍA, E., OBRADOR, J. J. & MORENO, G. 2010. Multiple pathways for tree regeneration in anthropogenic savannas: incorporating biotic and abiotic drivers into management schemes. *Journal of Applied Ecology,* 47**,** 1272-1281. DOI: 10.1111/j.1365-2664.2010.01865.x

PURINTON, B. & BOOKHAGEN, B. 2020. Multiband (X, C, L) radar amplitude analysis for a mixed sand-and gravel-bed river in the eastern Central Andes. *Remote Sensing of Environment,* 246**,** 111799. DOI: 10.1016/j.rse.2020.111799

QI, J., CHEHBOUNI, A., HUETE, A., KERR, Y. & SOROOSHIAN, S. 1994. A modified soil adjusted vegetation index. *Remote sensing of environment,* 48**,** 119-126. DOI: 10.1016/0034-4257(94)90134-1

QI, W. & DUBAYAH, R. O. 2016. Combining Tandem-X InSAR and simulated GEDI lidar observations for forest structure mapping. *Remote Sensing of Environment,* 187**,** 253-266. DOI: 10.1016/j.rse.2016.10.018

QI, W., LEE, S.-K., HANCOCK, S., LUTHCKE, S., TANG, H., ARMSTON, J. & DUBAYAH, R. 2019a. Improved forest height estimation by fusion of simulated GEDI Lidar data and TanDEM-X InSAR data. *Remote Sensing of Environment,* 221**,** 621-634. DOI: 10.1016/j.rse.2018.11.035

QI, W., SAARELA, S., ARMSTON, J., STÅHL, G. & DUBAYAH, R. 2019b. Forest biomass estimation over three distinct forest types using TanDEM-X InSAR data and simulated GEDI lidar data. *Remote Sensing of Environment,* 232**,** 111283. DOI: 10.1016/j.rse.2019.111283

R-CORE-TEAM 2018. R: A language and environment for statistical computing. Vienna (Austria): R Foundation for Statistical Computing.

RADFORD, D. D., CRACKNELL, M. J., ROACH, M. J. & CUMMING, G. V. 2018. Geological mapping in western Tasmania using radar and random forests. *IEEE Journal of Selected Topics in Applied Earth Observations and Remote Sensing,* 11**,** 3075-3087. DOI: 10.1109/JSTARS.2018.2855207

RAJENDRAN, S. & NASIR, S. 2021. ASTER mapping of gypsum deposits of Thumrait region of southern Oman. *Resource Geology*. DOI: 10.1111/rge.12245

RICHARDSON, A. J. & WIEGAND, C. 1977. Distinguishing vegetation from soil background information. *Photogrammetric engineering and remote sensing,* 43**,** 1541-1552

RIVAS-MARTINEZ, S. & RIVAS-SAENZ, S. 1996-2019. *Worldwide Bioclimatic Classification System* [Online]. Spain. Available: http://www.globalbioclimatics.org/form/tb_map/index.htm [Accessed July 2019].

RIVEST, D., ROLO, V., LÓPEZ-DÍAZ, L. & MORENO, G. 2011. Shrub encroachment in Mediterranean silvopastoral systems: Retama sphaerocarpa and Cistus ladanifer induce contrasting effects on pasture and Quercus ilex production. *Agriculture, ecosystems & environment,* 141**,** 447-454. DOI: 10.1016/j.agee.2011.04.018

ROUSE JR, J., HAAS, R., SCHELL, J. & DEERING, D. 1974. Monitoring vegetation systems in the Great Plains with ERTS. *Third Earth Resources Technology Satellite-1 Symposium.* Washington, D.C.: NASA.

SAJIKUMAR, N. & REMYA, R. 2015. Impact of land cover and land use change on runoff characteristics. *Journal of Environmental Management,* 161**,** 460-468. DOI: 10.1016/j.jenvman.2014.12.041

SANCHEZ-LOPEZ, N., BOSCHETTI, L., HUDAK, A. T., HANCOCK, S. & DUNCANSON, L. I. 2020. Estimating Time Since the Last Stand-Replacing Disturbance (TSD) from Spaceborne Simulated GEDI Data: A Feasibility Study. *Remote Sensing,* 12**,** 3506. DOI: 10.3390/rs12213506

SÁNCHEZ SÁNCHEZ, Y., MARTÍNEZ-GRAÑA, A., SANTOS FRANCÉS, F. & MATEOS PICADO, M. 2018. Mapping Wildfire Ignition Probability Using Sentinel 2 and LiDAR (Jerte Valley, Cáceres, Spain). *Sensors,* 18**,** 826

SCHNEIDER, F. D., FERRAZ, A. A., HANCOCK, S., DUNCANSON, L. I., DUBAYAH, R. O., PAVLICK, R. P. & SCHIMEL, D. S. 2020. Towards mapping the diversity of canopy structure from space with GEDI. *Environmental Research Letters*. DOI: 10.1088/1748-9326/ab9e99

SEIBERT, J. 1999. Regionalisation of parameters for a conceptual rainfall-runoff model. *Agricultural and forest meteorology,* 98**,** 279-293. DOI: 10.1016/S0168-1923(99)00105-7

SEIBERT, J. & VIS, M. J. P. 2012. Teaching hydrological modeling with a user-friendly catchment-runoff-model software package. *Hydrol. Earth Syst. Sci.,* 16**,** 3315-3325. DOI: 10.5194/hess-16-3315-2012

SILVA, C. A., HAMAMURA, C., VALBUENA, R. U., HANCOCK, S., CARDIL, A., NORTH BROADBENT, E., ALVES DE ALMEIDA, D. R., SILVA JUNIOR, C. H. L. & KLAUBERG, C. 2020. rGEDI: NASA's Global Ecosystem Dynamics Investigation (GEDI) Data Visualization and Processing. R package version 0.1.7 ed.

STAVRAKOUDIS, D., DRAGOZI, E., GITAS, I. & KARYDAS, C. 2014. Decision fusion based on hyperspectral and multispectral satellite imagery for accurate forest species mapping. *Remote Sensing,* 6**,** 6897-6928. DOI: 10.3390/rs6086897

STEINHAUSEN, M. J., WAGNER, P. D., NARASIMHAN, B. & WASKE, B. 2018. Combining Sentinel-1 and Sentinel-2 data for improved land use and land cover mapping of monsoon regions. *International Journal of Applied Earth Observation and Geoinformation,* 73**,** 595-604. DOI: 10.1016/j.jag.2018.08.011

STROMANN, O., NASCETTI, A., YOUSIF, O. & BAN, Y. 2020. Dimensionality Reduction and Feature Selection for Object-Based Land Cover Classification based on Sentinel-1 and Sentinel-2 Time Series Using Google Earth Engine. *Remote Sensing,* 12. DOI: 10.3390/rs12010076

TAVARES, P. A., SANTOS BELTRAO, N. E., GUIMARAES, U. S. & TEODORO, A. C. 2019. Integration of Sentinel-1 and Sentinel-2 for Classification and LULC Mapping in the Urban Area of Belem, Eastern Brazilian Amazon. *Sensors,* 19. DOI: 10.3390/s19051140

TEDELA, N. H., MCCUTCHEON, S. C., RASMUSSEN, T. C., HAWKINS, R. H., SWANK, W. T., CAMPBELL, J. L., ADAMS, M. B., JACKSON, C. R. & TOLLNER, E. W. 2012. Runoff Curve Numbers for 10 small forested watersheds in the mountains of the Eastern United States. *Journal of Hydrologic Engineering,* 17**,** 1188-1198. DOI: 10.1061/(ASCE)HE.1943-5584.0000436.

VAN LIER, O. R., FOURNIER, R. A., BRADLEY, R. L. & THIFFAULT, N. 2009. A multi-resolution satellite imagery approach for large area mapping of ericaceous shrubs in Northern Quebec, Canada. *International Journal of Applied Earth Observation and Geoinformation,* 11**,** 334-343. DOI: 10.1016/j.jag.2009.05.003

VAN TRICHT, K., GOBIN, A., GILLIAMS, S. & PICCARD, I. 2018. Synergistic Use of Radar Sentinel-1 and Optical Sentinel-2 Imagery for Crop Mapping: A Case Study for Belgium. *Remote Sensing,* 10. DOI: 10.3390/rs10101642

VERMA, A., KUMAR, A. & LAL, K. 2019. Kharif crop characterization using combination of SAR and MSI Optical Sentinel Satellite datasets. *Journal of Earth System Science,* 128. DOI: 10.1007/s12040-019-1260-0

WALEGA, A., AMATYA, D. M., CALDWELL, P., MARION, D. & PANDA, S. 2020. Assessment of storm direct runoff and peak flow rates using improved SCS-CN models for selected forested watersheds in the Southeastern United States. *Journal of Hydrology: Regional Studies,* 27**,** 100645. DOI: 10.1016/j.ejrh.2019.100645

WALEGA, A. & SALATA, T. 2019. Influence of land cover data sources on estimation of direct runoff according to SCS-CN and modified SME methods. *Catena,* 172**,** 232-242. DOI: 10.1016/j.catena.2018.08.032

WANG, N., LIU, W., SUN, F., YAO, Z., WANG, H. & LIU, W. 2020. Evaluating satellite-based and reanalysis precipitation datasets with gauge-observed data and hydrological modeling in the Xihe River Basin, China. *Atmospheric Research,* 234**,** 104746. DOI: 10.1016/j.atmosres.2019.104746

WARD JR, J. H. 1963. Hierarchical grouping to optimize an objective function. *Journal of the American statistical association,* 58**,** 236-244. DOI: 10.1080/01621459.1963.10500845

WEI, S., ZHANG, H., WANG, C., WANG, Y. & XU, L. 2019. Multi-temporal SAR data large-scale crop mapping based on U-Net model. *Remote Sensing,* 11**,** 68. DOI: 10.3390/rs11010068

WHYTE, A., FERENTINOS, K. P. & PETROPOULOS, G. P. 2018. A new synergistic approach for monitoring wetlands using Sentinels-1 and 2 data with object-based machine learning algorithms. *Environmental Modelling & Software,* 104**,** 40-54. DOI: 10.1016/j.envsoft.2018.01.023

YU, Q., XING, M., LIU, X., WANG, L., LUO, K. & QUAN, X. Detection of Land Use Type Using Multitemporal SAR Images. IGARSS 2019-2019 IEEE International Geoscience and Remote Sensing Symposium, 2019. IEEE, 1534-1537.

ZENG, Z., TANG, G., HONG, Y., ZENG, C. & YANG, Y. 2017. Development of an NRCS curve number global dataset using the latest geospatial remote sensing data for worldwide hydrologic applications. *Remote Sensing Letters,* 8**,** 528-536

ZHAO, Y., FENG, D., YU, L., WANG, X., CHEN, Y., BAI, Y., HERNÁNDEZ, H. J., GALLEGUILLOS, M., ESTADES, C., BIGING, G. S., RADKE, J. D. & GONG, P. 2016. Detailed dynamic land cover mapping of Chile: Accuracy improvement by integrating multi-temporal data. *Remote sensing of environment,* 183**,** 170-185. DOI: 10.1016/j.rse.2016.05.016

ZHOU, P., HUANG, J., PONTIUS, R. G. & HONG, H. 2014. Land classification and change intensity analysis in a coastal watershed of Southeast China. *Sensors,* 14**,** 11640-11658. DOI: 10.3390/s140711640

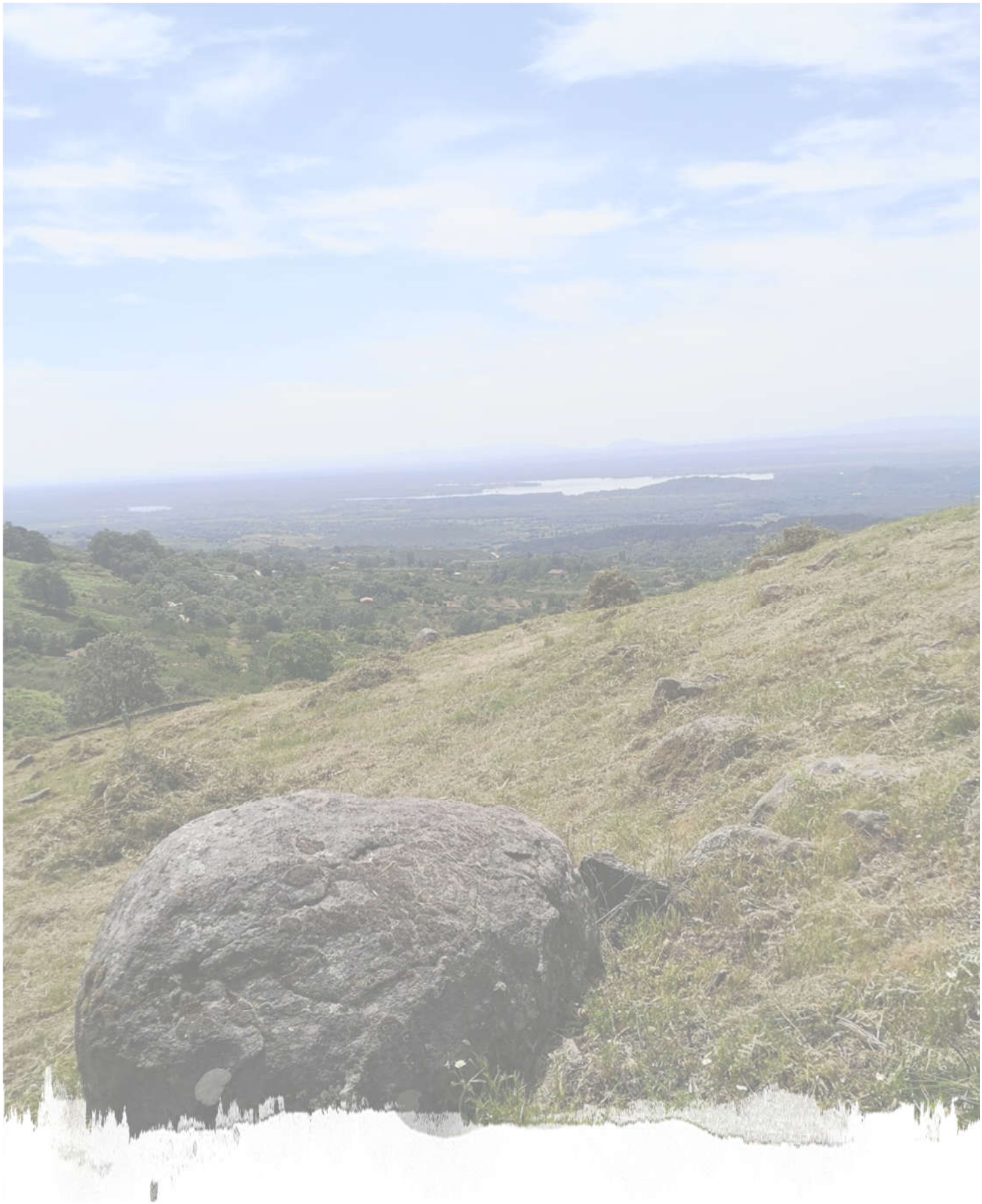

CAPÍTULO 3

Trabajos Publicados

3.1. Publicación N.º 1

Publicación	**Variability in estimated runoff in a forested area based on different cartographic data sources**				
Autores	**Fragoso, Laura** · Quirós, Elia · Durán-Barroso, Pablo				
Año	2017				
Revista	Forest Systems 26 (2), eRC02, 5 pages (2017)				
eISSN:	2171-9845				
DOI	10.5424/fs/2017262-10921				
Fuente de Impacto	Índice 5 años	Índice 2017	Categoría	Rank	Cuartil
WOS (JCR)	1,288	0,96	Forestry	44/66	Q3
Aportación de la doctoranda:	Concepción, análisis de datos, desarrollo de los experimentos, redacción del artículo y aprobación final de la versión.				

The final publication is available at **www.inia.es/Forestsystems**

Forest Systems
26 (2), eRC02, 5 pages (2017)
eISSN: 2171-9845
https://doi.org/10.5424/fs/2017262-10921
Instituto Nacional de Investigación y Tecnología Agraria y Alimentaria O. A., M. P. (INIA)

RESOURCE COMMUNICATION

OPEN ACCESS

Variability in estimated runoff in a forested area based on different cartographic data sources

Laura Fragoso, Elia Quirós, and Pablo Durán-Barroso
Universidad de Extremadura, Avda Universidad s/n 10005, Cáceres, Spain.

Abstract

Aim of study: The goal of this study is to analyse variations in curve number (CN) values produced by different cartographic data sources in a forested watershed, and determine which of them best fit with measured runoff volumes.

Area of study: A forested watershed located in western Spain.

Material and methods: Four digital cartographic data sources were used to determine the runoff CN in the watershed.

Main results: None of the cartographic sources provided all the information necessary to determine properly the CN values. Our proposed methodology, focused on the tree canopy cover, improves the achieved results.

Research highlights: The estimation of the CN value in forested areas should be attained as a function of tree canopy cover and new calibrated tables should be implemented in a local scale.

Additional keywords: runoff estimation; Soil Conservation Service curve number; land use map; Geographic Information System; forested watershed; tree canopy cover factor.

Abbreviations used: CLC (Corine Land Cover); CN (Curve Number); E (Nash-Sutcliffe efficiency); PBIAS (Percent bias); RSR (RMSE-observations standard deviation ratio); SCLUM (Spanish Cultivation and Land Use Map); SCS (Soil Conservation Service); SFM (Spanish Forestry Map); SLOIS (Spanish Land Occupation Information System); TCCF (Tree Canopy Cover Factor).

Authors´ contributions Conception, data analysis and final approval of the version: LF, EQ and PDB. Experiments and drafting the article: LF. Critical revision: EQ and PD-B.

Citation: Fragoso, L.; Quirós, E.; Durán-Barroso, P. (2017). Resource communication: Variability in estimated runoff in a forested area based on different cartographic data sources. Forest Systems, Volume 26, Issue 2, eRC02. https://doi.org/10.5424/fs/2017262-10921

Received: 17 Dec 2016 **Accepted:** 24 Jul 2017.

Funding: Government of Extremadura and FEDER (GR15129) has supported the English translation of the publication.
Competing interests: The authors have declared that no competing interests exist.
Correspondence should be addressed to Elia Quirós: equiros@unex.es

Introduction

The hydrologic response of a watershed in a rainfall-runoff event depends largely on the runoff threshold, which represents the volume of water that can be absorbed by the ground before surface runoff begins. Therefore, it is an essential component of flood forecasting and warning systems (Carpenter *et al.,* 1999). Determining this value is one of the first steps in a hydrological analysis of a watershed, and it depends on several factors that are partially chosen by non-objective criteria, resulting in a corresponding uncertainty in the value.

Even though the Soil Conservation Service curve number (SCS-CN) method has been widely studied for decades (NRCS, 2009), there are not several works focused on the validation of this approach in forested watershed. In this way, Kim & Lee (2008) concluded that the SCS-CN lookup tables depicts inaccurate runoff estimation especially in forested watersheds. Ajmal *et al.* (2016) applied tabulated SCS-CN in forested areas and they confirmed that those tables were unreliable due to a runoff overestimation in all of their studied watersheds.

Works like Choi *et al.* (2016) have also studied the SCS-CN from several experimental forest catchments in order to modify SCS-CN runoff for forest lands in Korea. In particular, Tedela *et al.* (2011) evaluated the consistency of the CN method from forested-mountainous watersheds in the eastern United States and runoff estimated by tabulated CN were unreliable in most cases.

Free open access to different data sources leads to the question of choosing the best cartographic

Table 1. Summary of information provided by each cartographic source for decision-making with regard to land use or hydrologic condition.

Data source [1]	Agricultural areas		Prairies / Forest (scrub)		Forest (tree)	
	Land use (Definition of the crop type)	Hydrologic condition (Cultivation practices)	Land use	Hydrologic condition (Degree of land use)	Land use	Hydrologic condition (Canopy cover)
SCLUM	●	-	●	-	●	○
SFM	×	-	●	-	●	●
CLC	●	-	●	-	●	-
SLOIS	●	●	●	-	●	-

[1] SCLUM: Spanish Cultivation and Land Use Map; SFM: Spanish Forestry Map; CLC: Corine Land Cover; SLOIS: Spanish Land Occupation Information System. ●: adequate data definition. ○: acceptable data definition (requires user interpretation). ×: poor data definition. - : not provided data

sources for performing hydrological studies. However, the effects that the mapping information source exerts on the estimation of runoff have not been analysed in detail. Consequently, the main goals of this study were to analyse the effects of the use of different cartographic data sources on the CN values of a forested watershed and to determine which cartographic data source fit the measured runoff values in our studied area.

Material and methods

The SCS-CN method is based on the hypothesis of equivalence between the maximum volumes of retention and rainfall and the effective volumes of runoff and infiltration. This methodology was modified for its use in Spain by Témez (1987) who adapted the original table of the SCS-CN method. Similar to the original method, the estimation of runoff is based on parameters such as land use, slope gradient, hydrologic condition, and soil type. In this adaptation the considered land uses are as follows: cultivated areas, prairies, regular forest plantations, forests and rocks. In the case of forests, five levels of hydrologic condition are established (very clear, clear, average, thick, and very thick). However, in the case of forests, the classification proposed by Témez (1987) includes no objective criterion, because it does not indicate the vegetation cover density value for each level.

The study area was a watershed of the Jerte River in Cáceres province (Spain) that is covered by the following land uses: 59% of forest cover (40% of forest and 19% of scrubland forest), 17% of prairie, 23% of cultivated areas, and the remaining area corresponds to urban areas, roads and other minor uses. Rainfall volumes were obtained from two automatic weather stations belonging to the Spanish National Meteorological Agency. The baseflow was separated from observed total flow using the WHAT tool (Automated Web GIS Based Hydrograph Analysis Tool) described by Lim *et al.* (2005).

The cartographic sources used in this study were: Spanish Cultivation and Land Use Map (SLUM)[1] performed within 2000-2010 and Spanish Forestry Map (SFM)[2] performed within 1997-2006, both at a scale of 1:50,000; Corine Land Cover (CLC)[3] version published in 2000 at a scale of 1:100,000 and Spanish Land Occupation Information System (SLOIS)[4] published in 2005 at a scale of 1:25,000. The most remarkable characteristics of each cartographic source are shown in Table 1.

Estimation of runoff using different cartographic sources

Firstly, the estimation of land use and hydrologic condition, based on the available sources was achieved. In the cases that the used cartography did not provide the necessary data, fair hydrologic condition was assumed. Particularly, for forested areas, in the absence of objective criteria for establishing the hydrologic condition levels, we used a classification focused on

[1] http://www.mapama.gob.es/es/cartografia-y-sig/publicaciones/agricultura/mac_2000_2009.aspx
[2] http://www.mapama.gob.es/es/biodiversidad/servicios/banco-datos-naturaleza/informacion-disponible/mfe50.aspx
[3] http://centrodedescargas.cnig.es/CentroDescargas/catalogo.do?Serie=CAANE
[4] http://www.siose.es/

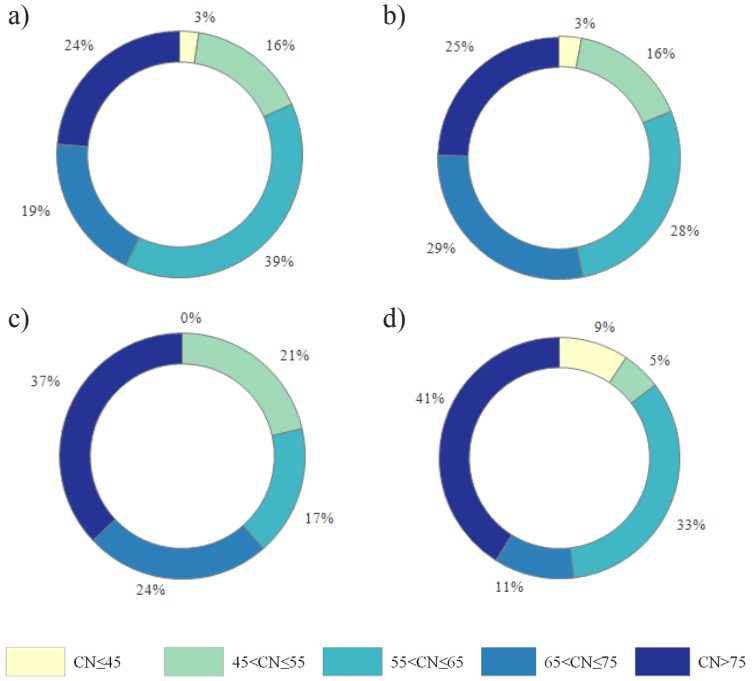

Figure 1. Fluctuations of obtained curve number (CN) values for each map: Spanish Cultivation and Land Use Map (SCLUM), (b) Spanish Forestry Map (SFM), (c) Corine Land Cover (CLC), (d) Spanish Land Occupation Information System (SLOIS).

Tree Canopy Cover Factor (TCCF). Our proposal for the assignment of hydrologic condition was: I-Very clear (< 20%), II-Clear (between 20 and 40%), III-Average (between 40 and 70%), IV-Thick (between 70 and 80%) and V-Very thick (> 80%).

Next, the slope was obtained from a Digital Elevation Model and the classification of soil groups was performed using the cartographic information developed by Ferrer i Juliá (2003), assigning soil group B throughout our studied area.

Finally, variations in CN values were analysed by comparing the four generated maps for land use and hydrologic condition.

Calibration

The observed runoff volumes (24 thunderous events from 2008 to 2014 period) were compared to the runoff volumes generated by each CN value obtained for each map. The comparison was attained by RMSE-observations standard deviation ratio (RSR), percent bias (PBIAS) and Nash-Sutcliffe efficiency (E) criteria.

Results and discussion

The estimation of CN value, as shown in Fig. 1, was dissimilar for each map. The range of CN values between 55 and 65 was the most variable: from 17% for the CLC up to 39% obtained for SCLUM. Those areas with CN value larger than 75, also presented significant fluctuations: from 24% for SCLUM to 41% for SLOIS. The most representative CN values for forest land use ranges from 55 to 65. These results are in substantial agreement with the outcomes attained in experimental forest catchments by Choi *et al*. (2016).

Otherwise, differences in CN spatial distribution (Fig. 2a) arranged from 1 (CN value coincidence in all maps) to 4 (none coincidence). The greatest differences (more than 15 points) in CN values (Fig. 2b) mostly corresponded with areas with no coincidence in CN

Table 2. Percent bias (PBIAS), Nash-Sutcliffe efficiency (E) criteria and RMSE-observations standard deviation ratio (RSR) values obtained from modelled volumes against the observed runoff volume.

Data source [1]	PBIAS	E criteria	RSR
SCLUM	-3.57	0.74	0.51
SFM	-2.04	0.74	0.51
CLC	4.41	0.71	0.54
SLOIS	15.58	0.62	0.61

[1] SCLUM: Spanish Cultivation and Land Use Map; SFM: Spanish Forestry Map; CLC: Corine Land Cover; SLOIS: Spanish Land Occupation Information System.

values. The highest variation in CN occurred in areas classified as scrubland forest and prairie, where none of the cartographic sources provided the TCCF values.

On average for the whole watershed, the CN obtained values were: 64.79 for SCLUM, 65.19 for SFM, 66.87 for CLC and 69.67 for SLOIS. Based on them, the runoff volumes associated to each thunderous event was calculated and compared with the observed runoff volume. The best results (Table 2) were attained by SCLUM and SFM based on RSR criterion. Comparing the PBIAS values, the best achievement was with the SFM map, with an overestimation of CLC and SLOIS. Similar results were obtained by Ajmal *et al*. (2016) in forested areas with a runoff overestimation using CN tabulated values. Finally, attending the E criteria, the best results (0.74) were obtained for SCLUM and SFM. It should be noted that this value was significantly better than those obtained in Tedela *et al.* (2011) in which the best of their forested basins showed a modest correlation (0.56).

Based on the performance rating proposed by Moriasi *et al.* (2007), a joint analysis reveals that the degree of suitability obtained in our CN estimation could be categorized as 'satisfactory' for SLOIS and 'good' for the rest of the maps, but being SCLUM and SFM located sorely close to the limit of 'very good'.

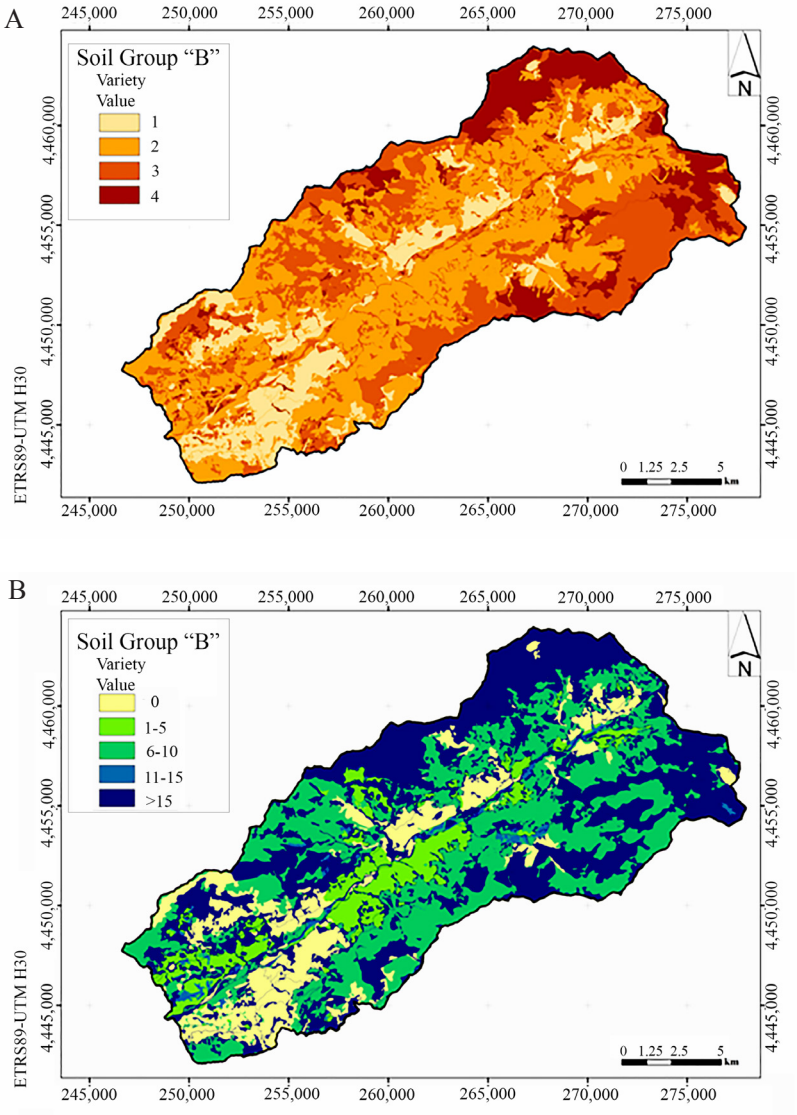

Figure 2. Results of variation in curve number (CN) for the four maps generated from each cartographic data source: (a) map of the variety in obtained CN values, (b) map of the range of variation in CN values.

In this work, the variation in CN, corresponding to the use of different cartographic data sources was studied. After the analysis of each of the data sources, it was observed that none of them provide all the information necessary to determine the land use and hydrologic condition. Based on the analysis of rainfall-runoff data in a forested watershed, the best cartographic data sources were the SCLUM and the SFM. Moreover, the ease to obtain the data of canopy cover from the SFM constitutes a distinct added value for this cartographic data source. Additionally, our proposed methodology for the assignation of the hydrologic conditions based on the TCCF, improves the achieved results, although the method could be validated over other cover ranges of forested watersheds. In short, we can conclude that the estimation of the CN in forested areas should be attained as a function of canopy cover and new calibrated tables should be implemented in a local scale.

Acknowledgements

We thank the Spanish National Meteorological Agency and the Tajo Hydrographic Confederation for providing the necessary data for de study.

References

Amal M, Kim TW, Ahn JH, 2016. Stability assessment of the curve number methodology used to estimate excess rainfall in forest-dominated watersheds. Arab J Geosci 9 (5): 1-14. https://doi.org/10.1007/s12517-016-2421-y

Carpenter TM, Sperfslage JA, Georgakakos KP, Sweeney T, Fread DL, 1999. National threshold runoff estimation utilizing GIS in support of operational flash flood warning systems. J Hydrol 224 (1–2): 21-44. https://doi.org/10.1016/S0022-1694(99)00115-8

Choi HT, Kim J, Lim HG, 2016. Estimating the SCS runoff curve number in forest catchments of Korea. EGU General Assembly Conference Abstracts.

Ferrer i Juliá M, 2003. Análisis de nuevas fuentes de datos para la estimación del parámetro número de curva: perfiles de suelos y teledetección. CEDEX, Spain.

Kim NW, Lee J, 2008. Temporally weighted average curve number method for daily runoff simulation. Hydrol Proces 22 (25): 4936-4948. https://doi.org/10.1002/hyp.7116

Lim KJ, Engel BA, Tang Z, Choi J, Kim KS, Muthukrishnan S, Tripathy D, 2005. Automated Web GIS based Hydrograph Analysis Tool, WHAT. JAWRA 41 (6): 1407-1416. https://doi.org/10.1111/j.1752-1688.2005.tb03808.x

Moriasi DN, Arnold JG, Van Liew MW, Bingner RL, Harmel RD, Veith TL, 2007. Model evaluation guidelines for systematic quantification of accuracy in watershed simulations. T ASABE 50 (3): 885-900. https://doi.org/10.13031/2013.23153

NRCS, 2009. National Engineering Handbook, section 4, Hydrology, version (1956, 1964, 1971, 1985, 1993, 2004, 2009). USDA, Washington, DC. Engineering Division

Tedela NH, McCutcheon SC, Rasmussen TC, Hawkins RH, Swank WT, Campbell JL, Adams MB, Jackson CR, Tollner EW, 2011. Runoff curve numbers for 10 small forested watersheds in the mountains of the Eastern United States. J Hydrol Eng 17 (11): 1188-1198. https://doi.org/10.1061/(ASCE)HE.1943-5584.0000436

Témez JR, 1987. Cálculo hidrometereológico de caudales máximos en pequeñas cuencas naturales. MOPU, Spain.

3.2. Publicación N.º 2

Publicación	**Overstory-understory land cover mapping at the watershed scale: accuracy enhancement by multitemporal remote sensing analysis and LiDAR**				
Autores	**Fragoso, Laura** · Quirós, Elia · Mora, Julián ·Gutiérrez Gallego, José Antonio ·Durán-Barroso, Pablo				
Revista	Environmental Science and Pollution Research (2020) 27:75–88				
eISSN	1614-7499				
DOI	10.1007/s11356-019-04520-8				
Fuente de Impacto	Índice 5 años	Índice 2019	Categoría	Rank	Cuartil
WOS (JCR)	3,056	3,306	Environmental Science	99/265	Q2
Aportación de la doctoranda:	Conceptualización, metodología, programas informáticos, análisis formal, investigación, redacción-borrador original, redacción-revisión y edición de la versión final.				

Environmental Science and Pollution Research (2020) 27:75–88
https://doi.org/10.1007/s11356-019-04520-8

CURRENT TRENDS ON SUSTAINABLE ENERGY, ENGINEERING, MATERIALS AND ENVIRONMENT

Overstory-understory land cover mapping at the watershed scale: accuracy enhancement by multitemporal remote sensing analysis and LiDAR

Laura Fragoso-Campón[1] · Elia Quirós[1] · Julián Mora[2] · José Antonio Gutiérrez Gallego[1] · Pablo Durán-Barroso[3]

Received: 19 October 2018 / Accepted: 6 February 2019 / Published online: 19 February 2019

Abstract

In forested watersheds, density, land cover, and its vertical structure are crucial factors for flood management, ecosystem monitoring, and biomass inventory. Nowadays, producing land cover maps with high accuracy has become a reality with the application of remote sensing techniques, but in some situations, it is not so easy to distinguish between the overstory and understory vegetation with only spectral information. The main goal of this study was to analyze the accuracy enhancement in overstory and understory land cover mapping at the watershed scale when using the data fusion of seasonal and annual time series of Sentinel-2 images complemented with low-density LiDAR and soil and vegetation indices. The study area was composed by two neighboring watersheds in Badajoz province (Spain). The accuracy of land cover classifications was trained in two ways: first, for each season and several soil-vegetation indices; and second, for the annual series and soil-vegetation indices. Next, LiDAR data were included in both analyses by means of a Boolean metric concerning the height. The obtained results showed that the overall accuracy was better with the annual evaluation when only spectral information was used for the classification. Additionally, if LiDAR data were included in the classification (data fusion), the overall accuracies were highly improved, especially in summer and autumn seasons. This improvement can be a significant issue in the analysis of vegetation structure and its spatial distribution as it is decisive for watershed ecosystem management.

Keywords Remote sensing · Sentinel-2A · Forest land cover · Overstory · Understory · Multitemporal analysis · LiDAR · Random forest

Responsible editor: Philippe Garrigues

✉ Laura Fragoso-Campón
laurafragoso@unex.es

Elia Quirós
equiros@unex.es

Julián Mora
jmora@unex.es

José Antonio Gutiérrez Gallego
jagutier@unex.es

Pablo Durán-Barroso
pduranbarroso@unex.es

[1] Department of Graphic Expression, Universidad de Extremadura, 10003 Cáceres, Spain

[2] Department of Art and Territorial Sciences, Universidad de Extremadura, 10003 Cáceres, Spain

[3] Department of Construction, Universidad de Extremadura, 10003 Cáceres, Spain

Introduction

Watersheds, from an environmental point of view, are ecosystems with hydrological, ecological, and environmental functions. They provide a suitable habitat for vegetation and wildlife that, to a greater or lesser extent, have interactions between the physical and biological characteristics of the water. Forest ecosystems can decrease the quantity of rainfall on the soil surface and, at the same time, reduce the runoff due to canopy and forest floor interceptions (Gökbulak et al. 2016). This reduction highly depends, not only on the intensity and quantity of the precipitation, but also on tree density, forest type, and its vertical structure.

One of the main characteristics of Mediterranean forests is the presence of branching formations: trees and shrubs coexisting in the same habitat. The original vegetation of the Mediterranean Iberian watersheds has been reduced in certain circumstances due to two opposing trends in land use:

Overstory-Understory Land Cover Mapping at the Watershed Scale: Accuracy Enhancement by Multitemporal Remote Sensing Analysis and LiDAR

Laura Fragoso-Campón [1*], Elia Quirós[1], Julián Mora[2], José Antonio Gutiérrez[1], Pablo Durán-Barroso[3]

[1]Department of Graphic Expression, Universidad de Extremadura, Cáceres, 10003, Spain; laurafragoso@unex.es; equiros@unex.es; jagutier@unex.es.

[2]Department of Art and Territorial Sciences, Universidad de Extremadura, Cáceres, 10003, Spain; jmora@unex.es.

[3]Department of Construction, Universidad de Extremadura, Cáceres, 10003, Spain; pduranbarroso@unex.es

*Correspondence author: laurafragoso@unex.es;

Abstract In forested watersheds, density, land cover, and its vertical structure are crucial factors for flood management, ecosystem monitoring, and biomass inventory. Nowadays, producing land cover maps with high accuracy has become a reality with the application of remote sensing techniques, but in some situations, it is not so easy to distinguish between the overstory and understory vegetation with only spectral information. The main goal of this study was to analyze the accuracy enhancement in overstory and understory land cover mapping at the watershed scale when using the data fusion of seasonal and annual time series of Sentinel-2 images complemented with low density LiDAR and soil and vegetation indices. The study area was composed by two neighboring watersheds in Badajoz province (Spain). The accuracy of land cover classifications was trained in two ways: first, for each season and several soil-vegetation indices; and second, for the annual series and soil-vegetation indices. Next, LiDAR data were included in both analyses by means of a Boolean metric concerning the height. The obtained results showed that the overall accuracy was better with the annual evaluation when only spectral information was used for the classification. Additionally, if LiDAR data were included in the classification (data fusion), the overall accuracies were highly improved, especially in summer and autumn seasons. This improvement can be a significant issue in the analysis of vegetation structure and its spatial distribution as it is decisive for watershed ecosystem management.

Keywords Remote sensing; Sentinel 2A; forest land cover; overstory; understory; multitemporal analysis; LiDAR; random forest.

Acknowledgments This research was funded by the Junta de Extremadura and the European Social Fund: A way of doing Europe, through the "Financing of Predoctoral Contracts for the Training of Doctors in Public Research and Development Centers belonging to the Extremadura System of Science, Technology, and Innovation [file PD16018]". This work was also supported by the Government of Extremadura (Spain) and co-funded by the European Regional Development Fund under Grants [Project: GR18052]. We thank the Junta de Extremadura (CICTEX) for providing the necessary high resolution ortophotographs PNOA 2007-CC-BY 4.0 scne.es.

Introduction

Watersheds, from an environmental point of view, are ecosystems with hydrological, ecological, and environmental functions. They provide a suitable habitat for vegetation and wildlife that, to a greater or lesser extent, have interactions between the physical and biological characteristics of the water. Forest ecosystems can decrease the quantity of rainfall on the soil surface and, at the same time, reduce the runoff due to canopy and forest floor interceptions (Gökbulak et al. 2016). This reduction highly depends, not only on the intensity and quantity of the precipitation, but also on tree density, forest type, and its vertical structure.

One of the main characteristics of Mediterranean forests is the presence of branching formations: trees and shrubs coexisting in the same habitat. The original vegetation of the Mediterranean Iberian watersheds has been reduced in certain circumstances due to two opposing trends in land use: progressive abandonment of practices in marginal rural areas and land use intensification in more productive areas (Palomo-Campesino et al. 2018)

Overstory is the highest strata of vegetation in a forest, usually forming the canopy and has been largely studied from the perspectives of distribution (Véga et al. 2016; Zhao et al. 2017) and density (González-Ferreiro et al. 2012; Ma et al. 2017). One the other hand, understory vegetation is also an important component in forest ecosystems, not only because of its contributions to forest structure, function and species composition, but also because of its essential role in supporting wildlife species and ecosystem services (Tuanmu et al. 2010). More specifically, in the Iberian Dehesa, a grazed Mediterranean open woodland, shrub encroachment has been proposed as an effective method to facilitate natural tree regeneration and ensure the sustainability of silvopastoral systems (López-Díaz et al. 2015). As stated in Caballero Díaz et al. (2015), in this Mediterranean environment, this type of understory species plays a crucial role in ecosystem dynamics.

Nevertheless, the analysis of vegetation structure and its spatial distribution is decisive for many other purposes like ecosystem monitoring and biomass inventory (García et al. 2010; Garcia et al. 2017; Latifi et al. 2015; Li et al. 2017; Nizami et al. 2017)

Nowadays, producing land cover maps with high accuracy has become a reality with the application of remote sensing techniques, but on some occasions, it is not so easy to distinguish between the overstory and understory vegetation by only using the spectral information.

There is a wide availability of satellites and sensors that offer a large range of spatial and spectral resolutions. In this field, Landsat imagery, which are available for free and have the longest time series, have been traditionally used because of its ability to discriminate between different types of coverage (eight spectral bands offered) with a good spatial resolution (30 m) (Ahmed et al. 2015; Akike and Samanta 2016; Bolton et al. 2018; Schultz et al. 2016; Zhao et al. 2016). Even so, with the appearance of Sentinel-2 imagery, new studies on land cover mapping can be performed (Ahmed et al. 2015; Godinho et al. 2017; Immitzer et al. 2016; Sánchez Sánchez et al. 2018).

Spectral information can be complemented by using the so-called vegetation indices (VI). These indices support the discrimination of the vegetal cover since they present characteristic values due to the coloration, water content, and photosynthetic action of the plants (Adamu et al. 2018; Godinho et al. 2016; Hill 2013).

Due to the seasonal cycle of the plants and to distinguish the vegetation with a temporal spectral signature, some authors like Gebhardt et al. (2014) and Zhao et al. (2016) showed how global accuracy in land cover mapping could be improved by the classification of multitemporal series instead of a single date image.

Moreover, and to distinguish between the overstory and understory vegetation, the inclusion of LiDAR data and machine learning techniques in the classification processes have proven to be one of the best improvements (Bork and Su 2007; Erdody and Moskal 2010; García et al. 2011; Mundt et al. 2006; Mutlu et al. 2008). This data fusion takes advantage of the information provided by LiDAR data on the vertical structure of the vegetation, and the capability of multispectral data to capture the horizontal distribution of vegetation as well as to differentiate vegetation types based on their spectral response (García et al. 2011).

More recently, works such as those of Stojanova et al. (2010), Ahmed et al. (2015) and Zald et al. (2016) have proposed the use of LiDAR and multitemporal series of multispectral images for estimating the LiDAR measured canopy structure using a time series of Landsat imagery. To reduce the costs associated with large-area acquisitions of LiDAR, in these works the LiDAR data are used only for the definition of sample data, extrapolating the estimation of the forest structure to the whole area covered by the satellite image. As mentioned in Zald et al. (2016) the most important limitation of the methodology is the inability of LiDAR by itself to provide information of map species composition. This restriction also applies to any variable that is only observable with field plot data or other sources of information.

The capacity of LiDAR data to represent the spatial structure of forest stands has been widely validated in this regard and the density of points per square meter is a crucial factor. When studying overstory, densities around 1 points/m² are enough to determine the coverage of the tree stratum (Ma et al. 2017) and, what is more, González-Ferreiro et al. (2012) suggested that, for forest stand variables estimation, density can be reduced to low values of 0.5 points/m² without a significant loss of information. In contrast, there are fewer works that focus on the study of the understory with LiDAR. In this regard, for the correct definition of this low strata, it is necessary to have a higher density of the LiDAR point cloud than for the overstory, reaching up to 8 points/m² as shown in Estornell et al. (2011) or even more than 13 points/m^2, as mentioned in Hellesen and Matikainen (2013). In order to counteract the lack of density, other works have proposed to enhance the classification with additional information like high resolution infrared orthophotography (Riaño et al., 2007) or by supplementing the analysis with a multispectral image of high spatial resolution (García et al., 2011).

The main goal of this study was to analyze the accuracy enhancement in overstory and understory land cover mapping at the watershed scale when using the data fusion of seasonal and annual time series of Sentinel-2 images complemented with LiDAR and soil and vegetation indices.

Materials and Methods

Studied Area

The study area is composed of two neighboring watersheds in Badajoz province (Spain) of 146 km^2 and 194 km^2, respectively (Fig. 1). According to the Spanish Cultivation and Land Use Map (MAPAMA 2018), the watersheds are mainly covered by the following vegetation types: perennial forest wooded with residual conifers at the overstory, and shrubs and herbaceous at the understory level.

The perennial forest wooded of the overstory is mainly composed of holm oaks (*Quercus Ilex*), cork oaks (*Quercus suber*) and Eucalyptus (*E. globulus* and *E. camaldulensis*). Regarding the understory, the evergreen shrubs are mainly *Pistacia lentiscus*, *Cistus ladanifer* and *Retama sphaerocarpa*. On the other hand, the herbaceous vegetation is predominantly located in the Dehesa below the holm oaks and also in agricultural areas. Finally, other covers like rocky outcrops and almost impervious surfaces (like roads and bare soil) are also present in the study area, but with less importance.

Sentinel 2 Data

The Sentinel-2 mission is composed of a constellation of two satellites (A and B) that has offered revisits every ten days since 2015 (A) and 2017 (B), so have a global revisit of five days since they started working together. The Sentinel 2 images offer different spatial resolutions depending on the spectral band considered. Bands B2, B3, B4, and B8 have a resolution of 10 m, while bands B5, B6, B7, B8a, B11, and B12 have a resolution of 20 m. Finally, bands B9 and B10 have a resolution of 60 m.

As shown in Fig.1, the studied area is located in tile T30STH. In this way, all cloud free images from April 2017 to April 2018 (twenty images) were processed. Moreover, the images were grouped according to their corresponding season: five autumn images, four winter images, five spring image321s, and six summer images.

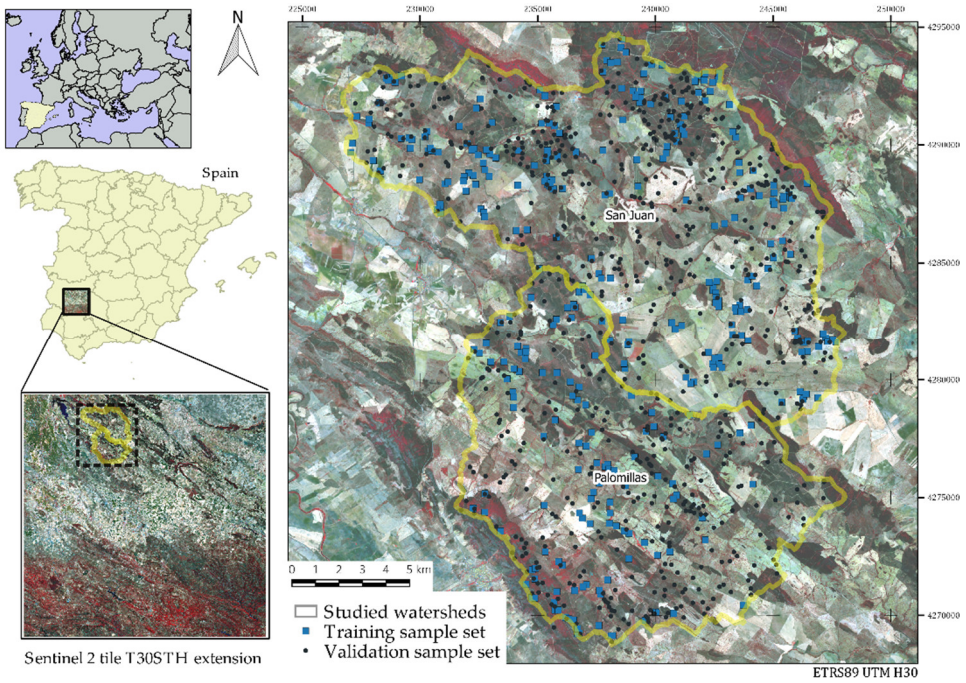

Fig.1 The two studied watershed in Badajoz province (Spain) represented within the Sentinel 2 tile T30STH (layout in infrared false color). The spatial distribution of the training and validation sample set are also represented

In addition to the spectral bands, various vegetation indices (VI) and soil indices (SI) were obtained for each single date image and included as predictors for the improvement of the classification accuracy (Table 1).

As shown in Table 1, the VI used were the well-known Normalized Difference Vegetation Index (NDVI) originally proposed by Rouse Jr et al. (1974), the Soil Adjusted Vegetation Index (SAVI) developed by Huete (1988) or the Second Modified Soil Adjusted Vegetation Index (MSAVI2) proposed by Qi et al. (1994), and the Green Normalized Difference Vegetation Index (GNDVI) developed by Gitelson et al. (1996). Additionally, Sentinel-2 imagery provide more indices rather than the classic ones such as the Normalized Difference Index (NDI45) proposed by Delegido et al. (2011) and the Sentinel-2 Red-Edge Position Index (S2REP), which is based on linear interpolation, as presented by Guyot et al. (1988). In addition, although they are not fully implemented in vegetation classifications yet, Soil Indices (SI) might be useful to improve the discrimination of low green vegetation canopy covers and the bare soil, as it has been evidenced in Huete et al. (1984) and Richardson and Wiegand (1977). The most extended SI are the Brightness Index (BI) and the Color Index (CI) (Escadafal 1993).

Table 1 Vegetation and soil indices relation considered in the supervised classification

Index	Use	Equation
GNDVI Green Normalized Difference Vegetation Index	Used to contrast the state of the vegetation between the NIR and the green band	GNDVI = (B7 – B3) / (B7 + B3)
NDVI Normalized Difference Vegetation Index	Used to measure the photosynthetic activity in correlation with the density and vitality of the vegetation	NDVI = (B8 – B4) / (B8 + B4)
NDI45 Normalized Difference Index	Employed to estimate biophysical variables, such as the leaf area index (LAI)	NDI45 = (B5 - B4) / (B5 + B4)

Index	Use	Equation
S2REP Sentinel-2 Red-Edge Position Index	Includes the information of both crop (chlorophyll content) and growth status of the vegetation	S2REP = 705 + 35 * ((B4 + B7)/2 - B5) / (B6 - B5)
SAVI Soil Adjusted Vegetation Index	Aims at minimizing the effect of the soil on the vegetation indices, especially evident on partially coated surfaces	SAVI = (1 + L) * (B8 – B4) / (B8 + B4 + L) With L=0.5
MSAVI2 Second Modified Soil Adjusted Vegetation Index	Similar to the SAVI index, but taking into account that not all soils are alike. Different soils have different reflectance spectra.	MSAVI2 = (1/2) * (2 * (B8 + 1) - sqrt((2 * B8 + 1) * (2 * B8 + 1) - 8 * (B8 – B4)))
BI Brightness Index	Uses the albedo of the terrestrial surface to differentiate between the vegetal covers and the ground	BI = sqrt(((B4 * B4) + (B3 *B3)) / 2)
CI Color Index	Related to the concentration of carbonates or sulphates in the soils	CI = (B4 – B3) / (B4 + B3)

B_i corresponds with the different spectral bands of the Sentinel 2 images.

LiDAR Data

LiDAR data correspond to the National Plan of Aerial Orthophotography (PNOA) of the Spanish National Geographic Institute with a point density of 0.5 points/m², and was acquired in September 2010. The data were downloaded from the Spanish National Geographic Institute website (Instituto-Geográfico-Nacional 2017), who provides it in tiles of 2 km x 2 km. The studied area corresponded to 116 tiles that were analyzed with FUSION software developed by the USDA Forest Service (McGaughey 2009).

The canopy height model (CHM), which represents the digital elevation model of the vegetation above the ground, was processed from the normalized height of the point cloud, creating a raster with pixel cell size of 2 m. The normalization was performed with a ground surface model with a RMSE of 0.114 m. Afterwards, to adjust the CHM to the Sentinel-2 spatial resolution, the raster was processed by generalizing the values to a pixel cell size of 10 m in a similar way to the procedure described in Ahmed et al. (2015). Then, two new rasters were obtained representing the mean and the maximum value in each generalized pixel.

The LiDAR data used is the only one available in Badajoz province up to the present. As a result, there is a time lag between the acquisition of the LiDAR data and the Sentinel images used in this work. Taking into account that the landscape in the studied area is quite stationary, it can be assumed that only phenological changes have occurred during the time lag. However, using a Boolean CHM instead of the physical LiDAR height values would contribute to avoid the noise of the height in low strata caused by the low density of the LiDAR, and to reduce the influence of the evolution in height of the vegetation cover during the time lag. With this regard, the Boolean threshold is crucial to properly define the limit between the overstory and understory, and it needs to be defined analyzing the characteristics of the studied vegetation. As stated before, the evergreen shrubs are composed mainly of *Cistus ladanifer,* whose height ranges from 0.5 to 2.0 m, *Retama sphaerocarpa,* whose height ranges from 0.5 to 3.0 m and *Pistacia lentiscus,* whose normal height ranges from 1 to 2.0 m. According to these measuring ranges, the limit height in the LiDAR metrics between shrubs and trees was fixed in 3 m above the ground. As a result, both generalized CHM (mean and maximum values) were transformed into Boolean values: one if LiDAR height was above 3 m and cero if not. These Boolean LiDAR-CHM metrics, unaffected by phenological changes, were included as predictor variables in the classification.

Training and Validation Areas Design

The training and validation samples were defined by photointerpretation over the High Spatial Resolution (HSR) imagery that also belongs to the National Plan of Aerial Orthophotography (PNOA) of the Spanish National Geographic Institute. In addition, the LiDAR metrics were considered to properly define the sample set. Thus, random stratified training areas were designed following the recommendation of Belgiu and Drăguţ (2016). The samples were selected under the criterion of not having suffered significant changes in the time lag between the LiDAR data and the Sentinel imagery. For this purpose, the changes in the vegetation were studied over the available HSR images as near to the date of the LiDAR flight and the date of the Sentinel images as possible. As a result, three series of HSR images were studied: images that date back to 2009 and 2011, those that were taken before and after the LiDAR flight and the images taken in 2016, which are the most recent ones to the acquisition of the Sentinel images in the studied area.

The land cover classes were grouped by their similar hydrologic response following the criteria of the National Engineering Handbook (NRCS, 2009). Therefore, five classes were considered according to their capacity for runoff generation (minor to major): wooded forest (overstory), shrub (understory), herbaceous and rock (which includes bare soil and impervious areas). Finally, the last class is composed of water bodies which have also been included in the land cover classification.

As a result, 364 sample locations were collected for training. Next, the size of each training area was obtained by expanding the spatial size, depending on the homogeneity around the sample location (Zhao et al. 2016). Finally, the resulting training area was around the 0.69% of the total area (more than 23,400 pixels) (see Fig. 1).

To ensure an objective accuracy assessment, the training and validation areas were designed independently. The appropriate validation sample size was defined using the multinomial distribution, following the guidelines proposed in Congalton and Green (2008) for five land cover classes with a desired confidence level of 95% and a desired precision of 5%. Therefore, 710 random stratified validation samples (cell size of 10 m) were used to generate a valid error matrix. A minimum number of 20 samples were used for water and rock covers due to their very small occupancy.

Supervised Classification

The analysis was carried out with the Sentinel Application Platform (SNAP) software developed by the ESA. A pixel based supervised classification was carried out for land cover mapping by applying the implemented Random Forest classifier (RF). The RF classifier (Breiman 2001) is an ensemble classifier that uses a set of classification and regression trees to make a prediction (classification), and works like that by Belgiu and Drăguţ (2016) have confirmed that it is suitable for data fusion analysis When using this classifier, two parameters are decisive to produce the forest trees: the number of decision trees to be generated (Ntree), and the number of variables to be selected and tested for the best split when growing the trees (Mtry). In this work, values of 500 and the square root of the number of input bands were considered respectively. Finally, 5000 pixels per run were considered for the randomization of the training to comply with the principle of the RF classifier.

Seasonal Analysis and Classification Accuracy Evaluation

In order to test the effectiveness of the data fusion of LiDAR and the seasonal analysis, the model was trained in two ways. First, the land cover classification was achieved for each season by combining all of the available images for each one as well as considering the VI and SI for each single date image. Second, the land cover classification was carried out for the annual series. Next, LiDAR data were included in the analysis, and as a result, new land cover classifications were achieved both for each season and the annual series. Afterwards, classification accuracies were evaluated by comparing the overall accuracy value derived from the error matrices and by separating differences into two components (Quantity and Allocation) defined by Pontius and Santacruz (2014). At the same time, the second component was divided into two derived statistics: one is the exchange, which is the component that pairwise confusion causes, and the other one is the shift, which is the one that nonpairwise confusions cause.

The flowchart of the used methodology for land cover mapping is shown in Fig. 2.

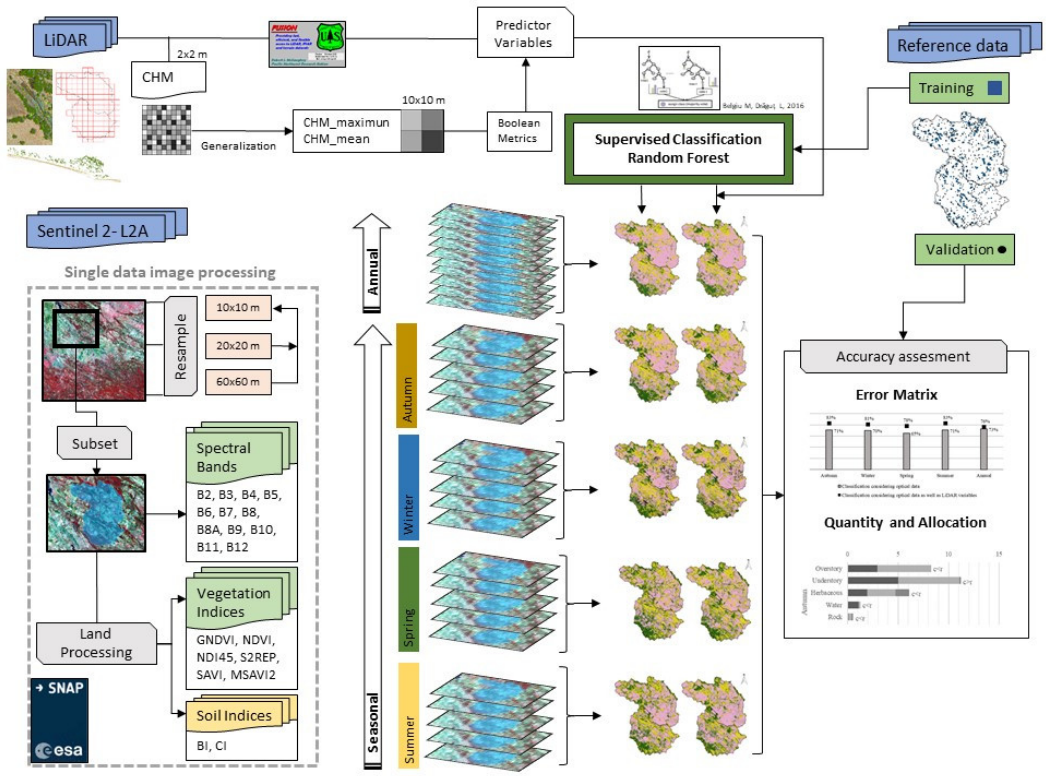

Fig. 2 Flowchart of the methodology used for land cover mapping

Results

Land cover maps obtained from the seasonal analysis are shown in Fig. 3 (Autumn), Fig. 4 (Winter), Fig. 5 (Spring), and Fig. 6 (Summer), representing both the considered scenarios of optical data (a), and optical data as well as LiDAR variables (b). Likewise, the results of the annual analysis are shown in Fig.7.

Land cover mapping from both the seasonal and annual analyses showed differences in the areal proportion for each cover class. The maximum differences in seasonal analysis were for overstory areas that ranged from 17.16% in winter (Fig. 4b) to 27.69% in spring (Fig. 5a). For understory areas, the differences ranged from 25.88% in summer (Fig. 6b) to 32.82% in autumn (Fig. 3b). For herbaceous areas, the differences ranged from 40.36% in spring (Fig. 5a) to 51.55% in summer (Fig. 6b). For the understory and overstory, a general decrease in the classification area was observed when considering the LiDAR variables; in contrast, the herbaceous classification increased.

The minimum variation between both analyses occurred in the annual one where the overstory areas range only increased from 15.25% (Fig. 7a) to 17.21% (Fig. 7b); the shrub areas slightly increased from 27.07% (Fig. 7a) to 27.77% (Fig. 7b); and the herbaceous areas slightly decreased from 53.84% (Fig. 7a) to 51.20% (Fig. 7b).

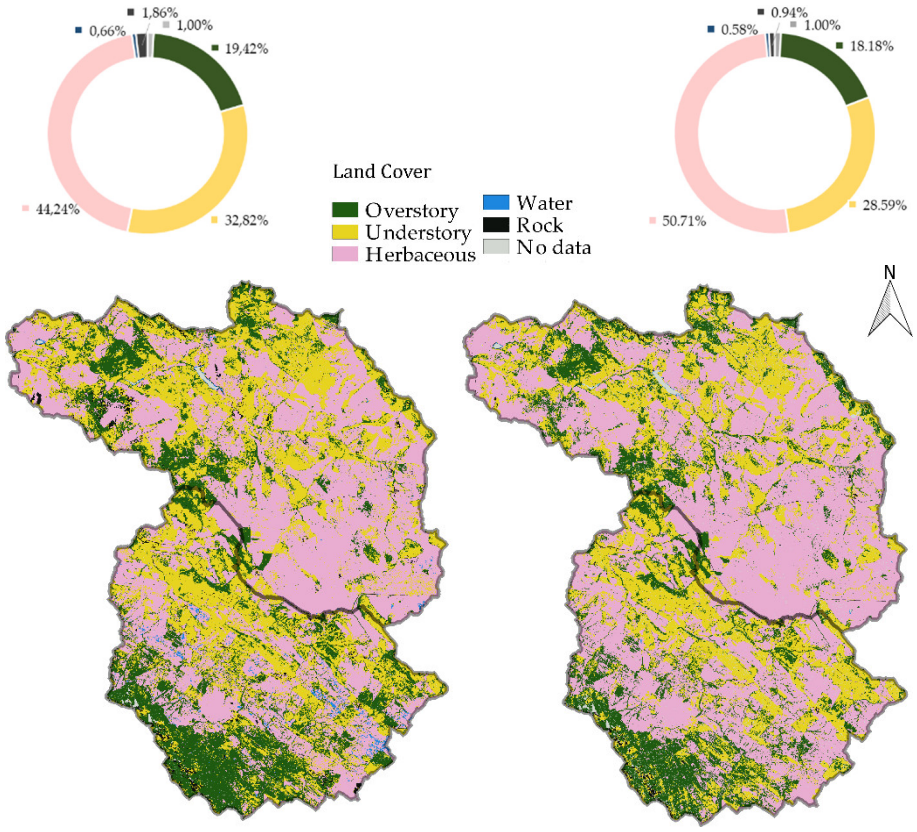

(a) (b)

Fig. 3 Land cover map obtained from the seasonal analysis in Autumn representing both the considered scenarios of optical data (a), and optical data as well as LiDAR variables (b)

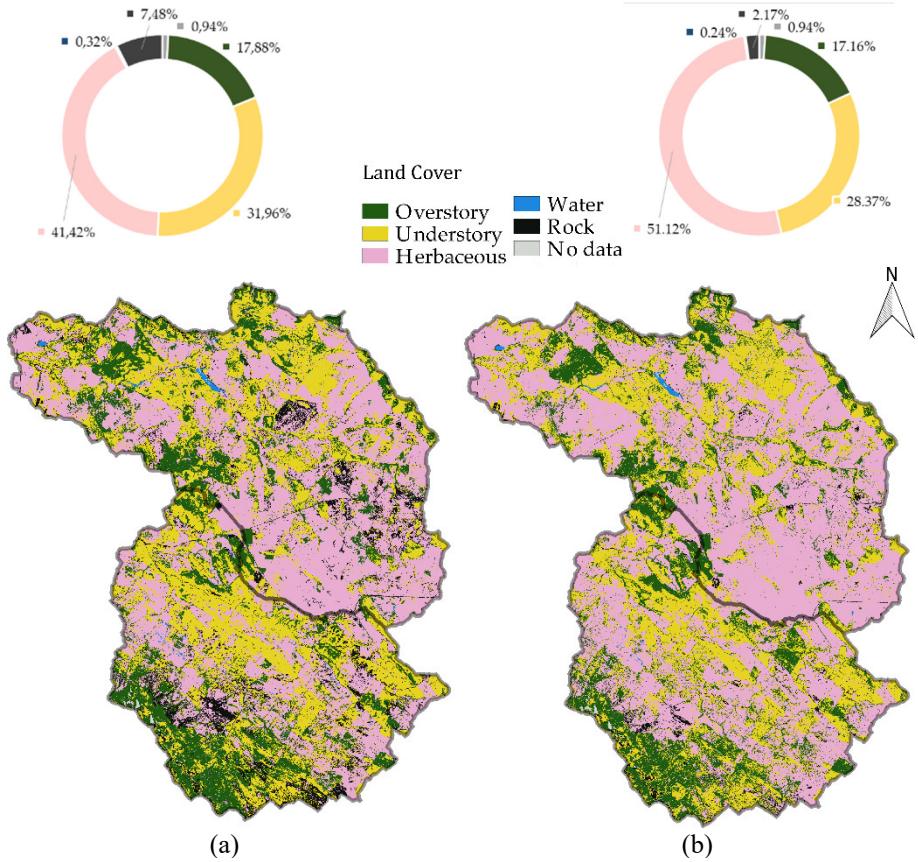

(a) (b)

Fig. 4 Land cover map obtained from the seasonal analysis in Winter representing both the considered scenarios of optical data (a), and optical data as well as LiDAR variables (b)

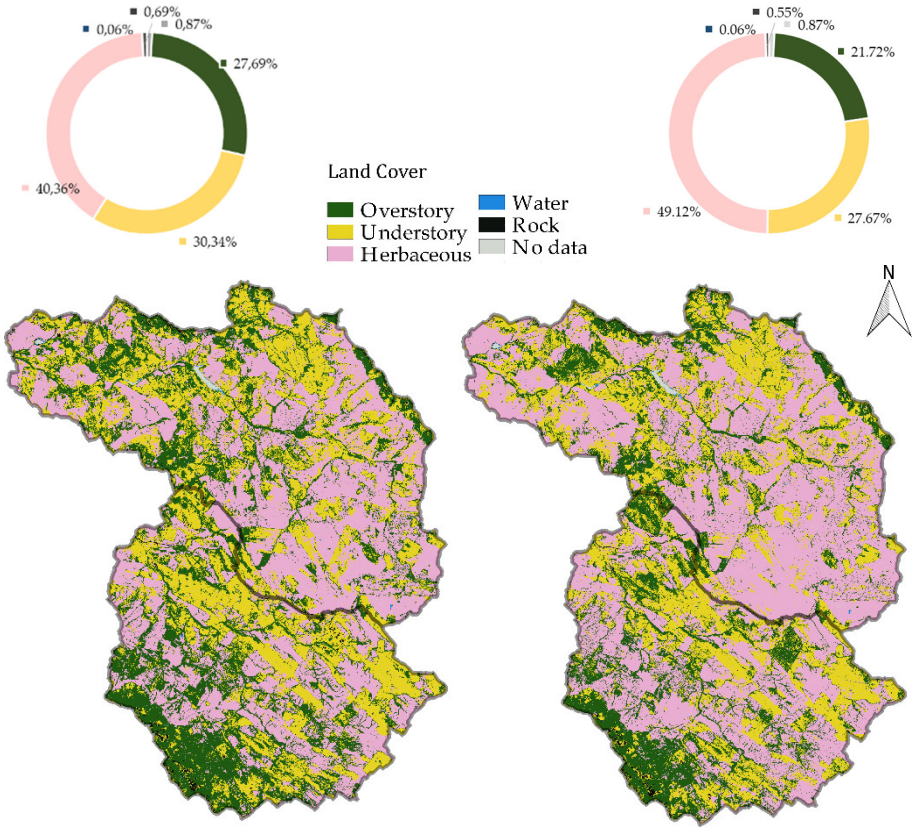

(a) (b)

Fig. 5 Land cover map obtained from the seasonal analysis in Spring representing both the considered scenarios of optical data (a), and optical data as well as LiDAR variables (b)

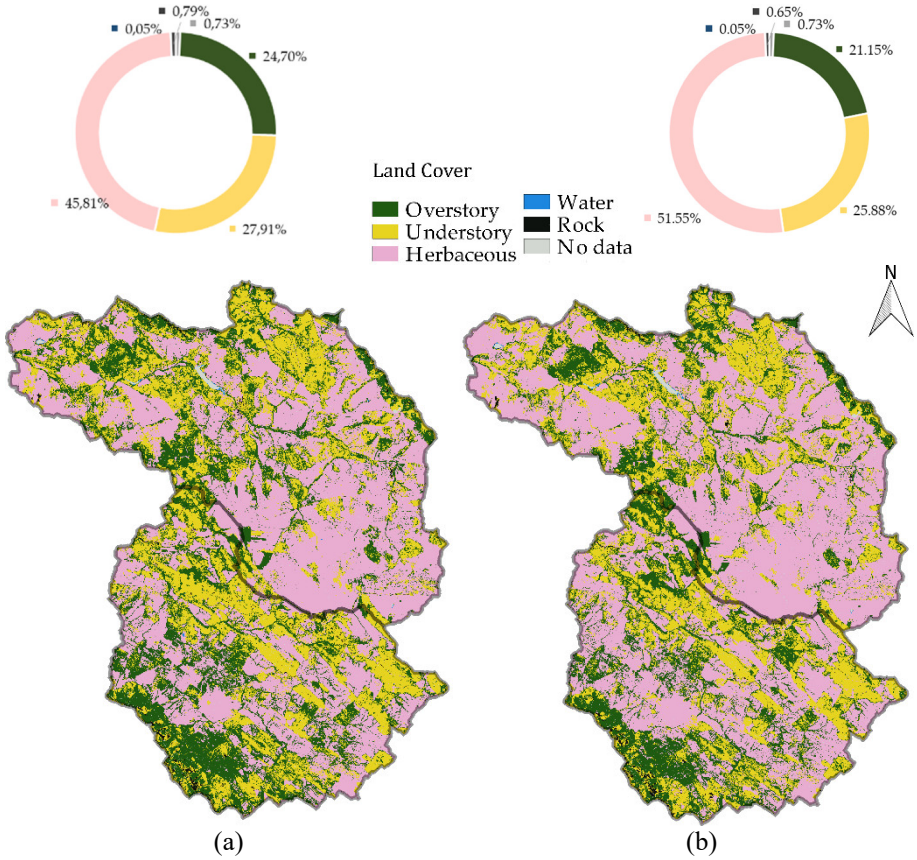

(a) (b)

Fig. 6 Land cover map obtained from the seasonal analysis in Summer representing both the considered scenarios of optical data (a), and optical data as well as LiDAR variables (b)

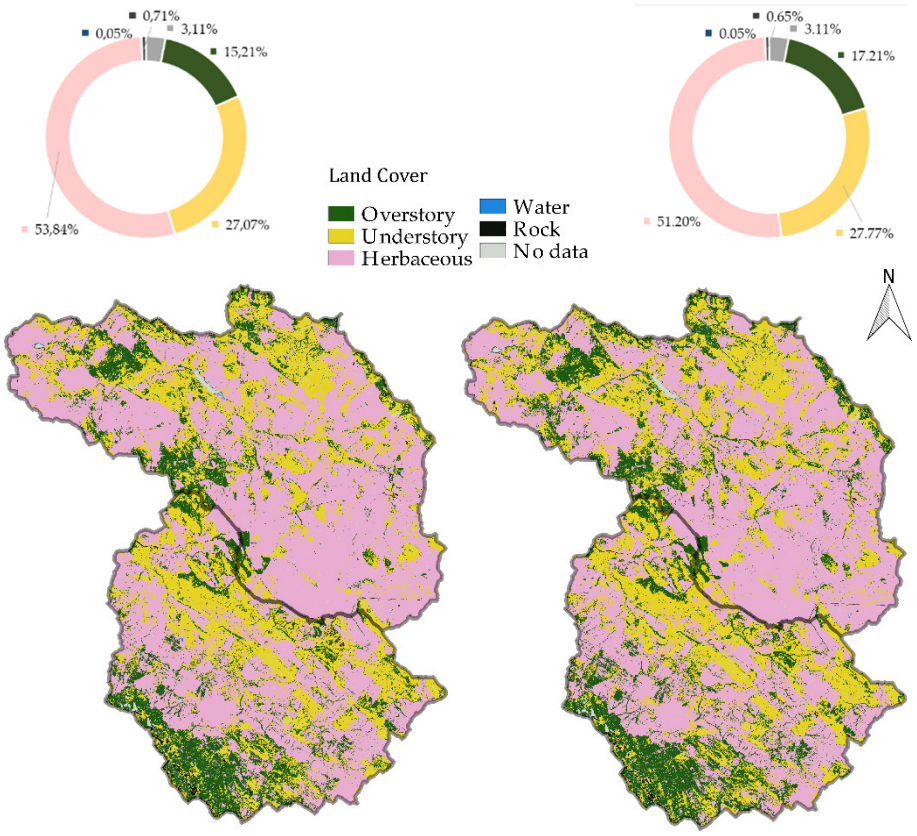

Fig. 7 Land cover map obtained from the annual analysis representing both the considered scenarios of optical data (a), and optical data as well as LiDAR variables (b)

For each land cover map, the error matrix was calculated and its corresponding overall accuracy values were compared. According to the results shown in Fig. 8, the annual analysis presented a higher accuracy than the seasonal classifications when only the optical data were used. Consequently, the number of images evaluated increased the accuracy of the results. Overall accuracy values ranged from 65% (spring) to 71% (summer and autumn) in the seasonal analysis, but the best value was slightly better for the annual analysis, reaching an overall accuracy of 73%.

In contrast, when the LiDAR data were included in the classification (also shown in Fig. 8), the seasonal overall accuracy as highly improved for every season. The best results were obtained for summer and autumn, where overall accuracy improved from 71% to 83%. In this case, the annual results were only slightly better (from 73% to 76%).

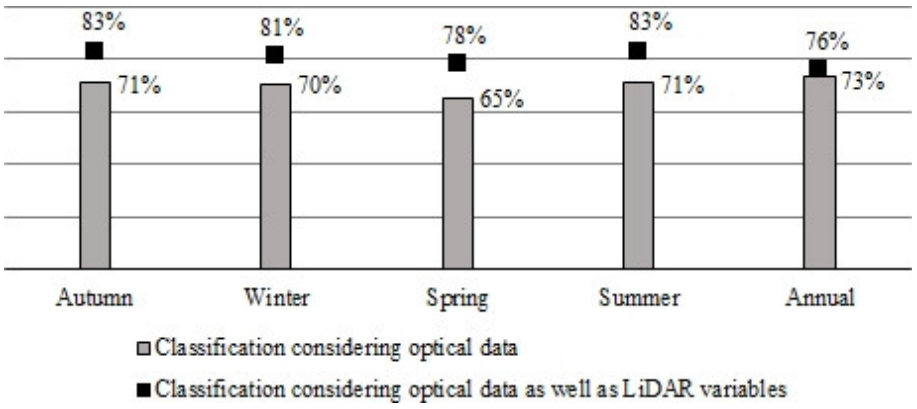

Fig.8 Overall accuracy (OA) of land cover classifications. The columns represent the OA obtained for each classification considering optical data. The black square plots represent the OA when considering optical data as well as LiDAR variables.

Both the user (Table 2) and producer (Table 3) accuracies performed better when considering the LiDAR data. For the overstory, the best user accuracy values ranged from 72% (spring) to 85% (autumn), and in the case of the understory, these values ranged from 64% (winter and spring) to 71% (autumn).

Table 2. User accuracy

	Classification considering optical data					Classification considering optical data as well as LiDAR variables				
	Au	Wi	Sp	Su	An	Au	Wi	Sp	Su	An
Overstory	60%	61%	54%	60%	69%	85%	82%	72%	84%	76%
Understory	54%	54%	48%	54%	59%	71%	68%	64%	70%	64%
Herbaceous	96%	97%	96%	96%	95%	96%	95%	96%	96%	96%
Water	67%	100%	100%	100%	100%	69%	100%	100%	100%	100%
Rock	62%	36%	100%	93%	100%	75%	57%	100%	94%	95%

Au: Autumn; Wi: Winter; Sp: Spring; Su: Summer; An: Annual

Table 3. Producer accuracy

	Classification considering optical data					Classification considering optical data as well as LiDAR variables				
	Au	Wi	Sp	Su	An	Au	Wi	Sp	Su	An
Overstory	51%	46%	58%	61%	49%	73%	68%	75%	80%	63%
Understory	74%	77%	69%	71%	81%	87%	80%	75%	86%	77%
Herbaceous	79%	76%	69%	80%	90%	88%	88%	85%	88%	85%
Water	50%	70%	15%	15%	40%	45%	70%	15%	10%	10%
Rock	90%	80%	75%	70%	89%	90%	85%	80%	80%	90%

Au: Autumn; Wi: Winter; Sp: Spring; Su: Summer; An: Annual

Additionally, the quantity, exchange and shift components of each classification, represented in figure 9, are in substantial agreement with the more accurate seasons (autumn and summer) and with the increase of OA when LiDAR metrics are included in the classification. Additionally, it can be observed that, in general, the exchange component is greater than the shift component. Therefore, the pairwise confusion is dominant in the classification, but it is considerably reduced when LiDAR variables are included in the classification, especially at the overstory and understory classes.

If the commission disagreement is greater than the omission disagreement for a particular category, the mapped points show more of that category than the reference points, that is the map overestimates the quantity of that category (Gao et al., 2011). This is the case of the understory in all classifications, considering optical data in isolation, or considering optical data in combination with LiDAR variables. As noted above, in this class, a general decrease in the classification area was observed when considering the LiDAR variables, so the overestimation shown in figure 9 decreases. On the other hand, if the omission disagreement is greater than the commission disagreement for a particular category, the map underestimates the quantity of that category. In this particular case we find the herbaceous in all classifications both considering optical data or considering optical data as well as LiDAR variables. As said before, in this class the classification area increased when LiDAR metrics were included, so the underestimation shown in figure 9 decreases.

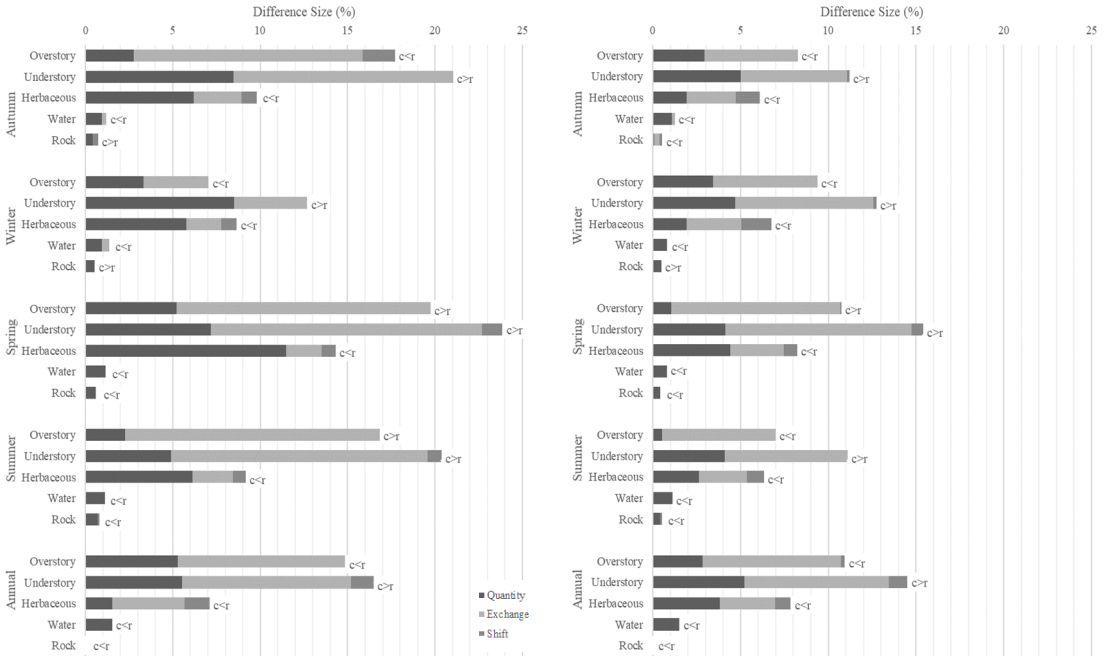

(a) (b)

Fig.9 Quantity, exchange and shift components of the classifications: (a) analysis when considering optical data exclusively and (b) analysis considering optical data as well as LiDAR variables. The label c < r means that the area of the category in the classification is less than the area of the class in the reference (underestimation), and the label c > r means that the area of the category in the classification is greater than the area of the class in the reference (overestimation).

As exposed in Breiman (2001), to verify the RF algorithm, after each tree is constructed, the values of each variable in the out-of-bag examples are randomly permuted and the out-of-bag data is run down the corresponding tree. In the SNAP software, each variable is perturbed three times and the percent of correct predictions are averaged, so the importance score is the original percent of correct prediction minus the averaged percent of correct prediction when the variable is permuted. In this way, higher values in the rank suggest that the variable adds information to the algorithm which is significant in the predictive accuracy when combined with the rest of variables. In this regard, Fig. 10 represents the importance of the predictor variables in the random forest model for the annual evaluation, and Fig. 11 represents the autumn analysis, which is the seasonal analysis that obtained the best results. In both analysis, the bands of Near-Infrared spectrum (NIR) were significant predictor variables in the evaluation (Fig 10a and Fig. 11a). In addition, when LiDAR metrics were considered, they were the most important predictors in the classifications (Fig 10b and Fig. 11b). Fig. 11a shows that the bands of NIR B9 and B8 and Short-Wavelength Infrared Spectrum (SWIR) bands B11 and B12 were the most important predictor variables in the evaluation. The soil index CI was ranked in fifth position and finally, with less importance, there were other vegetation indices such as S2REP, MSAVI2, GNDVI and NDVI. The most representative images were 18-11-2017, 08-12-2017 and 18-12-2017. On the other hand, Fig. 11b shows how the LiDAR metrics were the most important predictor variables, followed by the bands of NIR (B9, B8 and B8a) and SWIR (B11). In this evaluation, the NDVI is ranked sixth and the CI is ranked eighth. The indices SAVI, BI and NDI45 were given less importance. The most representative images were 09-10-2017, 18-11-2017, 08-12-2017 and 18-12-2017.

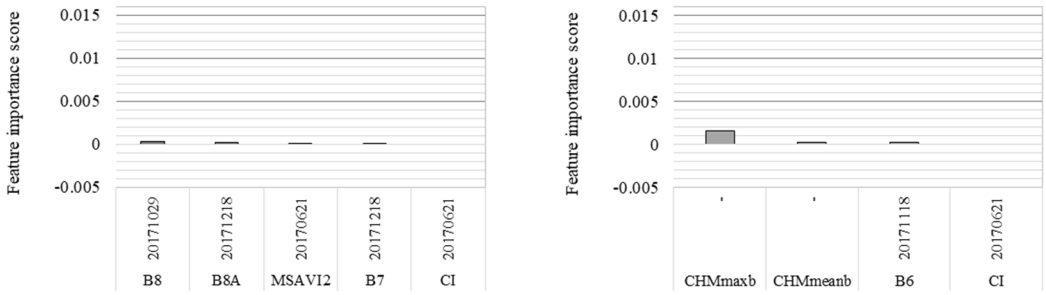

(a) (b)

Fig.10 Predictor variables in annual analysis. Feature importance score obtained in the supervised classification of the land cover applying the Random Forest algorithm. Higher feature importance suggests greater discriminatory power (a) when considering optical data exclusively and (b) the analysis when considering optical data as well as LiDAR variables.

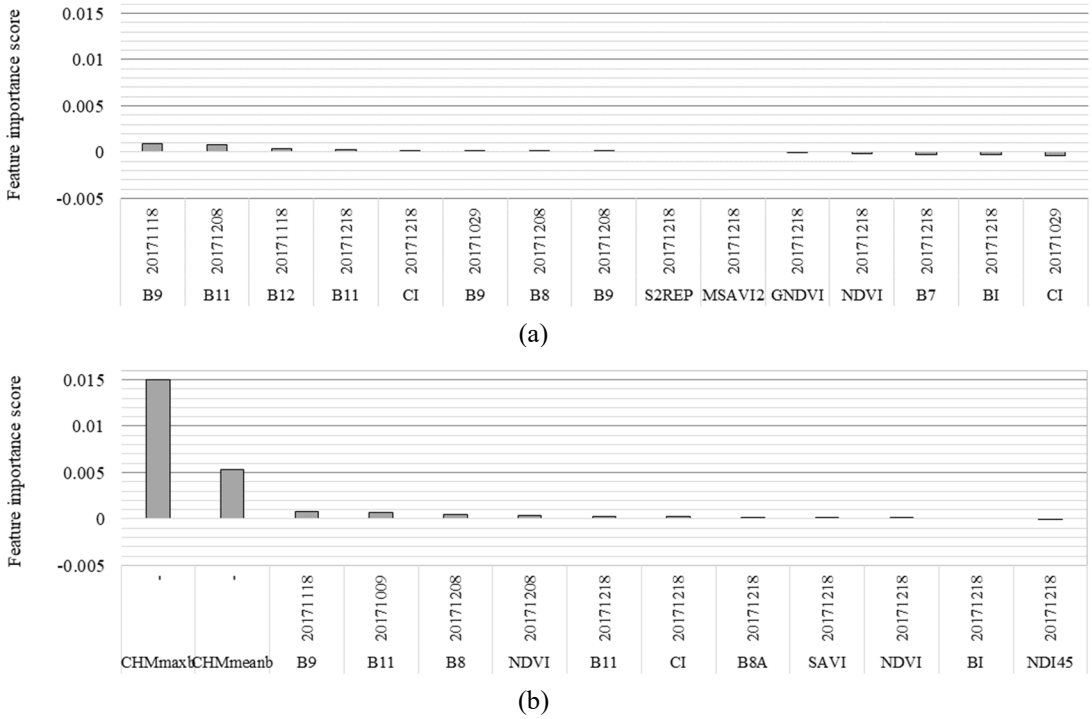

Fig.11 Predictor variables in seasonal analysis in autumn. Feature importance score obtained in the supervised classification of the land cover applying the Random Forest algorithm. Higher feature importance suggests greater discriminatory power (a) when considering optical data exclusively and (b) when considering optical data as well as LiDAR variables.

Discussion

Regarding the OA, the results obtained when exclusively considering the optical data showed that annual imagery classification had the best accuracy, reaching an OA of 73%. This value was in accordance with the results achieved in Gebhardt et al. (2014), which ranged from 70% to 77% in their multitemporal analysis of Landsat imagery and with those obtained in Zhao et al. (2016), where the OA reached ranged from 73% to 80% with the integration of Landsat multi-seasonal data.

On the other hand, when LiDAR data were included in data seasonal classification, the overall accuracy was highly improved for every season in a similar way to that of other previous studies (Ahmed et al. 2015; Erdody and Moskal 2010). The best results were obtained for summer and autumn with an OA of 83%. This value was slightly similar to the results obtained in Sánchez Sánchez et al. (2018) where the OA reached 88% with Sentinel-2 imagery and LiDAR-PNOA data, like in this work. However, this OA was lower than that shown in García et al. (2011) of 94%, although the LiDAR flight had better point density

(1.5–6 points/m² higher than the one available and considered in this work of 0.5 points/m²), and additionally, the analysis was performed with a high spatial resolution multispectral image of 2 m, which was also better than the Sentinel-2 spatial resolution of 10 m.

Regarding the seasonal evaluation, the best results reached in autumn could be due to the phenological variability of the vegetation in the studied watershed (perennial forest wooded, shrub, and herbaceous) that showed the best spectral separability in this season. Other single date studies like Godinho et al. (2016), Godinho et al. (2017) and Sánchez Sánchez et al. (2018) selected the image date under this criterion.

In any case, concerning the important predictor variables obtained for the annual analysis when considering only optical data, the most representative were the near infrared bands and MSAVI2, like the results shown in Vanselow and Samimi (2014), although in this work, only the NDVI was also considered as explanatory variables apart from the Rapid Eye optical bands. Despite this, the values of the importance score are quite low, ranging from 0.01% to 0.03%, and this is because the annual classification was performed using 380 variables (19 bands in each of the twenty Sentinel images used) and with this great deal of information there is not any specific variable that gives significant information to the classification algorithm. When the LiDAR data is used in the classification, the importance score of the Boolean LiDAR metrics reaches up to 0.16% of score, improving the accuracy of the RF algorithm, more than the rest of variables. In the same way, in the best seasonal analysis, the bands of NIR and SWIR were the most important predictor variables in the evaluation, with an importance score that ranges from 0.02% to 0.09%. When the LiDAR data is considered in the classification, the importance score of the Boolean LiDAR metrics reaches up to 1.5 %, improving the accuracy of the RF algorithm more than the rest of variables. This importance score is higher than the annual value because the autumn classification was performed using only 92 variables and the information of the LiDAR metrics has more influence than in the annual analysis.

Considering the user and producer accuracy, the best results were obtained for the scenario with LiDAR data, and showed how, in the case of shrubs, the producer accuracy was over 80% in the best seasonal analysis, similar to the results obtained by Zhao et al. (2016). These understory producer accuracies were even higher than the values obtained for the overstory. Focusing on the quantity and allocation evaluation, the obtained results, when considering optical data as well as LiDAR variables, are significantly better than the ones obtained by Zhou et al. (2014) and by Gao et al. (2011). On the other hand, Gao et al. (2011) attained an overestimation of temperate forest, but no agreement concerning the over or underestimation was found in dry forest. In our work, an overestimation in understory and an underestimation in herbaceous have been achieved in all classifications, but, similarly, no agreement has been obtained for the overstory (forest classes). In particular, understory and herbaceous classes are both below the limit of the stablished Boolean threshold, so the LiDAR variables, despite having greatly improved the accuracy of the classification, were not so precise.

Therefore, our results support the conclusions of González-Ferreiro et al. (2012), who considered LiDAR data from the National Plan of Aerial Orthophotography of the Spanish National Geographic Institute as a good source of information for forest management. However, even though the updates of the LiDAR data from the PNOA are not as frequent as desired, it is possible to minimize the effects of the time lag in vegetation heights. Even if the evolution of the vegetation could be despised in the period of the time lag between the LiDAR data and the acquisition of the satellite's images, the lack of accurate height information can be neutralized by applying the Boolean LiDAR metric values as proposed in this work. Nevertheless, the main limitation of this method is that these values might only be applied to separate high and low vegetation, and they probably could not be used to estimate accurate values of forest structure or biomass evaluation. Furthermore, with low density LiDAR data, the Boolean LiDAR metrics are useful to avoid the noise of the height in low strata. Thus, the confusion produced by the spectral similarities of the understory and overstory vegetation can be reduced by applying the variables derived from the LiDAR data, which allow for discrimination between the two strata.

Conclusions

In this work, the accuracy enhancement using LiDAR data with Sentinel 2 in multitemporal land cover classification in overstory and understory land cover mapping at the watershed scale was studied. The obtained results showed that the overall accuracies were better with the annual evaluation when only spectral information was used for the classification. Additionally, if LiDAR data were included in the classification (data fusion), the overall accuracies were highly improved, especially in the summer and autumn seasons where those two strata could be more easily differentiated. Thereby, LiDAR data from the National Plan of Aerial Orthophotography of the Spanish National Geographic Institute are a good improvement for data fusion analysis. The proposed methodology based on the use of Boolean LiDAR metrics allows the use of the PNOA LiDAR regardless of the time lag that exists between the LiDAR data and the satellite image acquisition. This improvement can be a significant issue in the analysis of vegetation structure and its spatial distribution as it is decisive for watershed ecosystem management, flood control, and many other purposes like ecosystem monitoring.

In any case, it must be pointed out that all the data have been obtained from open sources and the calculations have been achieved using free software. Therefore, there are no funding limitations to apply this methodology throughout the Spanish national territory or other regions with uniform LiDAR coverage.

References

Adamu B, Tansey K, Ogutu B (2018) Remote sensing for detection and monitoring of vegetation affected by oil spills International Journal of Remote Sensing 39:3628-3645

Ahmed OS, Franklin SE, Wulder MA, White JC (2015) Characterizing stand-level forest canopy cover and height using Landsat time series, samples of airborne LiDAR, and the random forest algorithm ISPRS Journal of Photogrammetry and Remote Sensing 101:89-101

Akike S, Samanta S (2016) Land Use/Land Cover and Forest Canopy Density Monitoring of Wafi-Golpu Project Area, Papua New Guinea Journal of Geoscience and Environment Protection 4:1

Belgiu M, Drăguţ L (2016) Random forest in remote sensing: A review of applications and future directions ISPRS Journal of Photogrammetry and Remote Sensing 114:24-31

Bolton DK, White JC, Wulder MA, Coops NC, Hermosilla T, Yuan X (2018) Updating stand-level forest inventories using airborne laser scanning and Landsat time series data International Journal of Applied Earth Observation and Geoinformation 66:174-183

Bork EW, Su JG (2007) Integrating LIDAR data and multispectral imagery for enhanced classification of rangeland vegetation: A meta analysis Remote Sensing of Environment 111:11-24

Breiman L (2001) Random forests Machine learning 45:5-32

Caballero Díaz J, Pérez F, Manuel A, Quirós Rosado E (2015) A state-and-transition model of Iberian dehesas based on spatial patterns Forest Systems 24 doi:http://dx.doi.org/10.5424/fs/2015242-06408

Congalton RG, Green K (2008) Assessing the accuracy of remotely sensed data: principles and practices. CRC press,

Delegido J, Verrelst J, Alonso L, Moreno J (2011) Evaluation of sentinel-2 red-edge bands for empirical estimation of green LAI and chlorophyll content Sensors 11:7063-7081

Estornell J, Ruiz LA, Velázquez-Martí B (2011) Study of shrub cover and height using LiDAR data in a Mediterranean area Forest Science 57:171-179

Erdody TL, Moskal LM (2010) Fusion of LiDAR and imagery for estimating forest canopy fuels Remote Sensing of Environment 114:725-737

Escadafal R (1993) Remote sensing of soil color: principles and applications Remote Sensing Reviews 7:261-279

Gao Y, Marpu P, Niemeyer I, Runfola DM, Giner NM, Hamill T, Pontius RG (2011) Object-based classification with features extracted by a semi-automatic feature extraction algorithm–SEaTH Geocarto International 26:211-226

García M, Riaño D, Chuvieco E, Danson FM (2010) Estimating biomass carbon stocks for a Mediterranean forest in central Spain using LiDAR height and intensity data Remote Sensing of Environment 114:816-830

García M, Riaño D, Chuvieco E, Salas J, Danson FM (2011) Multispectral and LiDAR data fusion for fuel type mapping using Support Vector Machine and decision rules Remote Sensing of Environment 115:1369-1379

Garcia M, Saatchi S, Ferraz A, Silva CA, Ustin S, Koltunov A, Balzter H (2017) Impact of data model and point density on aboveground forest biomass estimation from airborne LiDAR Carbon balance and management 12:4
Gebhardt S et al. (2014) MAD-MEX: automatic wall-to-wall land cover monitoring for the Mexican REDD-MRV program using all Landsat data Remote Sensing 6:3923-3943
Gitelson AA, Kaufman YJ, Merzlyak MN (1996) Use of a green channel in remote sensing of global vegetation from EOS-MODIS Remote sensing of Environment 58:289-298
Godinho S, Gil A, Guiomar N, Costa MJ, Neves N (2016) Assessing the role of Mediterranean evergreen oaks canopy cover in land surface albedo and temperature using a remote sensing-based approach Applied Geography 74:84-94
Godinho S, Guiomar N, Gil A (2017) Estimating tree canopy cover percentage in a mediterranean silvopastoral systems using Sentinel-2A imagery and the stochastic gradient boosting algorithm International Journal of Remote Sensing:1-23
Gökbulak F, Şengönül K, Serengil Y, Özhan S, Yurtseven İ, Uygur B, Özçelik MS (2016) Effect of forest thinning on water yield in a sub-humid Mediterranean oak-beech mixed forested watershed Water resources management 30:5039-5049
González-Ferreiro E, Diéguez-Aranda U, Miranda D (2012) Estimation of stand variables in Pinus radiata D. Don plantations using different LiDAR pulse densities Forestry 85:281-292
Guyot G, Baret F, Major D (1988) High spectral resolution: Determination of spectral shifts between the red and the near infrared International Archives of Photogrammetry and Remote Sensing 11
Hellesen T, Matikainen L (2013) An object-based approach for mapping shrub and tree cover on grassland habitats by use of LiDAR and CIR orthoimages Remote Sensing 5:558-583
Hill MJ (2013) Vegetation index suites as indicators of vegetation state in grassland and savanna: An analysis with simulated SENTINEL 2 data for a North American transect Remote Sensing of Environment 137:94-111
Huete AR (1988) A soil-adjusted vegetation index (SAVI) Remote Sensing of Environment 25:259-309 doi:10.1016/0034-4257(88)90106-X.
Huete AR, Post DF, Jackson RD (1984) Soil spectral effects on 4-space vegetation discrimination Remote sensing of environment 1984 v.15 no.2:pp. 155-165 doi:10.1016/0034-4257(84)90043-9
Immitzer M, Vuolo F, Atzberger C (2016) First experience with Sentinel-2 data for crop and tree species classifications in central Europe Remote Sensing 8:166
Instituto-Geográfico-Nacional (2017) Centro de Descargas. http://centrodedescargas.cnig.es/CentroDescargas/index.jsp. Accessed octubre 2017
Latifi H, Heurich M, Hartig F, Müller J, Krzystek P, Jehl H, Dech S (2015) Estimating over-and understorey canopy density of temperate mixed stands by airborne LiDAR data Forestry: An International Journal of Forest Research 89:69-81
Li A et al. (2017) Lidar aboveground vegetation biomass estimates in shrublands: Prediction, uncertainties and application to coarser scales Remote Sensing 9:903
López-Díaz M, Rolo V, Benítez R, Moreno G (2015) Shrub encroachment of Iberian dehesas: implications on total forage productivity Agroforestry systems 89:587-598
Ma Q, Su Y, Guo Q (2017) Comparison of Canopy Cover Estimations From Airborne LiDAR, Aerial Imagery, and Satellite Imagery IEEE Journal of Selected Topics in Applied Earth Observations and Remote Sensing 10:4225-4236
MAPAMA (2018) Mapa de Cultivos y Aprovechamientos de España 2000-2010. http://www.mapama.gob.es/es/cartografia-y-sig/publicaciones/agricultura/mac_2000_2009.aspx. Accessed Enero 2018
McGaughey RJ (2009) FUSION/LDV: Software for LIDAR data analysis and visualization US Department of Agriculture, Forest Service, Pacific Northwest Research Station: Seattle, WA, USA 123
Mundt JT, Streutker DR, Glenn NF (2006) Mapping sagebrush distribution using fusion of hyperspectral and lidar classifications Photogrammetric Engineering & Remote Sensing 72:47-54
Mutlu M, Popescu SC, Stripling C, Spencer T (2008) Mapping surface fuel models using lidar and multispectral data fusion for fire behavior Remote Sensing of Environment 112:274-285
NRCS (2009) National Engineering Handbook, section 4, Hydrology, version (1956, 1964, 1971, 1985, 1993, 2004, 2009). National Engineering Handbook. Engineering Division, US. Department of Agriculture, Washington, DC
Nizami SM, Yiping Z, Zheng Z, Zhiyun L, Guoping Y, Liqing S (2017) Evaluation of forest structure, biomass and carbon sequestration in subtropical pristine forests of SW China Environmental Science and Pollution Research 24:8137-8146

Palomo-Campesino S, Ravera F, González JA, García-Llorente M (2018) Exploring Current and Future Situation of Mediterranean Silvopastoral Systems: Case Study in Southern Spain Rangeland Ecology & Management

Pontius RG, Santacruz A (2014) Quantity, exchange, and shift components of difference in a square contingency table International Journal of Remote Sensing 35:7543-7554Qi J, Chehbouni A, Huete A, Kerr Y, Sorooshian S (1994) A modified soil adjusted vegetation index Remote sensing of environment 48:119-126

Qi J, Chehbouni A, Huete A, Kerr Y, Sorooshian S (1994) A modified soil adjusted vegetation index Remote sensing of environment 48:119-126

Riaño D et al. (2007) Estimation of shrub height for fuel-type mapping combining airborne LiDAR and simultaneous color infrared ortho imaging International Journal of Wildland Fire 16:341-348

Richardson AJ, Wiegand C (1977) Distinguishing vegetation from soil background information Photogrammetric engineering and remote sensing 43:1541-1552

Rouse Jr JW, Haas R, Schell J, Deering D (1974) Monitoring vegetation systems in the Great Plains with ERTS

Sánchez Sánchez Y, Martínez-Graña A, Santos Francés F, Mateos Picado M (2018) Mapping Wildfire Ignition Probability Using Sentinel 2 and LiDAR (Jerte Valley, Cáceres, Spain) Sensors 18:826

Schultz M, Clevers JG, Carter S, Verbesselt J, Avitabile V, Quang HV, Herold M (2016) Performance of vegetation indices from Landsat time series in deforestation monitoring International Journal of Applied Earth Observation and Geoinformation 52:318-327

Stojanova D, Panov P, Gjorgjioski V, Kobler A, Džeroski S (2010) Estimating vegetation height and canopy cover from remotely sensed data with machine learning Ecological Informatics 5:256-266

Tuanmu M-N, Viña A, Bearer S, Xu W, Ouyang Z, Zhang H, Liu J (2010) Mapping understory vegetation using phenological characteristics derived from remotely sensed data Remote Sensing of Environment 114:1833-1844

Vanselow KA, Samimi C (2014) Predictive mapping of dwarf shrub vegetation in an arid high mountain ecosystem using remote sensing and random forests Remote Sensing 6:6709-6726

Véga C, Renaud J-P, Durrieu S, Bouvier M (2016) On the interest of penetration depth, canopy area and volume metrics to improve Lidar-based models of forest parameters Remote Sensing of Environment 175:32-42

Zald HS, Wulder MA, White JC, Hilker T, Hermosilla T, Hobart GW, Coops NC (2016) Integrating Landsat pixel composites and change metrics with lidar plots to predictively map forest structure and aboveground biomass in Saskatchewan, Canada Remote Sensing of Environment 176:188-201

Zhao Y et al. (2016) Detailed dynamic land cover mapping of Chile: Accuracy improvement by integrating multi-temporal data Remote sensing of environment 183:170-185

Zhao Y, Hao Y, Zhen Z, Quan Y (2017) A Region-Based Hierarchical Cross-Section Analysis for Individual Tree Crown Delineation Using ALS Data Remote Sensing 9:1084

Zhou P, Huang J, Pontius RG, Hong H (2014) Land classification and change intensity analysis in a coastal watershed of Southeast China Sensors 14:11640-11658

European Commission

Science for Environment Policy

A tool for better forest management: LiDAR data improves accuracy of land-cover maps, Spain

A study of two forest ecosystems in Spain has found that land-cover maps of watersheds, ecosystems hosting key interactions between vegetation, wildlife, and water, are made more accurate by the inclusion of LiDAR data — a type of remote sensing that pulses laser light at a target to measure vertical distances for use in 3D-mapping an environment. This has important implications for ecosystem monitoring, flood mitigation, and forest management, fields in which accurately characterising an environment is key.

Watersheds are ecosystems with important hydrological, ecological, and environmental functions. They provide habitat for vegetation and wildlife that interact with the physical or biological characteristics of the water, and facilitate the flow of water throughout a natural environment. Forest ecosystems are important watersheds; tree canopies can decrease the quantity of rainfall falling upon the soil surface, and intercept and reduce run-off. These interactions depend heavily on the intensity and amount of rainfall, tree density and type, and the vertical structure of the forest.

Characterising and managing such watersheds is important in fields such as flood management and ecosystem monitoring; this is increasingly done by creating high-accuracy land-cover maps of forest watersheds, using remote sensing techniques, but it can be difficult to distinguish between different kinds of forest vegetation — namely 'overstory' (larger-scale trees and canopy cover) and 'understory' (plant life located beneath the canopy) — using this method.

This study explored two neighbouring Mediterranean forest watersheds in the Badajoz province of Spain: San Juan and Palomillas. The two watersheds span 146 and 194 square kilometres respectively, and mainly comprise a mix of perennial forest with residual conifers (at the overstory), and shrubs and herbaceous plants (at the understory). The researchers aimed to analyse how the accuracy of watershed-scale mapping of understory and overstory vegetation improved when using different combinations of seasonal and annual images from the Sentinel-2 satellites, soil and vegetation indices, and LiDAR (Light Detection and Ranging) data.

Using several soil-vegetation variations, the researchers first explored the accuracy of their mapping for each season, and then annually, before including LiDAR data in each scenario.

The results showed that, overall, annual mapping based on imagery was more accurate than seasonal mapping (with overall accuracies of 73% and 71%, respectively), and that the accuracy of both was highly improved by including LiDAR data, which allowed models to better discriminate between under- and overstory strata. The best results were obtained for summer and autumn, which hit accuracies of 83% when including LiDAR data. Autumn mapping was the most accurate overall; the researchers suggest that this may be due to the seasonal variability of the vegetation within the watershed at that time of year, which is more easily distinguishable spectrally.

These results suggest that data analysis and mapping for watersheds could benefit from the large-scale inclusion of LiDAR data. Improving the accuracy of forest ecosystem maps is crucial in understanding the structure and spatial distribution of vegetation, say the researchers, and is thus a central factor in successful and optimal ecosystem management.

08 August 2019
Issue 529
Subscribe to free weekly News Alert

Source: Fragoso-Campón, L., Quiros, E., Mora, J., Gutierrez Gallego, J. A., and Duran-Barroso, P. (2019) Overstory-understory land cover mapping at the watershed scale: accuracy enhancement by multitemporal remote sensing analysis and LiDAR. *Environmental Science and Pollution Research.* https://doi.org/10.1007/s11356-019-04520-8

Contact:
laurafragoso@unex.es

Read more about:
Forests, Flooding, Environmental information services

3.3. Publicación N.º 3

Publicación	**Dehesa environment mapping with transference of a Random Forest classifier to neighboring ultra-high spatial resolution imagery at class and macro-class land cover levels**				
Autores	**Fragoso-Campón, Laura** · Quirós, Elia · Gutiérrez Gallego, José Antonio				
Revista	Stochastic Environmental Research and Risk Assessment (2020) 34:2179–2210				
eISSN	1436-3259				
DOI	10.1007/s00477-020-01880-3				
Fuente de Impacto	Índice 5 años	Índice 2019	Categoría	Rank	Cuartil
WOS (JCR)	2.721	2.351	Statistics and Probability	21/124	Q1
			Water Science and Technology	37/94	Q2
			Civil Engineering	45/134	Q2
Aportación de la doctoranda:	Conceptualización, metodología, programas informáticos, análisis formal, investigación, redacción-borrador original, redacción-revisión y edición de la versión final.				

Stochastic Environmental Research and Risk Assessment (2020) 34:2179–2210
https://doi.org/10.1007/s00477-020-01880-3

ORIGINAL PAPER

Dehesa environment mapping with transference of a Random Forest classifier to neighboring ultra-high spatial resolution imagery at class and macro-class land cover levels

Laura Fragoso-Campón[1] · Elia Quirós[1] · José Antonio Gutiérrez Gallego[1]

Accepted: 19 September 2020 / Published online: 6 October 2020

Abstract

Accurate vegetation cover maps of forested areas are crucial for ecosystems monitoring, as well as for management of water balance, flood and fire risk, and other forest-associated resources. With this regard, remote sensing techniques have been used for land cover mapping worldwide. Here, we propose a vegetation-mapping methodology in a *dehesa* environment using ultra-high spatial resolution imagery (UHSR) with a spatial resolution of 0.25 m and four bands in the visible and near-infrared spectrum. Land cover categories were defined by their runoff generation capability and considered two levels of disaggregation: among species (macro-class level) and within species (class level). Additionally, we developed a method to reduce field campaigns and manual work by transferring random forest classifiers trained with a group of images (training group) to neighboring images (validation group). The training group was remarkably accurate, achieving an overall accuracy of 91.6% (k = 0.89) at the class level and 95.8% (k = 0.94) at the macro-class level. The results for the validation group were also very high, with an overall accuracy of 78.3% (k = 0.74) at the class level and 86.3% (k = 0.82) at the macro-class level. Moreover, we found that the blue band, soil color index, and texture features have a great influence on species discrimination, especially within shrub species in *dehesa* environments. Notably, having accurate land cover maps is crucial, given that the use of a global database led to underestimating the potential runoff in the most representative land cover in the *dehesa* environment. Future research will focus on the automatic generation of new samples extracted from the classified UHSR images, which could be used as training datasets for the supervised classification of other high spatial resolution images (e.g., Sentinel imagery) for regional-scale hydrological models.

Keywords Jeffries–Matusita distance · National Plan of Aerial Orthophotography (PNOA) · Run off · Shrub · Training-data · Tree grass ecosystem

1 Introduction

Accurate vegetation maps of forested areas are widely known to be crucial for forest management. Notably, vegetation cover has a great influence on biodiversity and ecosystem monitoring (Fang et al. 2018), water balance models (Becker et al. 2019; Dias et al. 2015; Dionizio and Costa 2019; Lima de Almeida et al. 2019), hydrological modeling and flood management (Chen et al. 2019a; Chymyrov et al. 2018; Dou et al. 2018; Fragoso-Campón et al. 2019; Melesse and Shih 2002; Niu and Sivakumar 2014; Van der Sande et al. 2003), soil erosion (Eroğlu et al. 2010), fuel type (García et al. 2011; Lasaponara and Lanorte 2007a; Riaño et al. 2007), and associated forest resources and biomass inventories (Castillo et al. 2017; Fassnacht et al. 2017; Garcia et al. 2017; Hawryło and

Electronic supplementary material The online version of this article (https://doi.org/10.1007/s00477-020-01880-3) contains supplementary material, which is available to authorized users.

✉ Laura Fragoso-Campón
laurafragoso@unex.es

Elia Quirós
equiros@unex.es

José Antonio Gutiérrez Gallego
jagutier@unex.es

[1] Department of Graphic Expression, Universidad de Extremadura, Escuela Politécnica, Avda. Universidad s/n, 10003 Cáceres, Spain

Dehesa environment mapping with transference of a Random Forest classifier to neighboring ultra-high spatial resolution imagery at class and macro-class land cover levels

Laura Fragoso-Campón [a,*], Elia Quirós [a], José Antonio Gutiérrez Gallego [a]

[a] Department of Graphic Expression, Universidad de Extremadura, Escuela Politécnica, Avda. Universidad s/n, 10003 Cáceres, Spain

laurafragoso@unex.es (orcid ID: 0000-0003-0397-6247), equiros@unex.es (orcid ID: 0000-0002-8429-045X), jagutier@unex.es (orcid ID: 0000-0002-2375-7087)

*Corresponding author: laurafragoso@unex.es

Abstract

Accurate vegetation cover maps of forested areas are crucial for ecosystems monitoring, as well as for management of water balance, flood and fire risk, and other forest-associated resources. With this regard, remote sensing techniques have been used for land cover mapping worldwide. Here, we propose a vegetation-mapping methodology in a *dehesa* environment using ultra-high spatial resolution imagery (UHSR) with a spatial resolution of 0.25 m and four bands in the visible and near-infrared (NIR) spectrum. Land cover categories were defined by their runoff generation capability and considered two levels of disaggregation: among species (macro-class level) and within species (class level). Additionally, we developed a method to reduce field campaigns and manual work by transferring random forest classifiers trained with a group of images (training group) to neighboring images (validation group). The training group was remarkably accurate, achieving an overall accuracy of 91.6% (k=0.89) at the class level and 95.8% (k=0.94) at the macro-class level. The results for the validation group were also very high, with an overall accuracy of 78.3% (k=0.74) at the class level and 86.3% (k=0.82) at the macro-class level. Moreover, we found that the blue band, soil color index, and texture features have a great influence on species discrimination, especially within shrub species in *dehesa* environments. Notably, having accurate land cover maps is crucial, given that the use of a global database led to underestimating the potential runoff in the most representative land cover in the *dehesa* environment. Future research will focus on the automatic generation of new samples extracted from the classified UHSR images, which could be used as training datasets for the supervised classification of other high spatial resolution images (e.g., Sentinel imagery) for regional-scale hydrological models.

Keywords: Jeffries–Matusita distance, National Plan of Aerial Orthophotography (PNOA), run off, shrub, training-data, tree grass ecosystem.

Declarations:

- **Funding:** This research was funded by the Junta de Extremadura and the European Social Fund: A way of doing Europe, through the "Financing of Predoctoral Contracts for the Training of Doctors in Public Research and Development Centers belonging to the Extremadura System of Science, Technology, and Innovation [file PD16018]." This work was also supported by the Government of Extremadura (Spain) and co-funded by the European Regional Development

Foundation under Grants GR18052 (DESOSTE) and GR18028 (KRAKEN). We thank the Junta de Extremadura (CICTEX) for providing the necessary high-resolution PNOA ortophotographs (PNOA 2007-CC-BY 4.0 scne.es).

- **Conflicts of interest/Competing interests:** The authors declare that they have no known competing financial interests or personal relationships that could have influenced the work reported in this paper.
- **Availability of data and material:** Not applicable.
- **Code availability:** Not applicable.
- **Authors' contributions: Laura Fragoso-Campón:** Conceptualization, Methodology, Software, Formal analysis, Investigation, Writing - Original Draft, Writing - Review & Editing. **Elia Quirós:** Conceptualization, Methodology, Resources, Writing - Original Draft, Writing - Review & Editing, Supervision. **José Antonio Gutiérrez Gallego:** Resources, Writing - Review & Editing.

1 Introduction

Accurate vegetation maps of forested areas are widely known to be crucial for forest management. Notably, vegetation cover has a great influence on biodiversity and ecosystem monitoring (Fang et al. 2018), water balance models (Becker et al. 2019; Dias et al. 2015; Dionizio and Costa 2019; Lima de Almeida et al. 2019), hydrological modeling and flood management (Chen et al. 2019a; Chymyrov et al. 2018; Dou et al. 2018; Fragoso-Campón et al. 2019; Melesse and Shih 2002; Niu and Sivakumar 2014; Van der Sande et al. 2003), soil erosion (Eroğlu et al. 2010), fuel type (García et al. 2011; Lasaponara and Lanorte 2007a; Riaño et al. 2007), and associated forest resources and biomass inventories (Castillo et al. 2017; Fassnacht et al. 2017; Garcia et al. 2017; Hawryło and Wężyk 2018; Li et al. 2017; Nizami et al. 2017; Rodriguez-Veiga et al. 2017).

Remote sensing techniques have been used to map land cover and land use worldwide. Many studies have addressed land cover from a general standpoint (Ahmed et al. 2015; Akike and Samanta 2016; Bolton et al. 2018; Qi et al. 2014; Zhao et al. 2016; Zhou et al. 2014) and others have focused on the study of a specific vegetation stratum. In the later studies, vegetation is typically divided into two strata: the overstory and the understory strata. The overstory is the highest vegetation level, which corresponds to the tree canopies. Many studies have focused on this stratum, particularly by characterizing forest structure, tree cover density, or tree species (Dalponte et al. 2012; Dalponte et al. 2014; Ferreira et al. 2016; Ghosh et al. 2014; Kim et al. 2011). The understory is the lowest level and includes shrubs and pasture. However, although this stratum plays a key role in forest ecosystems (Tuanmu et al. 2010), there are far fewer studies focusing on the understory than those addressing the overstory. Nonetheless, some works such as those by Magiera et al. (2016), Stavrakoudis et al. (2014), and van Lier et al. (2009) have focused on the mapping of understory habitats from remote sensing data. Additionally, several studies have focused on the detection of invasive shrubs (Malahlela et al. 2015; Müllerová et al. 2013; Niphadkar et al. 2017) and others have analyzed the relationship between low strata and the overstory, as well as the influence of shrubs on the reflectance of higher-level canopies (Eriksson et al. 2006; Landry et al. 2018; Tuanmu et al. 2010).

As shown in Fassnacht et al. (2016), the different remote sensing techniques used in vegetation cover analyses utilize either passive (multispectral or hyperspectral images) or active (SAR and LiDAR data)

optical data, or a combination of both. However, our study focused on passive optical data-based analyses, which require the spectral and spatial resolutions[1] to be considered in order to render accurate maps. In the case of passive remote sensing, whether its main sources are satellites or aerial platforms, the spectral resolution decreases when the spatial resolution increases (Dalponte et al. 2009). The spectral resolution in these types of sensors ranges from the visible (VIS), near-infrared (NIR), and shortwave-infrared (SWIR) of the electromagnetic spectrum. On the other hand, the spatial resolution ranges from coarse with a pixel size of more than 250 m (CSR), medium with a pixel size of 30 m (MSR), high with a pixel size of 10 m (HSR), very-high with a pixel size ranging from 1 m to 5 m (VHRS), and ultra-high with a pixel size of 1 m or less (UHSR).

Therefore, multispectral sensors can be classified into three groups depending on pixel size. The first group consists of MSR- or HSR-resolution approaches such as of Landsat-8, SPOT, and Sentinel-2 satellite imagery. The second group is comprised of high-resolution technologies such as GeoEye, Pleiades, IKONO, QuickBird, RapidEye, and WorldView, all of which achieve a VHSR resolution. See Table 1 for more details.

Table 1 Main characteristics of multispectral sensors.

Group[1]	Satellite[2]	Spatial Resolution	Number of Bands	Spectral bands[3]	Spectral range	Available[4]
MSR	Landsat-8	30 m	9	VIS-NIR-SWIR	15 nm to 180 nm	-
HSR	SPOT	10 m	5	VIS-NIR	70 nm to 170 nm.	-
	Sentinel-2	10 m	12	VIS-NIR-SWIR	15 nm to 180 nm	-
VHSR	GeoEye	2 m (PA 0.5 m)	5	PA-VIS-NIR	35 nm to 140 nm	€
	IKONO	4 m (PA 1 m)	5	PA-VIS-NIR	66 nm to 96 nm	€
	QuickBird	2.5-2.9 m (PA 0.6-0.9 m)	5	PA-VIS-NIR	60 nm to 140 nm	€
	RapidEye	6.5 m	5	VIS-RE-NIR	55 nm to 90 nm	€
	WorldView	2 m (PA 0.5 m)	8	VIS-RE-NIR1-NIR2	40 nm to 180 nm	€

[1]MSR: Medium Spatial Resolution, HSR: High Spatial Resolution, VHSR: Very-High Spatial Resolution
[2]Satellite Data from Labrador García et al. (2012)
[3]PA: Panchromatic
VIS: Red-Blue-Green
RE: Red Edge
NIR: Near-Infrared
SWIR: Shortwave-infrared
[4](-) available for free; (€) available under request and fee payment

UHSR-resolution approaches typically involve aerial imagery with a spatial resolution of <1 m, ranging from 0.25 to 0.50 m, such as those implemented by the National Plan of Aerial Orthophotography (PNOA) in Spain. The PNOA imagery provides a continuous coverage throughout the Spanish territory, with a spectral resolution of 4 bands including the VIS and NIR with an update period of 2 or 3 years, depending on the area.

[1] Please note that temporal resolution was not analyzed in this work.

The selection of a particular remote sensing sensor depends on the aim of the study. For instance, Landsat imagery is commonly used to map land cover from a general standpoint and when a long time series is needed, given that this technology possesses the longest time series capacity available (Ahmed et al. 2015; Bolton et al. 2018; Zhao et al. 2016; Zhou et al. 2014). In recent years, Sentinel-2 imagery has been proven as a viable alternative to Landsat, and many studies have adopted said technology for land cover mapping in forested areas (Fragoso-Campón et al. 2019; Godinho et al. 2017; Immitzer et al. 2016; Mura et al. 2018; Nomura and Mitchard 2018).

Additionally, spatial resolution plays a key role in heterogeneous landscapes due to the confusion between discrete and continuous cover types (Adam et al. 2014). In this regard, as mentioned by Ferreira et al. (2016), the differences in the spectral variability within species are significantly lower than the spectral variability among species. The potential of VHSR imagery has been demonstrated in vegetation species mapping in several ecosystems. For instance, heterogeneous coastal landscapes have been assessed with RapidEye (Adam et al. 2014), tree species discrimination with GeoEye, Pleiades, and WorldView2 (Fang et al. 2018), other applications with IKONOS (Kim et al. 2011), tree species crown mapping in African savannas with QuickBird (Boggs 2010), or a combination between VHSR and hyperspectral or LiDAR in the Southern Alps (Dalponte et al. 2012), Boreal forests (Dalponte et al. 2014), and tropical seasonal semi-deciduous forests (Ferreira et al. 2016). Regarding the study of the understory vegetation with VHSR, RapidEye was used to analyze the reflectance signatures of shrub species in the Caucasus (Magiera et al. 2016), whereas QuickBird and an EO-1 Hyperion (Stavrakoudis et al. 2014) or IKONOS were used in the study of ericaceous shrubs (van Lier et al. 2009). Fewer studies have employed UHSR imagery for vegetation mapping. One example is a study by Müllerová et al. (2013), which focused on the detection of an invasive species in the Czech Republic using RapidEye technology and a historical UHSR series. One more example, is the study by Wang et al. (2019) which used UHSR images to classify woody and herbaceous vegetation in a dryland ecosystem in China. Another study estimated tree crown delineation and tree cover from UHSR imagery obtained from the PNOA (Borlaf-Mena et al. 2019; Cantero Fauquier et al. 2017). Moreover, some studies (e.g., Riaño et al. (2007)) have used UHSR images to study the fuel-type map of a predominantly shrub-land area in central Portugal in conjunction with LiDAR data. Table 2 summarizes the main characteristics of these previous studies.

As previously mentioned, although these techniques have been proven to be effective in mapping vegetation species throughout various ecosystems, only a few studies have focused on *dehesa* landscapes. The *dehesa* is a Mediterranean agro-silvo-pastoral system that covers more than 3 million hectares in the Iberian Peninsula (Caballero Díaz et al. 2015; Diaz et al. 1997). There are many ways to define the *dehesa*. From an economic standpoint, Olea and San Miguel-Ayanz (2006) described it as "*an agrosilvopastoral system developed on poor or non-agricultural land and aimed at extensive livestock raising.*" Diaz et al. (1997) proposed another definition based on a landscape standpoint: "*Dehesas are pasturelands populated by holm (Quercus ilex) and/or cork (Quercus suber) oaks, with an understory of open grassland, cereal crops, or Mediterranean scrub."* As described by Olea et al. (2005), the *dehesa* is located in the southern region of the Iberian Peninsula, both in Spain and Portugal, where it is locally referred to as "*montado*," mainly in *Extremadura* (Spain), *Alentejo* (Portugal), and *Andalucía* (Spain), with extensions of approximately 12500, 8000, and 7000 km², respectively. The *dehesa* not only plays a key role in the rural economy, as they are a

source of cork, acorns, natural pastures, aromatic and medicinal plants, honey, and mushrooms (Canteiro et al. 2011), but also in preserving the ecosystem biodiversity, as they are the main feeding areas of a large number of endangered bird species, and also host a large number of wintering birds from northern Europe (Diaz et al. 1997).

In the *dehesa* environment, the spatial distribution of the vegetation cover plays a crucial role in the productivity of pastures and tree growth, and therefore many studies have focused on the relationship between them. However, characterizing the positive or negative relationship between understory and overstory species remains a challenge because different studies often reach conflicting conclusions. For example, Rivest et al. (2011) analyzed the effect of shrub encroachment on pasture yield, holm oak *(Quercus ilex)* growth, and acorn production, and concluded that encroachment affected pasture and tree production in Mediterranean *dehesa*s in a species- and climate-dependent manner. Other authors have analyzed how shrubs benefit tree recruitment. In this sense, Pulido et al. (2010) concluded that shrubs protect acorns and provide shadow, thereby allowing for better seedling establishment. An alternative point of view is the relationship between soil organic matter (i.e., a universal soil quality and land degradation indicator) and vegetation cover, studied by Pulido-Fernández et al. (2013). This study demonstrated that soil organic carbon stocks were closely related to the tree density and shrub cover, although further analysis is required. In another study, Santos-Silva et al. (2011) demonstrated that the tree canopy cover factor in *montados* was highly related with the macrofungal richness and sporocarp production, which highlighted the need for new management strategies to preserve *montados* with a canopy cover of 30–50%. Godinho et al. (2016b) investigated the influence of the environment, land management, and spatial factors on recent *montado* changes in Portugal, their results indicated that most of the variance in the large-scale distribution of recent *montado* loss was due to land management practices associated with grazing intensity and type, as well as shrub control techniques. Lastly, Godinho et al. (2016a) found that there was a significant statistical relationship between tree canopy cover factors in *montado* ecosystems and land surface albedo and temperature, and discussed how these two biogeophysical parameters are related with climate change, specifically in increasingly arid ecosystems. In this sense, the water balance is also related to the vegetation cover and affects several factors such as evapotranspiration, runoff, interflow, and infiltration (Becker et al. 2019; Dias et al. 2015; Dionizio and Costa 2019). Current approaches in hydrological calibration are based on spatially distributed models that require remote sensing data as input (Athira et al. 2016; Becker et al. 2019; Chen et al. 2019b). Therefore, it is necessary to know the spatial distribution of several parameters such as topography, soil and land cover characteristics, and meteorological details. Thus, knowing the spatial distribution of vegetation cover is essential to assess complex hydrological models, given that the vegetation cover factor reduces runoff and enhances infiltration, thereby increasing groundwater recharge (Netzer et al. 2019).

Despite the importance of having maps that accurately characterize the vegetation of the *dehesa*s ecosystem for hydrological modeling, water balance models, and management strategies of the regions in question, only a few studies have examined the *dehesa* vegetation using remote sensing techniques. Among these studies, we found a few that used MSR images such as Landsat (Carreiras et al. 2006; Godinho et al. 2016a) and HSR images of Sentinel imagery (Fragoso-Campón et al. 2019; Godinho et al. 2017). Moreover, hardly any researchers have used VHSR or UHSR in *dehesa*s ecosystems, most of which have focused on the

overstory stratum. For instance, Castillejo-González et al. (2010) applied QuickBird VHR images to obtain the tree canopy cover factor in a *dehesa* environment. Moreover, Cantero Fauquier et al. (2017) and Borlaf-Mena et al. (2019) mapped the tree crown shape of a *dehesa* environment using a segmentation approach with PNOA UHSR images, covering only three spectral bands (RBG) coupled with LiDAR data. Similarly, Lavado Contador et al. (2012) analyzed the temporal dynamics of the tree canopy cover factor in a *dehesa* ecosystem using PNOA UHSR images, also only covering three spectral bands (RBG). From a water balance standpoint, few studies have focused on the hydrological processes of *dehesa* environments. These studies include some of the earliest reports (Ceballos and Schnabel 1998; Cerda et al. 1998; Joffre and Rambal 1993), as well as more recent studies focused on soil water balance based on MODIS NDVI products (Campos et al. 2016; Campos et al. 2013). However, further research is needed to characterize hydrological processes in *dehesa* environments via spatially distributed models, where access to accurate vegetation spatial patterns is mandatory. Hence, this study attempted to go further by applying the current remote sensing techniques to render high accurate *ad hoc* land cover maps. Notably, the categories should be related to the potential runoff generation capability. Thus, it is applicable to hydrological modeling and, the precision is improved if compared to other global land cover database.

Therefore, our study sought to develop a methodology to characterize vegetation in a *dehesa* environment using PNOA UHSR imagery for future use in hydrological modeling. The specific goals of this study were: i) to obtain customized high-resolution maps of the vegetation in both the overstory and understory strata; ii) to develop a method to reduce field campaigns by transferring the information of the training dataset to different images for which ground data extraction was not necessarily performed; iii) to identify vegetation types based on ecosystem management approaches and runoff generation capability; iv) to evaluate the influence of the spatial resolution of land cover maps on potential runoff estimation in a *dehesa* environment.

Table 2 Overview of studies using Very High Spatial Resolution images for land cover mapping.

Study	Overstory/ Understory	Satellite/Sensor	Spectral Resolution	Spatial Resolution	Classification Algorithm	Predictors	Pixel/Object based	Accuracy assessment	Overall Accuracy
Adam et al. (2014)	O/U* *(not shrub)	Multispectral (RapidEye imagery)	5 bands (440–850 nm)	5 m	SVM, RF	Spectral Bands	Pixel	Error Matrix and McNemar's test	93.07% (RF); 91.80 % (SVM); Z= 1.96
Boggs, 2010	O	SPOT-5 and QuickBird	SPOT-5 (G-R-NIR) QuickBird (VNIR)	10 m (SPOT-5) and 0.6 m (QuickBird pan-sharpened)	Pixel threshold NDVI value and OBIA techniques	Spectral bands, VI and texture (OBIA)	Object	Error Matrix	85–97% (QuickBird); 53–81% (SPOT-5)
Eroğlu et al. (2010)	O/U	IKONOS	4 bands (VNIR)	4 bands (4 m) and 1 panchromatic band (1 m)	Parallelepiped non-parametric rule	Spectral Bands	Pixel	Error Matrix	82.5%
Burnett et al. (2019)	O/U	WorldView2	WorldView2 (VNIR+Y+RE+NIR 2)	2 m and 0.5 m (pan-sharpened)	RF	Spectral bands and texture features	Pixel	Error Matrix	97%
Dalponte et al. (2012)	O	VHR multispectral (GeoEye-1 satellite); VHR hyperspectral images (AISA Eagle sensor); LiDAR data	H: 126 bands (402.9–989.1 nm); M: 4 bands (450–920 nm) and panchromatic; LiDAR HR 8.6 points per m² LR 0.48 points per m²)	All datasets: 1 m	SVM, RF	Spectral Bands, LiDAR metrics	Pixel	Error Matrix	H+LiDAR: 74.1–83% (SVM); 70.8–80% (RF) M+LiDAR: 64.8–75.3% (SVM); 63.1–70.6% (RF)
Dalponte et al. (2014)	O	Hyperspectral (aerial) and LiDAR	160 bands (410–990 nm) LiDAR 7.4 echoes per m²	0.40 m	SVM	Spectral bands	Pixel	K-fold cross validation	85.4–93.5 %
Fang et al. (2018)	O	GeoEye, Pleiades, and WorldView2	GeoEye (VNIR), Pleiades (VNIR) and WorldView2 (VNIR+Y+RE+NIR 2) LiDAR 6.6 points per m²	2 m multispectral (MS) bands, as well as an approximately 0.5 m panchromatic band; LiDAR 0.5 m	RF	Spectral bands, vegetation indices, and Texture	Object	Error Matrix	62%
Ferreira et al. (2016)	O	Hyperspectral (aerial) and multispectral (Wordview-3)	260 bands (VNIR 450–970 nm; SWIR 970–2400 nm)	1.0 m H - 5.0 WV3	Lda, RBF-SVM, RF	Spectral bands, vegetation indices	Pixel	Error Matrix	70 % (VNIR); 75 % (VNIR+VI); 84% (VNIR-SWIR); 57.4% (WV-3 VNIR); 74.8% (WV-3 VNIR+SWIR)
Ghosh et al. (2014)	O	Hyperspectral: Two airborne (HyMAP) and one space-borne	Hympa 125 bands (450–2480 nm); Hyperion 146 bands (400–2500 nm);	4 m, 8 m, and 30 m	SVM, RF	Spectral bands, Minimum Noise Fraction, vegetation	Pixel	Error Matrix and McNemar's test	70–85%

Study	Overstory/ Understory	Satellite/Sensor	Spectral Resolution	Spatial Resolution	Classification Algorithm	Predictors	Pixel/Object based	Accuracy assessment	Overall Accuracy
		(Hyperion) and LiDAR	LiDAR 12 points per m²			indices (86 hympa and 84 hyperion)			
Kim et al. (2011)	O	IKONOS	4 bands (VNIR)	4 bands (4 m) and 1 panchromatic band (1 m)	MLC	Spectral Bands	Pixel & Object	Error Matrix	63.9% (PBC); 76.8% (SBC)
Magiera et al. (2016)	U	RapidEye & simulated satellite bands (IKONOS, Quickbird2, World-View2)	4 bands (VNIR)	RapidEye (5 x 5 m)	-	Spectral Bands	-	The Jeffries-Matusita distance (JMD) as a separation measure	-
Malahlela et al. (2015)	U	WorldView2	WorldView2 (VNIR+Y+RE+NIR 2)	2 m	Logistic regression	Spectral bands, vegetation indices and geographical data (DEM, Aspect)	Pixel	Error Matrix and ROC (AUC)	87%
Müllerová et al. (2013)	U	Aerial photographs, multispectral and RapidEye	Aerial (Panchromatic); Multispectral & RapidEye (VNIR)	0.5 (Aerial, multispectral); 2 m (RapidEye)	MLH (pixel) and C (Object-based)	Spectral bands and texture (OBIA)	Pixel Vs Object	Error Matrix	In terms of user's accuracy (UA), producer's accuracy (PA), quantity disagreement (QD), and allocation disagreement (AD)
Niphadkar et al. (2017)	U	GeoEye and WorldView2	GeoEye (VNIR) and WorldView2 (VNIR+Y+RE+NIR 2)	2 m	MLH (pixel) and NNC (Object based)	Spectral bands and vegetation indices	Pixel Vs Object	Error Matrix	60%
Stavrakoudis et al. (2014)	O/U	QuickBird and an EO-1 Hyperion	QuickBird (VNIR); 155 bands Hyperion (VNIR+SWIR)	QuickBird (2.4 m); Hyperion (30 m)	SVM	Spectral bands	Pixel	Error Matrix	67.58% (QuickBird); 77.21% (Fusion)
van Lier et al. (2009)	U	IKONOS and Landsat_TM	4 bands (VNIR)	3 m (IKONOS) 30 m (Landsat)	NNC	Spectral bands and vegetation indices (NDVI and TCC)	Object	Error Matrix	70–80% (VHR); 71–78% (Landsat)
Wang et al. (2019)	O/U	Aerial photograph	3 bands (RGB)	0.10 m	CART SMV RF GBDT	Spectral bands and derived color space	Pixel	Error Matrix	77.7% (CART) 76.9% (SMV) 78.1% (RF) 80.2% (GBDT)

[1]VIS: Red (G) -Blue (B) -Green (G)
RE: Red Edge
NIR: Near-Infrared
VNIR: Red-Blue-Green-Near-Infrared
SWIR: Shortwave-infrared

[2] If multiple algorithms were used, the best was underlined.

CART Classification and Regression Tree
C Combination of automated hierarchical, iterative, and ruled-based classification
GBDT Gradient Boosting Decision Tree
Lda Linear Discriminant Analysis
MLH Maximum Likelihood Classifier
NNC Nearest Neighbor Classification
RBF-SVM Support Vector Machine - Radial Basis Function
RF Random Forest
SVM Support Vector Machine

2 Materials

2.1 Study area

The study area corresponds to a *dehesa* environment in the Extremadura region in Spain. The area limits correspond with the two neighboring watersheds of the *Tamuja* and *Aljucén* rivers, which are approximately 458 and 253 km² respectively, and extends between latitudes 39°00'–39°30' N and longitudes of 6°21'–5°54' W (Fig. 1). Based on the Worldwide Bioclimatic Classification System (Rivas-Martinez and Rivas-Saenz 1996-2019), the area corresponds to the Mediterranean West Iberian biogeographic region (15a: Luso-Extremaduran), the Mediterranean pluviseasonal continental variant, and the mesomediterranean thermoclimatic belt. The overstory vegetation is mainly comprised of holm oaks (*Quercus rotundifolia*), although sparse areas of cork oaks (*Quercus suber*) and pyrenean oaks (*Quercus pyrenaica*) can also be found. The understory is more diverse and several evergreen shrub species are distributed in the study area. The main species in the *dehesa*s ecosystem are *Cistus ladanifer*, *Retama sphaerocarpa, Lavandula stoechas, Thymus mastichina, Genista hirsute, Phillyrea angustifolia, Erica arborea*, *and Erica australis* (Devesa Alcaraz 1995). The herbaceous vegetation is predominantly acidophilus pasture, which is characteristically ephemeral and with low coverage and spring phenology, followed lastly by dry agricultural areas (i.e., small grain, meadow, or forage lands for grazing). Finally, other non-vegetation land covers such as rocky outcrops, small cattle ponds, and impervious surfaces (e.g., roads or roofs of rural houses) are also present in the study area, albeit with a much lower occurrence.

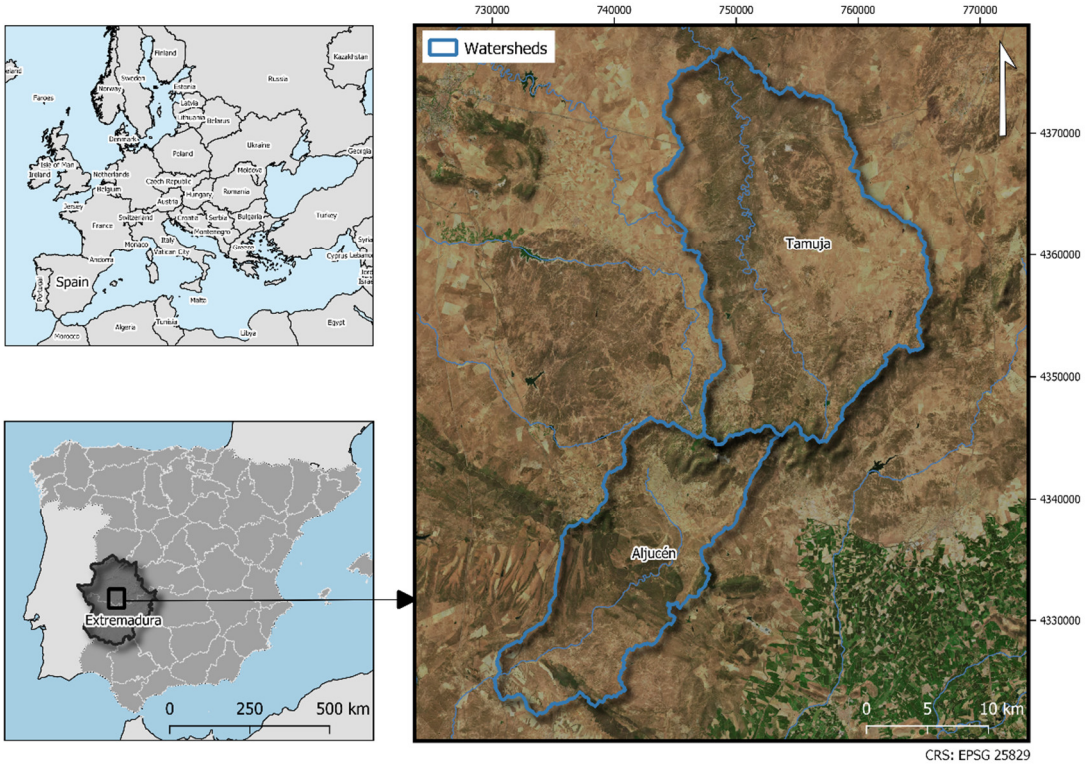

Fig. 1 Study area.

2.2 Imagery dataset

The UHSR imagery used in this study was obtained from the PNOA (Ministerio de Fomento 2019). As previously mentioned, the PNOA imagery has the great advantage of providing continuous coverage throughout the Spanish territory. The images analyzed in this study were taken with a 4-band multispectral sensor (visible and NIR) at a 0.25-m spatial resolution in June of 2016. The images are typically used as a cartographic background in numerous fields, including civil and forestry engineering, and as a basis for the photointerpretation of different surface elements (primarily in the combination of RGB bands) and to update the Spanish Land Occupation Information System (SIOSE) (Vila-García et al. 2015). Hernández-López et al. (2013) discussed the importance of the spectral information provided by PNOA images for applications related to the extraction of physical parameters, the evolution of forest cover, and agronomic analysis of plant species. However, few studies have taken advantage of the spectral information of the bands beyond their use as a cartographic background. Otherwise, only the visible spectrum (RGB) is typically used (Borlaf-Mena et al. 2019; Lavado Contador et al. 2012). This is probably due to the fact that RGB information can be downloaded for free from the National Geographic Institute's Download Center (IGN), whereas the NIR data is only available upon request.

In the study area, a total of twenty-five images were selected for the analysis, which represent the entire variability of the *dehesa* environment (Fig. 3). The pre-processing of the PNOA images is described in the metadata of the imagery and includes the following steps: mosaic making, radiometric correction, enhancement, and cutting of images with coating. The images are supplied in a 1:5000 tile and two products are available in parallel: one was made in the visible spectrum (RGB) and another in false infrared color (NIR-R-G), in this case, the metadata indicated that the infrared layer was not radiometrically corrected.

2.3 Field data

The field data in the *Tamuja* and *Aljucén* watersheds were randomly selected by visual interpretation of the UHSR images representing the wide range of cover types in the *dehesa*. As reported by Ferreira et al. (2016), only areas that were clearly distinguished by visual interpretation were drawn, thus ensuring the spectral responses of all the species considered in the analysis. Moreover, a field campaign was designed for the identification of ambiguous cases as proposed in Mas et al. (2010). As a result, the field dataset covered approximately 1.8 million pixels (Fig. 2). Thus, the land cover classes in the *dehesa* environment were grouped into two levels of disaggregation, as shown in Table 3 . On the one hand, the class-level, in which different classes within the species were defined, focused on the discrimination of understory strata. On the other hand, the different species in the *dehesa* environment were grouped in the macro-class level. This classification also fits a similar hydrologic response following the criteria of the National Engineering Handbook (NRCS 2009), and thus the different classes and macro-classes considered herein can be grouped according to their runoff generation capacity (Table 3).

Table 3 Land cover types analyzed.

Stratum	Land cover type	Class-level categories	Runoff generation	Macro-class-level categories
Overstory	Holm Oaks (*Quercus rotundifolia)*	Qc		Quercus (Qc)
	Cork oaks (*Quercus suber)*			
	Pyrenean oaks (*Quercus pyrenaica*)			
Understory	Mixed shrubs *(Lavandula stoechas, Thymus mastichina, Genista hirsute, Phillyrea angustifolia, Erica arborea and Erica australis)*	Smix		Shrub (S)
	Retama sphaerocarpa	Sret		
	Cistus ladanifer	Scis		
	Pasture	P		Herbaceous plants (H)
	Dry agricultural land	L		
Non-vegetation	Bare soil	B		B
	Roads	Rd		Impervious (I)
	Rocky outcrops	Rk		
	Roofs of rural houses	U		
	Shadows	Sh	-	Sh
	Waterbodies	W	-	W
Capacity for run off generation legend:	very high	high	medium	low

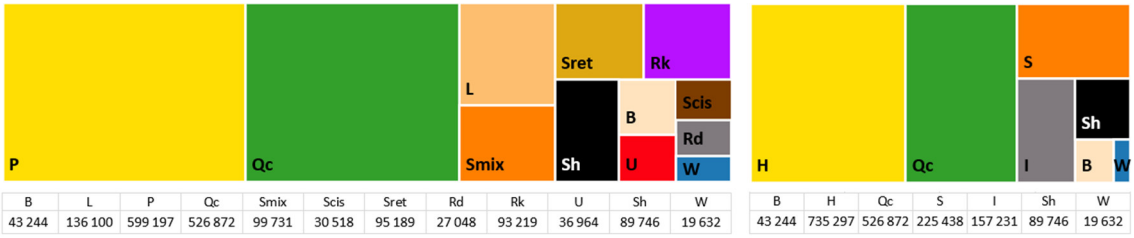

B	L	P	Qc	Smix	Scis	Sret	Rd	Rk	U	Sh	W
43 244	136 100	599 197	526 872	99 731	30 518	95 189	27 048	93 219	36 964	89 746	19 632

B	H	Qc	S	I	Sh	W
43 244	735 297	526 872	225 438	157 231	89 746	19 632

Fig. 2 Field dataset pixels grouped according to both levels of disaggregation considered (a) class level; (b) macro-class level.

2.4 Image pre-processing and predictors

A multiband raster stack was created for each image to account for the four spectral bands (i.e., NIR, red, green, and blue) in the analysis. Similar to previous studies (see Table 2), additional features (i.e., in addition to the spectral information) were used as predictors to improve the discrimination of the vegetation. These predictors included vegetation indices (VI), soil indices (SI), and textural features (TF). The PNOA imagery had an 8-bit color depth, and thus the pixel values ranged from 0 to 255. Therefore, similar to the method proposed by Borlaf-Mena et al. (2019), the digital numbers were first normalized from 0 to 1 using Eq. (1).

$$NIR_n = \frac{NIR}{255}; Red_n = \frac{Red}{255}; Green_n = \frac{Green}{255}; Blue_n = \frac{Blue}{255} \quad (1)$$

where NIR, Red, Green, and Blue are the digital values of the pixel in each band, and NIR_n, Red_n, $Green_n$, and $Blue_n$ are the normalized values of the pixels.

The VI, SI, and TF analysis was conducted using the Sentinel Application Platform (SNAP) software developed by the European Space Agency (ESA). The well-known normalized difference vegetation index (NDVI) is by far the most widely used index among the VI; however, other indices have also been proven to be useful (Fang et al. 2018; Ferreira et al. 2016). Due to the low spectral resolution of the PNOA imagery, only a limited number of indices can be computed with the available bands. Table 4 summarizes the indices considered in this study.

Regarding the use of SI, the most common indices are the Brightness Index (BI) and the Color Index (CI) (Escadafal 1993), and although they are not fully implemented in vegetation classifications (Fragoso-Campón et al. 2019), they have been proven to be useful as they can improve the discrimination between low green vegetation canopy covers and bare soil (Huete et al. 1984; Richardson and Wiegand 1977).

Table 4 Vegetation, water, and soil indices considered in this study.

Type	Index	Equation*		Reference
Vegetation	NDVI	$NDVI = \frac{\mathrm{NIR}_n - \mathrm{Red}_n}{\mathrm{NIR}_n + \mathrm{Red}_n}$	(2)	(Rouse Jr et al. 1974)
	SAVI**	$SAVI = (1+L)\cdot\frac{\mathrm{NIR}_n - \mathrm{Red}_n}{(\mathrm{NIR}_n + \mathrm{Red}_n + \mathrm{L})}$	(3)	(Huete 1988)
	MSAVI2	$MSAVI2 = \frac{1}{2}\cdot\left[(2\cdot(\mathrm{NIR}_n + 1) - \sqrt{(2\mathrm{NIR}_n+1)^2 - 8(\mathrm{NIR}_n - Red_n)}\right]$	(4)	(Qi et al. 1994)
Water	NDWI	$NDWI = \frac{\mathrm{Green}_n - \mathrm{NIR}_n}{\mathrm{Green}_n + \mathrm{NIR}_n}$	(5)	(Gao 1996)
Soil	BI	$BI = \sqrt{\frac{Red_n^2 + Green_n^2}{2}}$	(6)	(Mathieu et al. 1998)
	CI	$CI = \frac{\mathrm{Red}_n - \mathrm{Green}_n}{\mathrm{Red}_n + \mathrm{Green}_n}$	(7)	(Escadafal and Huete 1991)

* Adaptation of the traditional formulation to the normalized values of the bands
** L=0.50
NDVI (Normalized Difference Vegetation Index); SAVI (Soil Adjusted Vegetation Index); MSAVI2 (Second Modified Soil Adjusted Vegetation Index), NDWI (Normalized Difference Water Index); BI (Brightness Index); CI (Color Index).

Regarding the TF, the grey-level co-occurrence matrices (GLCM) (Haralick and Shanmugam 1973) is a widely used method to compute textures metrics. As reported by Burnett et al. (2019), the texture metrics

can be computed from a combination of bands or the principal component, but it is also possible to achieve good results using only a single band. In this case, we used only the NIR band to compute the derived textured measures due to the spatial resolution of the images and to the specific importance of this band in the vegetation response. As recommended by Hall-Beyer (2017), the descriptive statistics (mean and variance) of the GLCM texture measurements were applied. Specifically, means were utilized for classification and the variance was included as additional information, as these parameters were not expected to be highly correlated (Hall-Beyer 2017). The analysis was performed for all angles via probabilistic quantization, using a pixel displacement of 4 and a 7 × 7 window size.

2.5 Training and Validation Groups

Two different groups of PNOA images of the study area were considered in the analysis: the training group and the validation group (Fig. 3). The training group was used to train the model, whereas the validation group was used to perform an independent accuracy verification to evaluate the capability of the classifier to be used in neighboring images that were not used to train the model. The statistical analyses were performed with the R statistical computing software (R-Core-Team 2018).

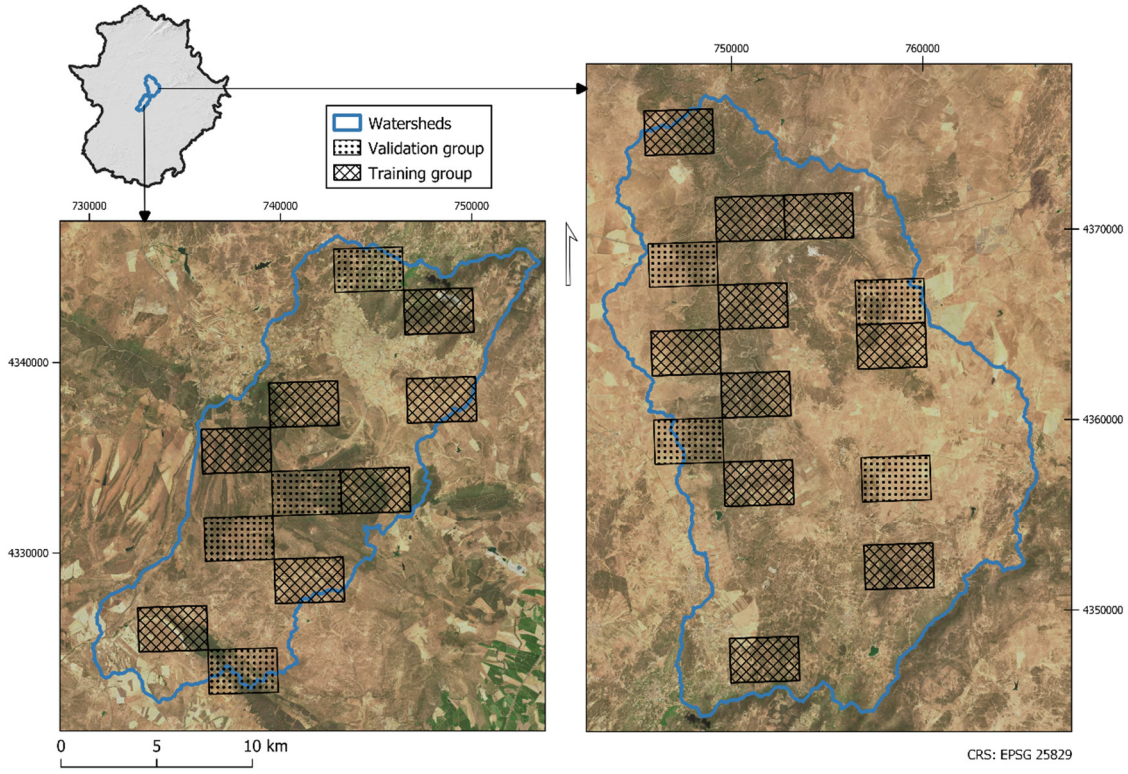

Fig. 3 Images of the PNOA tile used for training and validation.

First, a seventeen-image training group was used to obtain a training dataset. For each image, a different region of interest (ROI) dataset was randomly geolocalized, representing all the land cover types in each tile. Then, the values of the predictors in each category were obtained using the *raster R package* (Hijmans 2019). Afterward, all the ROI datasets were merged into one, representing all the ROI of the training group. At this point, the training dataset was randomly divided into two groups ensuring to maintain the class balance: ROI Dataset 1 and ROI Dataset 2 (complete data sets in Rdata format are provided in Online

Resource 1). The separability of the classes and macro-classes was tested based on the spectral response, VI, SI, and TF using the Jeffries-Matusita distance (JMD) for multiclass cases via the *varSel* R package (Dalponte and Ørka 2016). The JMD measures the separability among categories based on the information that each predictor can provide to the analysis. As shown in Lasaponara and Lanorte (2007b), the JMD bounds are between 0 and 1.41 (asymptotic to the value 2), whereby higher values indicate higher separability. JMD values below a threshold value of 1 are generally assumed to represent poor separability. Therefore, the separability of the proposed categories was verified using a JMD threshold of 1.

Secondly, an eight-image validation group was used to obtain the validation dataset. Following the procedure explained above, ROIs of each image were randomly geolocalized to represent the land cover in each tile.

2.6 Classification technique

When the input predictors for the classification are obtained from a mixed origin (spectra, indices, and textures), non-parametric machine learning methods such as the random forest (RF) (Breiman 2001) and the support vector machine classifier (SVM) have been proven effective in previous studies (Fassnacht et al. 2016). As shown in Table 2 , both algorithms have been widely used in previous studies and are well documented (Ghosh et al. 2014).

In this study, a pixel-level supervised classification was conducted using RF, as this approach is more time-efficient. Thus, the classifications were performed using the *RandomForest* R package (Liaw and Wiener 2002). The RF classifier was trained considering two scenarios as shown in Fig. 4 . Both training datasets, ROI Dataset 1 and ROI Dataset 2, were use twice (i.e., as training data or as independent test data each time). Finally, the RF classifier with the best performance in terms of overall accuracy was selected for the classification. The analysis was conducted for both the class and macro-class levels.

Two parameters had to be configured to train the RF classifier: the number of decision trees (Ntree), which was set to 500, and the number of variables to be selected and tested to achieve an optimal split when growing the trees (Mtry). In each scenario, the best Mtry values were trained before the classifier was defined.

2.7 Post-classification processing

When applying a pixel-level classification approach to an image with high spatial resolution, it is assumed that salt-and-pepper noise will occur. There are some techniques to reduce this noise in the final classification (Kim et al. 2011) and one of them is related to a classification post-process that improves the accuracy of the final maps (Stavrakoudis et al. 2014; Su 2016). In this work, the classified images were smoothed using the majority filtering and sieving methods (Mas et al. 2010). The filtering process was carried out with algorithms implemented in the QGIS software. First, the *SAGA majority filter* (Conrad 2010) was applied, considering a square search mode with a radius of 2. Afterward, the *GDAL sieve filter* (GDAL-documentation 2019), which removes groups of raster pixels smaller than a provided threshold size (in pixels), was set to a threshold value of 10 to replace the pixels with the pixel value of the largest neighboring pixels values.

2.8 Accuracy assessment

The accuracy measures used herein were based on error matrix information, which allows to obtain derived metrics to evaluate the performance of the RF (Congalton and Green 2008). The error matrices were performed with the *caret R package* (Kuhn et al. 2018). First, we considered an overall accuracy (OA) parameter, which represents the global ratio of correct predictions considering all the categories on the map. Additionally, the error matrix provides other information to test each category. Therefore, the metrics used for the accuracy assessment by categories (considering the class or macro-class level) were defined based on the procedures described by Franklin (2010), as summarized in Table 5 .

Table 5 Accuracy measures in each category based on error matrix information

Metric	Definition	Equation
Sensitivity	Proportion of predictions that are accurately classified as positive in each category. Also called producer's accuracy.	$\text{Sensitivity} = \frac{TP}{TP + FN}$ (8)
Specificity	Proportion of predictions that are accurately classified as negative.	$\text{Specificity} = \frac{TN}{TN + FP}$ (9)
Precision	Proportion of the reference area included accurately in each category to which it belongs. Also called user's accuracy.	$\text{Precision} = \frac{TP}{TP + FP}$ (10)
Balanced accuracy	The average proportion of predictions accurately classified, considering both the TP and TN possibilities.	$BA = \frac{1}{2} \cdot (sensivity + specificity)$ (11)

TP	True Positive	FP	False Positive
FN	False Negative	TN	True Negative

As shown in Fig. 4 , the accuracy evaluations were carried out in two phases. First, the best RF classifier in the training group was analyzed by comparing the OA in the two considered scenarios. Then, once the RF classifier with the best performance was selected, the accuracy metrics in each category were obtained for both class and macro-class analyses. Afterward, the capability of the RF classifier to be used in other validation group images that were not used to train the model was evaluated. Therefore, a zonal histogram of the ROI over the post-processed classified images was obtained for each tile, after which the information was merged to calculate a global error matrix of the validation group. In this case, the accuracy was based on polygons as sampling units (Congalton and Green 2008).

2.9 Influence of the spatial resolution of land cover maps on runoff

The hydrologic response was evaluated following the National Resources Conservation Service Curve Number method[2] (NRCS-CN) (NRCS 2009), where the runoff volume is calculated following Eq.(12).

$$Q = \frac{(P - 0.2S)^2}{P + 0.8S} \quad (12)$$

where Q is the surface runoff, P is the total rainfall and S is the potential maximum retention.

[2] It was not until 1994 that the Soil Conservation Service (SCS) changed its name to the National Resources Conservation Service (NRCS), so the methodology is also known as the SCS-CN method.

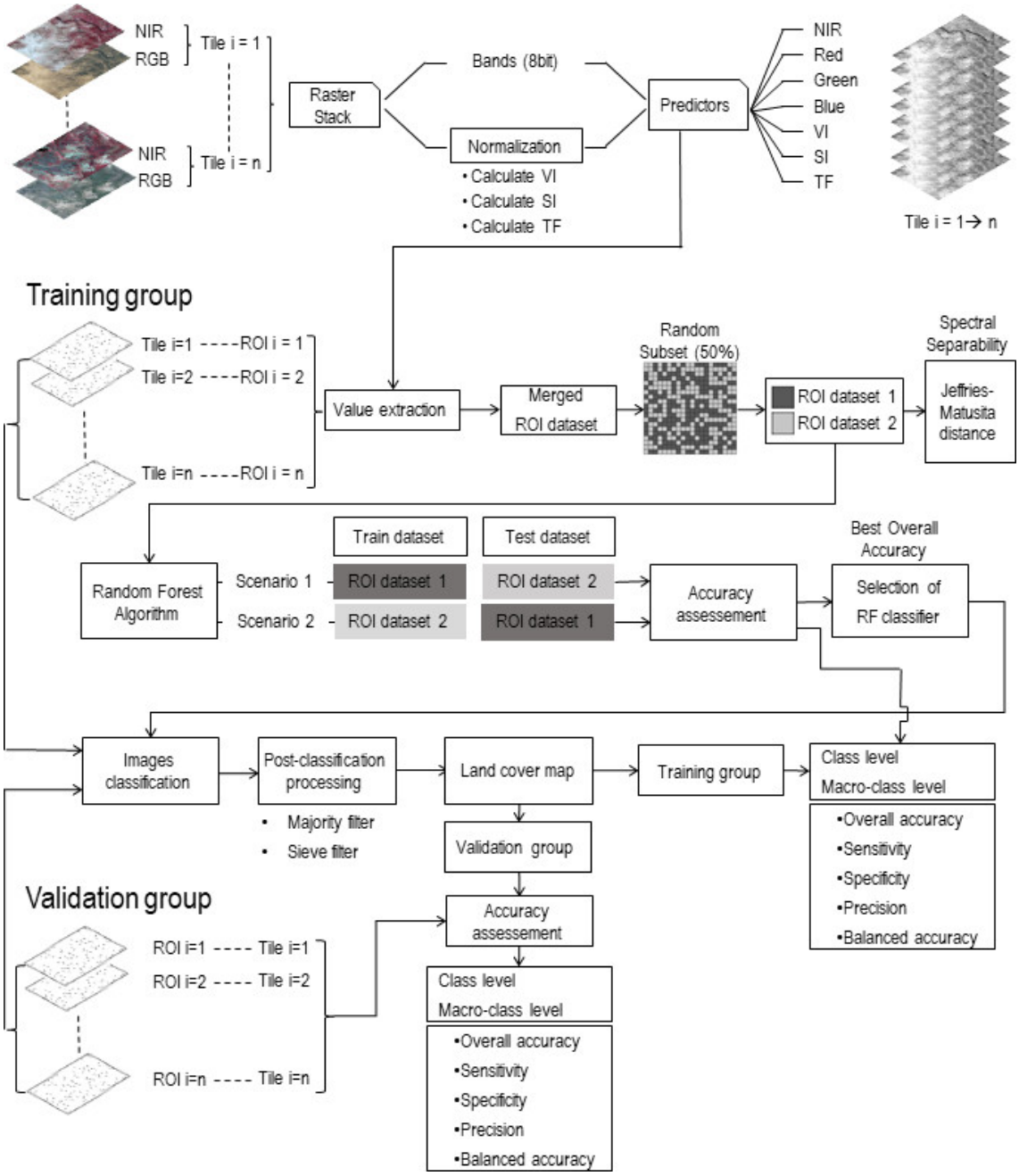

Fig. 4 UHSR imagery processing flowchart proposed in this study.

The S factor, which is measured in mm, is computed from the main factor of the method, the dimensionless curve number (CN) parameter following Eq.(13)

$$S = \frac{25400}{CN} - 254 \tag{13}$$

Subsequently, the CN refers to the potential runoff capability of a complex area, whereby the higher CN value indicates a higher potential runoff capability. Therefore, based on the criteria of the National Engineering Handbook, the CN depends on cover (land cover and treatment class) and soil type .The main limitation of the NRCS-CN is the soil initial antecedent moisture before the rainfall-runoff process begins (Durán-Barroso et al. 2016) and in this study an average condition was considered.

In this work, the influence of the spatial resolution of the land cover maps on runoff was conducted by comparing the CN values derived from the UHRS land cover maps with the CN values derived from the Corine Land Cover (CLC). CLC is a land cover database frequently used in Europe for hydrologic purpose (Petroselli and Grimaldi 2018; Psomiadis et al. 2020; Walega and Salata 2019) and, the version published in 2018 was used.

In the case of the UHSR land cover, given that the land cover was in fact grouped into categories depending on their hydrologic response, it is possible to obtain the CN values directly from the lookup tables of the National Engineering Handbook (NRCS 2004) and, the class-level categories were used with this aim. However, the CLC database, only provides general information of covertures. That is why, hydrological interpretation was needed and, the lookup table proposed in Spain by Ministerio de Fomento (2016) was used in terms of CN values. Finally, the soil group was chosen following the results in Ferrer i Juliá (2003) resulting in a soil group type B throughout the study area (Fragoso et al. 2017).

Table 6 NRCS runoff curve number (CN)

UHSR imagery				**Corine Land Cover**		
Class-level categories	NRCS land cover	Hydrologic condition	CN[1]	CLC-18	Description	CN[2]
Qc	Woods	Good	55	111	Continuous urban fabric	98
Smix	Range-Brush	Fair	56	131	Mineral extraction sites	85
Sret	Range-Brush	Poor	67	211	Non-irrigated arable land	75
Scis	Range-Brush	Good	48	223	Olive groves	64
P	Herbaceous vegetation	Fair	69	231	Pastures	61
L	Close-seeded	Good	72	242	Complex cultivation patterns	64
B	Gravel roads	--	85	243	Land principally occupied by agriculture, with significant areas of natural vegetation	77
Rd	Paved roads	--	98	244	Agro-forestry areas	69
Rk	Impervious		98	311	Broad-leaved forest	52
U	Impervious		98	313	Mixed forest	52
Sh	It is asummed that the shadow comprises the pasture around trees	--	69	321	Natural grasslands	69
W	--	--	100	323	Sclerophyllous vegetation	68
				324	Transitional woodland-shrub	60
				333	Sparsely vegetated areas	78

[1] Source: Table 9.1 and 9.5 in (NRCS 2004)
[2] Source: Table 2.3 in Ministerio de Fomento (2016) using the equation $CN=5080/(P_o+50.8)$

In order to compare the differences in the estimation of CN values, the weighted average CN values derived from both data sources were computed using a grid with a cell size of 100 x 100 m (Fig. 5), following Eq.(14)

$$CN_{grid} = \sum_{i=1}^{n} \frac{CN_i \cdot A_i}{A} \tag{14}$$

where, CN_i is the CN value in the i^{th} land cover portion within the grid cell, A_i is the i^{th} area of land cover portion, n is the total number of differences land covers portions in the grid cell and A is the total area of the grid cell. Consequently, in each grid cell, there was a pair of averaged CN values, corresponding to each land cover data sources: the UHSR-CN and the CLC-CN.

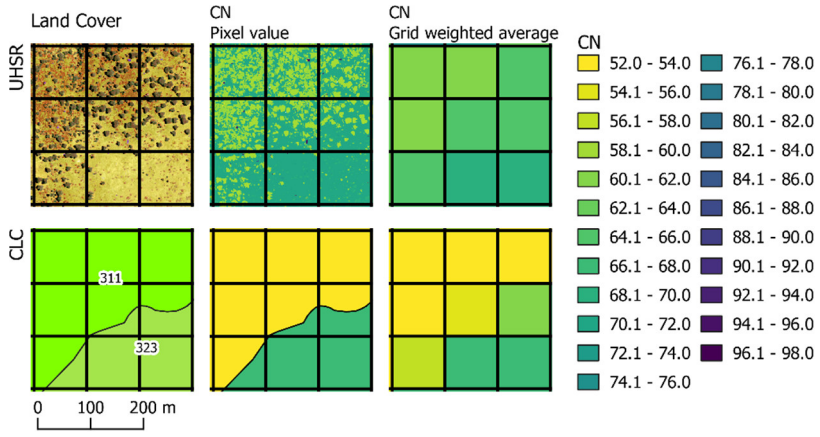

Fig. 5 Example of the grid cell weighted average CN values

Therefore, the analysis of the effect of land cover spatial resolution on the CN value, was conducted using the mean absolute difference (MAD) and the global root mean square difference (RMSD). The MAD measures the difference between the values in each grid cell expressing the comparisons of CLC-CN versus UHSR-CN. Therefore, it can be summarized if the disagreement between each pair means overestimation or underestimation of the CN value. The RMSD measures the difference between both land cover datasets in the estimation of the CN values. The MAD was computed for each CLC-CN value following Eq.(15), and the RMSD for the global dataset following Eq.(16)

$$MAD_{CN} = \frac{1}{N}\left(\sum_{i=1}^{N}(CN_{grid.CLC} - CN_{grid.UHSR})_i\right) \tag{15}$$

$$RMSD = \sqrt{\frac{1}{N}\left(\sum_{i=1}^{N}(CN_{grid.CLC} - CN_{grid.UHSR})_i^2\right)} \tag{16}$$

where, $CN_{grid.CLC}$ is the weighted average CLC-CN value in the i^{th} grid cell, $CN_{grid.UHSR}$ is the weighted average UHSR-CN value in the i^{th} grid cell and, N is the number of grid cells with the same $CN_{grid.CLC}$.

3 Results

3.1 Feature characterization

The feature characterization was inspired by a spectral signature of the categories. Due to the low spectral resolution of PNOA images, our approach considered not only the spectral information of the bands but also the information of all the predictors. Therefore, the characterization was based on a box-plot graph representing the values of the predictors from the first quartile to the third quartile, which is referred to as

the interquartile range (IQR). The analysis shows different responses among the categories at the class (Fig. 6) and macro-class (Fig. 7) levels.

The overstory stratum that represents the holm oaks presented high differences between the normalized optical bands, and presented the highest values in NIR band. In contrast, the red, green, and blue bands had much lower values, with an IQR below 0.20 in all cases, particularly the IQR of the blue band, with a value of 0.09. Regarding the indices, it is worth noting that holm oaks exhibit higher negative values in CI and NDWI2, but present higher positive mean values in terms of NDVI, second modified soil adjusted vegetation index (MSAVI2), and soil adjusted vegetation index (SAVI). The holm oaks also have a high response in terms of texture in both the GLCMm and GLCMv predictors.

The understory stratum categories presented different responses among categories at the macro-class level, which discriminated between shrubs and herbaceous plants. The shrub stratum also presented different responses within categories at the class level. However, in this case, herbaceous plant categories did not present significant differences at the class level. Therefore, understory categories exhibited a similar magnitude in all the optical bands, and no significant differences were observed compared to the overstory observations. Moreover, the values were lower for shrubs and higher for herbaceous plant categories. It is worth noting that, in this case, the blue band also presented a low IQR value of approximately 0.13 in both understory strata. Furthermore, when considering shrub species, Sret presented the highest values in all optical bands, whereas Scis had the lowest values. The IQR of the blue band was also very narrow, ranging from 0.8 to 0.10. Regarding the indices, the CI in the understory stratum was close to zero in all the categories, showing similar responses among and within species. When evaluating the VI, shrubs exhibited low values, showing different responses within species: the lowest values were observed for Sret and the highest values for Smix. The herbaceous stratum had negative VI values with a narrow IQR of 0.06, showing similar responses within species. The understory stratum presented different responses in terms of texture features. Particularly, while herbaceous plants had higher GLCMm and GLCMv predictor values (similar to the overstory stratum), the shrub stratum presented lower values and different responses within species, with Sret exhibiting the highest values. The lowest values were observed for Scis, which also had a narrow IQR.

Finally, the non-vegetation categories exhibited different responses at the macro-class level, distinguishing between impervious surface categories at class-level. First, related to the optical response, B presented the highest values of all bands, indicating that the IQR value of the green band in this category was very narrow, with a value of only 0.08. Additionally, impervious surfaces exhibited lower values in the NIR band; however, Sh and W presented by far the lowest values in all optical bands. Regarding the indices, impervious surfaces exhibited a CI value close to zero, with a narrow IQR but with similar responses within species. For this index, Sh and W exhibited high IQR values of over 0.70. Regarding the BI, the highest values were observed for B and U, which also had narrow IQR values of 0.017 and 0.09, respectively. Sh exhibited by far the lowest BI value, with a narrow IQR of 0.013. Concerning the NDWI2, not only did the highest values were observed for impervious surfaces and W, but the IQR values for Sh and W were also wider, with values higher than 1. Finally, in terms of texture, impervious categories presented low values

except for U, which had higher values in terms of both mean and IQR (> 0.5). The Sh and W classifications exhibited by far the lowest mean TF values, as well as a narrow IQR value of less than 0.04.

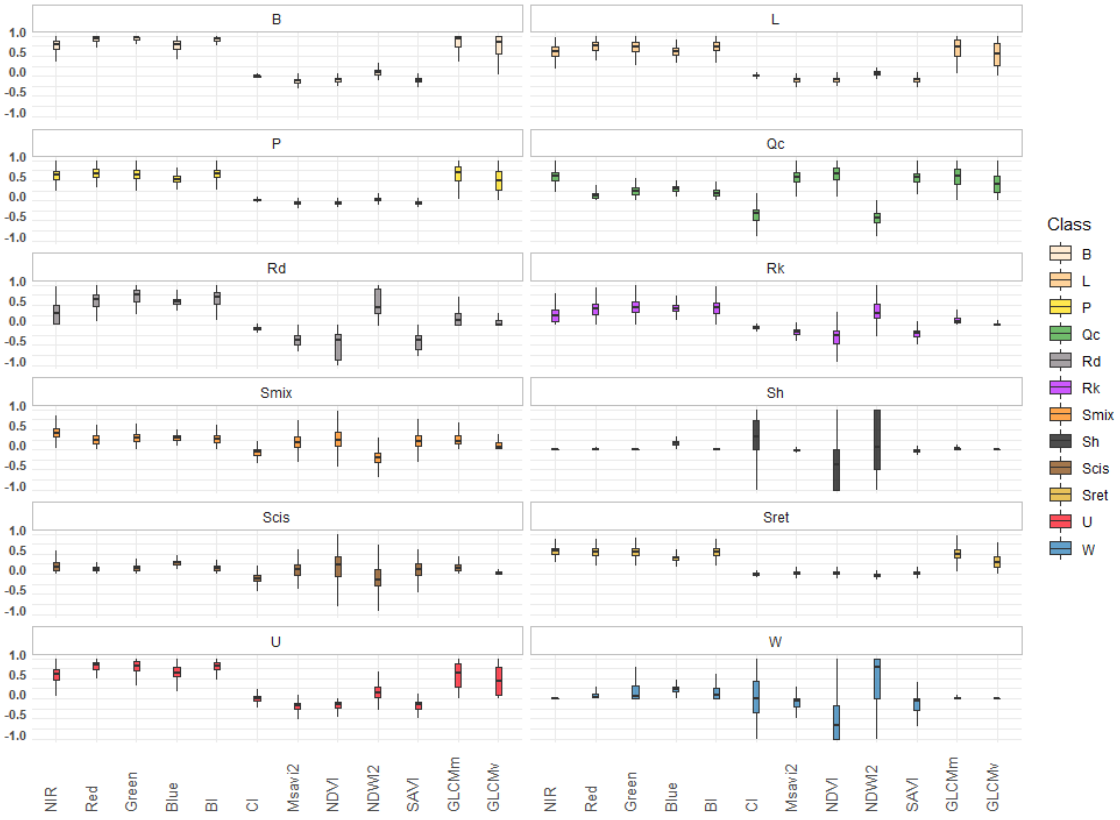

Fig. 6 Class-level feature characterization. The values of optical bands (NIR, red, green, and blue) and textures (GLCMm and GLCMv) are displayed as normalized values from 0 to 1.

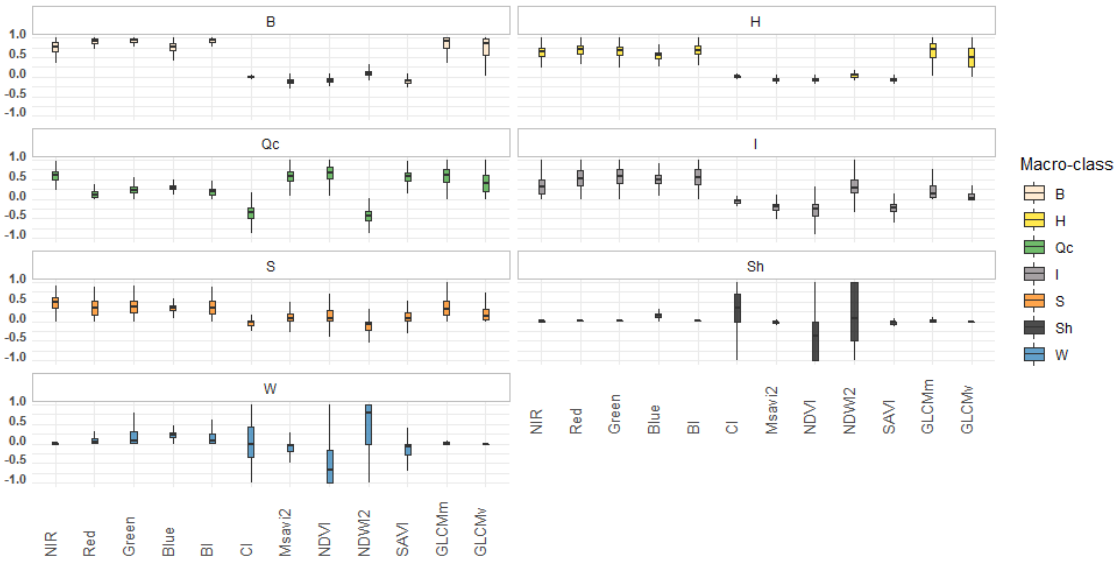

Fig. 7 Macro-class-level features characterization at (MC). The values of optical bands (NIR, red, green, and blue) and textures (GLCMm and GLCMv) are displayed as normalized values from 0 to 1.

The JMD showed a good spectral separation between the categories at both levels of disaggregation (Fig. 8). In the class-level analysis, the values ranged from 1.10 to 1.41. The lowest values occurred within the classes of the herbaceous macro-class. Specifically, P and L resulted in a JMD of 1.10. When considering the macro-class level, the highest JMD values remained at 1.41. However, the lowest values improved for the H and B pair, as well as the S and Qc pair, which achieved a JMD of 1.38.

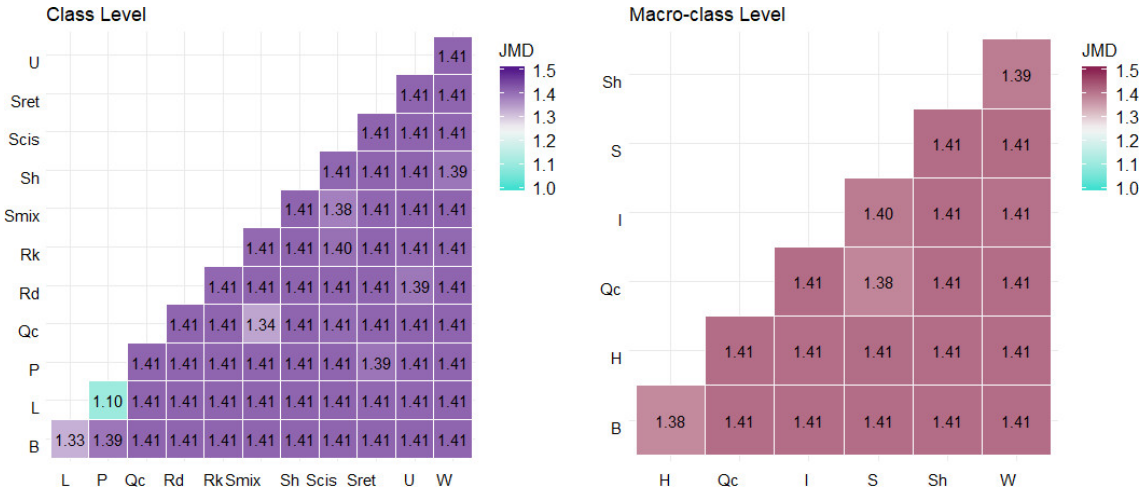

Fig. 8 Jeffries-Matusita distance (JMD) between the categories in both levels of disaggregation: class and macro-class.

3.2 Selection of the random forest classifier

As previously mentioned, the RF classifier was trained in two scenarios (Fig. 4) using the training dataset twice (i.e., each time either as a training or test set). The OAs achieved for each run are summarized in Table 7 , and demonstrate the robustness of our developed classifier, with an OA and kappa index of over 91% in both instances. The results in scenario 1 were slightly better, and thus the RF classifier obtained in scenario 1 was selected for image classification.

Table 7 Overall accuracies (OA) and kappa indices obtained from the error matrices in both considered scenarios.

			Class Level		**Macro-class Level**	
Scenario	Training	Test	OA (%)	kappa	OA (%)	kappa
1	ROI Dataset 1	ROI Dataset 2	91.6	0.8922	95.8	0.9412
2	ROI Dataset 2	ROI Dataset 1	91.5	0.8915	95.7	0.9407

Regarding the importance of the predictors, Fig. 9 shows the mean decrease in the predictive accuracy of the RF algorithm in Scenario 1. The RF algorithm uses the out of bag (OOB) samples that were not used to build the trees to measure the prediction capacity of each predictor. As explained in Hastie et al. (2009), when a tree is grown, OOB samples are used to measure the accuracy of the prediction. Then, each predictor is permuted in the OOB samples and the accuracy is calculated again. Afterward, the decrease in accuracy is averaged over all trees for each predictor. Higher values suggest a more important role of the predictor in the classification process.

CI, the blue band, GLCMm, and GLCMv were found to be the most important classification predictors, followed by other less important but also strong predictors, such as the green band, BI, and the NIR band. VI had the least importance, according to our analysis.

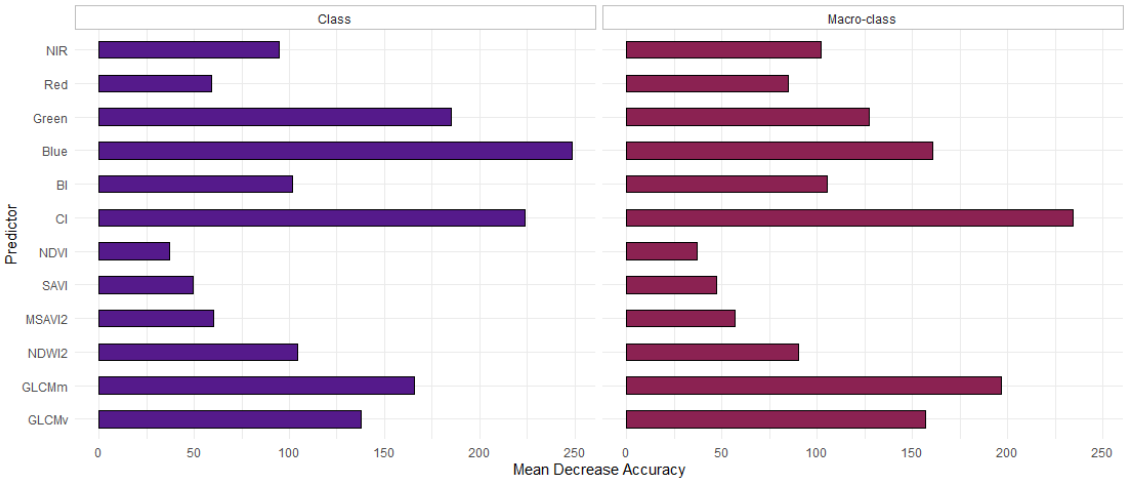

Fig. 9 Predictor importance in the RF algorithm based on mean decrease accuracy at the class and macro-class level.

Additionally, the importance of each predictor varied across the categories, as illustrated in Fig. 10 . The blue band became notably important to classify shrub species. Moreover, the most important predictors for herbaceous category classification were CI and GLCMm. Finally, CI was the most valuable predictor for impervious surfaces.

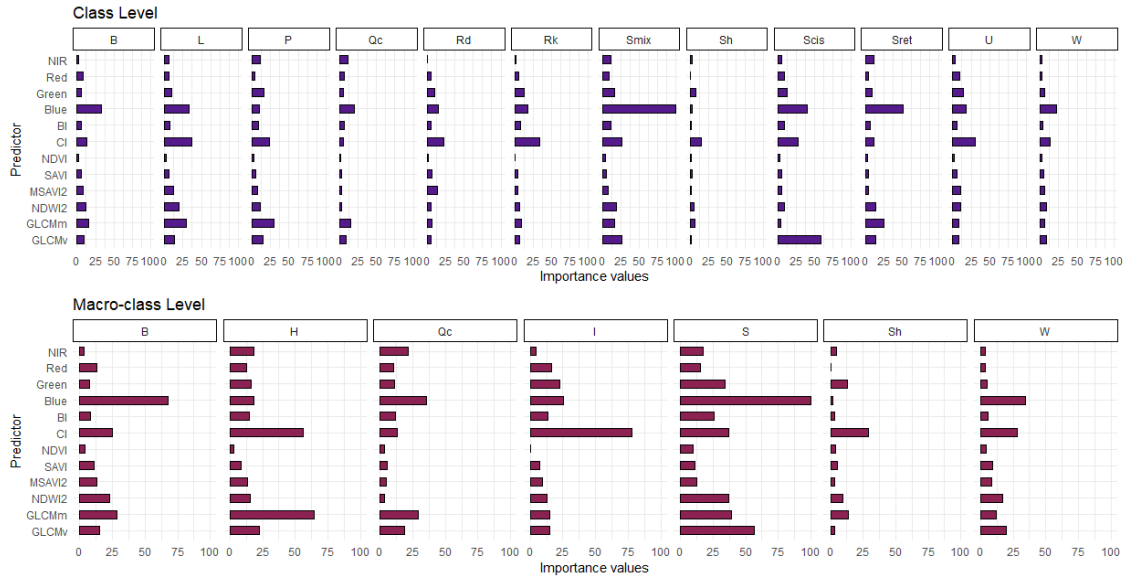

Fig. 10 Class- and macro-class-level predictor importance across categories in the RF algorithm.

3.3 Accuracy assessment

As indicated by Table 8 , the RF algorithm delivered accurate results. The OA values were higher for the macro-class level than for the class level analysis, and the results in the validation group were lower than those of the training group. However, despite these differences, the overall performance of our classifier was still outstanding.

Table 8 Overall accuracies (OA) and kappa indices obtained.

	Class Level		Macro-class Level	
Group	OA (%)	kappa	OA (%)	kappa
Training	91.6	0.89	95.8	0.94
Validation	78.3	0.74	86.3	0.82

The error matrices obtained herein are supplied as supplementary material for both groups. The matrices are expressed in terms of pixel count and percent of prediction for each category[3].

Overall, the training group rendered more accurate results than the validation group, based on the error matrix data (Fig. 11).

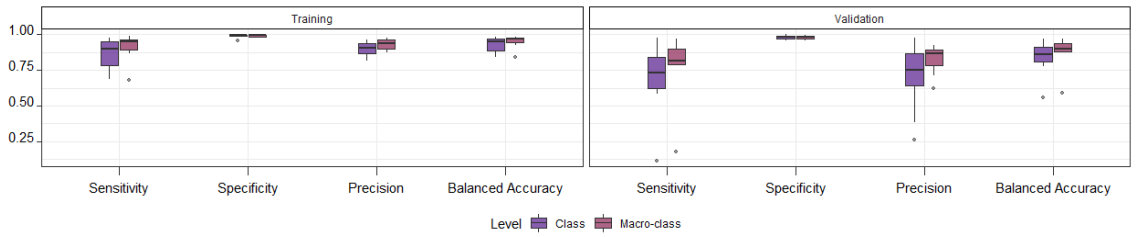

Fig. 11 Summary of the random forest classifier error matrix results.

When considering vegetation cover, the training group Qc classification (Fig. 12) achieved excellent results, with a sensitivity, specificity, and balanced accuracy of 0.98. Moreover, at the macro-class level, excellent results were achieved for the shrub stratum, showing a sensitivity of 0.80, a specificity of 0.97, and a balanced accuracy of 0.88. When considering the class-level disaggregation, the best results were observed for Sret, followed by Scis and Smix. Regarding the herbaceous stratum, the results were excellent at the macro-class level. However, at the class level, the statistics for the L class were poorer than those for P class. Specifically, L exhibited balanced accuracy and sensitivity values of 0.84 and 0.69, respectively, whereas P reached a 0.95 value for both parameters. Considering the non-vegetation covers, the results were excellent for B and I. Good results were also obtained when considering the class level disaggregation in Rk, Rd, and U. However, the values obtained for W were less accurate, with a sensitivity of 0.68 and a balance accuracy of 0.84.

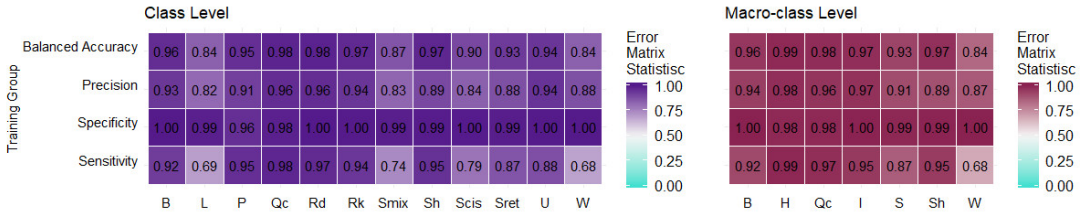

Fig. 12 Error matrix statistics of the training group random forest classifier

[3] Online Resource 2: see Tables S1 and S2 for more details on the training group at the class level. For the macro-class-level analysis, see Tables S3 and S4. For the validation group at class level, see Tables S5 and S6. For the analysis at the macro-class level, see Tables S7 and S8.

In terms of balanced accuracy, the results in the validation group (Fig. 13) showed values ranging from 0.56 to 0.97 at the class level and from 0.59 to 0.97 at the macro-class level. As previously mentioned, the accuracy values were lower than those for the training group, especially at the class level, where significant decreases in sensitivity and precision were observed. However, vegetation classifications remained accurate for Qc, H, and S. In contrast, a decrease in accuracy was observed for non-vegetation classes such as Sh, with W having the worst classification performance.

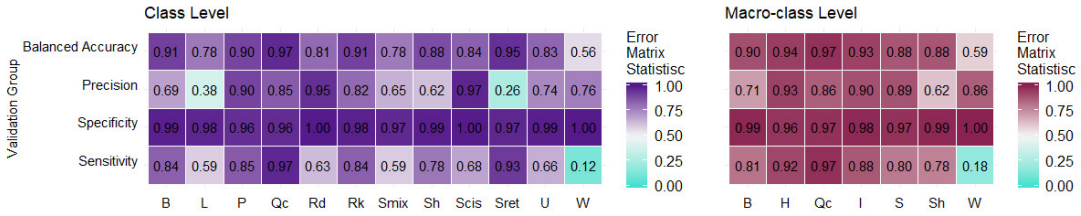

Fig. 13 Error matrix statistics of the random forest classifier in the validation group

3.4 Land cover results

Fig. 14 illustrates how the images were smoothed using the majority filtering and sieving methods to reduce salt-and-pepper noise. Fig. 15 illustrates the representative land cover types of the *dehesa* environment upon the application of post-classification processing. The final land cover maps for all the images of the training group are shown in Online Resource 2 from Fig S2 to Fig S5, and the land cover maps for the images of the validation group are shown in Fig S6 and Fig S7.

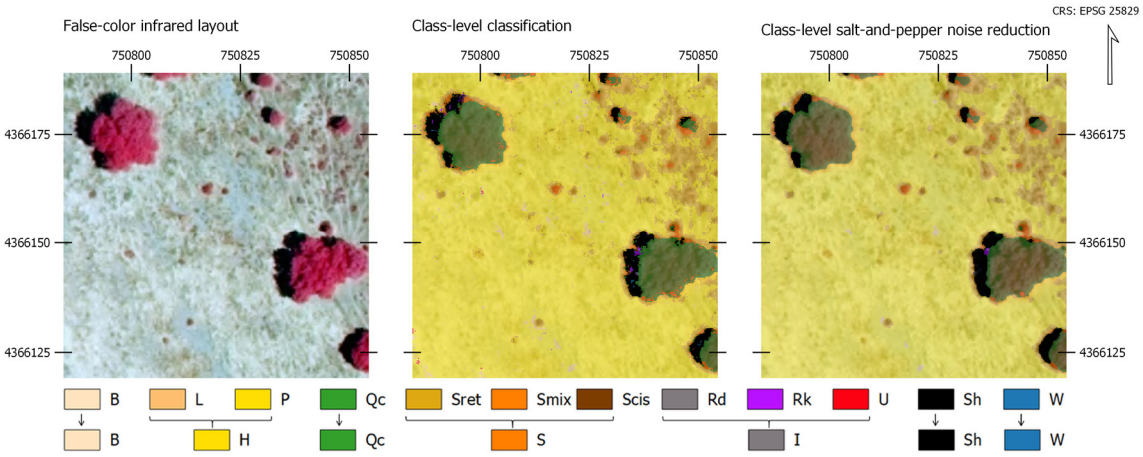

Fig. 14 Salt-and-pepper noise reduction post-classification processing results

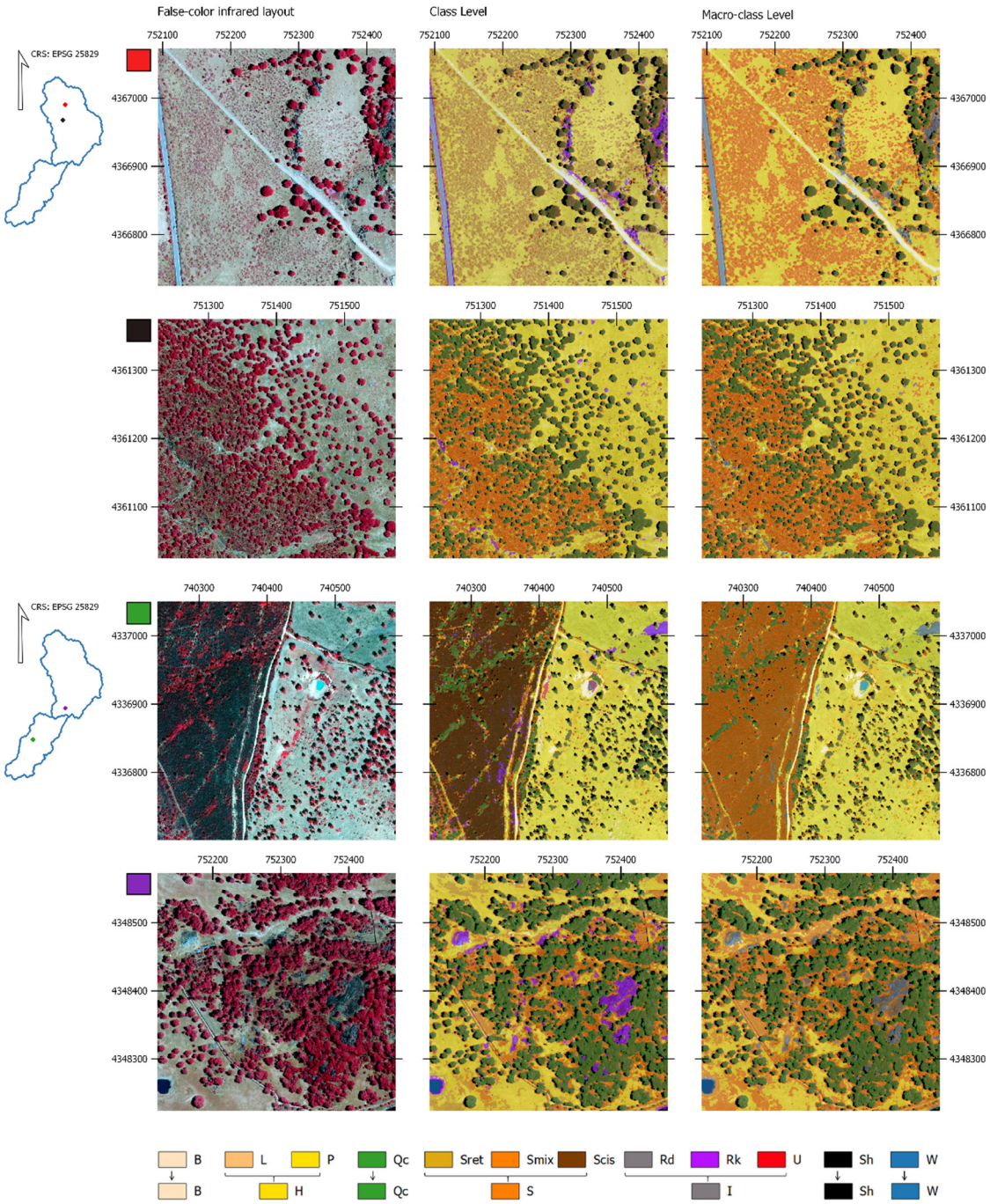

Fig. 15 Land cover maps of the *dehesa* environment

3.5 Influence of spatial resolution of land cover maps on runoff results

Fig. 16 illustrates an example of the spatial distribution of the grid cell weighted average CN values derived from the both data sources, the UHSR imagery developed in this study, and the CLC database. The results are different according to the first visual interpretation and they show several responses between the categories of land cover. Thus, the spatial distribution of the CN values depends on the spatial resolution of the land cover data source. The CN maps for the all the images used in this study are shown in Fig S8 to Fig S13.

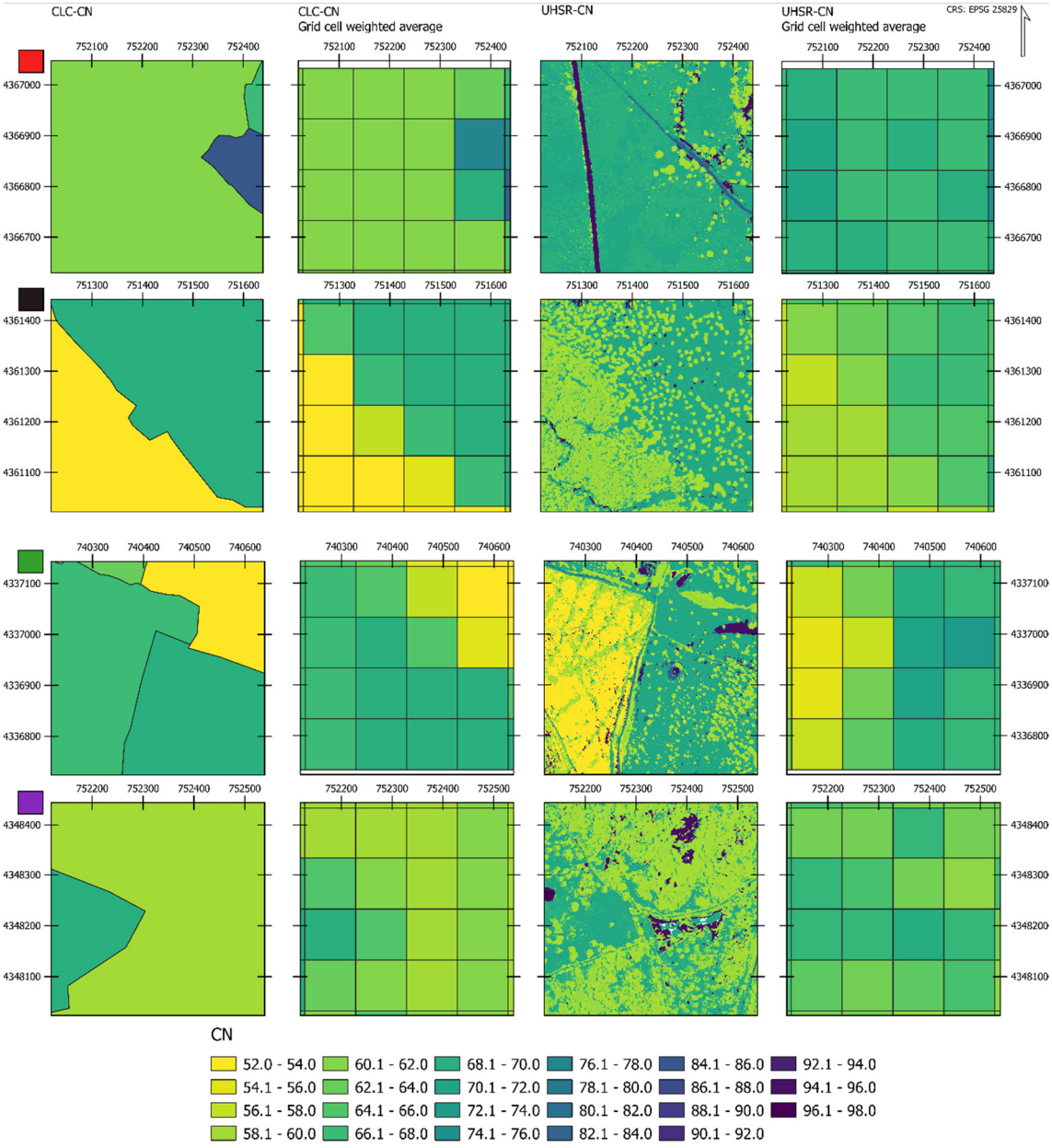

Fig. 16 Grid cell weighted average CN values derived from the UHSR land cover maps (UHSR-CN) and the CLC (CLC-CN) in a the *dehesa* environment

Given that the differences have physical sense, the MAD summarize if the disagreement between each pair means overestimation or underestimation of the CN value. As shown in Fig. 17 a, the CLC-CN values below, a threshold value of 66 are smaller than the UHRS-CN values, which means underestimation of the runoff of the CLC for the broad-leaved forest, mixed forest, transitional woodland-shrub, pastures, olive groves and complex cultivation patterns. On the other hand, the CLC-CN values over a threshold value of 66 are higher than the UHRS-CN values, which means overestimation of the runoff for the categories of sclerophyllous vegetation, agro-forestry areas, natural grasslands, non-irrigated arable land, land principally occupied by agriculture, with significant areas of natural vegetation, sparsely vegetated areas, mineral extraction sites and continuous urban fabric. The differences in the estimation of the CN values between the UHSR and CLC (Fig. 17 b) reached a RMSD of 6.26. Lastly, it is worth noting that the underestimation in runoff corresponds to the most representative land cover in the *dehesa* environment.

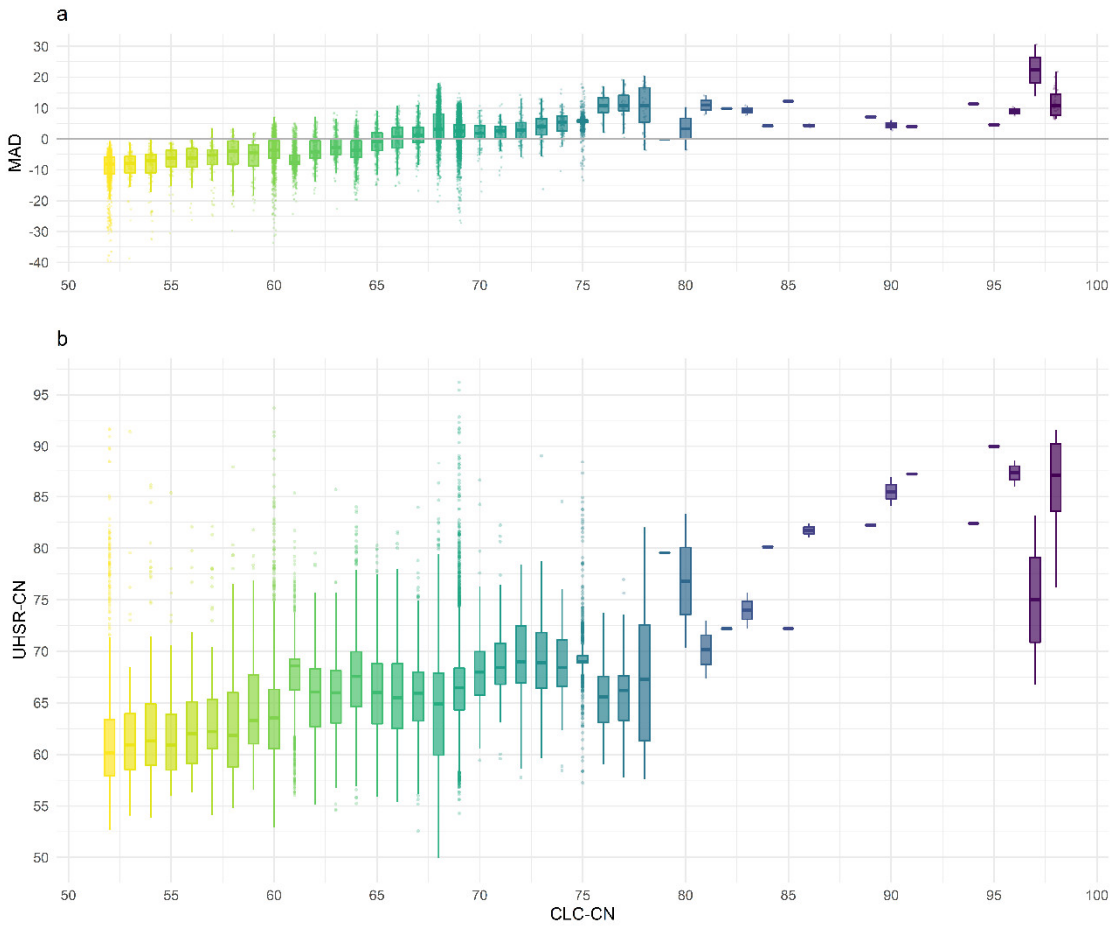

Fig. 17 Influence of the spatial resolution of the land cover maps in the CN comparing the grid cell 6weighted average CLC-CN value versus UHSR-CN values (a) mean absolute difference (MAD) (b) box-plot of CLC-CN values versus UHSR-CN values.

4 Discussion

In this work, the vegetation in a *dehesa* environment was studied using PNOA UHSR imagery considering both the overstory and understory strata. Here, we proposed the use of several UHSR images without the need for mosaic processing, using the information of the bands without further calibration. Therefore, the vegetation was analyzed considering the data available, which resulted in 4 optical bands (NIR, red, green, and blue) and the metrics derived from them, such as VI, SI, and TF.

Our results were presented in two different groups: the training and the validation group. The training group results could be compared to previous works, given that they derived from the application of a traditional process. In this sense, a supervised classification was carried out using the data collected from all the images of the training group. We verified that the ground data could be extracted from each independent tile and merged all data to build a global dataset that could be used for the characterization of land cover categories. Then, we tested our novel approach, which consisted of applying the information of the global dataset of the training group to the validation group, for which ground data extraction was not necessarily performed. The OA and kappa index results (Table 8) were excellent for the training group and very good for the validation group, reaching similar accuracy levels than those obtained in previous studies (Table 2).

Regarding the overstory classification, given that this stratum is mainly comprised of holm oaks, any necessary species discrimination was applied in this work. Therefore, the error matrix statistics for this category were excellent for the training group (Fig. 12) and very good for the validation group (Fig. 13). Importantly, our results were consistent with those reported by Boggs (2010), in which tree canopies were mapped using QuickBird imagery pan-sharpened to a spatial resolution of 0.5 m. In this work, the author used the same spectral bands used herein, but also considered NDVI data, thereby joining two approaches into an NDVI pixel- and object-based image analysis (OBIA). The OA values ranged from 85% to 95% for the NDVI pixel-based approach, and from 87% to 97% for the OBIA. Therefore, our training group results were slightly better than those obtained even with the OBIA approach. Considering other works that used VHSR, our results were comparable to those of Dalponte et al. (2014), which employed a spatial resolution of 0.40 m in their tree crown delineation and tree species classification in boreal forests using hyperspectral images. The best species classification producer's accuracy reached 97.5% for pine trees. Here, the sensitivity for holm oaks reached 98% in both training and validation groups. Moreover, it is important to point out that this was achieved using only 12 predictors in the classification versus the 160 spectral bands of their work, even though no species discrimination was applied in our study.

Regarding the understory classification, particularly the shrub species discrimination, our results were slightly better than those obtained in previous works that focused on understory strata, even though our work used UHSR instead of the more traditionally used VHSR (e.g.,Eroğlu et al. (2010), Malahlela et al. (2015), Niphadkar et al. (2017) and van Lier et al. (2009)). Eroğlu et al. (2010) and van Lier et al. (2009) reported an overall accuracy of 82.5% and 79.8% using IKONOS imagery. Similar to our macro-class-level analysis, van Lier et al. (2009) achieved a producer's accuracy of 87.8% for understory strata classification, pointing out that their method was weaker for areas with sparse cover of ericaceous shrubs or dense tree cover. Likewise, our results were better than those of Eroğlu et al. (2010) which reported a producer's accuracy of 65.9% and 93.75% for overstory and understory respectively, although they grouped shrub and herbaceous plants as an unique category. Moreover, Malahlela et al. (2015) used WordView2 imagery to study the probability of occurrence of a specific invasive shrub (*C. odorata*) in forest gaps, and achieved sensitivity, specificity, and precision values of 87%, 86%, and 87%, respectively. Finally, our results were much better than those of Niphadkar et al. (2017), who used Geo-eye and WordView2 imagery to map another invasive shrub (*Lantana camara*) in a tropical forest, with only an overall accuracy of approximately 60%.

Regarding our analysis of water bodies, it is worth noting that the results for water are by far the weakest of all categories for both the training and validation groups, where sensitivity decreased from 0.68 to 0.12. In the training group, the main confusion was between water and shadows, with a 27% confusion rate (Table S2). In the case of the validation group, low accuracies were attributed to the misclassification of 40% of the pixels. Further, confusion with shadows reached 21% and 10% with urban areas (Table S4). The water bodies in our study area were small cattle ponds and were likely misclassified in the validating group due to the considerable variability between the cattle ponds during the image acquisition period (June). This can be attributed to low depths, as well as suspended algae and sludge, all of which affects the surface's spectral response. Thus, even though the waterbody classification accuracy was poor in our specific case study, said surfaces only represented 0.5% of the studied area.

Regarding the importance of the predictors, our results demonstrated that CI, the blue band, GLCMm, and GLCMv were the most important classification parameters. The CI was the most important predictor, given that it was ranked first at the macro-class-level analysis and second at the class level. In turn, this ranking was not far from the blue band, which ranked first in the class level (Fig. 10). In our study, the CI was helpful to distinguish among vegetation categories, even more than the VI, especially for H and S. Moreover, regarding the non-vegetation categories, the CI was by far the most important for I. These results might be related to the fact that CI IQR values in these categories were very narrow. Therefore, a low dispersion was observed in the sample set. Consequently, the inclusion of CI as a predictor improved the discrimination of non-vegetated areas, as reported by Richardson and Wiegand (1977) and Huete et al. (1984). It is well known that the inclusion of VI facilitates the discrimination of vegetation and thus it is commonly used as a predictor (see Table 2). However, in our results, the VI seemed to have less importance. This may be explained by the seasonal phenology pattern typically observed during early summer in Extremadura (i.e., our study region), whereby the herbaceous stratum loses its greenness and evergreen shrubs become less vigorous, and thus the CI and BI become more effective for discrimination. Additionally, as shown in Fig. 18 , a negative correlation was observed between the VI and CI, making them less representative.

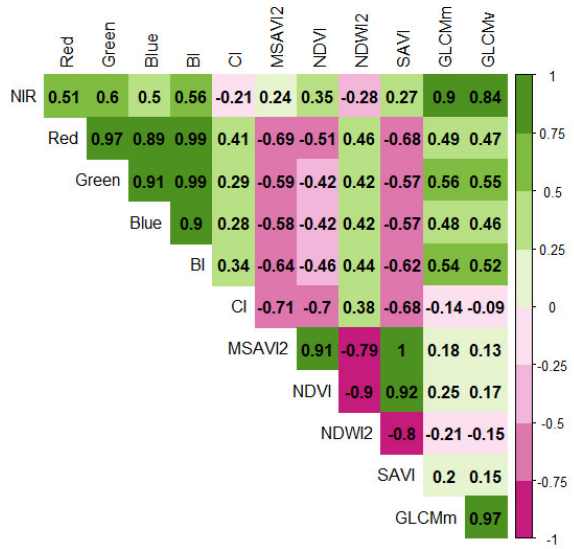

Fig. 18 Pearson correlation coefficient of the predictors.

The importance of the blue band and the texture features (GLCMm and GLCMv) are in concordance with the results of Burnett et al. (2019). In their study, coconut trees and native forests were mapped using WorldView2 images with a pan-sharpened spatial resolution of 0.5 m. The most important features were the coastal and blue band, ranking first and second in the average importance score, respectively. Moreover, different GLCM metrics were also ranked third to eighth. However, SI was not used in said work, and thus cannot be fully compared with ours. Burnett et al. (2019) concluded that the coastal and blue spectral bands facilitated the discrimination between broad vegetation classes in humid tropics. Although the environment in our study was Mediterranean and non-tropical, our results suggest that the blue band also facilitated discrimination, particularly in the shrub stratum (Fig. 10). Furthermore, based on the method described by Burnett et al. (2019), we ran a RF model in the training group without the blue band as a predictor, after which the accuracy decreased at both analysis levels. Specifically, the class-level OA decreased from 91.6%

(kappa=0.89) to 87.8% (kappa=0.84), and the macro-class-level OA decreased from 95.8 % (kappa=0.94) to 93.5% (kappa=0.91). Therefore, a general decrease in accuracy metrics was observed in all the categories (Fig. 19).

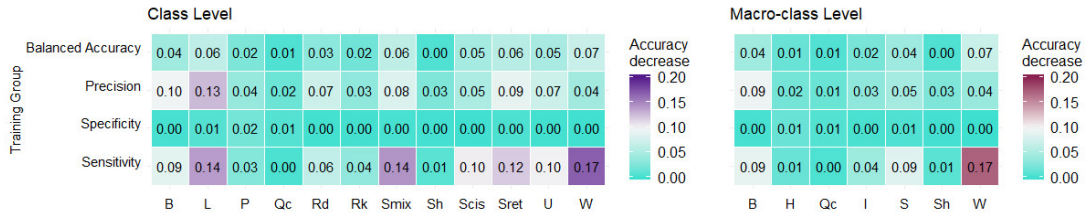

Fig. 19 Evaluation of the classification accuracy measure decreases for each category after eliminating the blue band as a predictor.

The most significant decrease was observed in the sensitivity of low strata vegetation (e.g., shrub species) and non-vegetated areas, such as urban areas and water bodies. This was likely because the blue band had a strong positive influence on the classification. Notably, the feature characterization demonstrated that the blue band had different responses within shrub species, and the IQR of the blue band was also very narrow in said categories.

Therefore, it is worth noting that our results confirmed the findings of Burnett et al. (2019) by establishing that the blue band facilitated species discrimination (particularly within shrub species) in a Mediterranean *dehesa* ecosystem. Considering the image acquisition dates, our results are also in agreement with those of Fang et al. (2018), which demonstrated that the blue wavelengths were among the most important variables during spring and summer.

Regarding spectral separability, the JMD was applied in this work. As previously mentioned, the JMD measures the separability between categories and depends on the information that each predictor can provide to the analysis. In our work, the JMD among categories ranged from 1.1 to 1.41 at the class level and from 1.38 to 1.41 at the macro-class level. Reaching a value of 1.41 for most pairs meant that the training data spanned the entire spectral variability between the categories. A low JMD value of 1.1 was observed for the P-L pair, which represented the species in the herbaceous macro-class. In this instance, the feature characterization established no significant differences between herbaceous categories at the class level. On the one hand, the class-level results exhibited a weighted-average confusion error between pairs (considering the 12 categories of the class-level disaggregation analysis) of 0.76%, as well as a related weighted-average JMD value of 1.397. On the other hand, the results at the macro-class level showed a weighted-average error of confusion between pairs (considering the 7 categories) of 0.70% as well as its related weighted-average JMD value of 1.408 (Fig. 20). In this regard, based on a multiclass JMD analysis, our results demonstrated that higher weighted-average JMD values (considering all categories) translated to lower weighted-average errors between categories. The weighted-average error between pairs was in concordance with the relationship between JMD and the classification error that was mentioned in Lasaponara and Lanorte (2007b) and Lee and Choi (2000), which suggested a classification error probability of approximately 5% or less for a JMD value above 1.24. Additionally, the best OA achieved was related to the higher weighted-average JMD value for the analysis of 7 categories at the macro-class

level, which represents an overall misclassification rate of 4.22%. In contrast, the analysis of 12 categories at the class level rendered an overall misclassification rate of 8.4%.

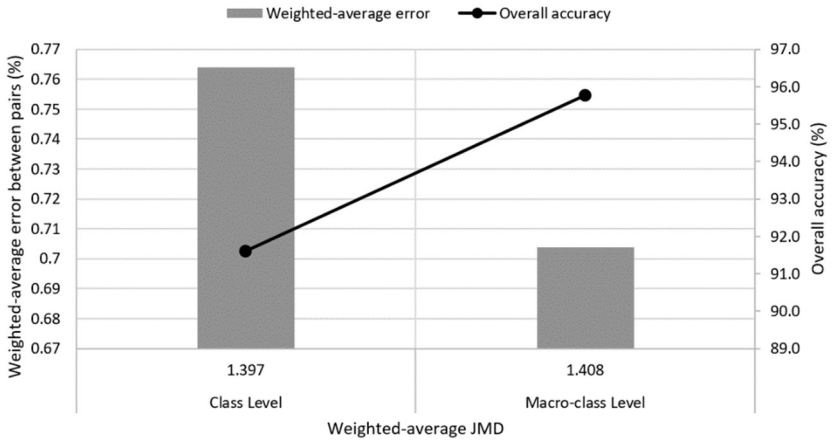

Fig. 20 Weighted-average Jeffries-Matusita distance (JMD) values at both level of analysis, weighted-average error between pairs, and final overall accuracy.

Regarding the tailored maps, we were able to design maps with very high accuracy for the main representative land cover types of the *dehesa* environment. The excellent results obtained for the overstory stratum, which was mainly comprised of holm oaks (*Quercus rotundifolia*) and had a 0.25-m UHSR resolution, allowed us to delineate the tree crown shape with high precision. Thus, the results could be very useful to calculate derived dendometric parameters of individual trees, such as crown area and crown diameter, as well as other dasometric variables related to the tree canopy cover factor and stand density. It is worth noting than shrub species were also classified with high accuracy, allowing us to study shrub cover spatial patterns, which play a crucial role in the hydrologic response of a given territory, as well as pasture productivity and tree growth (Pulido et al. 2010; Rivest et al. 2011), the occurrence of aromatic and medicinal plants and honey (Canteiro et al. 2011) and finally, but not the least important, the management of the *dehesa* ecosystem (Caballero Díaz et al. 2015; Godinho et al. 2016b).

Regarding the influence of the *ad hoc* land cover maps on the hydrologic process of the territory, the potential response of the UHSR land cover was compared with the potential response derived from a global database such as CLC. Our results, rendered a more precise estimation of the spatial distribution of the CN values, highlighting the influence of the spatial resolution, given that the global data base of CLC underestimate the potential runoff in the most representative land cover in the *dehesa* environment, such as those of broad-leaved forest, mixed forest, transitional woodland-shrub and pastures. This result, was consistent with those reported by Walega and Salata (2019) where the evaluation of the direct runoff using the NRCS-CN method was underestimated compared to the observed events. In this work, the authors pointed out that the differences strongly depend on catchment size due to the risk of over-generalization of the CLC land cover categories. In this regard, further investigation is needed, specially in Mediterranean forested watershed where a regional calibration of the CN is not yet available. Nevertheless, other works in forested areas in United States suggested uncertainties in the application of the CN lookup tables in forested watershed (Tedela et al. 2012; Walega et al. 2020).

For the classification of accurate UHSR land cover maps, the definition of reference data from fieldwork is a time-intensive, expensive, and subjective task (Ghimire et al. 2012). Image photointerpretation techniques could be used to minimize or avoid field campaigns; however, manual processing is also laborious, time-consuming, and impractical for extensive areas (Müllerová et al. 2013). In our work, we have proven the effectiveness of applying a classifier to neighboring images with similar environments that might not participate in the extraction of the training dataset, thereby reducing manual labor. Our approach uses UHSR image spectral information without further calibration, and thus reduces the need for labor-intensive field campaigns, which is especially useful in inaccessible regions. The main limitation of our proposed procedure is that images must have the same flight conditions to ensure the similarity of the spectral information.

Finally, once the UHSR images are classified for both the training and validation groups, the land cover information can be used for the definition of new training datasets for the supervised classification of HSR images, such as Sentinel or Landsat. In this regard, this approach was proposed by Paris et al. (2017) to avoid fieldwork by using the available information from another covering image of the same time series. Their methodology consisted of the definition of a "pseudo" training set from a thematic map analyzing the samples that had the highest probability of belonging to areas where no changes occurred on the ground. Finally, after a validation, these pseudo training samples could be used as training samples for supervised classification.

5 Conclusions

In this study, the vegetation of a *dehesa* environment was studied using PNOA UHSR imagery and a supervised classification algorithm based on the random forest approach. Both the overstory and understory strata were considered to obtain tailored maps of the land cover with high accuracy. During the classification process, the principal predictors were identified, demonstrating how the blue band, soil indices, and texture features were the most important classification parameters. The overstory stratum accuracy results were excellent and shrub species were also classified with high accuracy. This allows us to study shrub cover spatial patterns, which play a crucial role in pasture productivity and tree growth, the land management of the *dehesa* ecosystem, and the hydrologic response of the territory. Given that the land cover categories were also defined according to the runoff generation capability, the maps could be used as an input for future watershed hydrologic and water balance models. In addition, these maps characterize the environment in a precisely spatial distributed CN values, representing the potential runoff capability of the territory. In this sense, we found that having accurate tailored land cover maps is crucial, given that using a global land cover database, such as CLC, led to underestimating the potential runoff in the most representative land cover in the *dehesa* environment, such as those of broad-leaved forest, mixed forest, transitional woodland-shrub and pastures.

Moreover, we developed a method to reduce field campaigns by evaluating the performance of the classifier to map neighboring images that were not initially used to train the model, achieving good results. Given that our approach uses the spectral information of UHSR images without further calibration, it could be used to minimize the manual labor associated with photointerpretation and field campaigns. Future research will focus on the automatic generation of new samples extracted from classified UHSR images, which could

be used as training datasets for the future supervised classification of other HSR images, such as Sentinel imagery. Furthermore, future investigation is also needed to assess the regional calibration of the CN values of HSR land cover images in Mediterranean forested watershed.

References

Adam E, Mutanga O, Odindi J, Abdel-Rahman EM (2014) Land-use/cover classification in a heterogeneous coastal landscape using RapidEye imagery: evaluating the performance of random forest and support vector machines classifiers International Journal of Remote Sensing 35:3440-3458 doi:10.1080/01431161.2014.903435

Ahmed OS, Franklin SE, Wulder MA, White JC (2015) Characterizing stand-level forest canopy cover and height using Landsat time series, samples of airborne LiDAR, and the random forest algorithm ISPRS Journal of Photogrammetry and Remote Sensing 101:89-101 doi:10.1016/j.isprsjprs.2014.11.007

Akike S, Samanta S (2016) Land Use/Land Cover and Forest Canopy Density Monitoring of Wafi-Golpu Project Area, Papua New Guinea Journal of Geoscience and Environment Protection 4:1 doi:10.4236/gep.2016.48001

Athira P, Sudheer KP, Cibin R, Chaubey I (2016) Predictions in ungauged basins: an approach for regionalization of hydrological models considering the probability distribution of model parameters Stochastic environmental research and risk assessment 30:1131-1149 doi:10.1007/s00477-015-1190-6

Becker R, Koppa A, Schulz S, Usman M, Beek Tad, Schüth C (2019) Spatially distributed model calibration of a highly managed hydrological system using remote sensing-derived ET data Journal of Hydrology 577:123944 doi:10.1016/j.jhydrol.2019.123944

Boggs GS (2010) Assessment of SPOT 5 and QuickBird remotely sensed imagery for mapping tree cover in savannas International journal of applied earth observation and geoinformation 12:217-224 doi:10.1016/j.jag.2009.11.001

Bolton DK, White JC, Wulder MA, Coops NC, Hermosilla T, Yuan X (2018) Updating stand-level forest inventories using airborne laser scanning and Landsat time series data International Journal of Applied Earth Observation and Geoinformation 66:174-183 doi:10.1016/j.jag.2017.11.016

Borlaf-Mena I, Tanase MA, Gómez-Sal A (2019) Methods for tree cover extraction from high resolution orthophotos and airborne LiDAR scanning in Spanish dehesas Revista de Teledetección:17-32 doi:10.4995/raet.2019.11320

Breiman L (2001) Random forests Machine learning 45:5-32 doi:10.1023/A:1010933404324

Burnett MW, White TD, McCauley DJ, De Leo GA, Micheli F (2019) Quantifying coconut palm extent on Pacific islands using spectral and textural analysis of very high resolution imagery International Journal of Remote Sensing 40:7329-7355 doi:10.1080/01431161.2019.1594440

Caballero Díaz J, Pérez F, Manuel A, Quirós Rosado E (2015) A state-and-transition model of Iberian dehesas based on spatial patterns Forest Systems 24 doi:10.5424/fs/2015242-06408

Campos I, Gonzalez-Piqueras J, Carrara A, Villodre J, Calera A (2016) Estimation of total available water in the soil layer by integrating actual evapotranspiration data in a remote sensing-driven soil water balance Journal of Hydrology 534:427-439 doi:10.1016/j.jhydrol.2016.01.023

Campos I, Villodre J, Carrara A, Calera A (2013) Remote sensing-based soil water balance to estimate Mediterranean holm oak savanna (dehesa) evapotranspiration under water stress conditions Journal of hydrology 494:1-9 doi:10.1016/j.jhydrol.2013.04.033

Canteiro C, Pinto-Cruz C, Simões MP, Gazarini L (2011) Conservation of Mediterranean oak woodlands: understorey dynamics under different shrub management Agroforestry Systems 82:161-171 doi:10.1007/s10457-011-9375-6

Cantero Fauquier F, Tomé Morán J, Bravo Fernández J, Fernández-Landa A (2017) Herramientas de localización de árboles individuales con el módulo de procesado de QGIS a partir de información LiDAR y ortofotografía aérea. Paper presented at the 7º Congreso Forestal Español "Gestión del monte: servicios ambientales y bioeconomía", Plasencia, Cáceres (Spain), 26-30 junio

Carreiras JM, Pereira JM, Pereira JS (2006) Estimation of tree canopy cover in evergreen oak woodlands using remote sensing Forest ecology and management 223:45-53 doi:10.1016/j.foreco.2005.10.056

Castillejo-González IL, Medina Guerrero J, García-Ferrer Porras A, Mesas-Carrascosa FJ, Sánchez de la Orden M (2010) Utilización de imágenes de satélite de alta resolución espacial en la determinación de la fracción de cabida cubierta en sistemas adehesados. Paper presented at the XIV Congreso Nacional de Tecnologías de la Información Geográfica La información geográfica al servicio de los ciudadanos: de lo global a lo local, Sevilla (Spain),

Castillo JAA, Apan AA, Maraseni TN, Salmo III SG (2017) Estimation and mapping of above-ground biomass of mangrove forests and their replacement land uses in the Philippines using Sentinel imagery ISPRS Journal of Photogrammetry and Remote Sensing 134:70-85 doi:10.1016/j.isprsjprs.2017.10.016

Ceballos A, Schnabel S (1998) Hydrological behaviour of a small catchment in the dehesa landuse system (Extremadura, SW Spain) Journal of Hydrology 210:146-160 doi:10.1016/S0022-1694(98)00180-2

Cerda A, Schnabel S, Ceballos A, Gomez-Amelia D (1998) Soil hydrological response under simulated rainfall in the Dehesa land system (Extremadura, SW Spain) under drought conditions Earth Surface Processes and Landforms: The Journal of the British Geomorphological Group 23:195-209 doi:10.1002/(SICI)1096-9837(199803)23:3<195::AID-ESP830>3.0.CO;2-I

Chen H, Liang Q, Liang Z, Liu Y, Xie S (2019a) Remote-sensing disturbance detection index to identify spatio-temporal varying flood impact on crop production Agricultural and Forest Meteorology 269:180-191 doi:10.1016/j.agrformet.2019.02.002

Chen T et al. (2019b) Merging ground and satellite-based precipitation data sets for improved hydrological simulations in the Xijiang River basin of China Stochastic Environmental Research and Risk Assessment 33:1893-1905 doi:10.1007/s00477-019-01731-w

Chymyrov A, Betz F, Baibagyshov E, Kurban A, Cyffka B, Halik U (2018) Floodplain Forest Mapping with Sentinel-2 Imagery: Case Study of Naryn River, Kyrgyzstan. In: Vegetation of Central Asia and Environs. Springer, pp 335-347

Congalton RG, Green K (2008) Assessing the accuracy of remotely sensed data: principles and practices. CRC press,

Conrad O (2010) SAGA-GIS Module Library Documentation (v2.2.0)

Module Majority Filter. http://www.saga-gis.org/saga_tool_doc/2.2.0/grid_filter_6.html. Accessed October 2019

Dalponte M, Bruzzone L, Gianelle D (2012) Tree species classification in the Southern Alps based on the fusion of very high geometrical resolution multispectral/hyperspectral images and LiDAR data Remote sensing of environment 123:258-270 doi:10.1016/j.rse.2012.03.013

Dalponte M, Bruzzone L, Vescovo L, Gianelle D (2009) The role of spectral resolution and classifier complexity in the analysis of hyperspectral images of forest areas Remote Sensing of Environment 113:2345-2355 doi:10.1016/j.rse.2009.06.013

Dalponte M, Ørka HO (2016) varSel: Sequential Forward Floating Selection using Jeffries-Matusita Distance, R package version 0.1 edn.,

Dalponte M, Ørka HO, Ene LT, Gobakken T, Næsset E (2014) Tree crown delineation and tree species classification in boreal forests using hyperspectral and ALS data Remote sensing of environment 140:306-317 doi:10.1016/j.rse.2013.09.006

Devesa Alcaraz JA (1995) Vegetación y flora de Extremadura. Universitas Editorial,

Dias LCP, Macedo MN, Costa MH, Coe MT, Neill C (2015) Effects of land cover change on evapotranspiration and streamflow of small catchments in the Upper Xingu River Basin, Central Brazil Journal of Hydrology: Regional Studies 4:108-122 doi:10.1016/j.ejrh.2015.05.010

Diaz M, Campos P, Pulido FJ (1997) The Spanish dehesas: a diversity in land-use and wildlife. In: Pain D, Pienkowski M (eds) Farming and birds in Europe. Academic Press, London, pp 178-209

Dionizio EA, Costa MH (2019) Influence of land use and land cover on hydraulic and physical soil properties at the cerrado agricultural frontier Agriculture 9:24 doi:10.3390/agriculture9010024

Dou X, Song J, Wang L, Tang B, Xu S, Kong F, Jiang X (2018) Flood risk assessment and mapping based on a modified multi-parameter flood hazard index model in the Guanzhong Urban Area, China Stochastic environmental research and risk assessment 32:1131-1146 doi:10.1007/s00477-017-1429-5

Durán-Barroso P, González J, Valdés JB (2016) Improvement of the integration of Soil Moisture Accounting into the NRCS-CN model Journal of Hydrology 542:809-819 doi:10.1016/j.jhydrol.2016.09.053

Eriksson HM, Eklundh L, Kuusk A, Nilson T (2006) Impact of understory vegetation on forest canopy reflectance and remotely sensed LAI estimates Remote Sensing of Environment 103:408-418 doi:10.1016/j.rse.2006.04.005

Eroğlu H, Çakır G, Sivrikaya F, Akay AE (2010) Using high resolution images and elevation data in classifying erosion risks of bare soil areas in the Hatila Valley Natural Protected Area, Turkey Stochastic environmental research and risk assessment 24:699-704 doi:10.1007/s00477-009-0356-5

Escadafal R (1993) Remote sensing of soil color: principles and applications Remote Sensing Reviews 7:261-279 doi:10.1080/02757259309532181

Escadafal R, Huete A (1991) Etude des propriétés spectrales des sols arides appliquée à l'amélioration des indices de végétation obtenus par télédétection Comptes rendus de l'Académie des sciences Série 2, Mécanique, Physique, Chimie, Sciences de l'univers, Sciences de la Terre 312:1385-1391

Fang F, McNeil BE, Warner TA, Maxwell AE (2018) Combining high spatial resolution multi-temporal satellite data with leaf-on LiDAR to enhance tree species discrimination at the crown level International journal of remote sensing 39:9054-9072 doi:10.1080/01431161.2018.1504343

Fassnacht FE et al. (2016) Review of studies on tree species classification from remotely sensed data Remote Sensing of Environment 186:64-87 doi:10.1016/j.rse.2016.08.013

Fassnacht FE, Mangold D, Schaefer J, Immitzer M, Kattenborn T, Koch B, Latifi H (2017) Estimating stand density, biomass and tree species from very high resolution stereo-imagery - towards an all-in-one sensor for forestry applications? Forestry 90:613-631 doi:10.1093/forestry/cpx014

Ferreira MP, Zortea M, Zanotta DC, Shimabukuro YE, Filho CRdS (2016) Mapping tree species in tropical seasonal semi-deciduous forests with hyperspectral and multispectral data Remote Sensing of Environment 179:66-78 doi:10.1016/j.rse.2016.03.021

Ferrer i Juliá M (2003) Análisis de nuevas fuentes de datos para la estimación del parámetro número de curva: perfiles de suelos y teledetección. Monografía C48. CEDEX,

Fragoso-Campón L, Quirós E, Mora J, Gutiérrez Gallego JA, Durán-Barroso P (2019) Overstory-understory land cover mapping at the watershed scale: accuracy enhancement by multitemporal remote sensing analysis and LiDAR Environmental Science and Pollution Research:1-14 doi:10.1007/s11356-019-04520-8

Fragoso L, Quirós E, Durán-Barroso P (2017) Resource communication: Variability in estimated runoff in a forested area based on different cartographic data sources Forest Systems 26:02

Franklin J (2010) Mapping species distributions: spatial inference and prediction. Cambridge University Press, United State of America, New York

Gao B-C (1996) NDWI—A normalized difference water index for remote sensing of vegetation liquid water from space Remote sensing of environment 58:257-266

García M, Riaño D, Chuvieco E, Salas J, Danson FM (2011) Multispectral and LiDAR data fusion for fuel type mapping using Support Vector Machine and decision rules Remote Sensing of Environment 115:1369-1379 doi:10.1016/j.rse.2011.01.017

Garcia M, Saatchi S, Ferraz A, Silva CA, Ustin S, Koltunov A, Balzter H (2017) Impact of data model and point density on aboveground forest biomass estimation from airborne LiDAR Carbon balance and management 12:4 doi:10.1186/s13021-017-0073-1

GDAL-documentation (2019) gdal_sieve. https://gdal.org/programs/gdal_sieve.html. Accessed October 2019

Ghimire B, Rogan J, Galiano VR, Panday P, Neeti N (2012) An evaluation of bagging, boosting, and random forests for land-cover classification in Cape Cod, Massachusetts, USA GIScience & Remote Sensing 49:623-643 doi:10.2747/1548-1603.49.5.623

Ghosh A, Fassnacht FE, Joshi PK, Koch B (2014) A framework for mapping tree species combining hyperspectral and LiDAR data: Role of selected classifiers and sensor across three spatial scales

International Journal of Applied Earth Observation and Geoinformation 26:49-63 doi:10.1016/j.jag.2013.05.017

Godinho S, Gil A, Guiomar N, Costa MJ, Neves N (2016a) Assessing the role of Mediterranean evergreen oaks canopy cover in land surface albedo and temperature using a remote sensing-based approach Applied Geography 74:84-94 doi:10.1016/j.apgeog.2016.07.004

Godinho S, Guiomar N, Gil A (2017) Estimating tree canopy cover percentage in a mediterranean silvopastoral systems using Sentinel-2A imagery and the stochastic gradient boosting algorithm International Journal of Remote Sensing:1-23 doi:10.1080/01431161.2017.1399480

Godinho S et al. (2016b) Assessment of environment, land management, and spatial variables on recent changes in montado land cover in southern Portugal Agroforestry Systems 90:177-192 doi:10.1007/s10457-014-9757-7

Hall-Beyer M (2017) Practical guidelines for choosing GLCM textures to use in landscape classification tasks over a range of moderate spatial scales International Journal of Remote Sensing 38:1312-1338 doi:10.1080/01431161.2016.1278314

Haralick RM, Shanmugam K (1973) Textural features for image classification IEEE Transactions on systems, man, and cybernetics:610-621 doi:10.1109/TSMC.1973.4309314

Hastie T, Tibshirani R, Friedman J (2009) The elements of statistical learning: data mining, inference, and prediction. In. Springer Science & Business Media, pp 587-601. doi:10.1007/b94608

Hawryło P, Wężyk P (2018) Predicting growing stock volume of scots pine stands using Sentinel-2 satellite imagery and airborne image-derived point clouds Forests 9:274 doi:10.3390/f9050274

Hernández-López D, Felipe-García B, González-Aguilera D, Arias-Pérez B (2013) Web-based spatial data infrastructure: a solution for the sustainable management of thematic information supported by aerial orthophotography Dyna 80:123-131

Hijmans RJ (2019) raster: Geographic Data Analysis and Modeling., R package version 2.9-5. edn.,

Huete A (1988) A soil-adjusted vegetation index (SAVI) Remote Sensing of Environment 25:259-309 doi:10.1016/0034-4257(88)90106-X

Huete AR, Post DF, Jackson RD (1984) Soil spectral effects on 4-space vegetation discrimination Remote sensing of environment 1984 v.15 no.2:pp. 155-165 doi:10.1016/0034-4257(84)90043-9

IGN Centro de Descargas.

Centro Nacional de Información Geográfica. http://centrodedescargas.cnig.es/CentroDescargas/index.jsp. Accessed Julio 2019

Immitzer M, Vuolo F, Atzberger C (2016) First experience with Sentinel-2 data for crop and tree species classifications in central Europe Remote Sensing 8:166 doi:10.3390/rs8030166

Joffre R, Rambal S (1993) How tree cover influences the water balance of Mediterranean rangelands Ecology 74:570-582 doi:10.2307/1939317

Kim S-R, Lee W-K, Kwak D-A, Biging G, Gong P, Lee J-H, Cho H-K (2011) Forest cover classification by optimal segmentation of high resolution satellite imagery Sensors 11:1943-1958 doi:10.3390/s110201943

Kuhn M et al. (2018) caret: Classification and Regression Training., R package version 6.0-81. edn.,

Labrador García M, Évora Brondo JA, Arbelo Pérez M (2012) Satélites de Teledetección para la Gestión del Territorio.

Landry S, St-Laurent M-H, Nelson PR, Pelletier G, Villard M-A (2018) Canopy Cover Estimation from Landsat Images: Understory Impact onTop-of-canopy Reflectance in a Northern Hardwood Forest Canadian Journal of Remote Sensing 44:435-446 doi:10.1080/07038992.2018.1533399

Lasaponara R, Lanorte A (2007a) On the capability of satellite VHR QuickBird data for fuel type characterization in fragmented landscape Ecological Modelling 204:79-84 doi:10.1016/j.ecolmodel.2006.12.022

Lasaponara R, Lanorte A On the spectral separability of Prometheus fuel types in the Mediterranean ecosystems of the Italian Peninsula. In: Gitas I, Carmona-Moreno C (eds) Proceedings of the 6th International Workshop of The EARSeL Special Interest Group On Forest Fires - Advances in Remote Sensing and GIS Applications in Forest Fire Management: Towards An Operational Use of Remote Sensing in Forest Fire Management, Thessaloniki (Greece) 27-29 September 2007 2007b. European Commission. Joint Research Centre.

Institute for Environment and Sustainability, pp 115-118

Lavado Contador JF, Jariego García A, Schnabel S, Gómez Gutiérrez Á (2012) Análisis de la evolución histórica del arbolado de la dehesa mediante fotointerpretación y análisis OBIA. Paper presented at the Tecnologías de la información geográfica en el contexto del cambio global: XV Congreso Nacional de Tecnologías de Información Geográfica, Madrid (Spain), 19 al 21 de septiembre de 2012

Lee C, Choi E (2000) Bayes error evaluation of the Gaussian ML classifier IEEE Transactions on Geoscience and Remote Sensing 38:1471-1475 doi:10.1109/36.843045

Li A et al. (2017) Lidar aboveground vegetation biomass estimates in shrublands: Prediction, uncertainties and application to coarser scales Remote Sensing 9:903 doi:10.3390/rs9090903

Liaw A, Wiener M (2002) Classification and Regression by randomForest.

Lima de Almeida C, Anchiêta de Carvalho TR, de Araújo JC (2019) Leaf area index of Caatinga biome and its relationship with hydrological and spectral variables Agricultural and Forest Meteorology 279:107705 doi:10.1016/j.agrformet.2019.107705

Magiera A, Feilhauer H, Tephnadze N, Waldhardt R, Otte A (2016) Separating reflectance signatures of shrub species - a case study in the Central Greater Caucasus Applied Vegetation Science 19:304-315 doi:10.1111/avsc.12205

Malahlela OE, Cho MA, Mutanga O (2015) Mapping the occurrence of Chromolaena odorata (L.) in subtropical forest gaps using environmental and remote sensing data Biological Invasions 17:2027-2042 doi:10.1007/s10530-015-0858-7

Mas J-F, Gao Y, Navarrete Pacheco JA (2010) Sensitivity of landscape pattern metrics to classification approaches Forest Ecology and Management 259:1215-1224 doi:10.1016/j.foreco.2009.12.016

Mathieu R, Pouget M, Cervelle B, Escadafal R (1998) Relationships between satellite-based radiometric indices simulated using laboratory reflectance data and typic soil color of an arid environment Remote sensing of environment 66:17-28 doi:10.1016/S0034-4257(98)00030-3

Melesse AM, Shih SF (2002) Spatially distributed storm runoff depth estimation using Landsat images and GIS Computers and Electronics in Agriculture 37:173-183 doi:10.1016/S0168-1699(02)00111-4

Ministerio de Fomento (2016) Instrucción de Carreteras norma 5.2 - IC drenaje superficial.

Ministerio de Fomento (2019) Plan Nacional de Observación del Territorio. Plan Nacional de Ortofotografía Aerea (PNOA). http://pnoa.ign.es/presentacion. Accessed 22 abril 2019

Müllerová J, Pergl J, Pyšek P (2013) Remote sensing as a tool for monitoring plant invasions: Testing the effects of data resolution and image classification approach on the detection of a model plant species Heracleum mantegazzianum (giant hogweed) International Journal of Applied Earth Observation and Geoinformation 25:55-65 doi:10.1016/j.jag.2013.03.004

Mura M et al. (2018) Exploiting the capabilities of the Sentinel-2 multi spectral instrument for predicting growing stock volume in forest ecosystems International journal of applied earth observation and geoinformation 66:126-134 doi:10.1016/j.jag.2017.11.013

Netzer MS, Sidman G, Pearson TR, Walker SM, Srinivasan R (2019) Combining global remote sensing products with hydrological modeling to measure the impact of tropical forest loss on water-based ecosystem services Forests 10:413 doi:10.3390/f10050413

Niphadkar M, Nagendra H, Tarantino C, Adamo M, Blonda P (2017) Comparing pixel and object-based approaches to map an understorey invasive shrub in tropical mixed forests Frontiers in plant science 8:892 doi:10.3389/fpls.2017.00892

Niu J, Sivakumar B (2014) Study of runoff response to land use change in the East River basin in South China Stochastic environmental research and risk assessment 28:857-865 doi:10.1007/s00477-013-0690-5

Nizami SM, Yiping Z, Zheng Z, Zhiyun L, Guoping Y, Liqing S (2017) Evaluation of forest structure, biomass and carbon sequestration in subtropical pristine forests of SW China Environmental Science and Pollution Research 24:8137-8146 doi:10.1007/s11356-017-8506-7

Nomura K, Mitchard E (2018) More Than Meets the Eye: Using Sentinel-2 to Map Small Plantations in Complex Forest Landscapes Remote Sensing 10:1693 doi:10.3390/rs10111693

NRCS (2004) Chapter 9: Hydrologic Soil-Cover Complexes. In: NRCS National Engineering Handbook, Part 630: Hydrology. Engineering Division, US. Department of Agriculture

Washington, DC,

NRCS (2009) National Engineering Handbook, section 4, Hydrology, version (1956, 1964, 1971, 1985, 1993, 2004, 2009). National Engineering Handbook. Engineering Division, US. Department of Agriculture, Washington, DC

Olea L, López-Bellido R, Poblaciones M (2005) European types of silvopastoral systems in the Mediterranean area: dehesa Silvopastoralism and sustainable land management CABI, Oxfordshire:30-35

Olea L, San Miguel-Ayanz A The Spanish dehesa. A traditional Mediterranean silvopastoral system linking production and nature conservation. In: Sustainable Grassland Productivity, Badajoz (Spain), 2006. Sociedad Española para el Estudio de los Pastos

(S.E.E.P.), pp 3-13

Paris C, Bruzzone L, Fernández-Prieto D A novel automatic approach to the update of land-cover maps by unsupervised classification of remote sensing images. In: Geoscience and Remote Sensing Symposium (IGARSS), 2017 IEEE International, 2017. IEEE, pp 2207-2210. doi:10.1109/IGARSS.2017.8127426

Petroselli A, Grimaldi S (2018) Design hydrograph estimation in small and fully ungauged basins: a preliminary assessment of the EBA4SUB framework Journal of Flood Risk Management 11:S197-S210 doi:10.1111/jfr3.12193

Psomiadis E, Soulis KX, Efthimiou N (2020) Using SCS-CN and Earth Observation for the Comparative Assessment of the Hydrological Effect of Gradual and Abrupt Spatiotemporal Land Cover Changes Water 12:1386 doi:10.3390/w12051386

Pulido-Fernández M, Schnabel S, Lavado-Contador JF, Mellado IM, Pérez RO (2013) Soil organic matter of Iberian open woodland rangelands as influenced by vegetation cover and land management Catena 109:13-24 doi:10.1016/j.catena.2013.05.002

Pulido F, García E, Obrador JJ, Moreno G (2010) Multiple pathways for tree regeneration in anthropogenic savannas: incorporating biotic and abiotic drivers into management schemes Journal of Applied Ecology 47:1272-1281 doi:10.1111/j.1365-2664.2010.01865.x

Qi J, Chehbouni A, Huete A, Kerr Y, Sorooshian S (1994) A modified soil adjusted vegetation index Remote sensing of environment 48:119-126 doi:10.1016/0034-4257(94)90134-1

Qi Z-F, Ye X-Y, Zhang H, Yu Z-L (2014) Land fragmentation and variation of ecosystem services in the context of rapid urbanization: the case of Taizhou city, China Stochastic environmental research and risk assessment 28:843-855 doi:10.1007/s00477-013-0721-2

R-Core-Team (2018) R: A language and environment for statistical computing. R Foundation for Statistical Computing, Vienna (Austria)

Riaño D et al. (2007) Estimation of shrub height for fuel-type mapping combining airborne LiDAR and simultaneous color infrared ortho imaging International Journal of Wildland Fire 16:341-348 doi:10.1071/WF06003

Richardson AJ, Wiegand C (1977) Distinguishing vegetation from soil background information Photogrammetric engineering and remote sensing 43:1541-1552

Rivas-Martinez S, Rivas-Saenz S (1996-2019) Worldwide Bioclimatic Classification System. http://www.globalbioclimatics.org/form/tb_map/index.htm. Accessed July 2019

Rivest D, Rolo V, López-Díaz L, Moreno G (2011) Shrub encroachment in Mediterranean silvopastoral systems: Retama sphaerocarpa and Cistus ladanifer induce contrasting effects on pasture and Quercus ilex production Agriculture, ecosystems & environment 141:447-454 doi:10.1016/j.agee.2011.04.018

Rodriguez-Veiga P, Wheeler J, Louis V, Tansey K, Balzter H (2017) Quantifying Forest Biomass Carbon Stocks From Space Current Forestry Reports 3:1-18 doi:10.1007/s40725-017-0052-5

Rouse Jr J, Haas R, Schell J, Deering D (1974) Monitoring vegetation systems in the Great Plains with ERTS. Paper presented at the Third Earth Resources Technology Satellite-1 Symposium, Washington, D.C.,

Santos-Silva C, Gonçalves A, Louro R (2011) Canopy cover influence on macrofungal richness and sporocarp production in montado ecosystems Agroforestry systems 82:149-159 doi:10.1007/s10457-011-9374-7

Stavrakoudis D, Dragozi E, Gitas I, Karydas C (2014) Decision fusion based on hyperspectral and multispectral satellite imagery for accurate forest species mapping Remote Sensing 6:6897-6928 doi:10.3390/rs6086897

Su T-C (2016) A filter-based post-processing technique for improving homogeneity of pixel-wise classification data European Journal of Remote Sensing 49:531-552 doi:10.5721/EuJRS20164928

Tedela NH et al. (2012) Runoff Curve Numbers for 10 small forested watersheds in the mountains of the Eastern United States Journal of Hydrologic Engineering 17:1188-1198 doi:10.1061/(ASCE)HE.1943-5584.0000436.

Tuanmu M-N, Viña A, Bearer S, Xu W, Ouyang Z, Zhang H, Liu J (2010) Mapping understory vegetation using phenological characteristics derived from remotely sensed data Remote Sensing of Environment 114:1833-1844 doi:10.1016/j.rse.2010.03.008

Van der Sande C, De Jong S, De Roo A (2003) A segmentation and classification approach of IKONOS-2 imagery for land cover mapping to assist flood risk and flood damage assessment International Journal of applied earth observation and geoinformation 4:217-229 doi:10.1016/S0303-2434(03)00003-5

van Lier OR, Fournier RA, Bradley RL, Thiffault N (2009) A multi-resolution satellite imagery approach for large area mapping of ericaceous shrubs in Northern Quebec, Canada International Journal of Applied Earth Observation and Geoinformation 11:334-343 doi:10.1016/j.jag.2009.05.003

Vila-García D, Gil-Docampo M, Iniesto-Alba M (2015) Change detection in land use from unsupervised classifications for updating SIOSE. Implementation in Galicia Revista de Teledetección:63-76 doi:10.4995/raet.2015.3409

Walega A, Amatya DM, Caldwell P, Marion D, Panda S (2020) Assessment of storm direct runoff and peak flow rates using improved SCS-CN models for selected forested watersheds in the Southeastern United States Journal of Hydrology: Regional Studies 27:100645 doi:10.1016/j.ejrh.2019.100645

Walega A, Salata T (2019) Influence of land cover data sources on estimation of direct runoff according to SCS-CN and modified SME methods Catena 172:232-242 doi:10.1016/j.catena.2018.08.032

Wang H et al. (2019) Landscape-level vegetation classification and fractional woody and herbaceous vegetation cover estimation over the dryland ecosystems by unmanned aerial vehicle platform Agricultural and forest meteorology 278:107665 doi:10.1016/j.agrformet.2019.107665

Zhao Y et al. (2016) Detailed dynamic land cover mapping of Chile: Accuracy improvement by integrating multi-temporal data Remote sensing of environment 183:170-185 doi:10.1016/j.rse.2016.05.016

Zhou P, Huang J, Pontius RG, Hong H (2014) Land classification and change intensity analysis in a coastal watershed of Southeast China Sensors 14:11640-11658 doi:10.3390/s140711640

3.4. Publicación N.º 4

Publicación	**Optimization of land cover mapping through improvements in Sentinel-1 and Sentinel-2 image dimensionality and data mining feature selection for hydrological modeling**				
Autores	**Fragoso-Campón, Laura** · Quirós, Elia · Gutiérrez Gallego, José Antonio				
Revista	Stochastic Environmental Research and Risk Assessment (2021) *Published online: 17 april 2021*				
eISSN	1436-3259				
DOI	10.1007/s00477-021-02014-z				
Fuente de Impacto	Índice 5 años	Índice 2019	Categoría	Rank	Cuartil
WOS (JCR)	2.721	2.351	Statistics and Probability	21/124	Q1
			Water Science and Technology	37/94	Q2
			Civil Engineering	45/134	Q2
Aportación de la doctoranda:	Conceptualización, metodología, programas informáticos, análisis formal, investigación, redacción-borrador original, redacción-revisión y edición de la versión final.				

Stochastic Environmental Research and Risk Assessment
https://doi.org/10.1007/s00477-021-02014-z

ORIGINAL PAPER

Optimization of land cover mapping through improvements in Sentinel-1 and Sentinel-2 image dimensionality and data mining feature selection for hydrological modeling

Laura Fragoso-Campón[1] · Elia Quirós[1] · José Antonio Gutiérrez Gallego[1]

Accepted: 27 March 2021

Abstract
The characterization of land cover in a watershed has a remarkable influence on the water balance and, is a key factor in assessing complex hydrological models at the regional scale. Here, a method is proposed to generate accurate seasonal ad hoc land cover maps from a hydrological standpoint based on the runoff generation capabilities of the land cover types using remote sensing techniques with Sentinel-1 and Sentinel-2 data and a random forest approach. A multidate study is proposed, minimizing the images as much as possible: one single date for Sentinel-2 data and two dates for Sentinel-1 data. Then, the dimensionality of the satellite data is improved with texture metrics and derived spectral indices, after which a data mining feature selection is conducted through optimization of the classification algorithm, ensuring the accuracy of the final maps. The overall accuracies are remarkably high (93.29%) for the test dataset and still outstanding (85.24%) for the validation dataset. The texture metrics are the most important classification parameters and are mainly derived from VIS (B2 and B3), NIR (B5 and B6) and SWIR (B11). The results outperformed previous works that used large temporal image series and reduced the storage capacity requirements and computational time. Consequently, the hydrological response of the watersheds in terms of NRCS-CN is characterized truthfully, allowing the analysis of the potential runoff and its variation due to seasonal phenology. Future research will be focused on the analysis of rainfall-runoff models and the variability in seasonal runoff in forested watersheds in Mediterranean environments.

Keywords Land use · NRCS Curve number · Remote sensing · Runoff · SAR · Water resources

1 Introduction

Current trends in hydrological analysis require remote sensing data as input, such as digital terrain models, meteorological data, and soil and land cover maps (Athira et al. 2016; Becker et al. 2019; Chen et al. 2019; Martínez-Salvador and Conesa-García 2020; Parajuli et al. 2018). Among all parameters, vegetation has a remarkable influence on the water balance of a watershed (Astuti et al. 2019; Sajikumar and Remya 2015), and it is necessary to know the spatial distribution of the vegetation cover to assess complex hydrological models because vegetation cover is related to quite a few aspects, such as evapotranspiration, runoff, interflow, and infiltration capability (Becker et al. 2019; Dias et al. 2015; Dionizio and Costa 2019; Luan et al. 2018; Netzer et al. 2019; Parajuli et al. 2018). In a recent review by Marin et al. (2020), the performance of Soil and Water Assessment Tool (SWAT) models in small forested watersheds was analyzed, and the authors suggested that the Soil Conservation Service (SCS) runoff curve number (CN) was reported as one of the most sensitive parameters in the hydrologic processes in all the analyzed studies. The SCS-CN is dependent on land cover (land use and treatment class) and soil type (NRCS 2004).

Land cover maps, if available, can be obtained from public national databases or other global projects, and this information is usually provided at a coarse spatial

✉ Laura Fragoso-Campón
laurafragoso@unex.es

Elia Quirós
equiros@unex.es

José Antonio Gutiérrez Gallego
jagutier@unex.es

[1] Department of Graphic Expression, Universidad de Extremadura, Escuela Politécnica, Avda. Universidad s/n, 10003 Cáceres, Spain

Published online: 17 April 2021

Optimization of land cover mapping through improvements in Sentinel-1 and Sentinel-2 image dimensionality and data mining feature selection for hydrological modeling

Laura Fragoso-Campón [a,*], Elia Quirós [a], José Antonio Gutiérrez Gallego [a]

[a] Department of Graphic Expression, Universidad de Extremadura, Escuela Politécnica, Avda. Universidad s/n, 10003 Cáceres, Spain

laurafragoso@unex.es (orcid ID: 0000-0003-0397-6247), equiros@unex.es (orcid ID: 0000-0002-8429-045X), jagutier@unex.es (orcid ID: 0000-0002-2375-7087)

*Corresponding author: laurafragoso@unex.es

Abstract

The characterization of land cover in a watershed has a remarkable influence on the water balance and, is a key factor in assessing complex hydrological models at the regional scale. Here, a method is proposed to generate accurate seasonal *ad hoc* land cover maps from a hydrological standpoint based on the runoff generation capabilities of the land cover types using remote sensing techniques with Sentinel-1 and Sentinel-2 data and a random forest approach. A multidate study is proposed, minimizing the images as much as possible: one single date for Sentinel-2 data and two dates for Sentinel-1 data. Then, the dimensionality of the satellite data is improved with texture metrics and derived spectral indices, after which a data mining feature selection is conducted through optimization of the classification algorithm, ensuring the accuracy of the final maps. The overall accuracies are remarkably high (93.29%) for the test dataset and still outstanding (85.24%) for the validation dataset. The texture metrics are the most important classification parameters and are mainly derived from VIS (B2 and B3), NIR (B5 and B6) and SWIR (B11). The results outperformed previous works that used large temporal image series and reduced the storage capacity requirements and computational time. Consequently, the hydrological response of the watersheds in terms of NRCS-CN is characterized truthfully, allowing the analysis of the potential runoff and its variation due to seasonal phenology. Future research will be focused on the analysis of rainfall-runoff models and the variability in seasonal runoff in forested watersheds in Mediterranean environments.

Keywords: Land use, NRCS Curve number, Remote sensing, Runoff, SAR, Water resources.

Declarations:

- **Funding:** This research was funded by the Junta de Extremadura and the European Social Fund: A way of doing Europe, through the "Financing of Predoctoral Contracts for the Training of Doctors in Public Research and Development Centers belonging to the Extremadura System of Science, Technology, and Innovation [file PD16018]." This work was also supported by the Government of Extremadura (Spain) and co-funded by the European Regional Development Fund under Grants GR18052 (DESOSTE) and

GR18028 (KRAKEN). We thank the Junta de Extremadura (CICTEX) for providing the necessary high-resolution PNOA ortophotographs (PNOA 2016-CC-BY 4.0 scne.es). We thank the European Soil Data Centre (ESDAC) for providing the data about the topsoil physical properties for Europe.

- **Conflicts of interest/Competing interests:** The authors declare that they have no known competing financial interests or personal relationships that could have influenced the work reported in this paper.
- **Availability of data and material:** Online Resources.
- **Code availability:** Not applicable.
- **Authors' contributions: L. Fragoso-Campón:** Conceptualization, Methodology, Software, Formal analysis, Investigation, Writing - Original Draft, Writing - Review & Editing. **E. Quirós:** Conceptualization, Methodology, Resources, Writing - Original Draft, Writing - Review & Editing, Supervision. **J. A. Gutiérrez Gallego:** Resources, Writing - Review & Editing.

1 Introduction

Current trends in hydrological analysis require remote sensing data as input, such as digital terrain models, meteorological data, and soil and land cover maps (Athira et al. 2016; Becker et al. 2019; Chen et al. 2019; Martínez-Salvador and Conesa-García 2020; Parajuli et al. 2018). Among all parameters, vegetation has a remarkable influence on the water balance of a watershed (Astuti et al. 2019; Sajikumar and Remya 2015), and it is necessary to know the spatial distribution of the vegetation cover to assess complex hydrological models because vegetation cover is related to quite a few aspects, such as evapotranspiration, runoff, interflow, and infiltration capability (Becker et al. 2019; Dias et al. 2015; Dionizio and Costa 2019; Luan et al. 2018; Netzer et al. 2019; Parajuli et al. 2018). In a recent review by Marin et al. (2020), the performance of Soil and Water Assessment Tool (SWAT) models in small forested watersheds was analyzed, and the authors suggested that the Soil Conservation Service (SCS) runoff curve number (CN) was reported as one of the most sensitive parameters in the hydrologic processes in all the analyzed studies. The SCS-CN is dependent on land cover (land use and treatment class) and soil type (NRCS 2004).

Land cover maps, if available, can be obtained from public national databases or other global projects, and this information is usually provided at a coarse spatial resolution. However, as suggested by Sajikumar and Remya (2015), the coarse resolution of global maps may not be appropriate when addressing a regional analysis, in which maps with high spatial resolution are required and it is necessary to have local maps to achieve suitable hydrologic simulation. Therefore, in regional analyses, where detailed knowledge of the land cover is needed, it is recommended that *ad hoc* maps specially designed for a specific purpose are used, and remote

sensing techniques are a suitable choice to create these maps (Fragoso-Campón et al. 2020a). Hence, in the field of other geoscience disciplines, many studies worldwide have addressed this aim, showing the great capabilities of applying remote sensing techniques to the study of land cover from a general standpoint (Akike and Samanta 2016; Bolton et al. 2018), and, in particular, for forest structure and tree species studies (Fassnacht et al. 2016; Ferreira et al. 2016; Ghosh et al. 2014), studies conducted exclusively on the understory stratum (Magiera et al. 2016; Stavrakoudis et al. 2014; van Lier et al. 2009), studies focused on agricultural areas (Brinkhoff et al. 2020; Verma et al. 2019) and studies focused specifically on urban zones (Matikainen and Karila 2011; Tavares et al. 2019).

While it is important to obtain an accurate spatial landcover distribution for hydrological modeling and management strategies, only a few studies have addressed regional *ad hoc* vegetation maps using remote sensing techniques, including some works based on Landsat-8 imagery, with a spatial resolution of 30 m (Astuti et al. 2019; Martínez-Salvador and Conesa-García 2020; Wang et al. 2020), and another study that combined Landsat-5, Sentinel-1 (S1) and Sentinel 2 (S2) data, also with a spatial resolution of 30 m, to study the influence of land cover change on water resources and ecosystems in Tanzania (Leemhuis et al. 2017). Other work used the IRS LISS-IV, with a spatial resolution of 5.8 m, in India (Karunanidhi et al. 2020; Nageswara Rao 2020).

Currently, there are a large amount of remote sensing data available to be used for land cover mapping, and these data can be classified, according to the characteristics of the sensor, as optical passive (multispectral or hyperspectral) or active (synthetic aperture radar (SAR)), and can be used alone or in combination with other data. In addition, it is possible to add the temporal variable; hence, a land cover analysis could be addressed from several standpoints depending on the number of sensors and the temporality of the images analyzed. Many studies show that the final accuracy is higher when more information is used (Stromann et al. 2020; Zhao et al. 2016). Many studies have used multitemporal series of optical multispectral sensors, such as Landsat imagery (Ahmed et al. 2015; Bolton et al. 2018; Zhao et al. 2016), Sentinel-2 (Fragoso-Campón et al. 2020b; Hościło and Lewandowska 2019; Immitzer et al. 2019), or a combination of the two (Carrasco et al. 2019; Li et al. 2019). However, passive optical imagery is not always available as this kind of sensor is affected by atmospheric conditions; thus, in rainy regions with a high probability of cloud coverage, the use of SAR is mandatory, and multitemporal analysis is usually addressed (Wei et al. 2019; Yu et al. 2019). Moreover, in regions where climatology allows data from both sensors to be available, a fusion of the data can be incorporated, and good results can be achieved. In this regard, since the launch of the Sentinel satellites, this imagery has been used in many studies, and the capability of the fusion of S1 and S2 has been proven to be effective in

mapping vegetation and other coverages in several works, the main characteristics of which are summarized in Table 1.

There are many ways to combine the information of optical and SAR data. There are some studies in which the authors combine only the S1 backscattering in both polarizations with the S2 optical bands (Feng et al. 2019; Khan et al. 2020; Steinhausen et al. 2018). Other authors also added other information derived from S2, such as the spectral or biophysical indices (Brinkhoff et al. 2020; Denize et al. 2019; Heckel et al. 2020; Ienco et al. 2019; Lopes et al. 2020; Mahdianpari et al. 2020; Mercier et al. 2019; Whyte et al. 2018). Moreover, it is possible to combine the S1 backscattering information exclusively with the derived S2 spectral or biophysical indices (Van Tricht et al. 2018). In addition, other authors combine S1 backscattering with several optical sensors (S2, Landsat, LISS) and derived spectral or biophysical indices (Carrasco et al. 2019; Muthukumarasamy et al. 2019; Poortinga et al. 2019). Furthermore, other works added textural information of the gray level color matrix (GLCM) to the analysis, and there are several works that only used SAR texture measurements (Numbisi et al. 2019; Tavares et al. 2019; Verma et al. 2019), only used S2 texture measurements (Liu et al. 2018), or used both (Mishra et al. 2019; Stromann et al. 2020).

Nevertheless, the considerable increase in the amount of data to be processed causes the computational storage capacity and the computation time to also increase considerably. Therefore, the problems are not only about data availability (multitemporal series of cloud-free optical and SAR images) but also about the ability to manage and achieve the necessary computational requirements. Although most of the above studies proposed a multitemporal approach, other works, such as those of Khan et al. (2020), Mishra et al. (2019), Muthukumarasamy et al. (2019), Tavares et al. (2019) and Whyte et al. (2018), considered a single data evaluation and achieved high accuracies (see Table 1). In these examples, the low number of features was compensated by adding derived spectral or biophysical metrics from the optical data and the texture measurements. In contrast, studies that considered large time series solved the computational issues using the Google Earth Engine (GGE), which offers the possibility of managing a large amount of information (Brinkhoff et al. 2020; Mahdianpari et al. 2020; Poortinga et al. 2019; Stromann et al. 2020).

Therefore, the aim of our study was to develop a methodology for the generation of accurate land cover maps for future hydrological modeling. The specific goals of this study were i) to obtain accurate *ad hoc* land cover maps using the fusion of SAR and optical data, ii) to develop a method to achieve high-accuracy maps by data mining feature selection and minimizing the storage capacity requirements and the computational time, and iii) to identify hydrological land cover categories based on the seasonal runoff generation capability of the land cover types.

Table 1 Overview of studies combining Sentinel-1 and Sentinel-2 data for land cover mapping.

Study	SAR Sensor	SAR texture measures	Optical Sensor	Optical texture measures	Spectra Biophysical indices	Temporality	Classification Algorithm [1]	Pixel Object based	Sampling Design [2] Cross-Validation [3]	Overall Accuracy (%) (kappa coefficient)
Stromann et al. (2020)	S1	GLCM (9x9)	S2	GLCM (9x9)	NDVI, NDWI	summer images of 2015 and 2016; S2 (<15% cloud cover)	SVM	Object	70 % T : 30 % t ; k-fold (k=3, n=3)	93 - 94%
Mahdianpari et al. (2020)	S1	-	S2	-	NDVI	annual (S1); summer tri-monthly (S2) cloud free composite	RF (*ntree*=500)	Object	80 % T -t : 20 % V	79% (k= 0.75)
Lopes et al. (2020)	S1	-	S2	-	NDVI	annual (S2) Feb. 2018 to Feb. 2019 (<50% cloud cover); cloud gap filling	RF (*ntree*=100)	Pixel	70 % T : 30 % t; k-fold (k=20, n=1)	F-score = 73%
Khan et al. (2020)	S1	-	S2	-	-	single date	MLH	Pixel	-	84 - 85.60% (k= 0.8 - 0.82)
Heckel et al. (2020)	S1	-	S2	-	LAI, FAPAR	seasonal multitemporal from 2015 to 2017; S2 (<5% cloud cover) in summer 2016	RF (*ntree*=500)	Pixel	70 % T : 30 % t; k-fold (k=5, n=25)	84.3 - 93.7%
Brinkhoff et al. (2020)	S1	-	S2	-	NDVI	annual from May 2018 to April 2019	SVM, RF (*ntree*=128), CART	Object	66 % T : 33 % t; k-fold (k=3 n=3)	84.8 - 90.9%
Verma et al. (2019)	S1	GLCM	S2	-	-	monthly from June 2017 to November 2017	RF (ntree= not specified)	Pixel	-	83.87% (k=0.78)
Tavares et al. (2019)	S1	GLCM (5x5)	S2	-	NDVI, NDWI, SAVI	single date	RF (*ntree*=700)	Pixel	-	91.07% (k=0.87)
Poortinga et al. (2019)	S1	-	L8, S2	-	Nmetrics (several bands); SWIR1/NIR; RED/SWIR1; EVI; SAVI; IBI	S1: annual; L8, S2: seasonal rainy - dry (<40% cloud cover)	RF (*ntree*=100)	Pixel	Monte Carlo simulation process (100 times)	84%
Numbisi et al. (2019)	S1	GLCM (5x5)	RapidEye	-	NDVI, GNDVI, EVI2, SAVI, MSAVI	S1: seasonal rainy - dry from 2015 to 2017; RE: single date	RF (*ntree*=550)	Pixel	70 % T : 30 % t	88.1% (k=0.85)
Muthukumarasamy et al. (2019)	S1	GLCM (11x11)	LISS-IV, L8, S2	-	-	single date	SVM	Pixel	-	78.49% (k=0.68)

Study	SAR Sensor	SAR texture measures	Optical Sensor	Optical texture measures	Spectra Biophysical indices	Temporality	Classification Algorithm [1]	Pixel Object based	Sampling Design [2] Cross-Validation [3]	Overall Accuracy (%) (kappa coefficient)
Mishra et al. (2019)	S1 RISAT-1	GLCM (several windows)	LISS-III, LISS-IV, L8	GLCM (several windows)	-	single date	SVM	Pixel	75 % T: 25 % t	87.70 % (k=0.86)
Mercier et al. (2019)	S1	-	S2	-	EVI, NDVI, NDWI, SAVI	S1: annual from December 2016 to September 2017; S2: annual from December 2016 to August 2017	RF (*ntree*=100)	Pixel	50 % T : 50 % t; k-fold (k=30, n=1)	(k=0.89)
Ienco et al. (2019)	S1	-	S2	-	NDVI, NDWI, BI, NDVI and NDWI of infrared means (MNDVI and MNDWI), RNDVI	annual from April 2016 to May 2017 (S2 temporal gap-filling for cloudy observations)	TWIn Neural Networks	Pixel	-	89.88% (k=0.88)
Feng et al. (2019)	S1	-	S2	-	-	multidate (single date per season)	CNN	Pixel	1 T : 2 t	93.78% (k=0.93)
Denize et al. (2019)	S1	-	S2	-	NDVI, NDWI, SAVI, LAI, FAPAR, FCOVER	multidate (single date per month) from August 2016 to May 2017	SVM, RF (ntree=1000)	Pixel/Object	66 % T : 33 % t; k-fold (k=not specified, n=1)	81% (k=0.77)
Carrasco et al. (2019)	S1	-	L8, S2	-	L8: NDVI, NDMI, NDWI	S1: annual from October 2016 to September 2017; S2, L8: annual/seasonal from October 2016 to September 2017 (cloud-mask); S2: two-date composite	RF (*ntree*=200)	Pixel	1 T : 1 t	76.5% (k=0.70) (temporal composition); 77.9% (k=0.72) (two date)
Whyte et al. (2018)	S1	-	S2	-	NDVI, NDWI, MNDWI	single date	SVM (*RBF kernel*), RF (*ntree*= 900)	Object	80 % T : 20 % t	SVM: 79.8% (k=0.68); RF: 83.3% (k=0.72)
Van Tricht et al. (2018)	S1	-	S2	-	NDVI (mean value 10-day interval)	seasonal from March 2017 to August 2017	RF (*ntree*= not specified)	Pixel	10 % T - 90 % V	82% (k=0.77)
Steinhausen et al. (2018)	S1	-	S2	-	-	S1: November 2015 to May 2016; S2: multidate (2) cloud free	RF (*ntree*=1000)	Pixel	1 T : 1 t	91.53%

Study	SAR Sensor	SAR texture measures	Optical Sensor	Optical texture measures	Spectra Biophysical indices	Temporality	Classification Algorithm [1]	Pixel Object based	Sampling Design [2] Cross-Validation [3]	Overall Accuracy (%) (kappa coefficient)
Liu et al. (2018)	S1	-	L8, S2, DEM	GLCM	NDVI, RBI	S1: multidate (2) August 2016; L8: multidate (8) Feb. 2016 to Aug. 2016; S2: multidate (2) cloud-free Aug. 2016 and Sept. 2016	RF (*ntree*=20)	Object	75 % T : 25 % t	82.78% (k=0.78)

[1] If multiple algorithms were used, the best was underlined.
CART Classification and Regression Tree
MLH Maximum Likelihood Classifier
RF Random Forest
SVM Support Vector Machine
[2] T: training; t: test; V:validation; the sample design is indicated according to the nomenclature of each study.
(-) If the sample design information is not mentioned.
[3] If the cross-validation method is not specifically mentioned, it is assumed one-k-fold cross-validation without repetition.

2 Materials and Methods

2.1 Study area

The study area corresponds to the Extremadura region in Spain, which extends between latitudes 37°56'-40°29' N and longitudes 7°32'-4°39' W (Fig. 1). The climatic characteristics of the watersheds in the study area correspond to the Mediterranean pluviseasonal-continental variant and the meso-Mediterranean thermoclimatic belt for most of the watersheds, except the northern watersheds, which correspond to the supra-Mediterranean thermoclimatic belt; the highest-elevation watershed corresponds to the temperate, oceanic sub-Mediterranean climate region and to the oro-Mediterranean thermoclimatic belt (Rivas-Martinez and Rivas-Saenz 1996-2019). The analysis is focused on 20 gauged watersheds throughout the region that have been selected for hydrologic modeling and are not affected by any reservoir regulation (Table 2).

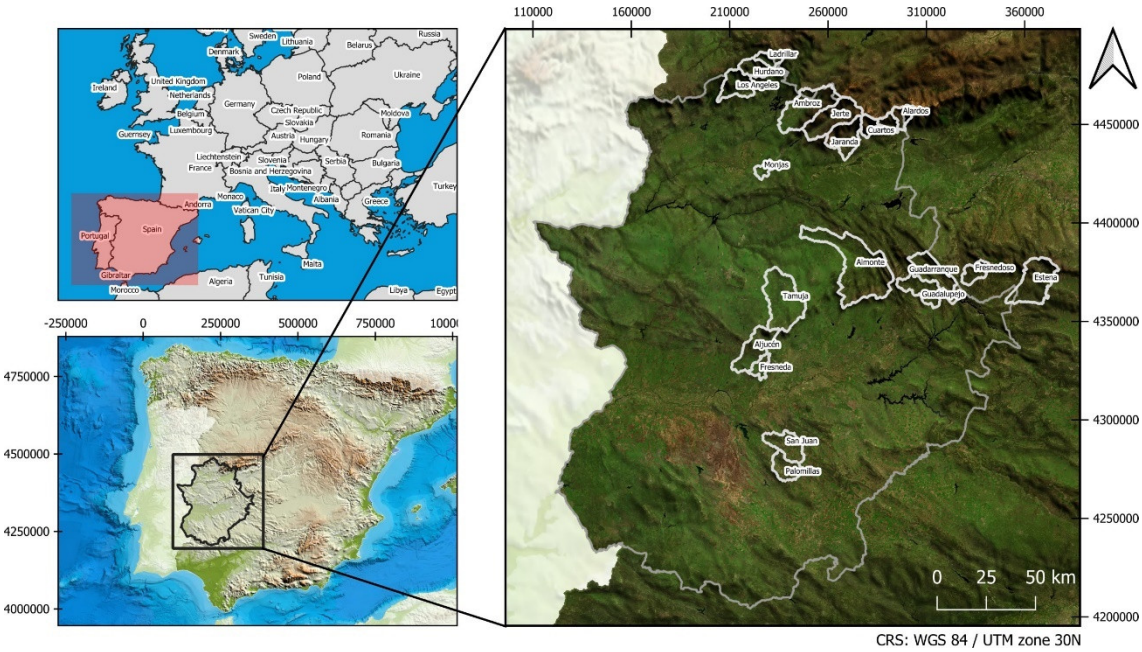

Fig. 1 Study area.

Table 2 Watersheds

Watershed	Hydrographic region	Area (km²)	Watershed	Hydrographic region	Area (km²)
Alardos	Tajo	87.80	Hurdano	Tajo	108.46
Aljucen	Guadiana	253.29	Jaranda	Tajo	225.18
Almonte	Tajo	781.00	Jerte	Tajo	314.89
Ambroz	Tajo	390.20	Ladrillar	Tajo	73.04
Cuartos	Tajo	68.39	Los Ángeles	Tajo	188.56
Estena	Guadiana	355.97	Minchones	Tajo	56.40
Fresneda	Guadiana	70.27	Monjas	Tajo	55.08
Fresnedoso	Guadiana	107.08	Palomillas	Guadiana	145.71
Guadalupejo	Guadiana	199.11	SanJuan	Guadiana	193.88
Guadarranque	Guadiana	256.55	Tamuja	Tajo	457.71
				Total area (km²)	4673.35

2.2 Land cover types

The land cover types in the Extremadura region can be divided into four general groups: forested areas, agricultural lands, water bodies and impervious surfaces. First, forested areas, which represent 67% of the Extremadura region, can be subdivided into woods, pastures, and *dehesas* landscapes; a *deseha* is a typical component of the Extremadura region and is a transition between those landscapes. Diaz et al. (1997) defined the *dehesa* as "pasturelands populated by holm and/or cork oaks, with an understory of open grassland, cereal crops, or Mediterranean scrub". Therefore, tree species mainly comprise holm oaks (*Quercus rotundifolia*), cork oaks (*Quercus suber*), Pyrenean oaks (*Quercus pyrenaica*), sweet chestnut (*Castanea sativa*) and pinus (*Pinus pinaster* and *Pinus pinea*). The shrub strata is composed of several evergreen species, the main species *Cistus ladanifer*, *Retama sphaerocarpa, Lavandula stoechas, Thymus mastichina, Genista hirstuta, Phillyrea angustifolia, Erica arborea*, and *Erica australis,* with *Cytisus* species at higher elevations (Devesa Alcaraz 1995). The pastures are composed of herbaceous vegetation and are predominantly acidophilic with plants that bloom in spring. Although rocky outcrops and bare soil are mostly impervious, they are also considered to be natural coverage in forested areas. Next, the agricultural lands in Extremadura, representing 32% of the region, can be divided into rainfed and irrigated areas. The rainfed crops are mainly olive trees and vineyards and cold-season annual crops such as oats, wheat and barley. Cherry trees also occur in the northwest valleys. The irrigated crops include seasonal warm crops such as corn, tomatoes, rice, tobacco and fruit trees. Finally, water bodies include rivers, reservoirs and small cattle ponds, and impervious surfaces represent urban areas and roads.

The analysis in this paper is focused on the identification of land cover categories based on their runoff generation capabilities, considering the specifications of the NRCS hydrologic soil-cover complex (NRCS 2004). In this regard, the variation in runoff capability due to seasonal phenology is also considered, which affects mainly deciduous trees and seasonal crops. Hence, for a given land cover class, two hydrologic conditions are defined in two periods: operational and nonoperational. The operational period refers to the phenological phase from planting to tillage in seasonal crops and to the leaf-on phase in deciduous trees in forested areas or cherry tree crops. Additionally, the operational period will be considered for pastures, which experience highly vigorous growth in spring. Thus, the nonoperational period refers to the rest of the period, until the next operational stage. Hence, Table 3 shows the proposed classification of the cover types.

Table 3 Land cover types and hydrologic conditions in operational and nonoperational periods.

	Land cover description [1]	Class code	NRCS land cover type		Hydrologic condition	
			Phenological Stage [2]		Phenological Stage [2]	
			Op	Non-op	Op	Non-op
Forested areas	Evergreen needleleaf forest (*Pinus pinaster, Pinus pinea*)	ENF	Woods	Woods	Good	Good
	Evergreen broadleaf forest (*Quercus rotundifolia, Quercus suber*) TCC>60%	EBF	Woods	Woods	Good	Good
	Evergreen broadleaf forest (*Quercus rotundifolia, Quercus suber*) 20<TCC<60%	DHS	Woods	Woods	Fair	Poor
	Deciduous broadleaf forest *(Quercus pyrenaica, Castanea sativa)*	DBF	Woods	Woods	Good	Fair
	Shrub	S	Brush	Brush	Fair	Fair
	Herbaceous vegetation	P	Pasture	Pasture	Fair	Poor
	Rocky outcrops	Rk	Impervious	Impervious	--	--
	Bare soil	B	Road Gravel	Road Gravel	--	--
Agricultural lands	Irrigated warm-season crops	AgIr	Row crops straight row	Fallow	Good	Fallow
	Rainfed cold-season crops	AgRc	Close seeded straight row	Fallow	Good	Fallow
	Crop residue cover	Agf	Fallow	Fallow	Poor	Poor
	Rainfed cherry tree plantations	Agc	Orchard/Tree farm	Orchard/Tree farm	Fair	Poor
	Rainfed olive tree plantations	Ago	Orchard/Tree farm	Orchard/Tree farm	Fair	Fair
	Rainfed vineyard plantations	Agv	Orchard/Tree farm	Orchard/Tree farm	Poor	Poor
Other	Urban and paved roads	Imp	Impervious	Impervious	--	--
	Water bodies	W	Water bodies	Water bodies	--	--

[1] TCC Tree Canopy Cover

[2] Op The operational stage refers to the phenological phase from planting to tillage in seasonal crops and to the leaf-on phase in deciduous trees in forested areas or cherry tree crops.

Non-op The nonoperational period refers to the rest of the period, until the next operational stage

2.3 Sentinel imagery

2.3.1 Data acquisition

The images used in this work were collected from the S1 and S2 missions of the Copernicus Program, which is managed by the European Commission in partnership with the European Space Agency (ESA). All the data were downloaded from the Copernicus Open Access Hub

(Copernicus Program 2020). The S1 is a C-band SAR sensor with dual VV and VH polarization. Specifically, the data used are from a Ground Range-Detected (GRD) product and were acquired in the interferometric Wide Swath (IW). The S2 is a multispectral sensor working in visible (VIS), near-infrared (NIR) and short wave infrared (SWIR) bands, and we used the Level 2A products representing the bottom-of-atmosphere (BOA) reflectance (Table 4).

First, we selected the summer period for the optical images since the study area is less affected by cloud coverage in the summer; additionally, it was also taken into account that, in the summer, the vegetation in the Mediterranean environment shows good spectral separability (Fragoso-Campón et al. 2020b; Godinho et al. 2017). To cover the study area, we processed four S2 tiles to obtain a cloud-free composition for the entire area. Next, we selected the S1 images, using an acquisition date in summer as close as possible to the S2 acquisition date, so that the vegetation could be represented in similar conditions for the optical and SAR information. In addition, we also used a winter date for S1 images, since these data are not affected by atmospheric conditions, so phenological differences in seasonal crops and deciduous trees could be considered. As a result, two S1 scenes per season were processed, both taken in ascending passes.

Table 4 Overview of the satellite information.

Sensor	Date		Product scene identification	Characteristic	
S1	Winter	11/01/2019	014450_01AE7E_5C38 014450_01AE7E_F036	Band: Product:	C (5.40 GHz) GRD
	Summer	28/06/2019	016900_01FCDB_9F6A 016900_01FCDB_A90D	Mode: Polarization:	IW VV VH (spatial resolution 10 m)
S2	Summer	01/07/2019	R137_T30TTK R137_T30STJ R137_T30SUJ R137_T30STH	Product: Bands:	S2MSI2A VIS: B2, B3, B4 (spatial resolution 10 m) NIR: B5, B6, B7, B8A (spatial resolution 20 m), B8 (spatial resolution 10 m) SWIR: B11, B12 (spatial resolution 20 m)

2.3.2 Data preprocessing

The preprocessing of the images was carried out using the Sentinel Application Platform (SNAP) software developed by the European Space Agency (ESA). The S1 scene preprocessing included calibration (radiometric normalization), terrain correction and speckle filtering. The S2 preprocessing included resampling, reprojection and mosaic-building.

The calibration of S1 was accomplished using the sigma naught method (σ^o) to obtain the radar backscattering coefficient for both polarization σ^o_{VV} and σ^o_{VH}. Then, a Lee sigma speckle filter

(window size 7x7) was applied to reduce speckle noise, and finally, terrain correction was applied using the digital elevation model from the Shuttle Radar Topography Mission (SRTM). The linear sigma naught (σ^o) values were used as predictors in the analysis to avoid mathematical errors when using logarithmic transformations, so that, as recommended in Flores-Anderson et al. (2019), the backscattering values were converted to dB only for color composite displays. Regarding the S2 preprocessing, first, the S2 bands with an original spatial resolution of 20 m were resampled to 10-m resolution using the S2 Resampling Operator implemented in SNAP and applying the mean downsampling method. Then, the tiles were mosaiced. Finally, the S1 scenes were mosaiced and eventually collocated to the S2 spatial resolution.

2.3.3 Indices and texture predictors

To add more information to the classification algorithm, we improved the dimensionality of the S1 and S2 images by considering the derived spectral metrics of the optical data and the texture metrics to be predictors in the analysis. As a result, the dimensionality was improved from 14 to 148 predictors (see Table 5).

Concerning the TF, as shown in Table 1, the well-known gray-level cooccurrence matrix (GLCM) (Haralick and Shanmugam 1973) is usually applied to compute texture metrics. Although texture metrics are rarely considered for both sensors, recent studies achieved good results when using them for both optical and SAR sensors (Mishra et al. 2019; Stromann et al. 2020). Therefore, we obtained the TF for both polarizations (VV, VH) in the SAR images and for all the bands of the S2 images. The analysis was performed for all angles via probabilistic quantization using a pixel displacement of 4 and a 9 × 9 window size.

Table 1 also shows that the most common vegetation indices used in other works are the normalized difference vegetation index (NDVI) (Rouse Jr et al. 1974) and the soil-adjusted vegetation index (SAVI) (Huete 1988) and the most commonly used water index is the normalized difference water index (NDWI) (Gao 1996). Here, we proposed to also use other S2 indexes, including the normalized difference index (NDI45) (Delegido et al. 2011), the second modified soil-adjusted vegetation index (MSAVI2) (Qi et al. 1994) and the green normalized difference vegetation index (GNDVI) (Gitelson et al. 1996). In addition, we also used some soil indices (SI), which are rarely used but have been proven to be very useful in previous works (Fragoso-Campón et al. 2020b; Huete et al. 1984); specifically, we used the color index (CI) (Escadafal and Huete 1991) and the brightness index (BI) (Mathieu et al. 1998).

Table 5 Predictors of S1 and S2 used for the supervised classification.

Sensor	Date	Bands	Texture features	Indices
S1	11/01/2019	σ^o_{VH-W} σ^o_{VV-W}	σ^o_{Vi-j}_ASM σ^o_{Vi-j}_Contrast σ^o_{Vi-j}_Dissimilarity σ^o_{Vi-j}_Energy σ^o_{Vi-j}_Entropy σ^o_{Vi-j}_Homogeneity σ^o_{Vi-j}_MAX σ^o_{Vi-j}_GLCMMean σ^o_{Vi-j}_GLCMVariance With i = VH, VV; j = w, s	-
S1	28/06/2019	σ^o_{VH-S} σ^o_{VV-S}		
S2	01/07/2019	B2 B3 B4 B5 B6 B7 B8 B8A B11 B12	B_i_ASM B_i_Contrast B_i_Dissimilarity B_i_Energy B_i_Entropy B_i_Homogeneity B_i_MAX B_i_GLCMMean B_i_GLCMVariance With i = 2 to 12	BI = sqrt(((B4 * B4) + (B3 *B3))/2) CI = (B4 – B3)/(B4 + B3) GNDVI = (B7 – B3)/(B7 + B3) MSAVI2 = (1/2) * (2 * (B8 + 1) - sqrt((2 * B8 + 1) * (2 * B8 + 1) - 8 * (B8 – B4))) NDI45 = (B5 - B4)/(B5 + B4) NDVI = (B8 – B4)/(B8 + B4) NDWI = (B3 – B8)/(B3 + B8) SAVI = (1 + L) * (B8 – B4)/(B8 + B4 + L) With L=0.5

BI (brightness index), CI (color index), GNDVI (green normalized difference vegetation index), MSAVI2 (second modified soil-adjusted vegetation index), NDI45 (normalized difference index), NDVI (normalized difference vegetation index), NDWI (normalized difference water index), SAVI (soil-adjusted vegetation index)

2.3.4 Dimensionality-increasing scenarios

In this work, we studied eighteen scenarios with different permutations of S1 and S2 predictors (Table 6) to analyze the influence of data fusion of features on the global accuracy and computational time of an analysis when increasing the dimensionality of the dataset.

Table 6 Scenarios considered in the RF algorithm optimization.

Scenario	Sensor	S1 σ^o_{VH-S} & σ^o_{VV-S}	S1 σ^o_{Vi-S}_ Textures	S1 σ^o_{VH-W} &σ^o_{VV-W}	S1 σ^o_{Vi-W}_ Textures	S2 Optical bands	S2 Textures: S2 Indices	S2 Textures: VIS (B2, B3, B4)	S2 Textures: NIR (B5, B6, B7)	S2 Textures: NIR (B8A)	S2 Textures: SWIR (B11, B11)	Total predictors
S1s	S1	×										2.00
S1w	S1			×								2.00
S1	S1	×		×								4.00
S2	S2					×						10.00
S2i	S2					×	×					18.00
S2tnir8A	S2					×				×		19.00
S1st	S1	×	×									20.00
S1wt	S1			×	×							20.00
S2tsw	S2					×					×	28.00
S1stS2	S1-S2	×	×			×						30.00
S2tnir57	S2					×			×			37.00
S2tvis	S2					×		×				37.00
S1t	S1	×	×	×	×							40.00
S1tS2	S1-S2	×	×	×	×	×						50.00
S1tS2i	S1-S2	×	×	×	×	×	×					58.00
S2t	S2					×		×	×	×	×	100.00
S2it	S2					×	×	×	×	×	×	108.00
S1tS2it	S1-S2	×	×	×	×	×	×	×	×	×	×	148.00

2.4 Classification technique

In this study, a pixel-level supervised classification was carried out by applying the random forest (RF) machine learning method (Breiman 2001) using the *RandomForest* R package (Liaw and Wiener 2002). This algorithm is suitable in this study due to the mixed origins of the inputs, and it has been widely used in previous studies with high effectiveness (Table 1). The number of decision trees (Ntree) was set to 500, and the number of variables (Mtry) was trained automatically by the classifier, as it depends on the number of predictors used in each scenario (Table 6).

2.5 Reference data and accuracy assessment

The reference data were defined to ensure the objectivity and consistency of the accuracy assessment, following the guidelines outlined in Congalton and Green (2008). First, a global region of interest (ROI) dataset was built to ensure the data collection consistency, and it was defined as polygons of homogeneous land cover categories. Second, the ROI dataset was

randomly split into two different groups, the train-test and validation datasets, ensuring their absolute independence.

The ROI dataset for forested areas was obtained from a supervised classification of ultrahigh spatial resolution (UHSR) data from the National Plan of Aerial Orthophotography (PNOA) in Spain following the methodology developed in Fragoso-Campón et al. (2020a). The ROI dataset for agricultural land was obtained from the database of the Common Agricultural Policy in the Extremadura region (CAP). The urban areas and water bodies were defined by photointerpretation of the PNOA UHSR.

As mentioned earlier, ROI dataset was randomly split into two independent groups, the train-test and validation datasets. This study considers sixteen categories to be classified (Table 3) and we proposed a random balance sample dataset to avoid that the RF tended to favor classification to the most representative category (Belgiu and Drăguţ, 2016) over such a large area. Thus, first we built an initial ROI dataset of unbalanced samples that was randomly split into an initial train-test and validation datasets in the ratio 75%-25% respectively, maintaining the class balance. Second, to create a balanced dataset avoiding selection bias, the subsample size of each class was again randomly split up to a maximum of 150 000 pixels whenever possible, in both train-test and validation datasets. This threshold of 150 000 was defined as the maximum value to avoid memory problems when addressing the RF algorithm ensuring that as much variability as possible between classes was taken into account. It is worth noting that the ROI dataset was finally quasi-balance because some classes, the least represented in the scheme, had less than 150 000 pixels. Finally, the ROI dataset was about 3,322 million pixels resulting in a ratio between train-test and validation of 57 % - 43 %.

Lastly, the area ratio of the ROI dataset compared to the extent of the S2 images was approximately 0.74 %. Specifically, the resulting training-test area ratio was 0.42 % and the validation area ratio was 0.32 %. These area ratios were in agreement with the analysis reported by Belgiu and Drăguţ (2016) where a ratio of about 0.25% of the total study area was mentioned as an approximate ratio for the training sample size.

Therefore, the accuracy assessment was performed in two ways: using the train-test dataset for the evaluation of the capability of the RF model and using the validation dataset for the independent accuracy evaluation of the final land cover map.

2.5.1 RF model accuracy evaluation

Using the train-test dataset, the pixel values of the 148 predictors were extracted for each land cover category using the *raster* R package (Hijmans 2019), resulting in approximately 1.9 million pixels. Then, the data were randomly split, maintaining the class balance, into 50% for training and 50% for testing, and the RF algorithm was evaluated in two ways. First, the RF algorithm

evaluated its own overall accuracy using the out-of-bag (OOB) samples of the training dataset that were not used to build the trees to measure the overall OOB error rate. Second, the RF model predictions were verified with the independent test dataset (not used to train the model) using the error matrix information (Congalton and Green 2008). During the data mining process, the accuracy assessment was analyzed in all scenarios using the same partition (50%-50%), and the scenario with the best performance was selected for the optimal feature selection (see details in 2.6). Once the optimal features were selected, to ensure the certainty of the cross-validation, we conducted a four *k*-fold cross-validation (k=4) with three repetitions of the RF algorithm in each fold (n=3), and the accuracy evaluation was performed for all the iterations in the *k*-fold cross-validation. Finally, the RF model with the best performance in the *k*-fold cross-validation was selected for the land cover classification.

2.5.2 Land cover accuracy assessment

The evaluation of the accuracy of the land cover maps was conducted after salt-and-pepper noise reduction postprocessing (Stavrakoudis et al. 2014; Su 2016). In this work, the classified land cover map was smoothed using the majority filtering and sieving methods (Mas et al. 2010) using QGIS software. Then, the validation dataset was used to evaluate the accuracy following a similar method to the one explained above. The categories of the *ad hoc* map were extracted in each land cover polygon of the validation dataset using the *raster* R package (Hijmans 2019) and were used to build the error matrix of the validation group.

2.5.3 Error matrix accuracy metrics

The error matrix accuracy metrics were calculated with the *caret* R package (Kuhn et al. 2018). The overall accuracy (OA) measures the ratio of correct predictions considering all categories on each map, and we also evaluated several accuracy metrics for each category derived from the error matrix information, such as sensitivity, precision, F1 and balanced accuracy, which are based on different relationships between the type of classification results: true positive (TP), false negative (FN), true negative (TN) and false positive (FP).

The sensitivity is a measure of the fraction of predictions that are properly classified as positive in each category (also known as producer's accuracy) and is calculated using Eq. (1).

$$\text{sensitivity} = \frac{TP}{TP + FN} \tag{1}$$

The precision is measure of the fraction of the reference area included accurately in each category to which it belongs (also known as user's accuracy); the precision is calculated using Eq. (2).

$$\text{precision} = \frac{TP}{TP + FP} \tag{2}$$

The F1, or F score, is calculated from the sensitivity and the precision following Eq. (3) and ranges from 0 to 1; higher values indicate a better fit.

$$\mathrm{F1} = \frac{(1+\beta^2)\cdot sensitivity \cdot\ precision}{(\beta^2 \cdot precision) + sensitivity} \qquad \text{With } \beta = 1 \tag{3}$$

Finally, the balanced accuracy, which is a measure of the average fraction of correct predictions, considering both the TP and TN possibilities, is calculated using Eq. (4):

$$balanced\ accuracy = \frac{1}{2}\left[\left(\frac{TP}{TP+FN}\right) + \left(\frac{TN}{TN+FP}\right)\right] \tag{4}$$

2.6 Data mining feature selection processing

As previously mentioned, the scenario with the best performance in terms of overall accuracy was selected for the optimal feature selection, which was based on the feature importance of the RF algorithm, specifically the mean decrease accuracy (MDA) measure. A higher MDA value implies a more important role of the predictor in the classification process (Hastie et al. 2009), so the RF computational requirements can be optimized by discarding the information of the predictors with less importance. To define how many predictors can be discarded, the data mining process includes several iterations, considering the breaks in the distribution of the MDA values. As a result, three iterations were defined: one considering the features with MDA values greater than 50%, one considering the features with MDA values greater than 40%, and, finally, one considering the features with MDA values greater than 30%. For each iteration, the accuracy and computational time of the RF model were evaluated. Selection of the optimal feature combination was conducted with consideration of both parameters.

Finally, Fig. 2 shows a flowchart of the methodology followed in this study.

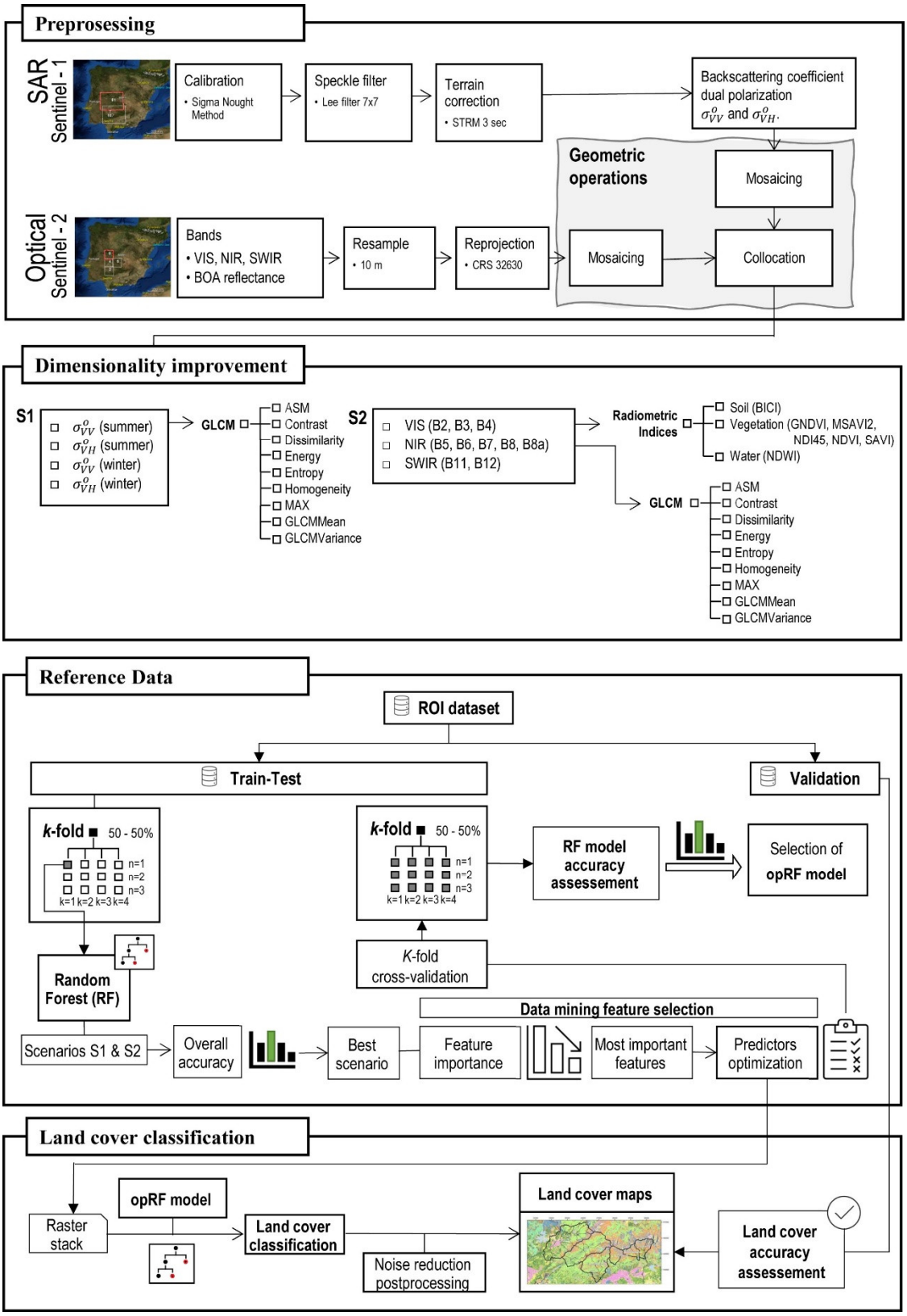

Fig. 2 Processing flowchart of the methodology proposed in this study.

2.7 Evaluation of potential runoff dependent on phenological stage

Once the land cover categories were mapped, five different phenological stages were defined considering the equivalences outlined in Table 3 of the classes and their respective NRCS land

cover types and hydrological conditions in each period (operational and nonoperational) (Fig. 3).

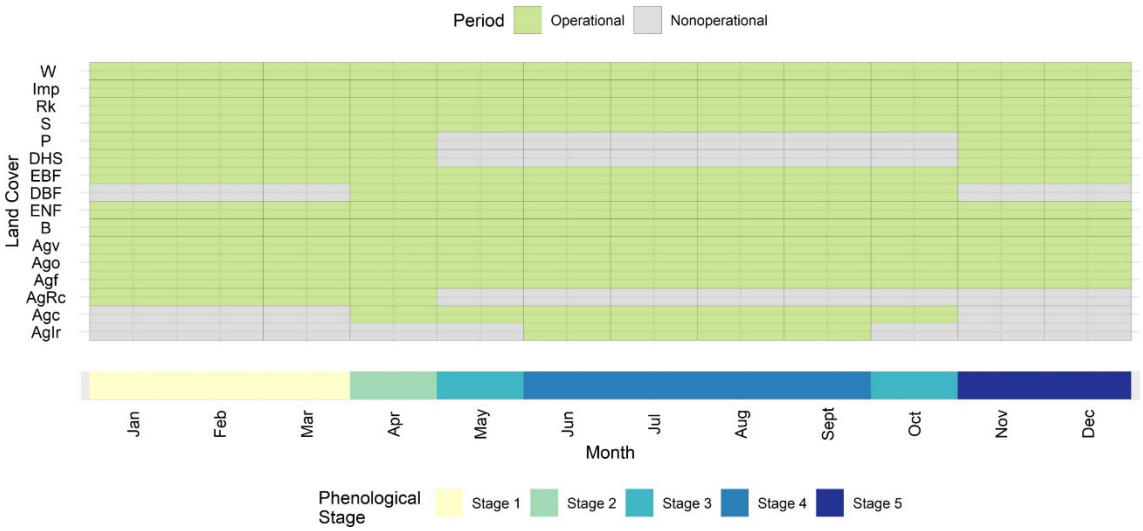

Fig. 3 Phenological stages of the land cover categories in the study area.

Finally, the hydrologic responses of the watersheds were analyzed for each stage following the National Resources Conservation Service curve number method (NRCS-CN) (NRCS 2009). The analysis was conducted in terms of the values of the CN parameter in the watersheds. The well-known CN parameter refers to the potential runoff capability of a watershed; a lower CN value indicates a lower potential runoff capability and vice versa. The CN depends on the land cover and soil type and was obtained in this study directly from the lookup tables of the National Engineering Handbook (Table 7). Please note that in this work, we considered an average soil initial antecedent moisture condition (AMC). Finally, to evaluate the hydrologic response in the watersheds, the weighted average CN values derived from each stage were computed at two levels: the watershed and the subwatershed level.

Table 7 NRCS-CN look up table for the land cover types identified in the study area.

Cover type and treatment	Hydrologic condition	CN for hydrologic soil group			
		A	B	C	D
Fallow	Poor	76	85	90	93
Row crops straight row	Good	67	78	85	89
Close seeded straight row	Good	58	72	81	85
Pasture	Poor	68	79	86	89
Pasture	Fair	49	69	79	84
Brush	Fair	35	56	70	77
Orchard/Tree farm	Poor	57	73	82	86
Orchard/Tree farm	Fair	43	65	76	82
Woods	Poor	45	66	77	83
Woods	Fair	36	60	73	79
Woods	Good	30	55	70	77
Road Gravel	-	76	85	89	91

Cover type and treatment	Hydrologic condition	CN for hydrologic soil group			
		A	B	C	D
Impervious	-	98	98	98	98
Water bodies	-	100	100	100	100

The soil type was obtained from the European Soil Data Centre (European Soil Data Centre (ESDAC) 2020), specifically from the results in Ballabio et al. (2016), in which the textural classes in Europe were proposed using the USDA classification based on the combination of three textural maps (clay, silt and sand), as shown in Fig. 4 . This database is publicly available upon request on the ESDAC website. The soil textural classes were transformed into the hydrologic soil group using the criteria in Hong and Adler (2008).

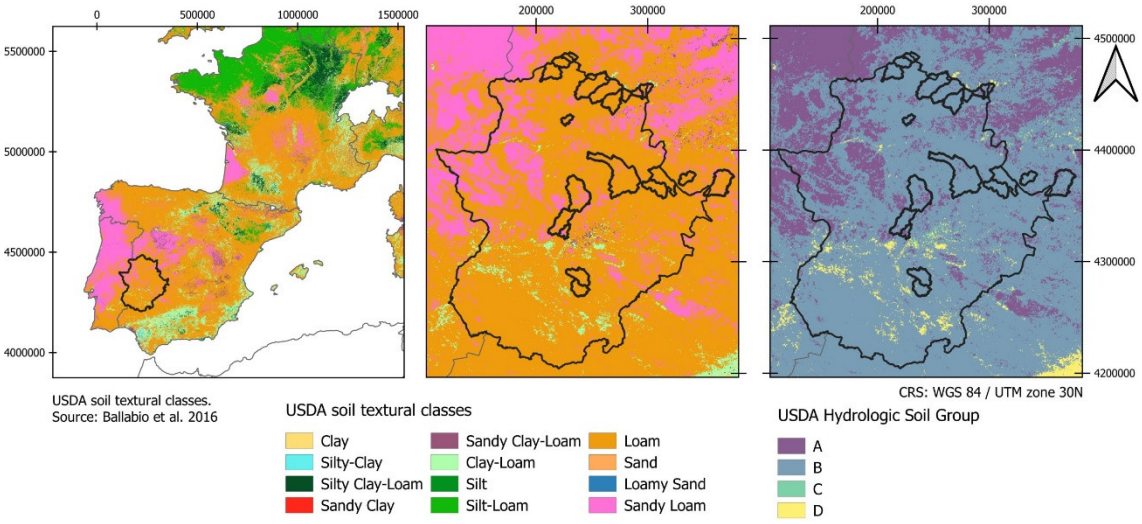

Fig. 4 USDA hydrologic soil group in the study area.

3 Results

3.1 Selection of the best scenario

Table 8 shows the results achieved for each scenario. The rows are listed based on the number of predictors. The computational time[1] increases with the number of predictors in all scenarios. Fig. 5 shows how the OA depends not only on the number of predictors but also on the sensor used. In terms of accuracy, OOB error rate and the OA, the S1 predictors show poorer results, and the scenarios that combined S1 and S2 reached accuracies over 85%. The scenario with the best performance is S1tS2it, which comprises all the available features, reaching an OA of 92.98% and is the scenario selected for the data mining of the optimal features.

Table 8 Overview of the overall accuracies and computational time for each scenario. The training dataset and test dataset are used for the split of the *k*-fold (k=1; n=1).

[1] System characteristics: Windows 10 Pro 64 bits; Common KVM processor 2.19 Gz; 100 GB RAM

Scenario	n predictors	RF OOB error rate [1]	RF OA (%) [2]	Time (h)
S1s	2	0.73	26.98	0.78
S1w	2	0.75	25.05	0.85
S1	4	0.62	38.00	0.94
S2	10	0.18	82.18	1.08
S2i	18	0.19	81.37	1.98
S2tnir8A	19	0.17	83.03	2.45
S1st	20	0.55	45.26	2.92
S1wt	20	0.61	39.07	3.00
S2tsw	28	0.15	84.69	2.71
S1stS2	30	0.15	84.75	2.93
S2tnir57	37	0.14	85.59	3.70
S2tvis	37	0.13	87.34	3.70
S1t	40	0.37	63.17	5.00
S1tS2	50	0.13	86.80	5.00
S1tS2i	58	0.14	86.47	5.78
S2t	100	0.08	91.80	9.44
S2it	108	0.09	91.06	10.79
S1tS2it	148	0.07	92.98	14.94

[1] RF OOB error rate: the overall error rate of the random forest algorithm using the out-of-bag samples from the training dataset.
[2] RF OA: the overall accuracy of the prediction using an independent testing dataset.

3.2 Feature data mining processing

Fig. 6 shows the measure of each predictor's importance based on the value of the MDA in the RF model scenario with the best performance, S1tS2it. Three ranges in the distribution of the MDA values were identified (Fig. 6 a), and we studied the capability of the RF when discarding features in three data mining iterations: the first iteration (DM1) discarded features with MDA values less than 50, the second iteration (DM2) discarded features with MDA values less than 40, and, finally, the third iteration (DM3) discarded the features with MDA values less than 30. Therefore, the RF model accuracy and computational time were evaluated for each iteration and compared with the results of the reference scenario S1tS2it.

As shown in Fig. 6 b, these most-important features are related almost exclusively to the texture metrics of both sensors, and remarkably, the dissimilarity has many features with MDA values over 30. Regarding the bands, only the narrow NIR red edge (B5) and SWIR (B11 and B12) bands were ranked as important predictors. Finally, related to the indices, only CI seems to be important. Fig. 6 c shows that the texture features are related mainly to the S2 bands and to the texture metrics of S1 in winter, mainly VV polarization, although there are also several important features of S1 in summer in VH polarization.

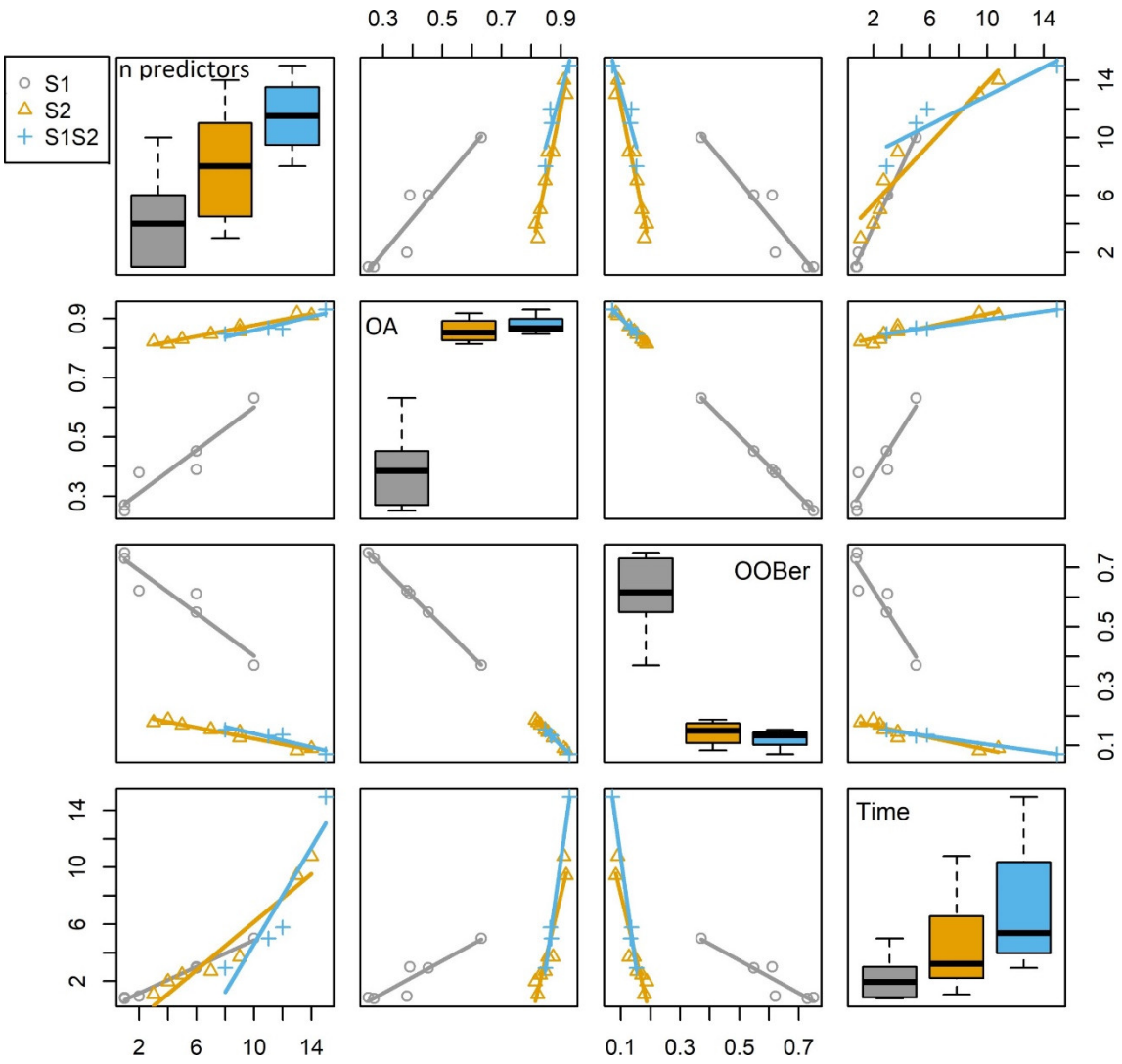

Fig. 5 Results for the scenarios of the permutations of S1 and S2 predictors considered in the RF algorithm optimization.

Fig. 6 d shows the OOB error rate, the OA achieved and the computational time of the iterations. The DM1, using the top 21 most important predictors, shows a decrease of 8.7% in terms of OA, with an optimization of the computational time of 86%. The DM2, using the top 42 most important predictors, has a decrease of 2.3% in terms of OA, with a reduction in the computational time of 74%. The DM3, using the top 75 most important predictors, shows the same OA as the original scenario, with a reduction in the computational time of 54%. In addition, Fig. 6 e shows the decrease in accuracy metrics for each land cover category for the three data mining iterations, and it can be observed how the iteration DM3 has almost the same performance for all the categories as the original scenario with approximately half of the features. Therefore, the features used in the DM3 iteration were selected for the optimization of the RF model.

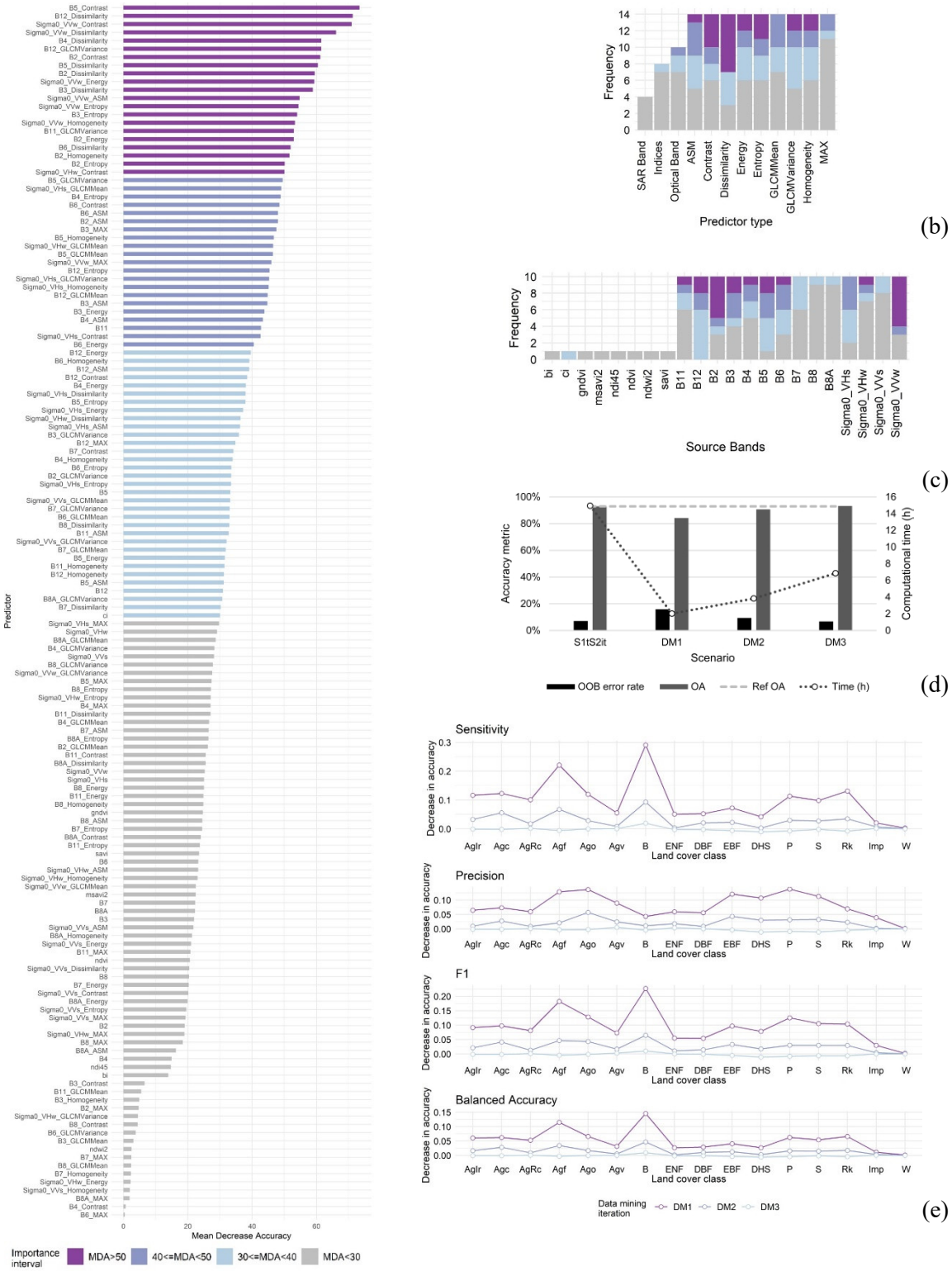

Fig. 6 Data mining results. (a) The predictor importance list in the RF model of the scenario with the best performance (S1tS2it). (b) The frequency of appearance of predictor types in the features selected as optimal. (c) The frequency of appearance of band-derived metrics in the features selected as optimal. (d) The accuracy metrics and the computational time achieved in the data mining iterations. (e) The decrease in accuracy metrics for each land cover category for the three data mining iterations with respect to the original scenario S1tS2it.

3.3 Cross validation and accuracy assessment

The selected features from the scenario S1tS2it and the DM3 iteration were set as the optimal features to be used to train the RF model, which was called the opRF model. From this point, to ensure the certainty of the cross validation, we conducted a four-*k*-fold cross-validation (k=4) with three repetitions of the opRF algorithm in each fold (n=3). Table 9 summarizes the accuracy metrics obtained, and it is worth noting that remarkable stability was achieved in the results of both the OOB error rate and the OA. Note that the results shown in 0 correspond to the k-fold (k=1, n=1).

Table 9 Accuracy metrics achieved in the k-fold cross-validation of the opRF model.

		k=1	k=2	k=3	k=4	Overall value
OOB error rate (%)	n=1	6.80	6.80	6.79	6.81	**6.80**
	n=2	6.81	6.79	6.79	6.82	
	n=3	6.81	6.79	6.80	6.81	
	mean value	6.81	6.79	6.79	6.81	
OA (%)	n=1	93.26	92.74	93.29	93.28	**93.23**
	n=2	93.27	93.25	93.29	93.29	
	n=3	93.26	93.26	93.28	93.28	
	mean value	93.26	93.08	93.29	93.28	

Finally, the opRF (k=3, n=2) model with an OA of 93.29% in the test had slightly better performance than the others and was selected for the land cover classification. Next, the validation dataset was used to evaluate the accuracy of the postprocessed land cover map, and this model reached an OA of 85.24%. However, despite being lower than the accuracy obtained for the test dataset, the overall performance of the opRF classifier was still outstanding. The accuracy metrics obtained by the opRF for each land cover category (Fig. 7 a) achieved excellent results in the test dataset, while those in the validation dataset were lower. In addition, the validation dataset showed better values in the forestland cover classes than in the agricultural cover classes and, the bare soil cover classes showed the weakest results. The area ratio of each land cover category in the final land cover map (Fig. 7 b) showed balanced accuracy values higher than 0.89 for the most representative classes in forested areas, except for S with a value of 0.82. Meanwhile, the most representative cover in agricultural areas was Agf with a balanced accuracy of 0.79. Finally, Fig. 7 c shows the diagram of misclassifications among categories. The low accuracies in S were attributed to confusion mainly with DBF (11%), P (7%) and EBP (5%), whereas misclassification of Agf was due to confusion mainly with AgRc (12%), Ago (11%) and S (7%).

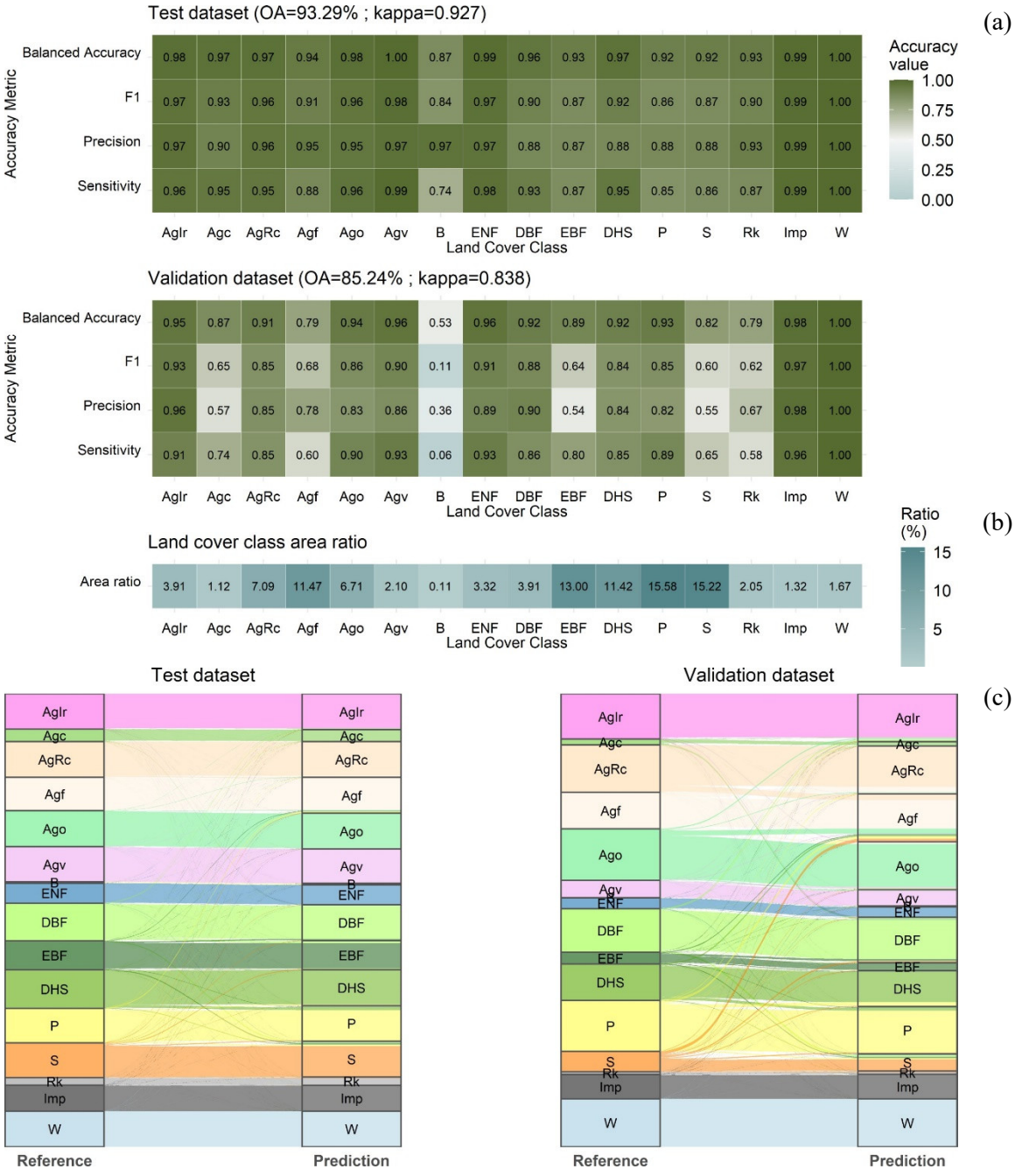

Fig. 7 Accuracy assessment (a) Accuracy metrics obtained for each category based on the error matrix information. (b) Area ratio of each land cover category in the final land cover map. (c) Diagram of misclassifications among categories.

3.4 Feature importance of opRF

Regarding the importance of the predictors, as shown in Fig. 8 , the most important features in the opRF were related to the texture metrics of both sensors, and dissimilarity, GLCMmean, GLCMvariance and contrast were the most relevant. Regarding the source bands of the texture metrics, the most important were mainly derived from B2, B3, B5 and B6. However, several

texture metrics derived from the SAR bands also had great importance in the classification scheme, which is not in vain; the metric VH-GLCMMean in winter is ranked first of all, with great influence in the discrimination of irrigated warm seasonal crops (AgI), rainfed cherry tree plantations (Agc), evergreen broadleaf forest (EBF), deciduous broadleaf forest (DBF) and impervious surfaces (Imp). In addition, the SWIR (B11) band had a great influence on the classification. In this regard, the land cover signature of the predictors was categorized using a box-plot graph representing the normalized values (from 0 to 1) from the first quartile to the third quartile and, as shown in Fig.S1 in Online Resource 1, different responses among the land cover categories were observed.

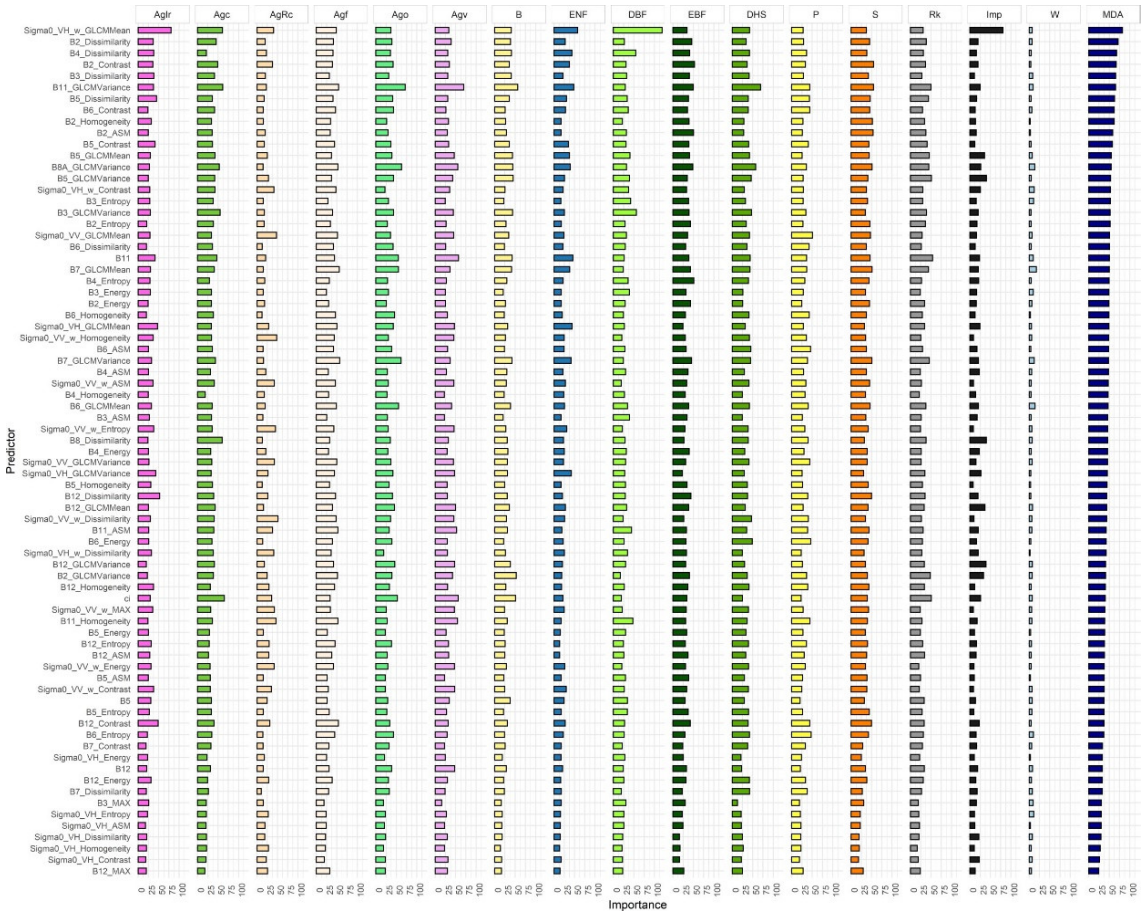

Fig. 8 Feature importance results of the optimal RF algorithm. Ranking of the predictor importances in terms of the mean decrease accuracy (MDA) measure, MDA from a global standpoint and MDA values for each category.

3.5 Land cover results

Fig. 9 shows the final land cover types after the application of postclassification processing. These maps were the starting point for the analysis of the variation of land cover and hydrologic

conditions in each phenological stage[2] and, finally, their equivalent maps in terms of CN values[3] (e.g., Fig. 10 in stage 3). Finally, Fig. 11 shows the weighted average CN values in each stage at the watershed and at the subwatershed levels. Two different behaviors can be observed depending on the variations in CN values throughout the year. One group included watersheds that mainly comprise land cover categories that remain invariant in both periods (operational and nonoperational); these watersheds showed an almost unchanging CN throughout the stages (e.g., *Alardos, Minchones, Estena, Hurdano* and *Ladrillar*). In contrast, the watersheds that are composed of land cover categories with different performances during the year showed shifting CN values in the stages: some had higher CN values from May to October (stages 3 and 4) (e.g., *Aljucen, Almonte, Fresneda* and *Tamuja*) and others had higher CN values from November to March (stages 1 and 5) (e.g., *Jaranda, Ambroz* and *Jerte).*

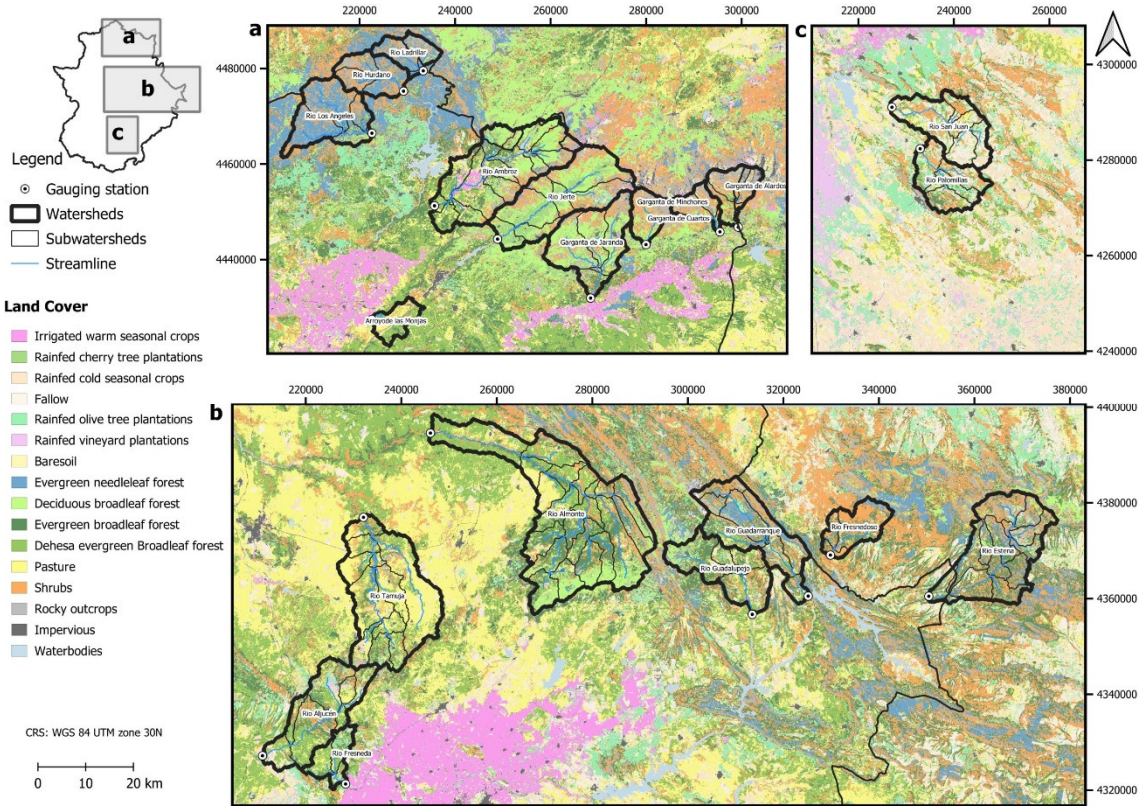

Fig. 9 Land cover maps.

[2] The variation of the NRCS cover types and hydrologic conditions through the phenological stages is shown in the animation in Online Resource 2.

[3] The variation of the NRCS-CN through the phenological stages is shown in the animation in Online Resource 3.

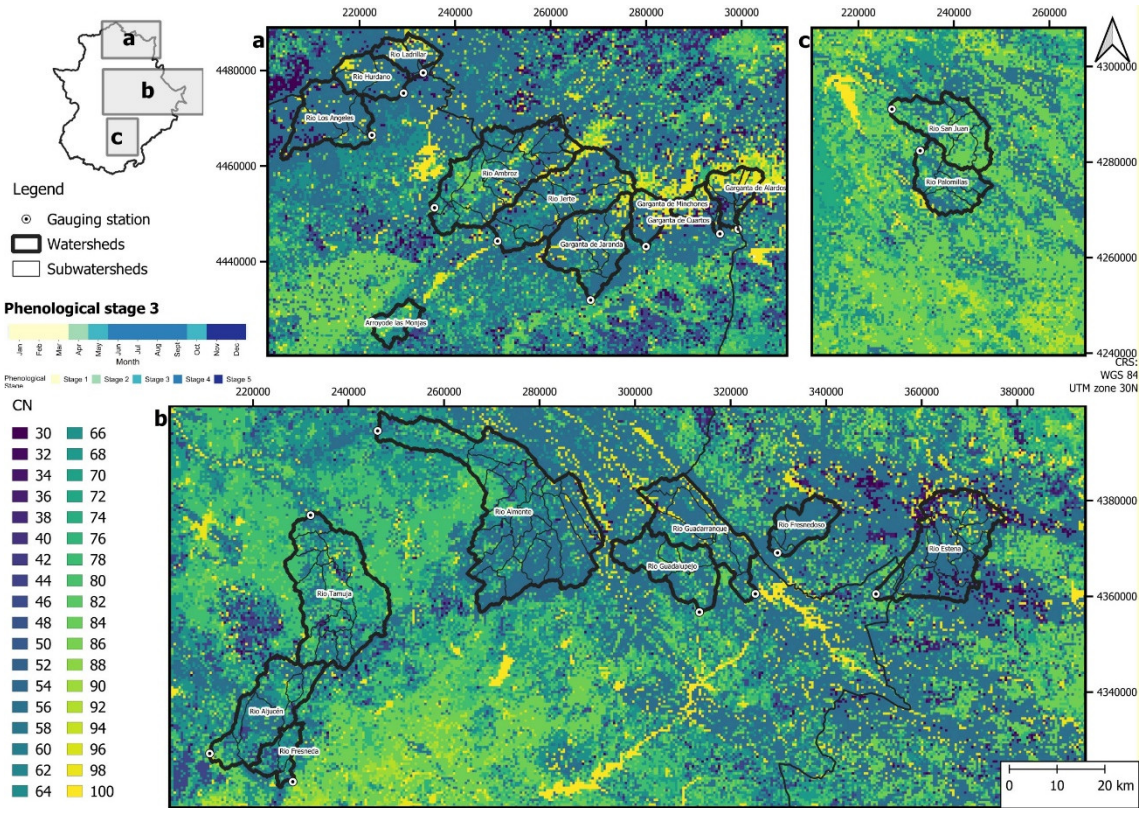

Fig. 10 Example of the NRCS-CN map in phenological stage 3.

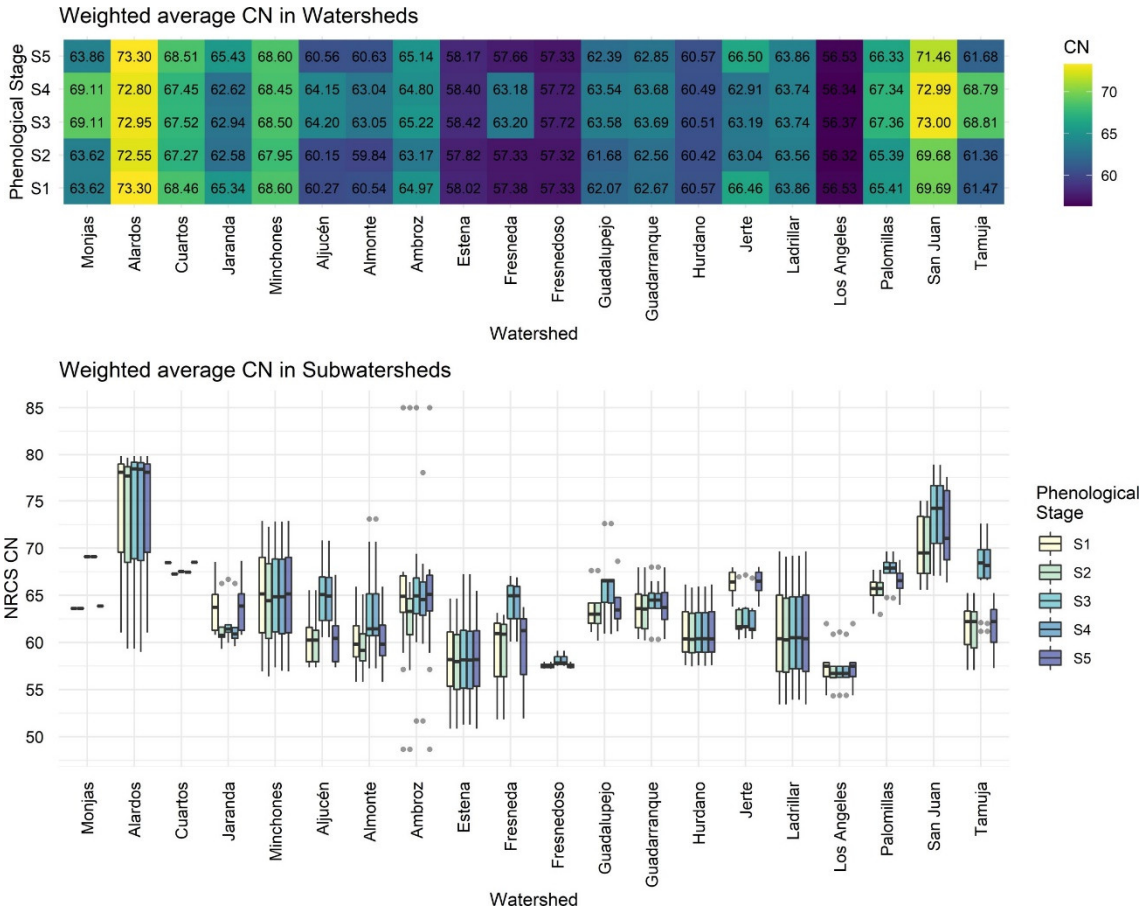

Fig. 11 Results of the CN values at the watershed and subwatershed levels.

4 Discussion

In this work, we developed a method to generate accurate *ad hoc* maps representing the spatial distribution of land cover categories from a hydrologic standpoint based on the runoff generation capabilities of the land cover categories. Here, we proposed a data fusion of SAR and optical data from the Sentinel satellites, minimizing computational issues in terms of storage capacity and computational time.

For that purpose, we carried out a multidate study requiring the data to be as minimized as possible: one single date was incorporated for optical data and two dates were used for SAR data. The acquisition dates were chosen to maximize the spectral separability of the vegetation in the Mediterranean environment. Then, we improved the dimensionality of the S1 and S2 information from 14 to 148 predictors by considering derived spectral metrics and texture metrics to be predictors. Then, we proposed a data mining process for the selection of the most important features to reduce computational issues without compromising the accuracy of the final maps. Finally, we analyzed the resulting *ad hoc* maps in terms of the variations in runoff capability due to seasonal phenology.

In terms of accuracy metrics, our results (four-k-fold cross-validation with three repetitions in each fold) achieved OAs of 93.29% (test) and 85.24% (validation), which were comparable to those of previous studies using data fusion of SAR and optical data (Table 1). Specifically, the results of this study are comparable to those of other studies that used single-date analyses in forested areas, such as those reported by Whyte et al. (2018) in their analysis focused on wetlands in South Africa, where an OA of 83.3% (k=0.72) was calculated using only the bands of S1 and S2 with derived optical indices where fifteen classes were classified. Regarding other previous works on a single date that used texture metrics as predictors, our results are better than those reported by Muthukumarasamy et al. (2019), who achieved a best OA of 78.49% (k=0.68) in the fusion of S1 and derived textures with Landsat-8 as the optical source (five classes were considered in the analysis). Finally, our results were slightly lower than those of Mishra et al. (2019), who reported an OA of 87.70% (k=0.86), although their analysis fused more data sources, such as S1 (VV, VH polarizations) and RISAT-1 (HH, HV polarizations) for SAR data and LISS-III, LISS-IV and Landsat-8 for optical data, and only seven classes were considered in their analysis, while we distinguished between sixteen land cover categories. In addition, our results are slightly better than other previous works based on multitemporal analyses and texture metrics, such as the OA of 83.97% reported by Verma et al. (2019), which used texture metrics only derived from SAR data to analyze six classes, or the OA 82.78% achieved by Liu et al. (2018), which used texture metrics only derived from optical data to classify eight land cover categories. In addition, it is worth noting that our results outperformed other previous works based on multitemporal analyses of S1 and S2 that did not incorporate texture information even if spectral

or biophysical optical indices were used (Carrasco et al. 2019; Denize et al. 2019; Mahdianpari et al. 2020; Poortinga et al. 2019; Van Tricht et al. 2018). Finally, as shown in Table 1, the aforementioned previous studies did not specifically mention the cross-validation method, so, we assumed one-k-fold cross-validation without repetition, except the analysis reported by Poortinga et al. (2019) where a Monte Carlo simulation with 100 repetition was carried out.

Regarding the differences in terms of the accuracy assessment between the test and validation datasets, the misclassification between categories in the validation dataset, especially between those with similar signatures, might be because the training data may not represent all the spectral variability of the land cover classes within a large expanse, as the one studied in this work, and the quality of the ROI is a crucial factor in obtaining accurate and trustworthy classification results (Heckel et al. 2020). Thus, the accuracy for the vegetation categories was remarkable, especially for forested areas; however, the accuracy was low for bare soil, which had by far the lowest accuracy among all of the land cover types. This category was less representative in the analysis, so the poor results must be related to the low representation of the spectral characteristics. In addition, even though the bare soil classification accuracy was poor, it only represented 0.11% of the studied area (Fig. 7 b), so it had less importance in the hydrologic response of the territory. Consequently, the accuracy achieved for the validation dataset, although lower than that achieved for the test dataset, remained outstanding, which confirmed the goodness of the proposed method of generating ROIs derived from the classification of UHSR imagery.

The results for the combinations of predictors (Table 6) showed how the SAR bands used alone or in seasonal fusion achieved the lowest accuracy results, obtaining OAs of only 25-27% (scenarios S1w – S1s) to 38% (scenario S1), with a great improvement with the addition of the SAR texture metrics to OAs of 39-45% (scenarios S1wt – S1st) to 63.2% (scenario S1t). However, the OA values obtained using only the SAR data were poor, in agreement with previous works that reported the same trend (Clerici et al. 2017; Muthukumarasamy et al. 2019; Tavares et al. 2019). Hence, the results obtained using only SAR data were weaker compared with the OA of 82.2% achieved using only the optical bands (scenario S2). The most important increment in terms of OA was the addition of the optical-derived textural features to the optical bands, which resulted in an increase in OA of 9.6 percentage points to reach an OA of 91.8% (scenario S2t). Our results are comparable to those of Mishra et al. (2019), who reported an increase in the OA of 8.1 percentage points for Landsat-8 or 14.32 percentage points for S1 after adding the textural features to the original bands. Additionally, it is worth noting that the inclusion of the indices did not improve the texture addition results, in agreement with other previous works (Numbisi et al. 2019; Tavares et al. 2019). Hence, it is important to point out that texture information in single-date analysis appeared to be more important than the use of multitemporal image series or spectral or biophysical derived indices.

Therefore, similar to findings in previous studies (Heckel et al. 2020; Mercier et al. 2019; Tavares et al. 2019), the fusion of SAR with optical data did not substantially enhance the OA of the classification in this study. However, SAR features, when applied in fusion with optical data, added supplementary information to the algorithm to enhance the discrimination between land cover categories, especially if the SAR data represented different phenological stages of the vegetation. In this sense, when adding SAR information to the optical bands, the OA increased by 4 percentage points (scenario S1tS2), but when the texture information of the optical bands was also used, the increment was less important only by 2 percentage points, achieving an OA of 93% (scenario S1tS2it). Although the improvement in accuracy was slight, it is worth noting that several metrics derived from SAR textures were selected in the data mining process. Finally, those SAR bands showed great importance in the classification scheme of the opRF (with a final OA of 93%), especially the GLCMMean and contrast of the VH polarization in winter; these factors ranked first and 15th. Considering this, the DM3 iteration was run again without the SAR information, and the decrease in terms of the OA remained at 2 percentage points (OA of 91% and kappa = 0.90). Thus, the range of improvement obtained in our results was also consistent with those reported by Heckel et al. (2020), in which an increase of 1.9-0.4 percentage points was achieved, or those reported by Tavares et al. (2019) (increase of 1.54 percentage points).

Regarding the importance of features, our results showed how texture metrics are the most important classification parameters, especially the dissimilarity, GLCMmean, GLCMvariance and contrast. The importance of these texture metrics is in agreement with the results reported by Mishra et al. (2019), while they pointed out that the best textural features depend on the sensor and the specific area, they found that the most important features were the mean, dissimilarity and entropy for optical data and the mean, variance, contrast and dissimilarity for SAR data. In addition, our results showed that the most important features are mainly derived from VIS (B2 and B3) and NIR (B5 and B6), and the SWIR B11 band also has a great influence on the classification due to its own properties.

Regarding the *ad hoc* maps, we mapped the main representative land cover types in the watersheds with high accuracy and enhanced the knowledge of the spatial distribution of the categories, which were classified according to their potential run-off capability; thus, the hydrological response of the watershed was characterized truthfully. The influence of seasonal phenology was also considered in the analysis of the hydrologic response of the watersheds; the basins composed of vegetation with higher phenology variation showed the highest differences in runoff capabilities, such as the watersheds in the *dehesa* environment, those composed of deciduous forest, and agricultural areas with seasonal crops. Our results were compared with those reported by Zeng et al. (2017), an updated version of the work by Hong and Adler (2008), who developed a global CN map from the Moderate Resolution Imaging Spectroradiometer (MODIS)

at a spatial resolution of 1 km. Although this dataset is not freely downloadable, we interpreted the results of their publication and, it seems that for the region of our study, the CN values range from 60 to 80, even with the uncertainty involved in the regionalization of a study on a global scale. Thus, our overall CN value results, ranging from 56 to 74, were consistent with the results in Zeng et al. (2017), which used fair hydrological conditions where applicable, while our study considered detailed hydrological conditions and phenological variations in vegetation.

Our results represent the territory truthfully at a high spatial resolution to address suitable seasonal hydrologic simulations at the regional scale and reducing the risk of overgeneralization of land cover categories in small watersheds (Sajikumar and Remya 2015; Walega and Salata 2019). In this regard, other previous work demonstrated that the use of a coarse global database led to an underestimation of the potential runoff in the most representative land cover in the *dehesa* environment (Fragoso-Campón et al. 2020a), underlining the importance of having accurate land cover maps in hydrological modeling; this is especially important in forested watersheds in which the NRCS-CN method is weaker than it is in nonforested watersheds (Tedela et al. 2012; Walega et al. 2020). In addition, considering the seasonal variability of CN has been proven to be efficient in runoff simulations (Gundalia and Dholakia 2014; Paik et al. 2005). Therefore, conducting analysis of rainfall-runoff models and the seasonal runoff variability influenced by the initial abstraction ratio and the AMC is still a challenge in forested watersheds in Mediterranean environments, and future works will be focused on the best calibration of the hydrologic parameters in this regard.

5 Conclusions

In this study, seasonal *ad hoc* land cover maps for hydrological modeling were developed with high accuracies based on the fusion of S1 and S2 data and the random forest approach. The information from the satellites was improved with texture metrics and derived spectral indices, after which data mining feature selection processing was conducted to reduce computational issues, ensuring the accuracy of the final maps.

We found that the fusion of SAR with optical data did not substantially enhance the OA of the classification when compared with the optical data results alone. However, the SAR features added supplementary information to the algorithm, enhancing the discrimination between land cover categories, especially if the SAR data represented different phenological stages of the vegetation. We found that incorporating texture metrics into the analysis added effective information to the classifier and resulted as the most important classification parameters, greatly improving the accuracy of the results. In contrast, as the optical data were obtained during the dry season when the vegetation was less vigorous, the addition of derived spectral optical indices did not enhance the classification algorithm, with the exception of the soil color index, which was

selected in the data mining process as one of the important features. It is worth noting that the method we proposed achieved high accuracies, with the best selection of predictors obtained after the data mining process, and outperformed other previous works using large temporal image series, simplifying cloud-removal processing and image management and, finally, reducing the storage capacity and computational time.

As the main research goal, this study mapped the main land cover types in several watersheds with high accuracy. The land cover types were classified according to their potential run-off capabilities in terms of the NRCS-CN parameter. Thus, the hydrological response of the watersheds was characterized by truthfully analyzing the potential runoff and its variation due to seasonal phenology. We found remarkable variation in seasonal CN values in the basins with higher phenological variation, proving that representing the territory truthfully, with a high spatial resolution, is required to address seasonal hydrologic simulations at regional scales in small watersheds. Future research will be focused on the analysis of rainfall-runoff models and the seasonal runoff variability in forested watersheds in Mediterranean environments.

References

Ahmed OS, Franklin SE, Wulder MA, White JC (2015) Characterizing stand-level forest canopy cover and height using Landsat time series, samples of airborne LiDAR, and the random forest algorithm ISPRS Journal of Photogrammetry and Remote Sensing 101:89-101 doi:10.1016/j.isprsjprs.2014.11.007

Akike S, Samanta S (2016) Land Use/Land Cover and Forest Canopy Density Monitoring of Wafi-Golpu Project Area, Papua New Guinea Journal of Geoscience and Environment Protection 4:1 doi:10.4236/gep.2016.48001

Astuti IS, Sahoo K, Milewski A, Mishra DR (2019) Impact of land use land cover (LULC) change on surface runoff in an increasingly urbanized tropical watershed Water Resources Management 33:4087-4103 doi:10.1007/s11269-019-02320-w

Athira P, Sudheer KP, Cibin R, Chaubey I (2016) Predictions in ungauged basins: an approach for regionalization of hydrological models considering the probability distribution of model parameters Stochastic environmental research and risk assessment 30:1131-1149 doi:10.1007/s00477-015-1190-6

Ballabio C, Panagos P, Monatanarella L (2016) Mapping topsoil physical properties at European scale using the LUCAS database Geoderma 261:110-123 doi:10.1016/j.geoderma.2015.07.006

Becker R, Koppa A, Schulz S, Usman M, Beek Tad, Schüth C (2019) Spatially distributed model calibration of a highly managed hydrological system using remote sensing-derived ET data Journal of Hydrology 577:123944 doi:10.1016/j.jhydrol.2019.123944

Belgiu M, Drăguţ L (2016) Random forest in remote sensing: A review of applications and future directions ISPRS Journal of Photogrammetry and Remote Sensing 114:24-31 doi:10.1016/j.isprsjprs.2016.01.011

Bolton DK, White JC, Wulder MA, Coops NC, Hermosilla T, Yuan X (2018) Updating stand-level forest inventories using airborne laser scanning and Landsat time series data International Journal of Applied Earth Observation and Geoinformation 66:174-183 doi:10.1016/j.jag.2017.11.016

Breiman L (2001) Random forests Machine learning 45:5-32 doi:10.1023/A:1010933404324

Brinkhoff J, Vardanega J, Robson AJ (2020) Land Cover Classification of Nine Perennial Crops Using Sentinel-1 and-2 Data Remote Sensing 12 doi:10.3390/rs12010096

Carrasco L, O'Neil AW, Morton RD, Rowland CS (2019) Evaluating Combinations of Temporally Aggregated Sentinel-1, Sentinel-2 and Landsat 8 for Land Cover Mapping with Google Earth Engine Remote Sensing 11 doi:10.3390/rs11030288

Chen T et al. (2019) Merging ground and satellite-based precipitation data sets for improved hydrological simulations in the Xijiang River basin of China Stochastic Environmental Research and Risk Assessment 33:1893-1905 doi:10.1007/s00477-019-01731-w

Clerici N, Valbuena Calderon CA, Manuel Posada J (2017) Fusion of Sentinel-1A and Sentinel-2A data for land cover mapping: a case study in the lower Magdalena region, Colombia Journal of Maps 13:718-726 doi:10.1080/17445647.2017.1372316

Congalton RG, Green K (2008) Assessing the accuracy of remotely sensed data: principles and practices. Second edn. CRC press,

Copernicus Program (2020) Copernicus Open Access Hub. https://scihub.copernicus.eu/dhus/#/home. Accessed 01/01/2020 2020

Delegido J, Verrelst J, Alonso L, Moreno J (2011) Evaluation of sentinel-2 red-edge bands for empirical estimation of green LAI and chlorophyll content Sensors 11:7063-7081

Denize J, Hubert-Moy L, Betbeder J, Corgne S, Baudry J, Pottier E (2019) Evaluation of Using Sentinel-1 and-2 Time-Series to Identify Winter Land Use in Agricultural Landscapes Remote Sensing 11 doi:10.3390/rs11010037

Dias LCP, Macedo MN, Costa MH, Coe MT, Neill C (2015) Effects of land cover change on evapotranspiration and streamflow of small catchments in the Upper Xingu River Basin,

Central Brazil Journal of Hydrology: Regional Studies 4:108-122 doi:10.1016/j.ejrh.2015.05.010

Diaz M, Campos P, Pulido FJ (1997) The Spanish dehesas: a diversity in land-use and wildlife. In: Pain D, Pienkowski M (eds) Farming and birds in Europe. Academic Press, London, pp 178-209

Dionizio EA, Costa MH (2019) Influence of land use and land cover on hydraulic and physical soil properties at the cerrado agricultural frontier Agriculture 9:24 doi:10.3390/agriculture9010024

Escadafal R, Huete A (1991) Etude des propriétés spectrales des sols arides appliquée à l'amélioration des indices de végétation obtenus par télédétection Comptes rendus de l'Académie des sciences Série 2, Mécanique, Physique, Chimie, Sciences de l'univers, Sciences de la Terre 312:1385-1391

Fassnacht FE et al. (2016) Review of studies on tree species classification from remotely sensed data Remote Sensing of Environment 186:64-87 doi:10.1016/j.rse.2016.08.013

Feng Q, Yang J, Zhu D, Liu J, Guo H, Bayartungalag B, Li B (2019) Integrating Multitemporal Sentinel-1/2 Data for Coastal Land Cover Classification Using a Multibranch Convolutional Neural Network: A Case of the Yellow River Delta Remote Sensing 11 doi:10.3390/rs11091006

Ferreira MP, Zortea M, Zanotta DC, Shimabukuro YE, Filho CRdS (2016) Mapping tree species in tropical seasonal semi-deciduous forests with hyperspectral and multispectral data Remote Sensing of Environment 179:66-78 doi:10.1016/j.rse.2016.03.021

Flores-Anderson AI, Herndon KE, Thapa RB, Cherrington E (2019) The SAR Handbook: Comprehensive Methodologies for Forest Monitoring and Biomass Estimation doi:10.25966/nr2c-s697

Fragoso-Campón L, Quirós E, Gallego JAG (2020a) Dehesa environment mapping with transference of a Random Forest classifier to neighboring ultra-high spatial resolution imagery at class and macro-class land cover levels Stochastic Environmental Research and Risk Assessment:1-32 doi:10.1007/s00477-020-01880-3

Fragoso-Campón L, Quirós E, Mora J, Gutiérrez Gallego JA, Durán-Barroso P (2020b) Overstory-understory land cover mapping at the watershed scale: accuracy enhancement by multitemporal remote sensing analysis and LiDAR Environmental Science and Pollution Research 27:75-88 doi:10.1007/s11356-019-04520-8

Gao B-C (1996) NDWI—A normalized difference water index for remote sensing of vegetation liquid water from space Remote sensing of environment 58:257-266

Ghosh A, Fassnacht FE, Joshi PK, Koch B (2014) A framework for mapping tree species combining hyperspectral and LiDAR data: Role of selected classifiers and sensor across three spatial scales International Journal of Applied Earth Observation and Geoinformation 26:49-63 doi:10.1016/j.jag.2013.05.017

Gitelson AA, Kaufman YJ, Merzlyak MN (1996) Use of a green channel in remote sensing of global vegetation from EOS-MODIS Remote sensing of Environment 58:289-298

Godinho S, Guiomar N, Gil A (2017) Estimating tree canopy cover percentage in a mediterranean silvopastoral systems using Sentinel-2A imagery and the stochastic gradient boosting algorithm International Journal of Remote Sensing:1-23 doi:10.1080/01431161.2017.1399480

Gundalia M, Dholakia M (2014) Impact of monthly curve number on daily runoff estimation for Ozat catchment in India Open Journal of Modern Hydrology 4:144 doi:10.4236/ojmh.2014.44014

Haralick RM, Shanmugam K (1973) Textural features for image classification IEEE Transactions on systems, man, and cybernetics:610-621 doi:10.1109/TSMC.1973.4309314

Hastie T, Tibshirani R, Friedman J (2009) The elements of statistical learning: data mining, inference, and prediction. In. Springer Science & Business Media, pp 587-601. doi:10.1007/b94608

Heckel K, Urban M, Schratz P, Mahecha MD, Schmullius C (2020) Predicting Forest Cover in Distinct Ecosystems: The Potential of Multi-Source Sentinel-1 and-2 Data Fusion Remote Sensing 12 doi:10.3390/rs12020302

Hijmans RJ (2019) raster: Geographic Data Analysis and Modeling., R package version 2.9-5. edn.,

Hong Y, Adler R (2008) Estimation of global SCS curve numbers using satellite remote sensing and geospatial data International Journal of Remote Sensing 29:471-477 doi:10.1080/01431160701264292

Hościło A, Lewandowska A (2019) Mapping forest type and tree species on a regional scale using multi-temporal Sentinel-2 data Remote Sensing 11:929 doi:10.3390/rs11080929

Huete A (1988) A soil-adjusted vegetation index (SAVI) Remote Sensing of Environment 25:259-309 doi:10.1016/0034-4257(88)90106-X

Huete AR, Post DF, Jackson RD (1984) Soil spectral effects on 4-space vegetation discrimination Remote sensing of environment 1984 v.15 no.2:pp. 155-165 doi:10.1016/0034-4257(84)90043-9

Ienco D, Interdonato R, Gaetano R, Dinh Ho Tong M (2019) Combining Sentinel-1 and Sentinel-2 Satellite Image Time Series for land cover mapping via a multi-source deep learning architecture Isprs Journal of Photogrammetry and Remote Sensing 158:11-22 doi:10.1016/j.isprsjprs.2019.09.016

Immitzer M, Neuwirth M, Böck S, Brenner H, Vuolo F, Atzberger C (2019) Optimal Input Features for Tree Species Classification in Central Europe Based on Multi-Temporal Sentinel-2 Data Remote Sensing 11:2599 doi:10.3390/rs11222599

Joint Research Centre (2020) European Soil Data Centre (ESDAC). European Commission. https://esdac.jrc.ec.europa.eu/. Accessed 20/07/2020

Karunanidhi D, Anand B, Subramani T, Srinivasamoorthy K (2020) Rainfall-surface runoff estimation for the Lower Bhavani basin in south India using SCS-CN model and geospatial techniques Environmental Earth Sciences 79:1-19 doi:10.1007/s12665-020-09079-z

Khan A, Govil H, Kumar G, Dave R (2020) Synergistic use of Sentinel-1 and Sentinel-2 for improved LULC mapping with special reference to bad land class: a case study for Yamuna River floodplain, India Spatial Information Research doi:10.1007/s41324-020-00325-x

Kuhn M et al. (2018) caret: Classification and Regression Training., R package version 6.0-81. edn.,

Leemhuis C et al. (2017) Sustainability in the food-water-ecosystem nexus: The role of land use and land cover change for water resources and ecosystems in the Kilombero Wetland, Tanzania Sustainability 9:1513 doi:10.3390/su9091513

Li L, Li N, Lu D, Chen Y (2019) Mapping Moso bamboo forest and its on-year and off-year distribution in a subtropical region using time-series Sentinel-2 and Landsat 8 data Remote Sensing of Environment 231:111265 doi:10.1016/j.rse.2019.111265

Liaw A, Wiener M (2002) Classification and regression by randomForest R News 2/3

Liu Y, Gong W, Hu X, Gong J (2018) Forest type identification with random forest using Sentinel-1A, Sentinel-2A, multi-temporal Landsat-8 and DEM data Remote Sensing 10:946 doi:10.3390/rs10060946

Lopes M, Frison P-L, Durant SM, to Buhne HS, Ipavec A, Lapeyre V, Pettorelli N (2020) Combining optical and radar satellite image time series to map natural vegetation: savannas as an example Remote Sensing in Ecology and Conservation doi:10.1002/rse2.139

Luan X-B, Wu P-T, Sun S-K, Li X-L, Wang Y-B, Gao X-R (2018) Impact of land use change on hydrologic processes in a large plain irrigation district Water Resources Management 32:3203-3217 doi:10.1007/s11269-018-1986-5

Magiera A, Feilhauer H, Tephnadze N, Waldhardt R, Otte A (2016) Separating reflectance signatures of shrub species - a case study in the Central Greater Caucasus Applied Vegetation Science 19:304-315 doi:10.1111/avsc.12205

Mahdianpari M et al. (2020) Big Data for a Big Country: The First Generation of Canadian Wetland Inventory Map at a Spatial Resolution of 10-m Using Sentinel-1 and Sentinel-2 Data on the Google Earth Engine Cloud Computing Platform Canadian Journal of Remote Sensing doi:10.1080/07038992.2019.1711366

Marin M et al. (2020) Assessing the vulnerability of water resources in the context of climate changes in a small forested watershed using SWAT: A review Environmental Research:109330 doi:doi.org/10.1016/j.envres.2020.109330

Martínez-Salvador A, Conesa-García C (2020) Suitability of the SWAT Model for Simulating Water Discharge and Sediment Load in a Karst Watershed of the Semiarid Mediterranean Basin Water Resources Management:1-18 doi:10.1007/s11269-019-02477-4

Mas J-F, Gao Y, Navarrete Pacheco JA (2010) Sensitivity of landscape pattern metrics to classification approaches Forest Ecology and Management 259:1215-1224 doi:10.1016/j.foreco.2009.12.016

Mathieu R, Pouget M, Cervelle B, Escadafal R (1998) Relationships between satellite-based radiometric indices simulated using laboratory reflectance data and typic soil color of an arid environment Remote sensing of environment 66:17-28 doi:10.1016/S0034-4257(98)00030-3

Matikainen L, Karila K (2011) Segment-based land cover mapping of a suburban area—Comparison of high-resolution remotely sensed datasets using classification trees and test field points Remote Sensing 3:1777-1804

Mercier A et al. (2019) Evaluation of Sentinel-1 and 2 Time Series for Land Cover Classification of Forest-Agriculture Mosaics in Temperate and Tropical Landscapes Remote Sensing 11 doi:10.3390/rs11080979

Mishra VN, Prasad R, Rai PK, Vishwakarma AK, Arora A (2019) Performance evaluation of textural features in improving land use/land cover classification accuracy of heterogeneous landscape using multi-sensor remote sensing data Earth Science Informatics 12:71-86 doi:10.1007/s12145-018-0369-z

Muthukumarasamy I, Shanmugam RS, Usha T (2019) Incorporation of textural information with SAR and optical imagery for improved land cover mapping Environmental Earth Sciences 78 doi:10.1007/s12665-019-8654-9

Nageswara Rao K (2020) Analysis of surface runoff potential in ungauged basin using basin parameters and SCS-CN method Applied Water Science 10:1-16 doi:10.1007/s13201-019-1129-z

Netzer MS, Sidman G, Pearson TR, Walker SM, Srinivasan R (2019) Combining global remote sensing products with hydrological modeling to measure the impact of tropical forest loss on water-based ecosystem services Forests 10:413 doi:10.3390/f10050413

NRCS (2004) Chapter 9: Hydrologic Soil-Cover Complexes. In: NRCS National Engineering Handbook, Part 630: Hydrology. Engineering Division, US. Department of Agriculture

Washington, DC,

NRCS (2009) National Engineering Handbook, section 4, Hydrology, version (1956, 1964, 1971, 1985, 1993, 2004, 2009). National Engineering Handbook. Engineering Division, US. Department of Agriculture, Washington, DC

Numbisi FN, Van Coillie FMB, De Wulf R (2019) Delineation of Cocoa Agroforests Using Multiseason Sentinel-1 SAR Images: A Low Grey Level Range Reduces Uncertainties in GLCM Texture-Based Mapping Isprs International Journal of Geo-Information 8 doi:10.3390/ijgi8040179

Paik K, Kim JH, Kim HS, Lee DR (2005) A conceptual rainfall-runoff model considering seasonal variation Hydrological Processes: An International Journal 19:3837-3850 doi:10.1002/hyp.5984

Parajuli PB, Jayakody P, Ouyang Y (2018) Evaluation of using remote sensing evapotranspiration data in SWAT Water resources management 32:985-996 doi:10.1007/s11269-017-1850-z

Poortinga A, Tenneson K, Shapiro A, Quyen N, San Aung K, Chishtie F, Saah D (2019) Mapping Plantations in Myanmar by Fusing Landsat-8, Sentinel-2 and Sentinel-1 Data along with Systematic Error Quantification Remote Sensing 11 doi:10.3390/rs11070831

Qi J, Chehbouni A, Huete A, Kerr Y, Sorooshian S (1994) A modified soil adjusted vegetation index Remote sensing of environment 48:119-126 doi:10.1016/0034-4257(94)90134-1

Rivas-Martinez S, Rivas-Saenz S (1996-2019) Worldwide Bioclimatic Classification System. http://www.globalbioclimatics.org/form/tb_map/index.htm. Accessed July 2019

Rouse Jr J, Haas R, Schell J, Deering D (1974) Monitoring vegetation systems in the Great Plains with ERTS. Paper presented at the Third Earth Resources Technology Satellite-1 Symposium, Washington, D.C.,

Sajikumar N, Remya R (2015) Impact of land cover and land use change on runoff characteristics Journal of Environmental Management 161:460-468 doi:10.1016/j.jenvman.2014.12.041

Stavrakoudis D, Dragozi E, Gitas I, Karydas C (2014) Decision fusion based on hyperspectral and multispectral satellite imagery for accurate forest species mapping Remote Sensing 6:6897-6928 doi:10.3390/rs6086897

Steinhausen MJ, Wagner PD, Narasimhan B, Waske B (2018) Combining Sentinel-1 and Sentinel-2 data for improved land use and land cover mapping of monsoon regions International Journal of Applied Earth Observation and Geoinformation 73:595-604 doi:10.1016/j.jag.2018.08.011

Stromann O, Nascetti A, Yousif O, Ban Y (2020) Dimensionality Reduction and Feature Selection for Object-Based Land Cover Classification based on Sentinel-1 and Sentinel-2 Time Series Using Google Earth Engine Remote Sensing 12 doi:10.3390/rs12010076

Su T-C (2016) A filter-based post-processing technique for improving homogeneity of pixel-wise classification data European Journal of Remote Sensing 49:531-552 doi:10.5721/EuJRS20164928

Tavares PA, Santos Beltrao NE, Guimaraes US, Teodoro AC (2019) Integration of Sentinel-1 and Sentinel-2 for Classification and LULC Mapping in the Urban Area of Belem, Eastern Brazilian Amazon Sensors 19 doi:10.3390/s19051140

Tedela NH et al. (2012) Runoff Curve Numbers for 10 small forested watersheds in the mountains of the Eastern United States Journal of Hydrologic Engineering 17:1188-1198 doi:10.1061/(ASCE)HE.1943-5584.0000436.

van Lier OR, Fournier RA, Bradley RL, Thiffault N (2009) A multi-resolution satellite imagery approach for large area mapping of ericaceous shrubs in Northern Quebec, Canada International Journal of Applied Earth Observation and Geoinformation 11:334-343 doi:10.1016/j.jag.2009.05.003

Van Tricht K, Gobin A, Gilliams S, Piccard I (2018) Synergistic Use of Radar Sentinel-1 and Optical Sentinel-2 Imagery for Crop Mapping: A Case Study for Belgium Remote Sensing 10 doi:10.3390/rs10101642

Verma A, Kumar A, Lal K (2019) Kharif crop characterization using combination of SAR and MSI Optical Sentinel Satellite datasets Journal of Earth System Science 128 doi:10.1007/s12040-019-1260-0

Walega A, Amatya DM, Caldwell P, Marion D, Panda S (2020) Assessment of storm direct runoff and peak flow rates using improved SCS-CN models for selected forested watersheds in the Southeastern United States Journal of Hydrology: Regional Studies 27:100645 doi:10.1016/j.ejrh.2019.100645

Walega A, Salata T (2019) Influence of land cover data sources on estimation of direct runoff according to SCS-CN and modified SME methods Catena 172:232-242 doi:10.1016/j.catena.2018.08.032

Wang N, Liu W, Sun F, Yao Z, Wang H, Liu W (2020) Evaluating satellite-based and reanalysis precipitation datasets with gauge-observed data and hydrological modeling in the Xihe River Basin, China Atmospheric Research 234:104746 doi:10.1016/j.atmosres.2019.104746

Wei S, Zhang H, Wang C, Wang Y, Xu L (2019) Multi-temporal SAR data large-scale crop mapping based on U-Net model Remote Sensing 11:68 doi:10.3390/rs11010068

Whyte A, Ferentinos KP, Petropoulos GP (2018) A new synergistic approach for monitoring wetlands using Sentinels-1 and 2 data with object-based machine learning algorithms Environmental Modelling & Software 104:40-54 doi:10.1016/j.envsoft.2018.01.023

Yu Q, Xing M, Liu X, Wang L, Luo K, Quan X Detection of Land Use Type Using Multitemporal SAR Images. In: IGARSS 2019-2019 IEEE International Geoscience and Remote Sensing Symposium, 2019. IEEE, pp 1534-1537. doi:10.1109/IGARSS.2019.8898077

Zeng Z, Tang G, Hong Y, Zeng C, Yang Y (2017) Development of an NRCS curve number global dataset using the latest geospatial remote sensing data for worldwide hydrologic applications Remote Sensing Letters 8:528-536 doi:10.1080/2150704X.2017.1297544

Zhao Y et al. (2016) Detailed dynamic land cover mapping of Chile: Accuracy improvement by integrating multi-temporal data Remote sensing of environment 183:170-185 doi:10.1016/j.rse.2016.05.016

3.5. Publicación N.º 5

Publicación	**GEDI Elevation Accuracy Assessment: A Case Study of Southwest Spain**				
Autores	Quirós, Elia · Polo, María-Eugenia · **Fragoso-Campón, Laura**				
Revista	Journal of Selected Topics in Applied Earth Observations and Remote Sensing (2021)				
eISSN	2151-1535				
DOI	10.1109/JSTARS.2021.3080711				
Fuente de Impacto	Índice 5 años	Índice 2019	Categoría	Rank	Cuartil
WOS (JCR)	3,909	3,827	Geography, physical	8/50	Q1
			Remote Sensing	11/30	Q2
Aportación de la doctoranda:	Metodología, programas informáticos, análisis estadístico, redacción-revisión del borrador y versión final.				

The final publication is available at https://ieeexplore.ieee.org/

GEDI Elevation Accuracy Assessment: A Case Study of Southwest Spain

Elia Quirós, María-Eugenia Polo, Laura Fragoso-Campón

***Abstract*— Information about forest structures is becoming crucial to Earth's global carbon cycle, forest habitats and biodiversity. The Global Ecosystem Dynamics Investigation (GEDI) provides 25-m diameter footprints of the surface for 3D structure measurements. The main goal of this study is to compare 12 031 footprints of GEDI data with other airborne and spaceborne Digital Elevation Models (DEMs) for Southwest Spain. Ground elevation differences (ELM) are analyzed by comparing GEDI measurements with ALS LiDAR- and TanDEM-X-derived DEMs. The vertical structure (RH100) is compared to the ALS LiDAR measurement. Ten zones are analyzed, considering different degrees of coverage and slopes. We achieved an RMSE of 6.13 m for the ELM when comparing GEDI and LiDAR data and an RMSE of 7.14 m when comparing GEDI and TanDEM-X data. For some of the studied areas, these values were considerably smaller, with RMSE values even lower than 1 m. For the RH100 metric, an RMSE of 3.56 m was achieved when comparing GEDI and LiDAR data, but again with a minimum value of 2.09 m for one zone. The results show a clear relation to coverage and slope, especially for the latter. This work also evaluates the positional uncertainty of GEDI footprints, shifting them ±10 and ±5 m along and across the track of the satellite orbit and their intermediate angular positions. The outcomes reveal a strong tendency to obtain better results in the ELM when setting the footprint to 270° and displacing it within 10 m of its positional uncertainty in comparison with the LiDAR and TanDEM-X data.**

***Index Terms*— Digital elevation models, Error analysis, Forestry, Uncertainty, Vegetation mapping.**

I. Introduction

In recent years, LiDAR technology has become a powerful tool for the study of the earth's surface from a three-dimensional perspective. LiDAR remote sensing from three platforms – ground, airborne, and spaceborne – has the potential to acquire direct three-dimensional measurements of the forest canopy that are useful for estimating a variety of forest inventory parameters [1].

Airborne laser scanning (ALS) has been, in recent decades, the main source of information used for forest structure modeling. Large areas or even whole countries are covered with 3D point clouds collected by ALS systems [2]. ALS data are used in multiple forest settings, such as to estimate aboveground biomass [3], to determine forest fuel characteristics of mortality-affected forests [4], to delineate crowns and classify tree species [5-7] or even to separate overstories and understories in forested areas [8], in some cases in combination with spectral images.

Two spaceborne laser scanners (SLSs) with the ability to scan vegetation structures, the ICEsat-2 and Global Ecosystem Dynamics Investigation (GEDI) missions, were launched in 2018. In the case of ICEsat-2, this was not its main objective, as its central mission was to enable the estimation of heights of ice sheets and sea ice thickness. However, it can provide an initial estimation of global vegetation height [9]. From its launch, it has been used to estimate aboveground biomass and forest canopy cover in Narine, et al. [10] and even to map forest canopy height in Li, et al. [11] with other satellite images.

On December 5, 2018, the National Aeronautics and Space Administration (NASA) launched the GEDI spaceborne LiDAR sensor, designed to measure the Earth surface structure and canopy structure of vegetation and to provide a biomass map at a 1 km spatial resolution [12]. The GEDI was deployed on the International Space Station (ISS) and started operations on March 25th 2019. The GEDI mission, which is scheduled to be operational for at least two years, is expected to collect approximately 10 billion cloud-free land surface observations. The goal of the GEDI mission is to provide data for studying forest structures and biomass in tropical and temperate environments of between 51.6° north and south, following the ISS path and being the first instrument specifically optimized to measure vegetation structures [13].

The GEDI instrument is comprised of 3 geodetic-class lasers, one of which is split into two weaker energy beams, resulting in four GEDI beams that are optically dithered to form 8 parallel tracks. These parallel tracks are spaced 600 m across the flight track direction, leaving a distance of 4.2 km between the first and last tracks. Each laser shoots 242 times per second, creating a footprint with a 25 m diameter on the surface on which the 3D structure is measured. The edge of every footprint is separated 35 m from the following or, equivalently, the footprint centers are separated 60 m apart [13, 14].

The GEDI provides some data products for each footprint that can be freely downloaded from the NASA EarthData

Manuscript received November 19, 2020. (Corresponding author: Elia Quirós). This work was supported in part by the Government of Extremadura (Spain) and co-funded by the European Regional Development Fund under Grants GR18028 (KRAKEN) and GR18052 (DESOSTE); and the participation of L. Fragoso-Campón was funded by the Junta de Extremadura and the European Social Fund under Grant PD16018.

Elia Quirós is with the Department of Graphic Expression, University of Extremadura, Polytechnic School, 10003 Cáceres, Spain (equiros@unex.es).

Maria-Eugenia Polo is with the Department of Graphic Expression, University of Extremadura, University Centre of Mérida, 06800 Mérida, Spain.

Laura Fragoso-Campón is with the Department of Graphic Expression, University of Extremadura, Polytechnic School, 10003 Cáceres, Spain.

Platform[1]. There are several levels of products available for download [13]. The raw waveforms collected by the system are delivered at the L1A level. Waveforms processed to identify ground elevation, canopy top height, and relative height (RH metrics) are included in the L2A dataset. In L2B, various canopy metrics are calculated. Level 3 products are gridded by spatially interpolating L2 footprint estimates of topography, canopy height, canopy cover, the Leaf Area Index (LAI), vertical foliage profiles and their uncertainties. Level 4 products are the highest levels GEDI products, and they measure above-ground biomass density. Level 1B, Level 2A, and Level 2B data from the GEDI are available from the Land Processes DAAC[2]. Gridded Level 3 GEDI data will be available from ORNL DAAC beginning in mid-2020 with Level 4 data to follow in early 2021.

GEDI data are being used for multiple purposes, such as to estimate time since the last stand-replacing disturbance to model forest ecosystem processes [15], estimate biomass [14, 16], estimate forest height [17], explore the relation between the vertical canopy structures and tree species [18], detect changes in forest structures [19], map the diversity of canopy structures [12] or even define the elevation for inland waterbody altimetry [20].

LiDAR systems are not the only systems with the ability to provide three-dimensional information about the surface of the earth. Synthetic aperture radar (SAR) has been used for forest monitoring for several years. SAR satellites have been proven to discriminate forest/vegetation [21, 22], not only to map forest vegetation [23-25] but also to characterize the vertical forest structure [26] to estimate forest aboveground biomass [27-29] and many other variables.

Several SAR satellites can be used for forest monitoring [30], such as SENTINEL 1 [31], ALOS PALSAR [32], ICESat GLAS [11], ENVISAT ASAR and RADARSAT [33] and one of the most used, TanDEM-X [34]. Since September 2010, a second satellite TanDEM-X (TDX) was added to TerraSAR-X (TSX) for the acquisition of a global digital elevation model (DEM) from bistatic X-band interferometric SAR acquisitions. The TanDEM-X mission was financed by a public-private partnership between DLR and Airbus Defense & Space. Since September 2016, the TanDEM-X DEM has been considered one of the most consistent, highly accurate and complete global DEM datasets of the Earth's surface [35]. There are several DEM products: the TanDEM-X DEM, the TanDEM-X Intermediate DEM and DEMs for special user requests. The first is a global product with a nominal pixel of 0.4 arcseconds that corresponds to approximately 12 m. The DEM's production includes the generation of other information layers, such as height error map data, which represent the height error (standard deviation), from rigorous error propagation. Many studies have confirmed the usefulness of the TanDEM-X DEM for various purposes. It is used mainly for flood detection [36] and other hydrological purposes [37]. However, works have also used the model to obtain canopy height models for forested areas [38].

As noted above, GEDI measurements of forest canopy height, canopy vertical structures, and surface elevation are used to characterize important carbon and water cycling processes, biodiversity levels, and habitats [39], but as the GEDI is a sampling mission, it is limited in the spatial resolution of grids (wall-to-wall) that can be produced. A finer, continuous spatial resolution can be achieved by combining these data with other remote sensing data [13, 40]. The fusion approach from GEDI and TanDEM-X indicates a great possibility for generating global-scale forest maps and biomass maps (where the GEDI data will be available) with unprecedented spatial resolution [41]. In this sense, GEDI data are combined with TanDEM-X measurements in Choi, et al. [42], Lee, et al. [41]and Lee, et al. [43] to express physical forest structure. This approach was also used for forest structure modeling before the GEDI launch [44] with simulated GEDI data.

Additionally, GEDI data have been combined with ALS, but in this case, this was not done to extrapolate the intermittent GEDI measurements but to evaluate the accuracy of both datasets, especially in quantifying the biomass and vertical structure of vegetation. The assessment of GEDI and ALS measurements has been carefully analyzed in Silva, et al. [45] and Hancock, et al. [46] but with simulated GEDI observations. It is challenging to interpolate the data between spotted data to match with the other optical images (continuous overage data). To prove the method and validate the height data, the ground locations between field measurement places and laser shot area have to be matched accurately [47].

Therefore, the study of differences in elevation between actual data captured by the GEDI satellite and other sources of information with which it is usually combined is now necessary. The GEDI is proving to spur a major revolution in global forest monitoring. As stated in Duncanson, et al. [14], the accuracy of vegetation metrics depends on the accuracy of the ground elevation estimation for each waveform. Its recent emergence means that its accuracy, in terms of measured elevations (terrain height and canopy height), has not been studied in detail, and it is necessary, while the GEDI mission's ground finding algorithm is still under development [14].

In this way, the overall goal of this study is to compare GEDI elevation real data with other airborne and spaceborne DEM data for Southwest Spain. For this purpose, ground elevation differences were analyzed by comparing GEDI measurements with ALS- and TanDEM-X-derived DEMs. Complementarily, and due to the great importance of vertical structure data for the GEDI sensor, differences between vegetation heights and the elevations of its upper end were compared to ALS measurements. Finally, all comparisons have been extended to the whole area of uncertainty in geolocation of the footprint, studying whether there is any predominant trend for a better fit between GEDI measurements and ALS- and TanDEM-X-derived DEMs.

[1] https://earthdata.nasa.gov/

[2] https://daac.ornl.gov/cgi-bin/dataset_lister.pl?p=40

II. Study Area and Datasets

The study areas are located in Southwest Spain in the region of Extremadura of the province of Cáceres, which extends across latitudes of 39.03° to 40.48° N and longitudes of 7.54° to 4.95° W. The climatic characteristics of the study area correspond to the Mediterranean pluviseasonal continental variant [48] (Fig. 1). Ten zones with varied vegetation cover, different elevations and diverse relief characteristics were chosen (Table I).

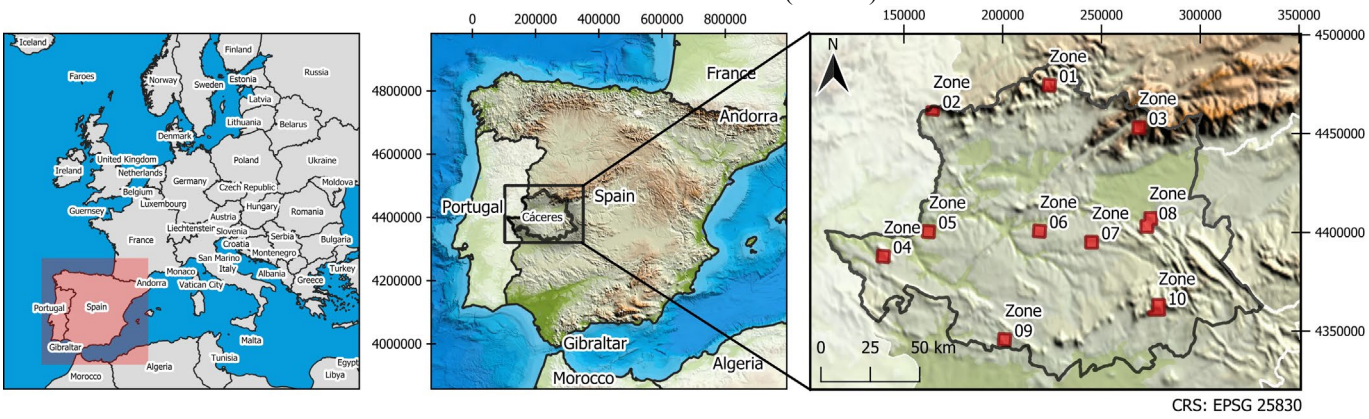

Fig. 1. Study area divided into 10 zones.

TABLE I.
General characteristics of each zone

Zone	Mean Elevation (m)	Mean Slope (º)	Predominant Coverage	Mean Percentage of Cover (%)
Zone 01	918	25.4	Mixed forest	35.0
Zone 02	766	18.1	Coniferous forest	41.7
Zone 03	1 397	22.6	Sclerophyllous vegetation	10.1
Zone 04	466	12.2	Sclerophyllous vegetation	26.0
Zone 05	286	13.3	Natural grassland	10.25
Zone 06	438	3.4	Agroforestry areas	4.6
Zone 07	449	6.8	Agroforestry areas	14.7
Zone 08	444	15.0	Agroforestry areas	22.2
Zone 09	484	9.3	Agroforestry areas	24.9
Zone 10	816	15.9	Broad-leaved forest	24.7

Three different datasets were used in this study: the GEDI dataset, which is the target dataset to be studied in terms of accuracy, the TanDEM-X dataset, which is our first source of comparative data, and the ALS LiDAR dataset, which is our second source of comparative data and, in terms of accuracy and temporal acquisition closeness, our most robust source of comparison.

GEDI is expected to obtain canopy heights generally accurate to about 1 m [49, 50]. Based on the prelaunch assessment and assuming full system calibration, the geolocation uncertainty of the data is 10 m [49]. Data were captured between May and September 2019.

The TanDEM-X DEM has an absolute horizontal and vertical accuracy level of 10 m in general. For slopes of less than 20%, the relative vertical accuracy is 2 m, and for slopes of greater than 20%, this relative accuracy is 4 m [35]. Data were acquired between 2011 and 2014.

LiDAR data were acquired between late 2018 and early 2019 with a resolution of 2 points/m^2. In terms of accuracy, LiDAR data have an altimetric RMSE of 0.15 m and planimetric RMSE of 0.30 m [51]. These features make these data the most accurate source used in this work.

The altimetric heights of the three data sources refer to the WGS-84 ellipsoid.

III. Methodology

A. Data Preparation

1) GEDI Data

GEDI data products are recorded for the full ISS orbits and are available for download at three levels of processing: Level 1B Geolocated Waveform Data, Level 2A Elevation and Height Metrics Data and Level 2B Canopy Cover and Vertical Profile Metrics Data. We used the GEDI Finder service to identify orbits over the study area. Then, the GEDI data were processed with the rGEDI R package [52].

First, we read the data for the full orbit and clipped within the boundary box of the Extremadura region. Second, the elevation and height metrics were extracted from GEDI Level 2A data for the selected footprints within the study area. The following GEDI information was extracted (Fig. 2):

- The *shot number*, which corresponds with the unique footprint identifier of every footprint in the orbit.
- *Degrade flags* indicating the degraded state of pointing and/or positioning information and showing a potential issue with the data.
- *Quality flags*, which indicate whether the waveform data are likely to be valid (1) or invalid (0).
- The *elevation of the highest return (EHR)* corresponding to the elevation of the highest detected return relative to reference ellipsoid.
- The *elevation of the lowest mode (ELM)* corresponding to the elevation of the center of the lowest mode of the received waveform in the footprint.
- *RH100* corresponding to the relative height metrics of the highest detected return (100%) and representing the difference in elevation between the highest detected return and mean ground elevation in the footprint.

The data were filtered, discarding all footprints with

degraded or invalid quality flags (0), and finally, the spatial position of the footprints was exported to shapefile format for their analysis in GIS software. As a result, a total of 12 031 footprints were used.

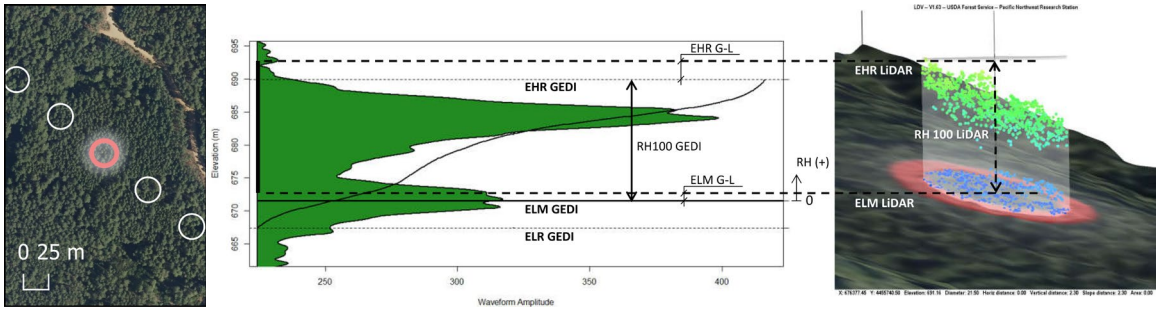

Fig 2. Interpretation of GEDI RH Metrics.

2) LiDAR Data

LiDAR data were processed with FUSION software [53], a primary research tool.

The first operation involved extracting the ground level. *GroundFilter* tool is designed to filter a cloud of LiDAR returns to identify returns that lie on the probable ground surface (bare-earth points) [54]. This algorithm is based on linear prediction and is implemented as an iterative process where some parameters need to be set. In the first step, a surface is computed with equal weights for all LiDAR points. This creates a surface that lies between the true ground and the canopy surface. Terrain points are more likely to be positioned below the surface while vegetation points are more likely to be positioned above the surface. The distance and direction to the surface are used to compute weights for each LiDAR point using the following weight function [54]:

$$p_{i=}\begin{cases} 1 & \text{If } v_i \le g \\ \dfrac{1}{1+(a(v_i-g)^b)} & \text{If } g<v_i \le g+w \\ 0 & \text{If } g+w<v_i \end{cases} \quad (1)$$

Parameters *a* and *b* determine the steepness of the weight function. The shift value, *g*, determines which points are assigned the maximum weight value of 1.0. The above ground offset parameter, *w*, is used to establish an upper limit for points to have an effect on the intermediate surface. In this study, values of *a*=1, *b*=4, *g*=-1, and *w*=1.25 were set. This combination is the one that works best for LiDAR low-density point resolution.

After the final iteration, bare-earth points are selected using the final intermediate surface. All points with elevations that satisfy the first two conditions of the weight function are considered bare-earth points [54].

The filtered bare earth point cloud was used to generate a digital elevation model (DEM) using the *GridSurfaceCreate* tool, which computes cell elevations using the average elevation of all points within a cell. Additionally, a digital surface model (DSM) was created to represent canopy cover using the *CanopyModel* tool, which creates a canopy surface model using the LiDAR point cloud and assigns to each pixel the elevation of the highest return. A spatial resolution of 2 m was used for the DEM and DSM.

Additionally, a cover analysis was performed by means of the *Cover* tool. Cover computes estimates of canopy closure using a grid. Output values for cover estimates range from 0.0 to 100.0 percent. Canopy closure is defined as the number of returns over a specified height threshold divided by the total number of returns within each pixel [54]. In our study, this height threshold was set at 1 m aboveground. The spatial resolution was also set to 2 m to generate this cover raster.

3) TANDEM-X Data

TanDEM-X DEM data did not need further preparation. The DEM contains the final global digital elevation of the land masses of the earth. It predominantly represents a DSM. Elevated objects are included, but heights might be affected by inherent SAR effects.

B. Height Extractions

Once all rasters were prepared, the heights were calculated within all GEDI footprints.

To draw a good comparison, heights were extracted following the same references of GEDI data. Thus, the most important metrics derived from GEDI measurements are as follows (Fig. 2):

- The elevation of the lowest mode (ELM): the mean ground elevation in the footprint.
- The elevation of the highest return (EHR): the highest detected return in the footprint.
- RH100: the difference in elevation between the highest detected return and the mean ground elevation in the footprint.

Following these metrics, the mean ground elevation in the footprint was calculated for the LiDAR DEM and TanDEM-X DEM in all zones. Additionally, the highest detected return was obtained for the LiDAR DSM. With the LiDAR extracted elevations, the RH100 metric (difference in elevation between the highest detected return and mean ground elevation) was also obtained for the LiDAR datasets.

B. Statistical Analysis

1) Global Statistics

As previously defined, the heights used are called the ELM, EHR and RH100. The mentioned heights together with the three available sources of data used in this study (GEDI, LiDAR

and TanDEM-X DEM) generate the following seven heights:

- ELM GEDI
- ELM LiDAR
- ELM TanDEM-X
- EHR GEDI
- EHR LiDAR
- RH100 GEDI
- RH100 LiDAR

From these variables, the following differences in heights were calculated, with their analysis being the focus of this paper:

- ELM G-L: the difference in the mean ground elevation in the footprint between GEDI and LiDAR data.
- ELM G-T: the difference in the mean ground elevation in the footprint between GEDI and TanDEM-X data.
- EHR G-L: the difference in the highest detected return in the footprint between GEDI and LiDAR data.
- RH100 G-L: the difference in elevation between the highest detected return and mean ground elevation in the footprint between GEDI and LiDAR data.

It should be noted that any observation classified as an outlier has been discarded using the interquartile range (IQR) criterion for RH100 LiDAR values, where some anomalous values were observed. This criterion means that all observations above third quartile +1.5·IQR are considered outlier values.

The statistical analysis was performed using R software [55]. First, the full set of 12 031 heights and differences in heights were analyzed to determine the behavior of both the heights and the differences. The statistical analyses involved the calculation of the mean value, standard deviation (SD), mean standard error (MSE), median, maximum and minimum values, interquartile rank (IQR) and coefficients of skewness and kurtosis. The root mean square error (RMSE) for the differences in the heights was also calculated, for GEDI-LiDAR differences in the ELM.

Box plots were drawn to graphically compare both the heights and the differences in heights. A scatterplot showing the correlation between each height and difference in heights with the terrain slope and the level of cover was plotted, and the correlation index for each case was also calculated.

A scale of slope ranges was established to identify a correlation between the heights and differences in heights and the slope of the terrain. The scale of terrain slopes measures at intervals of 5 over 5 units, with the first category referring to values of between 0 and 5, called “ts_00-05”, and with the last pertaining to values of greater than 40, called “ts_40”.

The same procedure was performed for the cover, cataloging this variable over five groups measured in intervals of 20 over 20 units, with the first called cc_00-20 and the last called cc_80-100.

Finally, the same analysis was performed considering the ranges of slope and cover in relation to the differences in heights in terms of descriptive statistics, RMSE values, box plots, scatterplots and correlation indexes.

On the other hand, it should be noted that the construction of the GEDI measuring instrument is divided into the three lasers, which are split into 4 beams that alternate to give 8 footprints. The information of which beam has performed the measurement is included in the data of each footprint. Therefore, a detailed analysis of the errors detected has been carried out to explore whether there is any pattern that leads to suggest that some beams are less accurate than others.

2) Zone Statistics

The 12 031 footprints of the study correspond to ten zones with different numbers of footprints, as shown in Table II.

TABLE II.
Number of footprints in each zone

Zone	Footprints	Zone	Footprints
Zone 01	1073	Zone 06	189
Zone 02	903	Zone 07	964
Zone 03	676	Zone 08	1672
Zone 04	2108	Zone 09	769
Zone 05	1237	Zone 10	2440

As the zones were chosen due to varied vegetation cover, different elevations and diverse relief characteristics, it should be useful to repeat the same calculations done for the whole set of data, but in this case for each of the ten zones.

The analysis involves considering each zone globally and analyzing it according to the range of slopes and coverage levels described above.

C. Uncertainty Analysis

As noted above, the location of the GEDI footprint has an uncertainty of ±10 m. For this reason, errors were estimated between the GEDI metrics and the other two data sources (LiDAR and TanDEM-X DEM), shifting the footprints both ±10 m (maximum error) and ±5 m (half the maximum error) along and across the satellite orbit and the intermediate angular position between them, depending on the orbit direction (Fig. 3).

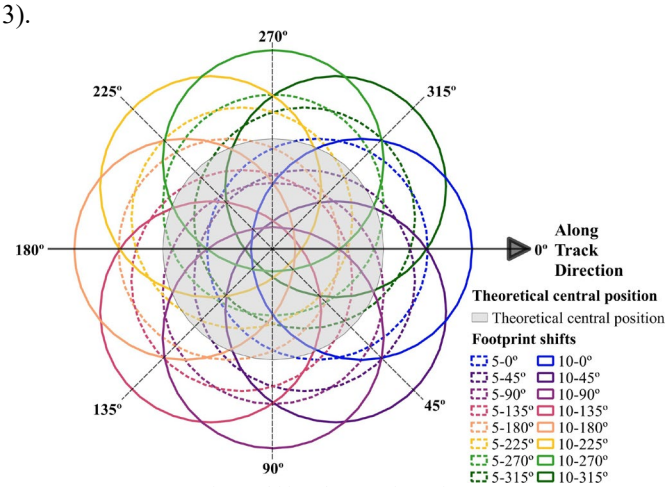

Fig 3. Shifts of GEDI footprints.

This shifting results in 16 new possible positions where all metrics were extracted following the method described in Section C. Finally, the best footprint location was defined by selecting the one of the 17 possibilities (including the central original position) with lower RMSEs.

This article has been accepted for publication in a future issue of this journal, but has not been fully edited. Content may change prior to final publication. Citation information: DOI 10.1109/JSTARS.2021.3080711, IEEE Journal of Selected Topics in Applied Earth Observations and Remote Sensing

IV. Results

A. LiDAR DEMs

Fig. 4 shows the resulting DEM, DSM and derived slope and canopy cover of the LiDAR data.

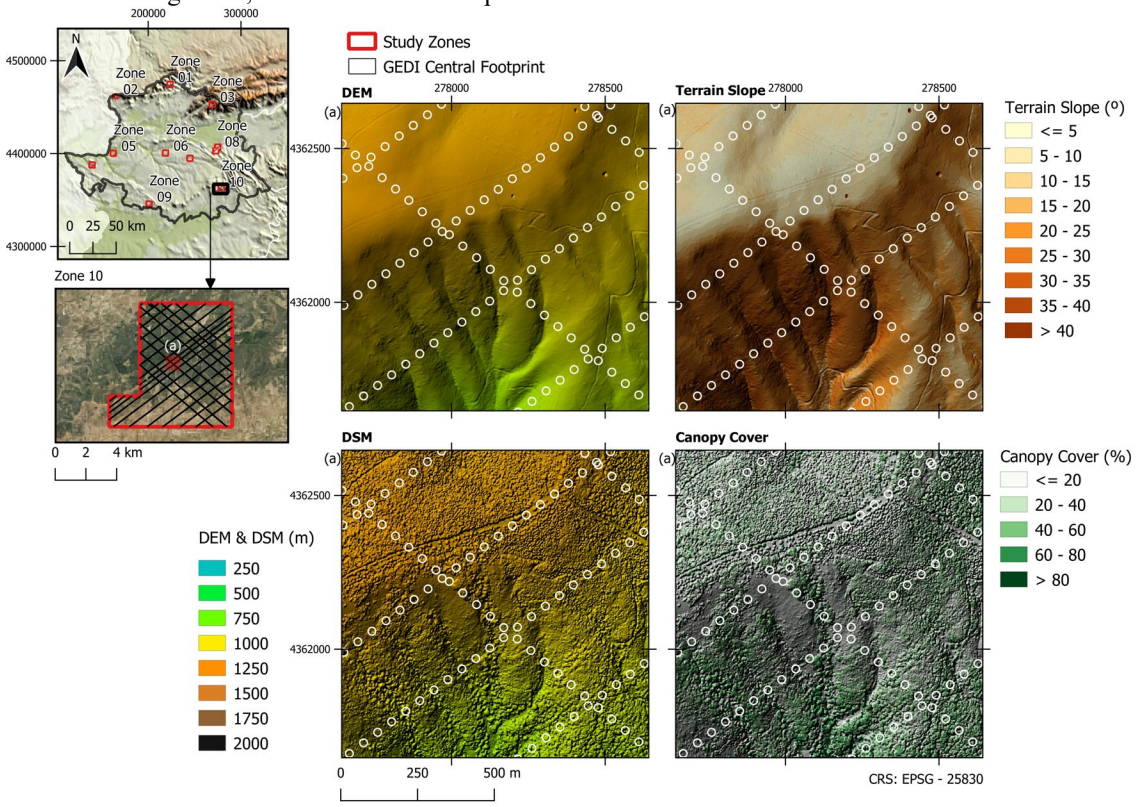

Fig 4. Digital Elevation Models.

B. Statistical Analysis

1) Global Statistics

The global statistics for the four differences in height are shown in Table III. The data show small skewness coefficients, which are fairly symmetrical, and slightly high kurtosis coefficients. The MSE, SD and RMSE, when comparing the GEDI ELM with the LiDAR data, are slightly lower than when comparing this dataset to the TanDEM-X.

TABLE III.
GLOBAL STATISTICS

	ELM G-L	ELM G-T	EHR G-L	RH100 G-L
Mean (m)	0.41	-0.85	0.77	0.35
SD (m)	6.04	6.93	6.44	3.54
MSE (m)	0.05	0.06	0.06	0.03
Median (m)	0.19	-0.63	0.77	0.57
RMSE (m)	6.05	6.99	6.49	3.56
R^2	1.00	1.00	1.00	0.52
IQR	4.61	6.29	5.75	3.50
skewness	0.21	-0.02	-0.59	-0.09
kurtosis	5.35	3.97	3.58	3.18

Fig. 5 shows the correlation between differences in heights for the global data. A high correlation is observed for all of them except in the case of the RH100 values due to the distribution of the data.

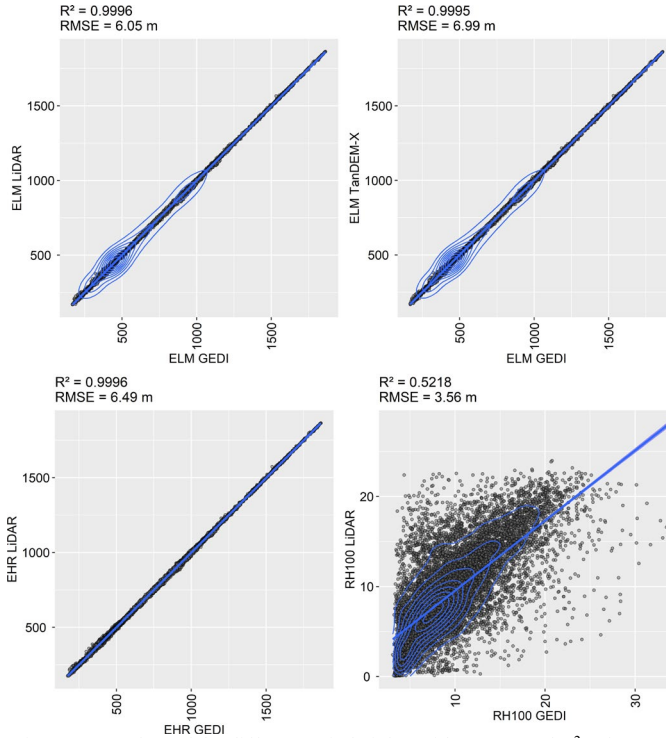

Fig 5. Scatterplots of the differences in heights with RMSE and R^2 values.

The calculations of the linear correlation index between each difference in height and the terrain slope and cover do not offer

This article has been accepted for publication in a future issue of this journal, but has not been fully edited. Content may change prior to final publication. Citation information: DOI 10.1109/JSTARS.2021.3080711, IEEE Journal of Selected Topics in Applied Earth Observations and Remote Sensing

significant values with R^2 values of close to zero.

Fig. 6 shows the RMSE of the four differences in heights for each abovementioned slope range.

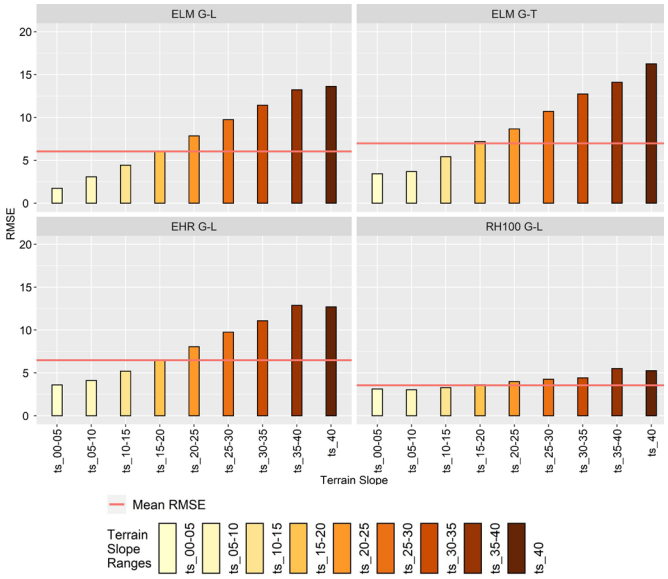

Fig 6. RMSE of ELM G-L, ELM G-T, EHR G-L and RH100 G-L values for each slope range.

In terms of the relation between the terrain slope and RMSE, nearly all comparisons show a positive tendency. In other words, the greater the slope, the greater the RMSE. This trendline has, in the case of the comparison between ELM and GEDI-LiDAR data, a noteworthy value of $R^2 = 0.9926$, and in the case of the comparison between ELM and GEDI-TanDEM-X data, a noteworthy value of $R^2 = 0.9892$. For the relation between the terrain slope and the RMSE of the RH100, the trendline is almost horizontal.

Fig. 7 shows boxplots on a scatterplot with the correlations of the ELM G-L and ELM G-T variables and the terrain slope values split by ranges of slopes.

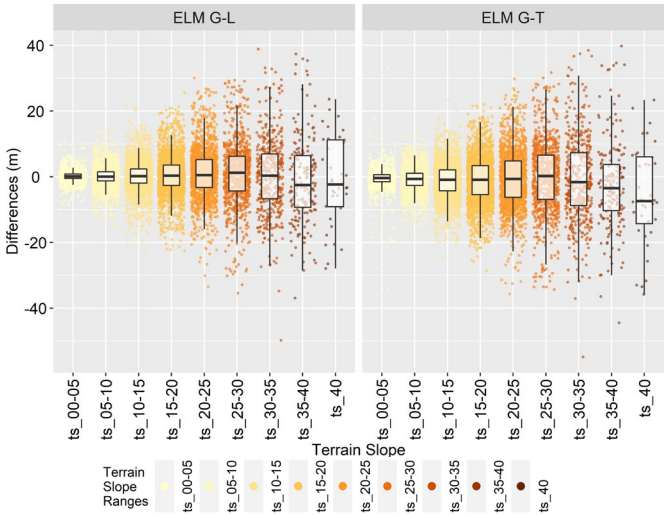

Fig 7. Boxplot on scatterplot of the ELM G-L and ELM G-T variables and the terrain slope values split by ranges.

As shown in Fig. 6 and Fig. 7, as the slope increases, the differences in elevation are dispersed, especially for slopes of greater than 40, although the dataset of this category is small.

Fig. 8 shows the boxplot for the EHR and RH100 variables. The figure shows more symmetrical distributions due to more proximity between the average mean and median values. According to the comparison with the RH100 metric, it has the lowest IQR value, which denotes less dispersion in differences.

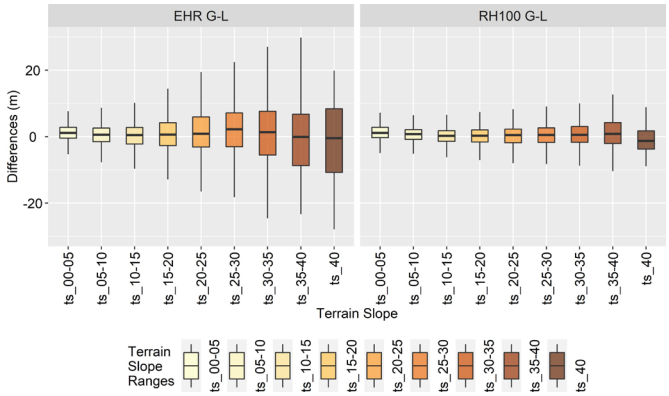

Fig 8. Differences in the EHR between GEDI and LiDAR data for each slope range.

On the other hand, Fig. 9 offers a similar analysis, where the RMSE values obtained from the four differences in heights and cover values split by ranges are plotted.

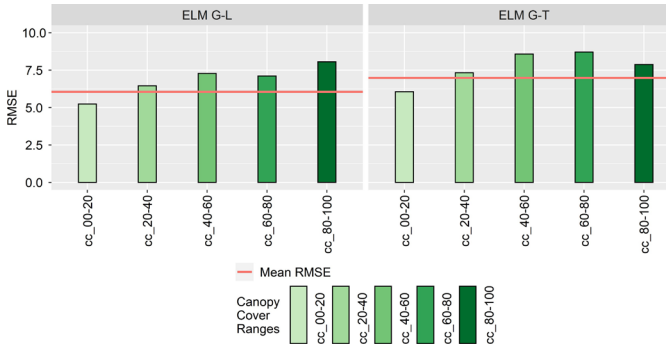

Fig 9. RMSE of differences between GEDI- LiDAR and GEDI-TanDEM-X data for each cover range.

From the relation between the percentage of vegetation cover and the RMSE and ELM of both comparisons, GEDI-LiDAR and GEDI-TanDEM-X show a positive tendency. In other words, the greater the coverage, the greater the RMSE. This relation shows, in the case of the GEDI-LiDAR comparison, a noteworthy value of $R^2 = 0.8870$ for the trendline. Additionally, the RMSE relation for RH100 and cover has also a worthy correlation ($R^2 = 0.8584$ for the trendline).

The boxplots of Fig. 10 show the differences in ELM values between the GEDI and LiDAR data split by cover ranges.

This article has been accepted for publication in a future issue of this journal, but has not been fully edited. Content may change prior to final publication. Citation information: DOI 10.1109/JSTARS.2021.3080711, IEEE Journal of Selected Topics in Applied Earth Observations and Remote Sensing

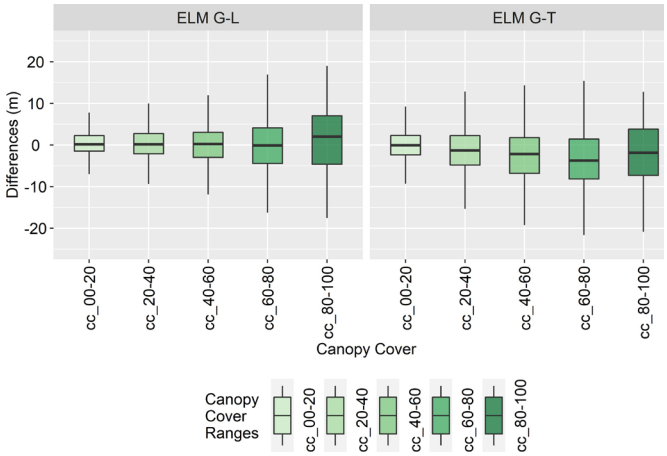

Fig 10. Differences in ELM values between GEDI and LiDAR data and between GEDI and TanDEM-X data for each cover range.

As shown in Fig. 9 and Fig. 10, as cover increases, the differences in elevation are dispersed, but not as much as for the slopes. The mean error, when comparing the GEDI ELM to the LiDAR ELM, is lower than when comparing it to the TanDEM-X DEM ELM in all cover ranges.

A similar comparison for the EHR and RH100 values can be observed in Fig. 11.

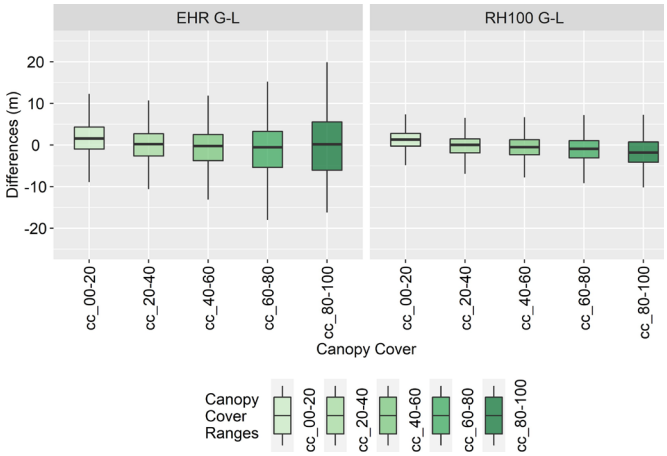

Fig 11. Differences in EHR and RH100 values between GEDI and LiDAR data for each cover range.

Fig. 11 shows more concentrated distributions of EHR and RH100 values, especially for the latter. From 20% coverage, the mean difference between the GEDI RH100 and LiDAR data begins to become negative.

Having analysed the possible influence of the measurement beam of the sensor on the errors committed, it can be seen in Fig. 12 that the beams with the highest errors for ELM are beams B-0000 and B-0011 and that, conversely, those with the lowest RMSE are beams B-1011 and B-1000 in both the GEDI-LiDAR and GEDI-Tandem-X comparisons. For EHR G-L the tendency is similar, but for RH100 G-L the tendency is not fulfilled, although in the latter case the differences are very small between the different beams.

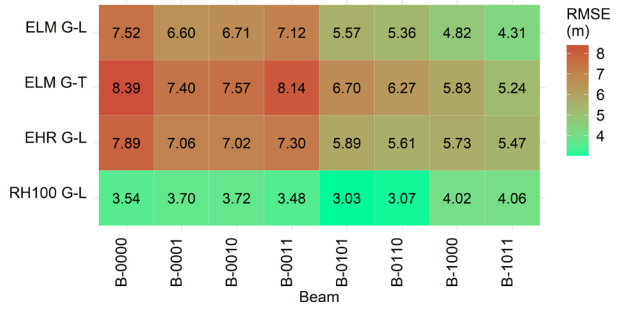

Fig 12. RMSE in GEDI central footprints for each beam (m).

2) Zone Statistics

A similar analysis was carried out with data from the ten areas into which the study was divided. Fig. 13 displays the RMSE values for each difference in height and zone.

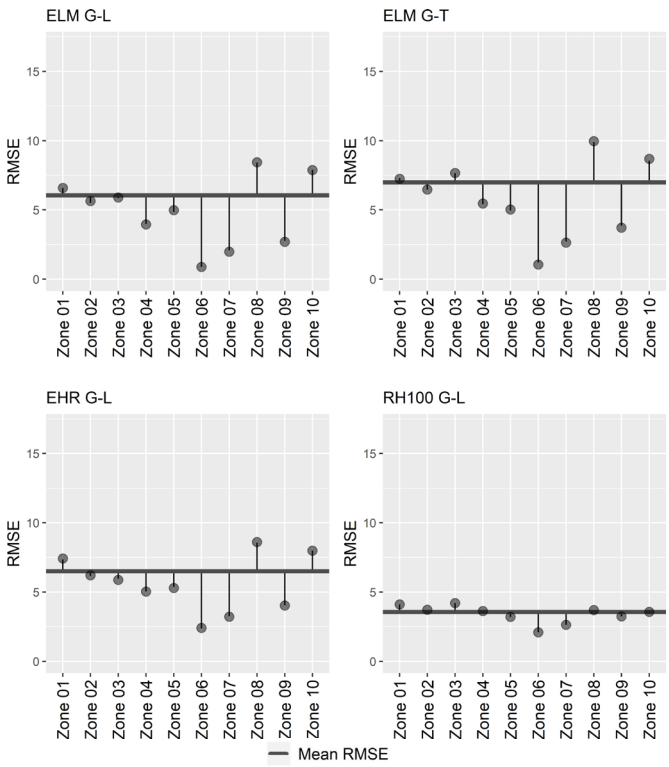

Fig 13. RMSE of differences between GEDI-LiDAR and GEDI-TanDEM-X data for each zone.

As shown in Fig. 13, the areas with lower RMSE values in general are zones 06 and 07, with RMSE values even lower than 1 m found in the ELM. These values correspond with the two areas with lower mean slopes (Table I). In contrast, the largest RMSE values correspond with zones 08 and 10, with similar medium both mean slope and mean percentage of cover. Additionally, those zones have in common that they both have the higher number of footprints (Table II).

The boxplots provided in Fig. 14 show the distributions of the ELM differences for the GEDI-LiDAR and GEDI-TanDEM-X DEM data.

This article has been accepted for publication in a future issue of this journal, but has not been fully edited. Content may change prior to final publication. Citation information: DOI 10.1109/JSTARS.2021.3080711, IEEE Journal of Selected Topics in Applied Earth Observations and Remote Sensing

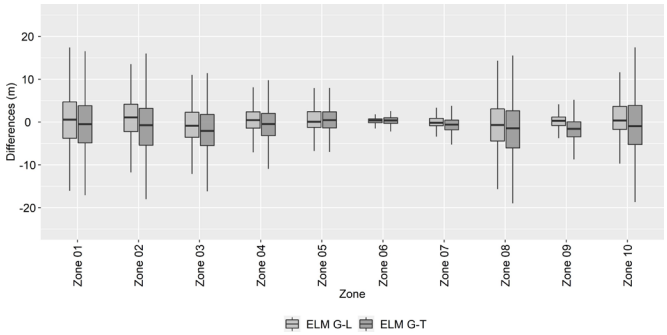

Fig 14. Differences in ELM values between GEDI-LiDAR and GEDI-TanDEM-X data for each zone.

Fig. 14 and Fig. 15 show how in zones 06, 07 and 09, there is much less error dispersion (lower IQR values). These zones correspond to zones of intermediate altitude (450-480 m) and the lowest slopes. Additionally, vegetation coverage is dominated by agroforestry areas.

When comparing the RH100 metric derived from the GEDI with that derived from the LiDAR dataset, we observe more concentrated errors in all zones with IQR values ranging from 2.15 m to 4.04 m (Fig. 15).

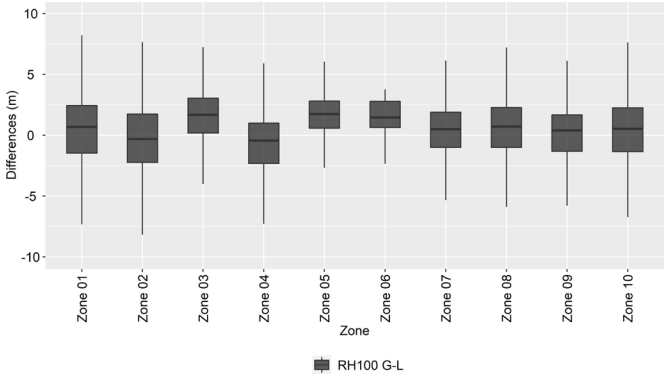

Fig 15. Differences in RH100 values between GEDI and LiDAR data for each zone.

It is worth noting that the analysis of zones by slope ranges and cover leads to similar results to the global one. As cover increases, the differences in elevation become dispersed, but not as much as for the slopes. For slopes, the differences in height show more dispersion from a value of 25°, especially for the ELM values. Zones 06 and 07 present nonsignificant results compared to the other zones because their maximum slope values are 11.4° for zone 06 and 37.19° for zone 07.

The RH100 differences offer a more concentrated distribution in all zones and slopes.

Zone 06 has a maximum cover value of 39.86%, and zones 01 and 02 have maximum values of 96.24% and 98.53%, respectively. The remaining zones do not reach the 80% cover value and present a moderate dispersion of the data, which is especially low in the RH100 comparison.

Table IV shows the relation between the RMSE of the RH100 G-L and the RH100 mean value for each zone. It can be observed that the worst values are obtained for zones 05, 06, 07 and 08, where the vegetation height is lower. The best percentage is for zones 01, 02, 03 and 04 with more prominent vegetation in height.

TABLE IV.
Percentage of RMSE for RH100 G-L in relation to vegetation height

RMSE	RH100 m	RMSE %
Total	9.19	21.10
Zone 01	10.57	5.08
Zone 02	12.01	6.04
Zone 03	8.30	9.57
Zone 04	9.67	6.98
Zone 05	4.84	15.91
Zone 06	2.99	36.03
Zone 07	6.87	26.27
Zone 08	7.92	44.25
Zone 09	9.69	17.47
Zone 10	11.70	12.79

C. Uncertainty Analysis

1) Global Statistics

The purpose of this section is to find the best location of the footprint once selecting one of the 17 possibilities (central or theoretical location of the footprint and 16 shifts) with less RMSE. As explained in part D of the methodology section, these 16 new proposed footprints are generated by shifting the theoretical position ±10 m and ±5 m along and across the satellite orbit and the intermediate angular position between them depending on the orbit direction. According to this, they are called 10-0° Shift, 10-45° Shift, 10-90° Shift, 10-135° Shift 10-180° Shift, 10-225°, 10-270° Shift, and 10-315° Shift for the maximum ±10 m error. In the same way, Shifts derived from half the maximum error (±5 m), are called 5-0° Shift, 5-45° Shift, 5-90° Shift, 5-135° Shift, 5-180° Shift, 5-225° Shift, 5-270° Shift, and 5-315° Shift. Fig. 16 shows as an example a portion of zone 07, with the central theoretical position in grey and the best footprint of the 17 possible footprints.

This article has been accepted for publication in a future issue of this journal, but has not been fully edited. Content may change prior to final publication. Citation information: DOI 10.1109/JSTARS.2021.3080711, IEEE Journal of Selected Topics in Applied Earth Observations and Remote Sensing

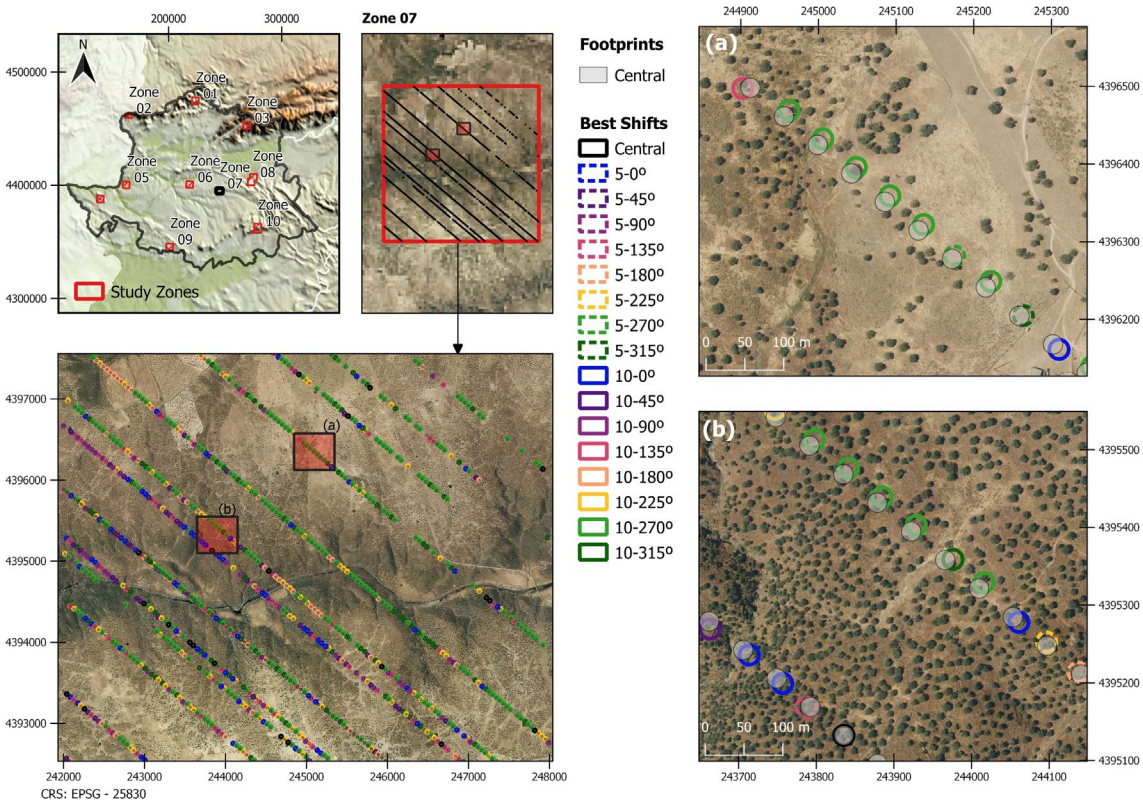

Fig 16. Best shifts of GEDI footprints relative to LiDAR data. Portion of zone 07 shown as an example.

From the RMSE analysis (Fig. 17), shows that the 10-270° Shift has the lowest values in all comparisons, and the 10-90° Shift has the worst value, except for the RH100 G-L data.

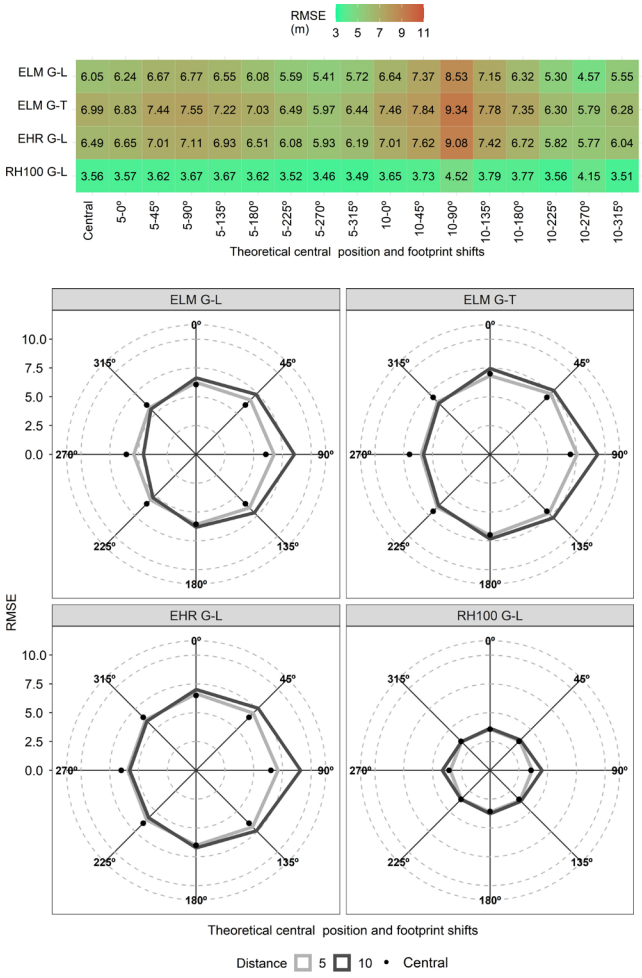

Fig 17. RMSE of shifts in GEDI footprints (m).

Fig. 18 shows the percentage of GEDI footprints whose heights are best fitted to the ELM LiDAR and ELM TanDEM-X elevations, respectively.

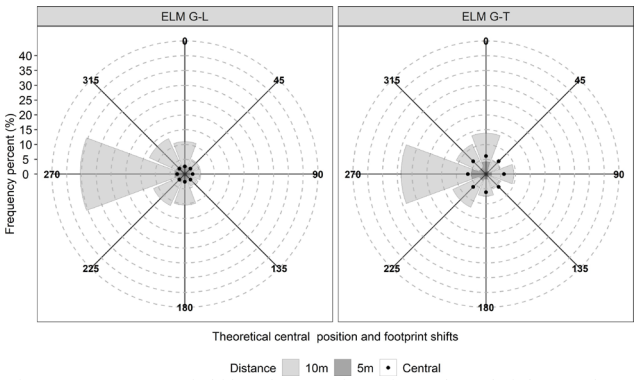

Fig 18. Percentage of shifts of GEDI footprints whose heights are best fitted to the ELM LiDAR elevations and to the ELM TanDEM-X elevations.

From the analysis of the ELM, we find that the percentage of best shifts located at 10-270° is notably larger in both comparisons with LiDAR and TanDEM-X data. Fig. 18 shows the 31.88% of the footprints have moved to 10-270° to fit better to the LiDAR ELM data. For TanDEM-X data this percentage decreases to 23.60%, but this value is still quite substantial. Furthermore, it should be noted that the central position (theoretical location of the footprint) in both figures has a very low percentage of adjustment in both ELM comparisons. If the 10-270° Shift is the best solution in both cases, the opposite position, the 5-135º Shift, presents the worst results with values of 5.1% and 4.76%, respectively. However, it is worth mentioning that, although this position of 5-135º Shift and 5-190º Shift are the ones with the fewest quantity of best positions, both in comparison with LiDAR and TanDEM-X data, they are not the ones with the highest errors, since, as mentioned above, the one with maximum errors is 10-90º Shift.

As was the case for the theoretical position of the footprint, when the slope increases, the RMSE of the differences in ELM comparisons between GEDI data and LiDAR and TanDEM data increases (Fig. 19). This increase is more pronounced for 10-90° Shift in both comparisons. Additionally, the results shown in the figures demonstrate that the footprint with less error is the one displaced at 10-270°.

The same study was performed for cover values and is illustrated in Fig. 20. The trend is repeated, and 10-270° Shift offers the best results with lower RMSE values.

This article has been accepted for publication in a future issue of this journal, but has not been fully edited. Content may change prior to final publication. Citation information: DOI 10.1109/JSTARS.2021.3080711, IEEE Journal of Selected Topics in Applied Earth Observations and Remote Sensing

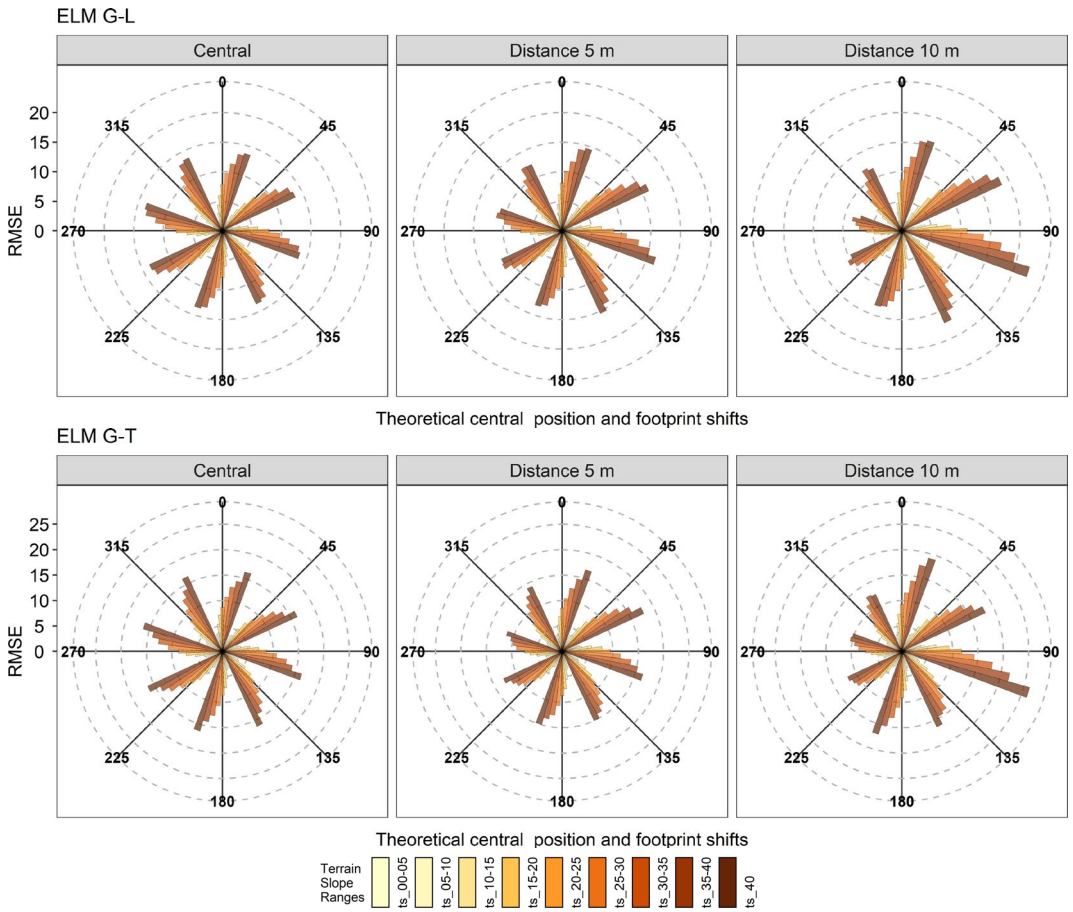

Fig 19. RMSE variation of theoretical footprints and shifts of ELM comparisons for GEDI and LiDAR data.

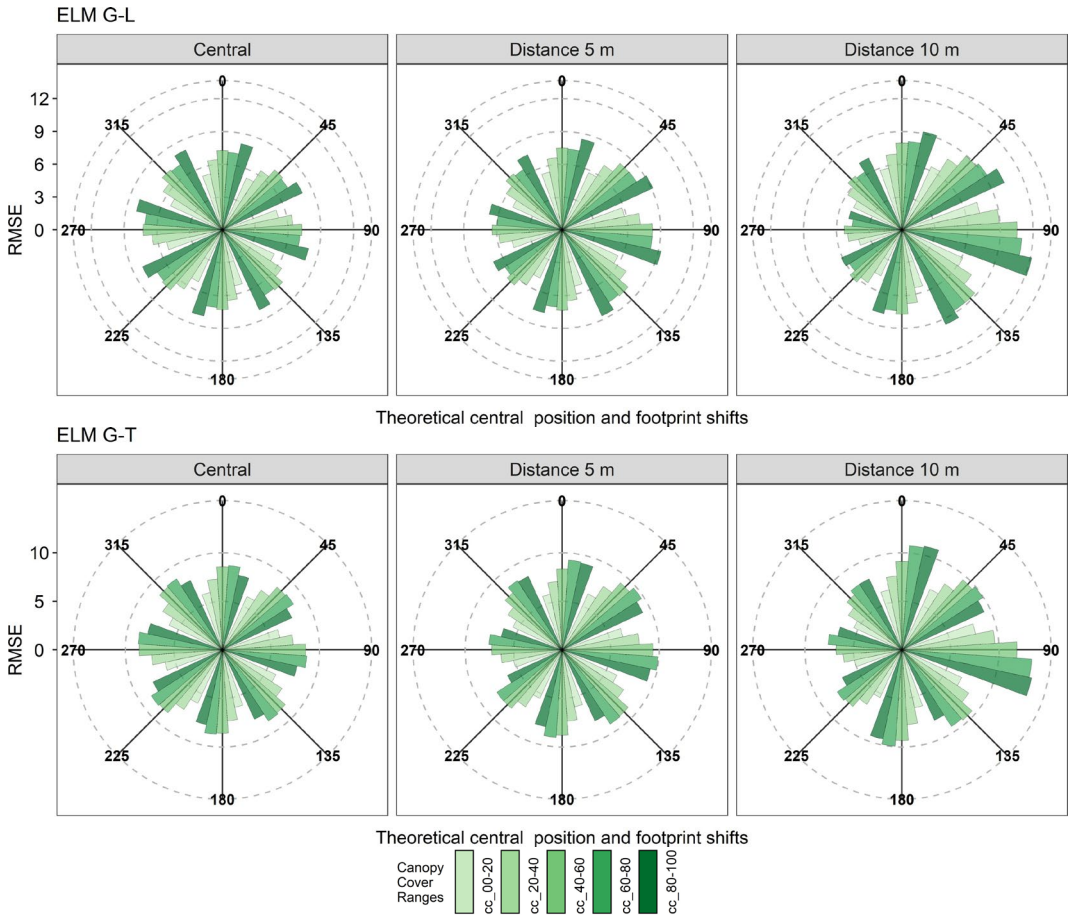

Fig 20. RMSE variations of theoretical footprints and shifts of ELM comparisons for GEDI and TanDEM-X data

This article has been accepted for publication in a future issue of this journal, but has not been fully edited. Content may change prior to final publication. Citation information: DOI 10.1109/JSTARS.2021.3080711, IEEE Journal of Selected Topics in Applied Earth Observations and Remote Sensing

2) Zone Statistics

Fig. 21 shows the RMSE values for the four variables considering the theoretical central position and the 16 possible proposed Shift splits by zone.

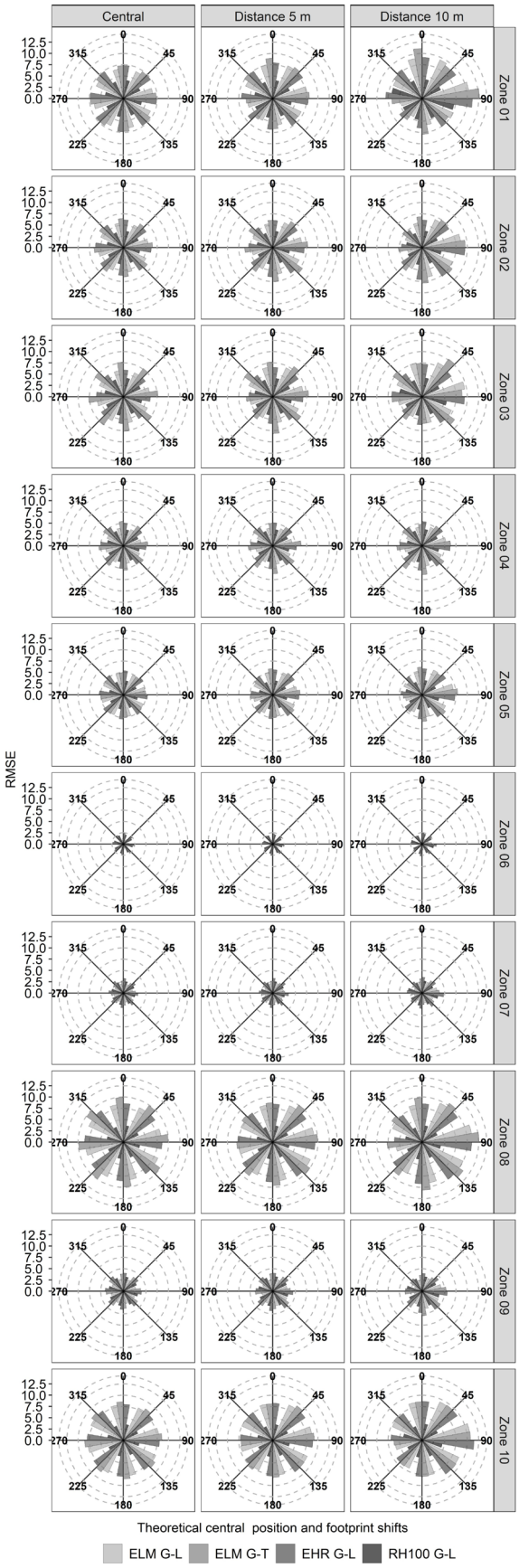

Fig 21. RMSE for all comparisons drawn for theoretical positions and shifts of GEDI footprints by zone.

Zones 06 and 07 are where the RMSE values are most evenly matched between shifts. As noted above, these zones correspond to the zones of intermediate altitude (450-480 m) and lowest slope. Additionally, vegetation in these areas is dominated by agroforestry land. On the other hand, zone 01 has the highest RMSEs values. Finally, it should be noted that the 10-270° Shift presents the lowest RMSE in all zones and, similarly, 10-90º Shift has the highest RMSE values in all zones.

V. Discussion

In our analysis, the real elevations and heights captured by the GEDI sensor have been compared to other Airborne and Spaceborne data sources. LiDAR-derived DEM data and DSM and TanDEM-DEM data were utilized to draw comparisons due to their greater accuracy. We also compared both sources of information to quantify the differences in elevation between them. Similar contrasts can be found in the recent literature. Wessel, et al. [35] compared the LiDAR DEM and TanDEM-X DEM and obtained a global RMSE of 6.78 m. The authors also calculated the error within several slope ranges and found that the steeper the slope, the higher the RMSE. We obtained an overall RMSE for differences between the LiDAR-derived DEM and TanDEM-X DEM of 3.35 m, a value that is much lower and therefore shows a better fit between the data sources with which we compared GEDI elevations and heights. As Wessel, et al. [35], we also found the error to increase with the slope of terrain (Fig 22). Additionally, we analyzed trends that occur with an increase in coverage and found that the greater the coverage, the greater the RMSE (Fig 22). In both cases, all RMSEs comply with the TanDEM-X Ground Segment DEM Products Specification Document [56], which indicates an absolute vertical accuracy value of less than 10 m.

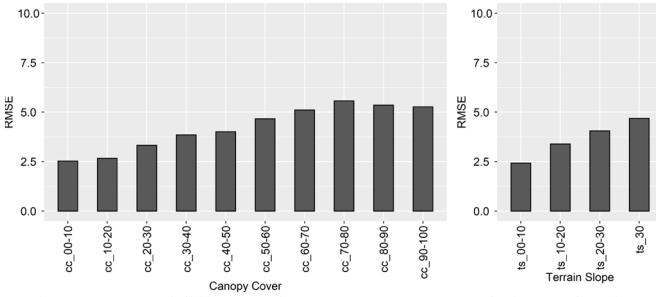

Fig 22. RMSE of differences between TanDEM-X and LiDAR data for different vegetation cover factors and slope ranges.

It is worth noting that the TanDEM-X DEM reproduces a surface model that includes above ground elevation tree canopies and built elements, which supports the positive trend of the RMSE related to coverage. However, as stated in Wessel, et al. [35], the mean errors for aboveground land cover classes are lower than expected for an interferometric SAR system such as TanDEM-X. In this sense, the TanDEM-X Ground Segment DEM Products Specification Document [56] confirms that in forested areas, the X-band SAR scattering center is located closer to the upper part of the vegetation volume rather than on the crown itself. Consequently, it can be considered, in almost all extensions, a measure of ground elevation. This conclusion is supported

by recent works such as that by Chimitdorzhiev, et al. [38], who found an error in canopy height, concluding that radar interferometric measurements underestimate the actual forest height by an average value of 5.5 m for high coverage and by 2-4 m for medium coverage. On the other hand, Gonzalez and Rizzoli [57] summarized the global relative height accuracy of the global TanDEM-X DEM for all continents and cover types. In our case, for Europe, the authors set accuracy levels of 1.64 m for forests, of 0.94 m for short vegetation and of 0.96 for shrubland, which account for most of our cover categories.

In terms of the main results of our work, we obtained an RMSE of 6.05 m when comparing the ELM of GEDI and LiDAR data and an RMSE of 6.99 when comparing GEDI and TanDEM-X data, but with an almost perfect correlation R^2 between them (0.9996 and 0.9995). Such values of a nearly perfect correlation were also obtained by Silva, et al. [45], but they obtained better RMSE results. These differences can be attributed to the fact that they used simulated data while we used real data. However, although from the global data our RMSE does not reach the values that Silva, et al. [45] obtained, for zones 06, 07 and 09, we do obtain RMSE values that fall within the range of their results (0.89-2.77 m) or that are even better.

Other notable results are those achieved for the RH100 metric. In the global results, we obtained an RMSE of 3.56 m. Qi and Dubayah [50] obtained RMSE values ranging from 3.53 m to 12.59 m when comparing RH100 values derived from different comparisons of LiDAR metric measurements with a combination of TanDEM-X and (synthetic) GEDI data. These results are in accordance with those obtained in our work, for both the original position of the footprint and most of its shifts, which are at the lower limit of their RMSE range.

In the same way, Hancock, et al. [46] assessed the accuracy of the GEDI simulator, which underpins the prelaunch calibration of GEDI data products. The authors calculated differences in RH2, RH5, RH25, RH50, RH75 and RH98 metrics compared to ALS datasets and obtained RMSEs of approximately 4.7-5.7 m. We obtained better results in all the studied zones, with a minimum value in Zone 06 of 2.09 that is even less than half their minimum RMSE. Healey, et al. [40] also performed RH98 predictions at 7615 focal sites using models calibrated at three scales, obtaining RMSEs ranging from 7.08 m to 9.2 m and IQR values of 6.89-11.19 m. Our general results show a significantly better general IQR of 3.50 m for RH100 differences and values ranging from 2.15 m to 4.04 m. If we focus on the percentages of the RMSE with respect to the RH100 value, our values are also better than those of Healey, et al. [40] since our maximum RMSE% (44%) is their minimum and we have zones with errors up to five times better than this error (zone 01). The highest RMSE% were found in areas with the lower vegetation. Additionally, in analyzing RH98 differences per vegetation type, Healey, et al. [40] achieved a minimum RMSE of 4.50 m for grasslands with the minimum work scale and a maximum RMSE of 10.58 m for evergreen broadleaf forests with the maximum work scale. We achieved a minimum RMSE of 2.09 m for the RH100 for zone 06 (agroforestry areas) and a maximum RMSE of 4.20 m for zone 03 (sclerophyllous vegetation). Globally, the RMSE obtained for the RH100 is 3.56 m, which is in accordance with the minimum general result given by Healey, et al. [40].

With regard to the EHR, our results achieve an RMSE of 6.49 m globally. In general, these altitudes generated the worst results of all of the work in spite of the fact that in zone 06 they reached better values with an RMSE of 2.37 m. None of the consulted studies using GEDI data provide results in on the elevations of the highest points of vegetation, so we cannot draw comparisons.

On the other hand, we used only elevations of footprints with a quality flag of 1 to ensure the quality of the elevation data. Fayad, et al. [20] used flag 0 or 1 to analyze the elevation of inland waterbodies and applied an elevation filter with SRTM elevations. Although they achieved more accurate results (studying areas without vegetation, without which there is less scope for confusing elevation), they noticed an improvement when applying the SRTM filter to the elevations, even for footprints with a quality flag of 1.

As stated in Luthcke, et al. [49], the GEDI instrument consists of three lasers producing a total of eight beam ground transects. These three lasers are: the “coverage” laser and two full power lasers. the “coverage” laser is split into two transects that are then each dithered producing four ground transects. The other two lasers are dithered only, producing two ground transects each. In our study area, beams B-0000, B-0001, B-0010 and B-0011, correspond to the “coverage” laser and beams B-0101, B-0110, B-1000 and B-1011, correspond to the other full power lasers. Thus, it can be clearly seen how the coverage laser has more error than the other two lasers for the EHR G-L, ELM G-L and ELM G-T. Nevertheless, it can be seen that for RH100 G-L, one of the two full power laser beams is the one with the lower RMSE.

Finally, in terms of our evaluation of the uncertainty of the footprint location, we obtained better results for almost 35% of our 12 031 footprints when shifting them 10 m and 270° in the orbit direction. Most of the literature using GEDI data works with simulated data. Using simulated GEDI data at precise locations to build footprint-level models obviates potential errors related to the positional uncertainty of GEDI footprints of ±10 m [58]. As stated by Luthcke, et al. [49], the intention is for GEDI mission geolocation to occur within the same frame and to use consistent geophysical corrections similar to those of ICESat-2 to facilitate the direct comparison and use of these laser altimeter mission data. The fusion approach applying GEDI and TanDEM-X data shows great potential for generating global-scale forest and biomass maps [43].

Despite being rather dense, with the comparison of 12 031 footprints and their respective parallels that have resulted in the study of 204 527 locations, the assessment carried out in this study, has been automated by means of R scripts and GIS programming, achieving an exhaustive analysis of the errors between the three sources of data studied. For further validation studies of GEDI with airborne LiDAR data, it would be recommended to establish a mathematical transformation model between both data sources for a correct extrapolation of the valuable information from GEDI data. It would also be advisable to explore the theory of authors such as Potapov, et al. [59] or Lang, et al. [60] who indicate that

such extrapolation could be carried out using multispectral images such as those of Landsat, Sentinel or many others.

VI. Conclusions

In this study, we compared real GEDI elevation data with other airborne and spaceborne DEM data for Southwest Spain. We analyzed agreement in ground elevation (ELM) across 12 031 real GEDI footprints and elevations obtained from LiDAR and TanDEM-X DEM data. In general, we achieved better agreement with the LiDAR data. Additionally, a comparison of the RH100 metric and the elevation of the highest point of vegetation (EHR) obtained from GEDI and LiDAR data was performed. In this case, the obtained results are in substantial agreement with other studies using simulated GEDI data.

Furthermore, the results show a clear relation between the errors obtained and the slope; the greater the slope, the greater the RMSE. This relationship has also been found by analyzing different degrees of coverage; as cover increases, differences in elevation become dispersed, but not as much as with slopes.

Finally, due to our initial predictions of uncertainty in GEDI footprints, a final evaluation of RMSE involved shifting 16 footprints in the ± 10 m uncertainty area. The obtained outcomes evidence a strong tendency to obtain better results (in terms of RMSE and frequency) on ground elevation when placing the footprint at 270°, displacing it to 10 m of its positional uncertainty, from comparative studies of LiDAR and TanDEM-X data.

The global results of this work show differences in elevation in relation to other data sources. These differences may or may not be important depending on the scale of work and the accuracy of forest mapping required. However, as it appears that future plans for the GEDI mission are to be placed within the same frame and to use consistent geophysical corrections similar to those of ICESat-2, improved positional uncertainty and height accuracy are to be expected. Following this, it would be highly desirable to conduct a new accuracy assessment of GEDI elevations to see if and by how much the differences found in this study vary. Additionally, many of our investigations point to a combination of GEDI data with TanDEM-X data to overcome the limitations of GEDI point sampling. This combination will also greatly reduce the differences between the two data sources. Future research is therefore needed to establish transformation models between these data sources.

Acknowledgments

This research was funded by the Government of Extremadura (Spain) and cofunded by the European Regional Development Fund under Grants GR18028 (KRAKEN) and GR18052 (DESOSTE).

The participation of L. Fragoso-Campón was funded by the Junta de Extremadura and the European Social Fund: A way of doing Europe through the “Financing of Predoctoral Contracts for the Training of Doctors in Public Research and Development Centers belonging to the Extremadura System of Science, Technology, and Innovation [file PD16018].”

We thank the Junta de Extremadura (CICTEX) for providing the LiDAR data (LiDAR-PNOA 2018 CC-BY 4.0 scne.es).

We thank the German Aerospace Centre (DLR) for providing TerraSAR-X/TanDEM-X © DLR <2020> satellite data.

References

[1] S. C. Popescu, K. Zhao, A. Neuenschwander, and C. Lin, "Satellite lidar vs. small footprint airborne lidar: Comparing the accuracy of aboveground biomass estimates and forest structure metrics at footprint level," *Remote Sensing of Environment,* vol. 115, pp. 2786-2797, 2011.

[2] X. Yu, A. Kukko, H. Kaartinen, Y. Wang, X. Liang, L. Matikainen*, et al.*, "Comparing features of single and multi-photon lidar in boreal forests," *ISPRS Journal of Photogrammetry and Remote Sensing,* vol. 168, pp. 268-276, 2020.

[3] M. Dalponte, T. Jucker, D. F. Burslem, S. L. Lewis, R. Nilus, O. Phillips*, et al.*, "Aboveground biomass estimation in tropical forests at single tree level with ALS data," in *2016 IEEE International Geoscience and Remote Sensing Symposium (IGARSS)*, Beijin (China), 2016, pp. 5334-5337.

[4] F. J. Romero Ramirez, R. M. Navarro-Cerrillo, M. Á. Varo-Martínez, J. L. Quero, S. Doerr, and R. Hernández-Clemente, "Determination of forest fuels characteristics in mortality-affected Pinus forests using integrated hyperspectral and ALS data," *International journal of applied earth observation and geoinformation,* vol. 68, pp. 157-167, 2018.

[5] M. Dalponte, H. O. Ørka, L. T. Ene, T. Gobakken, and E. Næsset, "Tree crown delineation and tree species classification in boreal forests using hyperspectral and ALS data," *Remote sensing of environment,* vol. 140, pp. 306-317, 2014.

[6] A. Harikumar, C. Paris, F. Bovolo, and L. Bruzzone, "A Crown Quantization-Based Approach to Tree-Species Classification Using High-Density Airborne Laser Scanning Data," *IEEE Transactions on Geoscience and Remote Sensing,* 2020.

[7] I. Arenas-Corraliza, A. Nieto, and G. Moreno, "Automatic mapping of tree crowns in scattered-tree woodlands using low-density LiDAR data and infrared imagery," *Agroforestry Systems,* vol. 94, pp. 1989-2002, 2020.

[8] L. Fragoso-Campón, E. Quirós, J. Mora, J. A. Gutiérrez Gallego, and P. Durán-Barroso, "Overstory-understory land cover mapping at the watershed scale: accuracy enhancement by multitemporal remote sensing analysis and LiDAR," *Environmental Science and Pollution Research,* vol. 27, pp. 75-88, 2020/01/01 2020.

[9] A. Neuenschwander, E. Guenther, J. C. White, L. Duncanson, and P. Montesano, "Validation of ICESat-2 terrain and canopy heights in boreal forests," *Remote Sensing of Environment,* vol. 251, p. 112110, 2020.

[10] L. L. Narine, S. Popescu, A. Neuenschwander, T. Zhou, S. Srinivasan, and K. Harbeck, "Estimating aboveground biomass and forest canopy cover with simulated ICESat-2 data," *Remote Sensing of Environment,* vol. 224, pp. 1-11, 2019.

[11] W. Li, Z. Niu, R. Shang, Y. Qin, L. Wang, and H. Chen, "High-resolution mapping of forest canopy height using machine learning by coupling ICESat-2 LiDAR with Sentinel-1, Sentinel-2 and Landsat-8 data," *International Journal of Applied Earth Observation and Geoinformation,* vol. 92, p. 102163, 2020.

[12] F. D. Schneider, A. A. Ferraz, S. Hancock, L. I. Duncanson, R. O. Dubayah, R. P. Pavlick*, et al.*, "Towards mapping the diversity of canopy structure from space with GEDI," *Environmental Research Letters,* 2020.

[13] R. Dubayah, J. B. Blair, S. Goetz, L. Fatoyinbo, M. Hansen, S. Healey*, et al.*, "The Global Ecosystem Dynamics Investigation: High-resolution laser ranging of the Earth’s forests and topography," *Science of Remote Sensing,* vol. 1, p. 100002, 2020.

[14] L. Duncanson, A. Neuenschwander, S. Hancock, N. Thomas, T. Fatoyinbo, M. Simard*, et al.*, "Biomass estimation from simulated GEDI, ICESat-2 and NISAR across environmental gradients in Sonoma County, California," *Remote Sensing of Environment,* vol. 242, p. 111779, 2020.

[15] N. Sanchez-Lopez, L. Boschetti, A. T. Hudak, S. Hancock, and L. I. Duncanson, "Estimating Time Since the Last Stand-Replacing Disturbance (TSD) from Spaceborne Simulated GEDI Data: A Feasibility Study," *Remote Sensing,* vol. 12, p. 3506, 2020.

[16] W. Qi, S. Saarela, J. Armston, G. Ståhl, and R. Dubayah, "Forest biomass estimation over three distinct forest types using TanDEM-X InSAR data and simulated GEDI lidar data," *Remote Sensing of Environment,* vol. 232, p. 111283, 2019.

[17] W. Qi, S.-K. Lee, S. Hancock, S. Luthcke, H. Tang, J. Armston, *et al.*, "Improved forest height estimation by fusion of simulated GEDI Lidar data and TanDEM-X InSAR data," *Remote Sensing of Environment,* vol. 221, pp. 621-634, 2019.

[18] S. M. Marselis, H. Tang, J. Armston, K. Abernethy, A. Alonso, N. Barbier, *et al.*, "Exploring the relation between remotely sensed vertical canopy structure and tree species diversity in Gabon," *Environmental Research Letters,* vol. 14, p. 094013, 2019.

[19] P. B. Boucher, S. Hancock, D. A. Orwig, L. Duncanson, J. Armston, H. Tang, *et al.*, "Detecting Change in Forest Structure with Simulated GEDI Lidar Waveforms: A Case Study of the Hemlock Woolly Adelgid (HWA; Adelges tsugae) Infestation," *Remote Sensing,* vol. 12, p. 1304, 2020.

[20] I. Fayad, N. Baghdadi, J. S. Bailly, F. Frappart, and M. Zribi, "Analysis of GEDI Elevation Data Accuracy for Inland Waterbodies Altimetry," *Remote Sensing,* vol. 12, p. 2714, 2020.

[21] G. V. Laurin, F. Del Frate, L. Pasolli, and C. Notarnicola, "Forest/vegetation types discrimination in an alpine area using RADARSAT2 and ALOS PALSAR polarimetric data and Neural Networks," in *2012 IEEE International Geoscience and Remote Sensing Symposium (IGARSS)*, Munich (Germany), 2012, pp. 5340-5343.

[22] C. Wecklich, M. Martone, P. Rizzoli, J.-L. Bueso-Bello, C. Gonzalez, and G. Krieger, "Production of a global forest/non-forest map utilizing TanDEM-X interferometric SAR data," in *2017 IEEE International Geoscience and Remote Sensing Symposium (IGARSS)*, Texas (USA), 2017, pp. 751-754.

[23] C. N. Koyama, M. Watanabe, M. Hayashi, T. Ogawa, and M. Shimada, "Mapping the spatial-temporal variability of tropical forests by ALOS-2 L-band SAR big data analysis," *Remote Sensing of Environment,* vol. 233, p. 111372, 2019.

[24] M. Martone, P. Rizzoli, C. Wecklich, C. González, J.-L. Bueso-Bello, P. Valdo, *et al.*, "The global forest/non-forest map from TanDEM-X interferometric SAR data," *Remote sensing of environment,* vol. 205, pp. 352-373, 2018.

[25] A. P. Nicolau, A. Flores-Anderson, R. Griffin, K. Herndon, and F. J. Meyer, "Assessing SAR C-band data to effectively distinguish modified land uses in a heavily disturbed Amazon forest," *International Journal of Applied Earth Observation and Geoinformation,* vol. 94, p. 102214, 2020.

[26] A. Toraño Caicoya, F. Kugler, M. Pardini, I. Hajnsek, and K. Papathanassiou, "Vertical forest structure characterization for the estimation of above ground biomass: First experimental results using SAR vertical reflectivity profiles," in *2014 IEEE International Geoscience and Remote Sensing Symposium (IGARSS)*, Québec (Canada), 2014, pp. 1045-1048.

[27] A. Kumar, B. Kishore, P. Saikia, J. Deka, S. Bharali, L. Singha, *et al.*, "Tree diversity assessment and above ground forests biomass estimation using SAR remote sensing: A case study of higher altitude vegetation of North-East Himalayas, India," *Physics and Chemistry of the Earth, Parts A/B/C,* vol. 111, pp. 53-64, 2019.

[28] Z. Liao, B. He, and X. Quan, "Potential of texture from SAR tomographic images for forest aboveground biomass estimation," *International Journal of Applied Earth Observation and Geoinformation,* vol. 88, p. 102049, 2020.

[29] Y. Liu, W. Gong, Y. Xing, X. Hu, and J. Gong, "Estimation of the forest stand mean height and aboveground biomass in Northeast China using SAR Sentinel-1B, multispectral Sentinel-2A, and DEM imagery," *ISPRS Journal of Photogrammetry and Remote Sensing,* vol. 151, pp. 277-289, 2019.

[30] A. L. Mitchell, A. Rosenqvist, and B. Mora, "Current remote sensing approaches to monitoring forest degradation in support of countries measurement, reporting and verification (MRV) systems for REDD+," *Carbon Balance and Management,* vol. 12, p. 9, 2017.

[31] J. Ruiz-Ramos, A. Marino, C. Boardman, and J. Suarez, "Continuous Forest Monitoring Using Cumulative Sums of Sentinel-1 Timeseries," *Remote Sensing,* vol. 12, p. 3061, 2020.

[32] X. Wang, Y. Zhang, P. M. Atkinson, and H. Yao, "Predicting soil organic carbon content in Spain by combining Landsat TM and ALOS PALSAR images," *International Journal of Applied Earth Observation and Geoinformation,* vol. 92, p. 102182, 2020.

[33] B. O. Tagnon, V. T. Assoma, J. M. O. Mangoua, A. G. Douagui, F. K. Kouamé, and I. Savané, "Contribution of SAR/RADARSAT-1 and ASAR/ENVISAT images to geological structural mapping and assessment of lineaments density in Divo-Oume area (Côte d'Ivoire)," *The Egyptian Journal of Remote Sensing and Space Science,* vol. 23, pp. 231-241, 2018.

[34] A. Mazza, F. Sica, P. Rizzoli, and G. Scarpa, "TanDEM-X Forest Mapping Using Convolutional Neural Networks," *Remote Sensing,* vol. 11, p. 2980, 2019.

[35] B. Wessel, M. Huber, C. Wohlfart, U. Marschalk, D. Kosmann, and A. Roth, "Accuracy assessment of the global TanDEM-X Digital Elevation Model with GPS data," *ISPRS Journal of Photogrammetry and Remote Sensing,* vol. 139, pp. 171-182, 2018.

[36] L. Hawker, J. Neal, and P. Bates, "Accuracy assessment of the TanDEM-X 90 Digital Elevation Model for selected floodplain sites," *Remote Sensing of Environment,* vol. 232, p. 111319, 2019.

[37] V. Vanthof and R. Kelly, "Water storage estimation in ungauged small reservoirs with the TanDEM-X DEM and multi-source satellite observations," *Remote Sensing of Environment,* vol. 235, p. 111437, 2019.

[38] T. Chimitdorzhiev, A. Dmitriev, I. Kirbizhekova, A. Sherkhoeva, A. Baltukhaev, and P. Dagurov, "Possible Inaccuracy of Canopy Height Model Estimation for Dense and Sparse Boreal Forest with Tandem-X DSM and ALOS Palsar DEM Fusion, Case Study from the Baikal Lake Region, Russia," in *2019 IEEE International Geoscience and Remote Sensing Symposium (IGARSS)*, Yokohama, Japan, 2019, pp. 6693-6695.

[39] J. Armston, M. Hofton, and S. Luthcke, "GLOBAL Ecosystem Dynamics Investigation (GEDI) Level 02 User Guide," 2020.

[40] S. P. Healey, Z. Yang, N. Gorelick, and S. Ilyushchenko, "Highly Local Model Calibration with a New GEDI LiDAR Asset on Google Earth Engine Reduces Landsat Forest Height Signal Saturation," *Remote Sensing,* vol. 12, p. 2840, 2020.

[41] S.-K. Lee, T. Fatoyinbo, W. Qi, S. Hancock, J. Armston, and R. Dubayah, "GEDI and TanDEM-X fusion for 3D forest structure parameter retrieval," in *2018 IEEE International Geoscience and Remote Sensing Symposium (IGARSS)*, Valencia (Spain), 2018, pp. 380-382.

[42] C. Choi, M. Pardini, and K. Papathanassiou, "A Structure-Based Framework for the Combination of GEDI and Tandem-X Measurements Over Forest Scenarios," in *2019 IEEE International Geoscience and Remote Sensing Symposium (IGARSS)*, Yokohama, Japan, 2019, pp. 4488-4490.

[43] S.-K. Lee, T. Fatoyinbo, S. M. Marselis, W. Qi, S. Hancock, J. Armston, *et al.*, "Spaceborne Data Fusion for Large-Scale Forest Parameter Estimation: GEDI Lidar & Tandem-X INSAR Missions," in *2019 IEEE International Geoscience and Remote Sensing Symposium (IGARSS)*, Yokohama, Japan, 2019, pp. 4491-4494.

[44] W. Qi and R. O. Dubayah, "Forest structure modeling of a coniferous forest using TanDEM-X InSAR and simulated GEDI lidar data," in *2017 IEEE International Geoscience and Remote Sensing Symposium (IGARSS)*, Texas (USA), 2017, pp. 914-917.

[45] C. A. Silva, S. Saatchi, M. Garcia, N. Labriere, C. Klauberg, A. Ferraz, *et al.*, "Comparison of small-and large-footprint lidar characterization of tropical forest aboveground structure and biomass: A case study from central gabon," *IEEE Journal of Selected Topics in Applied Earth Observations and Remote Sensing,* vol. 11, pp. 3512-3526, 2018.

[46] S. Hancock, J. Armston, M. Hofton, X. Sun, H. Tang, L. I. Duncanson, *et al.*, "The GEDI simulator: A large-footprint waveform lidar simulator for calibration and validation of spaceborne missions," *Earth and Space Science,* vol. 6, pp. 294-310, 2019.

[47] A. Kato, H. Wakabayashi, M. Bradford, A. Hudak, L. M. Moskal, and M. Watanabe, "Accurate Ground Positioning Obtained From 3d Data Matching Between Airborne and Terrestrial Data for Ground Validation of Satellite Laser," in *2019 IEEE International Geoscience and Remote Sensing Symposium (IGARSS)*, Yokohama, Japan, 2019, pp. 6632-6635.

[48] S. Rivas-Martinez and S. Rivas-Saenz. (1996-2019, July). *Worldwide Bioclimatic Classification System*. Available: http://www.globalbioclimatics.org/form/tb_map/index.htm

[49] S. B. Luthcke, T. Rebold, T. Thomas, and T. Pennington, "Algorithm Theoretical Basis Document (ATBD) for GEDI Waveform Geolocation for L1 and L2 Products," 2019.

[50] W. Qi and R. O. Dubayah, "Combining Tandem-X InSAR and simulated GEDI lidar observations for forest structure mapping," *Remote Sensing of Environment,* vol. 187, pp. 253-266, 2016.
[51] Centro Nacional de Información Geográfica, "Especificaciones Técnicas del Plan Nacional de Ortofotografía Aérea," 2018.
[52] C. A. Silva, C. Hamamura, R. u. Valbuena, S. Hancock, A. Cardil, E. North Broadbent*, et al.*, "rGEDI: NASA's Global Ecosystem Dynamics Investigation (GEDI) Data Visualization and Processing," R package version 0.1.7 ed, 2020.
[53] R. J. McGaughey, "FUSION/LDV: Software for LIDAR data analysis and visualization," in *US Department of Agriculture, Forest Service, Pacific Northwest Research Station: Seattle, WA, USA* vol. 123, ed, 2009.
[54] R. J. McGaugheey, "Manual FUSION/LDV Software for LiDAR Data Analysis and Visualization," in *US Department of Agriculture, Forest Service*, 4.00 ed, 2020.
[55] R-Core-Team, "R: A language and environment for statistical computing," ed. Vienna (Austria): R Foundation for Statistical Computing, 2018.
[56] B. Wessel, T. Fritz, and G. Krieger, "TanDEM-X Ground Segment DEM Products Specification Document," 2016.
[57] C. Gonzalez and P. Rizzoli, "Landcover-dependent assessment of the relative height accuracy in TanDEM-X DEM products," *IEEE Geoscience and Remote Sensing Letters,* vol. 15, pp. 1892-1896, 2018.
[58] P. L. Patterson, S. P. Healey, G. Ståhl, S. Saarela, S. Holm, H.-E. Andersen*, et al.*, "Statistical properties of hybrid estimators proposed for GEDI—NASA's global ecosystem dynamics investigation," *Environmental Research Letters,* vol. 14, p. 065007, 2019.
[59] P. Potapov, X. Li, A. Hernandez-Serna, A. Tyukavina, M. C. Hansen, A. Kommareddy*, et al.*, "Mapping global forest canopy height through integration of GEDI and Landsat data," *Remote Sensing of Environment,* vol. 253, p. 112165, 2021.
[60] N. Lang, K. Schindler, and J. D. Wegner, "Country-wide high-resolution vegetation height mapping with Sentinel-2," *Remote Sensing of Environment,* vol. 233, p. 111347, 2019.

Elia Quirós was born in 1972 in Cáceres, Spain. In 1999, she received a technical engineering degree in topography from the University of Extremadura, Spain; in 2001, she received an engineering degree in geodesy and cartography from the University of Extremadura, Spain; and in 2009, she received a Ph.D. in geodesy and cartography from the University of Extremadura, Spain.
She is an associate professor of digital photogrammetry at the Polytechnic School and of remote sensing at the Faculty of Philosophy and Arts, both at the University of Extremadura. She is the author of three books and 22 articles. Her publications are related to remote sensing and spatial photogrammetry.
Quirós is a member of the Spanish Society of Remote Sensing, and she is the head of the SNAP (Sentinel Application Platform) working group.

María-Eugenia Polo was born in Mérida, Spain in 1968. In 1990, she received a technical engineering degree in surveying from the University of Extremadura, Spain; in 2000, she received an engineering degree in geodesy and cartography from the University of Jaén, Spain; and in 2008, she received a Ph.D. in geodesy and cartography from the University of Extremadura, Spain. She is an associate professor in geomatics and surveying with the University Centre of Mérida, University of Extremadura, Spain. She is the author of 20 articles. Her publications are related to the analysis of errors in spatial databases and geomatics applied to cultural heritage.

Laura Fragoso-Campón was born in 1978 in Cádiz, Spain. In 1999, she received a technical degree in civil engineering from the University of Extremadura, Spain; in 2003, she received a master's degree in civil engineering (Ingeniera de Caminos, Canales y Puertos) from the Polytechnic University of Madrid, Spain.
She is a Ph.D. student in remote sensing and hydrology at the Polytechnic School at the University of Extremadura. She is the author of 5 articles, and her publications are related to remote sensing and hydrology. She is a member of the Spanish Society of Remote Sensing.

3.6. Publicación N.º 6

Analysing the Capability of the Catchment's Spectral Signature for the Regionalization of Hydrological Parameters

SAR | HBV | HYDROLOGY | RANDOM FOREST | RUNOFF | SENTINEL

Laura Fragoso-Campón, Pablo Durán-Barroso, Elia Rosado

The Preprint has been posted on Authorea and it is available on the website: https://www.authorea.com

https://doi.org/10.22541/au.162100995.56312514/v1

Cite as: Laura Fragoso-Campón, Pablo Durán-Barroso, Elia Rosado. Analysing the Capability of the Catchment's Spectral Signature for the Regionalization of Hydrological Parameters. *Authorea*. May 14, 2021.

DOI: 10.22541/au.162100995.56312514/v1

Preprint	**Analysing the Capability of the Catchment's Spectral Signature for the Regionalization of Hydrological Parameters**				
Autores	**Fragoso-Campón, Laura** · Durán-Barroso, Pablo · Quirós, Elia				
Año	2021				
Revista	Preprint in Authorea				
eISSN:					
DOI	10.22541/au.162100995.56312514/v1				
Fuente de Impacto	Índice 5 años	Índice 2017	Categoría	Rank	Cuartil
WOS (JCR)	-	-	-	-	-
Aportación de la doctoranda:	Conceptualización, metodología, programas informáticos, análisis formal, investigación, redacción-borrador original, redacción-revisión y edición de la versión final.				

3.7. Publicación N.º 7

Publicación	**Clasificación supervisada de imágenes PNOA-NIR y fusión con datos LiDAR-PNOA como apoyo en el inventario forestal. Caso de estudio: Dehesas**				
Autores	**Fragoso-Campón, Laura** · Quirós, Elia · Gutiérrez Gallego, José Antonio				
Revista	Cuadernos de la Sociedad Española de Ciencias Forestales (2019)				
eISSN	2386-8368				
DOI	10.31167/csecfv0i45.19882				
Fuente de Impacto	Índice 5 años	Índice 2019	Categoría	Rank	Cuartil
WOS (JCR)	-	-	-	-	-
Aportación de la doctoranda:	Conceptualización, metodología, programas informáticos, análisis formal, investigación, redacción-borrador original, redacción-revisión y edición de la versión final.				

Acceso abierto disponible en:

http://secforestales.org/publicaciones/index.php/cuadernos_secf/article/view/19882

Cuad. Soc. Esp. Cienc. For. 45(3): 77-96 (2019)
Doi: https://doi.org/10.31167/csecfv0i45.19882
Cuadernos de la Sociedad Española de Ciencias Forestales
Acceso abierto disponible en http://secforestales.org/publicaciones/index.php/cuadernossecf/index

Clasificación supervisada de imágenes PNOA-NIR y fusión con datos LiDAR-PNOA como apoyo en el inventario forestal. Caso de estudio: Dehesas

Supervised classification of PNOA-NIR images and datafusion with LiDAR-PNOA as support in a forest inventory: Case of study: Tree-grass environment "Dehesas"

Fragoso-Campón, L.[*1]; Quirós, E.[1]; Gutiérrez Gallego, J.A.[1]

[1]*Departamento de Expresión Gráfica, Universidad de Extremadura, Escuela Politécnica, Avda. de la Universidad s/n, 10003 Cáceres*

Autor para correspondencia: laurafragoso@unex.es

Resumen

La estimación de las métricas dasométricas como apoyo en un inventario forestal se puede abordar mediante la aplicación de distintas tecnologías y, si bien el muestreo de campo es la técnica más extendida, la aparición y desarrollo de las técnicas de teledetección aumentan las posibilidades de actuación en este ámbito. Estas nuevas técnicas de teledetección permiten minimizar los costes tanto económicos como en tiempo de la adquisición de datos sin menosprecio de la exactitud de las mediciones realizadas. En este sentido, las ortofotos del PNOA-NIR, que incluyen la información espectral del infrarrojo cercano, permiten obtener distintos índices de vegetación y suelo, aportando información valiosa en el análisis de la vegetación. En este trabajo se realiza una clasificación supervisada de las imágenes PNOA-NIR para, junto con los datos LiDAR-PNOA, determinar mediciones dendométricas en dehesas (área de copa, diámetro de copa y altura máxima de arbolado) y otros parámetros relacionados con la espesura (fracción de cabida cubierta y densidad). La metodología se plantea mediante la aplicación exclusivamente de software de código abierto. A través de los resultados obtenidos es posible delimitar de forma detallada la estructura de la copa, así como la reducción de la incertidumbre en las zonas de sombra del arbolado. La evaluación del clasificador empleado, Random Forest, alcanza un porcentaje de predicciones correctas del 96.72% con una confianza media en la clasificación de los píxeles de arbolado del 93%. Por tanto, el método propuesto resulta adecuado para su aplicación en dehesas y otras masas abiertas sin tangencia de copas.

Palabras clave: dasometría, dendometría, QGIS, SNAP (Sentinel Application Platform), Random Forest.

Abstract

Obtaining dasometric attributes as support in a forest inventory can be addressed through the application of different technologies and, although field sampling is the most widespread technique, the current development of remote sensing techniques offer new opportunities. These new techniques make it possible to minimize both economic and time-related costs of acquiring data without disregarding the accuracy of the measurements made. In this sense, the orthophotos of the PNOA-NIR, which include near infrared spectral information, allow us to obtain different indices of vegetation and soil, providing valuable information in the analysis of the vegetation. In this work a supervised classification of the PNOA-NIR images is carried out and a data fusion with the LiDAR-PNOA data is made, to obtain dendometric measurements on tree-grass environments *(dehesas)* (crown area, crown diameter and maximum tree height) and other parameters related to the canopy spatial distribution (tree canopy cover factor and density). The methodology is based on the application of open source software exclusively. The obtained results delineate the structure of the crown in detail, reducing the uncertainty of the crown perimeter in shaded areas The evaluation of the classifier used, Random Forest (RF), reaches a percentage of correct predictions of 96.72% and an average confidence when classifying tree pixels of 93%. Therefore, the proposed method is suitable for application in tree-grass environments and other forest areas without tree crown tangency.

Keywords: dasometry, dendrometry, SNAP (Sentinel Application Platform), Random Forest, QGIS.

1. Introducción

La estimación de las métricas dasométricas en un inventario forestal se puede abordar mediante la aplicación de distintas tecnologías, en concreto, para la medición de árboles y masas forestales puede llevarse a cabo mediante la técnica tradicional de muestreo en campo, así como con técnicas fotogramétricas y mediante el uso de la teledetección. Si bien el muestreo de campo es la técnica más extendida, la aparición y el desarrollo actual de las técnicas de teledetección ofrecen nuevas oportunidades (Ortiz-Reyes *et al.*, 2015).

Los datos de muestreo en campo son en muchos casos la única fuente de datos de las investigaciones (Diallo *et al.*, 2013), pero también se utilizan como muestras de entrenamiento y validación en caso de aplicación de otras tecnologías de medición indirecta a través de métodos estadísticos de regresión (Uzquiano Pérez, 2014; Ortiz-Reyes *et al.*, 2015; Guerra-Hernández *et al.*, 2016). Entre las técnicas de teledetección, existen distintas tecnologías que principalmente se han centrado en estudiar áreas de tamaño reducido, como por técnicas fotogramétricas (Panagiotidis *et al.*, 2017), con el LiDAR terrestre (Lin,Herold, 2016; López-Cortés *et al.*, 2019) y *small-foot print* LiDAR (Popescu *et al.*, 2004). Sin embargo, el uso del LiDAR aerotransportado a mayor escala (Popescu *et al.*, 2003; Koukoulas,Blackburn, 2005; Falkowski *et al.*, 2006) se ha convertido en los últimos años en una herramienta alternativa en mediciones de masas forestales (Uzquiano Pérez, 2014), que sirve de apoyo en posteriores análisis de regresión para la modelación de la relación entre variables dasométricas (Cancino, 2012; Navarro *et al.*, 2018), permitiendo obtener la estructura tridimensional y continua de la masa forestal útil para completar los trabajos de campo (Palop-Navarro *et al.*, 2016).

A la hora de plantear las mediciones dasométricas para un inventario forestal, entran en conflicto dos aspectos claves, por un lado, la exactitud de la información estructural detallada y, por otro, el coste económico y temporal que conlleva obtener esta información. La tendencia actual es la de minimizar los costes en tiempo y esfuerzo del trabajo de campo, pero sin menoscabar la calidad y exactitud de las mediciones. En este sentido, el uso tanto de información de acceso libre, así como su tratamiento posterior en software de código abierto (*open source*) permiten reducir los costes del inventario. En este sentido, España cuenta con la cobertura continua en todo el territorio del Plan Nacional de Ortofotografía Aérea (PNOA) que ofrece dos productos: imágenes orto rectificadas PNOA y nube de puntos LiDAR PNOA.

En primer lugar, imágenes orto-rectificadas se actualizan cada 2 o 3 años según las zonas y obtenidas como resultado del vuelo fotogramétrico realizado con una cámara digital multiespectral (Ministerio de Fomento, 2019). Estas imágenes están disponibles en dos formatos: PNOA-RGB, que incluyen la información espectral de las bandas visibles, y PNOA-NIR, que incluyen la información del infrarrojo cercano (NIR), rojo y verde. Los datos de la banda NIR complementan a los del espectro visible (RGB), y junto a ellos, permiten obtener distintos índices de vegetación y suelo, aportando información valiosa en el análisis de la vegetación.

Por otro lado, ofrece la cobertura de puntos 3D tomada con sensor LiDAR aerotransportado, cuya densidad de puntos es de 0.5 puntos·m^{-2} en la primera cobertura (vuelos de 2008 a 2010) y de 1 punto/m^{-2} en la segunda cobertura (vuelos de 2016 a 2018).

La aplicación de los datos LiDAR-PNOA en mediciones forestales ha sido ya validada en distintos trabajos. En González-Ferreiro *et al.* (2012) se aplica en el estudio del *P. radiata* en Galicia concluyendo que es una buena fuente de información para reducir costes en el inventario forestal. Otro trabajo como el de Sánchez Alberola *et al.* (2018) aplica los datos en el análisis de la especie *Pinus sylvestris* L. y concluye igualmente que se consiguieron estimar con buena precisión distintas variables forestales indicando que la tecnología LiDAR tiene un gran potencial en la realización de inventarios forestales incluso utilizando datos de baja densidad como es el caso del LiDAR-PNOA. En Palop-Navarro *et al.* (2016) se cuantifica los estados sucesionales avanzados en bosques caducifolios del norte de la Península Ibérica tomando como base el INF4 y el vuelo LiDAR-PNOA, concluyendo que la cobertura LiDAR de baja densidad de puntos, puede identificar estructuras forestales relacionadas con bosques caducifolios maduros. No obstante, la aplicación de los datos LiDAR PNOA con baja densidad de puntos en zonas forestales con arbolado disperso es complicada ya que dificulta la posibilidad de tener puntos suficientes para identificar de forma detallada el dosel arbóreo (Sánchez Alberola *et al.*, 2018). Este aspecto se agudiza aún más en las áreas de dehesas en las que la espesura del arbolado no supera el 60% (Pulido,Picardo, 2010).

Si bien el uso de los datos LiDAR-PNOA está más extendido, el uso de la ortofoto del PNOA no es tan común en la realización de inventarios forestales. En Lavado Contador *et al.* (2012) se analiza la dinámica temporal de la cobertura del arbolado en dehesas mediante clasificaciones de imágenes PNOA-RBG. En Borlaf-Mena *et al.* (2019) se utilizan de manera conjunta las imágenes PNOA-RGB y los datos LiDAR-PNOA para la extracción de la cobertura arbórea. En Navarro *et al.* (2018) se propone el uso de las imágenes PNOA-RGB para generar modelos digitales de la vegetación (MDV) por técnicas fotogramétricas, obteniendo buenos resultados siempre que exista un modelo digital del terreno (MDT) adecuado para poder normalizar las métricas de la vegetación.

En otros casos, el uso de las imágenes PNOA-RGB se reduce a la fotointerpretación de distintas coberturas o estimación de la fracción de cabida cubierta mediante el uso de platillas de densidad (Castillejo-González *et al.*, 2010).

Respecto al uso de las imágenes PNOA-NIR, hay una notable ausencia de trabajos que las utilicen siendo uno de los motivos que no sean de libre acceso y solo están disponibles previa solicitud al Instituto Geográfico Nacional u organismo autonómico competente en la materia. Sin embargo, en Fragoso-Campón, Laura, y Quirós (2019) se analiza cómo la información espectral de la imagen PNOA-NIR puede resultar muy útil para la caracterización de las masas forestales en paisajes de dehesa.

Ante esta situación, el objetivo general del presente trabajo es evaluar la aplicación de las imágenes PNOA-NIR junto con los datos LiDAR-PNOA en la deter-

minación de mediciones dendométricas en dehesas. Estas mediciones contemplan la extracción del perímetro de copa, medición del área y diámetro de copa, así como la estimación de la altura máxima de arbolado, y finalmente la aplicación en la determinación de otros parámetros dasométricos relacionados con la espesura de la masa como son la fracción de cabida cubierta y densidad del arbolado.

2. Material y métodos

2.1. Área de estudio

El análisis se ha llevado a cabo dentro del ámbito de la hoja del Mapa Topográfico Nacional a escala 1:50 000 (MTN50) nº 752 ubicada en la Comunidad Autónoma de Extremadura. En concreto, el área corresponde a la cuadrícula a escala 1:5000 con número 752-8-5 *(Fig. 1)*. El área se ubica dentro de la cuenca hidrográfica del río Aljucén caracterizada por un paisaje típico de la dehesa extremeña que, según la clasificación del Mapa Forestal de Extremadura, corresponde a encinar (*Quercus rotundifolia*).

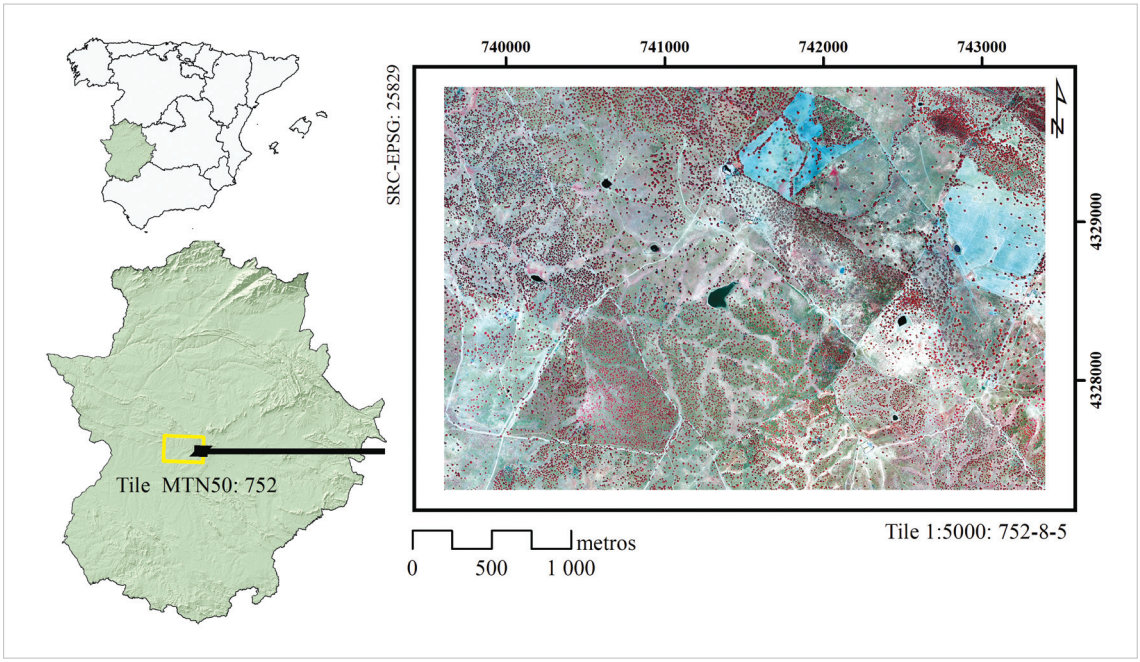

Figura 1. Delimitación de la zona de estudio. Hoja MTN50 nº 752-8-5.

2.2. Datos del Plan Nacional de Ortofotografía Aérea (PNOA)

La imagen utilizada en este trabajo corresponde al vuelo de 2016 del Plan Nacional de Ortofotografía Aérea (PNOA) que presenta una resolución espacial de

0.25 m. La imagen procede de un vuelo fotogramétrico realizado con una cámara digital de alta resolución, equipada con sensor pancromático y 4 sensores multiespectrales (Ministerio de Fomento, 2019). En concreto, se ha utilizado la ortofoto NIR que cuenta con las tres bandas correspondientes al infrarrojo cercano, rojo y verde, y que han sido facilitadas por el Centro de Información Cartográfica y Territorial de Extremadura (CICTEX). El vuelo disponible es de la época estival (junio de 2016) coincidiendo con la fase fenológica de la vegetación dominante en la que se observa una mayor separabilidad espectral entre la copa de arbolado y los estratos inferiores (Fragoso-Campón, Laura *et al.*, 2019).

Los datos LiDAR en el área de estudio corresponden al vuelo disponible del 2010 y abarcan la extensión de seis cuadrículas (EXT 738-4328 EXT 738-4330, EXT 740-4328, EXT 740-43, EXT 742-4328, EXT 742-4330). La información se ha procesado con ayuda del software FUSION desarrollado por el *Forest Service* del *USDA* (McGaughey, 2009), generando como información final el MDV, en el que se representan las alturas de vegetación normalizadas con una resolución espacial de 1.5 m que es la mejor que se puede obtener considerando la baja densidad de puntos del vuelo LiDAR. Para ello, en primer lugar, se unieron todas las cuadrículas del vuelo LiDAR y, posteriormente, se eliminaron los registros atípicos y se extrajeron los retornos del suelo. Ésta es la nube de puntos que sirve para generar el MDT calculando la elevación de cada celda como promedio de la elevación de todos los puntos dentro de la celda. Posteriormente, se genera el MDV que representa la altura normalizada de la vegetación sobre el MDT.

2.3. Procesado de la imagen

La imagen se ha procesado con el programa *Sentinel Application Platform* (SNAP) desarrollado por la Agencia Europea Espacial (ESA) siguiendo la metodología expuesta en Fragoso-Campón, Laura, y Quirós (2019). La *Fig. 3* muestra esquemáticamente el flujo de trabajo propuesto para el procesado de la imagen.

La información espectral disponible en la imagen PNOA se reduce únicamente a las tres bandas del NIR, rojo, verde y para completar la información puramente espectral, se han calculado varios índices de vegetación que faciliten la discriminación del estrato arbóreo como el NDVI, SAVI y MSAVI2; los índices de suelo BI y CI, así como el índice de agua NDWI (ver formulación en *Tab. 1*).

El análisis de las coberturas se ha realizado mediante una clasificación supervisada aplicando el algoritmo Random Forest (Breiman, 2001). Para ello se han definido las áreas de interés de manera aleatoria en el área de estudio, identificando las coberturas mediante fotointerpretación sobre la imagen, y finalmente se han considerado cinco clases: arbolado, pastizal, suelo desnudo y/o impermeable, masas de agua y sombras. Las áreas de interés se disponen en bloques de celdas de $1m^2$ sobre las distintas coberturas, extrayendo de forma aleatoria el 75% para entrenamiento y el 25% para validación o evaluación de la exactitud.

Tabla 1. Formulación de los índices de vegetación y suelos empleados.

Índice	Ecuación
Vegetación	$NDVI = \frac{\text{nir} - \text{red}}{\text{nir} + \text{red}}$
	$SAVI = (1 + L) \cdot \frac{\text{nir} - \text{red}}{\text{nir} + \text{red} + L}$ **
	$MSAVI2 = \frac{1}{2} \cdot \left[(2 \cdot (\text{nir} + 1) - \sqrt{(2nir + 1)^2 - 8(nir - red)}\right]$
Suelo	$BI = \sqrt{\frac{\text{red}^2 + \text{green}^2}{2}}$
	$CI = \frac{\text{red} - \text{green}}{\text{red} + \text{green}}$
Agua	$NDWI = \frac{\text{green} - \text{nir}}{\text{green} + \text{nir}}$

* Formulación tradicional adaptada a las bandas de las imágenes. ** L=0,5

Fuente: Tabla 1 de Fragoso-Campón y Quirós (2019).

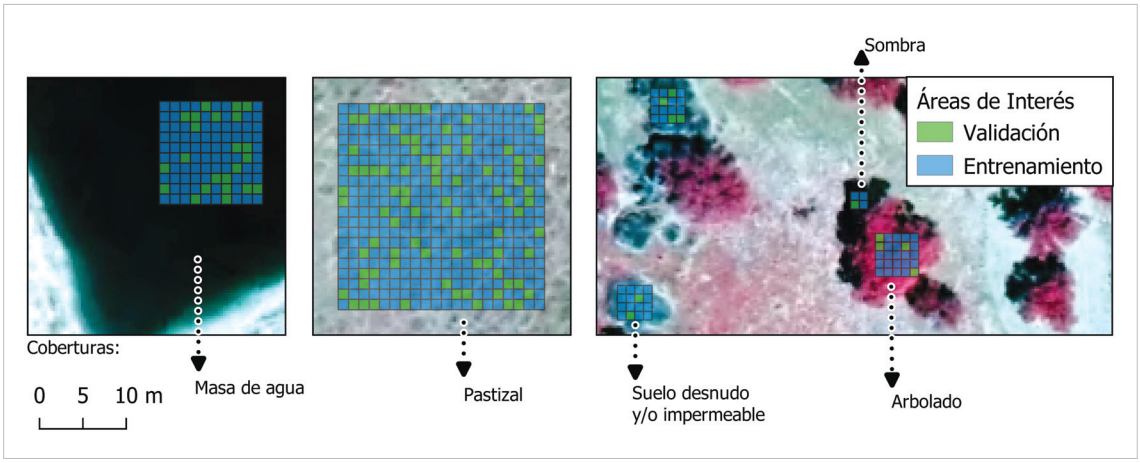

Figura 2. Áreas de entrenamiento y validación para evaluación de la exactitud.

La validación del mapa de coberturas obtenido se realiza mediante la validación cruzada del algoritmo de clasificación utilizado, así como con el mapa de confianza resultante en toda la extensión de la imagen obtenida.

2.4. Post-Proceso de los resultados

Una vez comprobada la validez del mapa ráster de la clasificación de coberturas, la siguiente fase se centra en obtener las variables dendométricas característi-

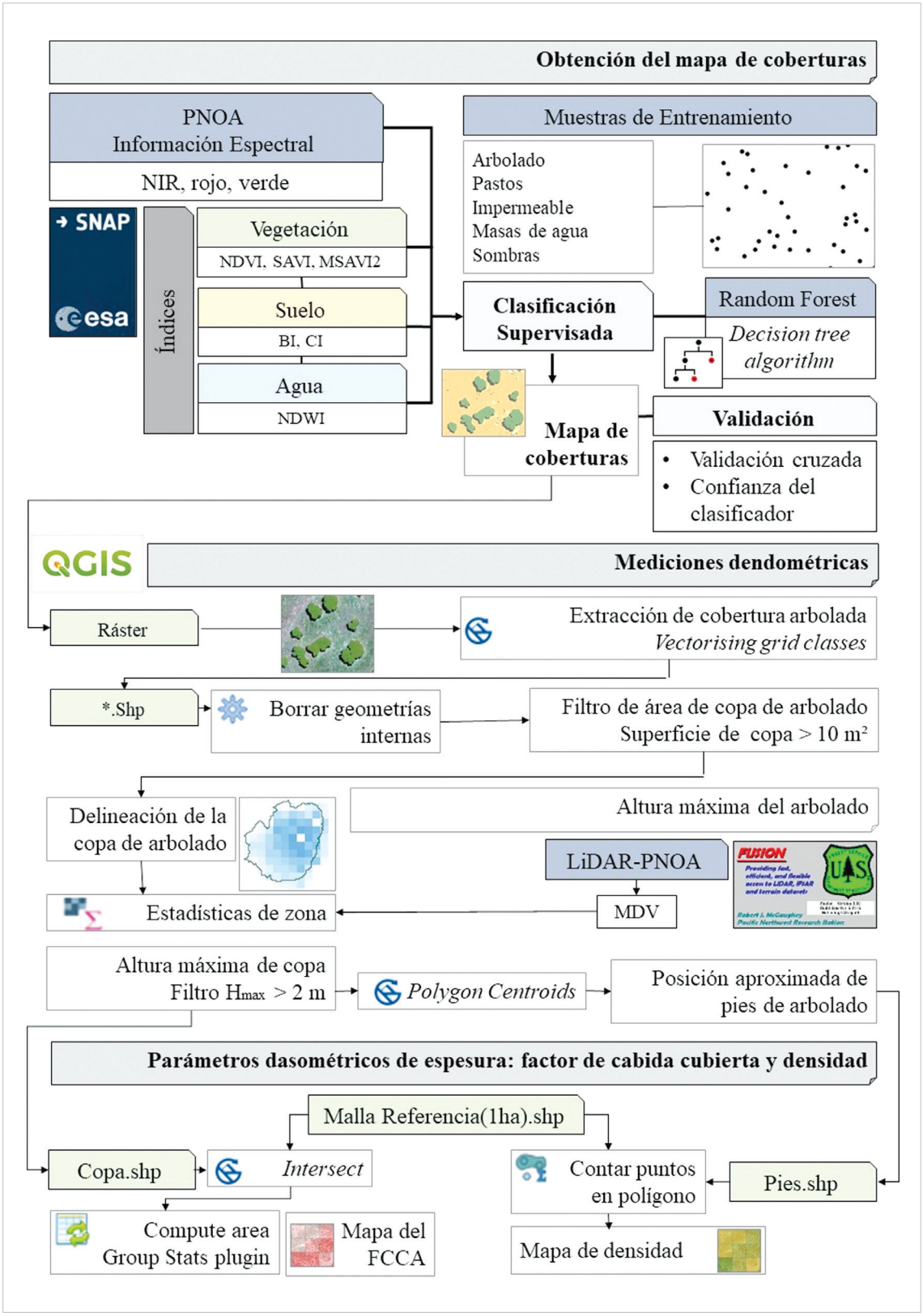

Figura 3. Metodología propuesta para el procesado de la imagen y el post-procesado de los resultados.

cas como son: una delineación detallada de la copa del arbolado, superficie de la copa, diámetro de copa, y estimación de la altura máxima de la vegetación según el vuelo LiDAR. Finalmente se obtienen los parámetros dasométricos relacionados con la espesura de la masa como la fracción de cabida cubierta arbórea (Fcca) y densidad. Para ello, se realiza el postproceso de la imagen en QGIS aplicando distintas herramientas y algoritmos (ver el flujo de trabajo esquemático en la *Fig. 3*).

En primer lugar, se vectoriza el mapa ráster de coberturas indicándole al algoritmo que vectorice únicamente la cobertura que queremos analizar que es la del arbolado. En segundo lugar, se depuran las geometrías eliminando huecos interiores dentro de la copa inferiores a 1 m^2, debidos a sombras superficiales por la rugosidad de la copa, y geometrías externas considerando un área mínima de copa de 10 m^2. Una vez depurado el archivo vectorial que representa el arbolado, se obtienen las estadísticas de zona en cada copa tomando como referencia el ráster del MDV, seleccionando como copa del arbolado aquellos elementos con una altura máxima superior a 2 m. Una vez depurado el archivo vectorial, se comprueba la exactitud de los resultados con la muestra independiente de evaluación obteniendo el porcentaje de acierto obtenido en la representación de las copas del arbolado. Finalmente, se obtiene la medición del área de copa y a partir de ella se estima su diámetro equivalente y la posición aproximada de los pies en el centro de gravedad de cada copa individual.

A partir de este punto, se define la malla (100 m x 100 m) en la que se van a calcular los estadísticos y posteriormente, se procede a obtener los parámetros de espesura de la masa forestal: el Fcca y la densidad (pies/ha) según se indica en la *Fig. 3*.

3. Resultados y discusión

Los resultados obtenidos en la clasificación supervisada de la imagen PNOA se muestran en las *Fig. 4* que representa la clasificación de las distintas coberturas en la zona de estudio.

La validación cruzada del algoritmo de clasificación Random Forest muestra un porcentaje de predicciones correctas dentro de la muestra de entrenamiento del 96.72% con un RMSE = 0.366 y Bias = –0.0049. Los resultados obtenidos para cada cobertura se muestran en la *Tab. 2*, alcanzándose exactitudes entre el 0.97 y 1.

Tabla 2. Resultados obtenidos en la validación cruzada de las muestras de entrenamiento.

Cobertura	Exactitud	VP	FP	VN	FN	Sensibilidad	Especificidad
Suelo desnudo - impermeable	100	996	5	3995	4	1.00	1.00
Pastizal	1.00	1000	0	4000	0	1.00	1.00
Sombras	0.97	925	86	3914	75	0.93	0.98
Arbolado	1.00	996	3	3997	4	1.00	1.00
Masas de agua	0.97	919	70	3930	81	0.92	0.98

Leyenda: VP — Verdadero Positivo VN — Verdadero Negativo FP — Falso Positivo FN — Falso negativo

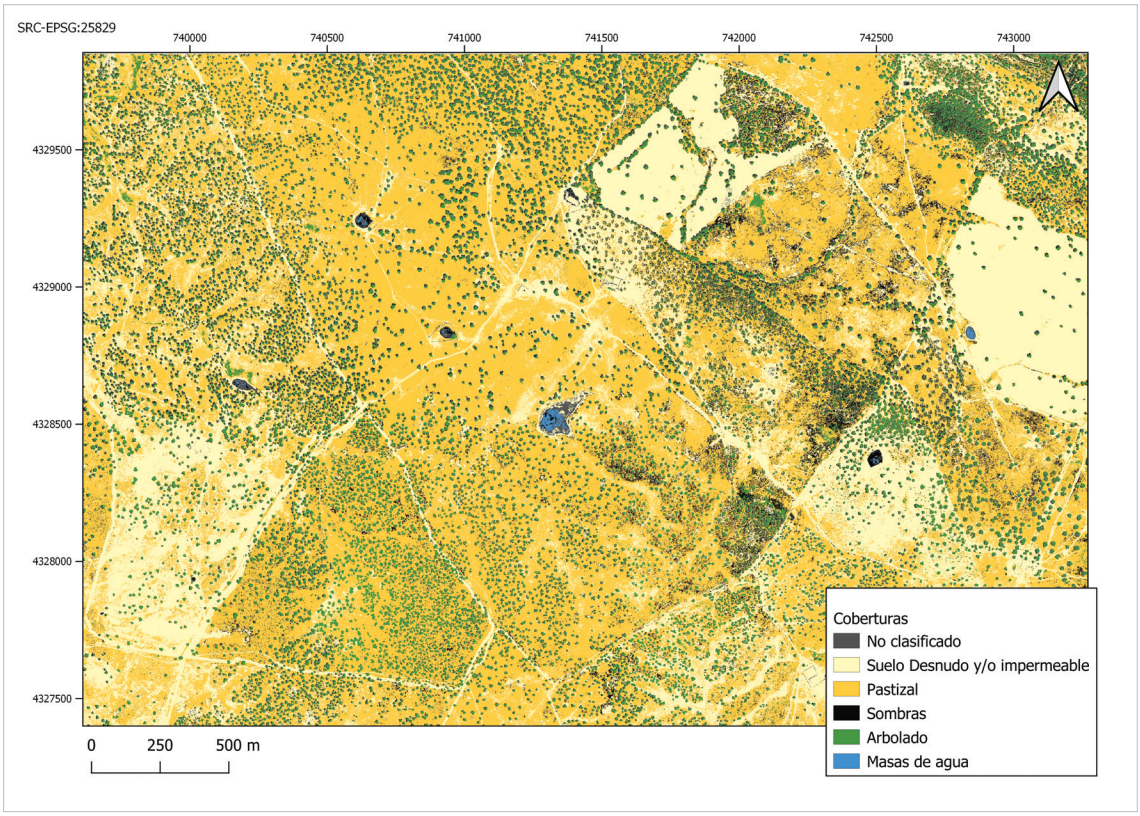

Figura 4. Mapa de coberturas.

Estos valores están en concordancia con los resultados obtenidos en Fragoso-Campón, Laura, y Quirós (2019) en otra área similar en la cuenca del río Tamuja en paisaje de dehesa.

Respecto a la confianza de la clasificación, la *Fig. 5* muestra la confianza del clasificador en la asignación de la cobertura en cada píxel y la *Tab. 3* muestra los valores medios de la confianza obtenidos en cada clase en toda el área de estudio.

Las coberturas de arbolado es la que se clasifica con mayor confianza, alcanzando un valor de confianza de 0.93 seguida de las coberturas de pastizal y suelo desnudo con un valor de 0.91. Las coberturas con peor valoración son las sombras y masas de agua, que son las que presentan mayor confusión entre ellas, observándose un número de errores por falsos positivos y falsos negativos más numerosos (ver *Tab. 2*).

De los predictores utilizados en la clasificación, son las bandas del rojo y verde, junto con los índices de suelo BI y CI, los que cuentan con mayor poder predictivo, seguidos del NDWI, la banda del NIR, y los índices de vegetación SAVI y NDVI.

El control de la exactitud obtenido en la representación de las copas del arbolado tomando como referencia la muestra de validación del arbolado muestra un porcentaje de acierto del 97.56%. Estos resultados están en concordancia con los

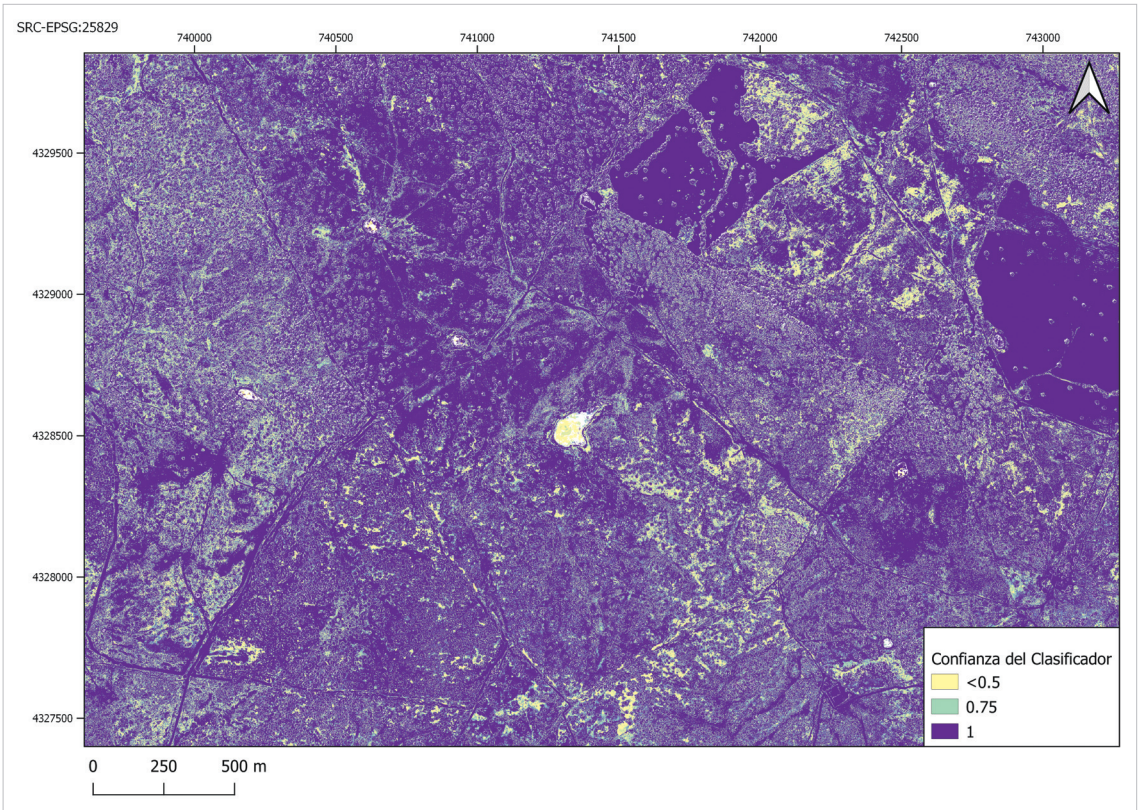

Figura 5. Confianza del clasificador.

Tabla 3. Confianza del clasificador Random Forest en la asignación de coberturas.

Cobertura	Valor medio	Desviación estándar
Suelo desnudo y/o impermeable	0.91	0.14
Pastizal	0.91	0.13
Sombras	0.79	0.20
Arbolado	0.93	0.14
Masas de agua	0.61	0.17

obtenidos en Castillejo-González *et al.* (2010) donde se analiza la capacidad de discriminación de copas de árboles en una dehesa a partir de imágenes QuickBird mediante técnicas de combinaciones de bandas (RGB, NIR y NDVI) y su posterior aplicación en el cálculo de la Fcca. En este trabajo se obtienen unas fiabilidades globales entre el 80 % y 98%. Así mismo, los resultados obtenidos mejoran los resultados obtenidos de Borlaf-Mena *et al.* (2019) para la clasificación realizada en base a las imágenes PNOA-RGB, resaltándose la influencia positiva que ejerce en la clasificación la disponibilidad de la banda NIR, y la utilización de índices derivados.

La evaluación de la exactitud y confianza obtenidas en la cobertura de arbolado ha permitido obtener con gran fiabilidad la delineación detallada de la copa. La *Fig. 6* muestra el resultado final obtenido y representándose el dosel arbóreo en distintos rangos de altura según el dato de la altura máxima de la copa obtenida del vuelo LiDAR-PNOA.

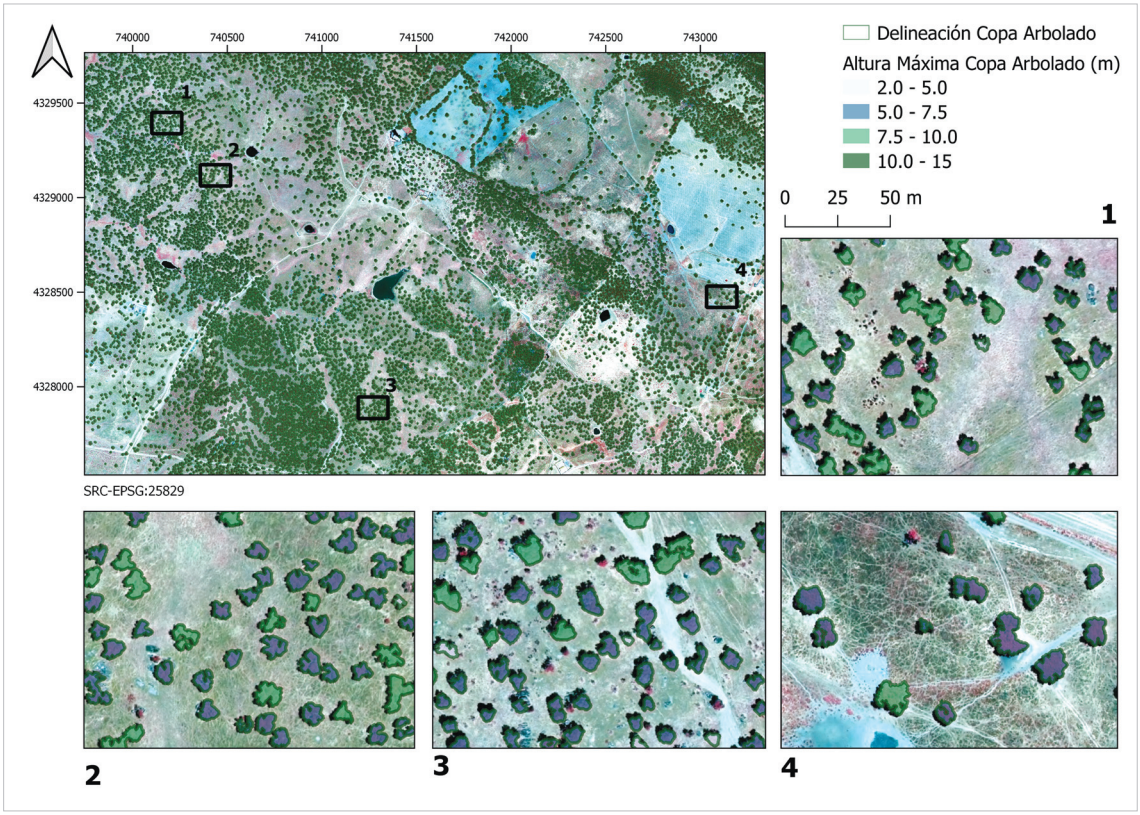

Figura 6. Mapa con la delineación detallada y altura máxima de la copa del arbolado.

El análisis visual de la delineación detallada de la copa del arbolado es más acertado que los resultados obtenidos en Cantero Fauquier *et al.* (2017) sobre todo la definición del perímetro y confusión en la zona de sombras. En Cantero Fauquier *et al.* (2017) se realiza una segmentación de la imagen PNOA-RGB y junto con datos derivados del modelo de altura procesados del LiDAR-PNOA, definen los contornos de copa. Si bien, no podemos cuantificar el margen de mejora, la clasificación supervisada de las imágenes PNOA-NIR junto con los predictores utilizados en el presente trabajo, como los índices de suelo y agua, mejoran la separabilidad de clases, permitiendo obtener mayor exactitud en la delineación del perímetro de copa, así como del diámetro de copa equivalente asignado a cada ejemplar de arbolado *(Fig. 7)*.

Se han extraído las mediciones de todos los ejemplares detectados en la zona de estudio procesándose posteriormente en R (R-Core-Team, 2018) para obtener las

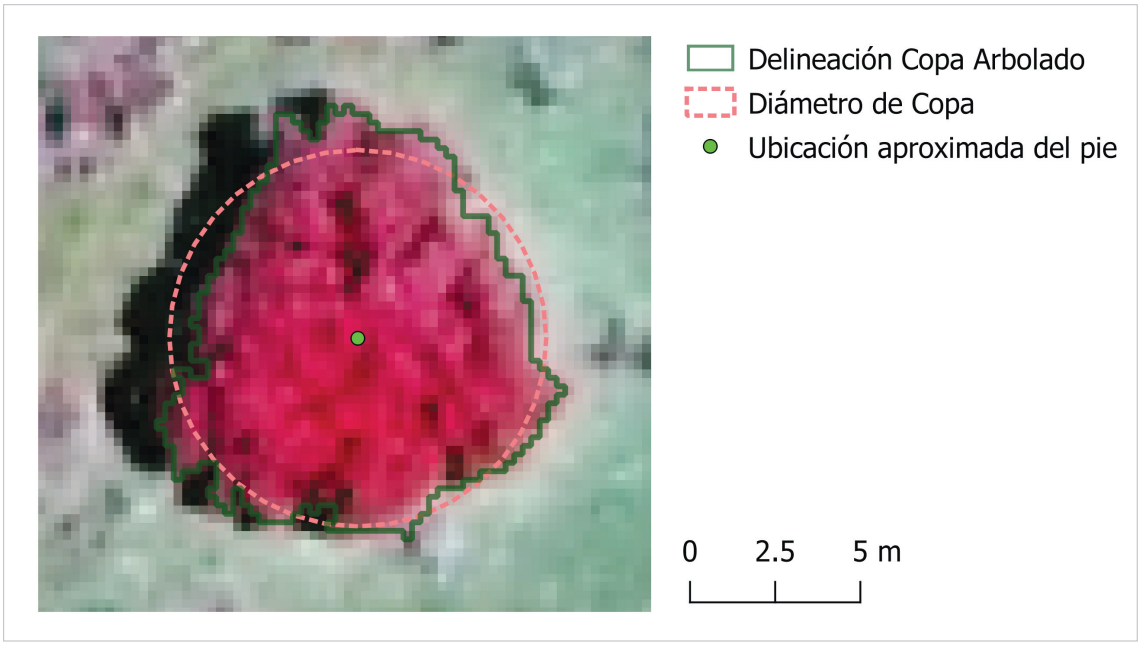

Figura 7. Detalle de la delineación detallada de la copa, el diámetro de copa equivalente y la ubicación aproximada del pie.

métricas representativas en el área estudiada. La *Tab. 4* muestra el resumen de las métricas obtenidas del área y diámetro de copa, así como de la altura máxima obtenida del vuelo LiDAR-PNOA.

Tabla 4. Resumen de métricas del arbolado.

Rango	Área de copa (m^2)	Diámetro de copa (m)	Altura Máxima (m)
Mínimo	6.19	2.81	2.00
1er cuartil	28.19	5.99	5.17
2º cuartil	46.88	7.73	6.21
3er cuartil	69.75	9.42	7.21
Máximo	123.69	12.55	12.40

En la *Fig. 8* se presenta la caracterización de las alturas del arbolado en cada uno de los segmentos de percentil descritos en la *Tab. 4*.

Por otro lado, la *Fig. 9* muestra la dispersión de la altura máxima de cada ejemplar y el diámetro equivalente de copa, así como los elipsoides de concentración para el 50% y 90% de los resultados, observándose que existe correlación positiva entre el tamaño de la copa y la altura máxima, presentando un coeficiente de correlación de Pearson de 0.55. Se observa por tanto una tendencia similar a lo señalado en Diallo *et al.* (2013). Esta tendencia, permitiría establecer modelos de predicción en toda el área de estudio, si se completara la información disponible con

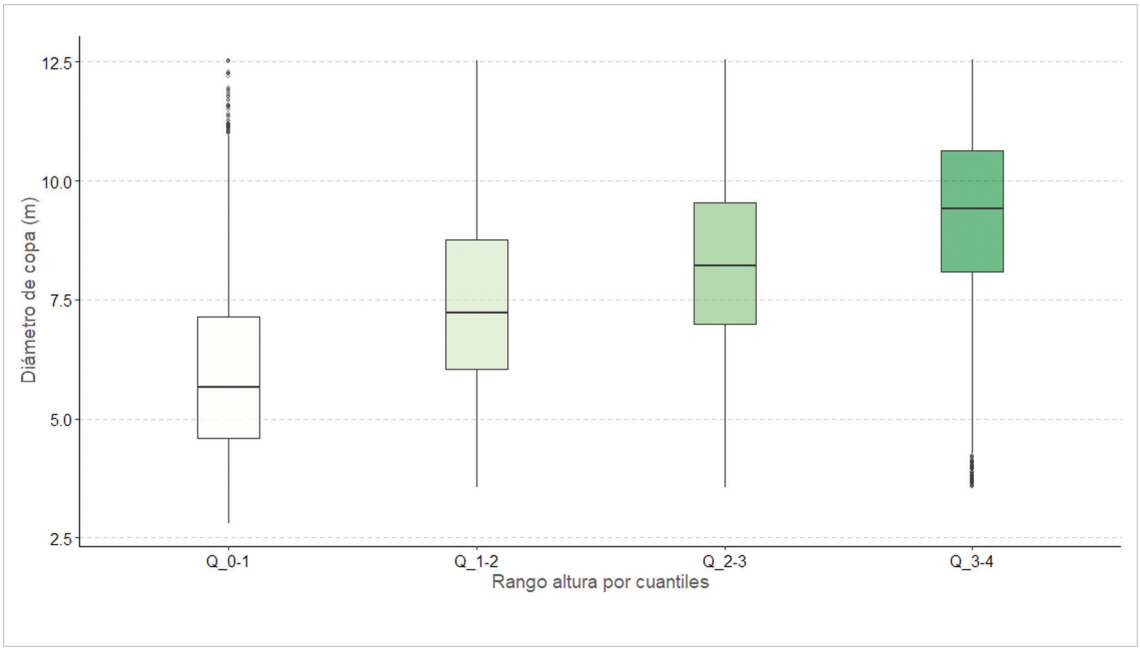

Figura 8. Distribución del diámetro de copas en cada rango de percentil de alturas.

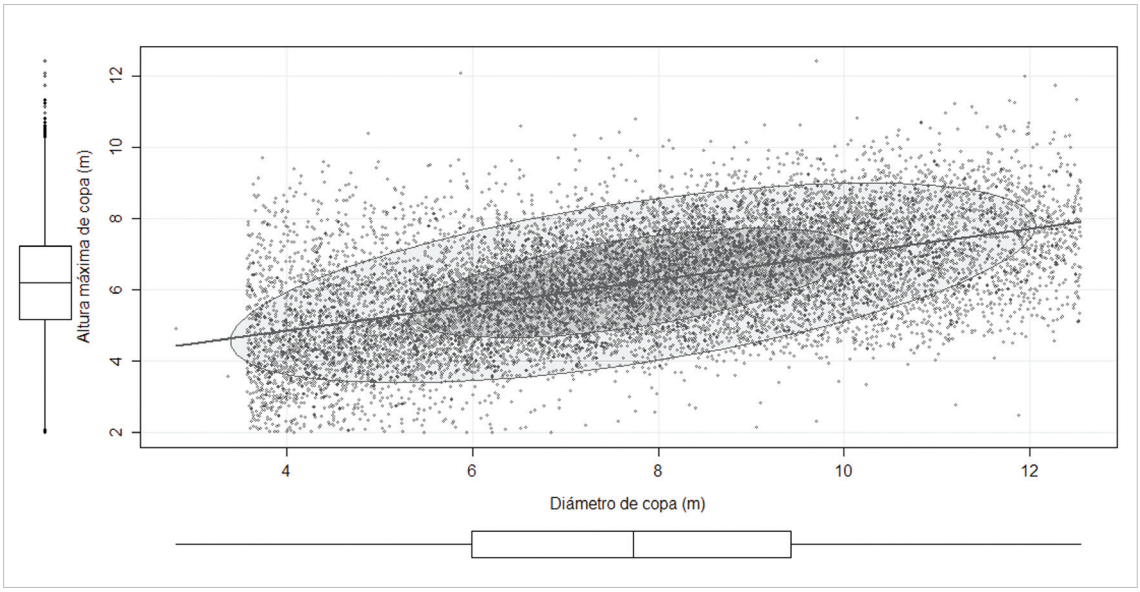

Figura 9. Diagrama de dispersión del diámetro de copa y la altura máxima de copa.

datos de campo considerando un muestreo representativo de otras variables dasométricas como el diámetro, área basimétrica, altura y volumen de copa o la estimación de la biomasa.

Por último, los resultados relacionados con la espesura se representan en la *Fig. 10* y la *Fig. 11* a través del mapa de la fracción de cabida cubierta y del mapa de densidad respectivamente.

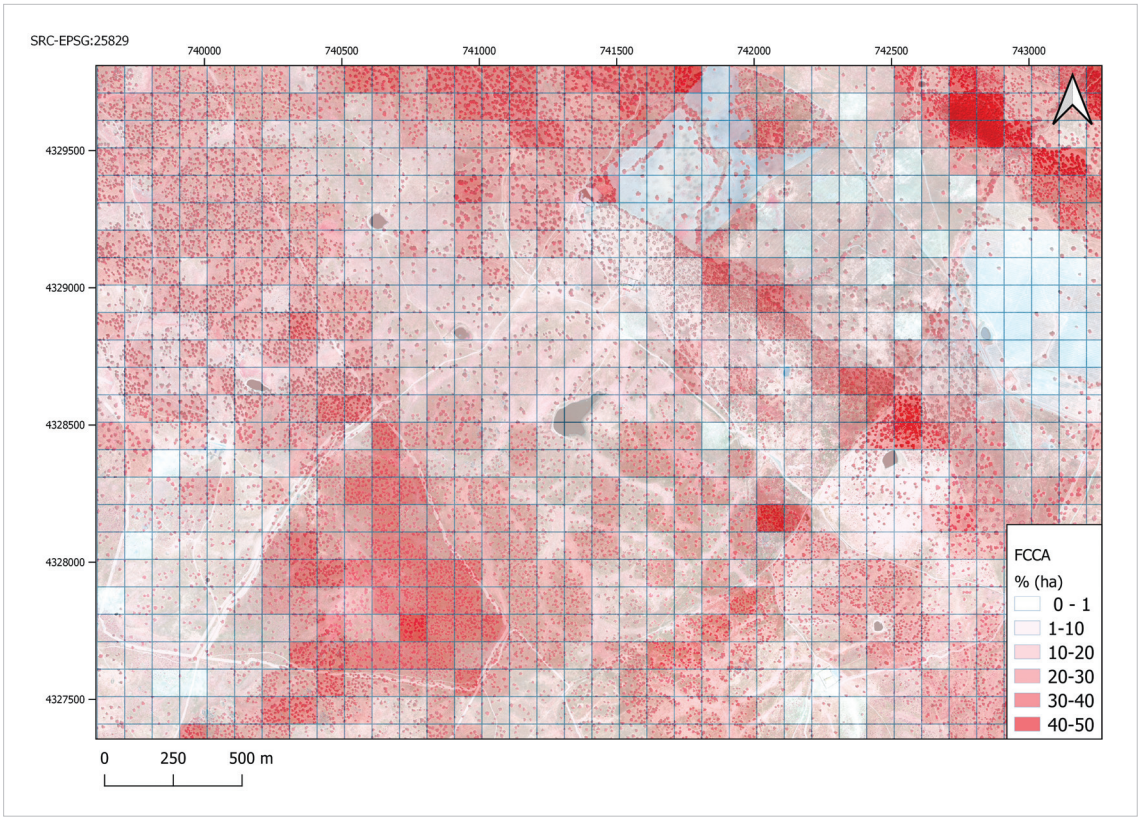

Figura 10. Mapa de la fracción de cabida cubierta arbórea (Fcca) por hectárea.

La mayor limitación de la metodología propuesta es la incertidumbre en la estimación de la densidad en las zonas en las que pueda existir tangencia de copas, sobre todo en las áreas con Fcca elevado. Al igual que se indica en Cantero Fauquier *et al.* (2017) la estimación de la densidad de pies y la identificación individual de las copas se complica en caso de tener alta cobertura y árboles con tangencia de copas, ya que una agrupación de distintos ejemplares estaría considerada como un único ejemplar y por tanto, la estimación de la densidad estaría infravalorada.

4. Conclusiones

En este trabajo se ha evaluado la aplicación de las imágenes PNOA-NIR junto con los datos LiDAR-PNOA en la determinación de mediciones dasométricas en dehesas. Se ha comprobado como la clasificación supervisada de las imágenes PNOA-NIR, basada en la información espectral y con ayuda de distintos índices de vegetación, suelo y agua derivados, permite la identificación detallada de cada copa individual del arbolado en zona de dehesa. La confianza de la clasificación supera el 93% lo que garantiza la exactitud de las mediciones dendométricas relacionadas con la superficie de copa de cada ejemplar. Así, ha sido posible obtener tanto la me-

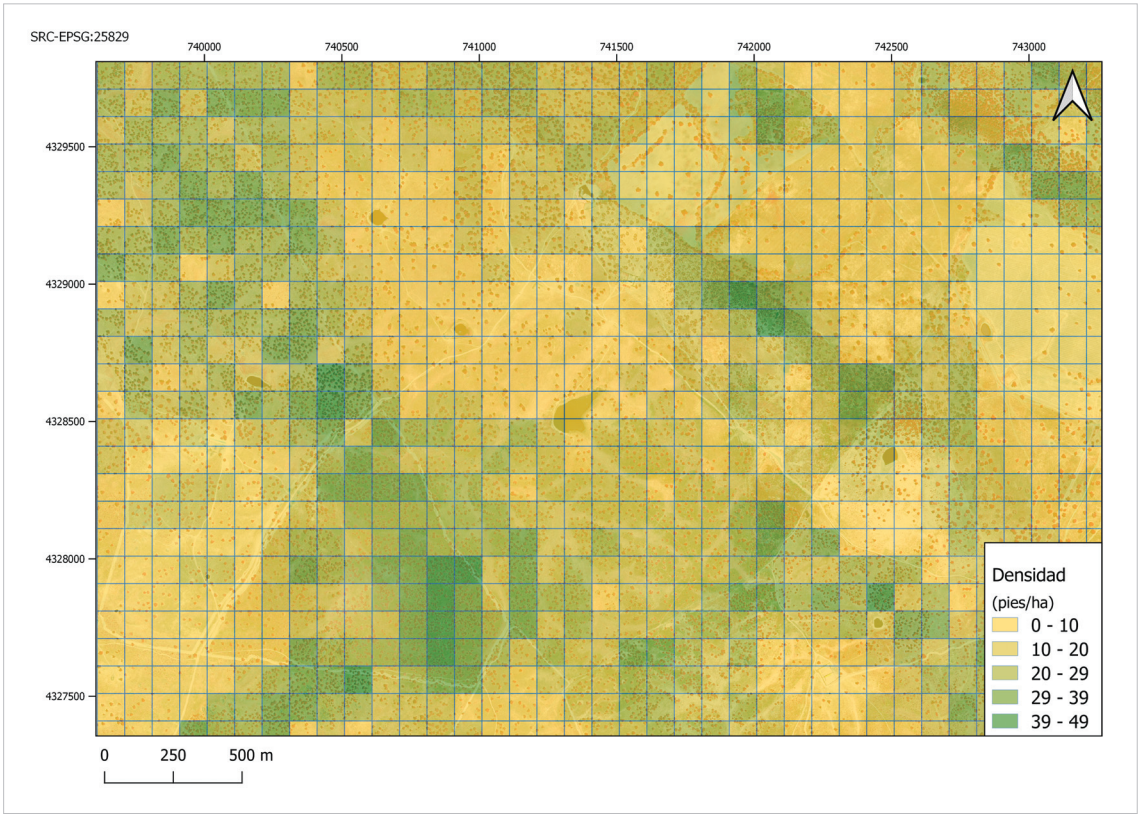

Figura 11. Mapa de la densidad del arbolado en pies por hectárea.

dición del área de copa y diámetro de copa, como otros parámetros dasométricos relacionados con la espesura de la masa como son la fracción de cabida cubierta y densidad del arbolado. Así mismo, la fusión de los resultados con la información derivada del vuelo LiDAR-PNOA ha permitido caracterizar la altura máxima de arbolado y estudiar la correlación existente con el resto de las variables en toda el área de estudio. Este proceso ha facilitado la caracterización de más de 13 000 ejemplares. Todo el desarrollo metodológico se ha elaborado mediante la aplicación exclusivamente de software de código abierto. La principal limitación de la metodología propuesta de cara a su aplicación en futuros trabajos es la incertidumbre en la estimación de la densidad en las zonas en las que pudiera existir tangencia de copas.

Agradecimientos

La presente investigación se ha realizado gracias a la financiación de la Universidad de Extremadura y el Fondo Social Europeo: Una manera de hacer Europa, mediante una Ayuda para la Financiación de Contratos Predoctorales para la Formación de Doctores en los Centros Públicos de I+D pertenecientes al Sistema Extremeño de Ciencia, Tecnología e Innovación (Expediente PD16018). La difusión de este trabajo en las Jornadas de "Retos y Aplicaciones de los Inventarios Forestales"

organizadas por la SECF ha sido posible también gracias a la ayuda del Fondo Europeo de Desarrollo Regional (FEDER) y Junta de Extremadura al grupo de investigación DESOSTE (GR18052). El CICTEX de la Junta de Extremadura ha proporcionado las imágenes del PNOA 2007 - CC-BY 4.0 scne.es.

5. Bibliografía

Borlaf-Mena, I.; Tanase, M.A.; Gómez-Sal, A.; 2019. Methods for tree cover extraction from high resolution orthophotos and airborne LiDAR scanning in Spanish dehesas. *Revista de Teledetección*, 53, 17-32. https://doi.org/10.4995/raet.2019.11320

Breiman, L.; 2001. Random forests. *Machine learning.* 45, 1, 5-32. https://doi.org/10.1023/A:1010933404324

Cancino, J.; 2012. *Dendrometría básica*: Universidad de Concepción. Facultad de Ciencias Forestales. Departamento Manejo de Bosques y Medio Ambiente.

Cantero Fauquier, F.; Tomé Morán, J.; Bravo Fernández, J.; Fernández-Landa, A.; 2017. Herramientas de localización de árboles individuales con el módulo de procesado de QGIS a partir de información LiDAR y ortofotografía aérea. In:SECF (ed.) 7º Congreso Forestal Español "Gestión del monte: servicios ambientales y bioeconomía". Plasencia, Cáceres (Spain).

Castillejo-González, I.L.; Medina Guerrero, J.; García-Ferrer Porras, A.; Mesas-Carrascosa, F.J.; Sánchez de la Orden, M.; 2010. Utilización de imágenes de satélite de alta resolución espacial en la determinación de la fracción de cabida cubierta en sistemas adehesados. In: Ojeda, J.; Pita, M.F.; Vallejo, I.; (ed.) XIV Congreso Nacional de Tecnologías de la Información Geográfica La información geográfica al servicio de los ciudadanos: de lo global a lo local. Sevilla (Spain).

Diallo, A.; Agbangba, E.C.; Ndiaye, O.; Guisse, A.; 2013. Ecological structure and prediction equations for estimating tree age, and dendometric parameters of Acacia senegal in the Senegalese semi-arid zone-Ferlo. *American Journal of Plant Sciences*. 4, 5, 1046. https://doi.org/10.4236/ajps.2013.45129

Falkowski, M.J.; Smith, A.M.; Hudak, A.T.; Gessler, P.E.; Vierling, L.A.; Crookston, N.L.; 2006. Automated estimation of individual conifer tree height and crown diameter via two-dimensional spatial wavelet analysis of lidar data. *Canadian Journal of Remote Sensing*. 32, 2, 153-161. https://doi.org/10.5589/m06-005

Fragoso-Campón, L.; Quirós, E.; 2019. Sentinel Toolbox Application (SNAP) aplicado a la clasificación supervisada de imágenes PNOA. In:UVA (ed.) XVIII Congreso de la Asociación Española de Teledetección: Hacia una visión global del cambio climático. Valladolid (España).

Fragoso-Campón, L.; Quirós, E.; Mora, J.; Gutiérrez Gallego, J.A.; Durán-Barroso, P.; 2019. Overstory-understory land cover mapping at the watershed scale: accuracy enhancement by multitemporal remote sensing analysis and LiDAR. *Environmental Science and Pollution Research*, 1-14. https://doi.org/10.1007/s11356-019-04520-8

González-Ferreiro, E.; Diéguez-Aranda, U.; Miranda, D.; 2012. Estimation of stand variables in Pinus radiata D. Don plantations using different LiDAR pulse densities. *Forestry.* 85, 2, 281-292. https://doi.org/10.1093/forestry/cps002

Guerra-Hernández, J.; Tomé, M.; González-Ferreiro, E.; 2016. Cartografía de variables dasométricas en bosques Mediterráneos mediante análisis de los umbrales de altura e inventario a nivel de masa con datos LiDAR de baja resolución. *Revista de Teledetección*. 46, 103-117. https://doi.org/10.4995/raet.2016.3980

Koukoulas, S.; Blackburn, G.A.; 2005. Mapping individual tree location, height and species in broadleaved deciduous forest using airborne LIDAR and multi-spectral remotely sensed data. *International Journal of Remote Sensing*. 26, 3, 431-455. https://doi.org/10.1080/0143116042000298289

Lavado Contador, J.F.; Jariego García, A.; Schnabel, S.; Gómez Gutiérrez, Á.; 2012. Análisis de la evolución histórica del arbolado de la dehesa mediante fotointerpretación y análisis OBIA. In: Martínez Vega, J.; Martín Isabel, P.; (ed.) Tecnologías de la información geográfica en el contexto del cambio global: XV Congreso Nacional de Tecnologías de Información Geográfica. Madrid (Spain).

Lin, Y.; Herold, M.; 2016. Tree species classification based on explicit tree structure feature parameters derived from static terrestrial laser scanning data. *Agricultural and Forest Meteorology*. 216, 105-114. https://doi.org/10.1016/j.agrformet.2015.10.008

López-Cortés, I.; Martí-Gavilá, J.; Estornell, J.; Fernández-Sarría, A.; 2019. Comparación de parámetros de olivos a partir de UAV y datos LiDAR aéreos. In:UVA (ed.) XVIII Congreso de la Asociación Española de Teledetección: Hacia una visión global del cambio climático. Valladolid (España).

McGaughey, R.J.; (2009). FUSION/LDV: Software for LIDAR data analysis and visualization.

Ministerio de Fomento, 2019. Plan Nacional de Observación del Territorio. Plan Nacional de Ortofotografía Aerea (PNOA). http://pnoa.ign.es/presentacion Accesed. 22 abril 2019.

Navarro, J.A.; Fernández-Landa, A.; Tomé, J.L.; Guillén-Climent, M.L.; Ojeda, J.C.; 2018. Testing the quality of forest variable estimation using dense image matching: a comparison with airborne laser scanning in a Mediterranean pine forest. *International Journal of Remote Sensing*. 39, 14, 4744-4760. https://doi.org/10.1080/01431161.2018.1471551

Ortiz-Reyes, A.D.; Valdez-Lazalde, J.R.; De-los-Santos-Posadas, H.M.; Ángeles-Pérez, G.; Paz-Pellat, F.; Martínez-Trinidad, T.; 2015. Inventario y cartografía de variables del bosque con datos derivados de LiDAR: comparación de métodos. *Madera y bosques*. 21, 3, 111-128. https://doi.org/10.21829/myb.2015.213461

Palop-Navarro, E.; Bañuelos, M.J.; Quevedo, M.; 2016. Combinando datos LiDAR e inventario forestal para identificar estados avanzadosde desarrollo en bosques caducifolios. *Revista Ecosistemas*. 25, 3, 35-42. https://doi.org/10.7818/ECOS.2016.25-3.04

Panagiotidis, D.; Abdollahnejad, A.; Surový, P.; Chiteculo, V.; 2017. Determining tree height and crown diameter from high-resolution UAV imagery. *International Journal of Remote Sensing*. 38, 8-10, 2392-2410. https://doi.org/10.1080/01431161.2016.1264028

Popescu, S.C.; Wynne, R.H.; Nelson, R.F.; 2003. Measuring individual tree crown diameter with lidar and assessing its influence on estimating forest volume and biomass. *Canadian Journal of Remote Sensing*. 29, 5, 564-577. https://doi.org/10.5589/m03-027

Popescu, S.C.; Wynne, R.H.; Scrivani, J.A.; 2004. Fusion of small-footprint lidar and multispectral data to estimate plot-level volume and biomass in deciduous and pine forests

in Virginia, USA. *Forest Science*. 50, 4, 551-565.

Pulido, F.; Picardo, A.; (2010). Libro verde de la dehesa. http://www.eweb.unex.es/eweb/accionporladehesa/documentos/libro_verde_dehesa.pdf

R-Core-Team. (2018). R: A language and environment for statistical computing. In R. F. f. S. Computing (Ed.). Vienna (Austria).

Sánchez Alberola, J.; Oliver, P.; Estornell, J.; Dopazo, C.; 2018. Estimación de variables forestales de Pinus sylvestris L. en el contexto de un inventario forestal aplicando tecnología lidar aeroportada. *GeoFocus*. *Revista Internacional de Ciencia y Tecnología de la Información Geográfica*, 21, 79-99. https://doi.org/10.21138/GF.509

Uzquiano Pérez, S.; 2014. Mediciones Dendrométricas y Dasométricas mediante Técnicas LiDAR y Fotograméticas. *Cuadernos de la Sociedad Española de Ciencias Forestales*. 40, 193-202. https://doi.org/10.31167/csef.v0i40.17360